9 NOVEMBER 1966

FINAL STUDY REPORT
(MAY THROUGH NOVEMBER 1966)

VOLUME I

BOOK 2

AN ADVANCED STUDY OF AN APPLICATION TECHNOLOGY SATELLITE (ATS-4) MISSION

NATIONAL AERONAUTICS AND SPACE ADMINISTRATION
GODDARD SPACE FLIGHT CENTER
GREENBELT, MARYLAND

FACILITY FORM 602
N67-24602 (ACCESSION NUMBER)
526 (PAGES)
CR-81767 (NASA CR OR TMX OR AD NUMBER)
(THRU)
1 (CODE)
31 (CATEGORY)

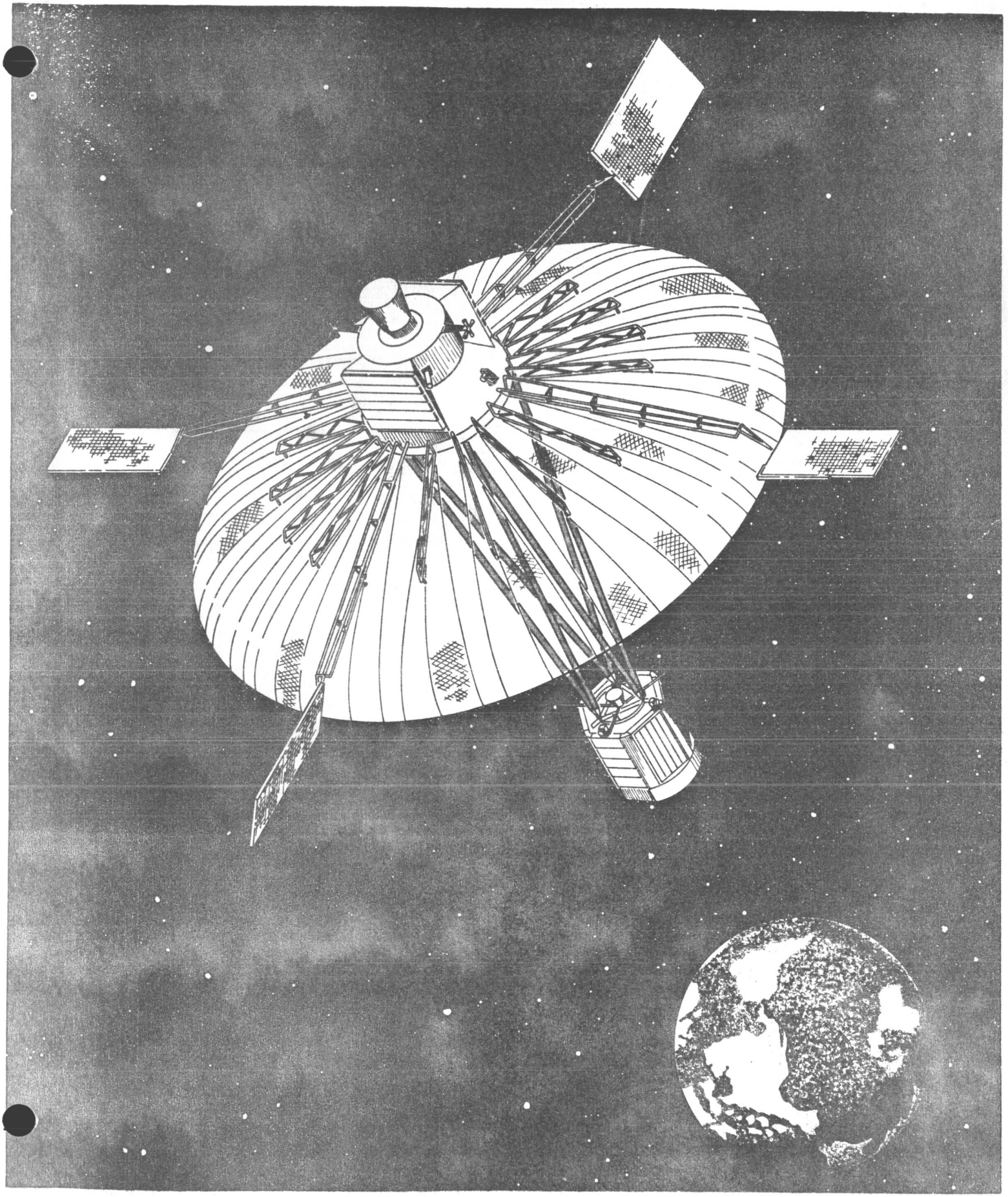


TABLE OF CONTENTS

VOLUME I
BOOK 1

Section			Page
1	INTRODUCTION		1-1
2	PROJECT OBJECTIVES		2-1
3	PROJECT FEASIBILITY		3-1
4	EXPERIMENT DESCRIPTION AND JUSTIFICATION		4-1
	4.1	General	4-1
	4.2	Parabolic Antenna Experiment	4-3
		4.2.1 Mechanical	4-3
		4.2.2 Electrical	4-4
	4.3	Orientation Control Experiment	4-11
	4.4	Phased Array Experiment	4-5
	4.5	Interferometer Experiment	4-6
	4.6	Secondary Experiments	4-7
5	SPACECRAFT DESCRIPTION		5-1
	5.1	Introduction	5.1-1
	5.2	Operational Concept	5.2-1
		5.2.1 Mission Requirements and Constraints	5.2-1
		5.2.2 Launch Vehicle and Apogee Motor Selection	5.2-2
		5.2.3 Mission Profile	5.2-3
		5.2.4 Payload Capability	5.2-5
	5.3	System Summary	5.3-1
		5.3.1 Configuration Description	5.3-1
		5.3.2 Subsystem Summary	5.3-9
		5.3.2.1 Power Subsystem	5.3-10
		5.3.2.2 Guidance and Control Subsystem	5.3-13
		5.3.2.3 TT&C Subsystem	5.3-15
		5.3.2.4 Experiments Subsystem	5.3-15
		5.3.2.5 Thermal Subsystem	5.3-16
		5.3.2.6 Module Interface	5.3-17
		5.3.3 System Performance	5.3-18
		5.3.3.1 Parabolic Antenna Experiment	5.3-18
		5.3.3.2 Orientation Control Experiment	5.3-19
		5.3.3.3 Phased Array and Interferometer	5.3-21
		5.3.3.4 Command and Telemetry Subsystem	5.3-24
		5.3.3.5 Power Subsystem Capability	5.3-25
		5.3.3.6 Spacecraft Weight and Balance	5.3-25

TABLE OF CONTENTS (Cont'd)

Section		Page
5.3.4	System Growth Capability	5.3-29
5.4	Parabolic Antenna	5.4-1
5.4.1	Selection of Antenna Concept	5.4-1
5.4.2	Description of Selected Design	5.4-2
5.4.2.1	Reflector and Feed	5.4-2
5.4.2.2	Packaging	5.4-7
5.4.2.3	Deployment	5.4-11
5.4.3	Antenna Performance	5.4-12
5.4.4	Reflector Design	5.4-15
5.4.4.1	Method of Construction	5.4-15
5.4.4.2	Material Selection	5.4-23
5.4.4.3	Structural Considerations	5.4-28
5.4.4.4	Stowage and Deployment Behavior	5.4-30
5.4.4.5	Performance in 1-g Environment	5.4-31
5.4.4.6	Spacecraft Interface	5.4-31
5.4.5	Deployment Mechanism Design	5.4-33
5.4.6	Feed Design	5.4-34
5.4.7	Thermal Design	5.4-36
5.5	Guidance and Control	5.5-1
5.5.1	Summary	5.5-1
5.5.2	Functional Description	5.5-9
5.5.2.1	Station Acquisition Modes	5.5-9
5.5.2.2	Orientation	5.5-25
5.5.2.3	Orientation Control Operational Modes	5.5-34
5.5.2.4	Station Capture and Station Change	5.5-42
5.5.2.5	Restabilization	5.5-45
5.5.3	Component Description	5.5-45
5.5.3.1	Spinup Motors	5.5-48
5.5.3.2	Coning Control Accelerometer	5.5-48
5.5.3.3	Precession Control Sun Sensor	5.5-49
5.5.3.4	Precession Control Rf POLANG Measurement	5.5-49
5.5.3.5	Station Acquisition Sensor Signal Processor	5.5-51
5.5.3.6	Station Acquisition and Despin Mass Expulsion Subsystem	5.5-51
5.5.3.7	Three Axis Gyro Package	5.5-58
5.5.3.8	Orientation Control Sun Sensors	5.5-60
5.5.3.9	Earth Sensor	5.5-64
5.5.3.10	Polaris Star Sensor	5.5-68
5.5.3.11	Orientation Control Sensor Signal Processor	5.5-70
5.5.3.12	Flywheel and Jet Controller	5.5-70
5.5.3.13	Mechanical Flywheel	5.5-70
5.5.3.14	Orientation Control and Stationkeeping Mass Expulsion Subsystem	5.5-73

TABLE OF CONTENTS (Cont'd)

Section		Page
	5.5.4 Command, Telemetry, and Programmer Interface	5.5-77
	5.5.4.1 Commands	5.5-77
	5.5.4.2 Telemetry	5.5-77
	5.5.4.3 Programmer	5.5-80
	5.5.5 Mounting and Field of View Interface	5.5-81
5.6	Experiment Equipment	5.6-1
	5.6.1 General	5.6-1
	5.6.2 Parabolic Antenna	5.6-2
	5.6.2.1 General	5.6-2
	5.6.2.2 Electronics and RF Equipment	5.6-4
	5.6.2.3 Geometric Instrumentation	5.6-11
	5.6.3 Orientation Control System	5.6-14
	5.6.4 Interferometer Experiment	5.6-15
	5.6.4.1 Introduction	5.6-15
	5.6.4.2 Basis of System Selection	5.6-16
	5.6.4.3 Interferometer Fundamentals	5.6-17
	5.6.4.4 Detailed Interferometer Design	5.6-21
	5.6.4.5 Weight and Power Estimates	5.6-26
	5.6.4.6 Thermal Effects	5.6-27
	5.6.5 Phase-Steered Array Antenna	5.6-28
5.7	Telemetry, Tracking and Command	5.7-1
	5.7.1 System Requirements	5.7-1
	5.7.2 Reference Design Summary	5.7-1
	5.7.3 Command Subsystem Operation	5.7-5
	5.7.3.1 Star Tracker Memory	5.7-11
	5.7.4 Telemetry Subsystem	5.7-12
	5.7.4.1 Telemetry Monitor Requiring Additional Circuitry	5.7-13
	5.7.5 Tracking Subsystem Operation	5.7-14
	5.7.6 TT&C Antennas	5.7-16
	5.7.6.1 Antenna Coverage	5.7-16
	5.7.6.2 Antenna Design	5.7-18
	5.7.7 Margin Calculations	5.7-22
	5.7.8 Implementation of Redundancy	5.7-27
	5.7.9 Power, Weight and Size Summary	5.7-27
5.8	Power	5.8-1
	5.8.1 Requirements	5.8-1
	5.8.1.1 Launch Load Profiles and Spacecraft Sun-orientation	5.8-1
	5.8.1.2 Orbit Load Profile and Spacecraft Sun-orientation	5.8-3
	5.8.2 Subsystem Description	5.8-6

TABLE OF CONTENTS (Cont'd)

Section			Page
	5.8.2.1	Subsystem Selection	5.8-6
	5.8.2.2	Subsystem Block Diagram	5.8-8
	5.8.2.3	General Operational Characteristics	5.8-10
	5.8.2.4	Solar Array Capability	5.8-11
	5.8.2.5	Battery Capability	5.8-20
	5.8.2.6	Subsystem Efficiency and Margins	5.8-21
	5.8.2.7	Operational Flexibility	5.8-21
	5.8.2.8	Growth Capability	5.8-22
5.8.3		Component Descriptions	5.8-22
	5.8.3.1	Solar Array	5.8-22
	5.8.3.2	Batteries	5.8-29
	5.8.3.3	Voltage Limiter	5.8-30
	5.8.3.4	Battery Charge Regulator	5.8-31
	5.8.3.5	PWM Regulator	5.8-31
	5.8.3.6	Inverter	5.8-32
	5.8.3.7	Power Control Unit	5.8-32
	5.8.3.8	Summary of Component Characteristics	5.8-32
5.9		Spacecraft Design	5.9-1
5.9.1		Introduction	5.9-1
5.9.2		Launch Phase and Orbital Constraints	5.9-2
	5.9.2.1	Launch Vehicle Constraints	5.9-2
	5.9.2.2	Coast Apogee Firing and Orbital Injection Constraints	5.9-10
	5.9.2.3	Orbital Constraints	5.9-20
5.9.3		Spacecraft Structural Design	5.9-21
	5.9.3.1	Earth Viewing Equipment Module	5.9-21
	5.9.3.2	Feed Support Truss	5.9-29
	5.9.3.3	Aft Equipment Module	5.9-34
	5.9.3.4	Solar Array Panels and Support Trusses	5.9-36
	5.9.3.5	Spacecraft Adapter	5.9-37
	5.9.3.6	Structure Weight Summary	5.9-38
5.9.4		Separation and Deployment	5.9-38
	5.9.4.1	Solar Panel Stowage and Deployment	5.9-38
	5.9.4.2	Combined Purpose Antenna Deployment	5.9-44
	5.9.4.3	Spacecraft/Booster Separation System	5.9-44
5.9.5		Structural Dynamic Considerations	5.9-48
	5.9.5.1	Introduction	5.9-48
	5.9.5.2	Launch Configuration Behavior	5.9-48
	5.9.5.3	Effect of Structural Damping on Cone Angle	5.9-53
	5.9.5.4	Orbital Configuration Behavior	5.9-53

Section			Page
5.9.6	Thermal Control		5.9-58
	5.9.6.1	Summary of Selected Configuration	5.9-58
	5.9.6.2	Equipment Mounting	5.9-59
	5.9.6.3	Semipassive Temperature Control	5.9-59
	5.9.6.4	Passive Temperature Control	5.9-61
	5.9.6.5	Configuration Thermal Analysis	5.9-62

TABLE OF CONTENTS

VOLUME I
BOOK 2

Section			Page
6	SPACECRAFT TRADEOFF AND ANALYSIS.		6.1-1
	6.1 Introduction		6.1-1
	6.2 Configuration Selection		6.2-1
	6.2.1 Approach to Configuration Selection		6.2-1
	6.2.2 Launch Vehicle Considerations		6.2-5
		6.2.2.1 Atlas/Agena-D Launch Vehicle	6.2-9
		6.2.2.2 TITAN III-C Launch Vehicle	6.2-10
		6.2.2.3 SLV3C/Centaur Launch Vehicle	6.2-11
	6.2.3 Early Conceptual Designs		6.2-22
		6.2.3.1 First Stage Designs	6.2-23
		6.2.3.2 Major Tradeoffs	6.2-27
		6.2.3.3 Second Stage Designs.	6.2-35
	6.2.4 Third Stage Designs		6.2-41
	6.2.5 Deployed Configuration		6.2-48
		6.2.5.1 Structural Considerations	6.2-52
		6.2.5.2 Equipment Module Deployment	6.2-56
	6.2.6 Alternate Fixed Feed Configuration		6.2-66
		6.2.6.1 Alternate Solar Panel Stowage Arrangement . .	6.2-68
		6.2.6.2 Aft Equipment Module Design	6.2-73
		6.2.6.3 Apogee Motor Packaging Provisions.	6.2-73
	6.3 Paraboloid Antenna.		6.3-1
	6.3.1 Rationale for Selected Reflector Concept		6.3-1
		6.3.1.1 Antenna Requirements	6.3-1
		6.3.1.2 Survey of Potential Reflector Concepts. . . .	6.3-1
	6.3.2 Design Studies of Selected Concept		6.3-26
		6.3.2.1 Paraboloid Reflector Configuration	6.3-26
		6.3.2.2 Thermal Considerations.	6.3-50
	6.3.3 Design Analysis of Selected Configuration.		6.3-65
		6.3.3.1 Design Criteria	6.3-65
		6.3.3.2 Structural Analysis	6.3-67
		6.3.3.3 Deployment Analysis.	6.3- 8
		6.3.3.4 Dynamic Analysis.	6.3-99
	6.3.4 Thermal Distortion Analysis		6.3-104
		6.3.4.1 Introduction.	6.3-104
		6.3.4.2 Thermal Analysis.	6.3-104
		6.3.4.3 Structural Deformation	6.3-105
	6.3.5 RF Performance Analysis		6.3-132
		6.3.5.1 Introduction.	6.3-132

Section			Page
	6.3.5.2	Feed Configuration Studies	6.3-136
	6.3.5.3	Selected Feed Configuration	6.3-144
	6.3.5.4	Monopulse	6.3-146
	6.3.5.5	Beam Steering	6.3-147
	6.3.5.6	RF Loss Budget Cassegrain vs Prime Focus	6.3-153
	6.3.5.7	Additional Strut Loss	6.3-157
	6.3.5.8	Thermal Distortion Loss	6.3-170
	6.3.5.9	RF Loss Budget-Final	6.3-171
	6.3 5.10	References for Section 6	6.3-172
6.4	Guidance and Control		6.4-1
	6.4.1	Summary	6.4-1
	6.4.2	Tradeoff Analysis	6.4-4
	6.4.2.1	Spacecraft Configuration Considerations	6.4-4
	6.4.2.2	Earth Sensor/Star Trackers	6.4-6
	6.4.2.3	Three Axis Control/Spin Stabilization During Station Acquisition Sequence	6.4-8
	6.4.2.4	Polaris Star Sensor/Gyrocompassing	6.4-9
	6.4.2.5	Momentum Storage Devices	6.4-11
	6.4.2.6	On-Off/Proportional Flywheel Control	6.4-15
	6.4.2.7	Spacecraft Orientation During Vernier Thrusting	6.4-16
	6.4.2.8	Yaw/Roll Axis Stabilization to the Sun	6.4-17
	6.4.2.9	Orientation Control/Stationkeeping Mass Expulsion Subsystem	6.4-18
	6,4.2.10	Accelerometer/Gryo for Coning Control	6.4-31
	6.4.2.11	Sattion Acquisition and Despin Mass Expulsion Subsystem	6.4-34
	6.4.2.12	Spinup Motor	6.4-42
	6.4.3	Design Analysis	6.4-46
	6.4.3.1	Transfer Orbit Disturbance Torques	6.4-47
	6.4.3.2	On-Station Disturbance Torques	6.4-52
	6.4.3.3	Control Static and Dynamic Performance Analysis	6.4-68
	6.4.3.4	Earth Pointing Error Analysis	6.4-113
6.5	TT&C Subsystem Tradeoffs and Analysis		6.5-1
	6.5.1	VHF vs S-Band Communication Link	6.5-1
	6.5.2	Tracking Analysis	6.5-3
	6.5.3	Antenna Configuration Tradeoff	6.5-7
	6.5.4	Analysis of Memory Requirements	6.5-11
6.6	Power		6.6-1
	6.6.1	Radiation Environment Requirements	6.6-1
	6.6.1.1	Trapped Radiation	6.6-1
	6.6.1.2	Solar Cosmic Radiation	6.6-2
	6.6.1.3	Primary Galactic Cosmic Rays	6.6-4

Section			Page
6.6.2	Energy Source Selection.		6.6-5
6.6.3	Array Configuration Selection.		6.6-6
	6.6.3.1	Array Location on Vehicle	6.6-6
	6.6.3.2	Array Configuration Studies	6.6-19
	6.6.3.3	Comparison of Four-Panel Configuration with Two-Panel Configuration	6.6-30
6.6.4	Array Design		6.6-33
	6.6.4.1	Array Sizing and Performance	6.6-33
	6.6.4.2	Solar Cell Selection	6.6-33
	6.6.4.3	Solar Cell Characteristics	6.6-35
	6.6.4.4	Solar Cell Loss Analysis	6.6-35
	6.6.4.5	Solar Cell Radiation Degradation Analysis.	6.6-38
	6.6.4.6	Cover Thickness Selection	6.6-40
	6.6.4.7	Launch Array Power Analysis.	6.6-42
6.6.5	Batteries.		6.6-43
	6.6.5.1	Requirements	6.6-43
	6.6.5.2	Selection of Battery Type	6.6-43
	6.6.5.3	Method of Sizing	6.6-44
	6.6.5.4	Effect of Two Paddles Versus Four Paddles	6.6-45
	6.6.5.5	Effect of Load Timing on Batteries	6.6-45
	6.6.5.6	Battery Description	6.6-47
	6.6.5.7	Battery Performance Summary	6.6-47
6.6.6	Power Subsystem Analysis.		6.6-50
	6.6.6.1	Power Distribution Selection (DC versus AC).	6.6-50
	6.6.6.2	Power Conditioning Equipment Selection	6.6-52
	6.6.6.3	Selected Power Subsystem Performance	6.6-61
6.6.7	References		6.6-66
6.7	Spacecraft Design		6.7-1
6.7.1	Structural Analysis		6.7-1
	6.7.1.1	Critical Loading	6.7-2
	6.7.1.2	Preliminary Design Philosophy	6.7-3
	6.7.1.3	Methods of Analysis	6.7-3
	6.7.1.4	Selected Configuration Design Rationale and Tradeoffs	6.7-5
6.7.2	Separation and Deployment.		6.7-48
	6.7.2.1	Design Criteria	6.7-48
	6.7.2.2	Deployment Mechanism Selection.	6.7-48
	6.7.2.3	Spacecraft/Booster Separation System	6.7-55
6.7.3	Structural Dynamics		6.7-58
	6.7.3.1	Design Criteria	6.7-58
	6.7.3.2	Dynamic Environment	6.7-59
	6.7.3.3	Methods of Analysis	6.7-61
	6.7.3.4	Configuration Selection Support Studies.	6.7-67

Section		Page
6.7.4	Electronic Packaging.	6.7-88
6.7.4.1	Design Criteria	6.7-88
6.7.4.2	Selected Configurations	6.7-89
6.7.4.3	Alternate Approaches	6.7-91
6.7.4.4	Areas for Further Study.	6.7-96
6.8	Apogee Motor Selection	6.8-1
6.8.1	Introduction.	6.8-1
6.8.2	Apogee Motor Requirements	6.8-2
6.8.3	Apogee Motor Selection - SLV-3A/Agena D	6.8-3
6.8.4	Apogee Motor Selection - SLV-3C/Centaur	6.8-5
6.8.4.1	Final Apogee Motor Selection Tradeoffs for the SLV-3C/Centaur	6.8-11
6.8.4.2	Recommended Apogee Motor for the Atlas/ Centaur Configuration	6.8-13
6.8.4.3	Surveyor Motor Development Requirements . .	6.8-13

TABLE OF CONTENTS

VOLUME I

BOOK 3

Section		Page
7	FLIGHT DYNAMICS	7-1
	7.1 Introduction	7-1
	7.2 Reference Design Sequence of Events - Summary	7-2
	7.2.1 Launch Trajectory - General	7-2
	7.2.2 Booster/Launch Phase	7-2
	7.2.3 Initial/Acquisition Phase	7-5
	7.3 Operating Longitude Evaluation	7-7
	7.4 Ascent Trajectory Selection	7-9
	7.4.1 Trajectory Influencing Parameters	7-9
	7.4.2 Launch Vehicle Constraints	7-13
	7.4.3 Trajectory Selection	7-13
	7.5 Initial Acquisition Phase Analyses	7-15
	7.5.1 Spin-Up Motors	7-16
	7.5.2 Transfer Trajectory Analysis	7-16
	7.5.2.1 Plane Change Velocity Requirements	7-16
	7.5.2.2 Apogee Motor Payload Analysis	7-18
	7.5.2.3 Reference Design Orbit Characteristics	7-24
	7.5.3 Vernier Velocity Requirements	7-26
	7.5.3.1 Reference Design Vernier Velocity Requirements	7-26
	7.5.3.2 Preliminary Velocity Requirements Analysis	7-31
	7.5.3.3 Injection Bias Analysis	7-46
	7.5.3.4 Despin	7-53
	7.6 Initial Stabilization and Deployment	7-54
	7.7 Synchronous Orbit Stationkeeping Requirements	7-54
	7.7.1 Dynamics	7-55
	7.7.1.1 Nominal Orbit	7-55
	7.7.1.2 Perturbations	7-60
	7.7.2 Velocity Requirements	7-63
	7.7.2.1 East-West	7-63
	7.7.2.2 North-South	7-65
	7.7.3 Tracking for Orbit Determination	7-65
	7.8 Operational System	7-70
	7.8.1 Launch and Parking Orbit	7-70
	7.8.1.1 Atlas Flight Phase	7-70
	7.8.1.2 Centaur Separation	7-70
	7.8.1.3 Launch-to-Injection Operations	7-70
	7.8.1.4 Perigee Burn	7-71

TABLE OF CONTENTS (Cont'd)

Section		Page
	7.8.2 Transfer Orbit	7-71
	7.8.3 Vernier Maneuvers	7-73
	7.8.4 Despin, Deployment, and Initial Stabilization	7-74
	7.8.5 Final Station Acquisition	7-76
	7.8.6 Operational Systems Contingency Planning	7-76
8	EXPERIMENT OPERATIONAL PHASE SEQUENCE	8.1-1
	8.1 General	8.1-1
	8.2 Experiment Axes Reference	8.2-1
	8.3 Parabolic Antenna	8.3-1
	8.3.1 General Discussion	8.3-1
	8.3.2 Technical Background of Measurements	8.3-2
	8.3.2.1 Introduction	8.3-2
	8.3.2.2 Direction and Gain	8.3-2
	8.3.3 Selection of Parameters	8.3-7
	8.3.3.1 General	8.3-7
	8.3.3.2 In-Space Measurements	8.3-8
	8.3.3.3 Ground Testing	8.3-9
	8.3.4 In-Space Measurement Techniques	8.3-11
	8.3.4.1 Gain	8.3-11
	8.3.4.2 Antenna Geometry Measurements	8.3-12
	8.3.4.3 Boresight	8.3-13
	8.3.5 Experiments	8.3-19
	8.3.5.1 Listing of Experiments	8.3-19
	8.3.5.2 Basic Electrical Measurements	8.3-25
	8.3.5.3 Basic Geometric Measurements	8.3-33
	8.3.5.4 Supporting Electrical Measurements	8.3-37
	8.3.6 Derivation of Equipment Requirements	8.3-40
	8.3.6.1 Electrical Measurements Experiments Equipment	8.3-40
	8.3.6.2 Geometric Measurement Experiment Equipment	8.3-54
	8.3.6.3 Summary of Required Equipment	8.3-55
	8.4 Orientation Control System	8.4-1
	8.4.1 General Discussion	8.4-1
	8.4.2 Listing of Experiments	8.4-3
	8.4.3 Basic Experiments	8.4-5
	8.4.3.1 General	8.4-5
	8.4.3.2 Pointing Performance	8.4-5
	8.4.3.3 Tracking Performance	8.4-8
	8.4.4 Equipment Requirements	8.4-10
	8.5 Interferometer	8.5-1
	8.5.1 General	8.5-1
	8.5.2 Listing of Experiments	8.5-2

TABLE OF CONTENTS (Cont'd)

Section		Page
8.5.3	Basic Experiments	8.5-4
8.5.3.1	General	8.5-4
8.5.3.2	Experiment I-1 - Verification of Operation	8.5-5
8.5.3.3	Experiments I-2 and I-3 - Internal Parameter Measurements	8.5-7
8.5.3.4	Experiment I-4 - Angle Error Measurement - Medium Accuracy	8.5-10
8.5.3.5	Experiment I-5 - Angle Error Measurement - High Accuracy	8.5-12
8.5.3.6	Experiment I-6 - Field of View	8.5-14
8.5.3.7	Experiment I-8 - Angle Difference Measurement	8.5-16
8.5.3.8	Experiment I-11 - Spacecraft Pointing	8.5-18
8.5.3.9	Experiment I-13 - System Life Verification	8.5-19
8.5.3.10	Experiment I-18 - Thermal Cycle Monitoring	8.5-21
8.5.4	Derivation of Equipment Requirements	8.5-23
8.6	Phase-Steered Array Antenna	8.6-1
8.6.1	General	8.6-1
8.6.2	Technical Background of Measurements	8.6-1
8.6.2.1	General	8.6-1
8.6.2.2	Component Similarity	8.6-2
8.6.2.3	Impedance Match	8.6-2
8.6.2.4	Physical Geometry	8.6-3
8.6.2.5	Radiation Characteristics	8.6-3
8.6.3	Parameter Selection	8.6-4
8.6.3.1	General	8.6-4
8.6.3.2	Internal Parameters	8.6-5
8.6.3.3	Gain	8.6-5
8.6.3.4	Beam Pointing Direction	8.6-5
8.6.4	Experiments	8.6-6
8.6.4.1	List of Experiments	8.6-6
8.6.4.2	Basic Electrical Measurements	8.6-11
8.6.5	Derivation of Equipment Requirements	8.6-20
8.7	Supplementary Experiments	8.7-1
8.7.1	General	8.7-1
8.7.2	Prime Experiment Augmentation	8.7-1
8.7.2.1	Parabolic Antenna Geometric Instrumentation	8.7-1
8.7.2.2	Parabolic Antenna Ultra-Wide Band Communications	8.7-2
8.7.2.3	Parabolic Antenna Side Lobe Measurement	8.7-2
8.7.2.4	Polarization Measurements from the Parabolic Antenna	8.7-2
8.7.2.5	Monopulse Installation	8.7-3

Section		Page
	8.7.2.6 Phase-Steered Array Monitoring.	8.7-5
	8.7.2.7 Interferometer Yaw Axis Stabilization	8.7-5
	8.7.2.8 Synthetic Angle Generation.	8.7-6
	8.7.2.9 Interferometer Transmit Mode	8.7-8
	8.7.3 Prime Experiment Applications	8.7-9
	8.7.3.1 High Data Rate Meteorological Sensor	8.7-9
	8.7.3.2 FM and TV Direct Broadcast	8.7-13
	8.7.3.3 Navigation and Air and Ship Traffic Control	8.7-21
	8.7.3.4 Communications with Low-Orbit Spacecraft	8.7-22
	8.7.3.5 Multiple Access Communications Satellite	8.7-25
	8.7.4 Passenger Experiments	8.7-26
	8.7.4.1 Millimeter Communications and Transmission	8.7-27
	8.7.4.2 Laser Communications and Transmission.	8.7-28
	8.7.4.3 Earth Radiation Measurements	8.7-28
	8.8 Operational System for Experiments	8.8-1
	8.8.1 General	8.8-1
	8.8.2 Experiment Operational System Requirements	8.8-2
	8.8.2.1 Operational Flow	8.8-2
	8.8.2.2 ATS-4 Ground Station Operational and Experimental Capability Requirements	8.8-5
	8.8.3 Experiment Control	8.8-12
	8.8.4 Data Acquisition, Processing and Display	8.8-21
	8.8.5 Contingency Planning.	8.8-24
	8.8.6 Reporting	8.8-24
9	SUPPORT OPERATIONS	9-1
	9.1 Introduction	9-1
	9.2 Summary	9-1
	9.3 Equipment Requirements	9-1
	9.4 Mechanical Support Equipment (MSE)	9-1
	9.4.1 Scope	9-1
	9.4.2 Study Approach.	9-5
	9.4.3 Mechanical Support Concepts	9-5
	9.4.3.1 Vehicle Assembly and Handling	9-5
	9.4.3.2 Alignment Equipment and Deployed Antenna Measurements	9-7
	9.4.3.3 Mass Properties, Spin Balance and Apogee Thrust Vector Alignment	9-7
	9.4.3.4 Deployment.	9-9
	9.4.3.5 Pneumatic and Fuel Servicing and Leak Testing.	9-10
	9.4.3.6 Vibration	9-10

TABLE OF CONTENTS (Cont'd)

Section		Page
	9.4.3.7 Structural Static Test	9-11
	9.4.3.8 Spin Test	9-11
	9.4.3.9 Acoustics Test	9-12
	9.4.3.10 RF Compatibility Tests	9-12
	9.4.3.11 Thermal-Vacuum Tests	9-12
	9.4.3.12 Attitude Control Demonstration	9-13
	9.4.3.13 Transportation and Shipping	9-13
	9.4.4 Equipment and Complexity Appraisal	9-14
9.5	Electrical Support Equipment (ESE)	9-16
	9.5.1 Scope	9-16
	9.5.2 Approach	9-16
	9.5.2.1 General	9-16
	9.5.2.2 Fail Safe	9-16
	9.5.2.3 Human Factors	9-16
	9.5.2.4 Isolation	9-16
	9.5.2.5 Accuracy	9-16
	9.5.2.6 Parts	9-17
	9.5.2.7 Use of Telemetry Subsystems for Testing	9-17
	9.5.3 Electrical Support Concepts	9-17
	9.5.3.1 General	9-17
	9.5.3.2 Subsystem Tests	9-17
	9.5.3.3 Earth Viewing Equipment Module Tests	9-18
	9.5.3.4 Aft Equipment Module Testing	9-18
	9.5.3.5 System Tests	9-18
	9.5.3.6 Thermal Vacuum Tests	9-19
	9.5.3.7 RF	9-19
	9.5.3.8 Pad	9-19
	9.5.4 Equipment List	9-19
9.6	Test Facilities	9-20
	9.6.1 Test Facility Support	9-20
	9.6.2 Test Facility Problem Areas	9-20
	9.6.2.1 Vibration, Deployed	9-20
	9.6.2.2 Large Antenna RF Testing	9-24
9.7	Launch Facilities	9-24
	9.7.1 Mechanical Support Operations	9-24
	9.7.2 Existing Launch Facilities	9-25
9.8	Orbital Support	9-28
9.9	Software	9-32

Appendix A. Parabolic Reflector Feed Selection Charts A-1

Appendix B. Launch Window Restriction Due to Precession Control Sun Sensors . . . B-1

Appendix C. Transfer Orbit Disturbance Torque Analysis C-1

Appendix D. On-Station Disturbance Torque Analysis D-1

Appendix E. Mathematical Model for Orientation Control Servo Analysis E-1

Appendix F. Stability Investigation and Pointing Error Analysis of the Three-Axis Star Tracker System F-1

Appendix G. Solar Array Computer Program G-1

Appendix H. Radiation Effects on Silicon Solar Cells H-1

Appendix I. Basic Design Data for Subsystem Comparison I-1

Appendix J. Coupling of Structural Flexibility with a Control System Feedback Loop . J-1

Appendix K. Coning Control K-1

Appendix L. Elements of Monopulse L-1

Appendix M. Plume Calculations for Walter Kidde Two-Pound Thrust Nozzle and for a Resistance Jet Ammonia Nozzle M-1

TABLE OF CONTENTS

VOLUME II

PRELIMINARY PROGRAM PLAN

Section		Page
1	INTRODUCTION	1-1
2	PROJECT SCHEDULE	2-1
	2.1 Introduction	2-1
	2.2 Phased Project Planning	2-1
	2.3 Overall Schedule	2-12
	2.4 Schedule of AGE Utilization	2-14
	2.5 Long Lead Items	2-15
3	ENGINEERING DEVELOPMENT	3-1
	3.1 Introduction	3-1
	3.2 Development Problem Areas	3-1
	3.2.1 Parabolic Antenna Development	3-2
	3.2.2 Spacecraft Structure	3-3
	3.2.2.1 Ascent Environment Design	3-3
	3.2.2.2 Orbital Environment Design	3-4
	3.2.3 Thermal Environment Control	3-4
	3.2.3.1 The Earth Viewing Module	3-5
	3.2.3.2 Aft Equipment Module	3-5
	3.2.4 Electrical Power and Distribution	3-6
	3.2.4.1 Batteries	3-6
	3.2.4.2 Power Profile	3-7
	3.2.5 Attitude Sensing and Control	3-7
	3.2.5.1 IR Sensor and Star Tracker	3-7
	3.2.5.2 Ground Station - Orientation Control Interface	3-8
	3.2.5.3 Attitude Control During Initial Acquisition	3-9
	3.2.5.4 Long Life Reliability	3-10
	3.2.5.5 Orientation Control System Operational Ground Test	3-10
	3.2.6 Telemetry Tracking and Command	3-10
	3.2.7 Propulsion	3-10
	3.2.7.1 Vernier Propulsion Unit	3-11
	3.2.7.2 Stationkeeping System	3-11
	3.2.8 Operational Experiments	3-12
	3.2.8.1 Parabolic Antenna Experiment	3-12
	3.2.8.2 Phased Steered Array Experiment	3-15
	3.2.8.3 Interferometer Experiment	3-16
	3.2.8.4 Orientation Control Experiment	3-18

TABLE OF CONTENTS (Cont'd)

Section		Page
	3.2.9 Ground Station Operation and Data Analysis	3 20
	3.2.9.1 Determination of Experiment Down Link Equipment and Functions to be Provided at Each ATS-4 Station	3-20
	3.2.9.2 Data Acquisition, Logistics, Merging, Storage	3-20
	3.2.9.3 Attitude Determination During Transfer Orbit, Apogee Burn and Achievement of Synchronous Orbit	3-21
	3.2.9.4 Determination of Spacecraft and Experiment Axes Orientation During Flight	3-21
	3.2.10 Ground Handling, Test and Checkout Equipment	3-22
	3.3 Development Approach	3-22
	3.3.1 Attitude Control Subsystem	3-23
	3.3.2 Telemetry, Tracking and Command Subsystem	3-23
	3.3.3 Propulsion Subsystem	3-23
	3.3.4 Solar Arrays	3-24
	3.3.5 Structure	3-24
	3.3.6 Power Conditioning Equipment	3-25
	3.3.7 Batteries	3-25
4	INTEGRATED TEST	4-1
	4.1 Principal Features	4-1
	4.2 Component Test	4-4
	4.3 System Test	4-4
	4.3.1 In-House System Tests	4-4
	4.3.2 Field Tests	4-11
	4.3.3 Development Test Hardware	4-11
	4.3.3.1 Engineering Development Spacecraft	4-11
	4.3.3.2 Structural Dynamic Model	4-12
	4.3.3.3 Attitude Control Engineering Model	4-13
	4.3.3.4 Parabolic Antenna Development Model	4-13
	4.3.3.5 RF Antenna Models	4-13
	4.3.3.6 Clearance Model	4-13
	4.3.3.7 Harness Mockup	4-13
	4.3.3.8 Vehicle Mockup	4-14
	4.4 Summary	4-14
5	MANAGEMENT AND SUPPORT ASPECTS	5-1
	5.1 Project Control	5-1

Section

Page

5.1.1 Uniform Project Control 5-2
5.1.2 Schedule Integration 5-4
5.1.3 Project Visibility 5-4
5.1.4 Interface Control 5-5
5.1.5 Approach 5-6
5.2 Configuration Management 5-7
5.2.1 Introduction 5-7
5.2.2 Guidelines 5-8
5.2.2.1 Configuration Identification 5-8
5.2.2.2 Configuration Control 5-9
5.2.2.3 Configuration Accounting 5-9
5.2.3 Requirements 5-10
5.2.4 Approach 5-10
5.2.5 Implementation 5-11
5.3 Data Management 5-12
5.3.1 Introduction 5-12
5.3.2 Approach 5-13
5.3.3 Requirements 5-13
5.3.4 Critical Areas 5-14
5.3.4.1 Data Identification 5-14
5.3.4.2 Acquisition, Storage and Retrieval 5-14
5.3.4.3 Timely and Accurate Input/Output 5-15
5.3.5 Implementation 5-15
5.4 Manufacturing/Facilities 5-16
5.4.1 Introduction 5-16
5.4.2 Manufacturing 5-16
5.4.2.1 In-Process Handling 5-17
5.4.2.2 Alignment of Critical Subsystems and Components 5-18
5.4.2.3 Solar Array Fabrication 5-20
5.4.3 Facilities 5-20
5.5 Procurement 5-20
5.5.1 Make or Buy 5-24
5.5.2 Source Selection 5-24
5.5.3 Subcontractor Management and Control 5-26
5.6 Product Assurance 5-26
5.6.1 Introduction 5-26
5.6.2 Problems 5-27
5.6.3 Approaches to Problem Solutions 5-27

Section		Page
	5.6.3.1 Long Life System Requirements	5-27
	5.6.3.2 Handling of Equipment	5-28
	5.6.3.3 Traceability	5-29
	5.6.3.4 Subcontractor and Associate Contractor Controls	5-30
5.7	Reliability	5-31
	5.7.1 Introduction	5-31
	5.7.1.1 Objective of the Program	5-31
	5.7.1.2 Special Attention to the Long-Life Problem	5-32
	5.7.2 Program Elements	5-32
	5.7.3 Contractor/Customer Relationships	5-33
5.8	Safety	5-35
	5.8.1 Introduction	5-35
	5.8.2 Approach	5-36
	5.8.3 Safety Plan Requirements	5-36
	5.8.4 Associated Safety Program Requirements	5-37
	5.8.5 Hazard Identification	5-38
5.9	Parts Program	5-39
	5.9.1 Introduction	5-39
	5.9.2 Parts Policy	5-39
	5.9.3 Selection and Approval	5-40
	5.9.3.1 Approved Lists	5-40
	5.9.3.2 Standardization of Parts, Materials, and Processes	5-40
	5.9.3.3 Qualification	5-41
	5.9.3.4 Nonstandard Parts Approval	5-41
	5.9.3.5 Use of Approved Lists	5-42
	5.9.3.6 Parts and Materials Application Review	5-43
	5.9.4 Parts Screening	5-43
	5.9.4.1 Test Program	5-43
	5.9.4.2 Typical Screening	5-44
	5.9.5 Specifications	5-44
	5.9.5.1 Standards	5-44
	5.9.5.2 New Drawings	5-45
	5.9.5.3 Document Approval	5-45
	5.9.6 Product Engineering Standards	5-45
	5.9.6.1 Design Standards	5-45
	5.9.6.2 Process Standards	5-46
	5.9.7 Failure Reporting and Analysis	5-46
	5.9.8 Subcontractor Requirements and Controls	5-47
	5.9.8.1 General	5-47
	5.9.8.2 Parts Program	5-47
	5.9.8.3 Subcontractor Parts Lists	5-47

TABLE OF CONTENTS (Cont'd)

Section		Page
6	COST	6-1
	6.1 Cost Breakdown	6-1
	6.2 Expenditure Rate	6-5
	6.3 Phasing Alternatives	6-5
	6.3.1 Four-Month Breakpoint	6-6
	6.3.2 Six-Month Breakpoint	6-6
	6.3.3 Eight-Month Breakpoint	6-6
	6.3.4 Twelve-Month Breakpoint	6-7
	6.3.5 Summary	6-8

LIST OF ILLUSTRATIONS

Figure		Page
5.2-1	ATS-4 Mission Sequence	5.2-4
5.3-1	Selected Configuration (Orbital View)	5.3-2
5.3-2	ATS-4 Selected Configuration, Inboard Profile and Orbital Configuration	5.3-5
5.3-3	ATS-4 System Block Diagram	5.3-11
5.3-4	ATS-4 Payload Growth	5.3-30
5.4-1	Petaline Rigid Reflector Configuration	5.4-3
5.4-2	Deployment Drive Mechanism	5.4-5
5.4-3	Feed Configuration	5.4-7
5.4-4	Stowed Configuration	5.4-9
5.4-5	Reflector, Typical Sector	5.4-16
5.4-6	Panel Structure Composite	5.4-17
5.4-7	Deviation from True Contour	5.4-18
5.4-8	Configuration of Expanded Metal for RF Reflecting Material	5.4-19
5.4-9	Deployment Trusses	5.4-21
5.4-10	Interface Ring	5.4-25
5.4-11	Three-Foot Diameter Demonstration Model	5.4-32
5.4-12	Composite Feed on Earth Viewing Equipment Module	5.4-34
5.4-13	Influence of Open Area on Antenna Design	5.4-37
5.4-14	ATS-4 Parabolic Antenna Temperature Distribution	5.4-38
5.4-15	Antenna Isotherms 39-90	5.4-39
5.5-1	ATS-4 Guidance and Control Subsystem Block Diagram	5.5-4
5.5-2	Spacecraft Configuration -- Station Acquisition	5.5-11
5.5-3	Coning and Precession Control	5.5-12
5.5-4	Principle of Orientation Measurement	5.5-16
5.5-5	Sun Sensor	5.5-17
5.5-6	Rhumb Line Precession	5.5-19
5.5-7	ATS-4 Reference Design: Antenna Half-Beam Angle During Transfer Orbit	5.5-22
5.5-8	Impulse Requirement versus Spin Rate	5.5-24
5.5-9	Sun Acquisition	5.5-26
5.5-10	ATS-4 Configuration-Orientation Control	5.5-28
5.5-11	On-Station Orientation Control	5.5-32
5.5-12	Integrated Stationkeeping-Wheel Unloading Mass Expulsion System Control Logic	5.5-39
5.5-13	Thrust and Impulse Required for East-West Station Change	5.5-44
5.5-14	Spin Sun Sensor Output	5.5-49
5.5-15	Polarized RF Antenna	5.5-50
5.5-16	Pulse Lengths for Various RPM's and θ's	5.5-54
5.5-17	Effect on I_{sp} for Various Pulse Widths for Hydrazine	5.5-55
5.5-18	Radial Impulse Efficiency	5.5-55
5.5-19	Station Acquisition System Schematic	5.5-56

LIST OF ILLUSTRATIONS (Cont'd)

Figure		Page
5.5-20	RAPS Rate Mode Total Uncertainty Limits	5.5-59
5.5-21	Miniature Rate Integrating Gyro	5.5-61
5.5-22	Director, Cone Angle Sun Sensor, Coarse Eye Assembly	5.5-62
5.5-23	Control Axes Coarse Sun Sensor Set Relative Response Characteristic.	5.5-62
5.5-24	Single Eye Output versus Angle Characteristic.	5.5-63
5.5-25	Acquisition Scan Pattern	5.5-65
5.5-26	Possible Tracking Scan Patterns	5.5-65
5.5-27	OAO Flywheel Cross Section.	5.5-71
5.5-28	General Electric Resistance Jet System	5.5-74
5.5-29	Liquid Ammonia, Zero-g Storage Tank Schematic	5.5-75
5.5-30	Polaris Sensor View Angles	5.5-83
5.5-31	Pitch and Roll Sun Sensors Fields of View	5.5-84
5.5-32	Station Acquisition and Yaw Sun Sensor Fields of View	5.5-85
5.6-1	Large Parabolic Antenna Experiment Subsystem	5.6-7
5.6-2	Typical Receiver.	5.6-9
5.6-3	Typical Transmitter	5.6-9
5.6-4	Relation of Incident Signal to Interferometer Antennas	5.6-17
5.6-5	Phase Comparison System	5.6-19
5.6-6	Phase Diagram for Σ-Δ System	5.6-19
5.6-7	Σ-Δ System	5.6-19
5.6-8	Pilot Tone Concept	5.6-21
5.6-9	Antenna Location on Cannister	5.6-22
5.6-10	ATS-4 Interferometer System, Block Diagram.	5.6-23
5.6-11	System Block Diagram.	5.6-30
5.7-1	TT&C Subsystem Block Diagram Reference Design	5.7-6
5.7-2	Goddard R&R S-Band Transponder.	5.7-7
5.7-3	Command Decoder, Functional Block Diagram.	5.7-8
5.7-4	Relay Logic	5.7-10
5.7-5	Typical Main Frame	5.7-14
5.7-6	ATS-4 Reference Design: Antenna Half-Beam Angle During Transfer Orbit	5.7-17
5.7-7	Half-Beam Angle Definition	5.7-17
5.7-8	ATS-4 Reference Design: Antenna Half-Beam Angle During Vernier Maneuvers While in Synchronous Orbit	5.7-18
5.7-9	Antenna Coverage	5.7-19
5.7-10	Antenna Switching Reference Configuration	5.7-20
5.7-11	Antenna Design	5.7-21
5.7-12	TT&C Block Diagram, Redundant Configuration	5.7-29
5.7-13	Antenna Switching, Redundant Configuration	5.7-31

LIST OF ILLUSTRATIONS (Cont'd)

Figure		Page
5.8-1	Load Power Requirements During Launch Transfer Orbit	5.8-2
5.8-2	Load Power Requirements During Near-Synchronous Orbit Vernier Maneuvers	5.8-2
5.8-3	ATS-4 Reference Design Load Requirements	5.8-4
5.8-4	Power Subsystem, Block Diagram	5.8-9
5.8-5	Solar Array Power	5.8-12
5.8-6	Daily Average Array Power versus Time in Orbit (For Equinox and Summer Solstice Orbits)	5.8-13
5.8-7	End-of-Life Array Power for Equinox Orbits	5.8-14
5.8-8	End-of-Life Array Power for Summer Solstice Orbit	5.8-15
5.8-9	Solar Array Power Capability of Loads for Equinox Orbits	5.8-16
5.8-10	Solar Array Power Capability of Loads for Summer Solstice Orbits	5.8-16
5.8-11	Solar Array V-I Curves	5.8-17
5.8-12	Solar Array Output During Stowed Launch Spin Mode	5.8-19
5.8-13	Solar Array Power Capability at Loads During Stowed Launch Spin Mode	5.8-20
5.8-14	Y-Axis Panels Area Growth Capability	5.8-22
5.8-15	ATS-4 Solar Cell Arrangements	5.8-25
5.9-1	Inboard Profile and Orbital Configuration	5.9-3
5.9-2	Static and Dynamic Envelope	5.9-7
5.9-3	Launch Availability versus Limit Bending Moment	5.9-10
5.9-4	Nozzle Locations and Plume Details	5.9-11
5.9-5	Delta Motor (TE-364-3)	5.9-14
5.9-6	Maximum Expected Outside Surface Temperature versus Time for TE-M-364-4-3	5.9-15
5.9-7	TE-M-364-3 Altitude Thrust and Chamber Pressure versus Time	5.9-17
5.9-8	G-Loading Versus Time During Apogee Burn	5.9-17
5.9-9	Thrust and Chamber Pressure versus Time, Motor B	5.9-19
5.9-10	Relation of Major Structural Elements of Selected Configuration	5.9-25
5.9-11	Truss Tube End Design Concept	5,9-31
5.9-12	Solar Panel Latching	5.9-41
5.9-13	Separation Nut Operation	5.9-47
5.9-14	Response of Upper Mass (Mass 1) versus First Mode Shape	5.9-50
5.9-15	Typical Shutter Assembly	5.9-59
5.9-16	Typical Shutter System Characteristics	5.9-60
5.9-17	Earth Viewing Equipment Module	5.9-64
5.9-18	EVM Panel Temperature Distribution (^{o}R) Based on Continuous Experiment Operation	5.9-66
5.9-19	EVM Panel 4 Transient Thermal Performance	5.9-67
5.9-20	Aft Equipment Module Overall Component Installation	5.9-68
5.9-21	AFT Equipment Module	5.9-69
5.9-22	AEM Panel Temperature Distribution (^{o}R)	5.9-74
5.9-23	Truss Nodal Designation	5.9-75

Figure		Page
5.9-24	Transient Strut Temperature Profile (^{o}R), $\alpha/\epsilon = 1$	5.9-75
5.9-25	Transient Strut Temperature Profile (^{o}R), $\alpha/\epsilon = 1$	5.9-76
5.9-26	Transient Strut Temperature Profile (^{o}R), $\alpha/\epsilon = 2$	5.9-76
5.9-27	Transient Strut Temperature Profile (^{o}R), $\alpha/\epsilon = 2$	5.9-77
5.9-28	Transient Strut Temperature Profile (^{o}R), $\alpha/\epsilon = 3$	5.9-77
5.9-29	Transient Strut Temperature Profile (^{o}R), $\alpha/\epsilon = 3$	5.9-78
5.9-30	Maximum Solar Flux Distribution During Equinox	5.9-80
5.9-31	Maximum Solar Flux Distribution During Summer Solstice	5.9-81
5.9-32	Maximum Solar Flux Distribution for Inclined Paddles	5.9-82
5.9-33	Average Solar Paddle Temperature for the Antenna-Mounted Four-Paddle Spacecraft	5.9-83
5.9-34	Absorbed Free Molecule Heat Flux for Parking Orbit of 80 Nautical Miles	5.9-85
5.9-35	Absorbed Free Molecule Heat Flux for Parking Orbit of 90 Nautical Miles	5.9-85
5.9-36	Absorbed Free Molecule Heat Flux for Parking Orbit of 100 Nautical Miles	5.9-85
6.2-1	Basic Spacecraft Arrangements Used in Configuration Tradeoff Studies	6.2-3
6.2-2	Candidate Launch Vehicles and Early Conceptual Approaches	6.2-7
6.2-3	Launch Availability versus Limit Bending Moment	6.2-15
6.2-4	Launch Availability versus Engine Deflection	6.2-16
6.2-5	Static and Dynamic Envelope	6.2-17
6.2-6	First Stage Design, Split Module Concept	6.2-23
6.2-7	First Stage Design, Single Module Concept	6.2-25
6.2-8	First Stage Design, Deployed Phased Array Concept	6.2-29
6.2-9	Star Tracker System for Orientation Control, View Angles	6.2-32
6.2-10	Polaris Tracker System for Orientation Control, View Angles	6.2-33
6.2-11	Second Stage Design, Phased Array Concept	6.2-37
6.2-12	Second Stage Design, Deployed Feed Concept	6.2-38
6.2-13	Third Stage Design, Tandem Concept	6.2-43
6.2-14	Third Stage Design, Deployed Phased Array Concept	6.2-45
6.2-15	Deployed Configuration	6.2-49
6.2-16	Structural Load Paths	6.2-55
6.2-17	Electrically Powered Deployment System	6.2-57
6.2-18	Mechanically Powered Deployment System	6.2-59
6.2-19	Alternate Fixed Feed Design, Extended Surveyor Apogee Motor	6.2-69
6.2-20	Alternate Fixed Feed Design, Antares I Apogee Motor	6.2-71
6.3-1	Wire-Grid Structure	6.3-4
6.3-2	Wire-Grid Structural Member	6.3-5
6.3-3	Tolerance Limitation of Mesh Attachment Method	6.3-5
6.3-4	Solar Collector Orbital Sequence	6.3-8

Figure		Page
6.3-5	Chemically Rigidized Reflector (Two-Foot Model)	6.3-9
6.3-6	Mirror-Supported by Rigid Foam (44.5-Foot Model)	6.3-9
6.3-7	Cross Section of Rigidized Solar Concentrator	6.3-10
6.3-8	Solar Concentrator (Initial and Final Fabrication Phases)	6.3-11
6.3-9	Stretched-Screen Reflector Surface Contour Accuracy	6.3-12
6.3-10	Thermal Deflection Comparison	6.3-13
6.3-11	Design with Cables Behind Reflector Surface	6.3-14
6.3-12	Swirlabola Antenna	6.3-15
6.3-13	Deployment of a Petal Antenna	6.3-19
6.3-14	Aluminum-Sandwich Frame Member	6.3-20
6.3-15	Typical Sector of Petal Lattice Pattern	6.3-27
6.3-16	Ultimate Tensile Strength versus Temperature for Aluminum and Titanium	6.3-32
6.3-17	Yield Strength versus Temperature for Aluminum and Titanium	6.3-32
6.3-18	Modulus of Elasticity versus Temperature for Aluminum and Titanium	6.3-33
6.3-19	Coefficient of Thermal Expansion versus Temperature for Aluminum and Titanium	6.3-33
6.3-20	Possible Configuration of Expanded Metal for RF Reflecting Material	6.3-35
6.3-21	Reverse Folding Pattern, Triangular Petals Folded Outward	6.3-41
6.3-22	Deployment Scheme	6.3-45
6.3-23	Reverse Folding Pattern, Triangular Petals Folded Radially Outward	6.3-51
6.3-24	Reverse Folding Pattern, Triangular Petals Folded Towards Center	6.3-51
6.3-25	Causes of Thermal Deflections	6.3-52
6.3-26	Heat Inputs	6.3-54
6.3-27	Internal Geometry Effects - Antenna Blockage	6.3-54
6.3-28	Two-Node Thermal Model	6.3-56
6.3-29	One-Dimensional Heat Transfer	6.3-59
6.3-30	Analytical Model.	6.3-59
6.3-31	Average Antenna Temperature	6.3-60
6.3-32	Temperature Differentials Through the Thickness	6.3-61
6.3-33	Temperature Differentials Tip-to-Tip	6.3-62
6.3-34	Isotherms for Solid-Rod Antenna	6.3-63
6.3-35	Isotherms for Solid and Open Antenna at 90-Degree Orbital Position	6.3-64
6.3-36	Folded Reflector Load Distribution and Geometry.	6.3-69
6.3-37	Radial Petal Member, Typical Section	6.3-70
6.3-38	Approximate Loading of a Beam	6.3-75
6.3-39	Computer Loads Printout, Stress Analysis and Margin of Safety Calculation	6.3-77
6.3-40	Computer Loads Printout, Stress Analysis, and Margin of Safety for One of Six Members Common to Truss Point 89	6.3-79

Figure		Page
6.3-41	Computer Loads Printout, Stress Analysis, and Margin of Safety for One of Six Members Common to Truss Point 89	6.3-80
6.3-42	Computer Loads Printout, Stress Analysis, and Margin of Safety for One of Six Members Common to Truss Point 89	6.3-81
6.3-43	Computer Loads Printout, Stress Analysis, and Margin of Safety for One of Six Members Common to Truss Point 89	6.3-82
6.3-44	Computer Loads Printout, Stress Analysis, and Margin of Safety for One of Six Members Common to Truss Point 89	6.3-83
6.3-45	Computer Loads Printout, Stress Analysis, and Margin of Safety for One of Six Members Common to Truss Point 89	6.3-84
6.3-46	Member Loads at Joint 89	6.3-85
6.3-47	Model Used for Face Sheet - Core Thermal Compatibility Analysis	6.3-85
6.3-48	Truss Members	6.3-92
6.3-49	Two-Node Diameter Mode of Vibration	6.3-100
6.3-50	45-Degree Sector of Antenna Representing Overhanging Beam on Two Supports.	6.3-100
6.3-51	Antenna Isotherms 39-90	6.3-106
6.3-52	Antenna Isotherms 39-0	6.3-106
6.3-53	Antenna Isotherms 39-45	6.3-106
6.3-54	Antenna Isotherms 39-135	6.3-106
6.3-55	Antenna Isotherms 39-180	6.3-106
6.3-56	Deformed Shape at Below Ambient Temperatures (Free Hub, No Deployment Trusses)	6.3-111
6.3-57	Deformed Shape at Below Ambient Temperature (Fixed Hub, No Deployment Trusses)	6.3-111
6.3-58	Structural Simulation for Digital Computer Program.	6.3-114
6.3-59	Computer-Drawn Schematic (or a Structural Antenna Simulation)	6.3-115
6.3-60	Contour Deflection for Fixed Hub	6.3-118
6.3-61	Contour Deflection for Free Hub	6.3-118
6.3-62	Antenna Deflections Due to Temperature Gradients, Displacements of Radial Members θ = 180 Degrees	6.3-119
6.3-63	Antenna Deflections Due to Temperature Gradients, Displacements of Radial Members θ = 160 Degrees	6.3-119
6.3-64	Antenna Deflections Due to Temperature Gradients, Displacements of Radial Members θ = 140 Degrees	6.3-120
6.3-65	Antenna Deflections Due to Temperature Gradients, Displacements of Radial Members θ = 120 Degrees	6.3-120
6.3-66	Antenna Deflections Due to Temperature Gradients, Displacements of Radial Members θ = 100 Degrees	6.3-121
6.3-67	Case 39-90, Deviation Plot (Symmetrical about Centerline)	6.3-122
6.3-68	Truss Geometry and Nomenclature used for Feed Distortion Analysis	6.3-130
6.3-69	0.3 f/D Geometry	6.3-132
6.3-70	0.4 f/D Geometry	6.3-133

Figure		Page
6.3-71	0.5 f/D Geometry	6.3-133
6.3-72	Cassegrain Antenna Nomenclature	6.3-135
6.3-73	Subreflector Blocking Gain Loss	6.3-136
6.3-74	Subreflector Included Angle versus 2f/d for 30-Foot Diameter Parabola	6.3-136
6.3-75	Horn Aperture and Length versus Secondary Focus H, F/D = 0.3	6.3-137
6.3-76	Horn Aperture and Length versus Secondary Focus H, F/D = 0.4	6.3-137
6.3-77	Horn Aperture and Length versus Secondary Focus H, F/D = 0.5	6.3-138
6.3-78	Syncom SHF Feed Patterns	6.3-148
6.3-79	Feed Configuration	6.3-148
6.3-80	Gain Degradation versus Scan Angle	6.3-149
6.3-81	Gain Performance for Scanning Scheme	6.3-150
6.3-82	Loci of Best Azimuth Focus for Various Elevation Angles θ	6.3-151
6.3-83	Comparison of Point Source and Line Source E-Plane Patterns, 15-Degree Steering	6.3-151
6.3-84	Coma Coefficient versus Scan Angle	6.3-153
6.3-85	Subreflector Grid Sizes	6.3-158
6.3-86	Strut Model Configuration	6.3-159
6.3-87	Three-V Strut Model Configuration	6.3-159
6.3-88	Four-Strut Model	6.3-160
6.3-89	Three V Struts on 2-Foot Diameter Circle	6.3-160
6.3-90	Three V Struts on 54-Inch Diameter Feed Circle	6.3-161
6.3-91	450-Foot Test Range, From Source	6.3-161
6.3-92	Measured Patterns	6.3-163
6.3-93	Case 39-90, Deviation Plot (Symmetrical About Centerline)	6.3-171
6.4-1	Star Tracker Field of View Requirements	6.4-7
6.4-2	Antenna Half-Beam Angle During Vernier Maneuvers During Synchronous Orbit	6.4-17
6.4-3	Data for GE Resistance Jet	6.4-21
6.4-4	Resistance Jet Stationkeeping/Orientation Control Subsystem (GE)	6.4-22
6.4-5	Propellant Weight versus Total Impuse at 1800°F (GE System)	6.4-23
6.4-6	Total System Weight versus Total Impulse (GE System)	6.4-23
6.4-7	Mollier Chart of Properties of Ammonia	6.4-25
6.4-8	AVCO Resistance Jet Subsystem	6.4-27
6.4-9	Propellant Weight versus Total Impulse (I_{sp} = 150 sec), AVCO System	6.4-28
6.4-10	Total System Weight versus Total Impulse (AVCO System)	6.4-28
6.4-11	GE Resistance Jet and AVCO Resistance Jet Operating Temperatures	6.4-30
6.4-12	Coning Control Sensor Location	6.4-33
6.4-13	Regulated and Blowdown Monopropellant System	6.4-37
6.4-14	Bipropellant System Schematic	6.4-40
6.4-15	Total Impulse for Various Spin Rates and Ir/r	6.4-43

Figure		Page
6.4-16	Candidate Spinup Motors	6.4-45
6.4-17	ATS-4 Spacecraft Configuration.	6.4-48
6.4-18	X_B and Y_B Components of Aerodynamic Torque	6.4-50
6.4-19	X_B and Y_B Components of Magnetic Torque.	6.4-51
6.4-20	X_B and Y_B Components of Gravity Gradient Torque	6.4-53
6.4-21	Assumed Configuration for Disturbance Torques	6.4-56
6.4-22	Disturbance Torque Profile (Yaw Axis Pointed to Local Vertical)	6.4-57
6.4-23	Disturbance Torque Profile (Yaw Axis Pointed to 0^o Pitch, 8.7^o Roll)	6.4-58
6.4-24	Disturbance Torque Profile (Yaw Axis Pointed to Rosman Station)	6.4-59
6.4-25	Disturbance Torque Profile (Yaw Axis Pointed to Mojave Station)	6.4-60
6.4-26	Flywheel Momentum Profile (Yaw Axis Pointed to Local Vertical)	6.4-62
6.4-27	Flywheel Momentum Profile (Yaw Axis Pointed to 0^o Pitch, 8.7^o Roll)	6.4-63
6.4-28	Flywheel Momentum Profile, Autumnal Equinox, (Yaw Axis Pointed to Rosman Station)	6.4-65
6.4-29	Flywheel Momentum Profile (Yaw Axis Pointed to Mojave Station)	6.4-67
6.4-30	Locus of Spin Axis After Booster Separation	6.4-71
6.4-31	Coning Damper	6.4-72
6.4-32	Thruster Efficiency versus Pulse Width	6.4-77
6.4-33	Apogee Motor Burn	6.4-81
6.4-34	Initial Stabilization Pitch Axis	6.4-84
6.4-35	Sun Stabilization System, Block Diagram	6.4-85
6.4-36	Gyroscopic Torques	6.4-86
6.4-37	Attitude and Sun Sensor Geometry	6.4-87
6.4-38	Phase Plane Diagram	6.4-90
6.4-39	Earth Stabilization Roll Axis, E1	6.4-93
6.4-40	Earth Stabilization Pitch Axis, E2	6.4-93
6.4-41	Earth Stabilization Roll Axis, E3	6.4-93
6.4-42	Earth Stabilization Pitch Axis, E4	6.4-93
6.4-43	Earth and Star Stabilization System	6.4-94
6.4-44	Nonlinear Flywheel	6.4-95
6.4-45	Velocity-Momentum Transfer Function for Rigid Vehicles with Flexible Appendages.	6.4-95
6.4-46	Attitude Geometry	6.4-97
6.4-47	Earth Scanner Geometry	6.4-98
6.4-48	Flywheel Unloading Jet Controller	6.4-99
6.4-49	Signal Processing Null.	6.4-100
6.4-50	Open Loop Frequency Response.	6.4-100
6.4-51	Sun Sensor Geometry for Star Stabilization	6.4-102
6.4-52	Primary Pointing System, Block Diagram	6.4-103
6.4-53	Roll Axis Pointing, P2.	6.4-105
6.4-54	Pitch Axis Pointing, P5	6.4-105
6.4-55	Yaw Axis Pointing, P8.	6.4-105

Figure		Page
6.4-56	Roll Axis Pointing, P1.	6.4-106
6.4-57	Pitch Axis Pointing, P4	6.4-106
6.4-58	Yaw Axis Pointing, P7.	6.4-106
6.4-59	Roll Axis Pointing, P3.	6.4-107
6.4-60	Pitch Axis Pointing, P6	6.4-107
6.4-61	Roll Axis Slew, S1	6.4-108
6.4-62	Roll Axis Slew, S2	6.4-108
6.4-63	Roll Axis Slew, S3	6.4-108
6.4-64	Pitch Axis Slew, S4.	6.4-108
6.4-65	Roll/Pitch Axis Slew, Yaw Axis, S5	6.4-109
6.4-66	Gravity Gradient Rod, Roll Axis Slew, S6	6.4-109
6.4-67	Roll Axis Track, T6	6.4-111
6.4-68	Roll Axis Track, T1	6.4-111
6.4-69	Roll Axis Track, T2	6.4-111
6.4-70	Roll Axis Track, T3	6.4-112
6.4-71	Pitch Axis Track, T4	6.4-112
6.4-72	Roll Axis Track, T5	6.4-112
6.5-1	Results of Tracking Analysis	6.5-4
6.5-2	Minimum Δt for Memory	6.5-11
6.5-3	Maximum Δt for Memory.	6.5-13
6.6-1	Trapped Electron Environment	6.6-2
6.6-2	Solar Flare Environment	6.6-3
6.6-3	Segment of 30-Foot Diameter Petal Antenna Reflector	6.6-11
6.6-4	Segment of 30-Foot Diameter Petal Antenna Reflector	6.6-11
6.6-5	Sun Shadow Distribution	6.6-13
6.6-6	Bypass Diode Functional Arrangement	6.6-14
6.6-7	Comparison of V-I Curves for a Partially Shaded Array Series String, With and Without Bypass Diodes	6.6-15
6.6-8	Illustration of Effects of a Number of Elements Shaded on Degradation of an Array Series String Operating at String Peak Power Voltage.	6.6-16
6.6-9	Illustration of Effects of a Number of Elements Shaded on Degradation of an Array Series String When Operating Voltage is Off Peak Power Point of Array	6.6-16
6.6-10	Array Located in Shadow of Antenna Reflector Structure	6.6-18
6.6-11	Dependence of Solar Cell Output on Angle of Incidence	6.6-22
6.6-12	Orbital Variations of Geometry Factor $K_G/\cos\psi$	6.6-25
6.6-13	Comparison of Four-Panel and Two-Panel Solar Array Power Capability at Loads	6.6-32
6.6-14	Efficiencies of 1-Ohm Centimeter and 10-Ohm Centimeter Cells Subjected to Radiation Degradation	6.6-34
6.6-15	Solar Cell Degradation After Two Years.	6.6-38

Figure		Page
6.6-16	One Ohm-Centimeter Solar Cell Degradation versus Orbit Time	6.6-39
6.6-17	Maximum Power Degradation versus Orbit Time	6.6-40
6.6-18	Ten Ohm-Centimeter Solar Cell Degradation versus Orbit Time	6.6-41
6.6-19	Solar Cell Cover Thickness Optimization	6.6-42
6.6-20	Power Distribution Comparison	6.6-51
6.6-21	Power System Block Diagram, Series Regulator	6.6-53
6.6-22	Power System Block Diagram, Series Regulator with Voltage Limiter	6.6-54
6.6-23	Power System Block Diagram, Shunt Regulator	6.6-54
6.6-24	Load Sharing Problems	6.6-55
6.7-1	Coordinate and Normalized Sign Conventions	6.7-5
6.7-2	Primary Structure Model	6.7-6
6.7-3	Results of Feed Support Truss Tradeoff Study	6.7-8
6.7-4	Geometry of the Aft Structure	6.7-10
6.7-5	Tape Drive Deployment System	6.7-50
6.7-6	Solar Panel Latching and Deployment Design	6.7-53
6.7-7	Coordinate Convention and Locations, Deployed Configuration	6.7-58
6.7-8	Coordinate Convention and Locations, Selected Configuration	6.7-59
6.7-9	Coordinate Conventions and Locations, Antenna-Mounted Solar Array Configuration	6.7-70
6.7-10	Response Coordinate Locations, Selected Configuration	6.7-76
6.7-11	Launch Response Coordinate Locations, Deployed Configuration	6.7-77
6.7-12	Typical Electronic Panel, Alternate Approach	6.7-93
6.7-13	Voyager Standard Panel	6.7-95
6.8-1	Antares I (X254AI)	6.8-8
6.8-2	Antares II (X259A2)	6.8-9
6.8-3	Delta Motor (TE-364-3)	6.8-9
6.8-4	Extended Surveyor Motor	6.8-10
7.2-1	ATS-4 Reference Design Ascent Trajectory Ground Trace	7-4
7.2-2	Perigee Burn Description and Orientations	7-5
7.2-3	Apogee Burn-Circularizing and Plane Change Maneuver	7-6
7.4-1	Variation of Injection Longitude with Launch Azimuth, Perigee Burn Crossing, Apogee Burn Opportunity	7-12
7.4-2	Effect of Launch Azimuth on: (1) Apogee Longitude at Injection, λ_I, (2) Additional Apogee Inclination Change, Δi, (3) Corresponding Apogee Velocity Penalty, ΔV	7-12
7.5-1	Perigee Velocity Impulse versus Inclination Change at Perigee	7-19
7.5-2	Apogee Velocity Impulse versus Inclination Change at Apogee	7-19
7.5-3	Variation of Total Velocity Impulse (from 100 nm Circular Parking Orbit to Synchronous Circular Equatorial Orbit) versus Inclination Change at Perigee	7-19
7.5-4	Variation of Perigee Burn Thrust Direction with Inclination Change at Perigee	7-19

LIST OF ILLUSTRATIONS (Cont'd)

Figure		Page
7.5-5	Variation of Apogee Burn Thrust Direction with Inclination Change at Apogee.	7-21
7.5-6	Variation of Required Transfer Orbit Payload with Apogee Burn Velocity Impulse	7-21
7.5-7	Payload Loss, and Inclination Change, of Transfer Orbit as Function of Excess Perigee Velocity	7-22
7.5-8	Payload Determination (Non-Optimum Apogee Motors)	7-23
7.5-9	Determination of Payload Capabilities for Modified Surveyor and Antares I Apogee Motors as a Function of Maximum Centaur P/L Capability.	7-24
7.5-10	Variation of Useful Payload into Synchronous Orbit with Maximum Centaur Capability	7-26
7.5-11	Growth Capability as a Function of Maximum Centaur Capability and Various Retro Motors	7-26
7.5-12	Description of Orbit Injection Error Sources and Vernier Engine Thrust Directions	7-28
7.5-13	Variation of Vernier Velocity Requirements with Apogee Burn Orientation Error	7-38
7.5-14	Variation of Total Payload Weight Cost with Launch Azimuth (or Injection Longitude) and Orientation Errors at Apogee Burn	7-43
7.5-15	Variation of Total Payload Weight Cost with Apogee Motor Orientation Errors	7-43
7.7-1	Variation of Maximum Longitude Excursion with Synchronous Orbit Inclination	7-59
7.7-2	Variation in Maximum Longitude Excursion with Eccentricity or Apogee-Perigee Distance	7-60
7.7-3	Variation of Individual Velocity Impulse Magnitude with Time Duration Between Thrusting	7-62
7.7-4	ΔV Requirement per Year as a Function of Synchronous Position.	7-62
7.7-5	ΔV Required to Zero Out Inclination (Impulse Applied at Nodal Crossing)	7-64
7.7-6	Thrust Inefficiency versus Error in Longitude of Nodal Crossing	7-64
7.7-7	Determination of Uncertainty in Nodal Location	7-67
7.8-1	ATS Ground Station Activity During Vernier Maneuvers.	7-75
8.3-1	Spillover Efficiency and Illumination Efficiency	8.3-4
8.3-2	Composite Patterns Measured on 30-Foot Paraboloid at 1700, 1820 and 1900 MHz	8.3-5
8.3-3	Sidelobe Level Versus Edge Illumination.	8.3-7
8.3-4	Large Aperture Antenna Equal Power Contours at 8.0 GHz Frequency.	8.3-14
8.3-5	Large Aperture Antenna Main Lobe Patterns	8.3-16
8.3-6	Graphic Representation of RF Boresight Measurement Technique	8.3-16
8.3-7	Curve Fitting Angle Data	8.3-17

Figure		Page
8.3-8	Boresight Error Combination Illustration	8.3-18
8.3-9	Thirty-Foot Antenna Gain Measurement Test Set-Up, ATS-4 Experiments	8.3-27
8.3-10	Alternate 30-Foot Antenna Gain Measurement Test Set Up, ATS-4 Experiments	8.3-27
8.3-11	Large Parabolic Antenna Experiment	8.3-34
8.3-12	Typical Receiver	8.3-53
8.3-13	Typical Transmitter	8.3-53
8.7-1	Yaw Axis Stabilization Geometry	8.7-7
8.7-2	Spacecraft Transmit System	8.7-8
8.7-3	Ground Station Circuitry for Transmit Experiment	8.7-9
8.8-1	Operational System Simplified Functional Flow Diagram	8.8-3
8.8-2	Experiment Analysis Reporting Schedule	8.8-26
9.3-1	ATS-4 Major Article Test Flow	9-3
9.7-1	Cape Kennedy Launch Sites	9-26
9.7-2	Launch Complex 36B Gantry Service Tower	9-29

LIST OF TABLES

Tables		Page
4.1-1	Value of ATS-4 Experiments to Operational Missions	4-2
5.2-1	Launch Vehicle Capability	5.2-6
5.3-1	Parabolic Antenna Performance	5.3-19
5.3-2	Orientation Control System Three-Sigma Error Budget	5.3-20
5.3-3	Orientation Control Subsystem Performance Summary	5.3-21
5.3-4	Performance Requirements Summary - Phase-Steered Array Antenna	5.3-22
5.3-5	Interferometer Performance Summary	5.3-23
5.3-6	Interferometer Error Budget	5.3-23
5.3-7	Command and Telemetry Subsystem Capability	5.3-24
5.3-8	Power Subsystem Capability	5.3-26
5.3-9	Detail Weight Summary of Selected Design	5.3-27
5.3-10	Inertia and Center-of-Mass Summary	5.3-28
5.4-1	Parabolic Antenna Experiment Loss Budget	5.4-13
5.4-2	Comparison of Feed System Requirements	5.4-35
5.5-1	Error Budget	5.5-7
5.5-2	Weight and Power Summary for Initial Acquisition and Orientation Control Subsystems	5.5-8
5.5-3	Station Acquisition Impulse Requirements	5.5-10
5.5-4	Mass Expulsion Subsystem Requirements for Orientation Control and Stationkeeping	5.5-37
5.5-5	Component Description	5.5-46
5.5-6	Impulse Requirements for Station Acquisition and Despin Mass Expulsion Subsystem	5.5-52
5.5-7	Station Acquisition System Weight	5.5-58
5.5-8	Resistance Jet System Weight	5.5-76
5.5-9	Command Requirements	5.5-78
5.5-10	ATS-4 Telemetry Requirements	5.5-79
5.5-11	O/C Component Mounting, Alignment and Field of View Requirements	5.5-86
5.6-1	Large Parabolic Antenna Experiment Equipment Characteristics	5.6-5
5.6-2	Geometric Instrumentation	5.6-12
5.6-3	Weight and Power Estimates for the Interferometer System	5.6-26
5.6-4	Major Characteristics of Phase-Steered Array Antenna System	5.6-31
5.7-1	Telemetry Requirements	5.7-3
5.7-2	Significant Reference Configuration Parameters	5.7-5
5.7-3	Margin Calculations-Telemetry Data	5.7-23
5.7-4	Margin Calculations-Tracking	5.7-24
5.7-5	Margin Calcularions-Command Link	5.7-25
5.7-6	Summary of Component Power, Weight and Size	5.7-26
5.7-7	Summary of Design Status	5.7-32
5.8-1	Summary of Array Power and Energy Capability	5.8-12
5.8-2	Battery Depths of Discharge for New and Old Arrays	5.8-21
5.8-3	Summary of Power Conditioning Equipment Operating Efficiencies	5.8-33
5.8-4	Summary of Power Subsystem Weights and Sizes	5.8-34
5.8-5	Summary of Power Conditioning Equipment Thermal Dissipations	5.8-37
5.9-1	Atlas/Centaur Qualification Test Specifications	5.9-9

LIST OF TABLES (Cont'd)

Tables		Page
5.9-2	Payload Capability Using TE-364-3 Improved Delta Motor	5.9-16
5.9-3	Performance and Physical Data on the Improved Delta Motor (TE-364-3)	5.9-18
5.9-4	Performance Parameters for Optimum Motor Extended Surveyor	5.9-19
5.9-5	Summary of Spacecraft Design Constraints and Significance to Selected Design	5.9-22
5.9-6	Major Structural Elements	5.9-27
5.9-7	Structure Weight Summary	5.9-39
5.9-8	Response Accelerations to Base Excitation.	5.9-52
5.9-9	Comparison of Analog Simulation Transfer Functions with Transfer Functions used for Selected Configuration	5.9-55
6.2-1	Launch Vehicles Comparison	6.2-9
6.2-2	Titan III C-Flight Loads Environment	6.2-12
6.2-3	Summary of Maximum Measured Flight Loads (Atlas/Centaur Flight AC-2 to AC-6)	6.2-21
6.2-4	Deployed Antenna Frequency Comparison	6.2-31
6.2-5	Performance of Deployed Configuration.	6.2-52
6.2-6	Deployed Configuration Weight Summary	6.2-53
6.2-7	Deployment System Comparison	6.2-67
6.3-1	Comparison of Space Deployable Antennas	6.2-23
6.3-2	ATS-4 Structural Parameters	6.3-29
6.3-3	Mechanical Properties of Aluminum and Titanium	6.3-34
6.3-4	Effect of Temperature on the Tensile Strength of FM-1000 Adhesive Bonded Aluminum Honeycomb Panels.	6.3-37
6.3-5	Effect of Temperature and Vacuum on the Tensile Strength of FM-1000 Adhesive Bonded Aluminum Honeycomb Panels.	6.3-38
6.3-6	Estimate of Mass Properties	6.3-59
6.3-7	Maximum Compression Load Launch Condition	6.3-68
6.3-8	Truss Member Loads.	6.3-94
6.3-9	Directional Displacements for Structural Joints (1 of 6) thru (6 of 6)	6.3-123
6.3-10	Feed Thermal Displacements	6.3-131
6.3-11	Antenna Loss Budget No. 1	6.3-154
6.3-12	Antenna Loss Budget No. 2	6.3-155
6.3-13	Antenna Loss Budget No. 3	6.3-156
6.3-14	Final Configuration Loss Budget	6.3-171
6.4-1	Body Rate and Acceleration Amplitude for Practical Sensor Locations	6.4-35
6.4-2	Atlantic Research Corporation Spinup Motor Data	6.4-42
6.4-3	Atlantic Research Corporation Motor Data.	6.4-44
6.4-4	Spacecraft Parameters Associated with On-Station Disturbance Torque Computation.	6.4-55
6.4-5	Sun Stabilization System Nomenclature	6.4-88
6.4-6	Sun Stabilization System Parameter Values	6.4-89

Tables		Page
6.4-7	Three-Sigma Error Budget Data	6.4-114
6.5-1	136 HMZ TLM (Carrier and Data)	6.5-2
6.5-2	Position and Velocity Error	6.5-5
6.5-3	Antenna Configuration Tradeoff For Alternate Design Configuration	6.5-8
6.6-1	Yearly Integrated Intensities of Solar Cosmic Rays	6.6-4
6.6-2	Abundancy of Cosmic Rays	6.6-5
6.6-3	Power Equation Factors for Various Array Configurations $P = K(A_T)(K_G) F_T F_S$	6.6-26
6.6-4	Array Area Requirements for Various Configuration (300 watt maximum array)	6.6-29
6.6-5	Maximum Power Required from Battery-Watt Hours	6.6-44
6.6-6	Battery Sizing and Performance	6.6-46
6.6-7	Time and Power Required to Recharge Batteries (33 A-HRS)	6.6-49
6.6-8	Power Distribution Weight Comparison	6.6-52
6.6-9	Power Conditioning Equipment Weight Summary	6.6-56
6.6-10	Power Systems Comparison Summary	6.6-60
6.7-1	Ultimate Launch Loads (g)	6.7-2
6.7-2	Separation Device Tradeoff Chart	6.7-56
6.7-3	Sinusoidal Vibration Testing Specifications	6.7-59
6.7-4	Transfer Functions for ATS-4 Configuration with Antenna-Mounted Solar Arrays	6.7-72
6.7-5	Maximum Acceleration Due to Unit Load or Moment Impulse at Point One on Deployment Column	6.7-72
6.7-6	Antenna with f/D = 0.4	6.7-75
6.7-7	Frequency Shift with f/D Variation	6.7-75
6.7-8	Launch Accelerations for the Selected and Deployed Configuration Due to A1 g or RAD/sec^2 Input	6.7-77
6.7-9	Mass Distributions	6.7-78
6.7-10	Frequency Comparison Selected and Deployed Feed Configuration	6.7-81
6.7-11	Dirac Delta Response Comparison	6.7-82
6.7-12	Control Transfer Functions	6.7-84
6.7-13	Transfer Functions for Gravity Gradient Rods	6.7-86
6.8-1	Payload Capability Using TE-364-3 Delta Motor	6.8-3
6.8-2	Apogee Motor Tradeoff Matrix	6.8-4
6.8-3	Physical and Performance Data of Six Motors Considered	6.8-7
6.8-4	Data on Candidate Apogee Motors	6.8-7
6.8-5	Apogee Motor Puff Chart	6.8-12
7.2-1	Sequence of Events	7-3
7.4-1	Perigee of Transfer Orbit at First Equatorial Crossing of Parking Orbit	7-11
7.4-2	Perigee of Transfer Orbit at Second Equatorial Crossing of Parking Orbit	7-11

LIST OF TABLES (Cont'd)

Tables		Page
7.5-1	Summary of Total Vernier Maneuver Impulse Requirements	7-27
7.5-2	Vernier Weight Tradeoff Summary	7-42
7.5-3	Injection Bias Summary (θ_ϵ = 1 degree)	7-52
7.7-1	In-Orbit Stationkeeping Velocity Requirements	7-66
7.7-2	Orbit Determination Summary	7-69
8.3-1	Individual Experiments - Parabolic Antenna	8.3-20
8.3-2	Required Signal Characteristics - Parabolic Antenna Measurements	8.3-42
8.3-3	Gains and Beamwidths - Perfect 30-Foot Parabolic Antenna	8.3-43
8.3-4	System Performance Parabolic Antenna Transmission Measurements.	8.3-45
8.3-5	System Performance Gain Standard Antenna Transmission Measurements	8.3-45
8.3-6	System Performance Parabolic Antenna Receiving Measurements	8.3-45
8.3-7	Limiting Power and Bandwidth Requirements Parabolic Antenna	8.3-48
8.3-8	On-Board Equipment Characteristics Parabolic Antenna Measurements.	8.3-49
8.3-9	Experiment Equipment Summary	8.3-55
8.4-1	Individual Experiments - Orientation Control System	8.4-3
8.5-1	Individual Experiments - Interferometer	8.5-2
8.5-2	Interferometer Telemetry Monitoring Signals	8.5-6
8.6-1	Individual Experiments - Phased Array Antenna	8.6-6
8.6-2	System Performance Steered Phase Array Antenna-Transmission and Reception Measurements (RF Bandwidth: 30 MHz)	8.6-21
8.7-1	System Performance High Data Rate Meteorological Sensors - Satellite to Surface (10 GHz; TV Data Rates).	8.7-11
8.7-2	Weight and Power Requirements of Sensors and Optics.	8.7-13
8.7-3	Transmission Link Characteristics Audio FM Broadcast to Home TV Receiving Sets	8.7-15
8.7-4	User Accessibility Versus Field Strength	8.7-17
8.7-5	Field Strength Versus On-Board Radiated Power.	8.7-17
8.7-6	Limited Area Audience Experiment	8.7-18
8.7-7	TV Broadcast Configurations Link Calculations	8.7-19
8.7-8	System Performance MOL Relay - MOL to Satellite - TV Bandwidths	8.7-24
8.8-1	Experiment and Ground Station Capability Tradeoffs	8.8-6
8.8-2	Required and Recommended Transmitting/Receiving Frequencies for Ground Stations	8.8-8
8.8-3	ATS-4 Operational Ground Station Configuration Matrix Assuming Additional ATS-4 Antenna at Rosman	8.8-10
8.8-4	ATS-4 Operational Ground Station Configuration Matrix Assuming One Antenna Per Station with Interchangeable Feeds	8.8-13
8.8-5	Operational Integration of Experimental Tasks, Facilities and Schedule.	8.8-15

LIST OF TABLES (Cont'd)

Tables		Page
8.8-6	Experiment Combinations	8.8-18
8.8-7	Contingency Matrix	8.8-25
9.2-1	Ground Support Summary Matrix	9-2
9.4-1	Equipment List (MSE)	9-15
9.5-1	Equipment List (ESE)	9-21
9.8-1	Ground Station Equipment Requirements Summary	9-30
9.9-1	ATS-4 Computer Program Requirements	9-33

SECTION 6

SPACECRAFT TRADEOFF AND ANALYSIS

6.1 INTRODUCTION

Early in the tradeoff studies, it became apparent that the interrelated selection of launch equipment and spacecraft configurations could only be resolved through the development of prime experiment concepts most capable of meeting the contract requirements. The best example of this is the parabolic antenna experiment. An industry-wide survey of potential antenna concepts indicated that only a rigid petal design would approach meeting the high system efficiency (≥ 50 percent) requirement at the high operating frequencies. The packaging geometry of rigid petal antennas is the most significant factor in establishing a launch vehicle fairing selection criteria. Additionally, the high-efficiency antenna requirement dictates a minimum rf blockage criteria for the spacecraft design. Similarly, the development of each of the other prime experiment concepts identified additional selection constraints, many of which were conflicting. System and subsystem tradeoff iterations resolved many of the conflicts but the actual selection of configurations involves compromises in operational performance, design complexity, and cost.

The selected configuration presented in Section 5 was optimized to the SLV-3C/Centaur launch vehicle, TEM-364-3 apogee motor, and extended (15 feet) Surveyor fairing. Many spacecraft configurations were developed during the study. Some of these offered the potential of significantly shorter fairing extensions and/or better system rf performance. However, each of these introduce additional design or operational complexity which would have to be traded off against development cost or performance goals. Optimization of rf and system performance, deployment reliability, and low development cost were the major factors in the configuration study. Minimization of fairing extensions was a major tradeoff object. However, during the study the NASA/GSFC Program Manager concluded that a 15-foot extension to the Surveyor fairing would be available for the ATS-4 launch period. Most of the spacecraft configurations which were in evaluation could be packaged within the selected fairing, and fairing extension minimization was no longer a major consideration.

This section of the report presents a discussion of the system and subsystem tradeoff considerations which led to the selection of the preferred spacecraft approach and identifies an alternate approach which offers slightly better rf performance at the expense of deployment complexity. The in-depth design analyses which substantiate the selected configuration performance are also included in this section.

6.2 CONFIGURATION SELECTION

The configuration studies were performed within the framework of satisfying the basic mission requirements and design goals with maximum performance and margin available for growth.

The two most significant influences on the design were the parabolic antenna, both from a mechanical and an rf performance point of view, and the restraints imposed by the candidate launch vehicle and shroud systems. Because of the extreme sensitivity of the design to these factors, iterations and revised ground rules forced radical changes in configuration approaches, in many cases, obsoleting "preferred" approaches at a point in time where detail design analysis was commencing. This necessitated that a much larger portion of the study phase be devoted to configuration studies than originally planned. However, the beneficial result has been a comprehensive study of all feasible spacecraft configurations, the scope of which gives confidence that the selected configuration best meets the basic ATS-4 mission requirements.

6.2.1 APPROACH TO CONFIGURATION SELECTION

The ATS-4 mission requires demonstration of four prime experiments: (1) the parabolic antenna, (2) the phased array, (3) an interferometer experiment, and (4) an orbit control system. All must vie for valuable unobstructed earth viewing. For the latter three experiments, this creates no particular problem. However, the multitude of design approaches, potentially feasible for the parabolic antenna and major "housekeeping" subsystems, when added to the desire to investigate three separate launch vehicle and fairing systems, leads to an almost infinite number of candidate spacecraft configurations. In order to proceed in an orderly manner, the extent of the influence on the design of each of the system's elements had to be evaluated. Basically, the design variables were classified into three categories as follows:

a. Launch Vehicle Considerations (Discussed in Section 6.2.2). These are the basic constraints that are applicable to all configurations. Selection of preferred approaches is on a system basis; therefore, these variables are fixed constraints of competing designs.

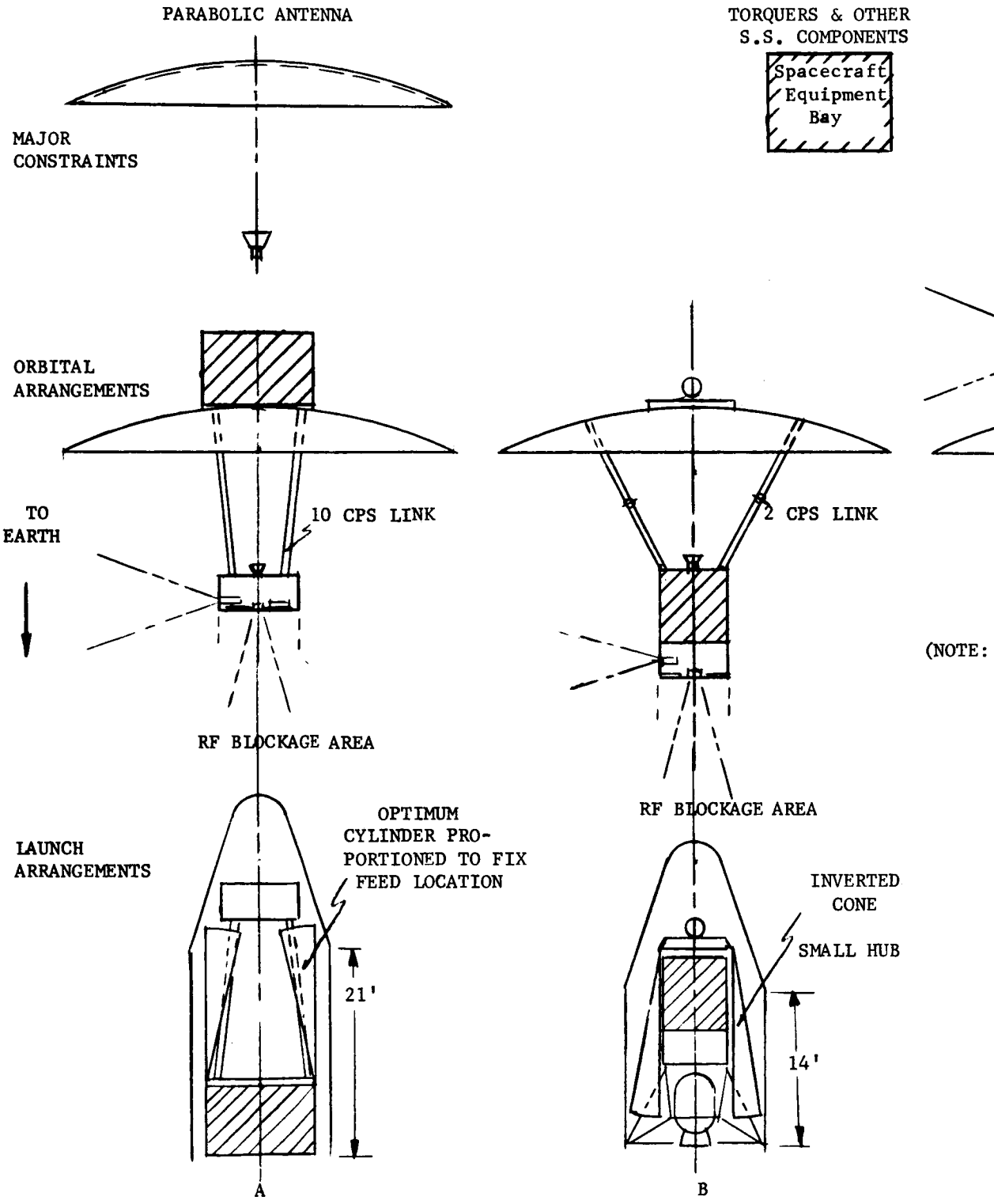
b. Primary Configuration Influencing Approaches. These are basic subsystem alternatives which have the most influence on the design. Basic decisions on the selection of the preferred approach are required prior to formulation of conceptual designs. Examples of these alternatives are the various antenna approaches discussed in Section 6.3 and the orientation control system philosophy.

c. Secondary Configuration Influencing Approaches. These subsystem alternatives have a more subtle effect on the design, and are basically areas of optimization studies which can be performed wholly within the concept of a particular configuration. The selected approach may alter the configuration slightly, but not to the extent of forcing an entirely different conceptual approach. Examples of these factors are solar array configuration approaches as reported in Section 6.6 and the apogee motor selection presented in Section 6.8.

Concurrent with subsystem selection approaches, basic spacecraft arrangements were investigated from the standpoint of offering unobstructed earth-viewing area to the four prime experiments. Initially this effort was designed to give some bounds to the subsystem selection; however, it was apparent that in many instances the selection between some subsystem alternatives could only be performed on an overall system basis.

The phased array, orientation control sensors, and interferometer, which can be readily packaged into one reasonably-sized earth-viewing area; the parabolic antenna; and an additional spacecraft equipment section form the basic building blocks for the configuration. The most likely spacecraft arrangements, and the constraints exerted by the major experiments, are schematically depicted in Figure 6.2-1. It was planned that the configuration evolution process would progress by factoring into each conceptual arrangement the most promising design approaches for the major subsystems until three competing designs remained. These three designs would then be studied in more detail in order to select the configuration which best met the ATS-4 requirements. This approach was followed with the

MAJOR INFLUENCE - EARTH ORIENTATION OF MAJOR EXPERIMENTS



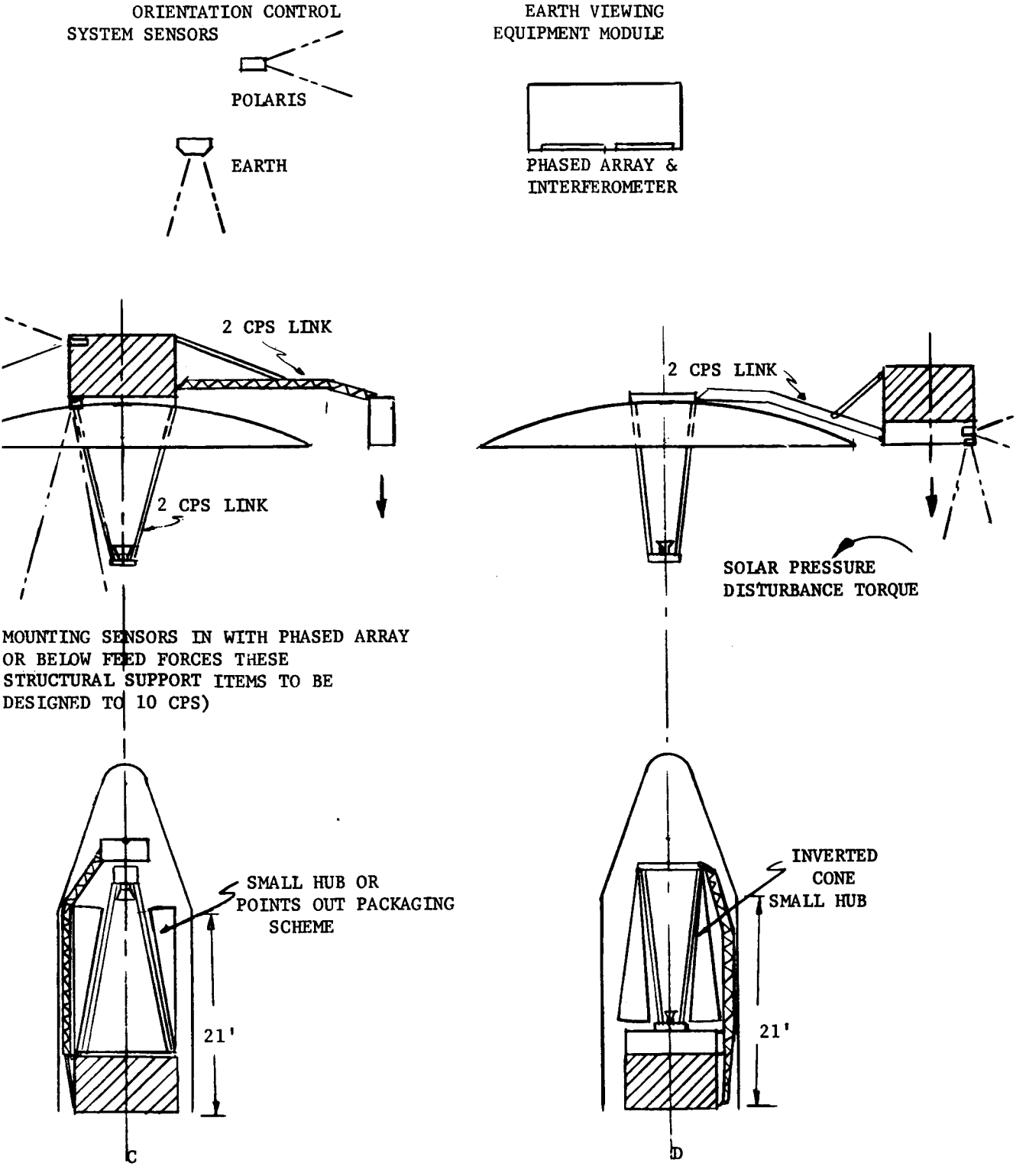


Figure 6.2-1. Basic Spacecraft Arrangements Used in Configuration Tradeoff Studies

development of early designs discussed in Sections 6.2.3 and 6.2.4, leading to the preliminary selected configuration, discussed in Section 6.2.5, which was based on superior antenna rf performance and a compact launch configuration featuring structural rigidity and a minimum shroud extension. Subsequent to this selection another configuration was developed. This new design featured a fixed feed and was predicated by the following factors:

a. The emphasis on optimum rf performance was reduced in favor of simplicity of deployment.

b. Rf far-field tests were performed which indicated that the rf losses due to blockage and reflectance of fixed-feed support structure were not as severe as earlier near field tests indicated. In addition, these tests showed that diagonal truss structure, with members off-axis to the beam, did not induce higher rf losses than on-axis structural arrangements.

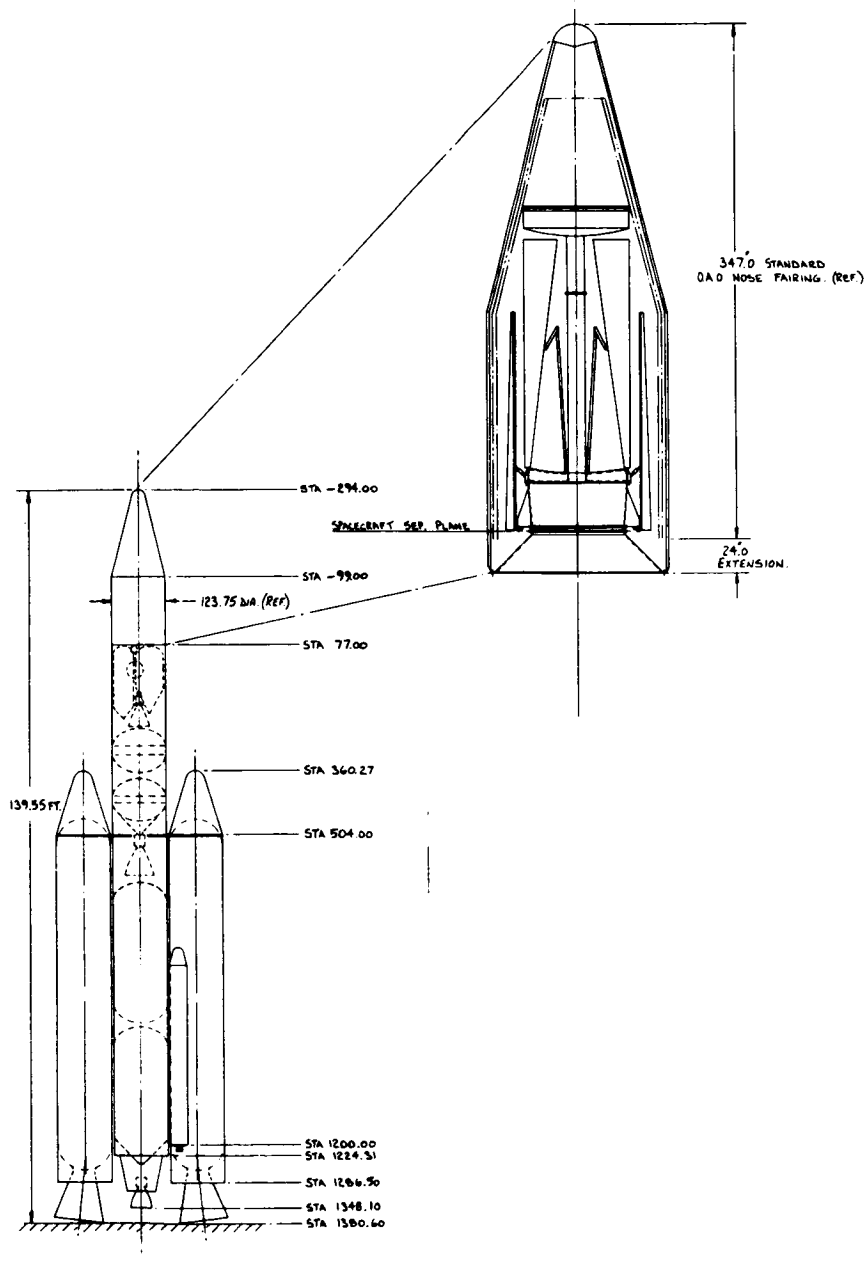
c. The emphasis on shroud minimization was reduced with the clarification that the 15-foot shroud extension was not a maximum allowable length but a 1969/70 probability.

This fixed-feed configuration was selected as the most suitable for the overall ATS-4 mission.

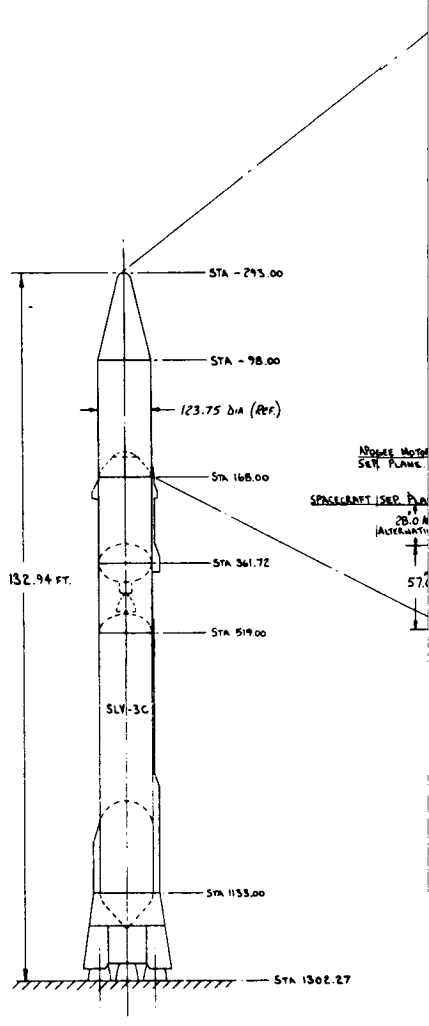
Modifications to the selected configurations to make it applicable to other apogee motors, as well as launch vehicle interface characteristics, are discussed in Section 6.2.6.

6.2.2 LAUNCH VEHICLE CONSIDERATIONS

The three competing launch vehicle systems to be considered in the ATS-4 design are shown in Figure 6.2-2. During the study it became apparent that a tightly constrained design was required for an Atlas/Agena launch; however, designs tailored for the Centaur, while not optimum for Titan, were representative of potential Titan-launched spacecraft designs. A tabular comparison of the launch vehicles is shown in Table 6.2-1. In the tradeoff comparisons, cost was heavily weighted, and, as such, use of the Atlas Agena was desired. However, in view of its low payload capability and limiting fairing dimensions, it was



TITAN III C



ATLAS / CENTAUR COMBI

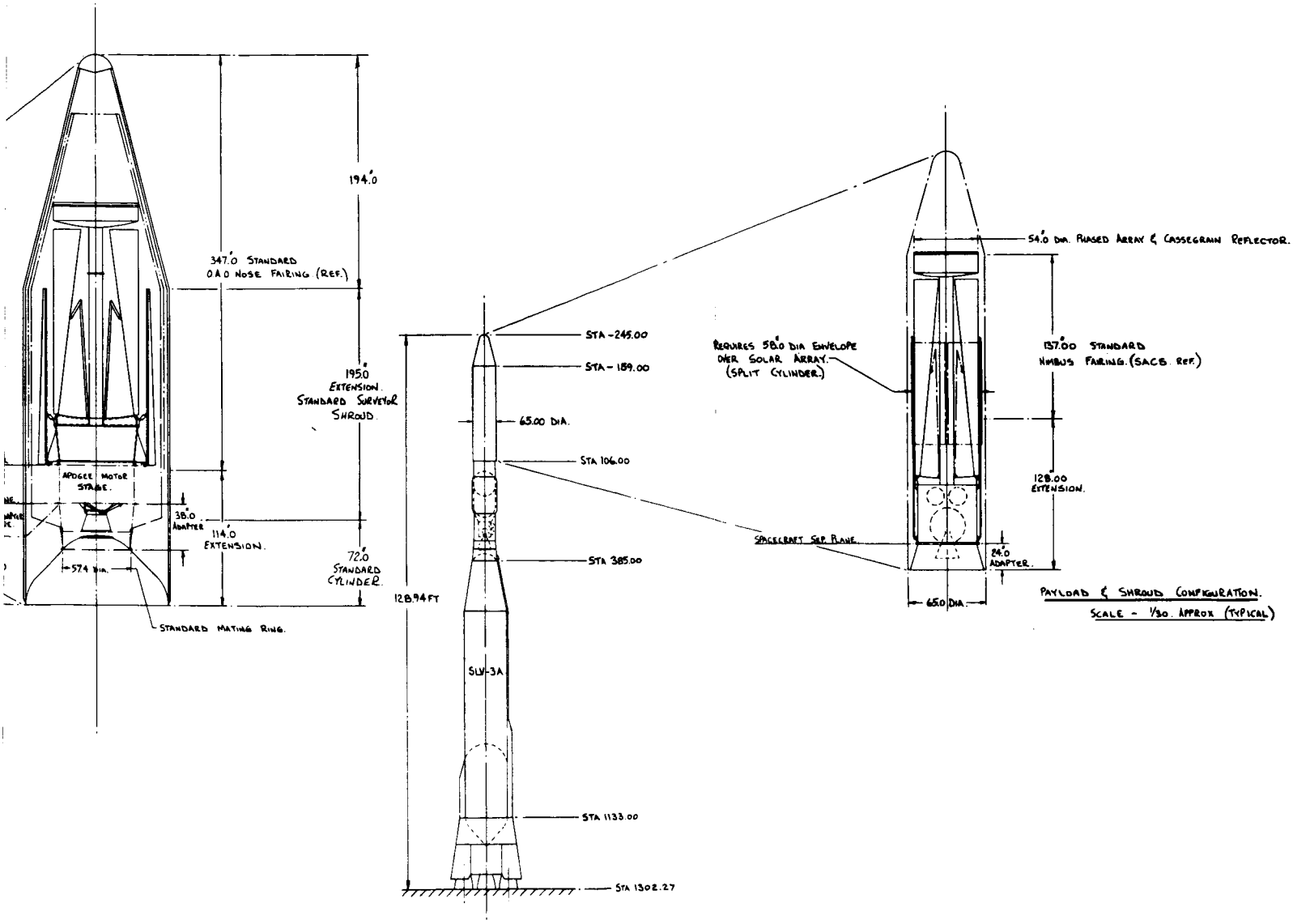


Figure 6.2-2. Candidate Launch Vehicles and Early Conceptual Approaches

eliminated early from further consideration. The Centaur booster has the capability of meeting ATS-4 requirements and, though requiring an apogee motor and the associated coast period control equipment, it is recommended over the costlier Titan III-C.

Table 6.2-1. Launch Vehicles Comparison

	SLV-3A AGENA	SLV-3C/ CENTAUR	TITAN III C
Payload Capability			
In Orbit	1060 lb	1990 lb	2100 lb
Transfer	2270 lb	4000 lb	---
Available Fairings	SACS	SURVEYOR	OAO
Dimensions	(NIMBUS)		
Payload diameter fairing length	~56 in. I. D. 223 in. Long	~110 in. I. D. 265 in. Long	~110 in. I. D. 347 in. Long
Maximum Allowable Fairing Extensions	~5 ft	15 ft	~12 ft
Launch Constraints	--- ---	25 Min. Coast	6-1/2 hr Transstage Life
Cost	$ 7.9M	$ 13.4M	$ 17.6M

6.2.2.1 Atlas/Agena-D Launch Vehicle

To determine the restrictions imposed on the spacecraft by the launch vehicle, the entire family of Atlas/Agena-D vehicles were investigated. Much of the information was obtained from General Dynamics/Astronautics prior to the designation of NASA/Lewis as the authority on launch vehicle performance and design parameters. In order to efficiently package the rigid petal antenna, it was hopeful to use the OAO shroud with an uprated version of the modified SLV-3 which launched the OAO vehicle. However, the only uprated Atlas specifi-

cally designed for use with the Agena upper stage is the SLV-3A. Use of the OAO shroud with this vehicle is not practical, since the tapered interstage adapter would have to be redesigned to accommodate the shroud; also, the aft shroud section would be longer than with the OAO vehicle.

As later reiterated by NASA/Lewis, the Standard Agena Clamshell (SACS) was the only shroud economically feasible both from cost and payload in-orbit capability to consider with the SLV-3A/Agena-D vehicle. This shroud imposes a diameter restriction on the payload of approximately 56 inches. In order to package a cylindrically folded pre-formed 30-foot rigid reflecting surface, an additional foot of shroud length is required for antenna alone. A conceptual design developed for use with this vehicle required a much longer extension in order to package all the spacecraft elements, since the narrow diameter forces a stacked arrangement of components. NASA/Lewis cautioned that no performance analysis had been performed for extended versions of the SACS shroud, and while a 5-foot extension did appear possible, longer extensions were not practical without at least some rework of selected portions of the launch vehicle's structural system. Therefore, the Atlas/Agena-D was deemed a desirable launch vehicle only for spacecraft employing antennas with nonrigid reflecting surfaces which could be packaged into low silhouette volumes, which was not compatible with the system selection of a rigid surface interlocking petal antenna. Furthermore, the 1060-pound payload in-orbit capability forced a minimum experimental subsystem, leaving no room for growth and redundancy. System development costs would probably increase in order to develop minimum weight structural approaches, microminiaturization of cricuitry, and other lightweight subsystem items.

In view of the preceding information, it appeared that the SLV-3A/Agena-D was not compatible with the ATS-4 mission objectives, and the development of an Atlas/Agena spacecraft design was not pursued further than the initial conceptual stage.

6.2.2.2 TITAN III-C Launch Vehicle

The data presented in the following paragraphs have been obtained through direct contact

with the Martin Company and from SSD-CR-65-18 (Revision 1), the Titan III definition for payload contractors.

Initial interest in the Titan III launch vehicle was centered about the use of a Titan bulbous shroud, which would allow a broader choice of antenna schemes. However, in view of a development cost of 5 million dollars for a 12- to 15-foot diameter shroud, the 10-foot diameter OAO shroud is recommended. Trajectory analysis performed by the Martin Company indicated that shroud cylindrical lengths of 25 feet could be flown with no significant reductions in either launch availability of payload in orbit capability, since the flight trajectory from ETR is restricted in order for the first stage to subrange Africa.

The Titan III-C features a 10-foot diameter mating ring with eight tie-down bolts. The environmental constraints, given in Table 6.2-2 are less severe structurally than the Atlas/Centaur specifications. It is apparent then, in consideration of like shroud dimensions, potentially compatible mating ring provisions, and the loads environment, that any spacecraft configuration developed for Centaur can be adapted to the Titan.

Therefore, in view of the cost effectiveness of the Centaur and the fact that no radical configuration approaches or design concepts are required for Titan flights, the major emphasis in the study was the development of a minimum weight, minimum cost spacecraft, the successful accomplishment of which has ruled out the Titan III-C as a mandatory requirement.

6.2.2.3 SLV3C/Centaur Launch Vehicle

6.2.2.3.1 Fairing/Selections

The initial studies with this launch vehicle also considered use of a modified OAO fiberglass fairing. This was in keeping with General Dynamic/Astronautics and the Martin Company's desires to adapt this lightweight, flight-proven fairing for future use with their respective launch vehicles.

Table 6.2-2. Titan IIIC - Flight Loads Environment

Accelerations

Based on 2200-lb Payload

Longitudinal Accelerations (Sustained)

Step 0	3.26 g
Step 1	4.18 g
Step 2	2.90 g
Step 3	0 to 1.68 g

Lateral Accelerations

Low cycle sinusoidal 0.4 g peak - 0 to 10 cps

Vibratory Accelerations

Sinusoids 0.25 g (0 to peak) Between 9 & 19 (Narrow band filtered data)

Random Overall Level 7.6 g rms
For payloads in excess of 2000 lb

Frequency	g^2/cps
10 to 22	0.015 to 0.033
22 to 180	0.033
180 to 530	0.033 to 0.1 g^2/cps
530 to 1000	0.1 g^2 cps
1000 to 2000	0.1 g^2 cps to 0.025

NASA/Lewis' selection of the heavier Surveyor shroud was based on a superior separation and jettison system and the fact that the Surveyor shroud was flight-qualified as part of the Atlas/Centaur launch system. Since both shrouds are 10 feet in diameter, the selection had no influence on configuration arrangement. It did however, introduce a design philosophy which has been strictly adhered to in the study effort, namely, that of maintaining as many of the features of the qualified Surveyor launch vehicle as possible.

A maximum fairing extension of 15 feet has been allowed, which gives a maximum overall fairing length of 445 inches.

6.2.2.3.2 Launch Availability

The effect of a shroud extension on the launch vehicle's structural capability is measured in terms of reduced launch availability, which is an expression of the probability that flight-induced loads (as a function of wind profile and pitch programs) will be within the boosters structural and guidance capability. For the SLV3C/Centaur, the design limitation is the bending moment strength across the Atlas main tank walls. Launch availability percentages are calculated below for both the selected design and the alternate deployed configuration, which utilized a shroud with only an 8-foot extension. In order to use the launch availability data in the General Dynamics/Astronautics' Centaur capability handbook prepared specifically for the Surveyor spacecraft, the difference in bending moments between the ATS-4 flight vehicle and the Surveyor launch vehicles is calculated.

SLV-3C bending moment capability $= 7.1\ (10)^6$ in.-lb

(Based on post buckling strength capability determined by NASA/Lewis tests)

The partial of bending moment with respect to increased fairing length is

$$\frac{\partial\ BM}{\partial\ L} = 0.84 \times 10^4 \text{ (in.-lb)/in.}$$

including both aerodynamic and inertial forces.

The bending moment is reduced however, by an inertial relief caused by the payload being acted upon by an acceleration opposite to that of the launch vehicle. A Surveyor weight of 2100 lb, CG location 55 inches above the base, and a 700-inch moment arm to the critical section from the CG are used in conjunction with a 0.06 g lateral load to determine the increase in inertial relief obtained from the longer, heavier, ATS-4 spacecraft.

Case 1 - Configuration with 8-foot shroud extension

Cylindrical Length	=	14 feet total
Payload Weight	=	4000 pounds
CG Actual	=	81.6 inches above Station 172.45 base; distance from critical Atlas station = 726.6 inches

Bending mement increase $\Delta BM_A = \frac{\partial\ BM}{\partial\ L}\ (\Delta L)$

$$\Delta BM_A = 0.84\,(10)^4\,(96) = 0.81\,(10)^6 \text{ in-lb}$$

Inertia Relief:

$$\Delta BM_R = \left|(\text{Wt})\,(\text{arm}) - \text{Surveyor}\,(\text{wt})\,(\text{arm})\right| \left[\text{lateral g}\right]$$

$$\Delta BM_R = \left|4000\,(726.6) - 2100\,(700)\right| \; 0.06\,g = 0.09\,(10)^6 \text{ in.-lb}$$

Total Bending Moment Increase

$$\Delta BM_T = \Delta BM_A - \Delta BM_R$$

$$\Delta BM_T = 0.81 - 0.09 = 0.72\,(10)^6 \text{ in.-lb}$$

Case 2 - Selected Configuration

Cylindrical Length	=	21 feet (15-foot extension)
Payload Weight	=	3350 pounds
CG	=	92.6 inches above base distance; from critical Atlas station = 742.6 inches

$$\Delta BM_A = 0.84\,(10)^4\,(180) = 1.51\,(10)^6 \text{ in-lb}$$

Inertial Relief

$$\Delta BM_R = \left|3350\,(742.6) - 2100\,(700)\,(0.06\,g)\right| = 0.06\,(10)^6 \text{ in.-lb}$$

$$\Delta BM_T = 1.51 - 0.06 = 1.45\,(10)^6 \text{ in.-lb}$$

The curve shown in Figure 6.2-3 gives launch availability in percent versus the limit bending moment for monthly expected wind profiles. The curves are based on the two different pitch profiles used during the winter and summer months. Line A designates the current Surveyor/Atlas/Centaur capability and lines B and C show the reduction for the deployed configuration and the selected configurations. From this curve it is determined the minimum launch availability for the selected configuration is 45 percent in January and February, with a maximum value of 97 percent being obtained during the favorable summer months.

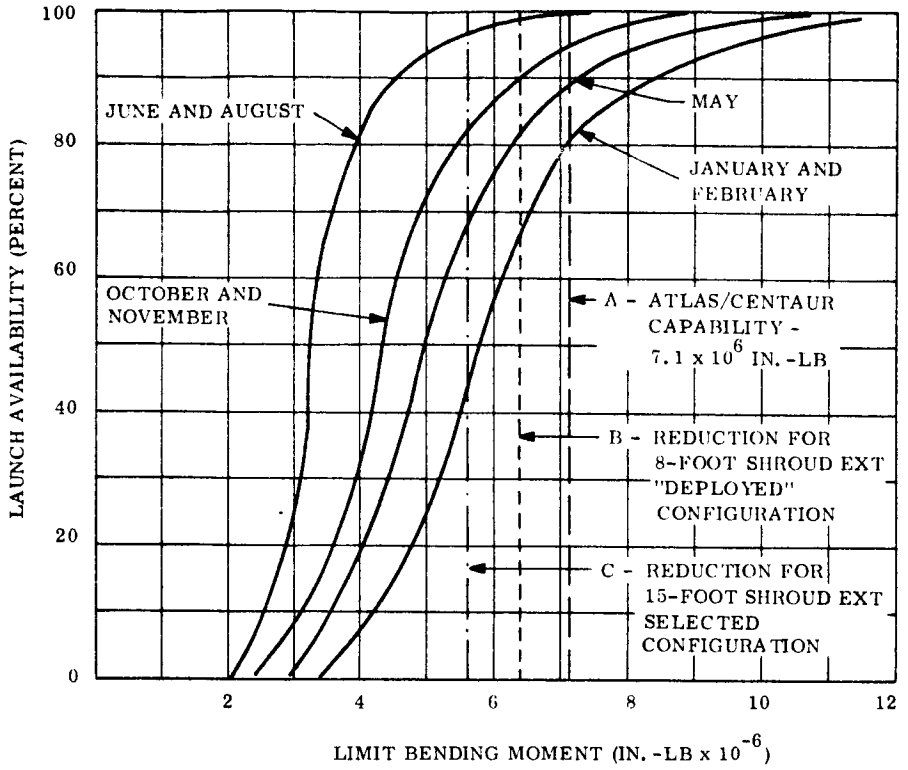


Figure 6.2-3. Launch Availability vs Limit Bending Moment

Launch availabilities of 67 percent and 98 percent, respectively can be expected for the deployed configuration. These values are comparable to Surveyor's prior to the introduction of the increased buckling strength. In view of the day-to-day unrestricted launch window for the ATS-4 mission, the increased fairing length is not detrimental. Launch availability reductions can also occur from engine deflection limitations; however, this is not limiting, in that bending moment strength restrictions as induced by increased shroud length are always the most severe.

The substantiating analysis is shown below for the selected design.

$$\Delta S_\theta = 0.45 \times 10^{-6} \Delta BM$$

where ΔS_θ is the reduction in pitch angle

$$\Delta S_\theta = 0.45 \times 10^{-6} (1.45) (10)^6$$

$$= 0.65^o$$

and 0.45×10^{-6} is a conversion factor.

From the curve shown in Figure 6.2-4 it is determined that the reduction in launch capability is only 9 percent due to engine deflection constraints.

6.2.2.3.3 Static and Dynamic Clearance

The static and dynamic payload envelopes have been derived for the extended version of the Surveyor shroud using the Surveyor payload envelope (Convair-Astro drawings 55-00050 (SHT. -1, Rev. Z and SKC-2) received from NASA/Lewis as a reference. These have been shown in Section 5 and are repeated in Figure 6.2-5. In view of the ease of encountering clearance problems with large flexible structures, a conservative approach has been

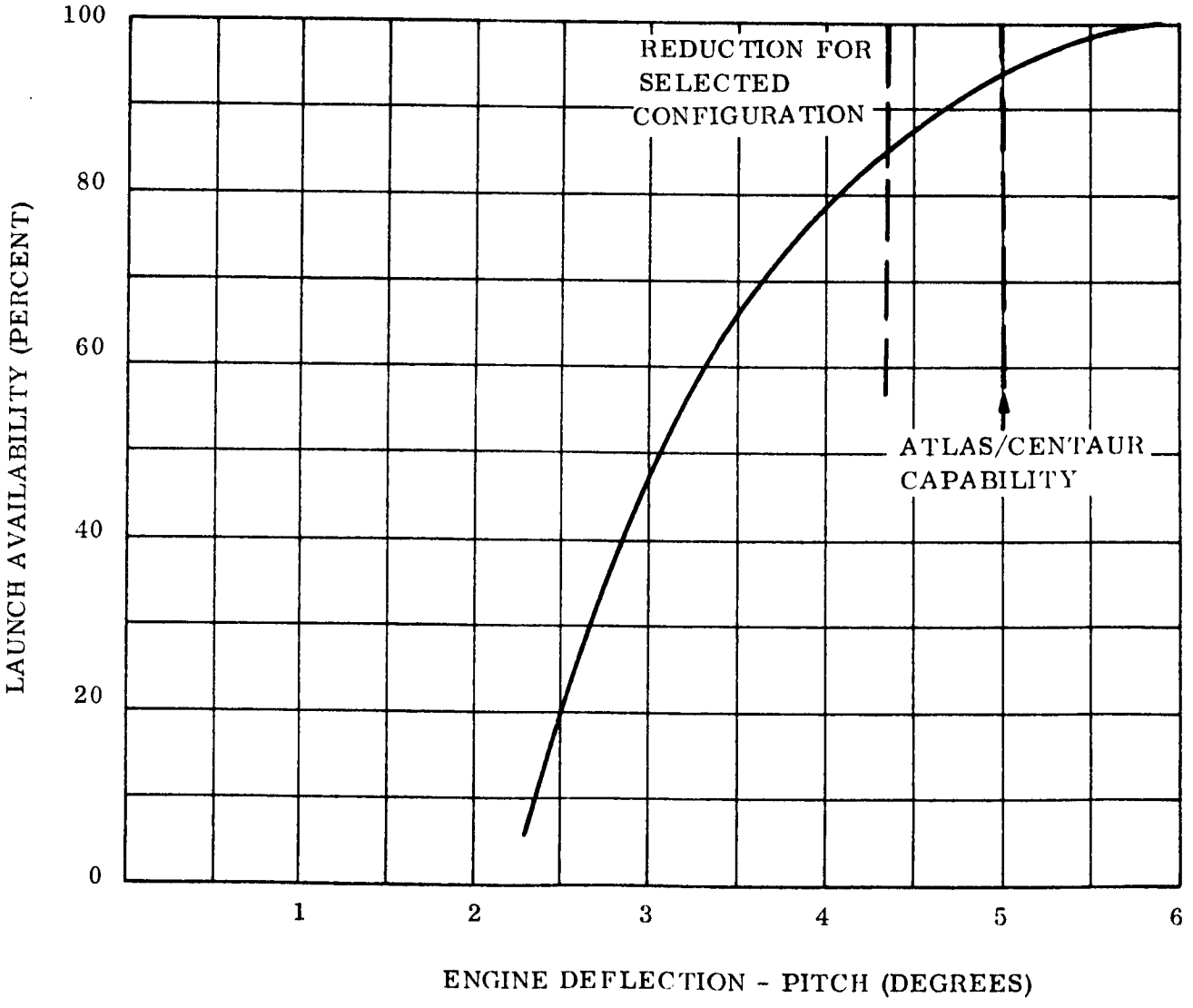
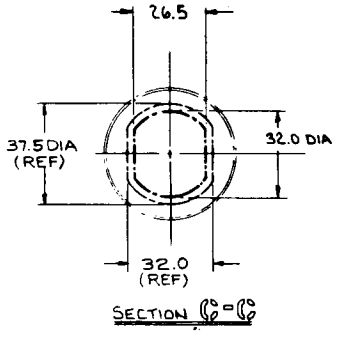
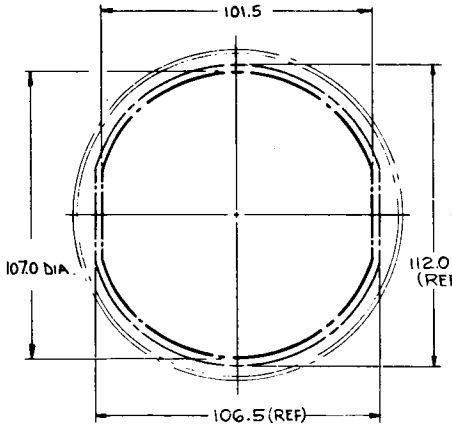


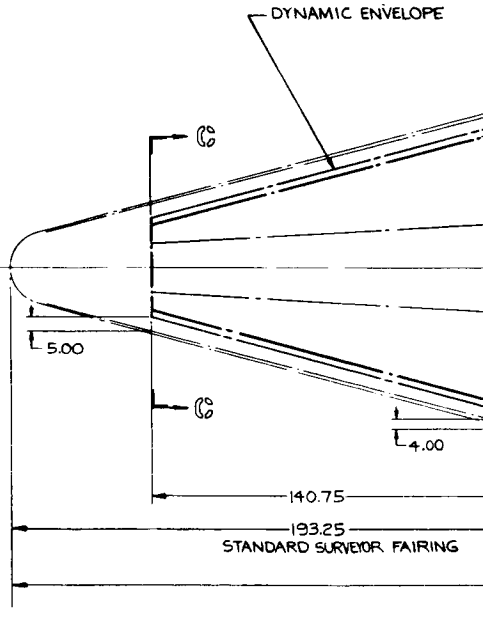
Figure 6.2-4. Launch Availability vs Engine Deflection



SECTION ℄ = ℄



SECTION B = B



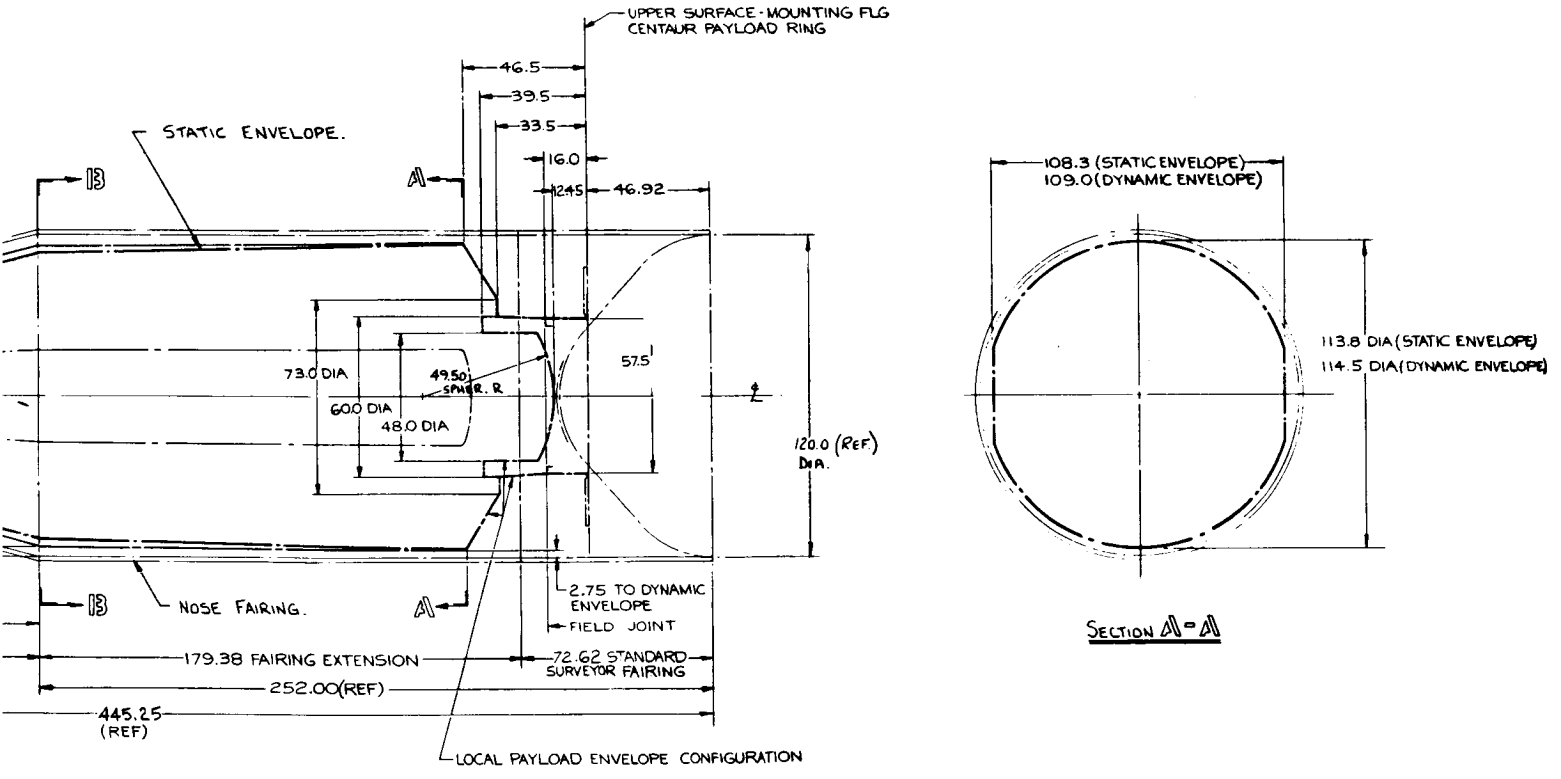


Figure 6.2-5. Static and Dynamic Envelope

taken at this early time to ensure that when detail deflection values are available for the extended shroud, they will not force changes in the launch configuration design. The minimum dynamic clearance maintained on the existing Surveyor shroud was 2-1/2 inches at an air conditioning duct location. In anticipation of greater shroud deflections for the longer shroud, a generous shroud deflection curve has been developed which coincides with the Surveyor shroud in the lower cylindrical portion but increases to 4 inches at the junction of the conic and cylindrical portions, and 5 inches at the extreme top of the usable portion. The section shown is across the flat portion of the inside diameter, i.e., the additional clearance area required for the separation joint which protrudes 2-3/4 inches inside the fairing. At shroud separation this joint parts, and each half is ejected straight out, requiring that this additional clearance be maintained along a chord rather than only at a point.

The static envelope has been developed with the same conservatism in mind. Dynamic analysis indicated that the antenna petal tip could undergo an excursion of approximately 0.7 inch when subjected to flight lateral loads. But a 3-inch deflection has been assumed to locate a reference point which linearly increases to the top of the shroud and decreases to 0 at the launch vehicle interface. Therefore, a total of 7-1/4 inches has been maintained at the critical clearance point, consisting of 4-1/4 inches for shroud excursion and 3 inches for spacecraft excursion.

At the base, an additional inch of longitudinal clearance over that held for Surveyor, has been maintained between the apogee motor nozzle and Centaur tank, to account for expected increased axial deflections of the heavier spacecraft.

6.2.2.3.4 Payload Mating Provisions

The selected design is mated to the Atlas/Centaur at the mating ring provided at station 172.45. This ring is a modified tee section, designed to receive uniformly distributed loads. In its present configuration, it can support a 3000-pound payload. In order to support the 3350-pound spacecraft, structural rework will be required. It is realized that integrity and vehicle stability on the Centaur is maintained with internal pressure, and

providing this structural capability may require more complex redesign in the forward bulkhead area than is apparent.

A less costly approach from a structural veiwpoint is to mate the spacecraft at Centaur station 219. This would require only an increase in gage of the ring at station 219. The spacecraft adapter would mate to an open trusswork adapter through a field joint at Centaur station 162. The lower portion of this adapter is a 20-inch high sheet-stringer cylinder which distributes loads to the ring at station 219. The significant advantage to this approach is that mating to the larger diameter results in a more rigid design enabling the Centaur frequency requirements to be met with a smaller expenditure of structure which must be injected into final orbit.

It is understood that NASA/Lewis is currently investigating this area and is trading off the relative merits of a more complex structural rework on the forward bulkhead as against rework in the shroud separation joint at station 219.

The significant point to be made is that the selected configuration is readily adaptable to either mating location, but in view of its long length and high lateral loading, structural advantages can be realized by supporting on a broader base.

6.2.2.3.5 Environmental Factors

The structural design criteria specified by NASA/ Goddard (see Section 5.9.2) conservatively ensures that the spacecraft will survive the launch environment. A composite of actual measured flight levels is given in Table 6.2-3 for comparison. The data presented include the information obtained from NASA/Lewis which was used as design criteria until the latter stages of the program.

A design goal to meet a minimum cantilever bending frequency of 10 Hz has also been specified in order to avoid structural coupling with the launch vehicle. The first and second lateral frequencies for the presently configured Centaur occurs at 2.5 and 6.0 cps, well below the range of the specified value. However, of equal importance is a design frequency

Table 6.2-3. Summary of Maximum Measured Flight Loads
Atlas/Centaur Flights AC-2 to AC-6

	Nz	Nxy
Steady State Accelerations*		
At Max q	2.3	±1.8
At BECO	6.3	±0.4
Centaur Eng. Start	1.7	±0.9
Centaur Eng. Cutoff	-1.6	±0.9

Vibration Environment - 0 to Peak g's (Sinusoidal)

	Nz	Frequency	Nxy	Frequency
At Liftoff	0.5	7.4 cps	0.04	2.1 cps
Flight	0.16	12.0 cps	0.04	2.2 cps
BECO	1.5	70-90 cps	0.12	5.5 cps

Torsion - 60 rad/sec^2 short pulse - Duration 0.1 to 0.2 sec

at 60-90 cycles

(Note: This is a conservative approximation of a pulse to simulate BECO torsion transient.)

REFERENCE: NASA/Lewis information
Distributed to ATS-4 Study Contractors June 1966

*G/D Astronautics Data

which will be outside of the range which can affect the control dynamics for the existing autopilot system.

Either decreasing frequency, or increasing the mass associated with the bending mode may require a control system redesign. If the change is radical, such as a 5-cps frequency associated with a 1000-pound mass, a revised design philosophy of the autopilot system may be required, resulting in additional development costs. The 10-cps bending mode frequency criteria has been specified for the structure with the thought that the mass in motion at 10-cps will be less than 500 pounds. This will require a check on the adequacy of the Centaur autopilot system, and possibly some redesign in filters and sensor bandwidths.

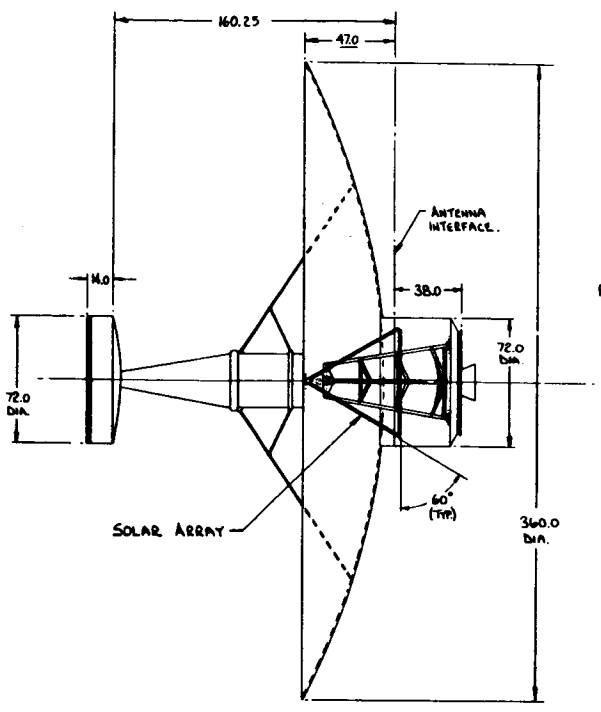
It is recommended that early in the subsequent design phase, a coupled launch vehicle/ spacecraft structural system dynamic analysis be performed to verify spacecraft design efficiency and compatibility with the launch vehicles' autopilot system.

6.2.3 EARLY CONCEPTUAL DESIGNS

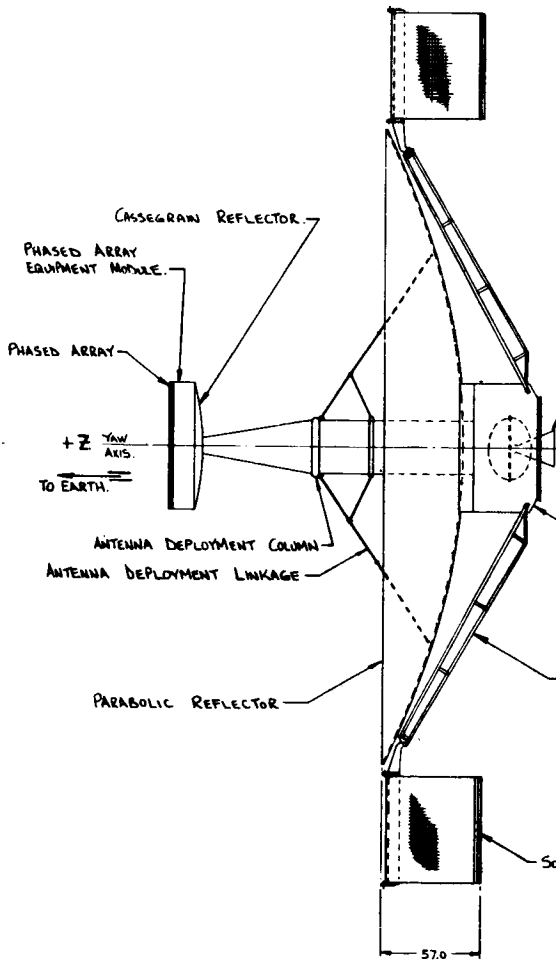
6.2.3.1 First Stage Designs

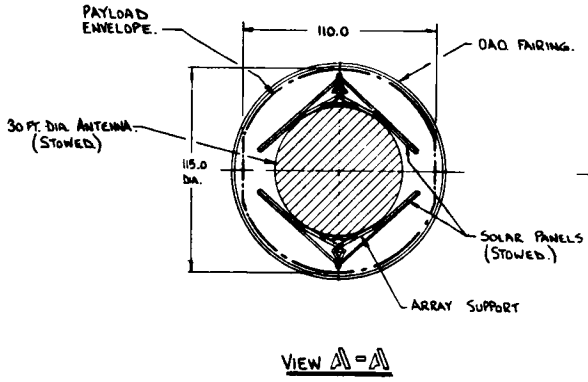
The first spacecraft configuration concepts developed for this application featured the front deployment of the parabolic antenna and a Cassegrain feed approach. The front deployment scheme was a sound mechanical design which deployed the antenna by application of a positive thrust force vectored normal to the antenna surface. The mechanism consisted of folded tubular struts located on hinge lines in each of the antenna sectors and attached through linkage to a movable center ring. This center ring, when driven by screw jacks, formed the fourth member of a four bar sliding linkage, and provided the motive power needed for rate control during the release of stored strain energy in the petals. It also provided the force necessary to drive the petals past the top dead center position. The center column, required to provide rigid guidance to the actuator ring and house the screw jack drive, was extremely compatible with a Cassegrain feed antenna design, since this column could also be used to support the prime feed horn.

The mounting of the earth-viewing experiments and sensors below the existing blockage area of the Cassegrain was compatible with the overall approach to minimizing rf blockage. Additionally, the already functional column formed the support structure for the earth viewing module during launch. This arrangement formed the framework about which the design in Figure 6.2-6 was developed. However, a significant problem was recognized with this aprroach in that the weight penalty for the center support structure could be high, about 140 pounds, when using conventional aluminum construction to meet the frequency requirement of 10 cps, necessitated for compatibility with the launch vehicle. The same comments are applicable to the conceptual design shown in Figure 6.2-7. In this case some structural and thermal control advantages result by the common packaging of all components. Of more significance is the location of the orientation control subsystems momentum wheels



VIEW ON ARROW 13





VIEW A-A

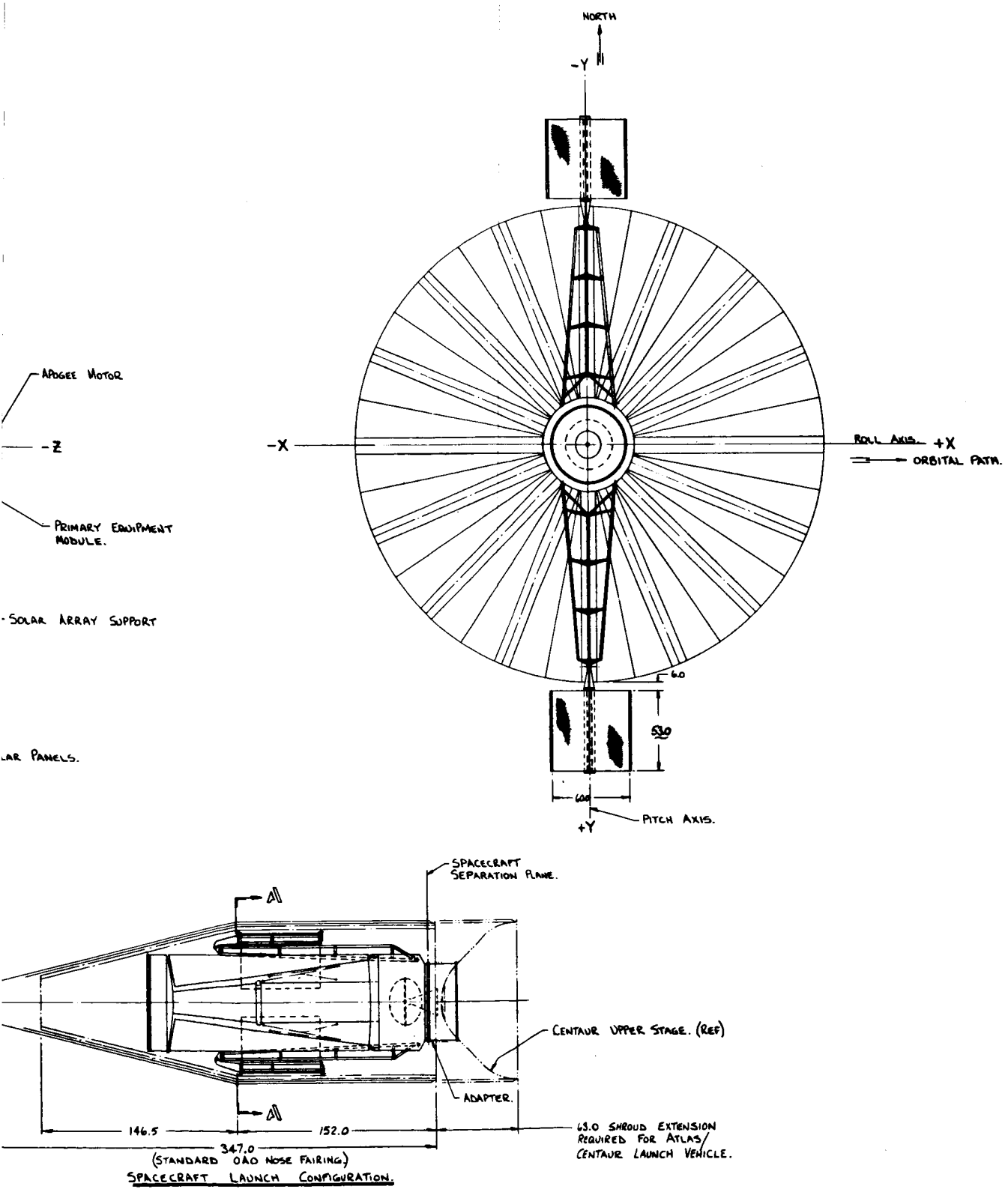
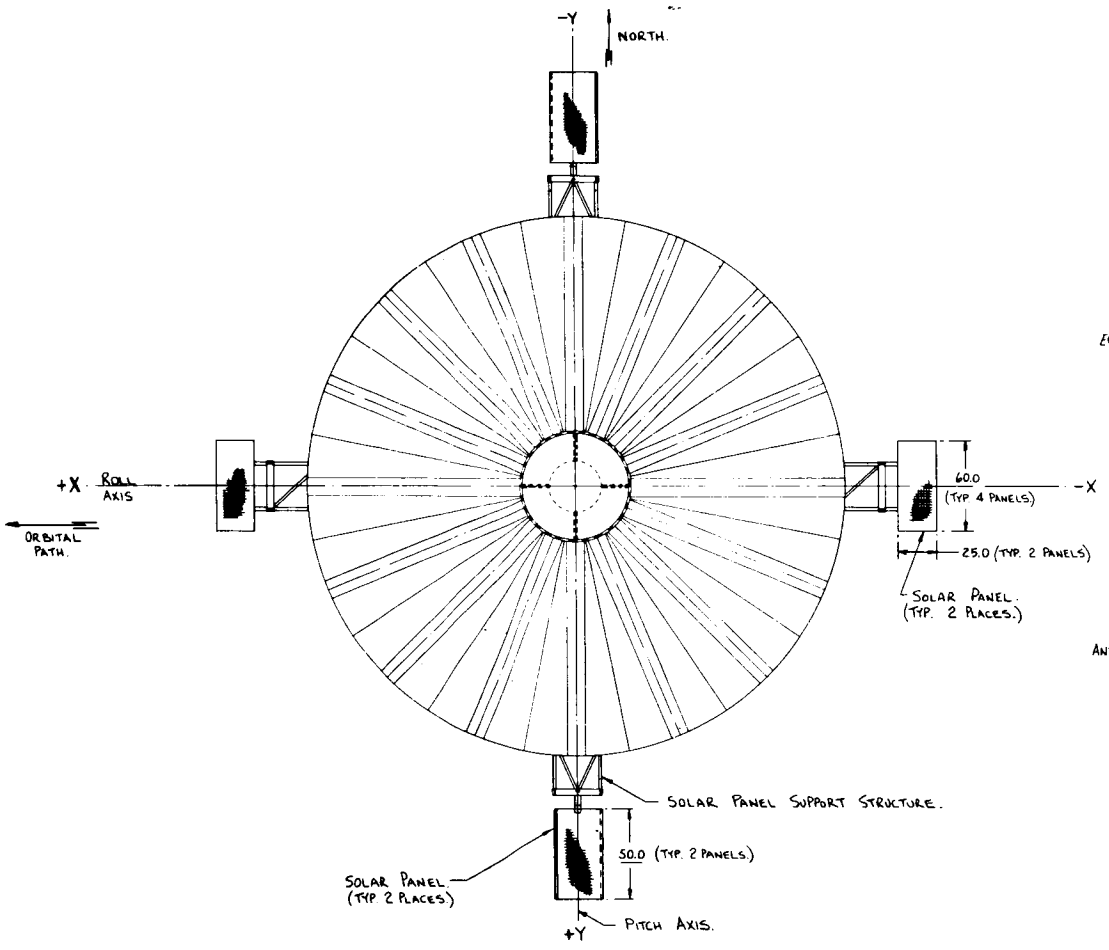
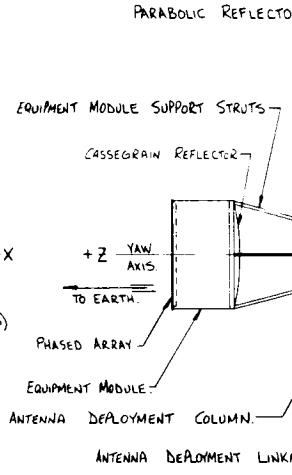
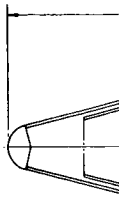


Figure 6.2-6. First Stage Design Split Module Concept


-Y
NORTH.
+X ROLL AXIS
ORBITAL PATH.
60.0 (TYP. 4 PANELS)
-X
25.0 (TYP. 2 PANELS)
SOLAR PANEL. (TYP. 2 PLACES.)
SOLAR PANEL SUPPORT STRUCTURE.
50.0 (TYP. 2 PANELS)
SOLAR PANEL (TYP. 2 PLACES)
PITCH AXIS.
+Y


PARABOLIC REFLECTO
EQUIPMENT MODULE SUPPORT STRUTS
CASSEGRAIN REFLECTOR
+Z YAW AXIS.
TO EARTH.
PHASED ARRAY
EQUIPMENT MODULE
ANTENNA DEPLOYMENT COLUMN.
ANTENNA DEPLOYMENT LINK



6.2-25

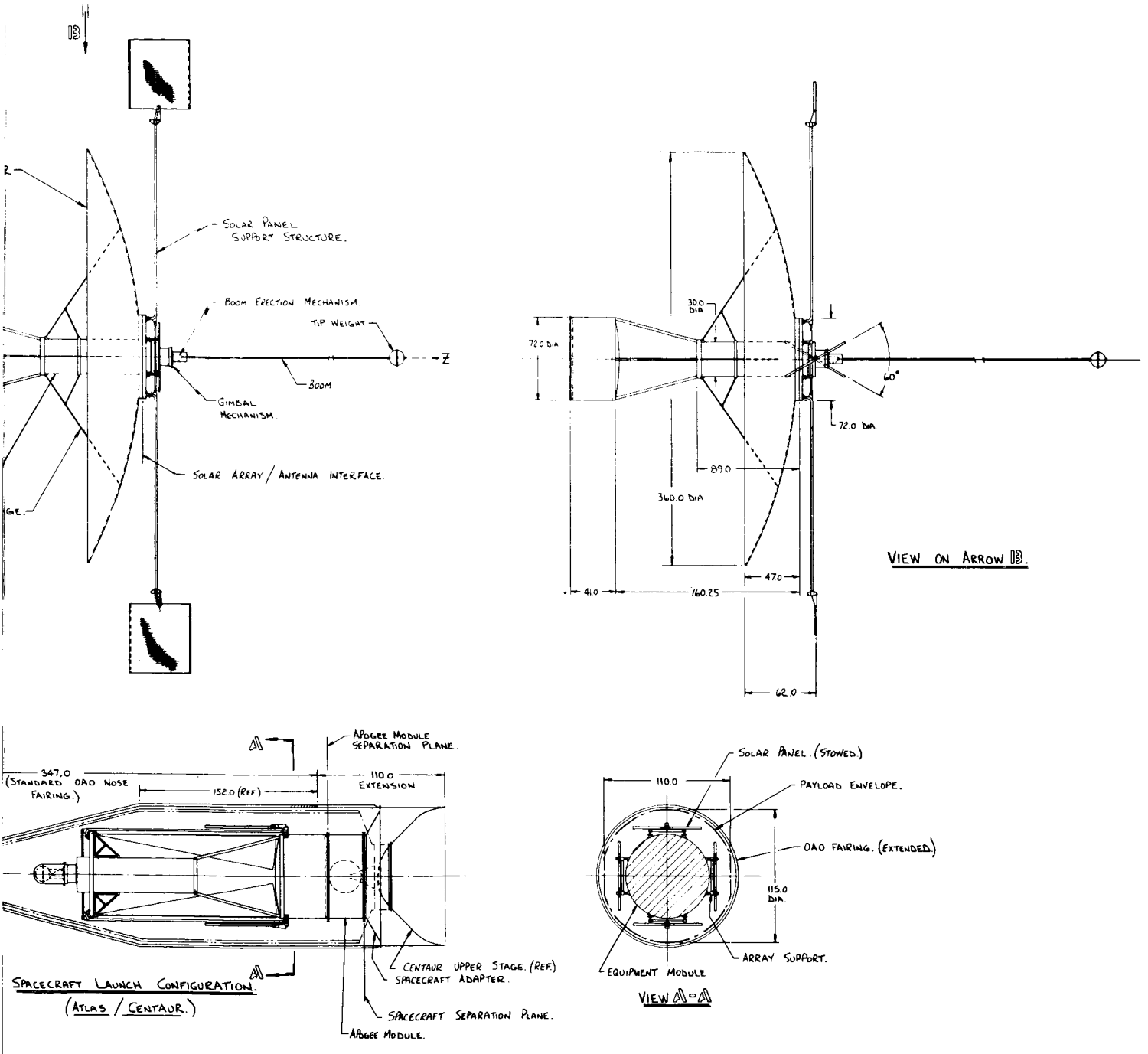


Figure 6.2-7. First Stage Design Single Module Concept

on the same reference axes as the sensors, which also coincide with the reference axis of the phased array. In the launch configuration, structural savings are available, since the antenna and supported solar arrays are lighter than the equipment module previously supported by the column. The launch arrangement, presented in Figure 6.2-7, illustrates that a separate apogee module would be required. This module would have to be separated from the spacecraft prior to orbital operation.

One other early design, presented in Figure 6.2-8, featured a deployed earth-viewing package. This offered the least rf blockage and promised some structural weight savings in the feed support structure, in return for deployment complexity. However, later studies indicated that the structure required to deploy the phased array and interferometer experiments exceeded any potential weight savings in the feed column. This design pointed out the relative inefficiency of the front deployment method, if the rigid structure required was not also used for close tolerance location, and support of the prime earth viewing experiments.

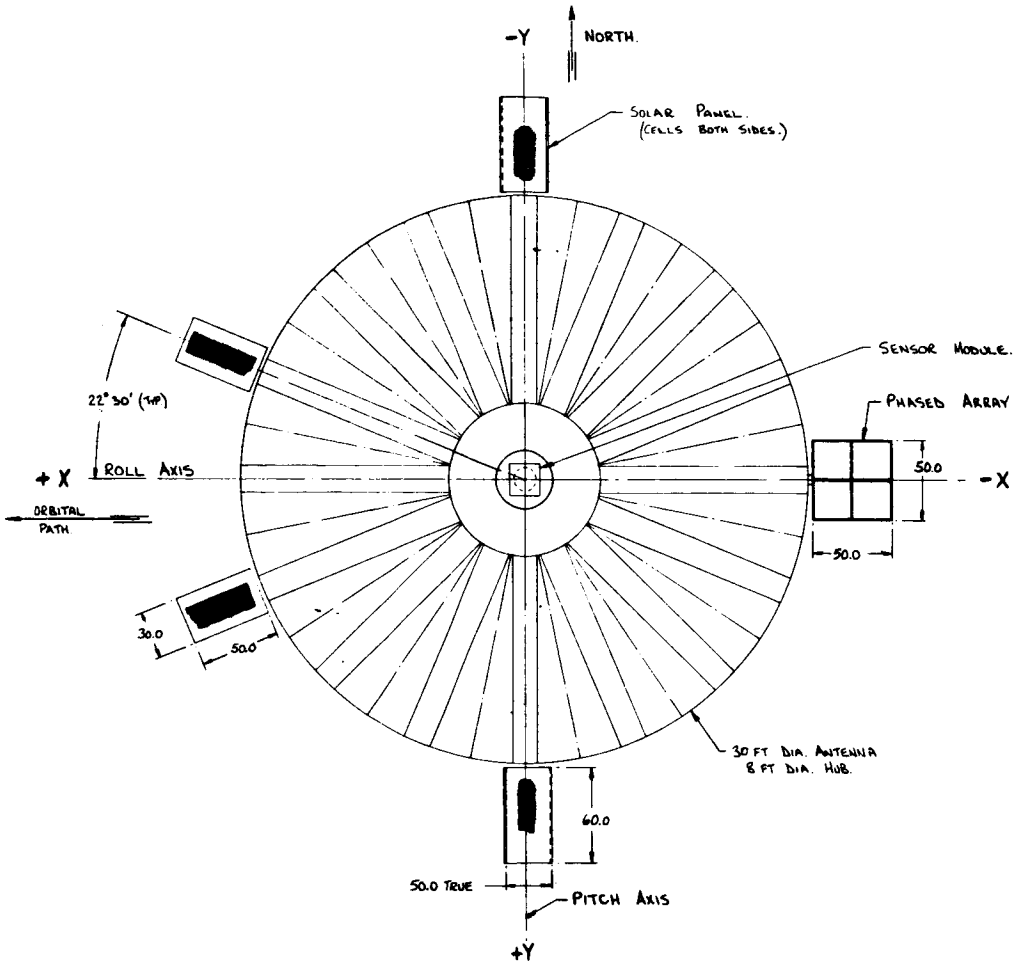
In summary, the configuration concepts generated during the first phase of the study indicated the importance of the antenna deployment scheme and also emphasized that more compact stowage arrangements, introducing deployments as necessary, were required in order to minimize structural loadings and shroud extensions. These designs were quite useful for a background about which various system and subsystem tradeoff studies were performed.

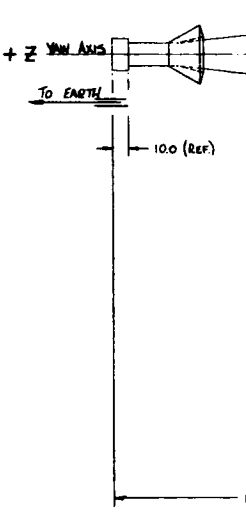
6.2.3.2 Major Tradeoffs

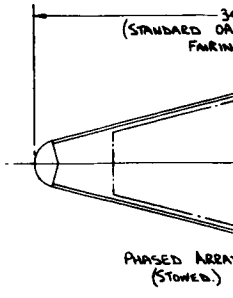
The major tradeoff studies which were performed following the first stage design effort, formed the basis for the next configuration development cycle. The major elements of this effort are summarized in the following paragraphs.

6.2.3.2.1 RF Analysis

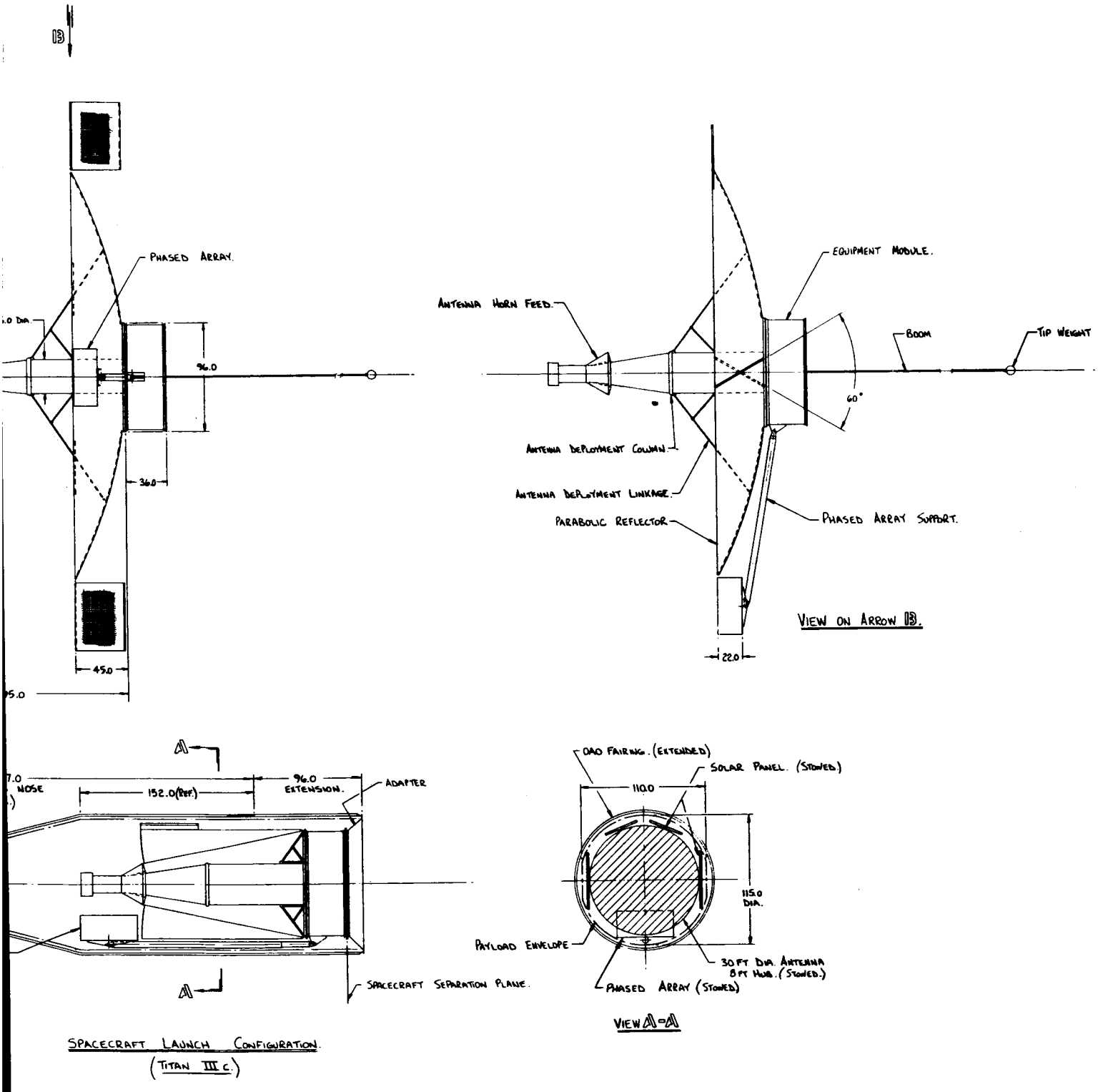
An rf loss budget analysis determined that the 50 percent efficiency at the high frequencies could not be achieved with a front deploying antenna because of blockage losses and







PHASED ARRA
(STOWED.)



SPACECRAFT LAUNCH CONFIGURATION.
(TITAN III C.)

Figure 6.2-8. First Stage Design Deployed Phased Array Concept

reflectance phase errors caused by the deployment struts. Elimination of the consideration of this deployment method removed the consequential configuration advantages resulting from use of a Cassegrain feed and enabled the comparison of feed types to be based on rf factors only.

6.2.3.2.2 Dynamic Analysis

Comparative dynamic analyses were performed to evaluate; (1) the reduction in stiffness offered to the deployed antenna by a back deployment method, (2) mounting the solar array panels directly to the antenna, and (3) the effects of varying the f/D ratio, which is significant because of the major contribution of curvature to antenna stiffness. The results, summarized in Table 6.2-4, indicated that sufficient stiffness to meet a 2-cps design criteria could be obtained with a more flexible back deployment truss providing antenna midpoint support. However, direct mounting of arrays was aggravating, especially at the higher f/D ratios.

Table 6.2-4. Deployed Antenna Frequency Comparison

	f/D = 0.3	f/D = 0.4	f/D = 0.5
Front compression struts	5.0 cps	4.5 cps	3.6 cps
Front compression struts with antenna-mounted arrays	3.0	2.7	2.2
Back support trusses	3.9	3.5	2.8
Back support trusses with antenna-mounted arrays	2.4	2.0	1.7

6.2.3.2.3 Fields of View

An investigation of the required free fields of view, with no sunlight reflection, of the Polaris sensor was included in the general conceptual studies, since it was apparent that the deployed antenna offers a significant constraint to maximizing view angles. The layouts shown in Figures 6.2-9 and 6.2-10 show sensor locations for two conceptual orbit control systems. In each case, the sensors had to be located as far from the antenna as possible in

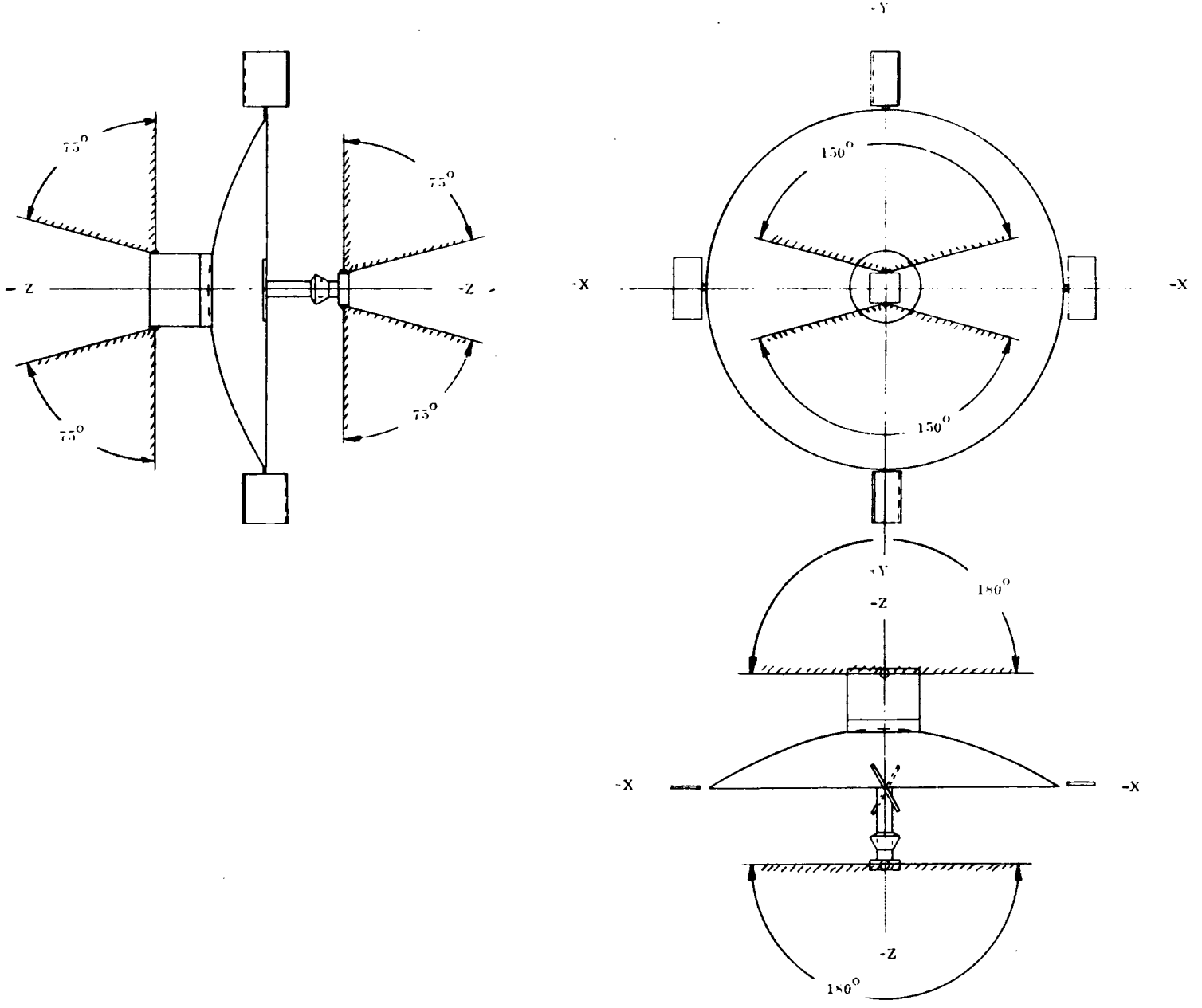


Figure 6.2-9. Star Tracker System for Orientation Control, View Angles

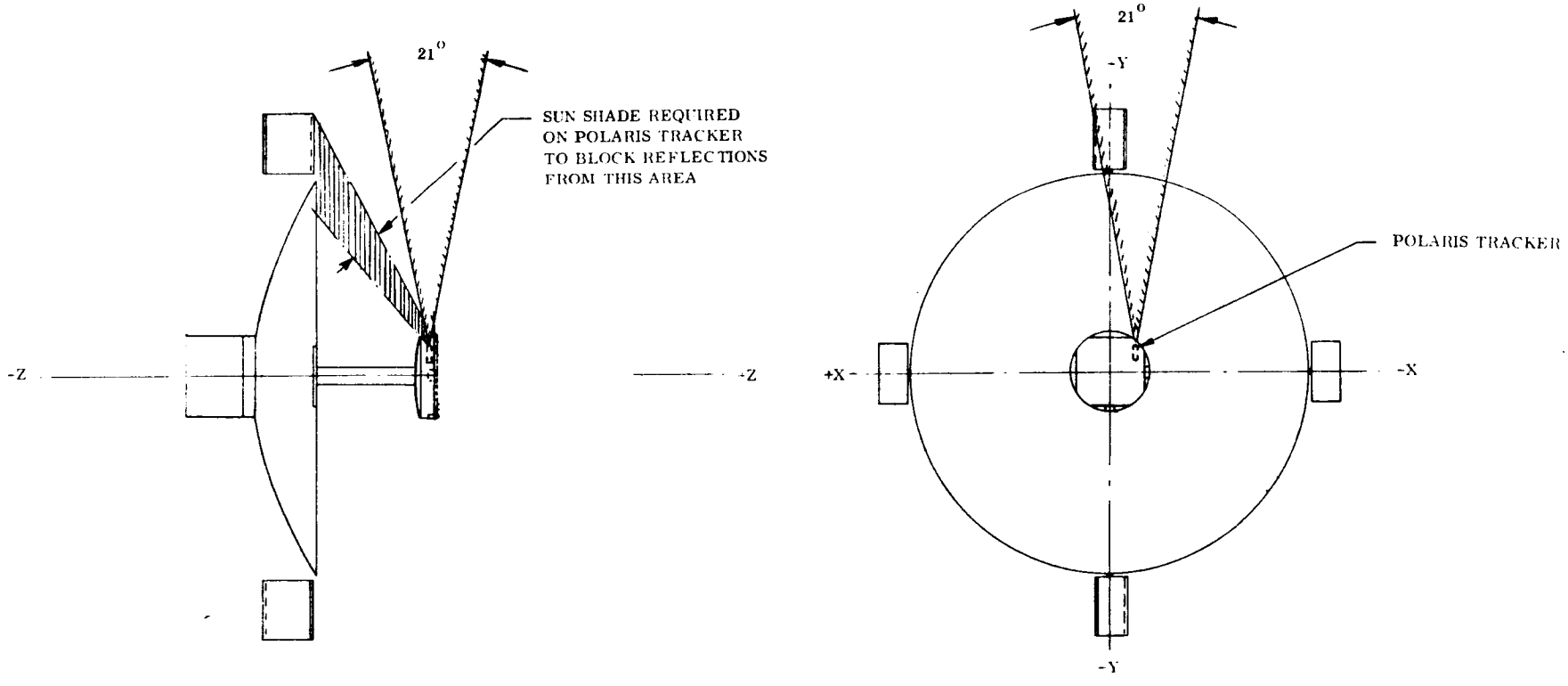


Figure 6.2-10. Polaris Tracker System for Orientation Control, View Angles

order to obtain the free fields of view required. The star tracker orientation control system requires an unobstructed 70-degree half-cone-angle field of view. Within the antenna and solar array constraints, two approaches could be taken. First, the sensors could be mounted on deployed structure to a location where the free field of view could be obtained. This is not efficient, since a severe weight penalty is incurred to provide a structural link sufficiently rigid to avoid servoelastic coupling. Furthermore, the sensor's inertial axes would not coincide with either the momentum wheels or any of the other prime experiments. The second approach consists of using duplicate sensors. This is illustrated in Figure 6.2-9 and results in a more complex system and an additional weight of 40 pounds. The earth sensor, Polaris tracker concept illustrated in Figure 6.2-10 is much more desirable from a configuration point of view. The field of view required by the tracker, 21-degree cone, is compatible with the antenna. It was concluded that:

a. The star tracker system was not compatible with configuration approaches meeting the viewing requirements of the Polaris system.

b. Mounting of the Polaris sensor at a point behind the antenna feed was preferred to mounting in the primary equipment module.

c. A sun shield of the OAO type is required to eliminate reflections from the antenna and solar panels into the sensing eye.

d. Suitable constraints have to be placed on the location and (possibly) aspect ratio of solar array panels to avoid a sun shield extension.

6.2.3.2.4 Solar Panel Configurations

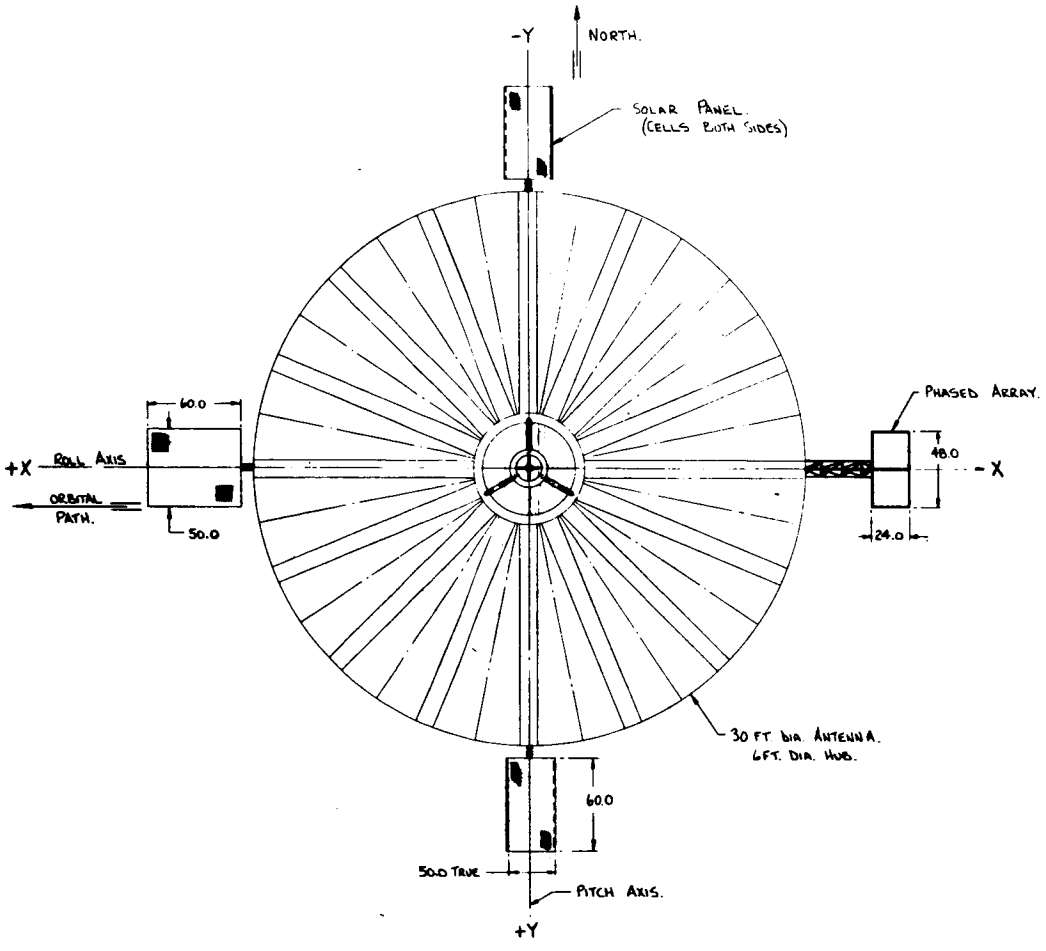
Parametric studies of many non-sun-oriented solar array configurations were performed as discussed in Section 6.6. The two most efficient concepts were: a four paddle system with cells on both sides, which is the arrangement used in the design shown in Figure 6.2-7, and a two-panel system, with a North and South panel at right angles to each other. In view of, (1) packaging constraints with two larger panels, (2) the desire to distribute loads on the antenna (if they were so connected), (3) the possible reduction of free field of view on the Polaris sensor, and (4) the power design considerations of higher battery charge and discharge rates, the four panel configuration was tentatively selected. In the succeeding

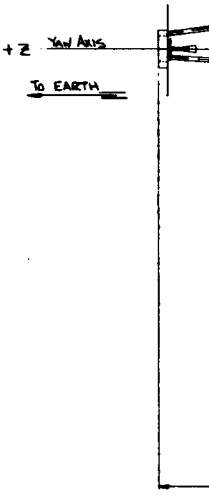
configuration development phase, no additional factors were introduced which gave the two-panel system preference. For the selected design, additional studies on growth, deployment complexity, and structural support weight reiterated the selection of a four-panel approach.

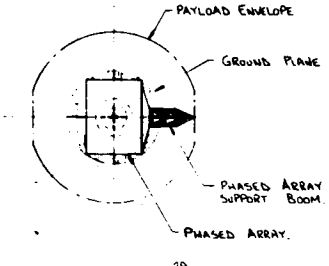
6.2.3.3 Second Stage Designs

The design shown in Figure 6.2-11 was an up dating of the deployed phased array approach (Figure 6.2-8), incorporating the results of the tradeoffs just discussed. The outstanding feature is the inclusion of a back deployed antenna scheme which was found to be quite favorable for antenna performance and acceptable structurally and mechanically. The design was meant to be optimum from an rf standpoint, in that the feed support structure, a small diameter tubular tripod, would support only the feed and Orientation Control sensors in launch. The heavier phased array structure would be deployed out of the path of the antenna, thereby reducing direct blockage and the losses that would occur from the larger members in the feed support truss. The most significant tradeoff study performed with this configuration approach was the investigation of rf losses due to feed support structure. Near-field rf testing was performed which indicated high blockage and reflectance losses resulting from feed support truss members being located in the high-power density portion of the beam. Moving the feed support struts radially outward, towards the rim of the reflector, was considered to be optimum. As a compromise, deploying the feed structure from the back deployment trusses was chosen as the selected approach for future designs. This, and the still important desire to reduce fairing extension lengths, led to the design shown in Figure 6.2-12, the first deployed conceptual design. A Cassegrain reflector approach was selected to avoid the deployment of waveguide and coax feed.

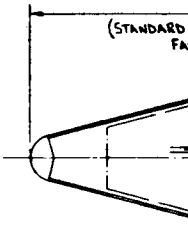
The obvious solution to minimizing shroud height was to stow the basic spacecraft within the folded antenna package. In order to accomplish this, the open end of the antenna cylinder, which had the least internal clearance because of petal geometry, had to be located at the widest portion of the shroud in order to allow this diameter to be enlarged. This led to an inverted cone packaging arrangement of the antenna. The dimensions of the prime feed were such as to force mounting of spacecraft components above the antenna hub in order to leave







VIEW ON ARROW 'G'.



PHASED A
(SUPPORT BO
OMITTED FO

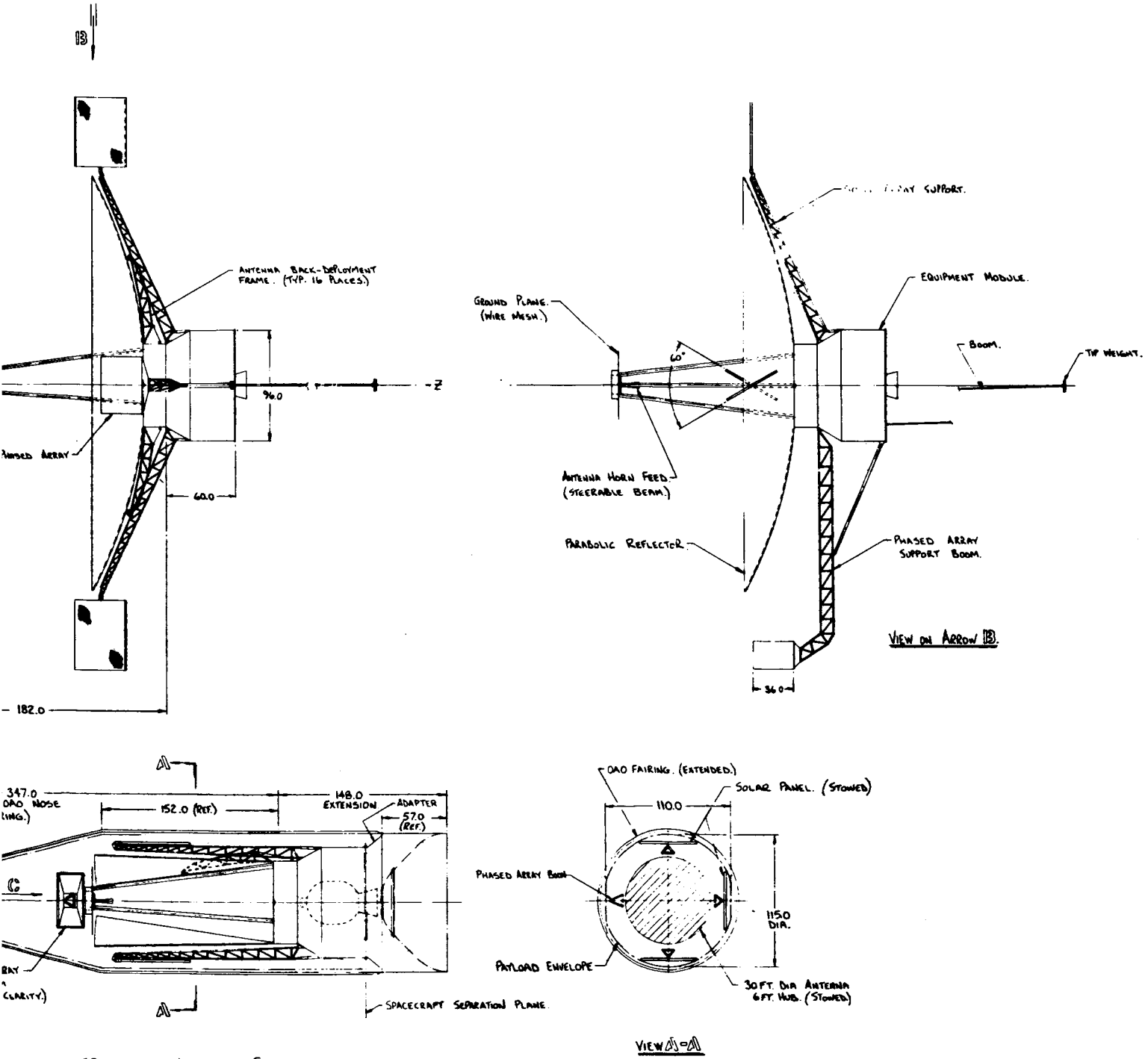
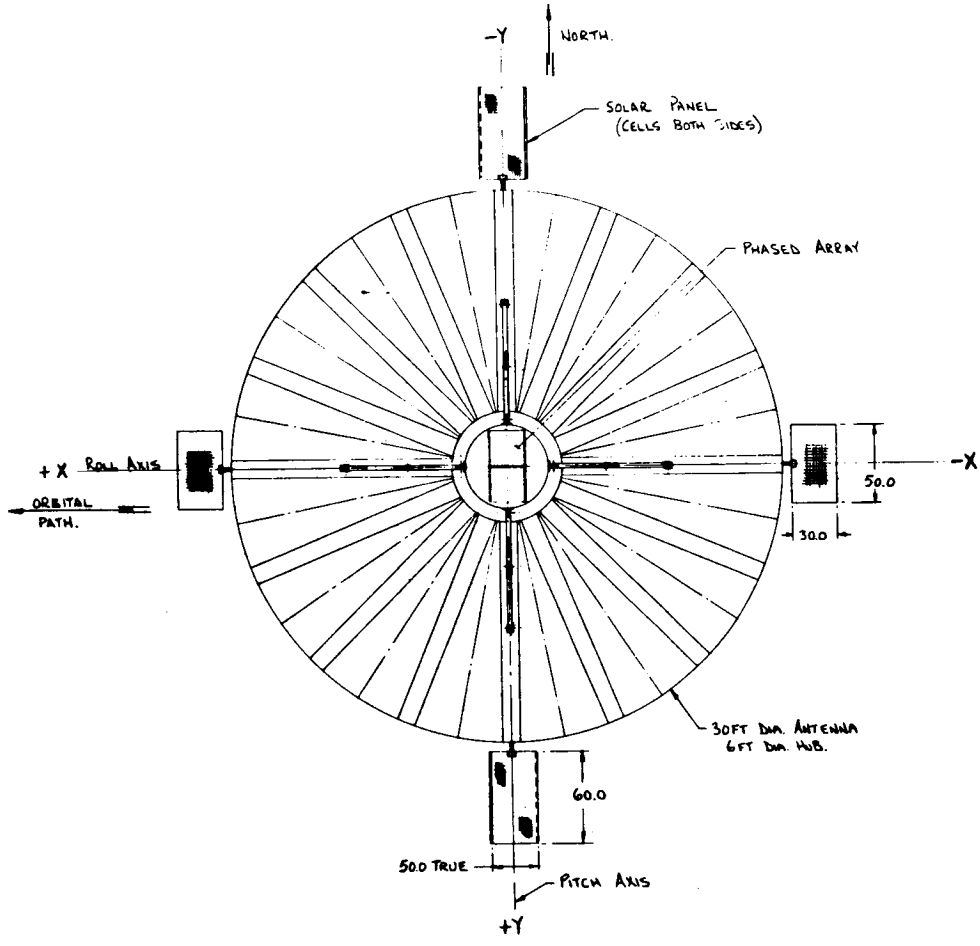
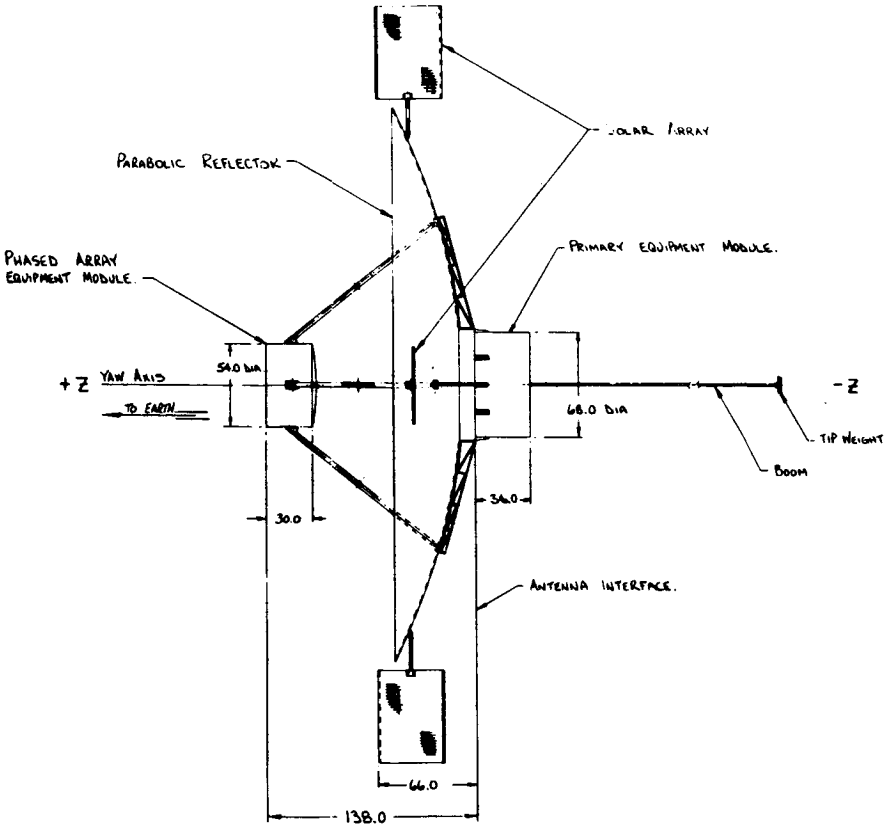
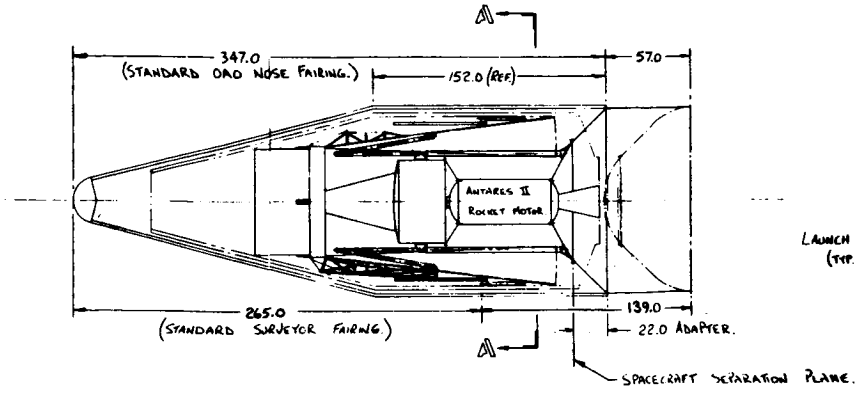


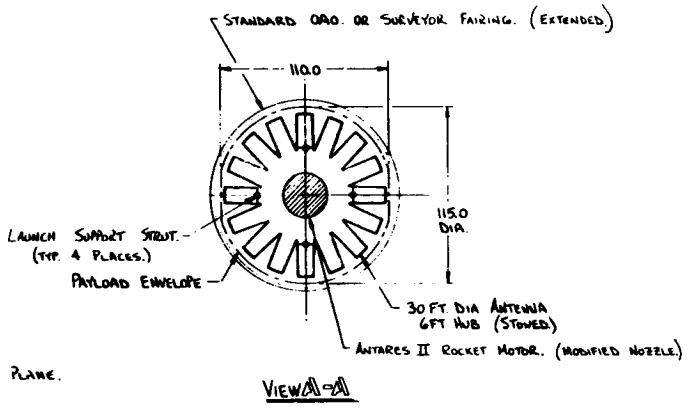
Figure 6.2-11. Second Stage Design Deployed Phased Array Concept


-Y
NORTH.
SOLAR PANEL
(CELLS BOTH SIDES)
PHASED ARRAY
+X ROLL AXIS
ORBITAL
PATH.
-X
50.0
30.0
30FT DIA. ANTENNA
6FT DIA. HUB.
60.0
50.0 TRUE
PITCH AXIS
+Y





SPACECRAFT LAUNCH CONFIGURATION.
(ATLAS / CENTAUR SHOWN)



VIEW

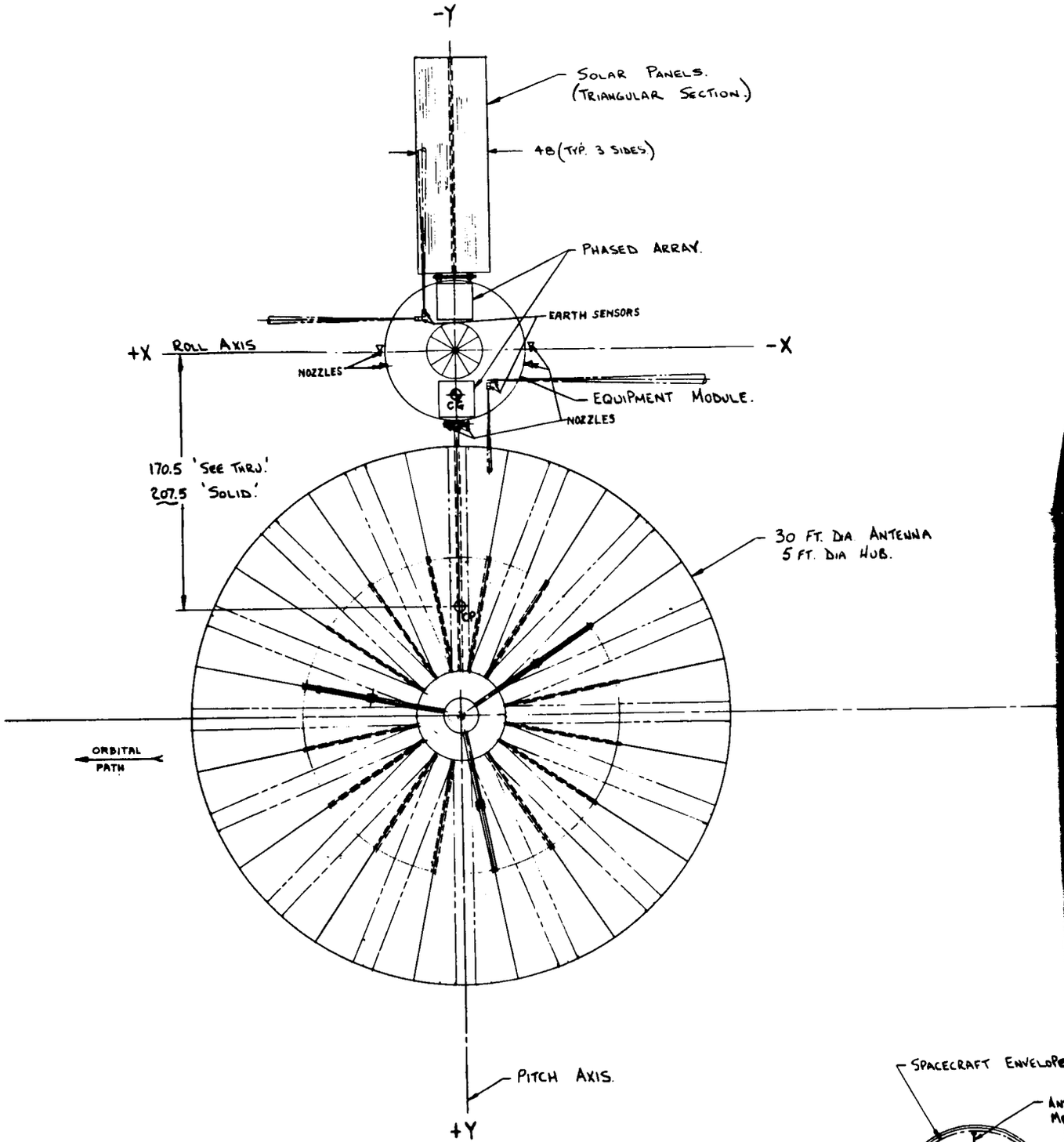
Figure 6.2-12. Second Stage Design
·Deployed Feed Concept

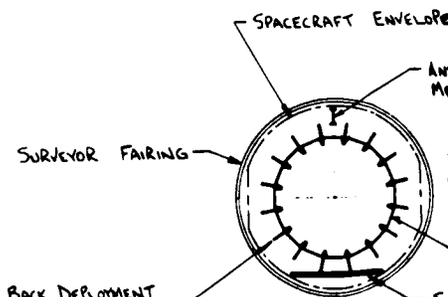
packaging area for the Antares II apogee motor. In orbit, the Antares II was jettisoned and the Cassegrain reflector, with the earth-viewing experiments mounted behind it, deployed into position. Studies performed at this time determined that the structural arrangement of mounting heavy spacecraft components above the antenna hub was not efficient during launch. In addition to which, the Antares II was not overly desirable for the ATS-4 mission. Therefore, while the configuration concept solved the antenna performance and shroud height problems, a redesign was planned.

6.2.4 THIRD STAGE DESIGNS

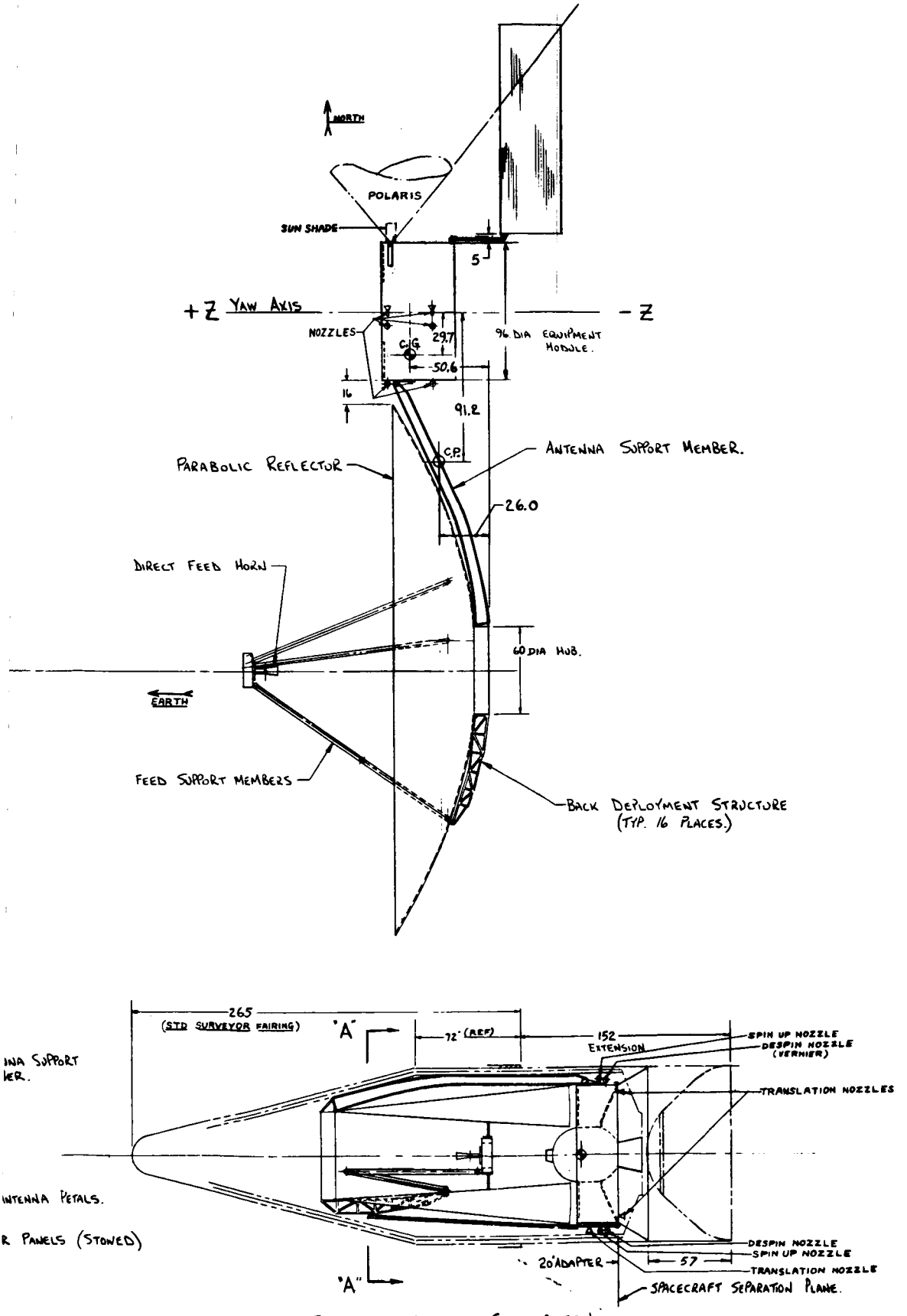
The many advantages of mounting all components in one spacecraft module was evident throughout the studies. Besides efficient structural and thermal control designs, the advantages of packaging the Orientation Control sensors and thrustors in one compartment and the utilization of one reference axis for the spacecraft could also be obtained. Therefore, still in an rf optimum design framework, the tandem configuration shown in Figure 6.2-13 was developed. However, only preliminary analysis was required to show that the Cp/Cm mismatch resulting from this orbital arrangement would result in prohibitive momentum wheel weights and would probably dictate a new approach to the Orientation Control experiment. In addition to this, the structural support provisions for the antenna were also heavy and complex. Therefore, this design did not appear to be competitive in comparison to the other configuration approaches.

The deployed earth-viewing equipment package concept presented in Section 6.2.3 was updated to include deploying feed support struts. This design, shown in Figure 6.2-14, was also successful in packaging the Orientation Control sensors into the primary spacecraft, viewing past the feed. This eliminated two major objections to deploying the sensors: (a) the high structural weight penalty incurred to maintain a 10 cps link between sensors and torques and (b) the misalignment errors which can result from a deployment. Thus, this configuration was approaching an optimum experimental platform for the antenna and orientation control system, with no degradation of performance for either the phased array or the interferometer. However, the cost in structural weight and deployment complexity was becoming prohibitive.


-Y
SOLAR PANELS. (TRIANGULAR SECTION)
48 (TYP. 3 SIDES)
PHASED ARRAY.
EARTH SENSORS
+X
ROLL AXIS
-X
NOZZLES
CG
EQUIPMENT MODULE.
NOZZLES
170.5 'SEE THRJ.'
207.5 'SOLID'
30 FT. DIA ANTENNA
5 FT. DIA HUB.
CP
ORBITAL PATH
PITCH AXIS.
+Y

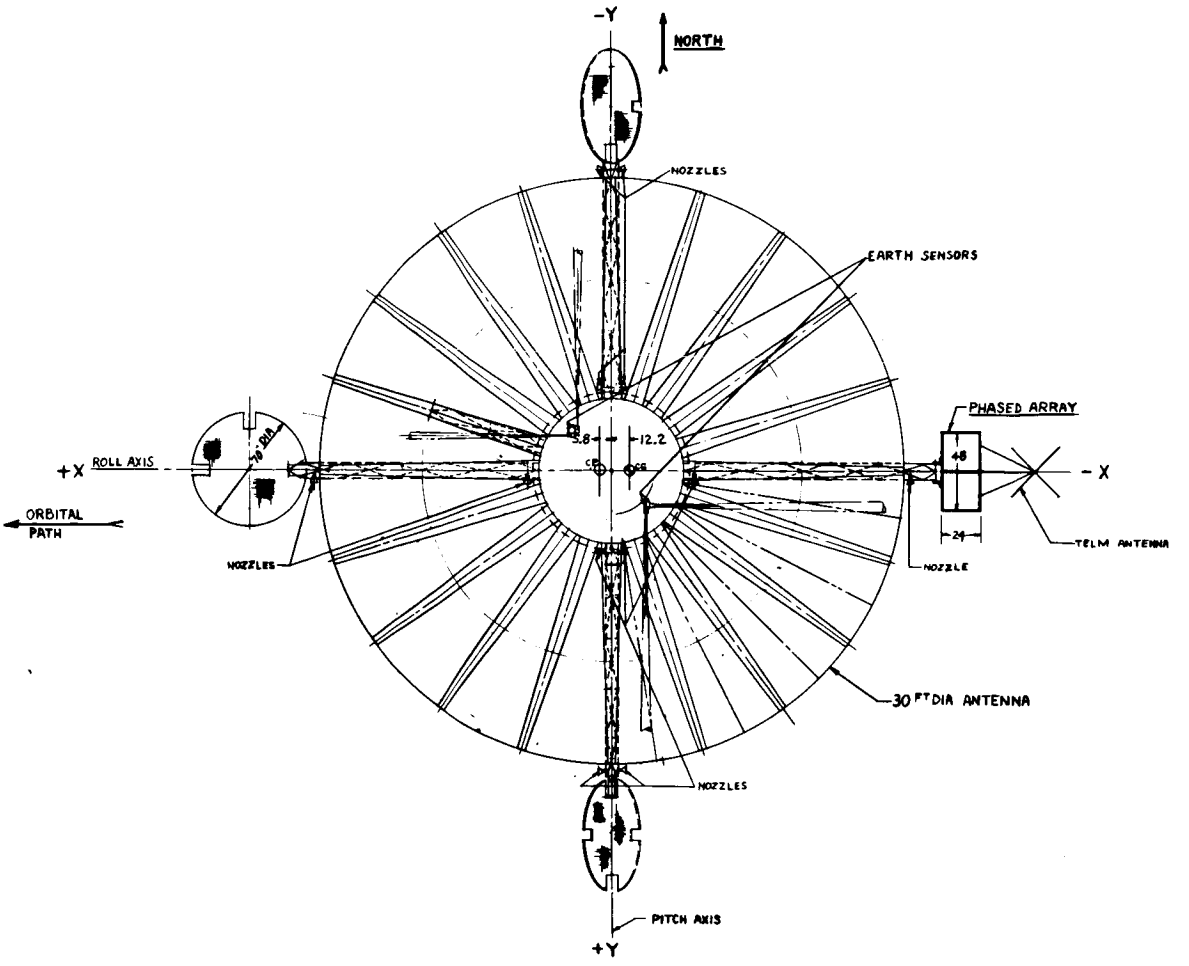

SPACECRAFT ENVELOPE
SURVEYOR FAIRING
BACK DEPLOYMENT STRUCTURE

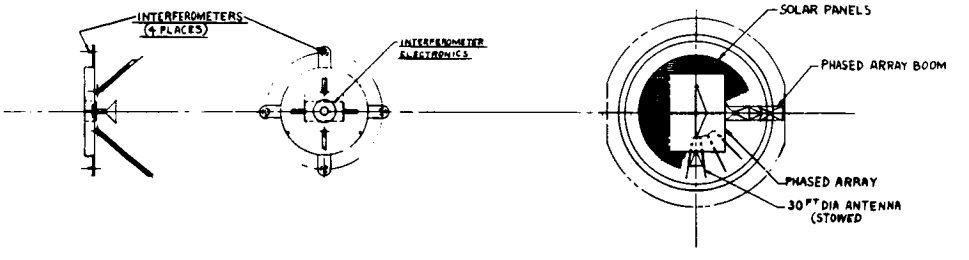
VIEW 'A-A'



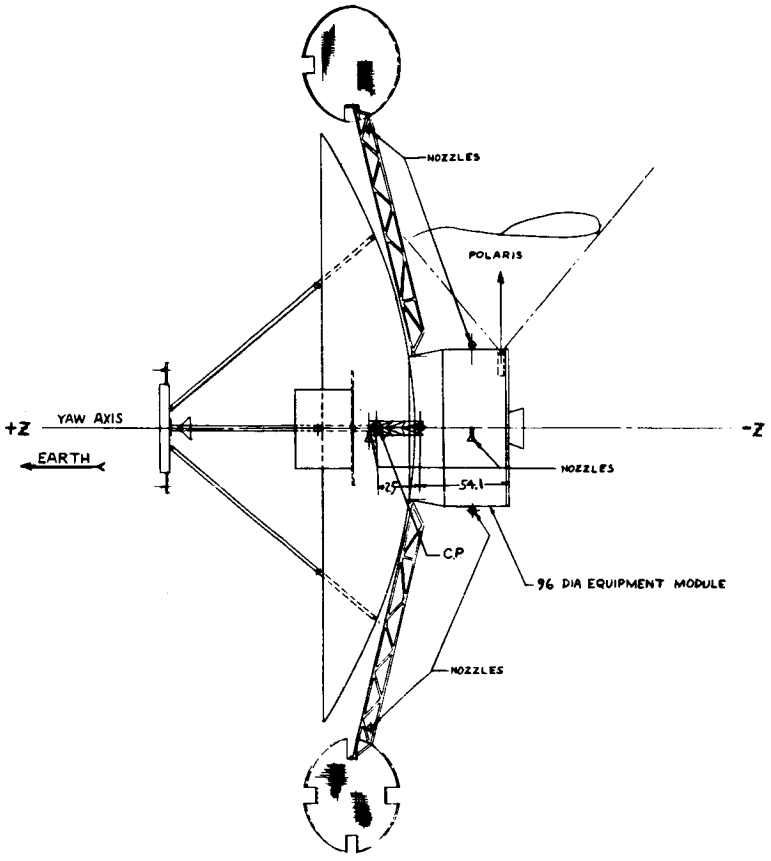
SPACECRAFT LAUNCH CONFIGURATION.
(ATLAS/CENTAUR.)

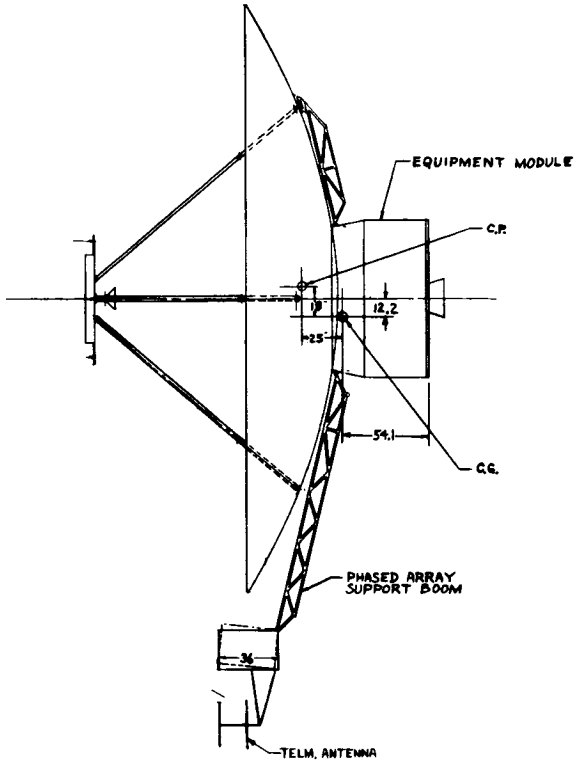
Figure 6.2-13. Third Stage Design Tandem Concept

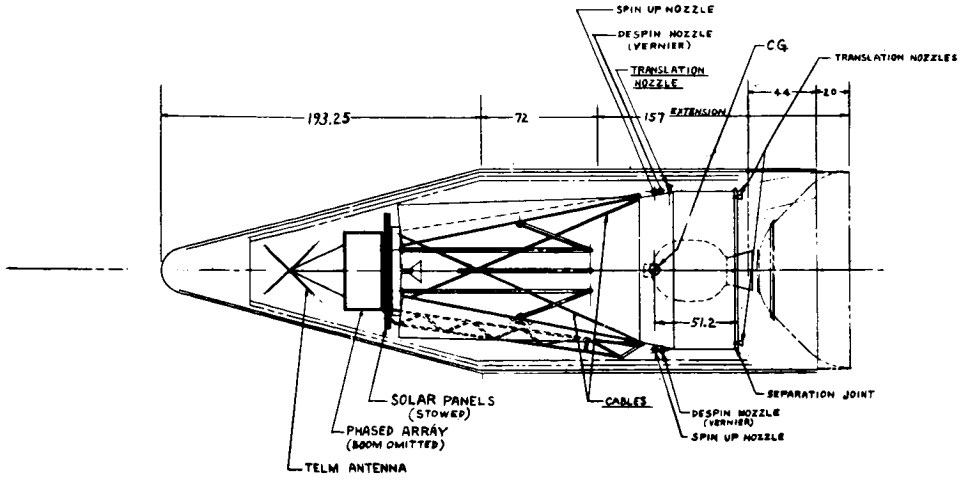

-Y
NORTH
NOZZLES
EARTH SENSORS
PHASED ARRAY
+X
ROLL AXIS
- X
ORBITAL PATH
NOZZLES
NOZZLE
TELM ANTENNA
30 FT DIA ANTENNA
NOZZLES
PITCH AXIS
+Y


INTERFEROMETERS (4 PLACES)
INTERFEROMETER ELECTRONICS
SOLAR PANELS
PHASED ARRAY BOOM
PHASED ARRAY
30 FT DIA ANTENNA (STOWED

6.2-45







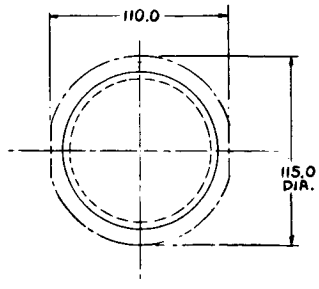


Figure 6.2-14. Third Stage Design Deployed Phased Array Concept

A feature of the design worthy of discussion,because of its applicability to the selected design, revolved about the introduction of deploying the solar array panels with the antenna deployment mechanism. A "points out" antenna packaging arrangement was selected, since this would allow more generous volume between petals on the back side of the antenna. The antenna arrangement requires the same volume as the "points in" approach used in the selected design and could easily be substituted with the advantage of enabling a more efficient structural design of the solar array support trusses, and allowing a reduction in the size of the linkage connecting the antenna petals to the deployment trusses. The primary reason for its exclusion, but not rejection, from the selected design was that the antenna deployment forces must be applied at the center of the trapezoidal segments rather than directly at a hinge line. This requires a small bending member to transfer the required deployment force to the hinge lines, the inclusion of which may alter uniform strain energy release of the antenna at deployment. Analytically, the scheme appears acceptable, but all previous deployment test models have used hinge line actuation methods. This lack of test data, and the successful design of rigid solar array trusses which are stowable between petals in the selected configuration, relegate the "points out" folding arrangement to a feasible alternate approach.

A review of all the potential designs indicated that the most desirable spacecraft performance qualities could be achieved via the redesign of the deployed configuration shown in Figure 6.2-12. The following attributes were available:

a. Orientation Controller experiment efficiency by packaging of all equipment in one module

b. Optimum parabolic antenna, phased array, and interferometer performance via a single feed and earth-viewing equipment deployment

c. A compact, efficient structural arrangement

d. A minimum shroud height

e. Minimization of harness runs and an efficient thermal control design, also by single spacecraft module design

Consequently, the improved deployed concept, discussed in detail in the following paragraph was selected for further study.

6.2.5 DEPLOYED CONFIGURATION

The configuration selection studies, discussed previously in this section, evolved one strong configuration potential for this application. The elements that led to this selection are summarized below for emphasis:

a. Atlas (SLV-3C)/Centaur launch vehicle with an extended Surveyor fairing

b. Rigid petal antenna approach

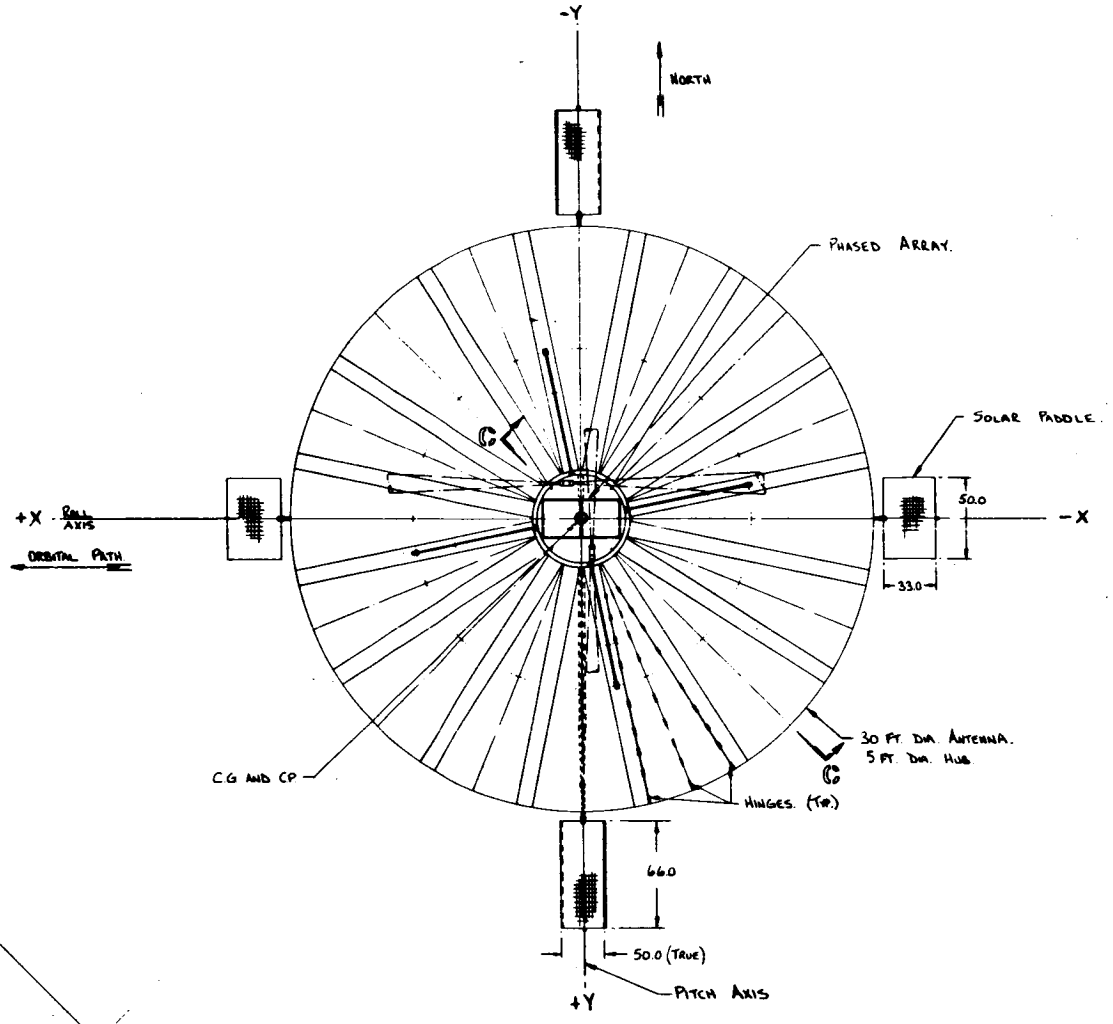
c. Antenna back deployment

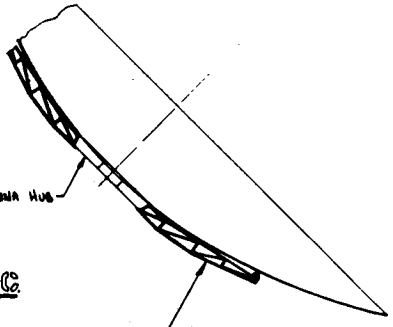
d. Solar array panels extended beyond the antenna

e. Direct feed approach

f. Deployed feed support truss

The incorporation of these elements into a spacecraft configuration led to the design illustrated in Figure 6.2-15, which features a deployable prime feed module. In the stowed position, the equipment/feed module is nested within the folded antenna, and four sets of articulated links connect the antenna to the module. The antenna hub is attached to the module by explosive nuts which effectively create an assembly of the antenna/module package during launch. At the other end of the equipment module, the apogee motor is housed in a separate structure which in turn interfaces with the booster adapter ring, thus creating two separation planes. In the deployed condition, the equipment module is supported at the focal point of the antenna by the support tubes, which are removed as far as practical from the high rf density region of the antenna pattern. The solar panels are deployed beyond the antenna on elongated back deployment trusses to maximize their efficiency. The equipment module support tubes act as conduits for the power leads from the solar panels, as well as for command and telemetry lines to the vernier system, which is mounted off the antenna hub. The apogee module is separated from the spacecraft after

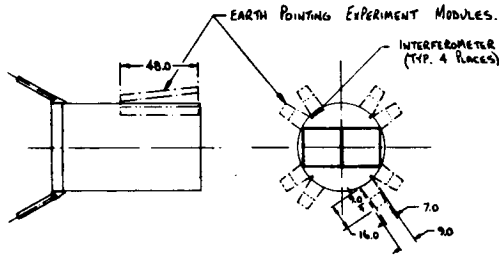




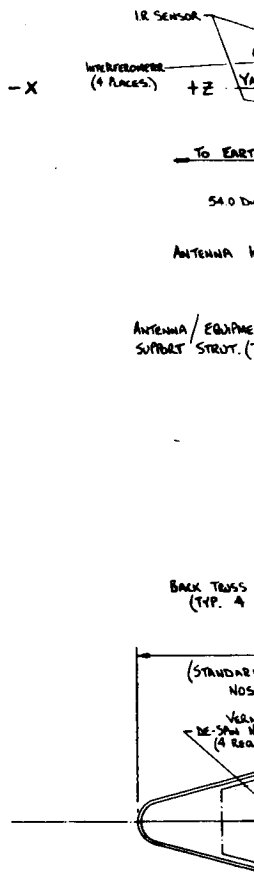
VIEW C-C.

ANTENNA BACK-DEPLOYMENT TRUSS
11 REQUIRED AS SHOWN.
1 REQUIRED - MODIFIED SLIGHTLY TO SUPPORT VERNIER TRANSLATION NOZZLE FOR INITIAL ACQUISITION.
4 REQUIRED - EXTENDED TO SUPPORT SOLAR ARRAY.

IN ADDITION TO ABOVE - 4 BACK-UP TRUSSES REQUIRED AT ANTENNA/EQUIPMENT MODULE SUPPORT STRUTS.



VIEWS SHOWING POSSIBLE GROWTH POTENTIAL



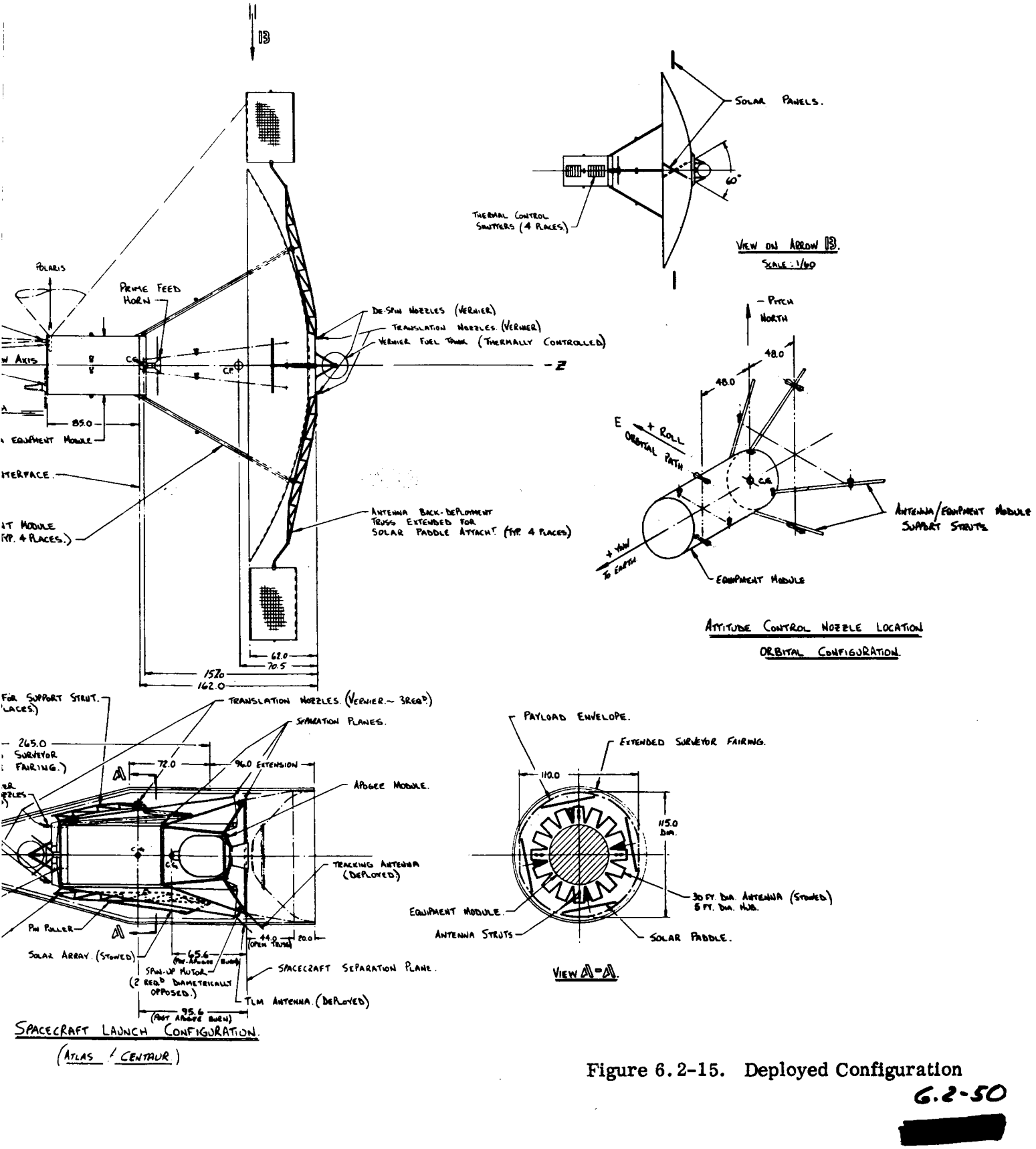


Figure 6.2-15. Deployed Configuration

deployment. The remainder of the spacecraft equipment is packaged into the single equipment module, such that the three prime experiments and the feed for the parabolic antenna have the same coordinate axes, thereby eliminating a large source of mechanical boresight errors.

The separation/deployment sequence of this configuration is basically as follows:

a. The stowed spacecraft - including the antenna, the feed module, and the apogee module separates from the launch vehicle.

b. After apogee motor burn and vernier thrusting, the antenna cinch-up band is released and the back-deployment drive motor is activated, deploying the antenna

c. The explosive nuts connecting the antenna hub to the feed module are actuated. This event severs the fixed interface between the two components allowing the spring-loaded articulated links to straighten and deploy the feed module to the focal distance of the deployed antenna.

d. The apogee motor module is then separated by explosive devices from the feed module, thus creating the orbiting spacecraft configuration consisting of the deployed antenna connected to the feed module by four rigid struts.

The performance summary of the deployed configuration is presented in Table 6.2-5. The performance of the prime experiments and spacecraft subsystems would be as presented in Section 5, with the exception of the parabolic antenna; its performance with this configuration is discussed in Section 6.3. The spacecraft weight and inertia summary is presented in Table 6.2-6.

The deployed configuration maximizes the rf performance of the parabolic antenna, within the constraints of the study, and offers some unique structural advantages over other configurations which have been considered. However, three major disadvantages of the configuration are: (1) the required deployment and rate control of the equipment module, (2) the necessity of separating the apogee module so that the earth-viewing equipment can be operated, and (3) the inability to use the sensors or thrusters of the equipment module during initial acquisition and in the event of an antenna deployment failure. Two of these

elements, the structural advantages and the module deployment, warrant further discussion and are presented in the following sections.

Table 6.2-5. Performance of Deployed Configuration

Selected booster - SLV-3C/Centaur	
Shroud required - std. surveyor with 8-ft cylindrical extension	
Payload penalty into synchronous	15 lb
Launch availability penalty	17%
Kick stage - surveyor type, TE-M-364-Modified	
Payload to synchronous orbit	1852.1 lb
Present design weight (to synchronous)	1589.0 lb
Payload margin available	263.1 lb
Payload volume available	110 cu ft
Spacecraft system volume required	37 cu ft
Volume margin available	73 cu ft

6.2.5.1 Structural Considerations

The structural advantages of this configuration are centered around the rather unique packaging concept of the spacecraft in the launch configuration. This approach embraces many of the aspects of an ideal boost phase design philosophy such as:

a. The use of a standard shroud with a minimum extension

b. Combined spacecraft center of gravity located near the payload mounting interface

c. Highly efficient structural arrangement for supporting large mass items during the design critical launch environment

d. Provisions for the forward mounting of the rather flexible antenna and solar array trusses in such a manner as to ensure their stability under the significant launch thrust.

Table 6.2-6. Deployed Configuration Weight Summary

A.	**Basic Spacecraft**		
	Structure		283.2 lb
	Equipment Module	91	
	Apogee Module	104	
	Struts, Fittings, etc.	88.2	
	Parabolic Antenna		266.0 lb
	Reflector & Hub	124	
	Feed	10	
	Deployment	102	
	Thermal Control	30	
	Attitude Control & Stationkeeping		479.8 lb
	Electronics	117	
	Momentum Storage	72	
	Mass Expulsion	196	
	Thrustors Tankage, Valve, etc.	94.8	
	Experiments		217.5 lb
	Phased Array	110	
	Interferometer	35	
	Other	72.5	
	Power		254.0 lb
	Array	100	
	Batteries	100	
	Electronics & Harness	54	
	Thermal Control		34.0 lb
	TT&C		54.4 lb
			1588.9 lb
B.	Redundancy 10% (158.9 lb)		1747.8
C.	Growth 6% (104.3 lb)		1852.1 Lbs.

D. Mass Moments of Inertias

Orbital	Prior to Apogee Burn
I_{ox} = 3786 slug-ft^2	2486.4 slug-ft^2
I_{oy} = 3357 slug-ft^2	2471.0 slug-ft^2
I_{oz} = 1635 slug-ft^2	355.6 slug-ft^2

Little amplification is needed relative to the obvious merits of requiring a minimum shroud extension or maintaining a low center of gravity, but some detail is warranted concerning the beneficial structural aspects of the launch configuration.

The shell of the equipment module, together with the angled struts surrounding the apogee module, from the basic path for transferring all launch loads to the open truss spacecraft adapter (see Figure 6.2-16). Typical construction of such a module, housing large heat dissipating components, entails the use of thermal panels with generous thicknesses for heat conduction. This concept would make full use of the thermal control panels for structural purpose necessitating only a structural skeleton for its framing support members. Thus, instead of the thermal panels being a "dead load" requiring additional structure for its support, these elements are integrated into the structure, thereby conserving weight and allowing for greater future growth.

The advantages of mounting the parabolic antenna from the forward end of the equipment module are important from a standpoint of system reliability considerations. The probability of antenna deployment is enhanced if the individual segments undergo no deformations during launch that would tend to wedge the segments into the antenna lateral restraint devices. Since the forward mounting of the antenna ensures that only tensile loads are developed in the segments during axial thrust, the problem of excessive deformation due to compression buckling is eliminated.

The solar array support truss also benefits in a like manner, with the elimination of column buckling as a mode of failure during launch environment.

The advantages derived from this packaging concept are even more pronounced when considering the orbital or deployed condition of the spacecraft.

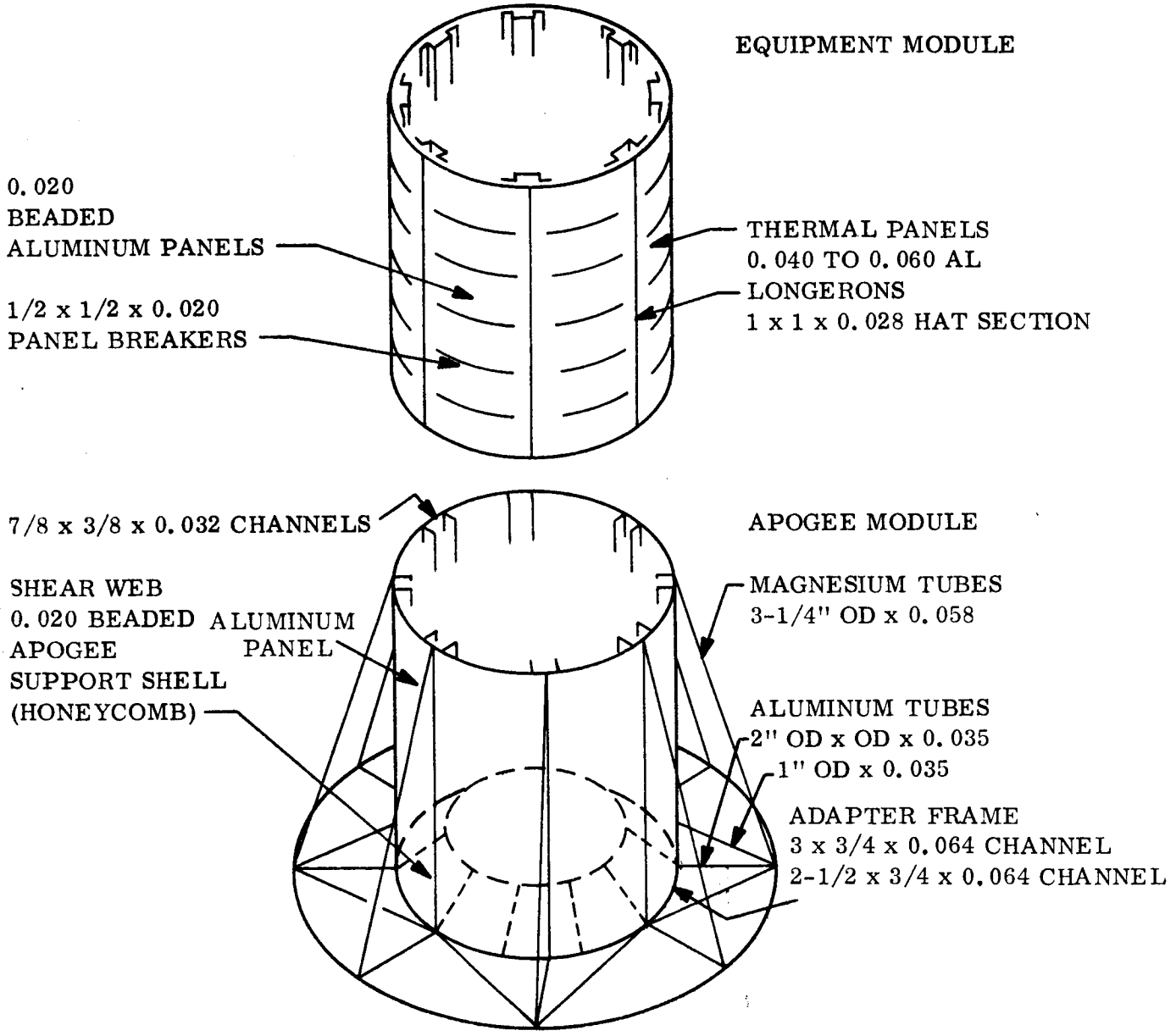


Figure 6.2-16. Structural Load Paths

6.2.5.2 Equipment Module Deployment

In view of the dependency of the configuration approach on deployment of the equipment module, the mechanism to achieve deployment was investigated in some detail. Two techniques - one electrically powered, one mechanically powered - were studied to evaluate the feasibility of separating and extending the feed module from the antenna and to assess the relative complexity of the two approaches. For the study, it was assumed that the antenna deployment mechanism is a separate mechanism and that antenna deployment has already been successfully achieved.

The electrically powered system is shown in Figure 6.2-17. This system utilizes three motor-driven screw jacks to separate the two masses. At full deployment, the folded links lock in place and the screw jacks are withdrawn and discarded.

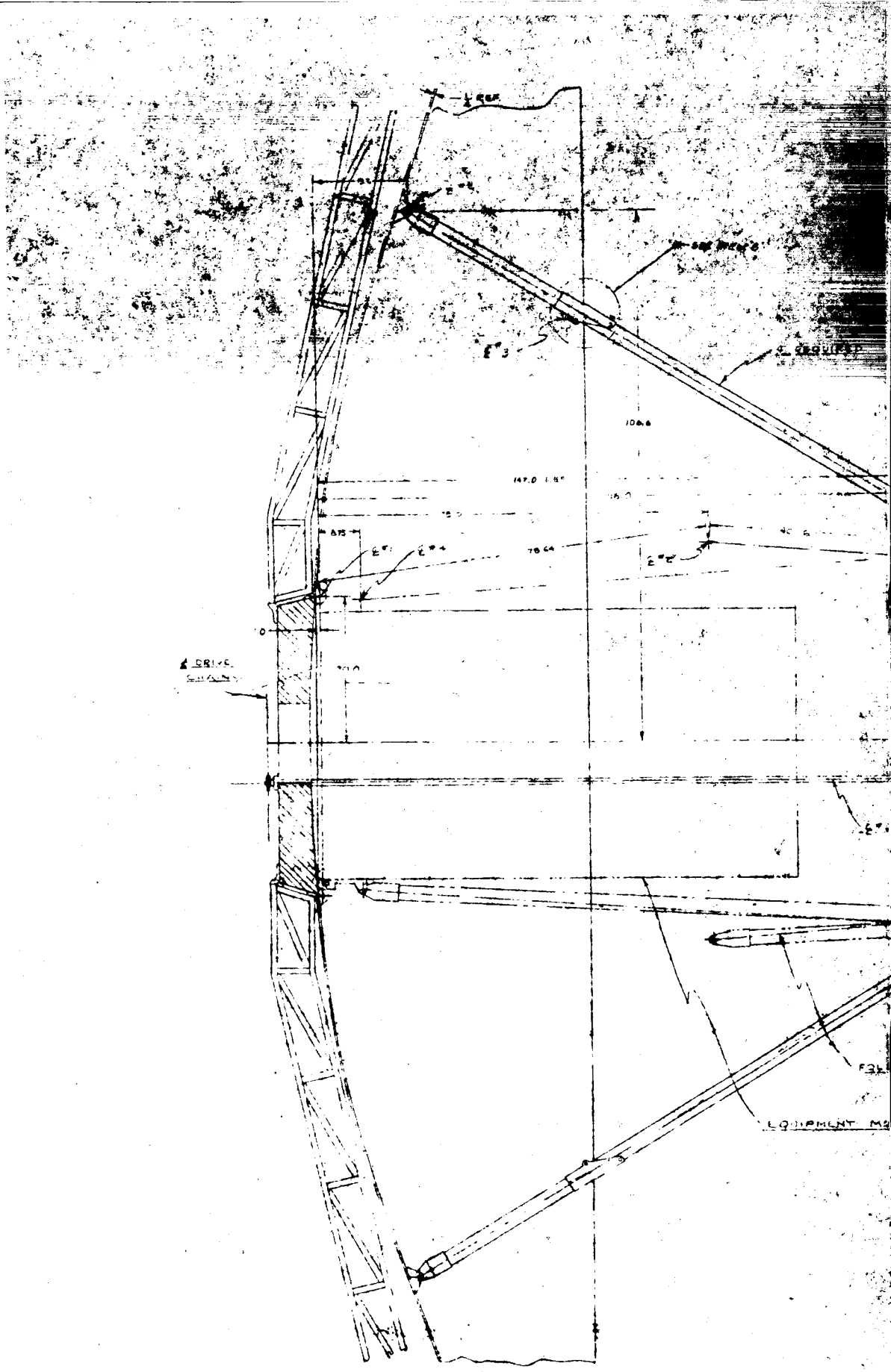
The mechanically powered system is presented on Figure 6.2-18. During deployment this system is provided by a cable/pulley system which synchronizes the motion of the spring-actuated links.

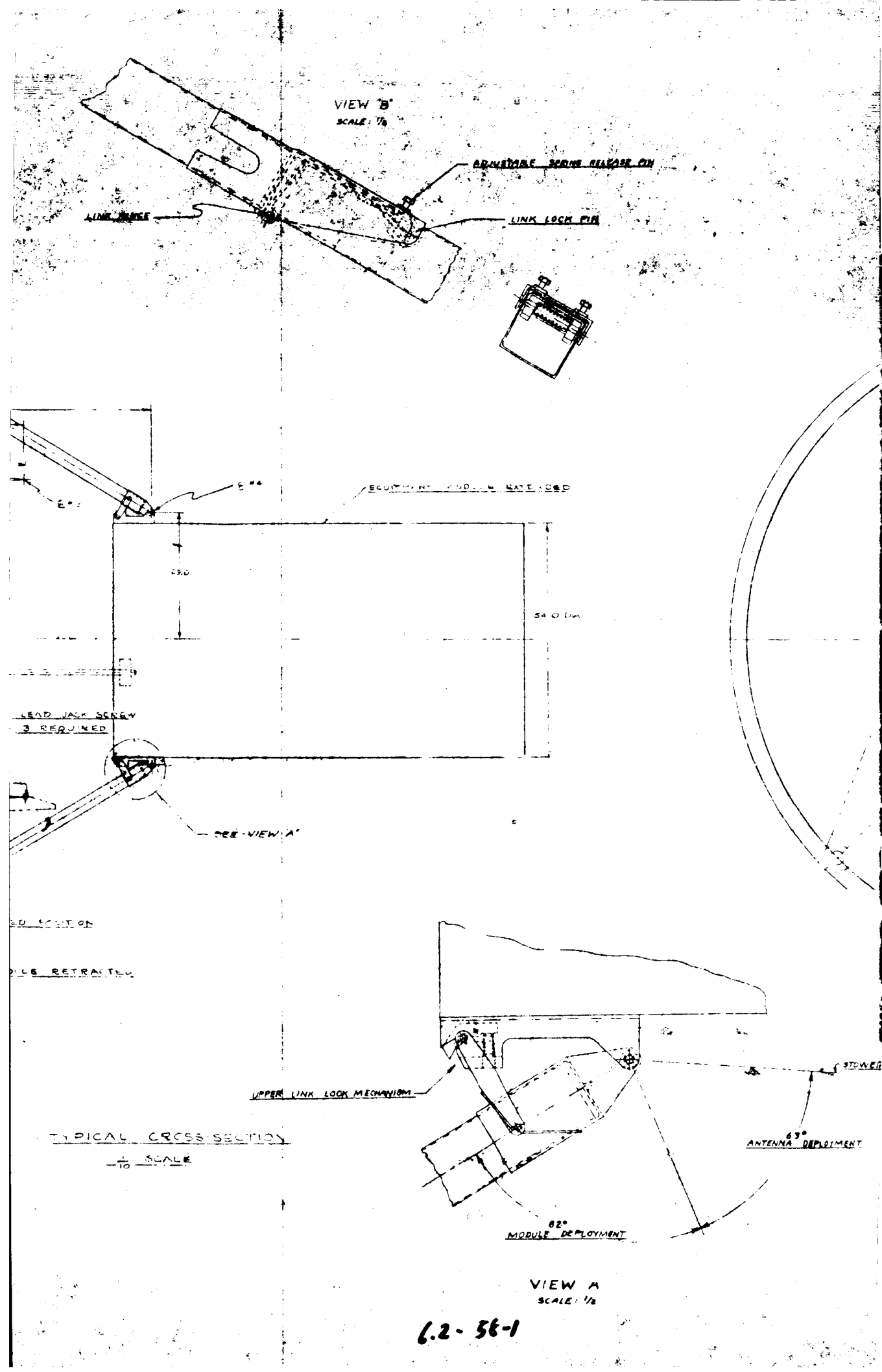
A detailed description of each system follows.

6.2.5.2.1 Electrically Powered System

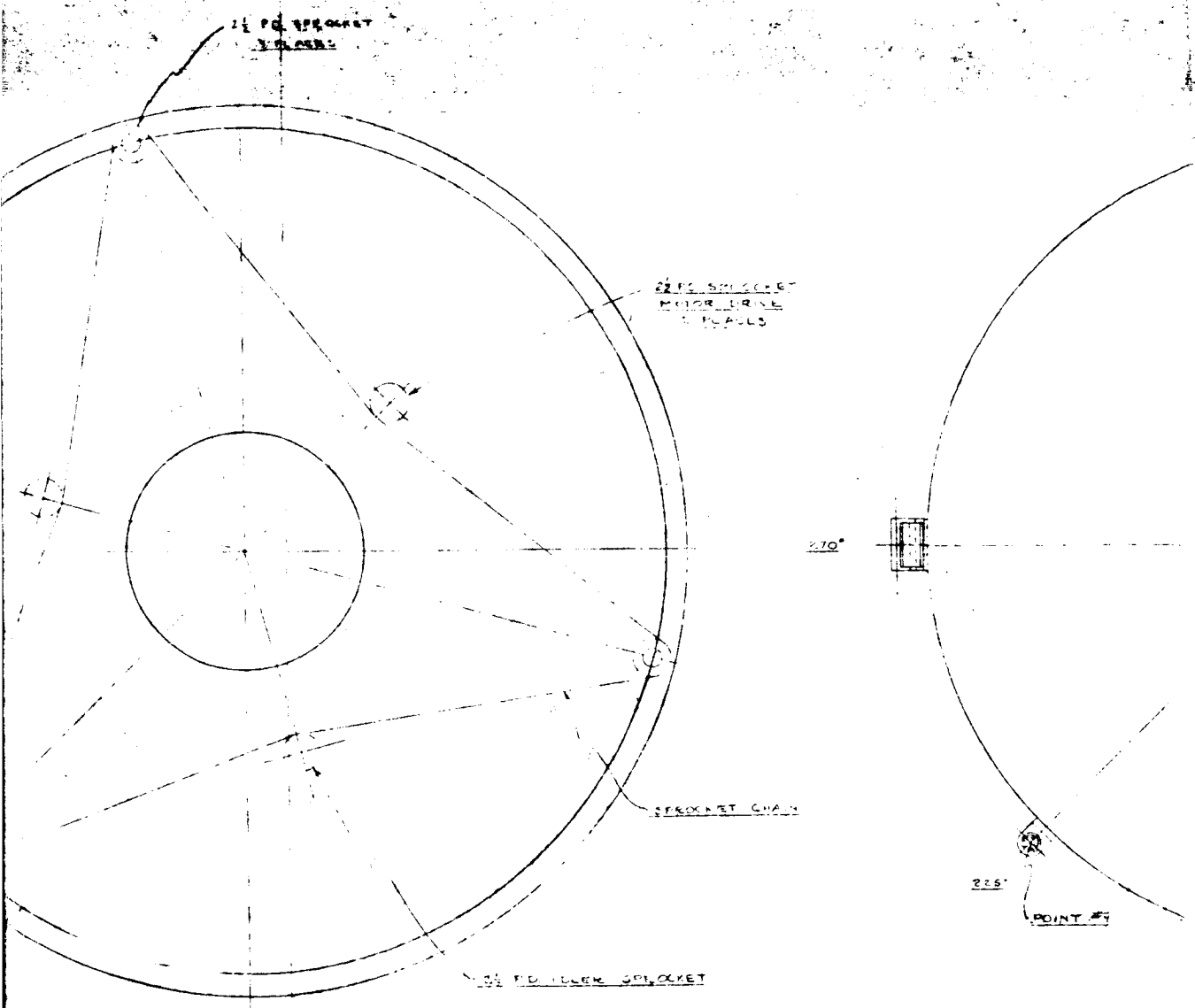
Deployment is accomplished by three equally spaced screw jacks which also provide lateral and rotational stability of the two masses during deployment. Four sets of articulated links are unfolded by the deployment motion and have been assumed to contribute nothing to the stability until full deployment has been achieved. At that time, the articulated links are automatically locked and the screw jacks are withdrawn and ejected into space leaving the articulated links to provide stiffness and stability for operational requirements. For the motor system investigated deployment time is approximately 14.7 minutes.

Actuation of the screw jacks is accomplished by two redundant motors with self-contained gearboxes. Sprockets on the output shafts drive a continuous chain. Although a chain has been shown on the drawing, this is considered a generic term. More detailed study might




VIEW B
SCALE: 1/8
ADJUSTABLE SPRING RELEASE PIN
LINK LOCK PIN
LINK BRACE
EQUIPMENT POD (N. RATED)
54.0 DIA
LEAD JACK SCREW
3 REQUIRED
SEE VIEW A
UPPER LINK LOCK MECHANISM
STOWED
63°
ANTENNA DEPLOYMENT
82°
MODULE DEPLOYMENT
TYPICAL CROSS SECTION
1/10 SCALE
VIEW A
SCALE: 1/2

6.2-56-1

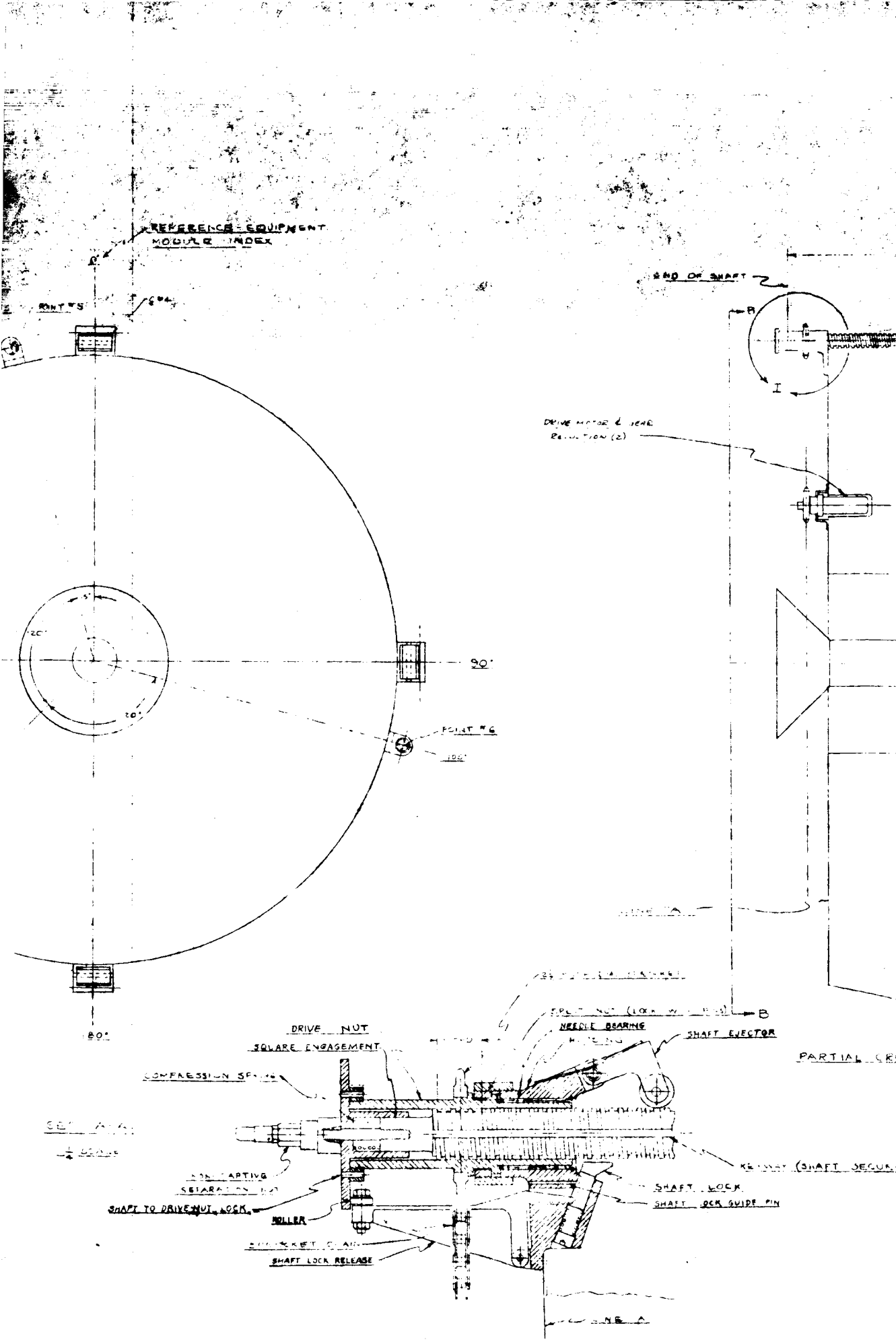


SECTION

SEC. E-E

¼ SCALE

6.2-58-2



DETAIL I

FULL SCALE

6.2-58-3

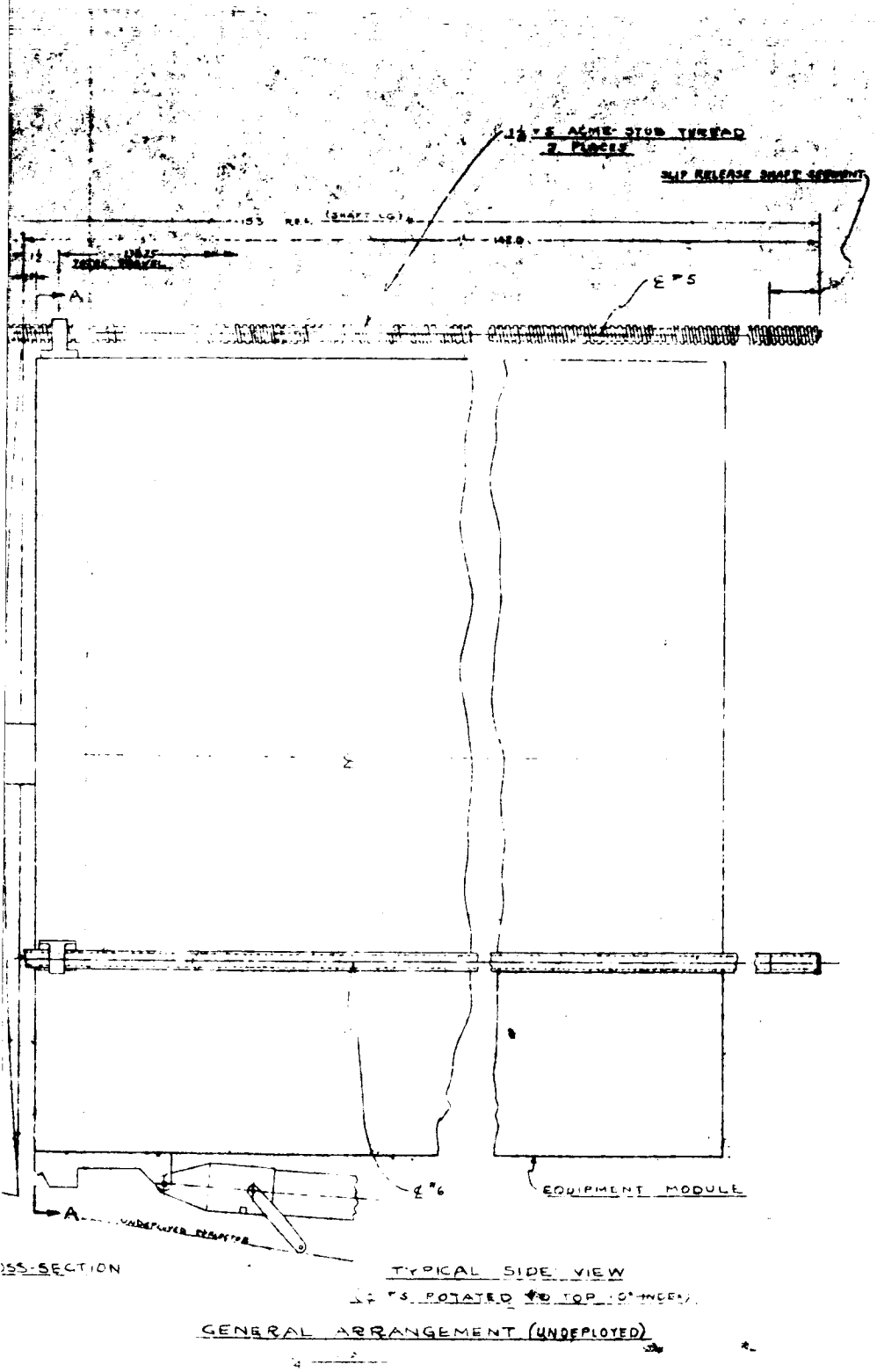
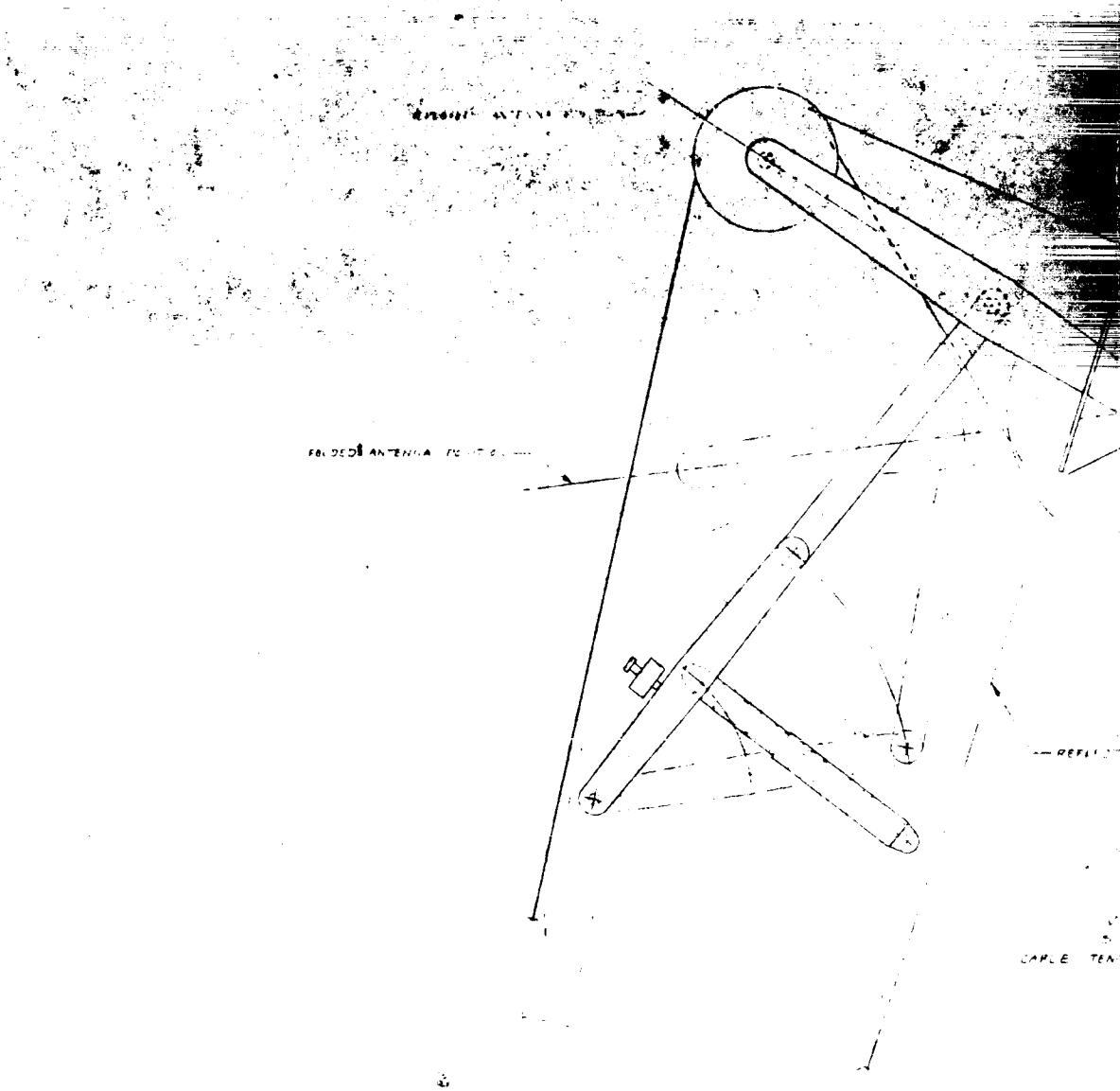
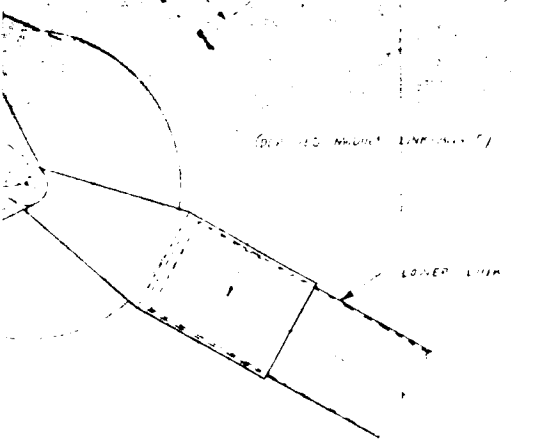
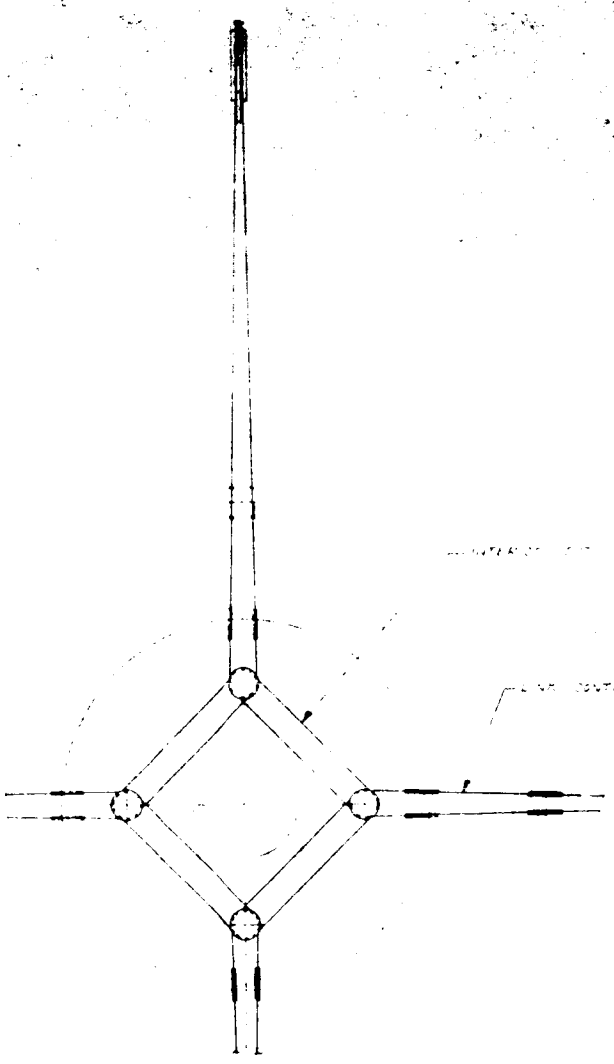


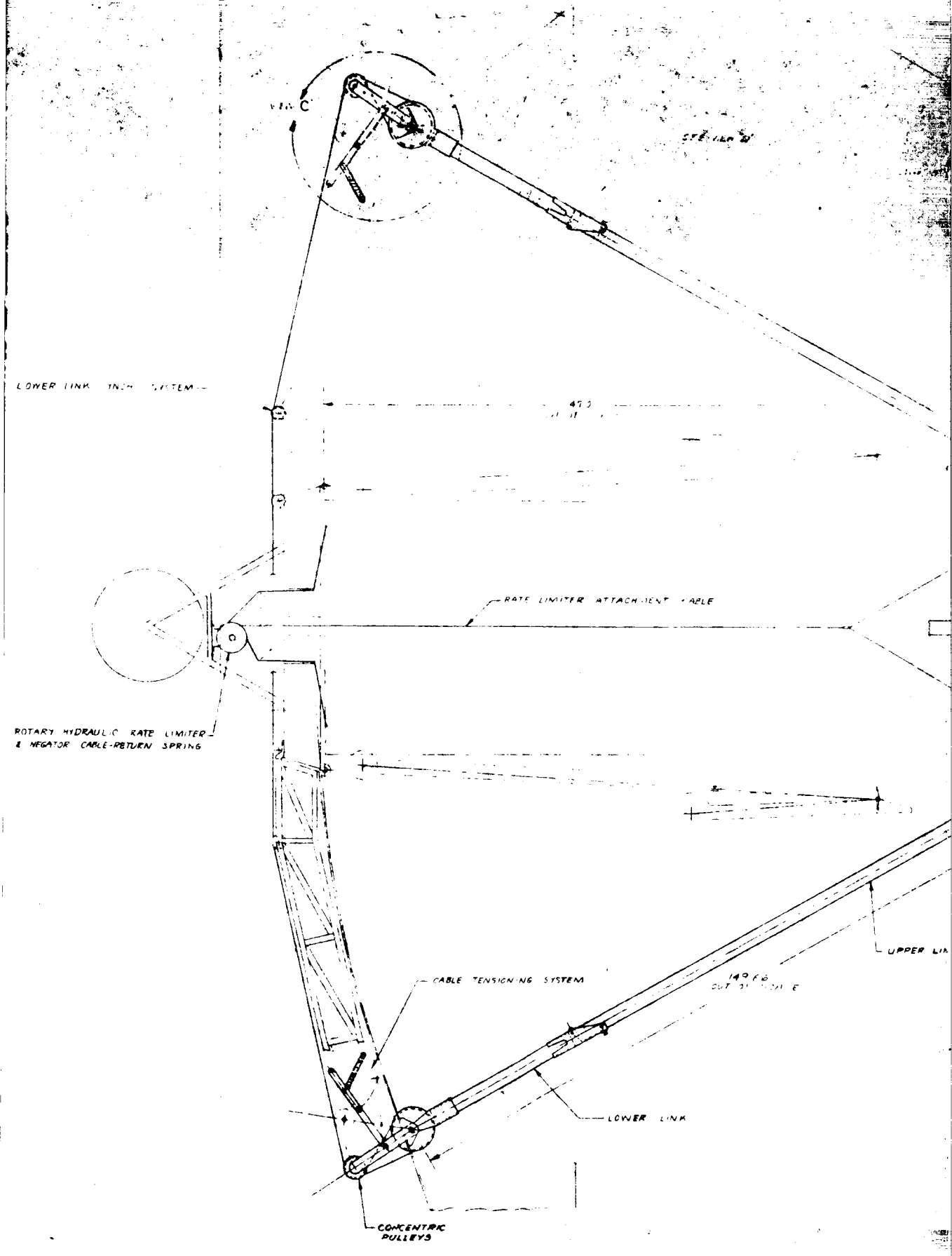
Figure 6.2-17. Electrically Powered Deployment System



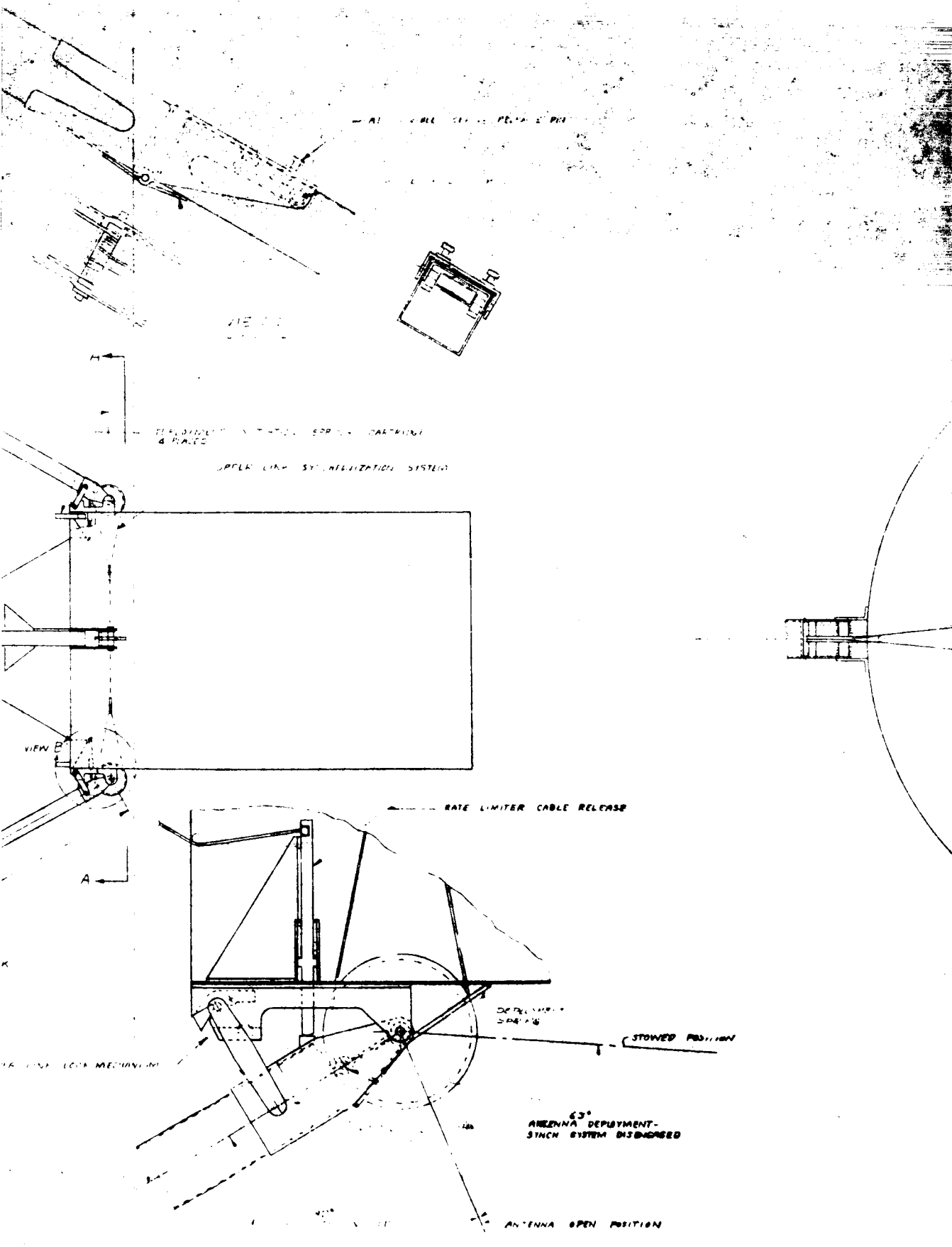




LOWER LINK SYNCH SYSTEM


LOWER LINK
RATE LIMITER ATTACHMENT CABLE
ROTARY HYDRAULIC RATE LIMITER
& NEGATOR CABLE-RETURN SPRING
CABLE TENSIONING SYSTEM
LOWER LINK
CONCENTRIC
PULLEYS

6.2-60-2


RATE LIMITER CABLE RELEASE
STOWED POSITION
63°
ANTENNA DEPLOYMENT-
SYNCH SYSTEM DISENGAGED
ANTENNA OPEN POSITION
VIEW B

6.2-60-3

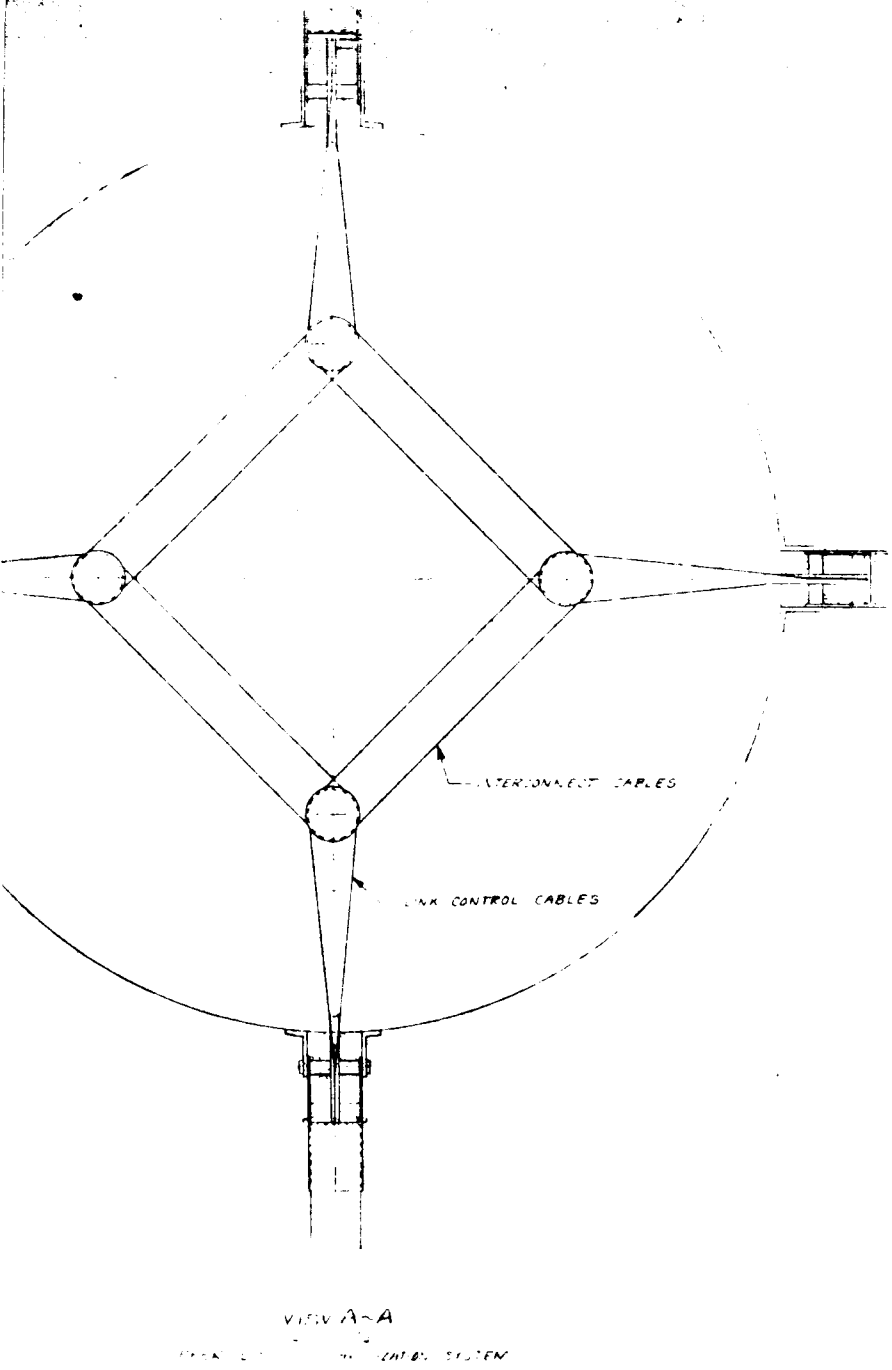


Figure 6.2-18. Mechanically Powered Deployment System

6.2-60-4

show that a thin steel band would be more advantageous weight-wise. Perforations in the band would allow it to be driven by a sprocket much in the manner of movie film.

When deployment is completed, a microswitch closes to initiate screw jack withdrawal. The microswitch can be triggered by the action of the upper link in rotating into its locked position. The withdrawal signal reverses the motors and simultaneously fires the separation nuts which retain the drive nut/screw jack lock plate. The lock plate is ejected by a compression spring, and the screw jack is no longer locked to the drive nut.

Before withdrawing the screw jack, a positive means of preventing it from rotating must be implemented. The ejection of the lock plate frees the shaft lock release, which in turn releases the shaft lock. The shaft lock is spring-loaded to engage a full-length keyway in the screw jack and thereby prevents rotation. At the end of deployment, the screw jack is still engaged in the fixed nut on the module. In order to permit screw jack axial withdrawal, the last few inches are made of a separate dissimilar material or teflon-coated material and joined to the main screw by a light press fit and square tongue engagement.

Thus, to withdraw the shaft, the separation nuts are fired, the motors reversed; the drive nut turns on the jack screw, withdrawing it from the "screw extension" and translating it toward the hub.

This system is satisfactory until the last jack screw thread has passed through the drive nut and a few inches of the square-ended screw have yet to progress through the nut and out to space. (It was deemed advisable not to retain the jack screws projecting out the back side of the hub because of the effect of their mass and inertia on system natural frequency and attitude control propellant consumption.) At this moment, a spring-loaded shaft ejector comes into action. This is a crank at the end of which is a roller which heretofore has been sliding (during deployment) or rolling (during withdrawal) against the threads. When the end of the screw comes by, the roller is in a position to drive it axially through the drive nut (the threads have become disengaged). A small amount of energy should be adequate to propel the screw jack through the nut and into space.

The geometry of the four support links is essentially as defined on the layout. Their function during the deployment process is merely to follow the rest of the action, although they will probably provide some additional lateral stability.

Their function after deployment is to provide a stiff connection between the reflector and the equipment module. The several degrees of freedom of the system must be eliminated by locking two joints in each set of links. This has been done at the link attachment of the equipment module and at the interlink joint. The remaining joint at the reflector is left pin-ended. Thus, each set of deployed links (when locked) is a cantilever beam with fixity at the equipment module. This fixity is provided by a pair of links which are pinned to the "upper" link and are spring-loaded to enter an over-center slot when deployment is completed. In addition to the spring load, a lock prevents the link from disengaging.

Tubes of square cross-section were selected for the link design for two reasons. First, the square section simplifies the design of hinge joints and latches. Second, for the same weight and moment of inertia a square tube of smaller width than an equivalent round tube can be used. Although the effect may not be great, it is in the direction of reducing aperture blockage. A 3-inch-wide tube with a 0.07-inch wall thickness was selected. The 3-inch x 0.07-inch tube support system has a natural frequency of 2.7 cps (assuming the antenna is infinitely stiff). In a detailed design it would be necessary to optimize the design in some fashion, such as use of tapered tubes, doublers, et al.

Although a detailed design of the drive motor system was not attempted, it was deemed prudent to make an approximate first cut at the requirements. To accomplish this task, some arbitrary assumptions were made:

a. A 5-pound thrust load was assumed on each of the three jack screws.

b. A friction factor of 1.0 was assumed for the thrust washers and the fixed nuts on the equipment module.

c. An efficiency of 70 percent was assumed for all bearings, sprockets, etc.

These assumptions, combined with the geometry shown on the drawing and the dimensions of the screw, resulted in a total torque of 34.5 in.-lb. This approximate output can be achieved with a 27-volt dc motor with a rated load of 6.0 in.-oz. and a starting load of 21 in.-oz. The dc voltage was chosen because of high starting torque capability, reversability, and ease of control. Rated load current is 1.4 amperes, and no load motor speed is 6400 rpm. A gear reduction of 117:1 with an efficiency of 85 percent results in an output torque of 37.3 in.-lb and a no load output speed of 54.7 rpm. With both motors operating and sharing the load, output speed is 47 rpm and deployment time is 14.7 minutes.

In order to take advantage of the redundant motors, the design must be such as to prevent one motor failure from preventing deployment. Consequently each motor output shaft could be coupled through a spring/solenoid ratchet/pall clutch. Thus failure of one motor would merely meal idling its ratchet. Under this condition, one motor would do all the work and deployment time would be increased to 17.5 minutes.

6.2.5.2.2 Mechanically Powered System

This type of system was selected for study because it appeared possible to provide deployment energy and rate control with no additional electrical events after the initial pyrotechnic release of the equipment module. However, the nature of the configuration and the dependence upon the links to provide stability during deployment as well as after deployment as well as after deployment present a unique set of problems.

In contrast to the electrically powered system, no built-in rate control exists, as was provided by the motor/screw jack system. Furthermore, the absence of the synchronizing and stabilizing influence of the screw jacks leaves a system having several degrees of freedom. This gross instability must be eliminated.

Stability can be provided if the four lower links (those attached to the reflector) are synchronized to deploy at the same rate, and if the four upper links (those attached to the equipment module) are similarly synchronized to each other. At the same time, the sync system must be such as to eliminate or at lease minimize any interaction between reflector deployment

and itself. Otherwise, any irregularities during reflector deployment will induce loads in the sync system.

The wide separation of the links to be synchronized made a cable system appear attractive. Several techniques of implementing a cable system might be followed, but the one selected seemed to present a minimum amount of aperture blockage. It is shown in Figure 6.2-18.

Two separate systems are used, one for the upper links and one for the lower links. Their operation is almost identical.

Cable sectors are supported by the same hinge pins which attach the upper links to the equipment module. Links and sectors are free to turn to the equipment module. Links and sectors are free to turn relative to each other until full deployment of the reflector has been achieved. The antenna deployment causes the upper link to rotate approximately 63 degrees relative to the equipment module (and relative to the cable sector). At that time, a spring-loaded pin locks each upper link to its sector.

Deployment energy is provided to each upper link by a torsion spring at the link support hinges. Rotation of the link through an angle of 82 degrees relative to the equipment module (in addition to the previous 63 degrees) results in full deployment. At that time, the upper link is locked in position by the same technique described for the electrically powered system. By locking the link, all further dependence upon the sync system and the driver springs is eliminated.

The lower links are synchronized in much the same fashion. At the attachment of each lower link to the reflector a concentric cable sector is pinned to a closed loop cable. The four cables pass through a pulley system to four sectors on the back side of the hub. These sectors are interconnected by a closed loop cable system to provide link synchronization as described for the upper links.

One additional problem is peculiar to the lower link system. Although the same idling technique for divorcing the sync system from antenna deployment motion is employed, the rotation of the antenna relative to the hub tends to shorten the link control cables. In order to compensate for this effect, one pulley on the antenna is not pinned to the support structure, but rather is pinned to an arm which can pivot about the sector hinge. A pair of spring-loaded toggle links maintains tension in the cable by driving the pulley-support arm as the reflector deploys. When antenna deployment is completed, the toggle links are over center and the system is locked.

Additional deployment energy is provided by torsion springs at the interlink joint. The upper and lower links are locked to each other by the same technique as was used for the electrically powered system. The link geometry in the early portion of the deployment cycle presents an apparent mechanical disadvantage for the eight deployment springs previously described. In order to alleviate this condition, four short stroke springs have been shown extending out of the equipment module. These springs, which react against the hub, are intended to impart sufficient kinetic energy to the separating masses to overcome the mechanical disadvantage. A separation velocity of 1 foot per second is probably more than adequate and not too difficult to achieve.

Although the system described thus far provides deployment in a synchronized fashion, it is also necessary to dissipate the excess kinetic energy which exists. The first approach utilized a hydraulic dashpot of the standard variety. The dashpot was incorporated into the interconnect system on the back side of the reflector hub. However, the concept of using a few inches of stroke to limit the rate of a body which is translating through a distance of 12 feet seemed rather undesirable. Morever, the route followed by the damping loads was extremely devious. It was resolved that the rate-limiting action should take place between the hub and the equipment module directly. Thus, the devious load path and the sensitivity of the short stroke system were eliminated by using a 12-foot stroke.

The system employs a cable attachment between the equipment module and a rotary hydraulic rate limiter located on the back of the hub. The cable divides into two pieces

at the module end in order to clear the feed horn. At the module, the cable passes through a slotted fitting upon which the cable's ball-end rests. The ball is captivated by a spring-loaded sliding rod. The rod is displaced by the upper link's final deployment motion, and the ball is freed. The cable is then free to be retracted. Retraction is accomplished by a negator spring motor mounted on the rotary damper. A small amount of spring load will be adequate to rewind the cable onto its pulley.

Prior to deployment, the rate limiter cable's routing is such as to provide some slack in the early portion of deployment. This was done to prevent the rate limiter from dissipating the system's kinetic energy too quickly.

Routing of the cable and its early motion must be studied carefully to provide positive assurance that no damage to the feed horn will occur during deployment.

6.2.5.2.3 Deployment System Comparison

Table 6.2-7 attempts to compare the two systems with regard to the parameters deemed important. In general, the comparison is qualitative, since an in-depth design and analysis was not performed and because certain parameters are functions of antenna characteristics.

The results of this study indicate that both systems appear feasible. However, the complexity and number of parts associated with the mechanical system render a lower verdict on deployment confidence than the electrically powered system, in spite of the latter's dependence on successful motor operation.

6.2.6 ALTERNATE FIXED FEED CONFIGURATIONS

The deployed configuration, presented in Section 6.2.5, represented an optimum design from an rf standpoint, but features a complex deployment. At this point in the study, additional rf testing was conducted to evaluate more precisely the far-field effects of the feed support truss. This test program is discussed in detail in Section 6.4. The results indicated that a nondeployed feed, with the truss mounted between the antenna hub and the top of the feed module, had poorer rf performance than the deployed feed approach, but the decision was made that the additional loss would be acceptable.

Table 6.2-7. Deployment System Comparison

	Electrically Powered System	Mechanically Powered System
Estimated Weight (lb)	125	110
Approximate number of parts (excluding bolts, nuts, springs)	75	100
Number of electrical events	5	1
Failure mode	a) Loss of power is total failure. b) Redundant motors and squibs.	Failure of any one part of system may not inhibit deployment if jam does not occur.
Stability during deployment	Determined by screw jack bending stiffness	Determined by link bending stiffness and cable stretch
Stiffness after deployment	Determined by link section (2.7 cps for weight shown)	Determined by link section (2.7 cps for weight shown)
Deployment time	Approximately 14.7 min. for motor system shown	To be established by allowable inertia loads and rate limiter design
Load-carrying ability	1 g	1 g
Testing considerations	Requires support in 1 g until fully deployed	Requires support in 1 g until fully deployed
Potential problem areas	Motor reliability under temperature variations between launch and deployment (several hours); microswitch reliability	a) Rigging b) Cable tension rements c) Effect of thermal environment on cable tension

The selection of a fixed-feed approach in lieu of the deployed configuration, incorporated the philosophy of deployment simplicity as the keynote of design activity. As a result, only one basic arrangement was practical, that of mounting the phased array and other earth-viewing equipment in front of the nondeploying feed with the remaining spacecraft components mounted behind the hub. This left only some of the secondary configuration elements such as structural design approaches and solar panel stowage to be investigated further.

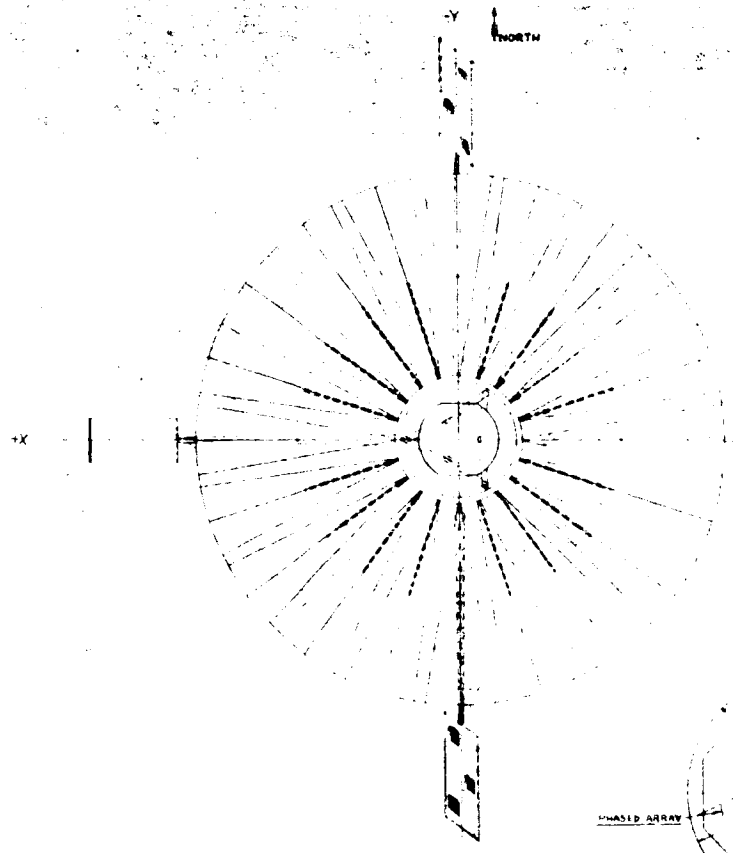
Figures 6.2-19 and 6.2-20 present an alternate approach to the design of the aft equipment module and solar panel stowage and deployment scheme. In this respect, designs are identical to each other, the duplication of drawings being made to indicate requirements of substituting either the TE-M-364-4 (Extended Surveyor Motor), or the Antares for the improved Delta apogee motor used in the selected design.

6.2.6.1 Alternate Solar Panel Stowage Arrangement

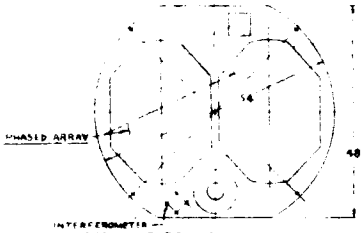
To discuss the solar panel stowage arrangement first, the approach taken was to align the solar arrays on their support trusses so that when the trusses are deployed, no additional rotation of the panels about an axis perpendicular to the truss plane was required. In this manner, the only motion of the panels, relative to the deployment trusses, required for proper orientation was a 60-degree rotation of the north and south panels about the axis of the support truss. This could easily be accomplished with a stored energy spring and damper device which could be activated upon release of the panels.

In the launch configuration, the panels are snubbed against the Earth-Viewing Module, by a preloaded release mechanism. Two objections make this scheme less desirable than the selected approach.

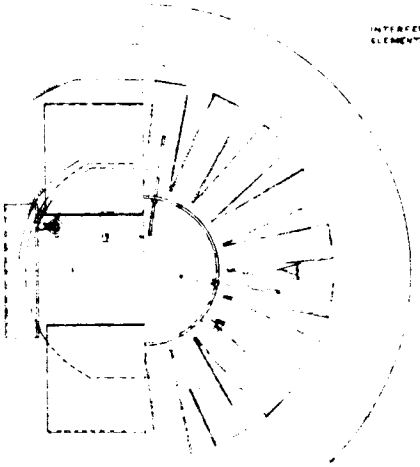
a. Failure of the snubbed-up panels to separate from the EVM means failure of the mission, since the antenna cannot deploy. Also, packaging of the panels about the EVM blocks Orientation Control sensors, phased array, and thermal radiation area, ruling out many degraded mode operational schemes. The selected design has the significant advantage of being capable of performing all but the parabolic antenna experiments while in the fully stored attitude.





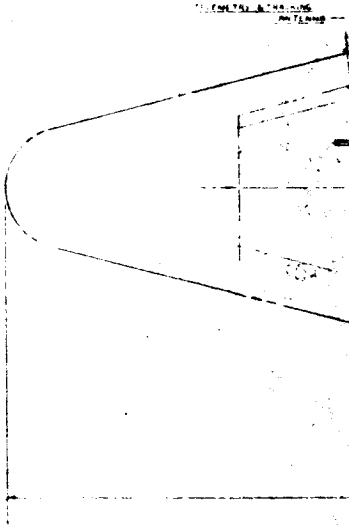


EARTH VIEW NO. 2
EQUIPMENT MODULE
VIEW B



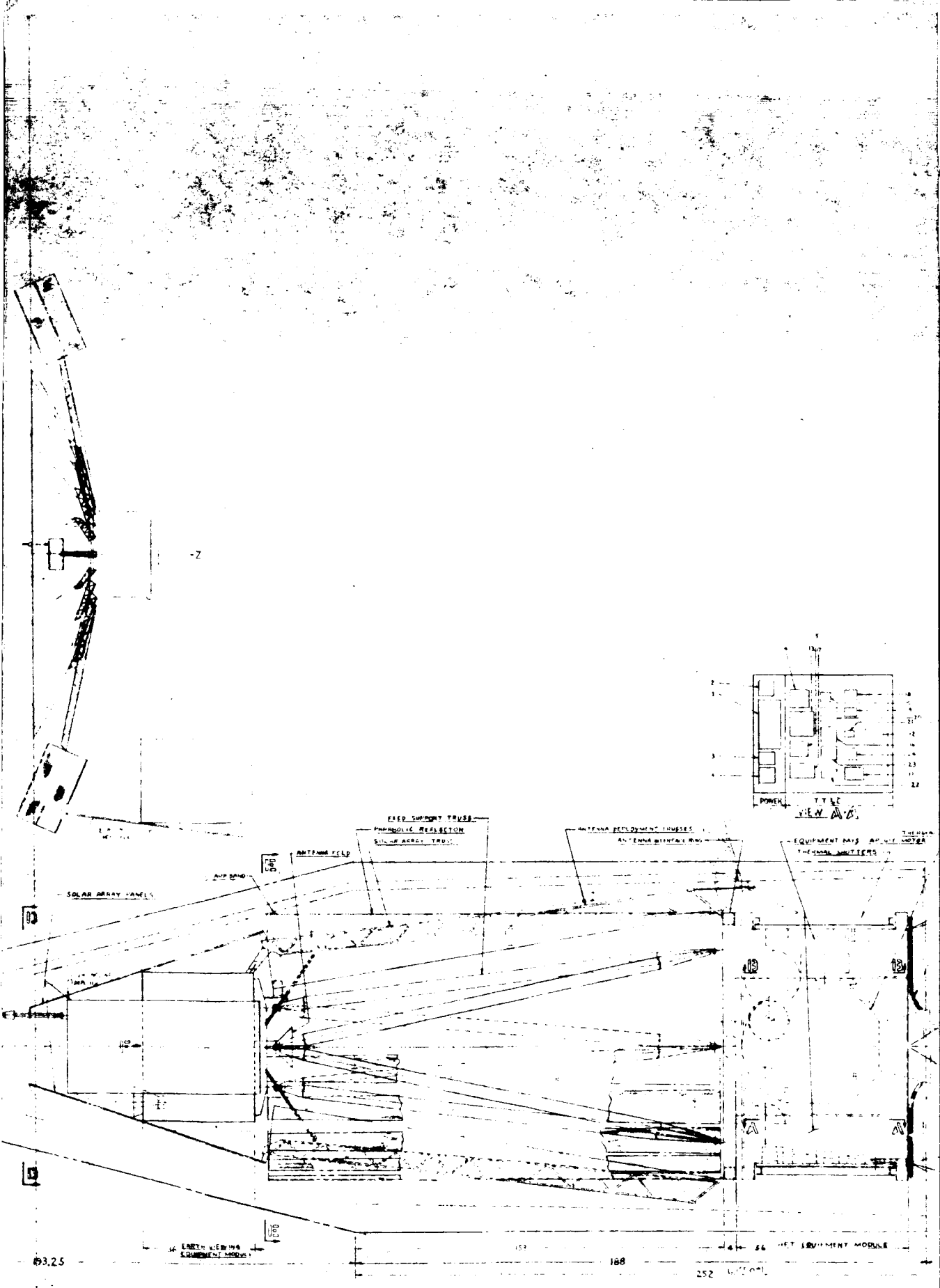
HALF SECTION A-A

HALF SECTION B-B



6.2-69

[redacted]


-Z
KEEP SUPPORT TRUSS
PARABOLIC REFLECTION
SOLAR ARRAY TRUSS
ANTENNA DEPLOYMENT TRUSSES
ANTENNA BEARING RING
EQUIPMENT BAYS
THERMAL LOUVERS
ANTENNA FEED
SOLAR ARRAY PANELS
EARTH VIEWING EQUIPMENT MODULE
193.25
188
252
POWER
VIEW A-A

6.2-10-1

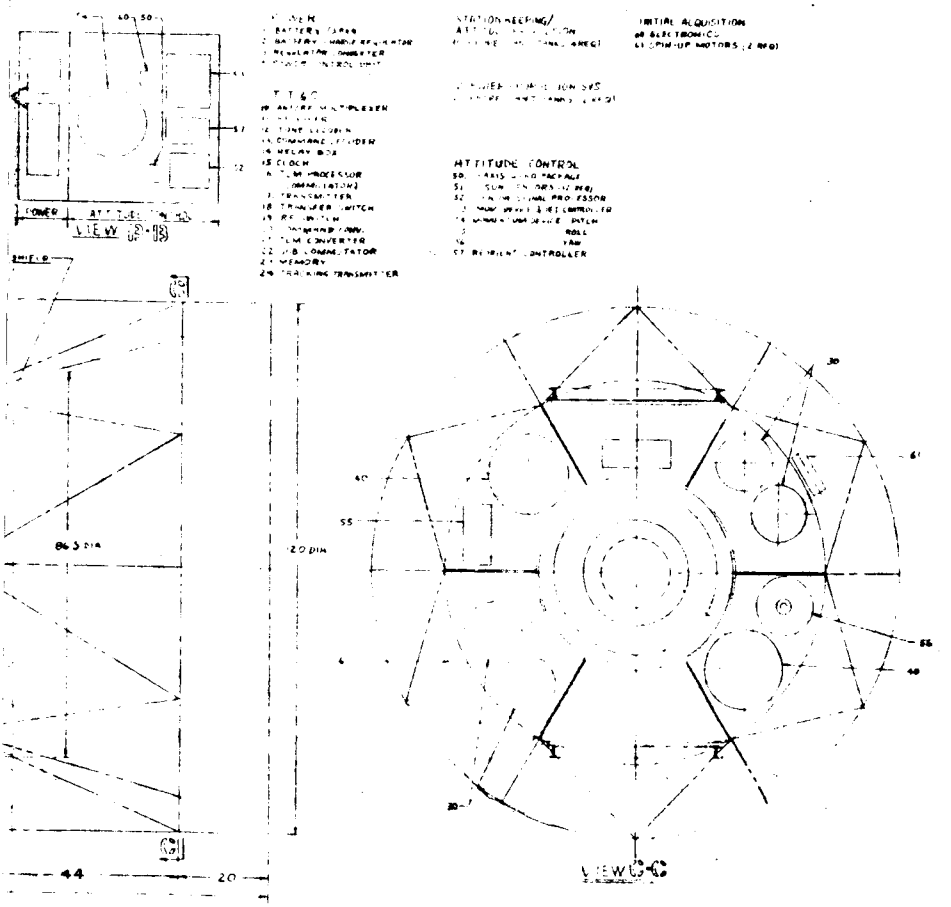
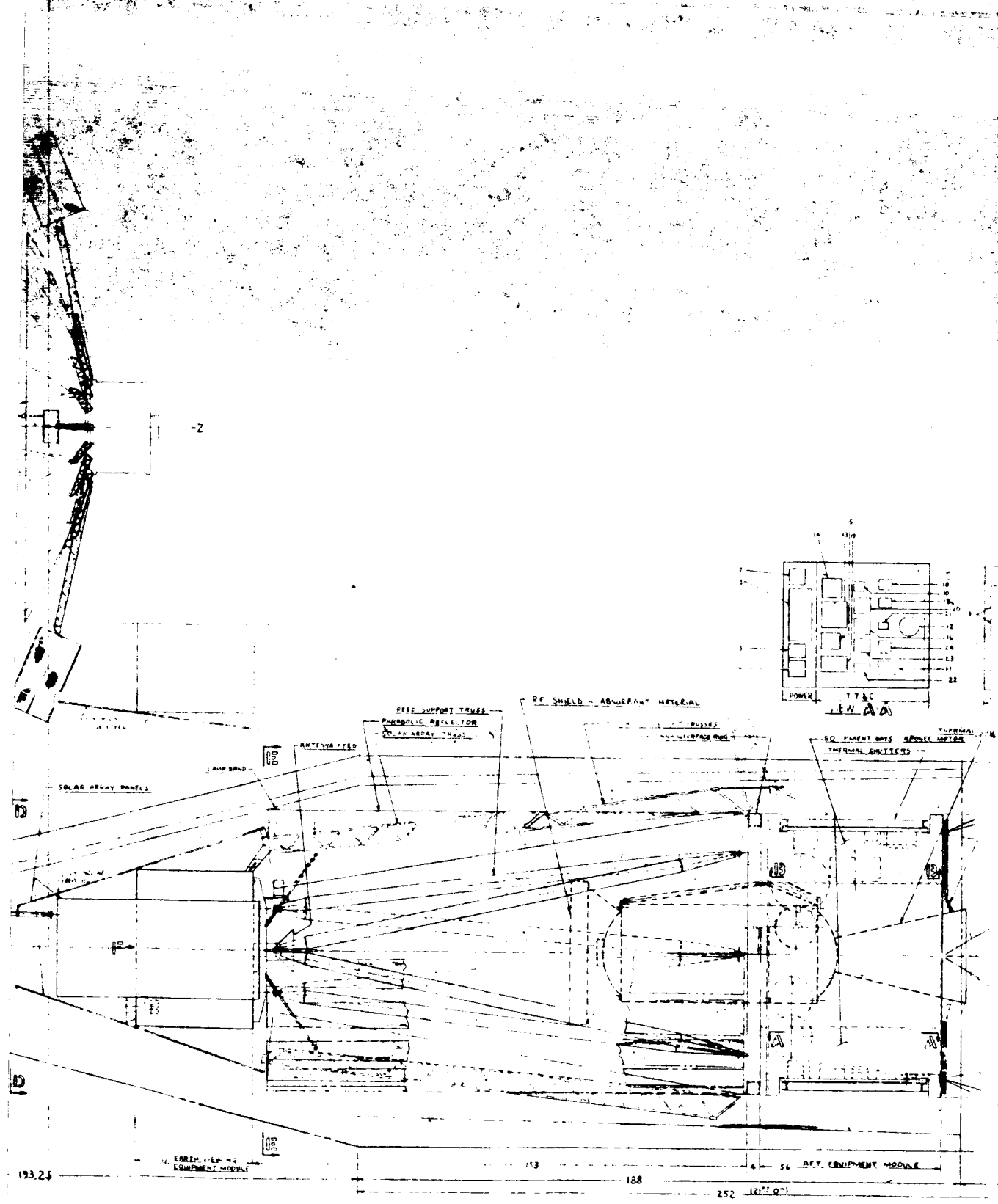


Figure 6.2-19. Alternate Fixed Feed Design Extended Surveyor Apogee Motor

NORTH
+Y
-X
+X
+Z YAW AXIS
EARTH
PHASED ARRAY
48
EARTH VIEW
EQUIPMENT MODULE
VIEW
HALF SECTION
HALF SECTION


-Z
VIEW AA
POWER
TT&C
RF SHIELD - ABSORBENT MATERIAL
FEED SUPPORT TRUSS
PARABOLIC REFLECTOR
ANTENNA FEED
SOLAR ARRAY PANELS
EQUIPMENT BAYS
THERMAL LOUVERS
193.25
153
56
AFT EQUIPMENT MODULE
188
252

6.2-72-1

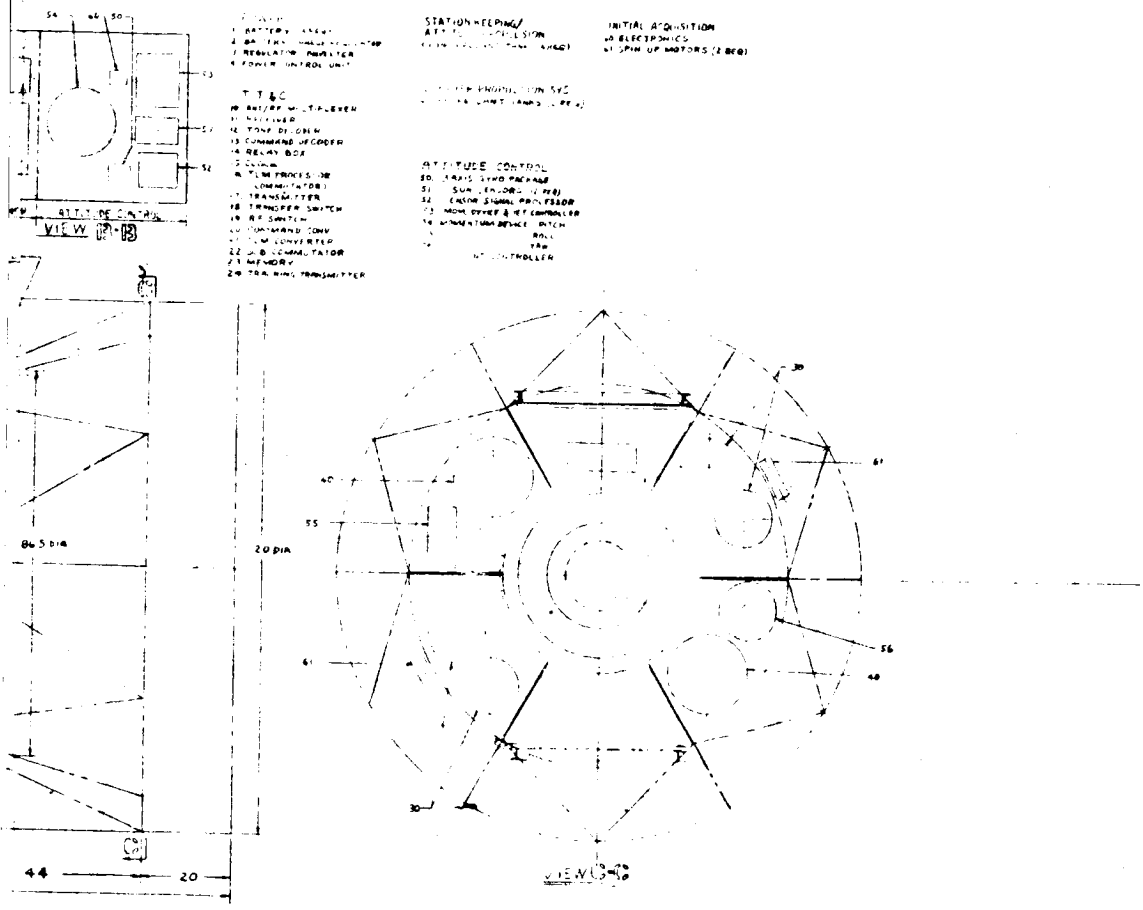


Figure 6.2-20. Alternate Fixed Feed Design
Antares I Apogee Motor

6.2-72-2

b. The tracking, telemetry, and polarization antennas must be mounted on a solar panel in order to obtain the proper field of view. This requires an excessive amount of harness to run from the antenna, down a deployment boom and then back through the feed support struts to the TT&C electronics mounted in the EVM.

6.2.6.2 Aft Equipment Module Design

The structural design of the aft equipment module is based on the use of a large-diameter spacecraft adapter which mates to the Centaur at Centaur station 219. The high probability of this launch vehicle mating interface being ultimately recommended by NASA/Lewis and its similarity to the Titan III-C mating provisions has been inferred in Section 6.2.2.

The primary load path consists of a semimonocoque cylinder, utilizing six longerons to transfer the loads from the feed support truss and the antenna to the truss adapter. Separation is accomplished through six explosive nuts as on the selected design. The thermal radiation panels, located on the flattened north and south sides of the AEM, are an integral part of the shear structure required to resist lateral loads, resulting in a more efficient usage of this normally thicker gage sheet material. Fuel tanks, nonheat-dissipating components, and the apogee motor are supported by internal radial webs which transfer loads to the main longerons by shear action.

6.2.6.3 Apogee Motor Packaging Provisions

This equipment module is ideally suited for the family of Surveyor apogee motors, in that the height can be tailored to suit any one, with more than sufficient packaging volume being available for mounting of components around it.

The adaptation for the installation of the Antares motor, shown in Figure 6.2-20 is not meant to be an optimum approach, but serves to illustrate the geometrical problems involved with packaging a 114-inch-long by 30-inch-diameter solid motor. The requirement to protude the motor into the reflecting area is dictated by shroud height limitations. However, this protrusion is into the blockage area created by the EVM, and an rf absorber or reflector is required here in any event. The most significant integration problem will be of a structural nature. The motor, fully loaded, weighs 2285 pounds, which is more than half of the total spacecraft weight.

Under lateral loading, the overturning moments on this high-mass item must be reacted by a truss work, whose geometry is not too favorable in this direction. In addition, the resulting high-mass center of the spacecraft is going to help incur a larger structural weight penalty. The narrow diameter means that axial loading must be sheared over greater distances in order to be reacted at the six main longerons.

In conclusion, use of the Antares I, which is not an efficient answer to the ATS-4 propulsion requirements, aggravates even further the structural problems posed with a high-silhouette spacecraft, and is, in fact, an extreme opposite to the optimally configured motor for this mission.

6.3 PARABOLOID ANTENNA

The large paraboloid antenna study included both the paraboloid reflector and the multi-frequency feed. The study was initiated with a broad review of the state-of-the-art which resulted in the selection of the Petaline packaging concept for the paraboloid and a combination of dipoles and coaxial horns for the feed. Variations of these selected concepts were studied to determine an optimum arrangement considering total system requirements. The study resulted in the preparation of preliminary design drawings which show the overall configuration and necessary details for understanding the design approach.

6.3.1 RATIONALE FOR SELECTED REFLECTOR CONCEPT

6.3.1.1 Antenna Requirements

The requirements for the large parabolic antenna are, that it must have a minimum aperture diameter of 30 feet and must be capable of both transmitting and receiving operations at frequencies up to 10 GHz. Specifically, the antenna feed system must be capable of transmitting at 100, 800, 2300, and 7300 MHz and also must be capable of receiving at 1700, 2100, and 8000 MHz. It is not necessary that either transmission or reception be simultaneous on all the above frequencies. Bandwidth capability of the system at the specified frequencies must be 10 percent and system antenna efficiency must be at least 50 percent.

6.3.1.2 Survey of Potential Reflector Concepts

The antenna study was based on a reflector diameter of 30 feet, which is the minimum specified. Consideration was given to reflector diameters in excess of 30 feet, since these have the potential of providing higher gain. However, the reflector surface accuracy needed with the 30-foot diameter to meet the 50 percent efficiency requirement approaches the limit of manufacturing capability. In addition, several adverse effects of the increase in diameter tend to negate or over compensate for the gain improvement and therefore make the larger reflector diameters less desirable:

a. Increased shroud length

b. More flexible structure, resulting in lower resonant frequencies and potential control coupling

c. Increased packaging and deployment problems

d. Increased thermal distortions and attendant rf losses

e. Increased weight

f. Increased possibility of interference with sensor view angles

It has been concluded that a 30-foot diameter reflector is compatible with the spacecraft design constraints and will best approach the 50 percent system efficiency specified in the contract.

6.3.1.2.1 Classification of Antennas

The use of large high-gain microwave antennas for space applications in the near future will require the development of reflector concepts that will be:

a. Lightweight

b. Packaged into a relatively small volume for launch to orbit

c. Deployed into an operational configuration with the required surface accuracy

d. Capable of withstanding the environment of space, especially the thermal extremes and gradients, without undue degradation in surface tolerances and/or other performance characteristics

Numerous structural and deployment concepts were studied for constructing antennas having these characteristics. Classifying the reflectors on the basis of their shape-maintenance techniques yields the major divisions and subdivisions noted below:

a. Wire-grid, formed reflectors

   1. Inflation-deployed wire grid (yielded)

   2. Thermally deployed and formed Nitinol wire grid (nickel titanium alloy, Naval Ordnance Laboratories)

b. Chemically rigidized textile or film reflectors

1. Solar-heat-activated, predistributed foam

2. Gas-catalyst-activated, resin-impregnated fabric

c. Mechanically deployed rigid reflectors

1. Umbrella configurations employing rigid ribs to support a mesh reflecting surface

2. Swirlabola configurations with preformed rigid reflecting surfaces or rigid ribs to support a mesh reflecting surface (these configurations form a cylindrical wafer when packaged)

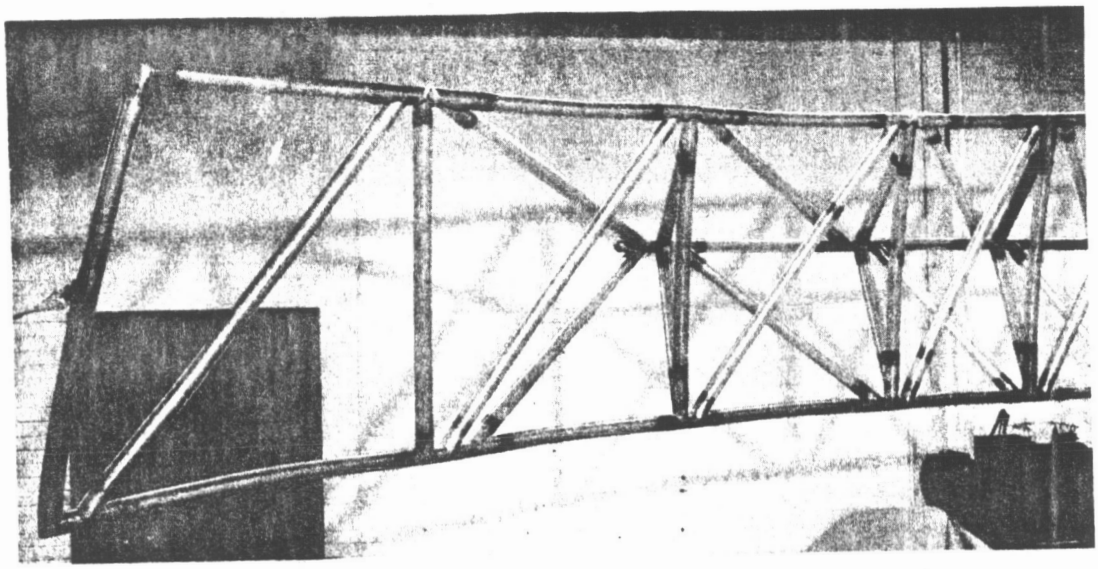
3. Petaline configurations using closely spaced foldable preformed frame elements to support a mesh reflecting surface or foldable preformed rigid reflecting surface (these configurations form a long cylinder when packaged).

The remainder of this section contains descriptions of these reflector concepts and notes their present status of development. Summarized at the end of this section are the relative merits of the various concepts with reference to the requirements of the ATS-4, large-aperture antenna.

6.3.1.2.2 Wire-Grid-Formed Reflector

Both industry-funded and government-sponsored programs have been pursued to develop space-deployable, lightweight, wire-grid-formed antenna concepts.

a. Inflation-Deployed Wire Grid. Illustrated in Figure 6.3-1 is a deployed 24 foot long, wire-grid antenna constructed to demonstrate the yielded wire approach to preforming and maintaining the preformed structural configuration in space. As shown, a wire-grid space-frame is used to support the parabolic reflecting surface. The tubular members of the space frame are made of a fabricated laminate of 12 mil aluminum wire oriented on the cylindrical surface of a film pressure barrier, so that each wire element is subjected to the same strain when the structure is pressurized internally. Therefore, when the pressure reaches the point at which the strain in the wire elements exceeds the yield stress, the wire-grid tubular members will not spring back and are effectively rigidized. The grid then will maintain its structural shape, capable of supporting imposed loading, when the pressure differential is removed. A typical frame element is shown in Figure 6.3-2.



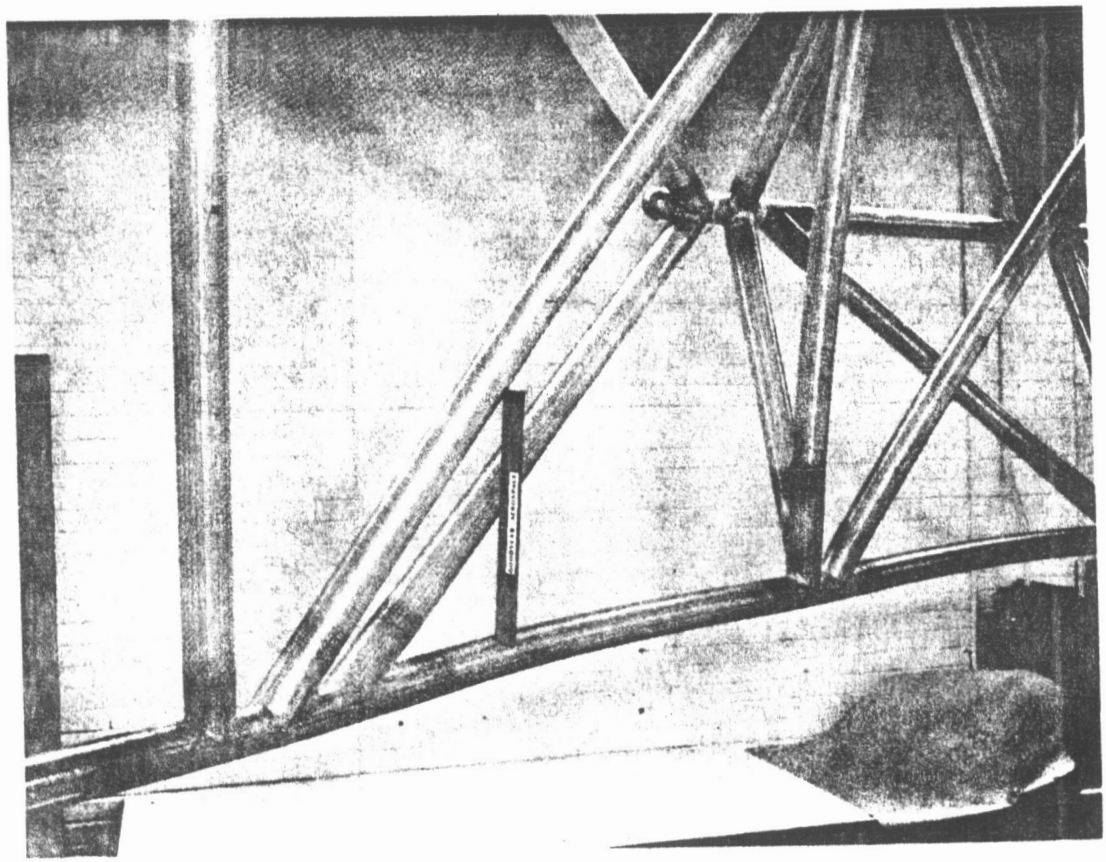


Figure 6.3-1. Wire-Grid Structure

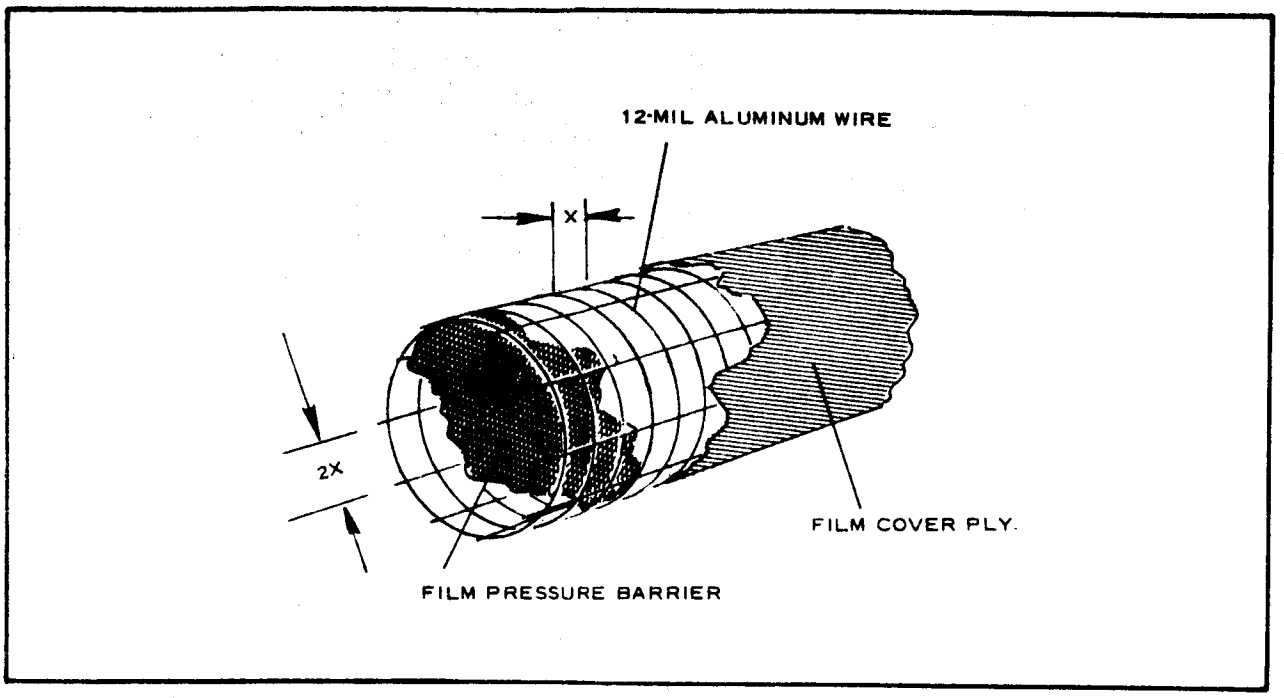


Figure 6.3-2. Wire-Grid Structural Member

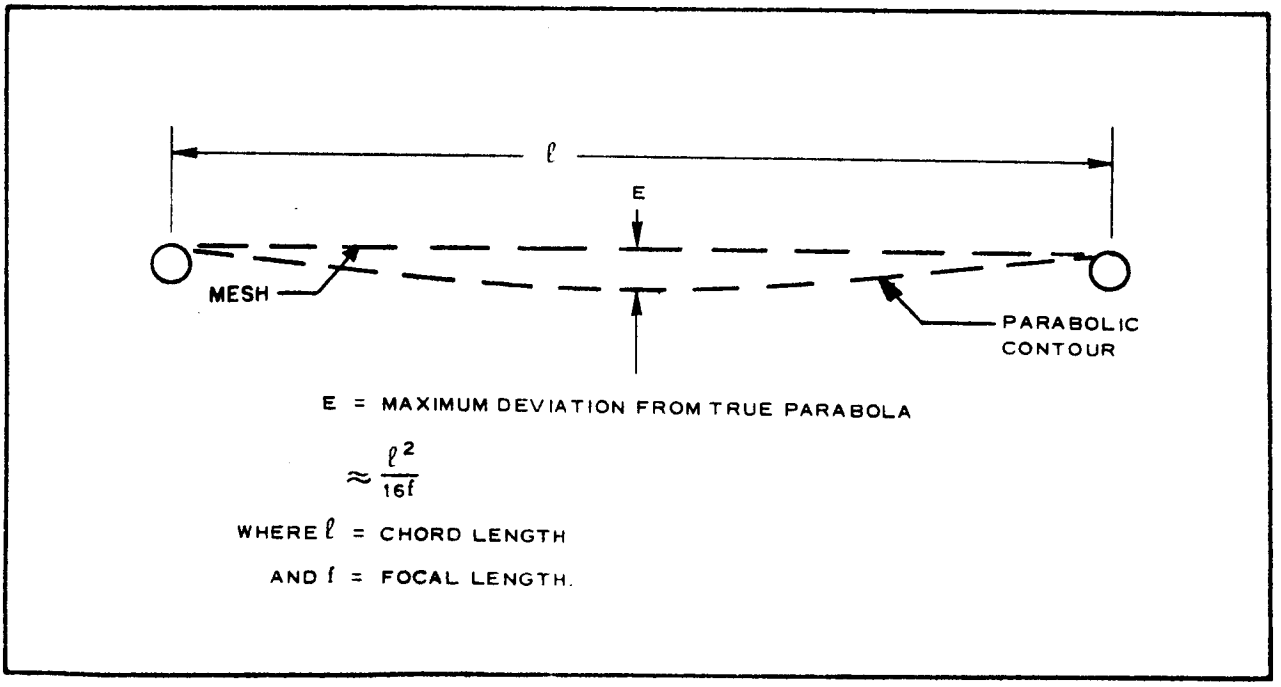


Figure 6.3-3. Tolerance Limitation of Mesh Attachment Method

The parabolic surface material is a lightweight, flexible, rf-reflecting mesh, such as Sucal, that is drawn taut between adjacent parabolically contoured frame members. Illustrated in Figure 6.3-3 is a tolerance limitation imposed by this mesh attachment method. Methods have been devised to pull the center of the screen nearer to the parabolic contour with lightweight tension elements extending between backsides of adjacent frame support members, thus reducing the magnitude of the surface error. The use of memory materials such as Nitinol and irradiated polyethyelene to create a true parabolic surface between frame members also is being investigated.

The wire-grid tube structural member is an ideal building block for fabricating large reflectors. Reflectors as the one shown in Figure 6.3-1 will weigh less than 0.1 psf of aperture area, including the inflation system. This type of antenna also will have a very efficient packaging factor.

Methods presently exist for analyzing wire-grid structures. Wire and film stresses have been related to inflation pressure throughout the entire inflation and rigidization cycle, including the residual stresses after the pressure differential reduces to zero. The entire inflation and rigidization process has been programmed for solution on a digital computer. In addition, critical moments and axial loads for wire-film cylinders based on overall, local, and general instability have been derived.

To verify analytical methods, test programs have been completed on wire-grid cylinders subjected to axial and bending loads. Packaging appears to have little effect on either compressive stiffness or the critical buckling load.

Present techniques of fabrication, as verified by the antenna model illustrated, would limit manufacturing and deployment tolerances attainable for a 30 foot dish to the region of 1 inch. Thermal distortions for this type of antenna may or may not be relatively significant depending upon the nature of the shadowing of solar energy inherent in a specific configuration. From the viewpoint of structural stiffnesses, it appears that local values will be limited but that very large values should be attainable for overall configurations since deep truss structures can be developed at little weight penalty.

b. Thermally Deployed Wire Grid. Another technique having future potential for attaining a space deployable antenna structure uses Nitinol as the structural material in some wire grid and/or foil forms. This material can be formed or have its shape set at a temperature of approximately 1200^{o}F, folded radically or deformed at room temperature, and then will return to its original formed shape following heating to a temperature of approximately 150^{o}F. The recovery characteristics of the material vary somewhat depending on various factors such as the severity of the packaging folds, the recovery temperature-time profile, degree of freedom during recovery, and specific alloy batch. These variables, especially alloy consistency, represent factors requiring additional effort prior to any major use of Nitinol in a space program. Limited use of Nitinol might be warranted if: (a) the folds can be limited, (b) one alloy batch of established properties is used, and (c) other variables can be closely controlled. Such use conceivably could include contour aids for screen or mesh reflector surfaces.

6.3.1.2.3 Chemically Rigidized Textile or Film Reflectors

In recent years a number of programs have been pursued to develop chemical rigidizing techniques for maintaining the shape of inflation-deployed textile or film structures in space. Most of this effort has been directed toward solar concentrator and airlock applications. Accordingly some of the characteristics of the rigidized fabric structures developed to date may or may not be particularly applicable to configurations designed specifically for reflecting microwave energy. However, as an overall indication of the present status of chemical rigidizing processes, the pertinent results from predistributed-foam and resin-impregnated fabric solar concentrator programs are summarized in the following paragraphs.

a. Heat-Activated Foam. Shown in Figure 6.3-4 is the orbital sequence presently envisaged for deploying and foam-rigidizing a solar reflector surface. This particular azide foam concept involves:

   1. Patterning and fabricating an accurately contoured, aluminized film mirror or reflecting surface

   2. Patterning, fabricating, and assembling a contoured film endcap to the reflecting surface

   3. Inflating the mirror endcap assembly and applying an azide foam in a paste form to the backside of the mirror surface

   4. Covering the predistributed foam paste with a film backflap that is attached to the mirror at its edge and hub

   5. Deflating the assembly and folding it into the desired form with the backflap now serving as a paste separator

   6. Packaging the folded assembly into a separable container and launching it to an orbital position

   7. Initiating orbital deployment and rigidization by ejecting the breakaway container, inflating the mirror-end-cap assembly, heating the predistributed foam to rigidize it, and separating the endcap by a primer chord or some other technique

   The heating required may be applied in several ways, i.e., by selective flap or mirror surfaces to use solar energy as the thermal initiator, by hot wires, or by pyrotechnics.

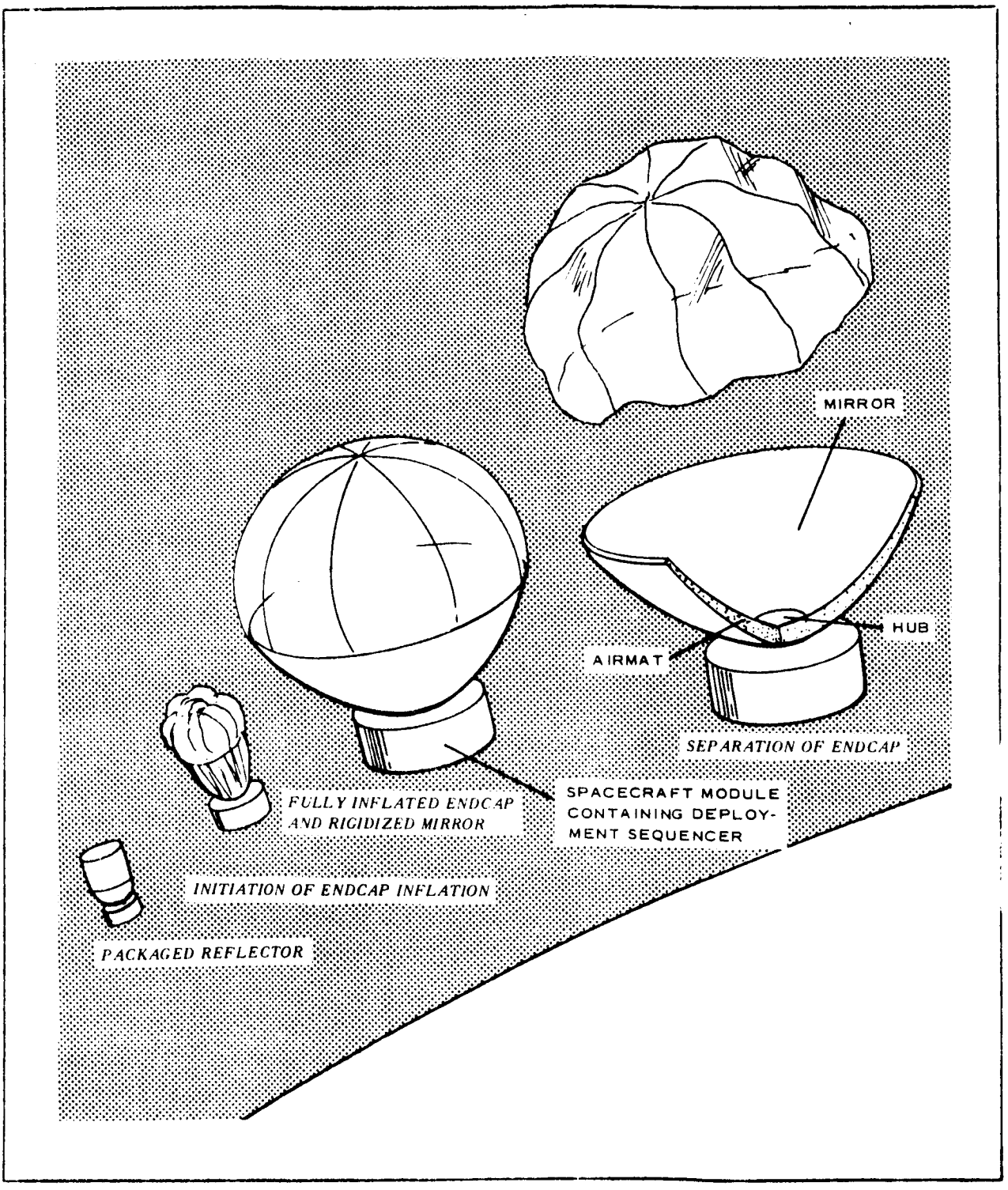


Figure 6.3-4. Solar Collector Orbital Sequence

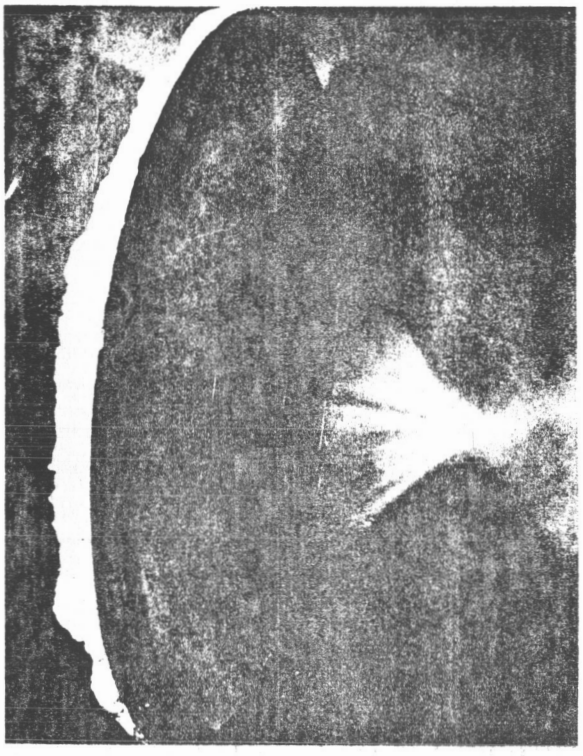


Figure 6.3-5. Chemically Rigidized Reflector (Two-Foot Model)

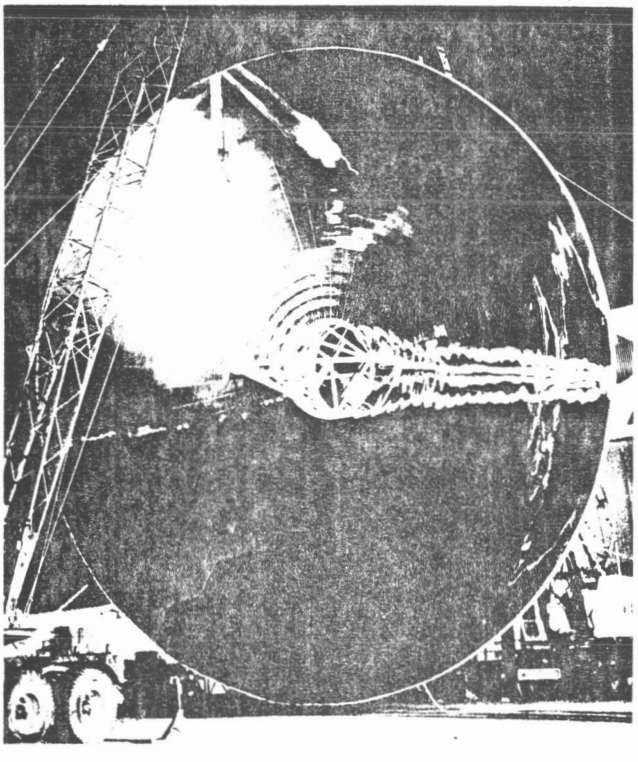


Figure 6.3-6. Mirror Supported by Rigid Foam (44.5-Foot Model)

Illustrated in Figure 6.3-5 is a 2-foot model that was formed in a vacuum chamber following the sequence just described with the exception that it did not unfurl from a packaged state. Figure 6.3-6 shows a 44.5-foot mirror that was constructed using the inflation-formed-mirror surface technique followed by rigidization with a mechanically mixed and deployed foam spread on the backside.

Based upon results achieved with the 44.5-foot mirror, it appears that a 30-foot paraboloid dish could be fabricated to accuracies within 0.10 inch following a predetermined inflation. However, the surface errors caused by orbital induced thermal differentials will be considerably greater in magnitude than 0.10 inch.

Other state-of-the-art limitations include allowable stresses of about 25 psi and modulus of elasticity values of less than a 1000 psi for expanded foam weights of approximately 4 pcf. Considering these allowable stresses and values in conjunction with a tapered foam backing, it appears that average reflector aperture weights approaching 0.8 to 1 psf are attainable.

b. Gas Catalyst-Activated Resin Impregnated Fabric. Figure 6.3-7 shows the cross section of an AIRMAT* structure supporting a solar reflector surface. In this concept it is envisaged that the surfaces and AIRMAT backing structure will be patterned accurately, fabricated, and assembled; the inner surfaces and drop yarns of the AIRMAT will be impregnated with a urethane resin prior to packaging for launch. As a final step of the orbital deployment sequence, a water-vapor or moist-gas inflation of the AIRMAT will reform the reflector shape and activate the resin to rigidize the structure in space.

*TM, Goodyear Aerospace Corporation, Akron, Ohio

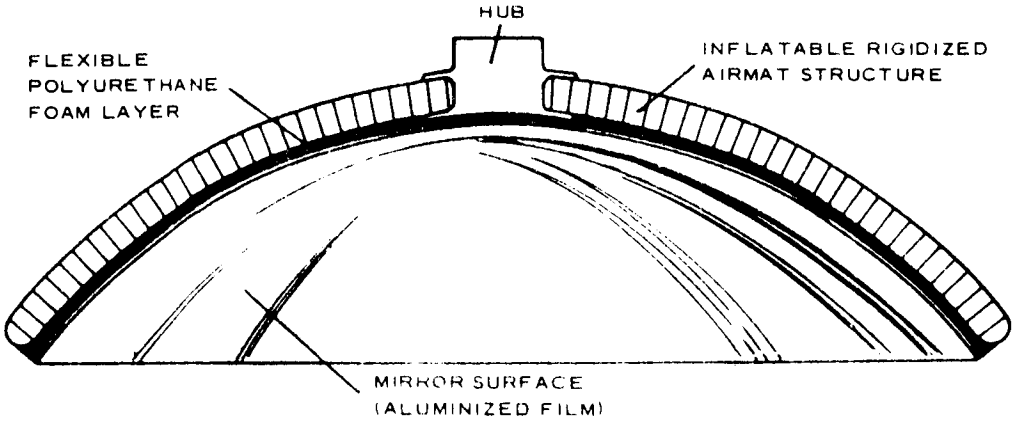


Figure 6.3-7. Cross Section of Rigidized Solar Concentrator

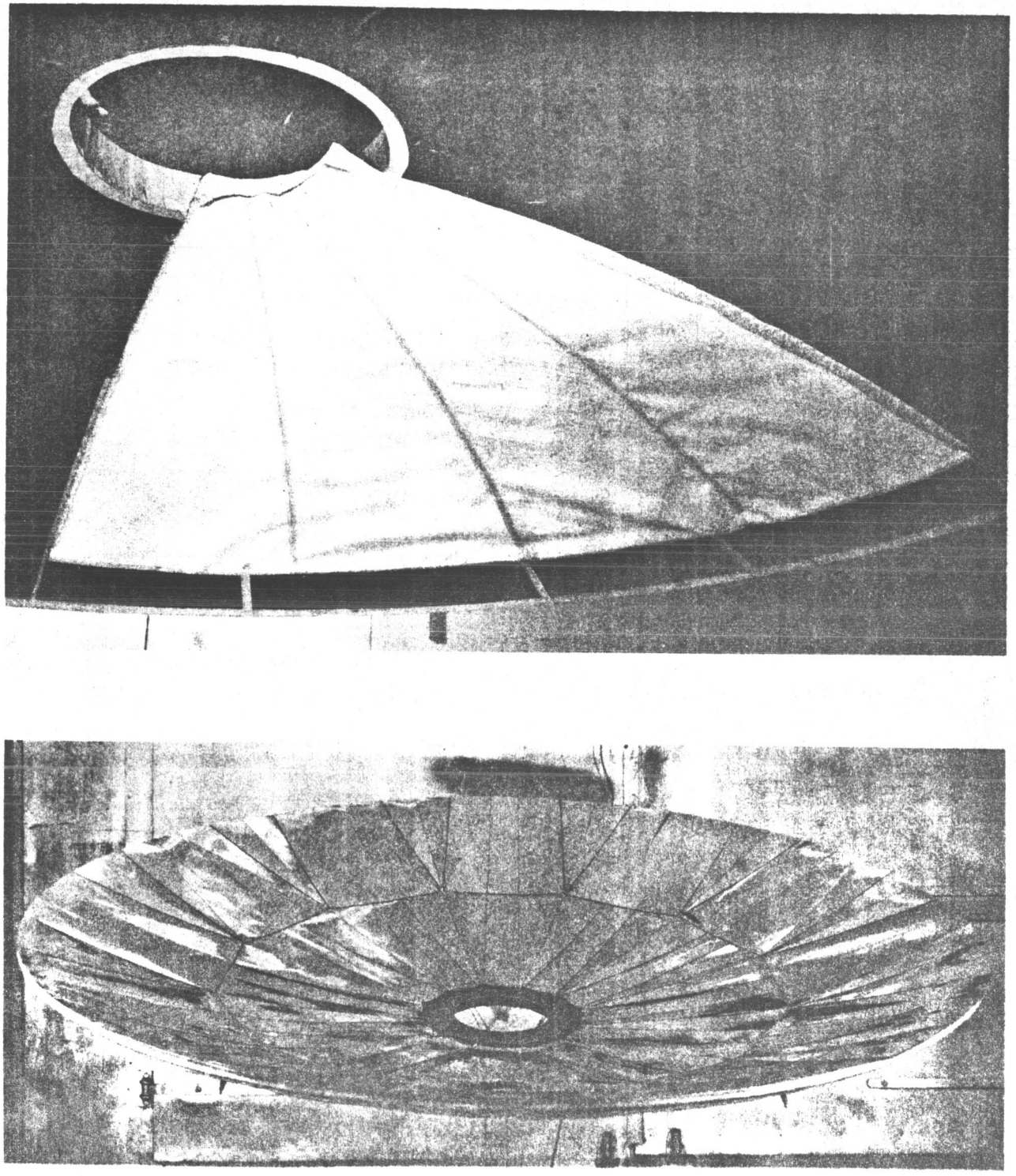


Figure 6.3-8. Solar Concentrator (Initial and Final Fabrication Phases)

Since the catalyst has certain temperature constraints, the deployment must also be within these constraints.

Figure 6.3-8 depicts a 10 foot model of a resin-impregnated AIRMAT solar concentrator during initial and final fabrication phases. Fabrication surface contour errors in this, the first model ever built,were less than 0.2 inch. Based upon some improvements in the fabrication approach, it appears that the error could be reduced considerably. When this type of antenna with its conductivity and thermal expansion properties orbits in the space environment, however, it will have significantly increased surface deviations. The deviations will be less than those for the predistributed azide foam.

Average aperture unit weights using this AIRMAT concept that appear to be attainable are 0.4 to 0.5 psf. From a stiffness viewpoint, this rigidized structural concept is dependent particularly upon the specific material and its arrangement in the AIRMAT.

6.3.1.2.4 Mechanically Deployed Umbrella Configurations

The umbrella space antenna concept has been proposed by a number of investigators. In its simplest form, it can be thought of as an umbrella-like structure with the handle representing the feed and the cloth canopy contoured by the deployed ribs as the reflecting surface. The bowstring antenna described in the following paragraphs is an upgraded version of the umbrella-type antenna and has been refined to reduce thermal distortions.

The bowstring antenna has tubular ribs extending radially from hinges on a central hub. Each rib has a contoured elasticity index to produce the desired paraboloidal deflection when a force is applied at the tip by a cable extending from the tip to the feed support tube. The rf-reflection mesh is stretched between and attached to adjacent ribs. Figure 6.3-9 illustrated the surface contour errors resulting from this mesh attachment technique as a function of the number of ribs used in the antenna (see Figure 6.3-3 for basic error principle).

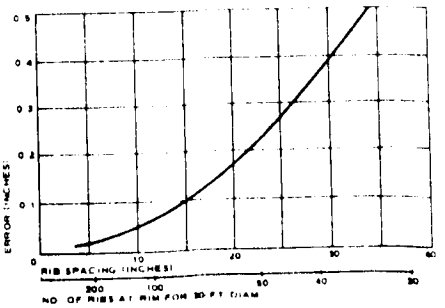


Figure 6.3-9. Stretched-Screen Reflector Surface Contour Accuracy

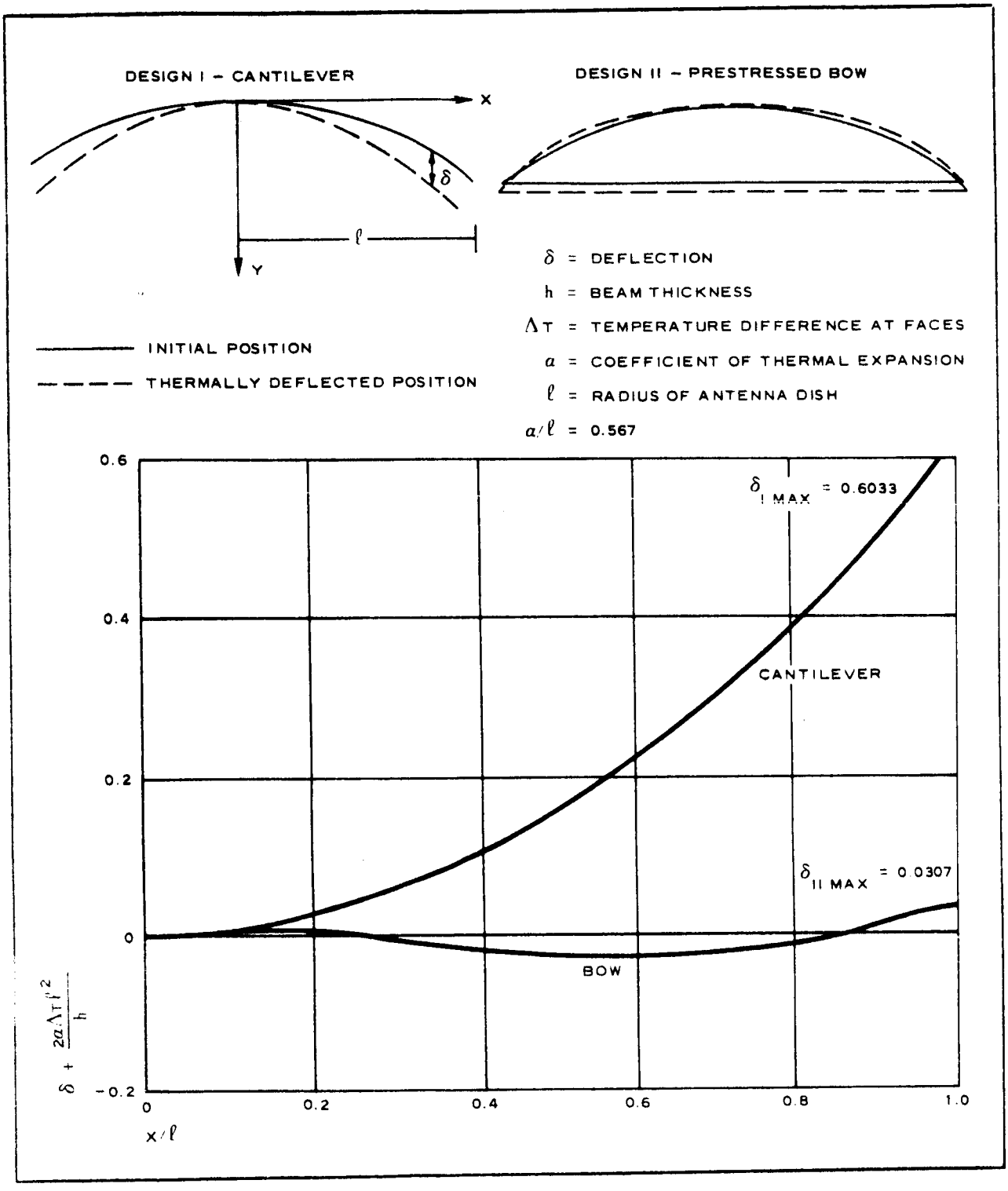


Figure 6.3-10. Thermal Deflection Comparison

In the launch configuration, the ribs are packaged parallel to the axis of the paraboloid forming a cylindrical package. At deployment the ribs are rotated outward. After the antenna is deployed and the ribs are locked, tension is applied at the tip by cables.

Thermal distortions of the reflection surface are minimized by using structural members with solid cross sections. The surface deflections caused by front-to-back temperature gradients are reduced further because of the rib prestressing induced by the tension cables as illustrated in Figure 6.3-10. If the same material is used for the prestressing cables, ribs, and feed support structure, variations in antenna geometry due to average temperature changes will all be in the same direction and only a slight defocusing and small loss in gain will result.

Assuming, as is likely at least at the higher frequencies, that the use of prestressing cables between the reflector surface and the feed would result in a significant gain loss, the design could be revised to place the cables behind the reflector surface. Illustrated in Figure 6.3-11 is one possible approach to implementing the rear pre-stressing cables. In this arrangement, the cables also could be used to aid in deploying the ribs. Though preloaded in the opposite sense with reference to rib root bending stresses, the prestressed thermal control technique (as applied for this antenna configuration) loses none of its ability to offset or minimize all types of thermally induced distortions.

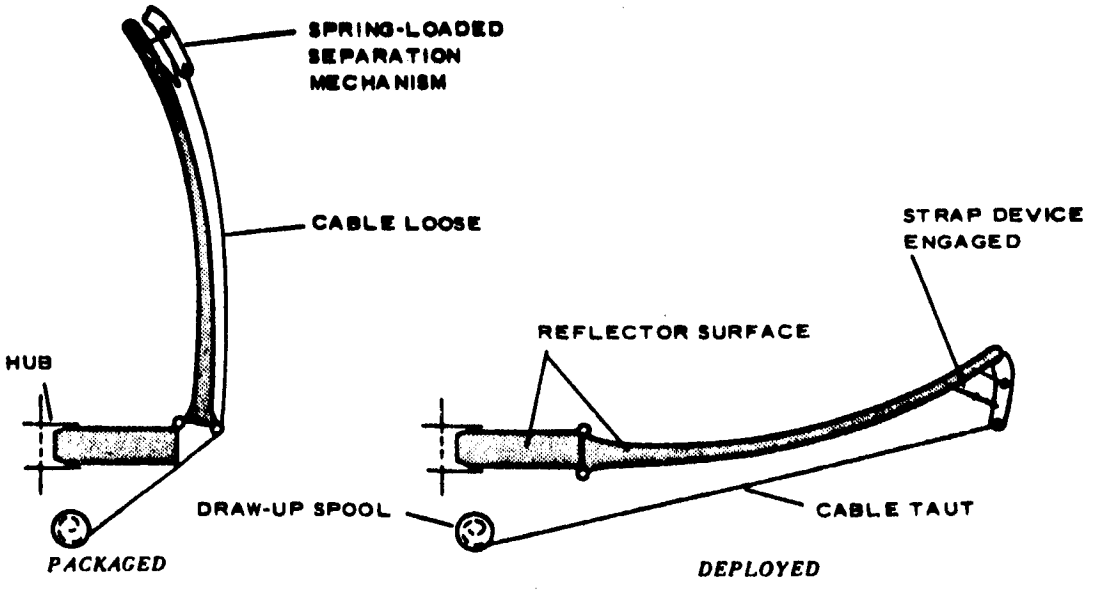


Figure 6.3-11. Design With Cables Behind Reflector Surface

Manufacturing and deployment accuracies attainable with the bowstring concept are yet to be demonstrated. However, with reference to a best fit paraboloid, rib contour surface errors of less than 0.10 inch are judged to be realistic following deployment. If a predetermined paraboloid must be matched, the rib contour surface errors conceivably could be held to within 0.3 inch or less. To these errors must be added the surface screen deviations, which as previously noted would be a function of the number of ribs.

For the 30-foot diameter dish size range, average antenna aperture weights of about 0.1 psf appear attainable assuming spline type rib members are used. Including a deployment system weight, where a significant load capability must be provided, could increase the system weight to more than 0.25 psf in reference to the antenna aperture area.

Though constructed of relatively soft components, the structural stiffness of this reflector concept may well be adequate since it will be primarily a function of the distance between prestressing cable and the rib at its root. Considering launch configuration aspects, the antenna ribs could be hinged at intermediate points to reduce significantly the cylindrical packaging height.

6.3.1.2.5 Mechanically Deployed Swirlabola Configurations

A high-gain, pencil-beam spacecraft Swirlabola antenna was developed by the Goodyear Aerospace Corp., under contract to the Jet Propulsion Laboratory (JPL). As shown in Figure 6.3-12, the concept is compatible with either a flexible mesh reflecting surface or a rigid solid reflecting surface. The flexible screen configuration has curved radial ribs that extend from the hub to the outer periphery to support the reflector screen and establish the parabolic contour outboard of the hub. These ribs pivot at the hub rim and, since they have the approximate radius of the hub, nest circumferentially around the hub rim in the packaged condition. The screen material is lightweight tin-plated, copper-wire mesh that is attached to the ribs; when packaged, it folds over the hub. The reflector is a conventional structure that is a continuation of the parabolic surface and provides the mounting structure for the radial ribs, feed, and spacecraft attachment.

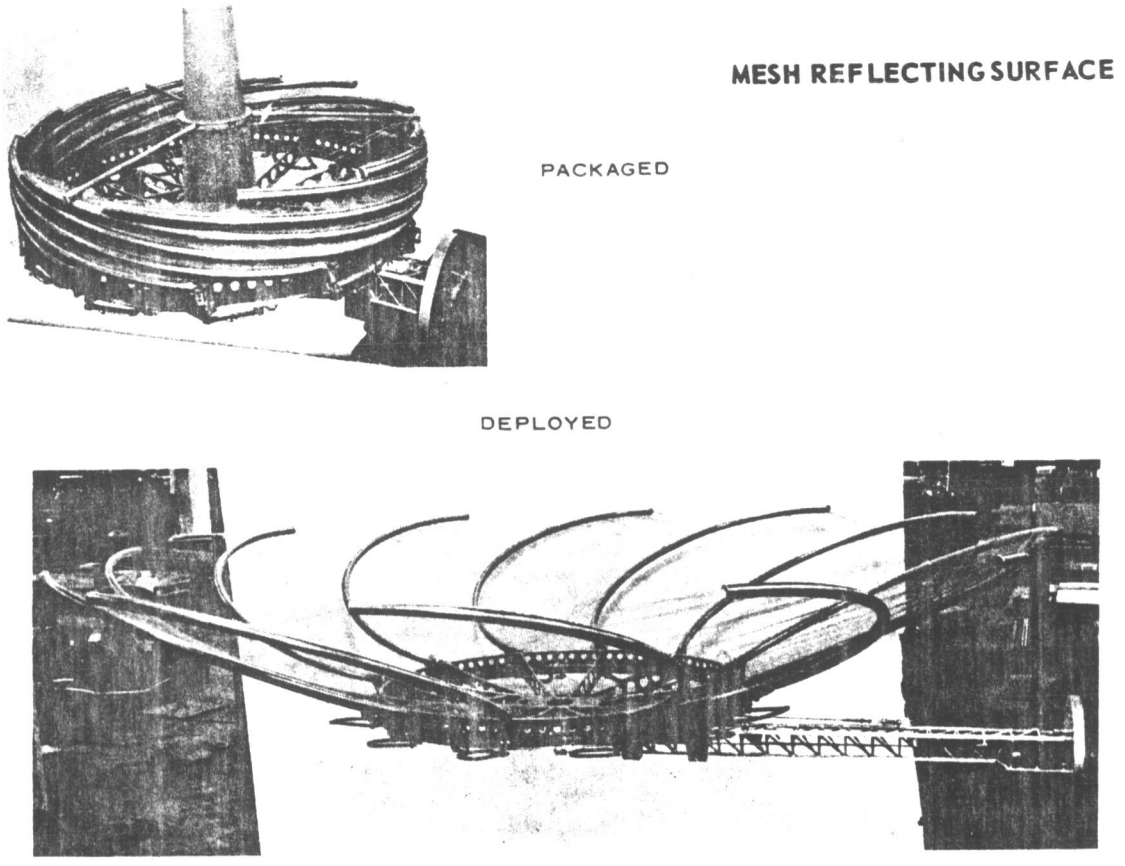


Figure 6.3-12. Swirlabola Antenna

The rigid-petal Swirlabola is similar to the flexible-screen Swirlabola with improved accuracy achieved by using double-curved rigid panels contoured to a parabolic shape. The configuration uses a deployment technique similar to that for the flexible-screen Swirlabola, but the curved radial ribs support the rigid panel in lieu of the flexible screen. Because these panels are rigid, there may be some friction between panels during the last part of the deployment sequence just before the petals reach the end of their travel and engage each other.

The Swirlabola concept provides a wide latitude in the selection of materials. As an illustration, the initial wire-screen Swirlabola fabricated for JPL used primarily Invar to meet the requirements of dimensional stability over extremely wide temperature ranges. In the subsequent model where low weight and 1-g deflection requirements were given high preference in the specification, the tradeoff study indicated that aluminum was the most desirable material. Other materials such as Lockalloy appeared promising in the tradeoff study. However, it was believed that further development of this material was required to understand completely the characteristics and fabrication processes.

The Swirlabola concept has been subjected both to full-scale and model testing to prove feasibility. The testing of the full-scale (nine-foot diameter) concept included packaging, deployment, 1g contour, rf range testing for gain and pattern, and vibration about all axes (both packaged and deployed). Testing of the model included structural tests of fabricated joints, thermal cycling of components in vacuum, vacuum and thermal tests of all moving joints, and waveguide tests of reflecting material new- and after-simulated aging.

The Swirlabola could be implemented in an ATS-4 type of configuration at about 0.3 lb/ft^2, including the deployment mechanism. Although the Swirlabola represents a sound and demonstrated concept, its packaged form for a 30-foot diameter dish is not compatible with a 10-foot diameter shroud because the packaged-to-deployed ratio is about 1 to 2.4.

6.3.1.2.6 Mechanically Deployed Petaline Configuration

The petal concept for packaging and deploying a paraboloidal space structure has received

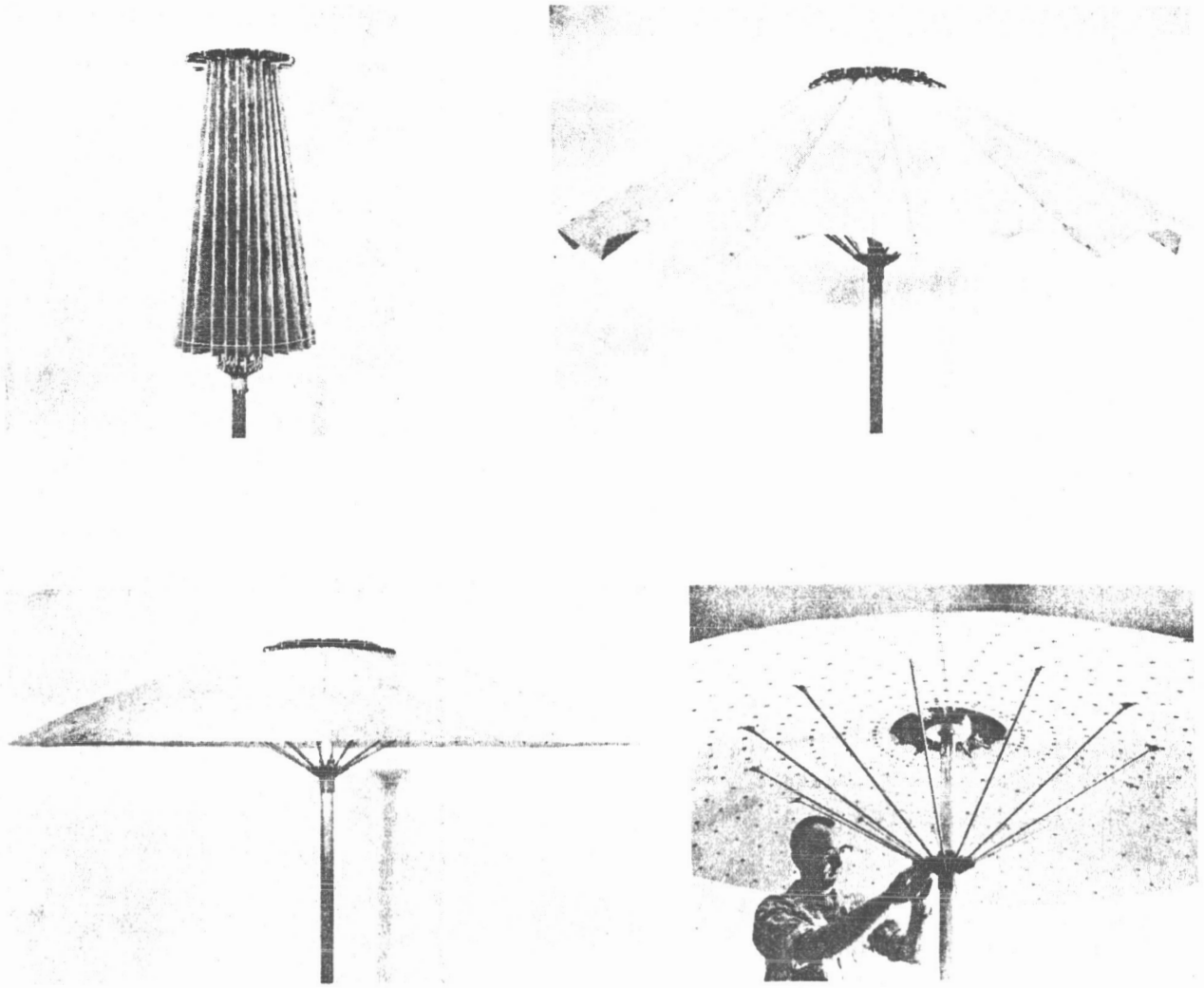
considerable attention in recent years for application in solar concentrator and antenna technology. Many configurations have evolved. However, published data indicate that all concepts treat the petals as individual rigid elements, each hinged from a center hub, so they can be packaged into a cylindrical envelope. When deployed, the petals are cantilevered from the hub, and, in some cases, one to three interconnecting latches are engaged between petals at the completion of deployment to provide hoop-tension continuity to the paraboloid.

The Goodyear Aerospace Corporation has developed a concept where each petal is attached structurally to its adjacent petals during final assembly and remains that way throughout the packaged condition, deployment cycle, and in full deployment. By having the petals interconnected as one of the final assembly operations, and at all stages of subsequent packaging and deployment, the launch loads on the antenna can be more efficiently withstood, the transient thermal deflections and loading conditions of deployment will have minimum adverse effects, and the deployed antenna will match closely the contour set during the final assembly and will have a high degree of structural shape continuity and stiffness.

The shape of each petal is a true, double-curved radial segment of a paraboloid of revolution. The petals are connected by hinges, uniformly spaced along the petal edges, that in effect establish curved hinge lines in the deployed paraboloid. The composite structure of petals and hinges approaches the equivalent of a one-piece paraboloid. Figure 6.3-13 shows a model and its deployment.

The curved hinge paraboloid is packaged by flattening the petals. This action places the hinge pins in a straight line and permits an accordion-like folding of the parabolic structure. The petal is designed so that the stress required to straighten the curved hinge line for packaging is well below its yield stress and no permanent deformation is introduced into the panels. At deployment, the petals return to the nominally zero-strain condition in which they initially were fabricated and assembled.

The petal structural requirements can be met by solid construction methods (possibly sandwich material) or by open construction with the frame members supporting a mesh.



TYPICAL PANEL

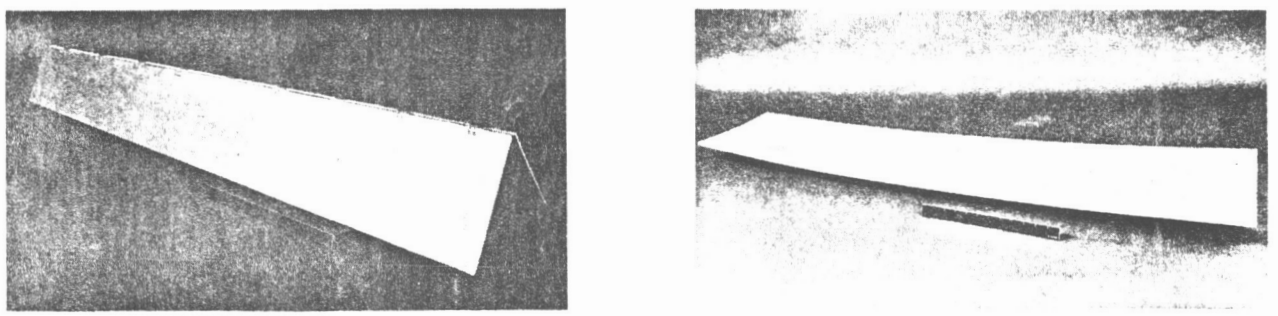


Figure 6.3-13. Deployment of a Petal Antenna

With either method the initially fabricated and finally deployed petal will be a double-contoured segment of a paraboloid. The frame member type construction using aluminum sandwich is shown in Figure 6.3-14.

Manufacturing tolerances for the petaline type antenna should not exceed and may well be considerably less than 0.04 inch. This value can be subdivided into an error of 0.02 inch for the final assembly jig and 0.02 inch for an error within the petal and screen attachment not affected by the total assembly function. No attempt has been made here to assess the 1-g effect, but based upon the large number of matchpoints in the final assembly jig, the 1-g effect should be small.

Deployment-induced deviations in the surface contour should be very small since relatively close tolerance bushings, stiff deployment trusses and stops, and low deployment rates will be used in arranging the antenna for space operation.

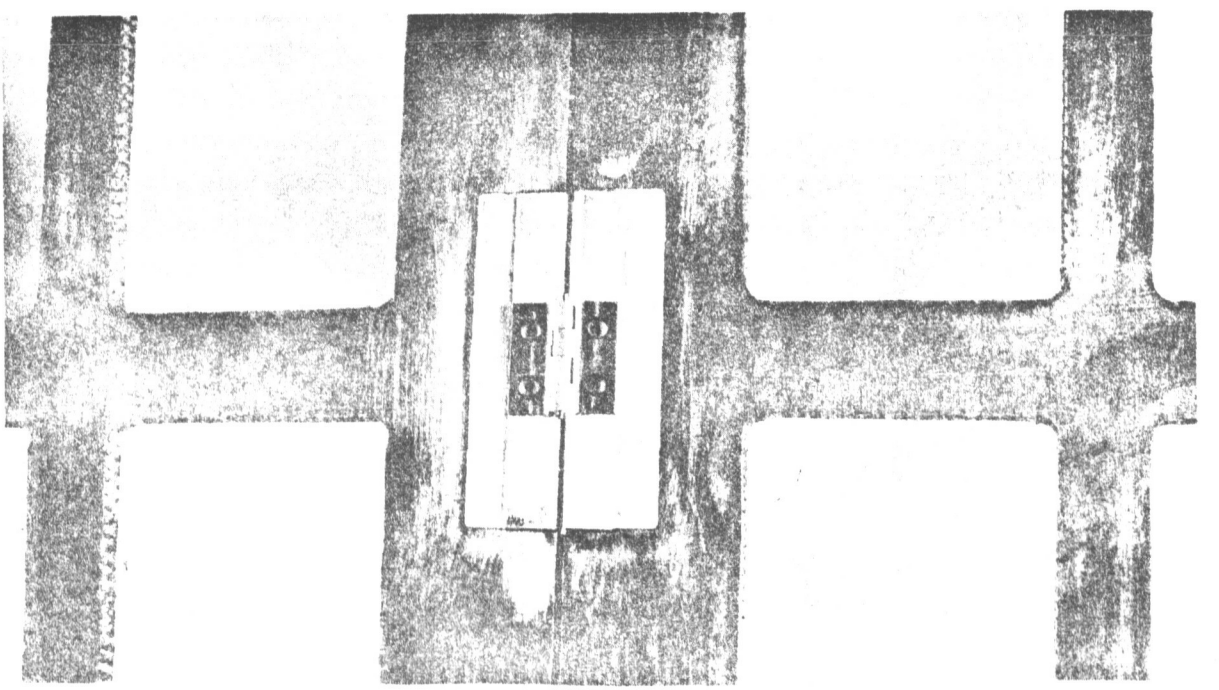


Figure 6.3-14. Aluminum-Sandwich Frame Member

Thermally induced surface errors represent a most significant problem. However, with an open-mesh, petaline-type antenna, the thermal distortion problem is as amenable to solution as with any of the other antenna types discussed.

From the aspect of stiffness, the structural continuity of the petaline shape results in a configuration approaching a spherical shell. Depending upon the material and its specific arrangement in the petaline concept, average weights of 0.15 lb/ft^2 or less for the reflector surface area may be attained. This weight, in conjunction with a comparable deployment system weight, should result in a total reflector and deployment system weight of 0.3 lb/ft^2 or less.

6.3.1.2.7 Antenna Configuration Selection

To ensure the selection of the best antenna concepts for detailed analysis, design, fabrication, and testing in this program, a number of antenna approaches were evaluated relatively in regard to packaging, deployment, structure, weight, tolerances, ground testing, development status, and cost. These areas of evaluation are modified here to the extent that the specific requirements of an ATS-4 antenna are used as a reference. To further enhance the validity of the evaluation, an attempt is made also to interpret the relative significance of the various parameters.

Of first order significance in the ATS-4 program is the development of an antenna that will withstand the launch environment, deploy in space, transmit and receive microwave energy. These functions were assigned a numerical value of 45, which was subdivided into 10 for packaging, 10 for deployment, 15 for structure, and 10 for weight. Packaging factors considered were volume, size, shape, ability to withstand launch loads and environment, and the effects of all the factors on shroud modifications and payload weight. Deployment factors evaluated were system simplicity; controlled sequences, rates, damping, and loads: and tolerance and environmental control requirements. Structural integrity, stiffness, damping, and openness, in addition to material adaptability, orbital life characteristics, and feed interface requirements were evaluated in considering the antenna structures. The antenna structure weight, including the deployment system, and the weight distribution were the evaluation factors noted in this area.

Development of an antenna that will satisfy and/or surpass the specifications and test requirements is also of prime significance and was assigned a value of 35. This number was subdivided into 10 for manufacturing and deployment tolerances, 15 for all other tolerances, and 10 for relative ease and significance of a ground test program. Under manufacturing and deployment tolerances, the overall ATS-4 specifications were weighed in conjunction with actual data where possible for the antennas. The degree to which a structure was usable after deployment also was considered under these tolerances. The other tolerance effects included acceleration deflections that were evaluated on the basis of structural stiffness; thermal deflections that considered structure openness; concept adaptability to different materials; and overall structure arrangement with reference to shadowing, thermal conduction and response characteristics, and other stress or design details that minimized the effects of thermally induced strains.

Under the ground test program, an attempt was made to assess the relative problems and validity of test results likely to be associated with the different antenna approaches. The ratings in this area were influenced by special support requirements, special data interpretation, and other special ground test requirement factors affecting costs and validity of test results.

The relative development of the various antenna approaches was given a value of 10 and the ATS-4 schedule compatibility and program costs also were given a total value of 10. To the degree possible, the antenna concepts and developed hardware were measured against the high frequency tolerances, unique packaging, and other special requirements of the ATS-4 antenna. Schedule compatibility and relative costs then were deduced from the magnitude that the different antenna approaches failed to fulfill the ATS-4 specifications.

The results of this evaluation are summarized in Table 6.3-1. The considerations for each concept that were of greatest significance are noted below.

The poorest reflector concept, with reference to the ATS-4 requirements, was the rigidized fabric approach. The need for more development and poor thermal-structural characteristics

Table 6.3-1. Comparison of Space Deployable Antennas

X-band, 30-ft diameter, parabolic antenna construction concepts	Packaging (10)* and deployment (10)	Space structure (15) and weight (10)	Tolerances (25)		Ground test and checkout (10)	Status of development (10) and costs (10)	Relative order and values of antenna concepts
			Manufacturing and deployment (10)	Other sources (15)			
Wire grid	Excellent packaging (10) efficiency. Random shape and minimum volume. No particular launch load or environment limitations Deployment by gas (8) inflation	Soft lateral structure. (5) Relatively high damping Reflector and deployment weight < 0.15 psf of aperture area (10)	Final assembly and (3) deployment tolerances < 1 in. Value may be better but presently unable to confirm	Thermal deflections (8) are dependent especially on material and configuration. Structure generally is open and has potential for low thermal distortions	Difficult to perform (4) or evaluate ground test with structure in space configuration (zero internal pressure). Would either have to design structure for ground test and pay weight penalty or test under internal pressure and evaluate results accordingly. Limited number of deployments possible	Structural elements (4) have been studied and tested. Some properties established but not to accuracy consistent with high performance X-band reflector design. Lower frequency antenna constructed and ground tested with good results. Additional development required with little assurance that antenna specifications and schedule could be satisfied Relatively high program (4) costs because additional development requirements would include significant physical test program and data analysis. Meaningful 0- and 1-g testing and data analysis for X-band antenna also represent formidable and costly tasks	Fourth (56)
Rigidized fabric	Fair to good packaging (4) efficiency. Reasonable shape variations and small volume Closely controlled (2) launch and deployment environment required. Deployment by gas inflation	Soft structure (2) Reflector and deployment system weight > 0.5 psf of aperture area (1)	Final assembly tolerances < 0.2 in. repeatable following inflation and repackaging. No way of accomplishing total deployment and rigidization and then repackaging (2)	Solid structure with (2) low thermal conductivity and high coefficient of expansion materials. Relatively large thermal distortions	Proof of environmental control necessary for deployment demonstration. Deployment and rigidization repeatable only if gelation approach used. A low stiffness-to-weight ratio probably will require support outside of the antenna structure during most tests (2)	Presently available (2) and relatively well-founded data indicate that wider deployment and rigidization environmental tolerances are needed. Better thermal properties are required. Both of the above items are materials dependent and thus basic research is required Antenna specifications (1) within schedule and possibly outside of schedule appear unattainable. Highest program costs since both basic research and development requirements are yet to be satisfied	Fifth (18)
Bowstring-umbrella	Good packaging efficiency (8) in cylindrical to conical shape and small volume Mechanically controlled (8) sequence and rate deployment	Lack of structural (10) hoop continuity and use of soft tie members results in medium stiffness. High damping Reflector and deployment system weight < 0.25 psf of aperture area (8)	Final rib assembly (3) tolerances < 0.3 in. are repeatable following packaging and redeployment	Thermal deflections (12) may be controllable to less than 0.1 in. Acceleration deflections will be greater than for Swirlabola or petaline concepts	Low stiffness of antenna may require extra support during some tests (6)	Concept studied for (5) different frequency range. Use at higher frequency dictates mesh-rib detail design revision and model test checkout. Also needed is design, fabrication and proof testing to show better manufacturing tolerances Therefore design de- (7) velopment is required and precludes assurance of schedule satisfaction although antenna specifications appear potentially attainable. Medium to lower costs with reference to other antenna approaches noted. If development requirements fulfilled early, costs may be reduced somewhat since analysis and tooling requirements appear simpler	Second or third (67)
Swirlabola	Fair packaging efficiency (2) in cylindrical wafer shape. Deployed-to-packaged diameter ratio is 2.4 to 1. Good launch load package configuration Mechanically controlled (6) sequence and rate deployment. Requires engagement of adjacent petals at completion	Structural hoop (10) continuity following petal engagement results in relatively high stiffness. Low damping Reflector and deployment system weight (6) ≈0.3 psf of aperture area	Final assembly tolerances < 0.04 in. are repeatable following packaging and redeployment (10)	Thermal deflections (12) depending upon material selected may be controlled to about 0.1 in. Acceleration deflections < 0.01	With reference to (7) other antennas, Swirlabola and petaline probably will require the least special handling and support during testing	Swirlabola mesh antennas (7) for lower frequencies have been designed, built, and ground-tested, including simulated launch loads and vibrations. Small, rigid-petal Swirlabola model built and deployment tested. Packaging ratio of present design is not compatible with 30 ft and 10 ft diameters for deployed and packaged requirements. Also the rigid petal packaging form is inconsistent with a fixed feed support. Thus significant design changes and development testing would be necessary Antenna specifications (7) appear potentially attainable but unlikely within schedule. Medium costs with reference to other antenna approaches	Second or third (67)
Petaline	Fair packaging efficiency (7) in long cylindric shape. Good launch load package configuration Mechanically controlled (8) sequence and rate deployment	Structural hoop (12) continuity results in relatively high stiffness. Low damping Reflector and deployment system weight (6) < 0.3 psf of aperture area.	Final assembly tolerances < 0.04 in. are repeatable following packaging and redeployment (10)	Thermal deflections (12) depending upon material selected may be controllable to about 0.1 in. Acceleration deflections < 0.01	With reference to (7) other antennas, Swirlabola and petaline probably will require the least special handling and support during testing	Considerable analysis, (9) design, and fabrication efforts completed in support of petaline concept. Four models constructed, each with a different petal-hinge line geometry. Full-scale panels constructed. Concept fits AIS-4 requirements, primary unresolved area is the selection of a material that will best satisfy thermal tolerances, weights, costs, and other antenna parameters Antenna specifications (9) appear attainable within the schedule and without any basic development efforts, thus costs should be minimum	First (80)

*Numbers in parentheses are relative values for antenna characteristics.

was enough to eliminate it from further consideration.

The primary deficiencies of the wire-grid antenna are the low tolerances attainable and the need for special testing. These deficiencies are inherent with the concept characteristics of good packaging and lightweight structure. The wire-grid concept is probably one of the better approaches for lower frequencies and possibly larger dimensions, but it may not be adaptable to the high frequency requirements of the ATS-4 system.

The Swirlabola and bowstring-umbrella approaches appear to have about the same potential for fulfilling the high-frequency, large aperture antenna requirements. However, both will also require significant design revisions in accomplishing this goal. In the present configuration, the Swirlabola packaging ratio (deployed-to-packaged diameter) will not satisfy the ATS-4 needs. In addition, going to a rigid petal will involve a major design revision if the feed support system is fixed to the antenna hub. Although considerable development effort has been completed on the Swirlabola, major redesign and development work still would be required to increase the packaging ratio.

The bowstring-umbrella concept has a good potential for minimizing thermal deflections, but must be revised to include a contoured skin or reflector surface. Proof of the ability to form an accurate surface with the rib-screen as a part of the manufacturing and deployment functions also must be shown. In addition, the basic stiffness of the antenna structure may have to be supplemented to arrive at the required natural frequency. Developing a contoured skin in space could be pursued by using a pressure deployment or rigid, expanded-metal skins attached to the ribs. In either case, considerable design and proof testing would be necessary to show the validity of the proposed solution. The attainment of the accurate rib contour from a fabrication and assembly viewpoint may or may not be necessary, depending upon which screen approach would be selected. Independent of this fact, however, it appears that adapting a rib-screen design to the tolerances pertinent to x-band operation would involve major design and development effort for the bowstring-umbrella concept.

The petaline concept was selected as the best approach for fulfilling the ATS-4 large-aperture

antenna requirements. The packaging form and its modest flexibility in arriving at a specific shape appears amenable to the shroud and feed interface requirements.

The most significant advantage of the petaline approach is its inherent structural continuity available for the launch, deployment, and operational loads and tolerance control functions. Considerable development effort has been expended on the petaline design for antennas as well as for solar concentrators and most of this work appears applicable to the ATS-4 needs. Little, if any, basic development work will be required and the schedule appears attainable within reasonable costs.

6.3.2 DESIGN STUDIES OF SELECTED CONCEPT

Having selected the petaline concept, the objective of the design studies then was to investigate various configurations of the petaline-type antenna and to determine their overall applicability to the ATS-4 mission, with the ultimate objective being the selection of a configuration for more detailed study and preliminary design. The configuration variables selected for study were petal size and arrangement, petal construction, package configuration, deployment, and hub construction. Each of these variables were evaluated for manufacturing feasibility, weight, tolerance, and general adaptability to the utlimate configuration.

The following paragraphs discuss the results of these studies. Due to the importance of the paraboloid thermal studies, special emphasis is given to thermal analysis, thermal distortions and associated rf losses due to thermal distortions.

6.3.2.1 Paraboloid Reflector Configuration

The 30-foot paraboloid reflector configuration studies were conducted to determine the configuration, environment, and construction constraints as applied to the ATS-4 system. As a result of the concept selection work described in Section 6.3.1, these studies were limited to the petaline antenna concept and resulted in the selection of a specific configuration recommendation.

The discussion in the following paragraphs gives the approach to each of the significant problem areas, methods of analysis, and the results obtained.

6.3.2.1.1 Petal Construction

In order to achieve a minimum weight, 30-foot diameter, parabolic dish, with a reflective surface accuracy commensurate with the rf requirements of this system, it became evident that the petals forming the reflector should have a lattice work of accurately contoured members covered with a lightweight radar reflective screen.

A typical petal sector depicting the lattice work pattern is shown in Figure 6.3-15.

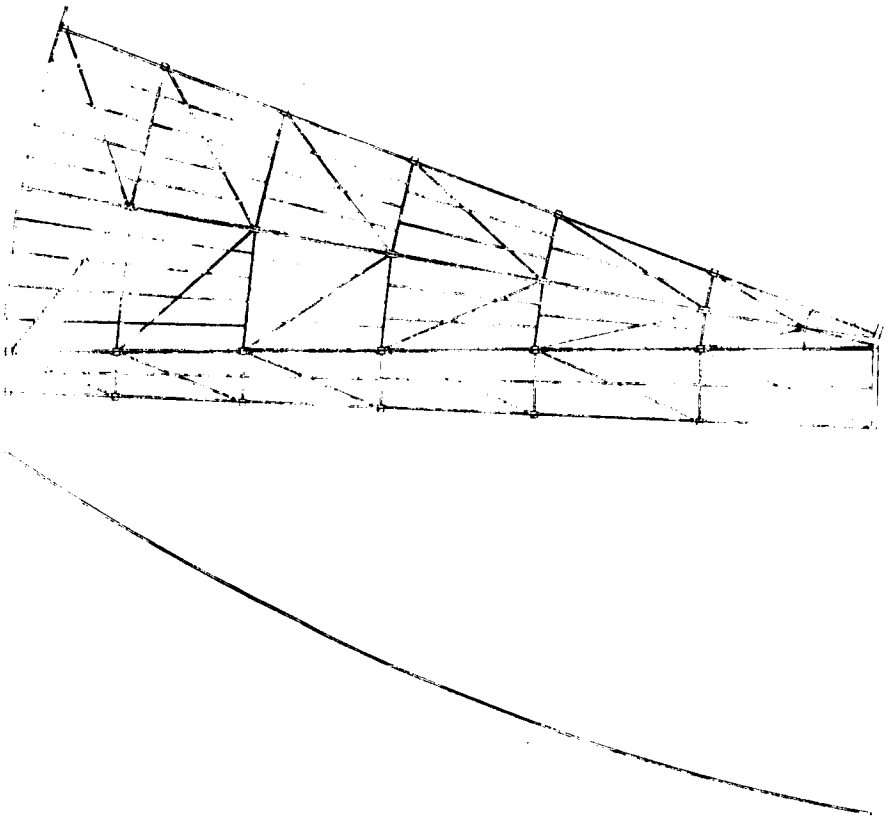


Figure 6.3-15. Typical Sector of Petal Lattice Pattern

In regard to the above, a number of petal constructions and fabrication methods were considered using weight as a common denominator. Each method has been evaluated against several tangible items that affect selection, such as the following:

a. Overall structural efficiency - static deflection and natural frequency

b. Structural stability and dimensional tolerances under thermal-induced stress

c. Ease of manufacture

d. Shop-handling characteristics

e. Adaptability to the continuous-hinge reflector concept

f. Ease of installing the required reflective screen surface on the petals

g. Complexity of the installation required to withstand the launch environment

h. Cost

i. State-of-the-art

Applying the above criterion to the design of the reflector petals, the summary of the initial study parameters are presented in Table 6.3-2.

The aluminum bar configuration is fabricated by stretching 0.200-inch-thick stock over a parabolic-contoured form and routing the formed sheets to the lattice pattern. The primary structural members which are the petal outer frame, the circumferential rings, and the diagonals are routed so that they have a 0.20 x 0.20 square inch cross-section. The secondary members which are the radial, intermediate members are routed to a width of 0.10 inch and the back surface is then milled to form a 0.10 x 0.10 square inch cross-section.

This configuration rates high from a thermal stability standpoint but rates low for natural frequency, is the heaviest, and has the poorest member column strength of the configurations under consideration.

The beryllium configuration is fabricated by hot die-forming the individual lattice members from square bar stock, to contour, providing gussets for both the top and the bottom surfaces at the member junctures, and utilizing structural bonding to assemble the petal over a parabolic-contoured mold.

This configuration is far superior to any of the others under consideration and rates the highest from a thermal stability standpoint. The disadvantage of this concept is the extremely high cost for material and fabrication.

The titanium configuration is fabricated by laying up a honeycomb sandwich of titanium face sheets and an aluminum core on a parabolic contoured mold and bonding the components into a composite panel. The panels are then cut out to form the lattice pattern.

This configuration compares favorably with the beryllium bar concept as far as weight is concerned, but offers a lower percentage of open areas, and a lower launch load column strength and natural frequency. However, even though the load column strength and natural frequency are lower, they still meet the requirements of the ATS-4 program.

Table 6.3-2. ATS-4 Structural Parameters

Parameters → / Configuration ↓	Member Sizes		% Open	Total* Dish Wt. W ~ lb	E lb/in.^{2}	I (in.^{4})	A (in.^{2})	Launch Load Column Strength Parameter		Nat. Frequency Parameter	
	Primary (inches)	Secondary (inches)						EI/W	Rating	$\sqrt{EI/W}$	Rating
Alum. Bar	0.2 x 0.2	0.1 x 0.1	90	106	10×10^6	1.33×10^{-4}	0.0400	13	3	3.5	3
Be Bar	0.16 x 0.16	0.1 x 0.1	93	65	40×10^6	0.546×10^{-4}	0.0256	34	1	5.8	1
Ti Sand	0.75 x 0.3 x 0.0025	0.375 x 0.3 x 0.0025	80	66	15.5×10^6	0.845×10^{-4}	0.00375	20	2	4.5	2
Alum. Sand.	0.75 x 0.3 x 0.004	0.375 x 0.3 x 0.004	80	64	0.10×10^6	1.35×10^{-4}	0.0060	21	2	4.6	2

*Screen and Hinge Weight Included

The aluminum-sandwich configuration is fabricated in the same manner as the titanium sandwich except that the face sheets and core are of aluminum. The aluminum and titanium sandwich configurations have practically identical ratings in the parameters chart.

The sandwich configuration was chosen for the reflector, in lieu of the beryllium-bar concept, on strictly economic grounds.

The titanium face sheets were chosen for the sandwich because titanium has a lower coefficient of thermal expansion than aluminum (see Figure 6.3-19), and thus with the same temperature distribution for a given area, smaller thermal deflections affecting the reflector surface accuracy will exist.

6.3.2.1.2 Materials

Materials must be carefully selected to provide a structure that will perform successfully for two years in space environment. The reflector materials must provide several functions including:

a. Structural

b. Thermal control

c. Rf reflection

d. Adhesive bonds

e. Lubrication

The following properties are considered the most important in selecting basic structural materials:

a. Basic mechanical characteristics

    1. Modulus of elasticity

    2. Tensile and yield strengths

3. Weight-to-stiffness ratio

4. Coefficient of thermal expansion

5. Thermal conductivity

6. Electrical conductivity

7. Magnetic characteristics

b. Fabrication characteristics

1. Compatibility or suitability for application of thermal control coatings to attain the required α/ϵ values

2. Availability

3. Machinability

4. Notch sensitivity

5. Corrosion resistance

6. Damping coefficient

When considering these properties, aluminum and titanium appear to be the most desirable. They can be obtained in the skin thickness required, have satisfactory workability, and are nonmagnetic. A summary of their mechanical properties is shown in Table 6.3-3. Variation of these mechanical properties with temperature is listed as follows:

a. Figure 6.3-16 - Ultimate tensile strength versus temperature for aluminum and titanium

b. Figure 6.3-17 - Yield strength versus temperature for aluminum and titanium

c. Figure 6.3-18 - Modulus of elasticity versus temperature for aluminum and titanium

d. Figure 6.3-19 - Coefficient of thermal expansion versus temperature for aluminum and titanium

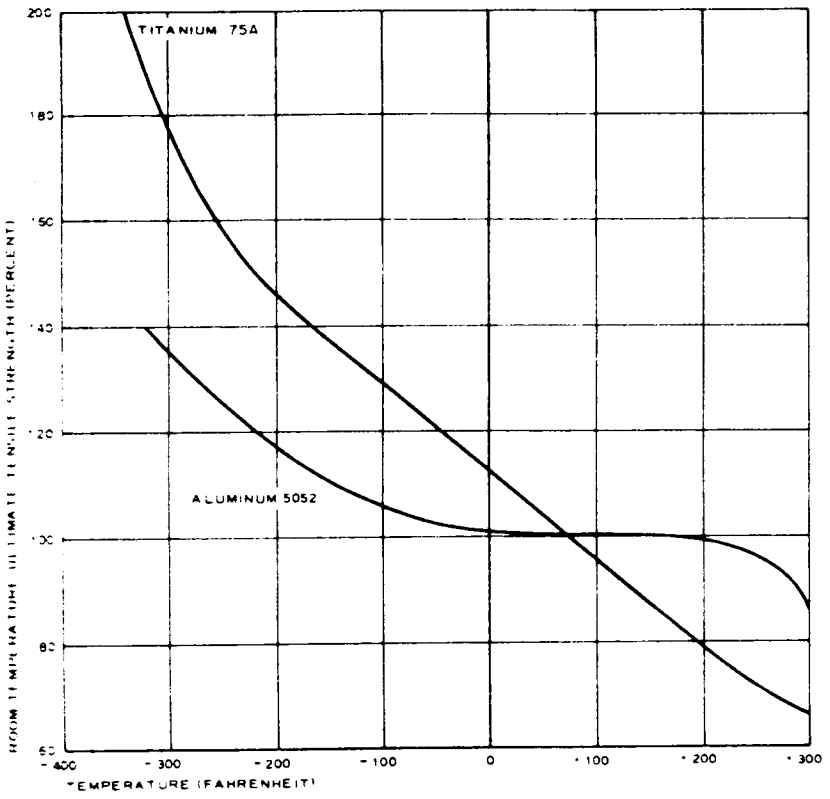


Figure 6.3-16. Ultimate Tensile Strength vs Temperture for Aluminum and Titanium

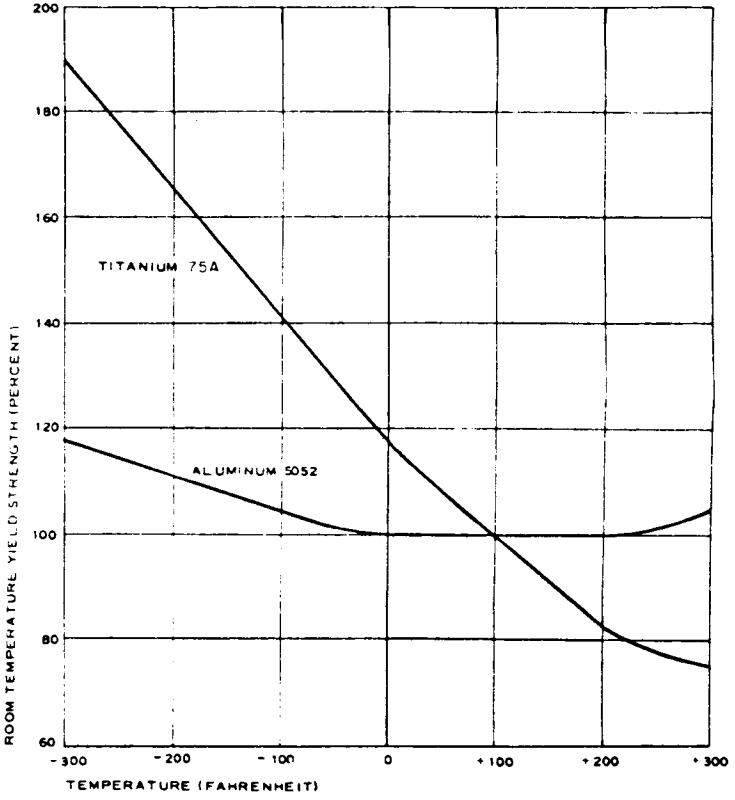


Figure 6.3-17. Yield Strength vs Temperature for Aluminum and Titanium

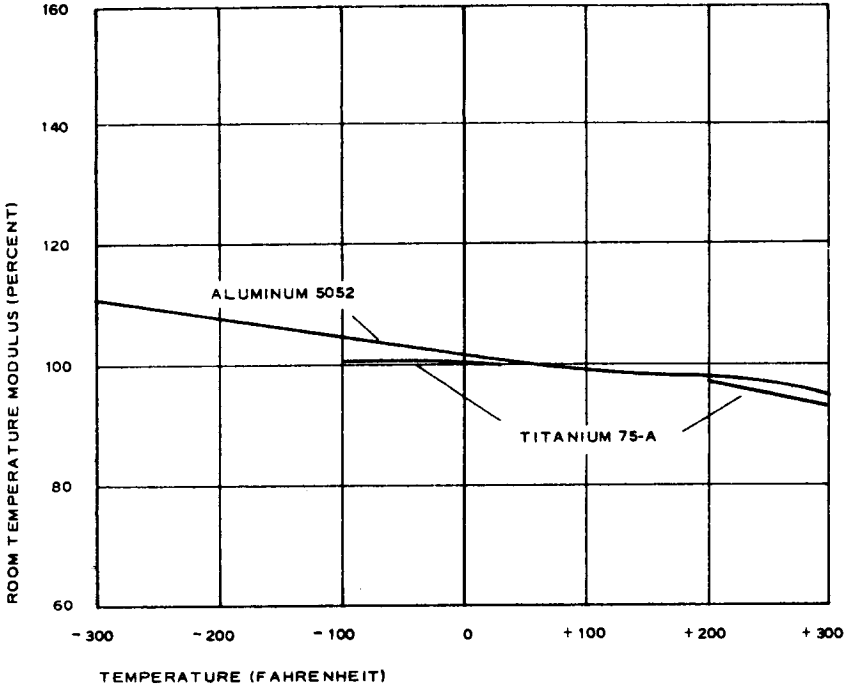


Figure 6.3-18. Modulus of Elasticity vs Temperature for Aluminum and Titanium

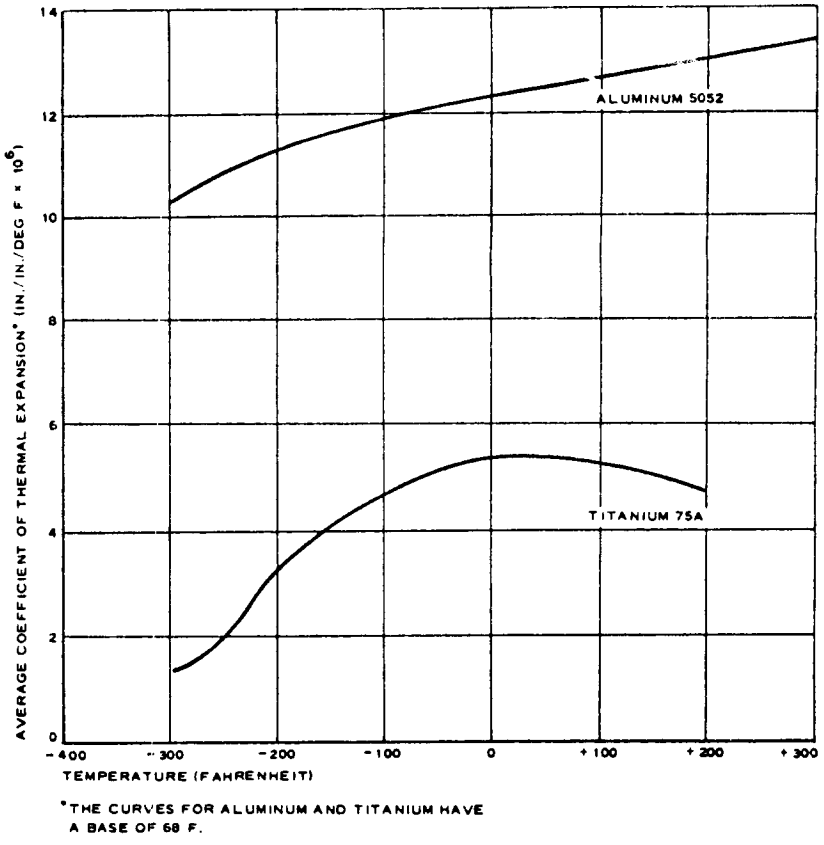


Figure 6.3-19. Coefficient of Thermal Expansion vs Temperature for Aluminum and Titanium

Both aluminum and titanium may be used for face sheets on honeycomb built-up structure. They are very compatible with forming and adhesive-bonding techniques.

If honeycomb is used for the basic structural material, an aluminum honeycomb core 0.3 inch thick will be used with either skin material. The core will be 0.0007-inch aluminum foil with 1/8-inch cellular openings (minimizing these dimensions is optimum for thin panels). Aluminum is chosen primarily from a weight savings standpoint and because it is thermally compatible with the titanium face material and the adhesive.

Table 6.3-3. Mechanical Properties of Aluminum and Titanium

Property	Aluminum 5052	Titanium 75A commercially pure
Density (pounds per cubic inch)	0.097	0.163
Tensile strength (psi)	39,000	80,000
Yield strength (psi)	33,000	70,000
Elastic Modulus (psi x 10^{-6})	10.2	16.2

For the rf reflecting material, expanded metal mesh has been selected. The mesh will be stretched into a rectangular form, rolled, and chemically etched to remove burrs. Titanium was selected to maintain similar coefficients of thermal expansion between the basic structure and screening material.

All ductile metals available in foil or thin sheet form (including titanium, steel, invar, and aluminum) can be obtained in the expanded form. Figure 6.3-20 shows the configuration for the expanded metal.

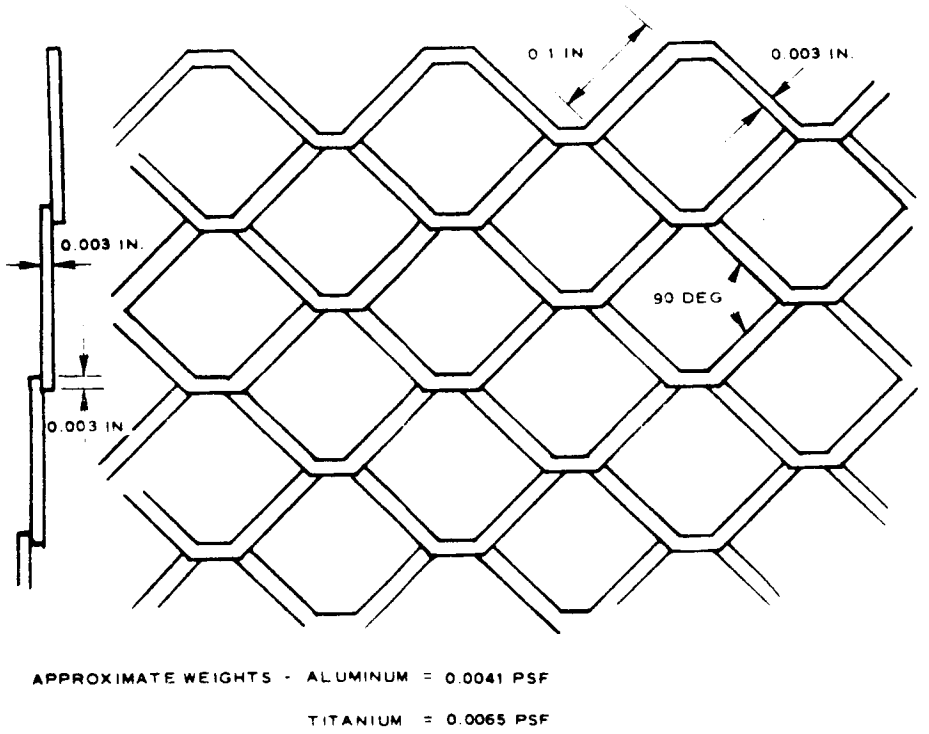


Figure 6.3-20. Possible Configuration of Expanded Metal for RF Reflecting Material

Various methods of attachment are available such as:

a. Applying the adhesive to the honeycomb skin and laying of the mesh over the adhesive.

b. Applying the adhesive to the mesh and laying it on the petal surface.

c. Positioning the screen on the petal surface and then overspraying with an adhesive.

d. Mechanically attaching the mesh to the petal.

Applying the adhesive to the mesh is preferred from the standpoint of contaminating the thermal coatings on the reflector.

The primary areas of concern in selecting an adhesive are mechanical properties, thermal properties, and stability in a space environment.

These properties have been examined and the FM-1000 adhesive selected. FM-1000 is provided as a film weighing 0.025 lb/ft^2. Since FM-1000 is a film, uneven distribution inherent in brushing or spraying is eliminated. The lightweight and high peel strength of FM-1000 makes it ideally suited for a honeycomb structure. The most desirable method for applying the adhesive onto the reflecting screen will require further development during the design program.

Evaluation has been made of FM-1000 for another space program, which influenced the selection of this adhesive. Some honeycomb panels consisting of aluminum skins, aluminum core, and FM-1000 adhesive were tested by the Lockheed Missile and Space Company to:

a. Determine the basic thermophysical, optical, and mechanical properties of materials developed by the solar-collector industry for use in the ASTEC program.

b. Test the degrading effects of various segregated and combined elements of the space environment on these materials.

Table 6.3-4 shows the effect of temperature on the strength of FM-1000 adhesive-bonded honeycomb in tension. These tests were conducted at -200^{o}F, room temperature, and +250^{o}F. Table 6.3-5 gives similar data for specimens exposed to elevated temperature (250^{o}F) and vacuum for various lengths of time.

Differences in coefficients of thermal expansion between the face skins of the honeycomb and the FM-1000 adhesive do not produce excessive stresses in the bond, due to the low elastic modulus (E) of the bond and the cutout configuration.

Teflon has been selected as the basic lubricant for the hinges and actuating mechanisms.

The thermal control necessary to maintain dimensional uniformity will be base metal patterns and highly reflective surfaces in combination with vapor-deposited coatings (e.g., aluminum and silicone monoxide), and also thermally reflective or absorbent paints.

Table 6.3-4. Effect of Temperature on the Tensile Strength of FM-1000 Adhesive-Bonded Aluminum Honeycomb Panels

Temperature (^{o}F)	Specimen No.	Modulus E (psi)	Elastic Limit (psi)	Maximum Stress (psi)	Final Strain (percent)
-200	1*	4.46×10^3			
	2*	4.08×10^3	512	550	16.8
	3*	3.80×10^3	564	573	14.5
	Average	4.11×10^3	538	561	15.6
Room temperature	1*	11.5×10^3	237	322	3.30
	2+	12.2×10^3	139		
	3*	15.8×10^3	167	230	1.90
	Average	13.2×10^3	181	271	2.60
+250	1±	9.25×10^3	102	125	2.08
	2±	9.41×10^3	120	145	2.33
	3±	10.55×10^3	128	140	2.48
	Average	9.74×10^3	117	137	2.30

*Core material tensile failure

+Test equipment failure

±Glue line failure

Table 6.3-5. Effect of Temperature and Vacuum on the Tensile Strength of FM-1000 Adhesive Bonded Aluminum Honeycomb Panels*

Exposure+	Modulus E (psi)	Elastic Limit (psi)	Maximum Stress (psi)	Final Strain (percent)
Thermal/vacuum environment (100 hr)	3.08×10^3	155	349	14.4
Thermal/vacuum environment (1000 hr)	5.01×10^3	301	364	8.3
Thermal/vacuum environment (1000 hr)	2.47×10^3	326	360	15.0
Thermal/vacuum environment (6000 hr)	5.75×10^3	297	332	5.75
Thermal/vacuum environment (6000 hr)	6.65×10^3	291	351	5.62
Thermal cycling (100 cycles)	3.95×10^3	360	396	10.5
Thermal cycling (1000 cycles)	5.93×10^3	362	390	9.53
Thermal cycling (6000 cycles)	6.27×10^3	295	346	5.75

*All testing performed at room temperature

+Thermal/vacuum environment - +250°F with vacuum of 5×10^{-6} torr or less.

Thermal/cycling - specimen heated to +250°F and allowed to cool for 36 minutes in a vacuum between 10^{-6} and 5×10^{-5} torr.

These coatings will be necessary to provide the correct temperature gradients to maintain the dimensional stability previously mentioned and were chosen from materials that have been used in previous programs or have had substantiating data for their suitability in resistance to vacuum, sunlight, and hard radiation. The application of these coatings and their resistance to earth atmosphere during storage and manufacturing also were considered.

Some special requirements are listed below:

a. Space Environment Effects on Material - Although the behavior of materials at pressures below 10^{-4} atmospheres may usually be extrapolated from data in the range 10^{-4} to 1 atmosphere, certain minute phase changes may occur that may cause difficulty with the system. In these cases, data will be developed to establish the validity of the particular extrapolation during the detail design phase of the program.

b. Polymeric Materials, Lubricants, and Insulation - Consideration was given to the properties of these materials for the required environment. Such factors as out-gassing, radiation degradation, and UV degradation were considered and sub factors such as natural shielding also were taken into account.

c. Protection of Surfaces During Manufacture and Storage - In many cases, the inorganic coating treatments, such as anodic films or conversion coatings, provide corrosion protection while also providing a particular α/ϵ ratio. In other cases, strippable protective films can be used or, in some cases, a photolyzable film which will disintegrate in space.

6.3.2.1.3 Weight Data

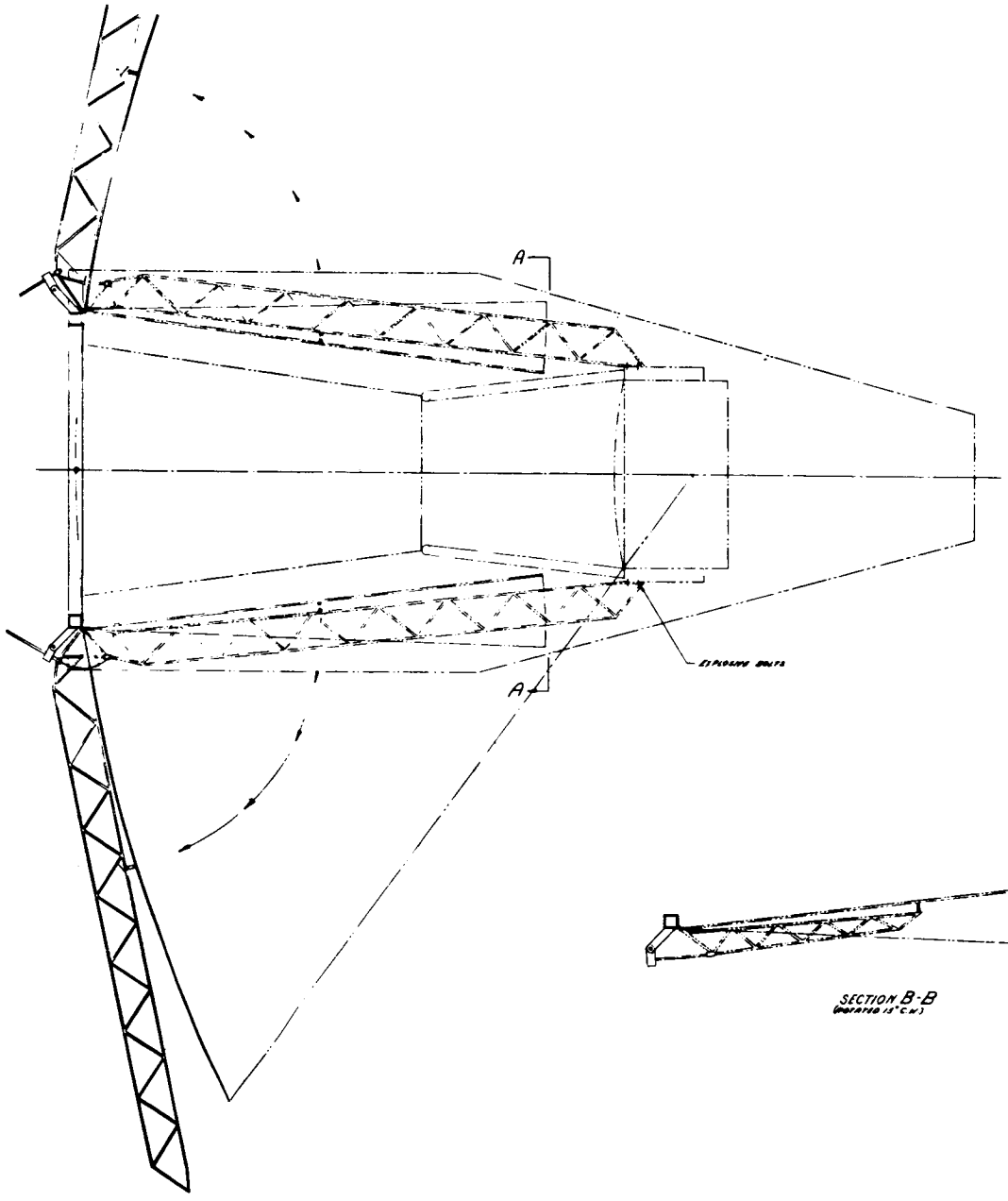
An estimate of the mass properties for the selected design is shown in Table 6.3-6. Also shown for comparison is the aluminum bar configuration.

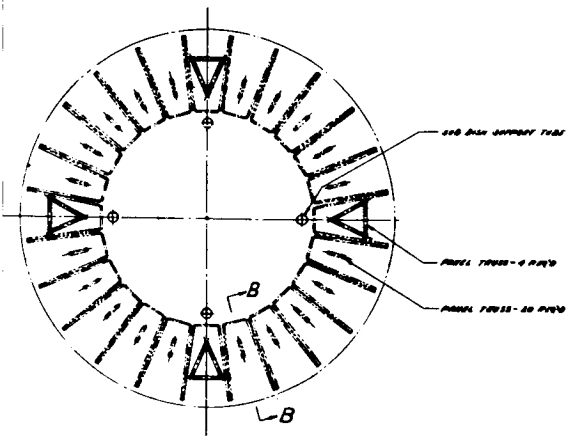
In all designs,the deployment mechanism provisions are somewhat conservative and present a potential weight reduction area.

6.3.2.1.4 Packaging and Deployment

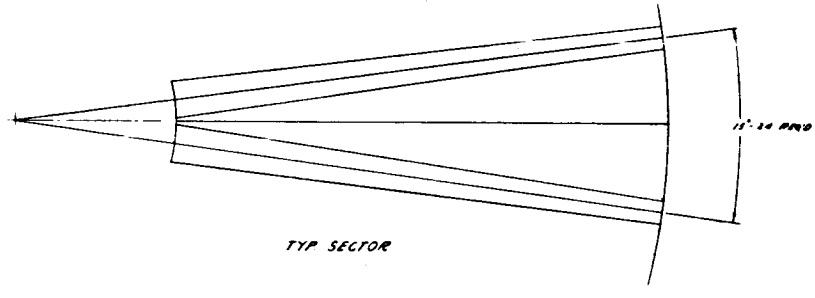
The flexibility of the folded petal concept for parabolic dishes is best illustrated by a few of the alternate packaging and deployment approaches that were under consideration during the conceptual phase of the study program.

Figure 6.3-21 shows a reverse folding pattern that has the trapezoidal petals folded in toward the package center and the triangular petals folded out. This would provide space to place four trusses of triangular cross-section that serve the dual purpose of being part of the deployment system and aid in supporting an experiment equipment package mass located behind the focal point of the parabolic dish. This additional support would increase the


A
A
SECTION B-B



SECTION A-A



TYP SECTOR

Figure 6.3-21. Reverse Folding Pattern, Triangular Petals Folded Outward

stiffness of the total package in the launch environment. Explosive bolts would release the trusses from the experiment equipment package for reflector deployment.

Several deployment schemes are adaptable to moving the reflector from its packaged cylindrical form to the deployed dish. The basic requirement for the deployment is to move the petals hinged at the central hub, in an outward arc until the petals interconnecting hinge lines become straightline elements of a cone. At this point, a force must be applied at the midpoint of the hinge line to "pop" the hinge lines from the straightline elements of the cone to the parabolic-curved lines of the deployed dish (see Figure 6.3-13).

The initial application for which the folded dish was developed was a solar concentrator and utilized deployment linkages in front of the reflective surface. This scheme provided for a maximum diameter central hub and a minimum height of the packaged cylinder for a given diameter of the deployed dish (see Figure 6.3-22, Sheet 1).

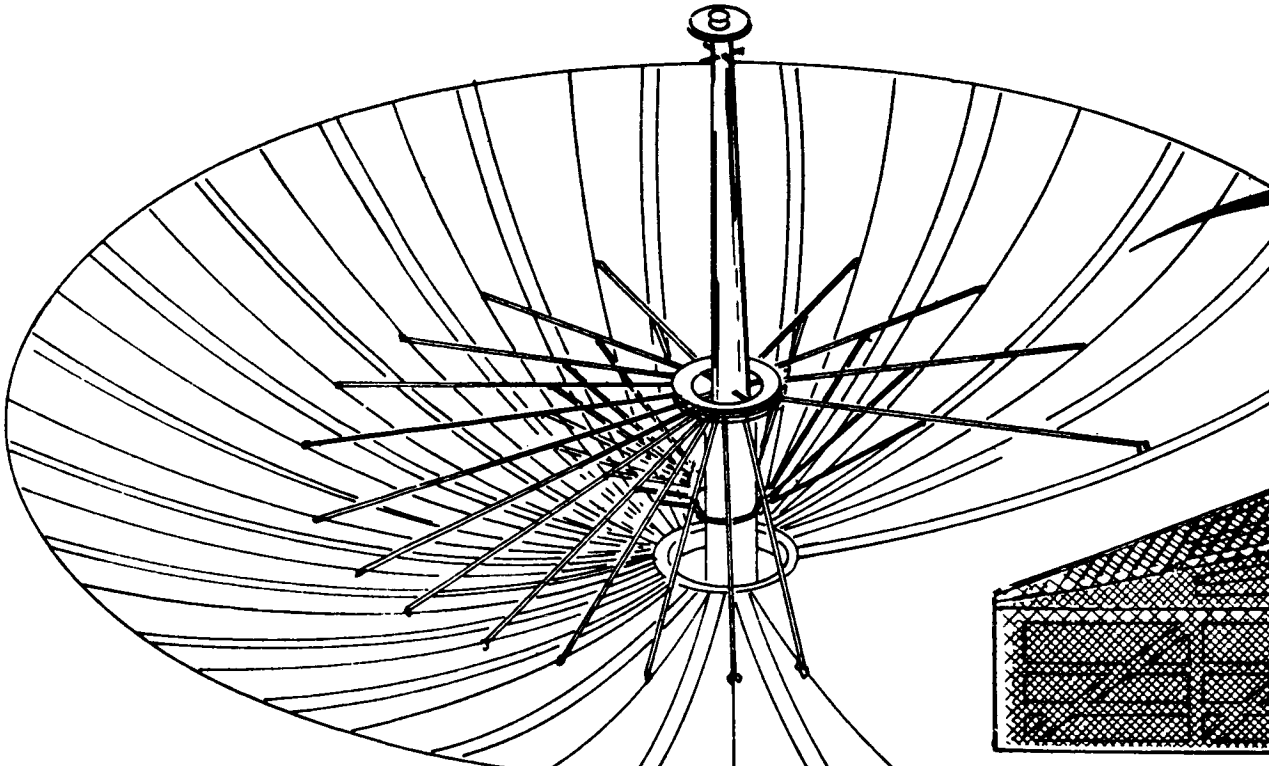
This method of deployment was suitable for the solar concentrator application but has a definite disadvantage for antenna applications due to the frontal blockage caused by the actuation linkage elements.

For the antenna application proposed herein a scheme of deployment that has the mechanism behind the reflective surface was developed (see Figure 6.3-22, Sheet 2).

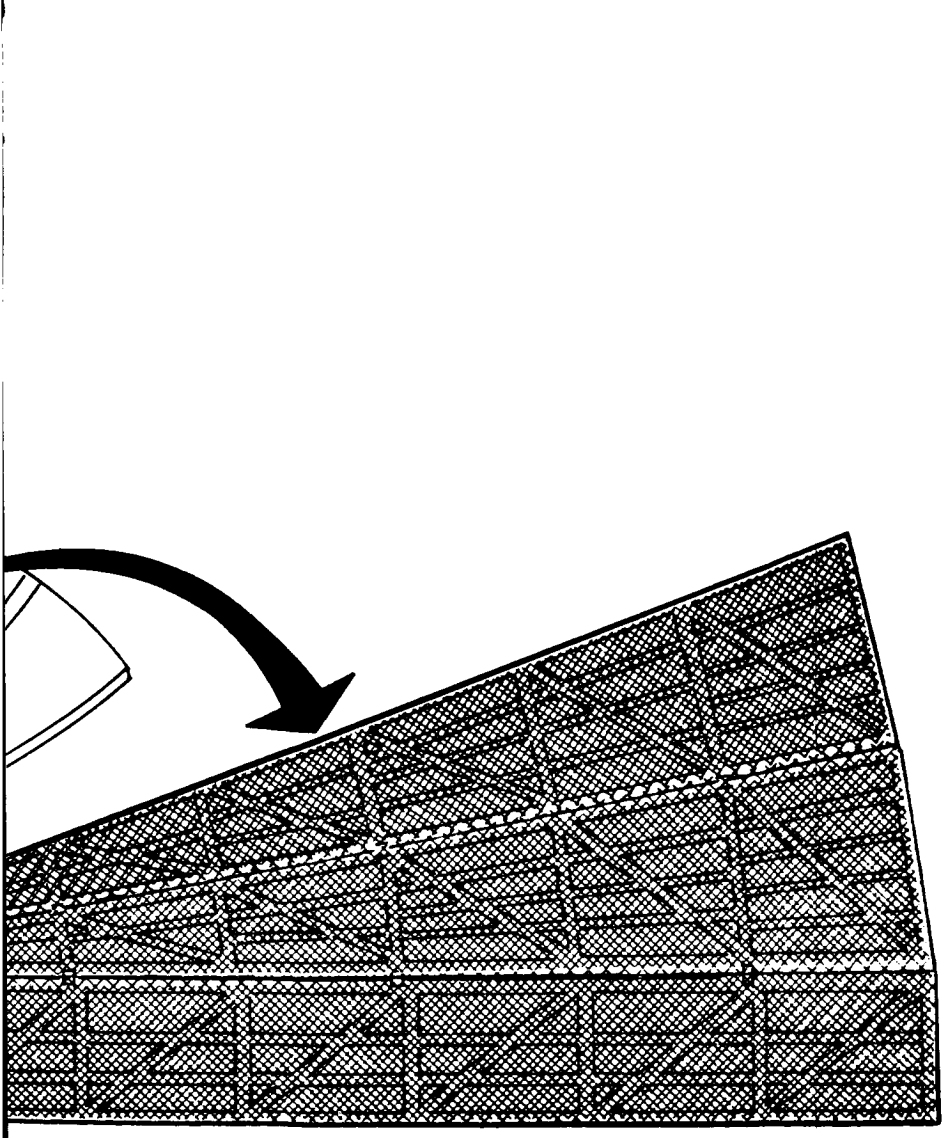
This scheme necessitates a smaller central hub for a given package diameter to provide space for the actuating mechanism, and thus presents a slightly taller cylindrical packaged form for a given diameter of deployed reflector.

The back deployment method was chosen for the proposed antenna as it eliminates the rf blockage inherent in the frontal deployment scheme.

Another innovation that may be employed to increase the reflector accuracy under induced thermal stresses is to design the interconnecting hinges of adjacent petals so that they are close-toleranced in the circumferential direction and free for a small movement in the radial



6.3-45



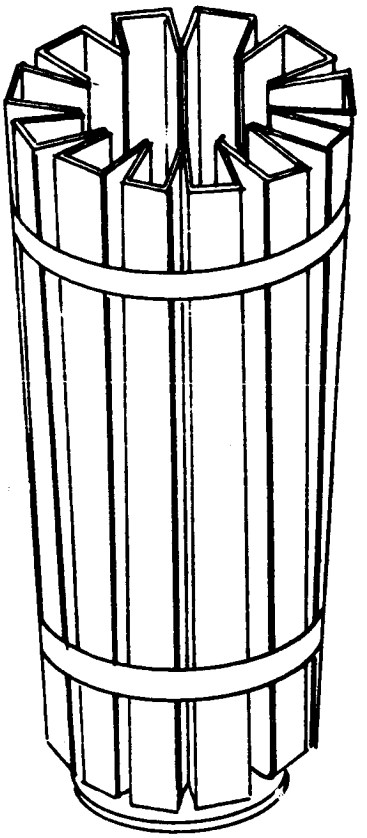
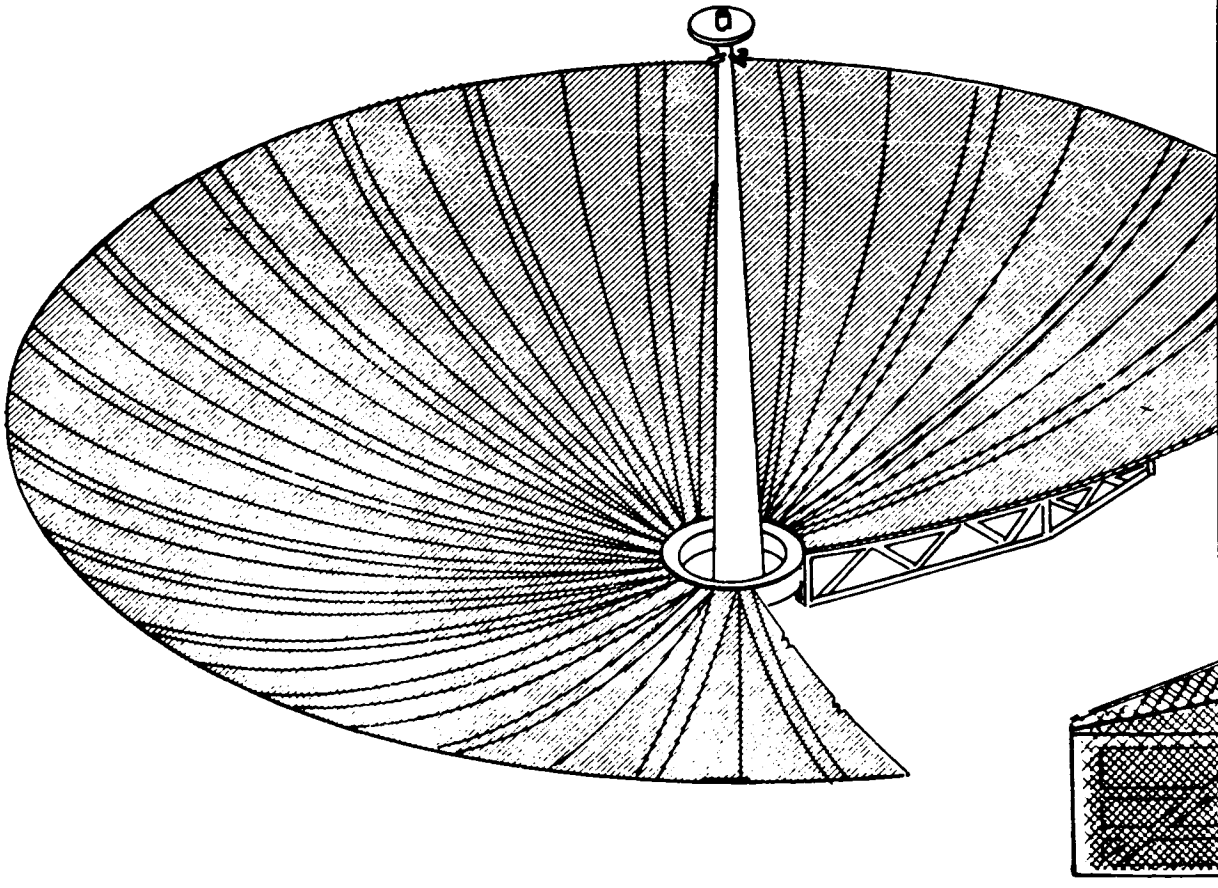
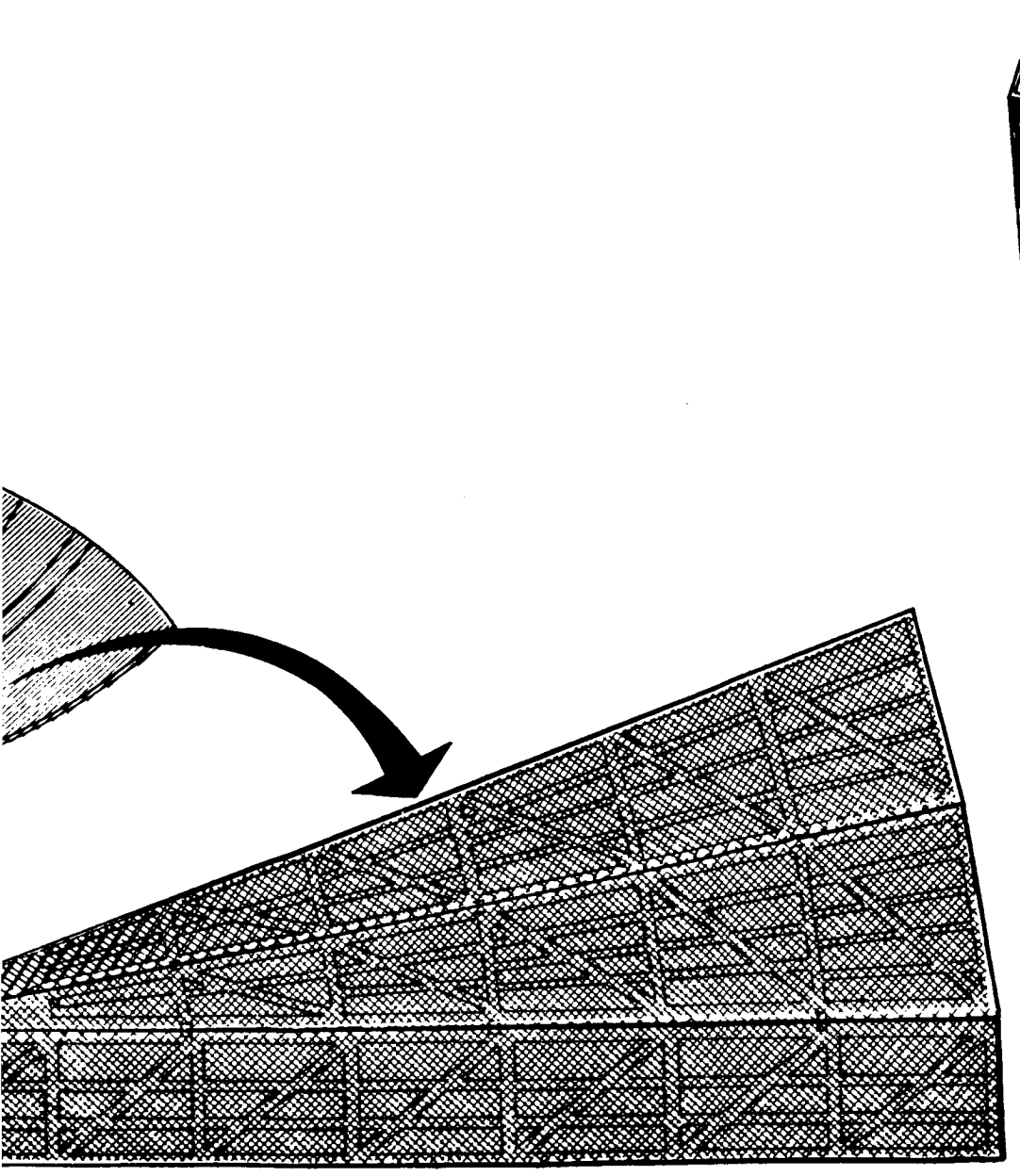


Figure 6.3-22. Deployment Scheme
(Sheet 1 of 2)



6.3.47



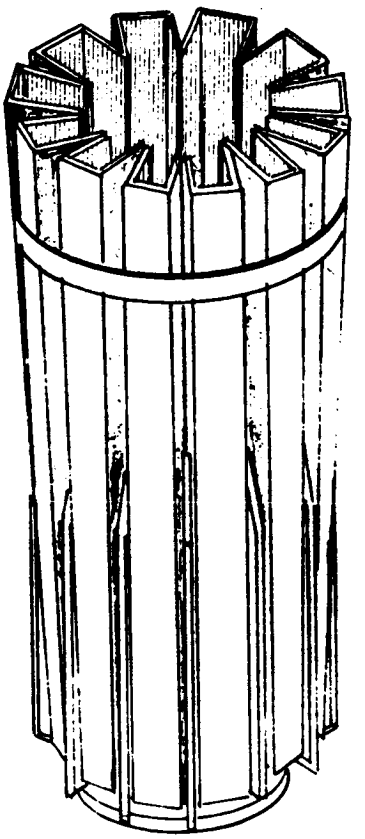


Figure 6.3-22. Deployment Scheme
(Sheet 2 of 2)

Table 6.3-6. Estimate of Mass Properties

Item	Aluminum Bars	Titanium Honeycomb
Reflector	(118.30)	(66.40)
Panel Framework	95.00	43.10
Screen and Bonding	10.70	10.70
Interpanel Hinges	9.50	9.50
Thermal Finish	1.50	1.50
Miscellaneous	1.60	1.60
Deployment Mechanism	(102.60)	(102.60)
Interface Mounting Ring	30.00	30.00
Hinges and Pins (20 sets)	8.80	8.80
Actuators (20)	45.10	45.10
Torque Tubes (20)	.80	.80
Universals (1)	3.00	3.00
Trusses (16)	11.80	11.80
Motor Drive (1)	3.10	3.10
Launch Stewage Provisions	(8.70)	(8.70)
Channel and Stowage Brackets	7.10	7.10
Clamping Band	1.60	1.60
Total - Reflector, Deployment, and Launch Stowage	229.6	177.70

direction. The hinges nearest the interface hub would be tight-toleranced in all directions, but the outboard hinges could be designed to provide this radial clearance allowing for differential movement between adjacent petals if it appears desirable in the final analysis.

Adaptations can also be made to the reflector to alter the packaged form. If it becomes desirable (to accommodate a smaller diameter hub, for example), the reflector proposed herein could be packaged approximately 1 foot higher in the confines of the enclosing shroud

by making angular cuts in the corners of the triangular petals. Such cuts can also permit a shorter, larger diameter, cylindrical package. To do this, a reverse folding pattern is again required with the trapezoidal petals on the inside of the package and the triangular petals folded radially outward (see Figure 6.3-23).

These cuts would result in a series of triangular scallops on the periphery of the deployed dish which would be covered with flexible radar reflective mesh so as to minimize the rf losses of the dish.

With the reflector folded so that the trapezoidal panels are on the outside of the package with the triangular panels folded in towards the center (see Figure 6.3-24), the same cut could be made to accommodate any shear bracing whose diameter at the feed is maximized in order to minimize rf strut losses. The reflector cannot be raised in the shroud with this configuration.

6.3.2.2 Thermal Considerations

6.3.2.2.1 General

The ATS-4 antenna was analyzed thermally for the periods prior to and during operation. Both of these phases required that antenna temperatures encountered should not affect structural properties or mechanical functions adversely. For the operational phase, there exists the additional requirement that the thermal deflections must not degrade the antenna performance.

There are three temperature effects that could be detrimental to the antenna performance (see Figure 6.3-25).

a. Temperature gradient through the antenna (front to back)

b. Temperature gradients across the antenna

c. An average antenna temperature quite different from that for which it was accurately fabricated

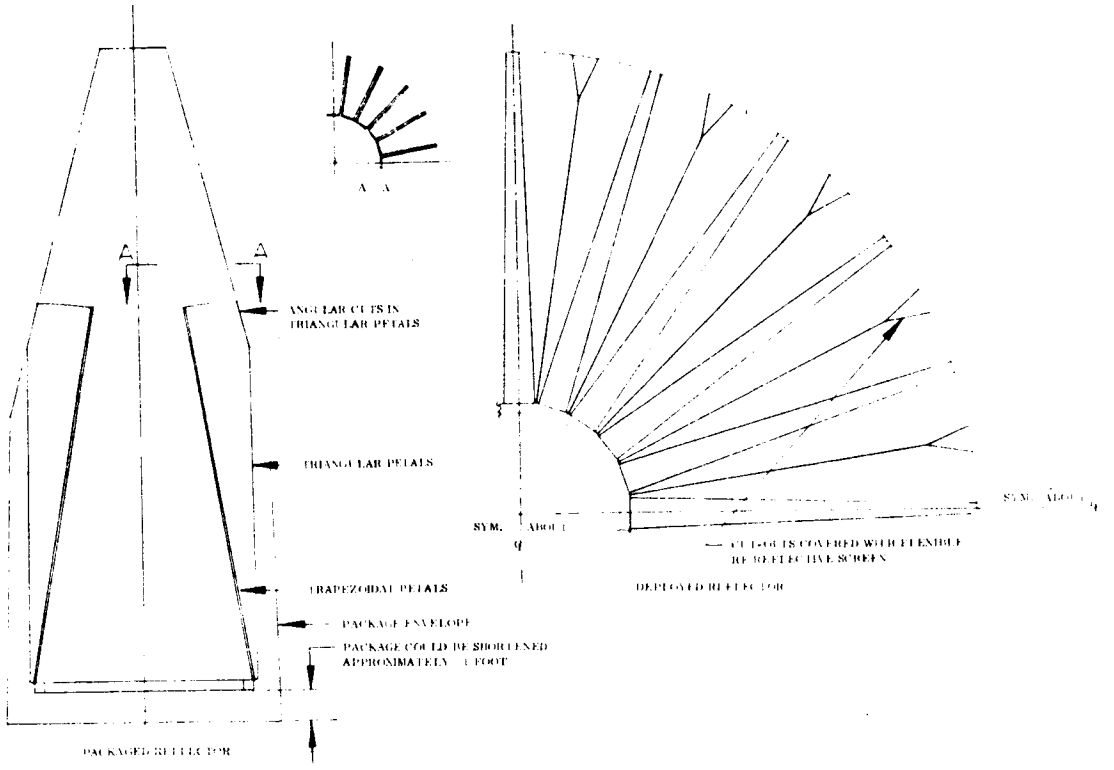


Figure 6.3-23. Reverse Folding Pattern, Triangular Petals Folded Radially Outward

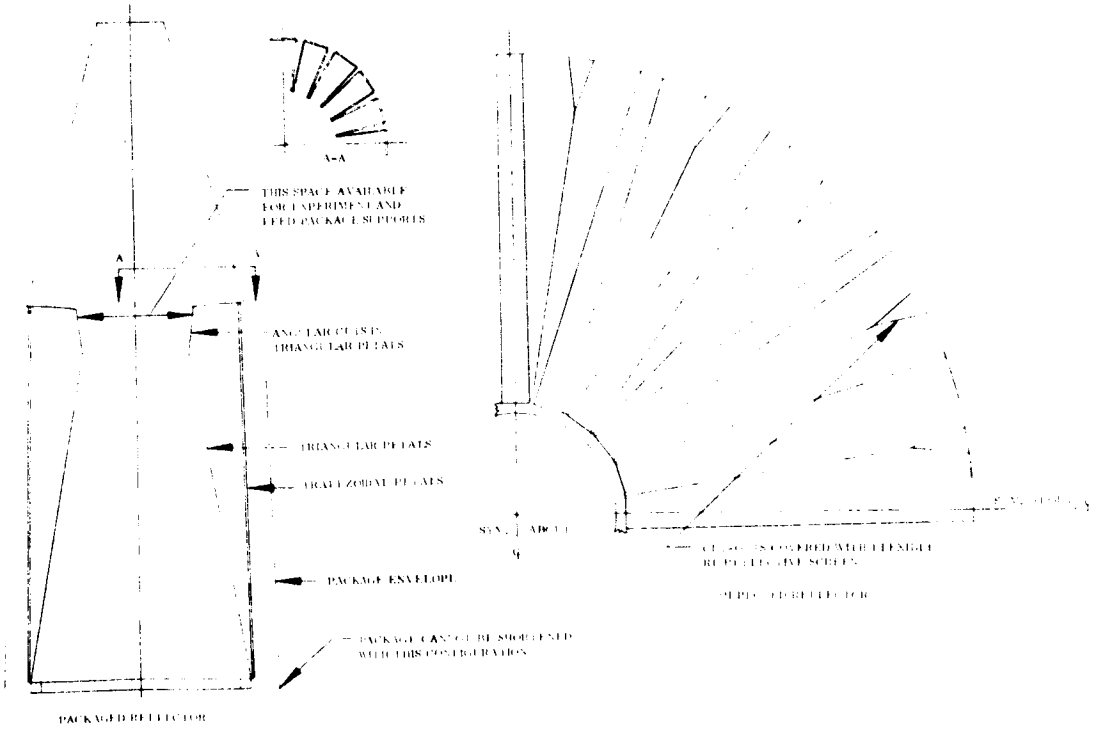


Figure 6.3-24. Reverse Folding Pattern, Triangular Petals Folded Towards Center

All three can produce thermal distortions of the antenna. The first temperature effects can be very small for an aluminum honeycomb panel and negligible for solid aluminum rods. The third effect can be alleviated by designing a free hub (free to expand and contract). The second effect will be the largest problem area because even when the antenna is 80 percent open there will be orbital positions when large temperature differentials will exist across the antenna. The third effect changes the f/D slightly.

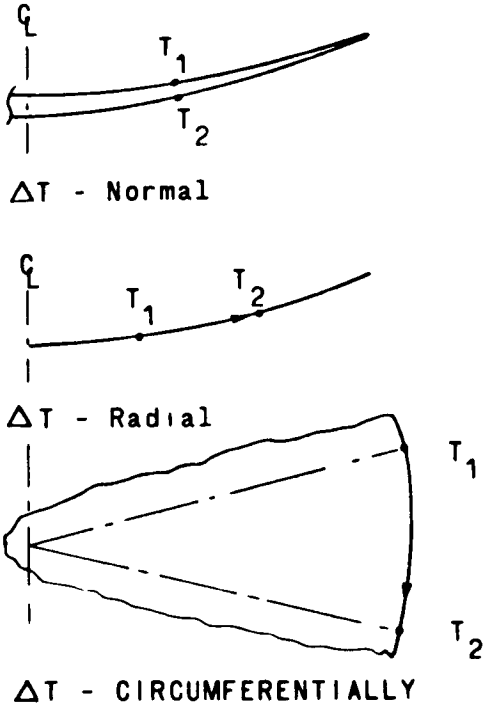


Figure 6.3-25. Causes of Thermal Deflections

During environmental prelaunch phase, which includes ground handling and time prior to launch, the antenna will be protected properly with coatings and shipping containers to protect both the optical properties of the surfaces and the structure itself. This is not a critical environmental phase. The launch phase set design criteria for the folded configuration. The operational phase, while in orbit, was the environmental phase considered in this study.

6.3.2.2.2 Approach to Problem

The thermal analysis included defining the thermal environment and the thermal model of the antenna. These models, along with different optical coatings, were used to calculate the time-temperature history of the antenna. Coatings that are considered space stable were used in the analysis. These would be coatings such as bare metal, or metallized surfaces and dark paints. Spacecraft and feed geometries were not included in the thermal models.

Two basic structural materials, solid aluminum rods and aluminum honeycomb, were investigated as the best possible candidates. The solid rod structure has a better thermal lagging characteristic and better conduction so that a transient orbital analysis would be more necessary in follow-on studies than for the honeycomb structure.

6.3.2.2.3 Symbols

The following symbols are used in the thermal analysis:

a = albedo

c = constant

C_p = specific heat

C_s = solar constant

F_p = planet view factor

H = altitude

I = infrared radiation

K = attitude parameter on thermal conductivity

N = normal vector

P = planet vector

R_p = planet radius

q = heat flux

Q = total heat flux

S = solar vector

T = temperature

W = weight per square foot

α = solar absorptance

ϵ = total emittance

η = blockage factor

ψ = angle between sun-planet and satellite-planet line

Ω = angle toward planet

σ = Stefan-Boltzmann constant

τ = time

Δ = increment

6.3.2.2.4 Thermal Environment

The heat fluxes used for an orbit environment included all three radiant heat fluxes although the albedo and earth-emitted heat fluxes are of minor importance (see Figure 6.3-26).

$$\dot{q}_S = C_S A_P$$
$$= C_S A \cos\beta$$
$$\dot{q}_E = (1 - a) C_S \frac{\pi R^2}{4\pi R^2}$$
$$= \frac{1 - a}{4} C_S$$

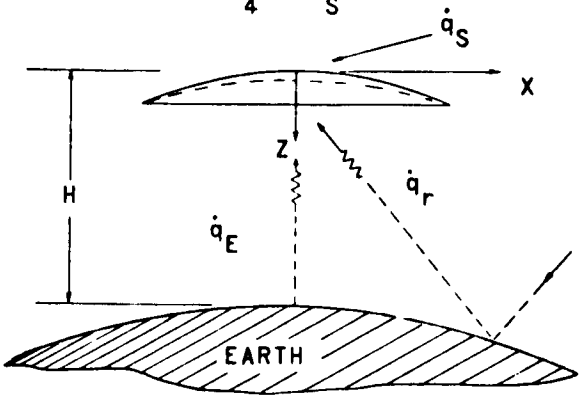


Figure 6.3-26. Heat Inputs

The sources of radiation that are included in the thermal analysis consist of direct solar radiation, $\dot{q}_s$; earth-reflected solar albedo, $\dot{q}_r$; and earth-emitted, $\dot{q}_E$. The direct solar radiation will be calculated on a projected area basis and therefore will be a function of the angle between the unit normal vector $\bar{N}$. and the unit solar vector, $\bar{S}$, the solar constant, C_s, and the solar absorptance, α, of the surface:

$$\dot{q}_s = \eta \alpha C_s \bar{N} \cdot \bar{S}$$

where η would be 1.0 when the sun shines directly on the surface and some value less than 1.0 for all points that would have a partially blocked view of the sun. When the sun passes through one side of the antenna having a transparency, μ, η will be $(\bar{N} \cdot \bar{S})$ for calculating the heat flux, $\dot{q}_s$, to the other side (see Figure 6.3-27).

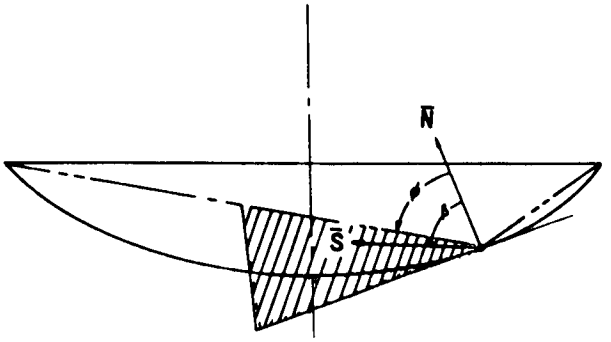


Figure 6.3-27. Internal Geometry Effects-Antenna Blockage

The infrared heating from the earth in its most general form is

$$\dot{q}_E = IF_p$$

where the flux intensity, I, is constant for any point around the planet based on the projected area of the planet absorbing that portion of solar heating which is not reflected (1 - a) and distributed over the entire area:

$$I = 1/4 \ (1 - a) \ C_s$$

The view factor, F_p, will be a function of altitude and the angle Ω between the unit normal vector and unit planet vector P.

$$F_p = f \ (\Omega, K^2)$$

where the altitude parameter K is

$$K = \frac{R_p}{R_p + H}$$

The planet-reflected solar albedo is similar to that of the earth-emitted except that the flux intensity is a function of the angle ψ between the unit planet vector $\overline{P}$ and the unit solar vector $\overline{S}$.

The albedo heat flux is

$$\dot{q}_r = \alpha \ F_p \ Q_a$$

$$= f \ (\alpha, \ a, \ C_s, \ \psi, \ \Omega, \ K^2).$$

The total radiation flux is then

$$Q_R = \dot{q}_s + \dot{q}_r + \dot{q}_E.$$

Previous work done for synchronous orbits indicates very low heat fluxes from the planet emitted and reflected, of about 5 Btu/hr/sq ft. For the concave surface of the antenna, multiple reflections are included in the steady-state network as shown in Figure 6.3-28.

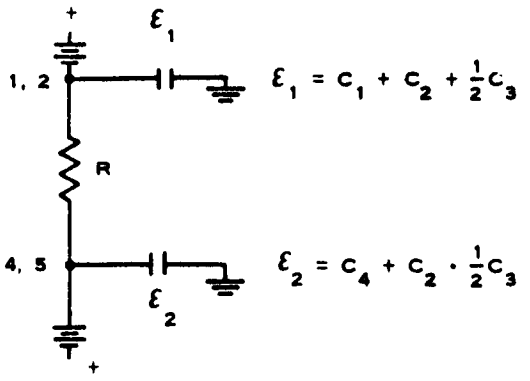


Figure 6.3-28. Two-Node Thermal Model

6.3.2.2.5 Analytical Thermal Model

A simple thermal model will be described here. The one-dimensional transient thermal programs for aluminum honeycomb have, for any node on the antenna, a two-node representation where the face sheet and the adhesive are at one temperature and the core temperature is averaged between the two face-sheet temperatures (Figure 6.3-28).

The heat transfer equations were written with the assumption that the heat flow is from the front to the back of the antenna:

$$Q_1 = W_1 \, C_p \, \frac{dT_1}{dT}$$

where

$$Q_1 = \sum \dot{q} - \left(-K \, \frac{dT}{dx}\right)$$

and

$$\Sigma \dot{q} = Q_R - \tau \epsilon T^4.$$

In finite difference form, the heat balance on node one is

$$-\tau \epsilon_1 (T_1^4) - \frac{K}{\Delta x} (T_1 - T_2) = W_1 C_p \frac{\Delta T_1}{\Delta \tau}$$

Using backward differences,

$$\tau \epsilon_1 (T_{1,\tau+\Delta\tau}^4) - \frac{K}{\Delta x}(T_{1,\tau+\Delta\tau} - T_{2,\tau+\Delta\tau}) = \frac{W_1 C_p}{\Delta x} (T_{1,\tau+\Delta\tau} - T_{1,\tau}).$$

Linearizing the equation,

$$T_{\tau+\Delta\tau} = T_\tau + \Delta T,$$

$$T^2_{\tau+\Delta\tau} = T^2_\tau + 2T_\tau \Delta T + \Delta T^2$$

$$\approx T^2_\tau + 2T_\tau \Delta T,$$

$$T^4_{\tau+\Delta\tau} \approx T^4_\tau + 4T_\tau \Delta T$$

Since

$$\Delta T = T_{\tau+\Delta\tau} - T_\tau$$

and

$$T^4_{\tau+\Delta\tau} = 4T^3_\tau T_{\tau+\Delta\tau} - 3T^4_\tau.$$

The front surface equation is then

$$-4\sigma\epsilon_1 T^3_{1,\tau} T_{1',\tau+\Delta\tau} + 3\sigma\epsilon_1 T^4_{1,\tau} - \frac{K}{\Delta x}(T_{1',\tau+\Delta\tau} - T_{2,\tau+\Delta\tau}) =$$

$$\frac{W_1 C_p}{\Delta x}(T_{1,\tau+\Delta\tau} - T_{1,\tau}).$$

The back surface equation is

$$(\dot{q}_s + \dot{q}_a + \dot{q}_{ir})_2 - 4\tau\epsilon_2 T^3_{2,\tau} T_{2',\tau+\Delta\tau} + 3\sigma\epsilon_2 T^4_{2,\tau} + \frac{K}{\Delta x}(T_{1,\tau+\Delta\tau} \cdot T_{2,T+\Delta T}) =$$

$$\frac{W_2 C_p}{\Delta x}(T_{2,\tau+\Delta\tau} - T_{2,\tau})$$

The two equations and two unknowns are then solved explicitly. The steady-state thermal program uses the same equations except that the one side of the equation, $WC_p\, dT/d\tau$ is set equal to zero. A multinode model as shown in Figure 6.3-29 was used for this study. As the design was being changed or optimized, the antenna geometry was redefined. The number of segments that the antenna is divided into is a variable and the number of orbital positions analyzed is also a variable as shown in Figure 6.3-30. Most cases studied here had 40 nodes on the one-half of the antenna and 5 orbital positions measured in degrees from the earth-sun line, 0, 45, 90, 135 and 180.

6.3.2.2.5 Results

Comparative approaches were made on various structural configurations. The first comparison was the open-to-solid antenna. The open dish, cases 1 and 4, eliminated complete shadowing of half the antenna but still had fairly large temperature gradients. This was greatly reduced by treating the inside edges of the cutouts with a coating having a high α/ϵ ratio. As the projected surface area decreases, the projected edge area increases, resulting in a more constant heating of the antenna as it rotates relative to the sun.

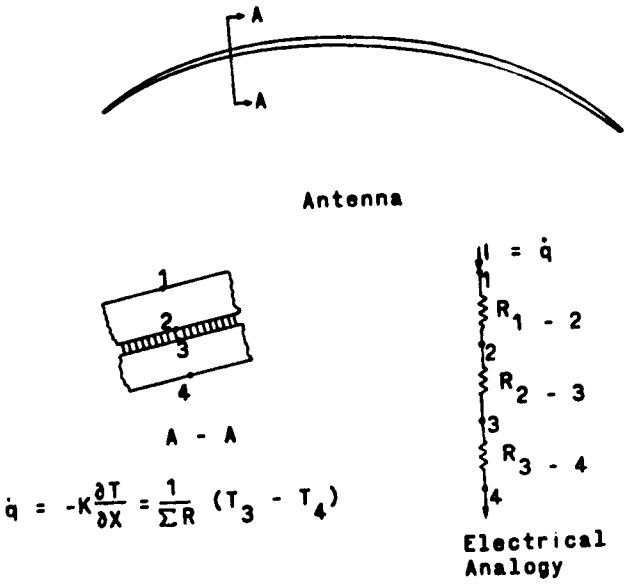


Figure 6.3-29. One-Dimensional Heat Transfer

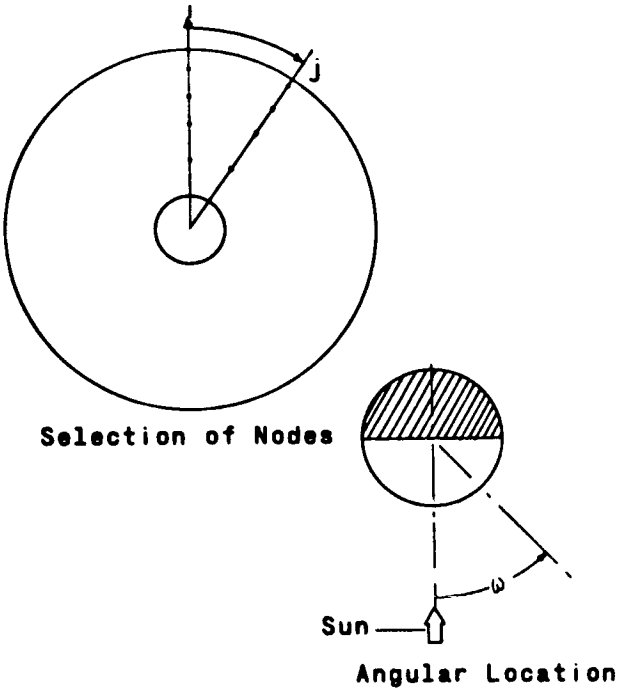


Figure 6.3-30. Analytical Model

An indication of some of the temperature excursions and gradients that could be expected are shown in Figures 6.3-31, 32 and 33. These are some of the cases for both aluminum honeycomb and solid aluminum rods. The open area was varied from 0 to 95 percent. Various coating combinations were used on all types of construction. A typical temperature distribution for a 90 percent open solid aluminum rod antenna is shown in Figure 6.3-34 (case No. 31). Figure 6.3-35 shows one for a solid aluminum honeycomb antenna (case No. 9) compared with a 60 percent open aluminum honeycomb antenna at the 90-degree orbital position. Figure 6.3-31 shows the average antenna temperature for several coatings investigated.

Figure 6.3-32 shows temperature differentials between the two surfaces of the antenna, and Figure 6.3-33 shows the differential for two edges 180 degrees apart.

CASE NO.	FRONT			BACK			EDGE			THERMAL CONDITION	OPEN (PERCENT)
	AREA (PERCENT)	α	ϵ	AREA (PERCENT)	α	ϵ	AREA (PERCENT)	α	ϵ		
4	50	0.22	0.9	50	0.12	0.03	0	. . .	. . .	25	60
9	50	0.22	0.9	50	0.12	0.03	0	. . .	. . .	25	0
18	32	0.32	0.11	32	0.12	0.04	36	0.9	0.9	25	80
31	25	0.39	0.09	25	0.18	0.31	50	0.57	0.75	5000	90

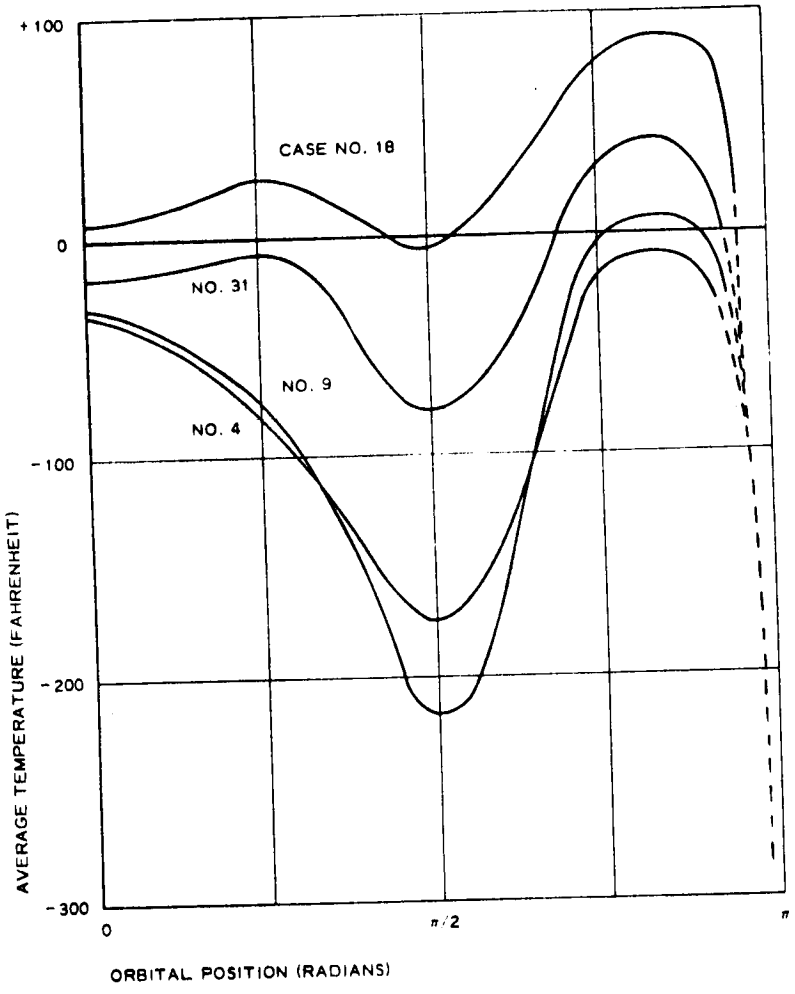


Figure 6.3-31. Average Antenna Temperature

CASE NO.	FRONT			BACK			EDGE			THERMAL CONDITION	OPEN (PERCENT)
	AREA (PERCENT)	α	ϵ	AREA (PERCENT)	α	ϵ	AREA (PERCENT)	α	ϵ		
4	50	0.22	0.9	50	0.12	0.03	0	. . .	. . .	25	60
9	50	0.22	0.9	50	0.12	0.03	0	. . .	. . .	25	0
18	32	0.32	0.11	32	0.12	0.04	36	0.9	0.9	25	80
31	25	0.39	0.09	25	0.18	0.31	50	0.57	0.75	5000	90

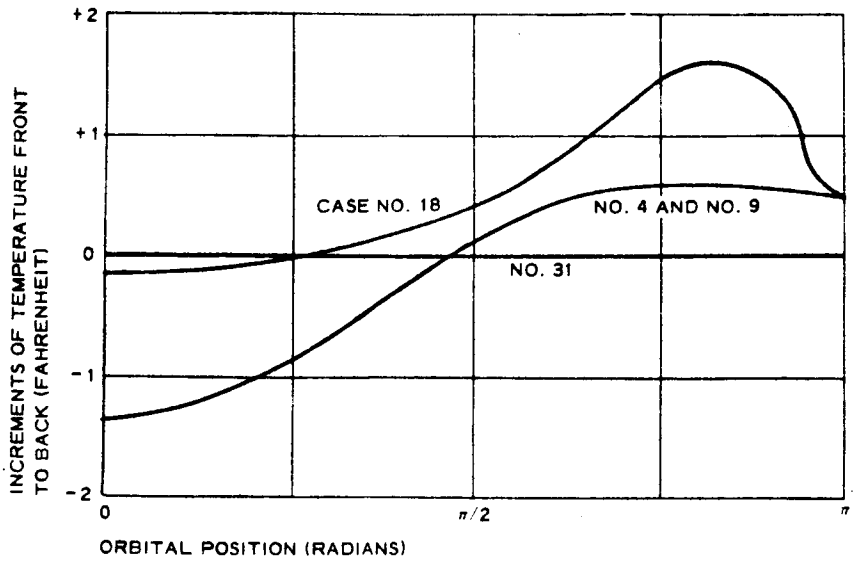


Figure 6.3-32. Temperature Differentials Through the Thickness

CASE NO.	FRONT			BACK			EDGE			THERMAL CONDITION	OPEN (PERCENT)
	AREA (PERCENT)	α	ϵ	AREA (PERCENT)	α	ϵ	AREA (PERCENT)	α	ϵ		
▷ 15	38	0.45	0.15	38	0.12	0.04	24	0.9	0.9	25	60
◇ 20	32	0.45	0.15	32	0.12	0.04	36	0.9	0.9	25	80
⬡ 28	25	0.45	0.15	25	0.12	0.04	50	0.9	0.9	5000	95
□ 29	25	0.34	0.11	25	0.18	0.31	50	0.4	0.67	5000	90
△ 30	25	0.34	0.11	25	0.18	0.31	50	0.57	0.75	5000	90
○ 31	25	0.39	0.09	25	0.18	0.31	50	0.57	0.75	5000	90

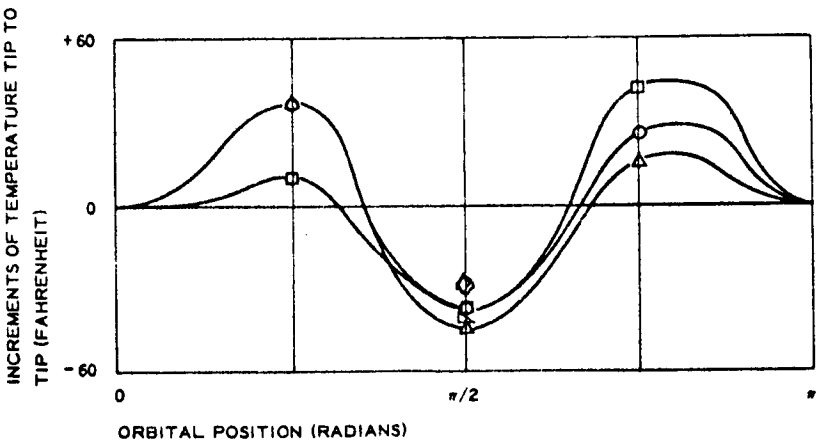


Figure 6.3-33. Temperature Differentials Tip-to-Tip

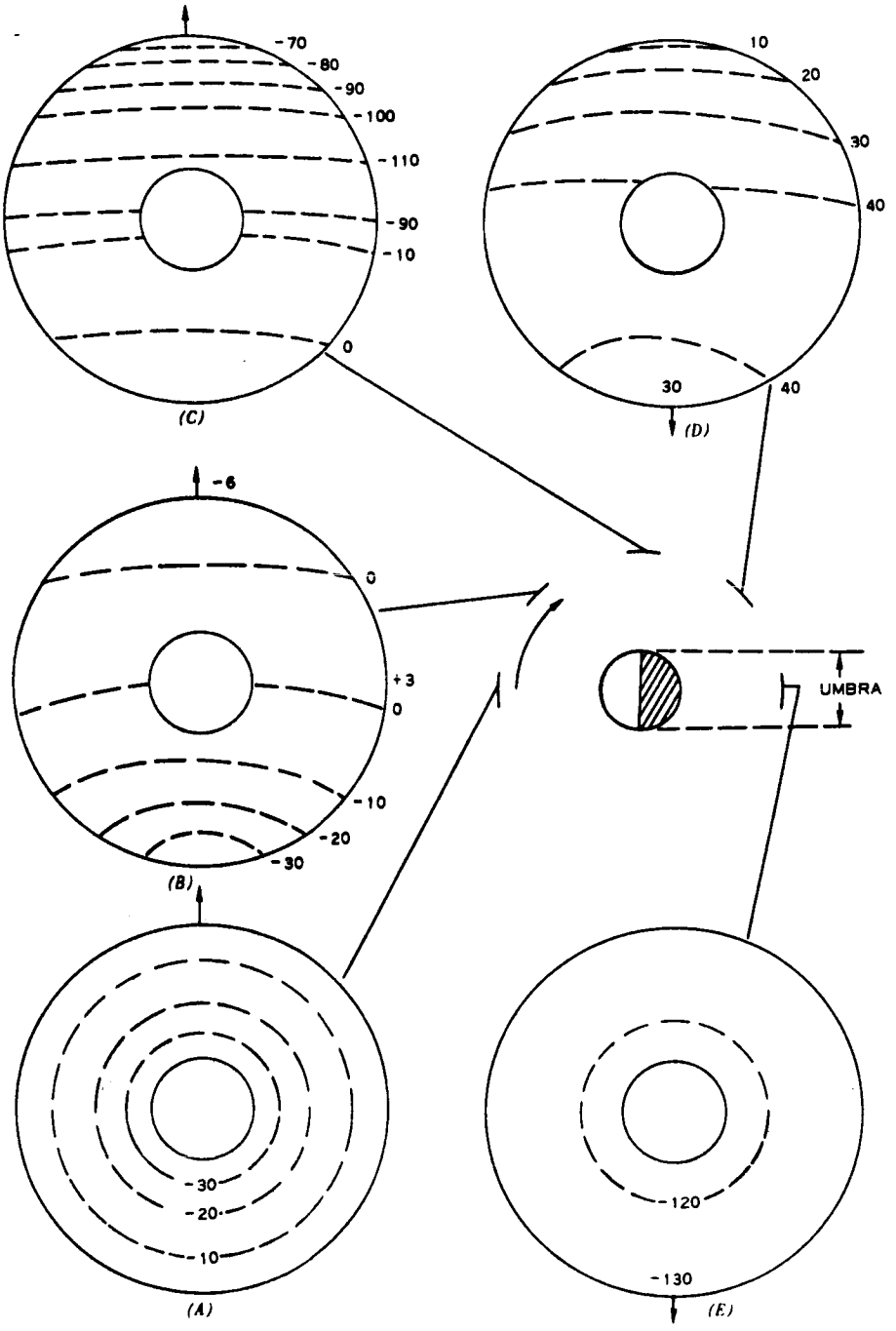


Figure 6.3-34. Isotherms for Solid-Rod Antenna

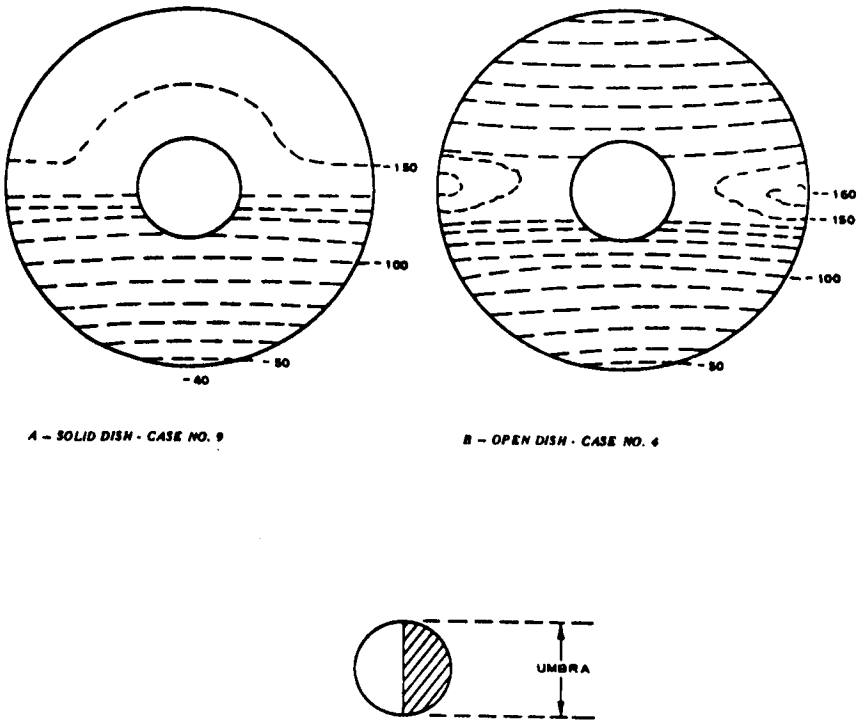


Figure 6.3-35. Isotherms for Solid and Open Antenna at 90-Degree Orbital Position

Different coatings and surface finishes were evaluated to minimize the thermal gradients. One of the best coating combinations for a honeycomb structure (case No. 18) is for a buffed-metal front surface, a black-painted edge, and a metallized (low-emittance) back surface. These would be stable for a two-year life.

Analysis of the selected configuration is shown in Section 6.3.4.

6.3.3 DESIGN ANALYSIS OF SELECTED CONFIGURATION

The design analysis was concerned with optimizing the antenna configuration and substantiating that the final design selected met all performance requirements. To do this, it was necessary to perform load analyses, tradeoff studies, and detailed stress and dynamic analyses. The required analyses are discussed relative to three environmental phases.

Phase I is concerned with events prior to launch (handling, transportation, etc.) that can affect the design of the antenna. The problem here is to properly integrate these requirements into the total program so that they have little or no effect on the final design.

Phase II is concerned with the ascent into orbit. In the packaged configuration, the structure must survive all combinations of steady-state acceleration, random vibration, shock, and acoustic levels that might be encountered without suffering damage that would affect its operational performance. Phase III is concerned with the performance of the antenna in orbit. There are two major problems that must be considered. The first concerns deployment without damage to the antenna. The second involves antenna deflections under the combined effects of the operating environment, accelerations and temperature distributions.

Solutions to the above problems are discussed in this section and typical analyses are presented where applicable.

6.3.3.1 Design Criteria

An antenna structural design criteria was established in order to ensure that the antenna would possess sufficient strength, rigidity and other physical characteristics necessary to insure high probability of a successful mission.

The following items were considered in performing the design analyses of the antenna:

a. Design conditions and environments

b. Material properties

c. Strength requirements

d. Stiffness requirements

e. Thermal requirements

f. Factors of safety

Design conditions were established to accommodate the three environmental phases:

a. Phase I includes the ground and pre-launch phases. This is defined as the time period which begins with assembly of the antenna at the antenna contractor's plant, continues through transportation, ground handling, testing, and ends with vehicle lift-off.

b. Phase II covers the ascent phase and covers the time period between vehicle lift-off, spacecraft separation, and the transfer orbit phase through completion of apogee motor burning.

c. Phase III covers the time period from completion of apogee motor burning, antenna deployment, and through the remaining life time of the spacecraft.

The ultimate loads for Phase II are:

a. Condition A - (Vibration test)

1. Longitudinal Acceleration - 30 g

2. Lateral accelerations - 13.65 g

These loads were obtained from the spacecraft response analysis (Reference Section 6.7.3) and represents an average loading on the stowed antenna system.

b. Condition B Spin - 71 rpm

The Phase III loads are:

a. Condition C - Deployment
This will be based on the load required to snap the antenna through to total deployment. This load is derived in the analysis given in Section 6.3.3.2.

b. Condition D - Orbital

This condition is concerned with temperature distributions and resulting thermal stresses. The analysis for this condition is given in Section 6.3.3.2.

The Phase I environment is not expected to significantly affect the basic antenna structural design and does not result in any critical design conditions. (The antenna has been designed to be deployable in a 1-g field.) Knowing the structural limitations of the basic design, handling equipment and shipping containers will be designed to meet these requirements without requiring modification of the basic structure.

In the event that this is not practical, modifications can be made to the basic structure in such a manner as to minimize the effect on the system requirements.

Material strengths and other physical properties were obtained from Section 6.3.2.1.2 and from authorized sources of reference (such as MIL Hdbk - 5). Strength allowables and other mechanical properties used were appropriate to the loading conditions, design environments, and stress states for each structural member.

Strength requirements were specified for limit load and ultimate load applications. At limit load the antenna structure was designed to have sufficient strength without experiencing excessive elastic or plastic deformation. At ultimate load the antenna structure was designed to have sufficient strength without experiencing failure. An ultimate load factor of safety of 1.5 was used.

Stiffness requirements were specified to be compatible with the launch vehicle constraints regarding shroud/antenna clearances and a spacecraft bending frequency of 10 cps. In addition, a 2 cps criteria for the deployed antenna configuration was established as a design goal (Reference Section 5.9.2.3).

6.3.3.2 Structural Analysis

This section provides the analysis of the antenna reflector for the critical design conditions. Strength analyses are shown for the antenna reflector for the launch environment and band

tension requirements are established for the spin-up conditions. A thermal stress analysis is provided for the critical structural members for the orbital environment as well as a face sheet-bond-core thermal compatibility analysis.

6.3.3.2.1 Reflector Analysis

a. Condition A - Launch Accelerations - The design ultimate accelerations are 30 g longitudinal and 13.65 g lateral. These loads are not combined and act separately.

The reflector is attached by 40 legs on a 43.25-inch radius to the interface mounting ring. The reflector weight is 65 pounds. The center of gravity of the folded reflector is 88 inches above the interface mounting ring. Petal-to-petal hinges are located at 71.75, 96.25, 119.75, 141.25, 160.75 and 180.0-inch radii. The weight distribution in the packaged configuration is approximately linear. The maximum limit load in any leg is calculated in the following paragraphs and tabulated in Table 6.3-7.

Table 6.3-7. Maximum Compression Load Launch Condition

x (in.)	A_i (lb/in.)	L_i (in.)	W_{Ri} (lb)	$\bar{L}_i$ (in.)	P'_{ci} (lb)	P_{bi} (lb)
43.25	0.0428	133.25	65.00	88.00	48.8	86.9
71.75	0.2215	108.25	61.37	64.71	46.0	60.4
96.25	0.3229	83.75	50.97	47.56	38.2	36.8
119.75	0.5400	60.25	42.71	31.79	32.1	20.6
141.25	0.6798	38.75	29.61	19.43	22.2	8.8
160.75	0.8065	19.25	15.10	8.94	11.3	2.1
180.00	0.9203	0	0	0	0	0

From the 43.25-inch radius to the first petal-to-petal hinge only one basic section carries the load. A 0.0075-inch doubler is used from the 71.75-inch radius hinge to the petal-to-hub hinges on the radial members of the trapezoidal panels.

Outboard of the 71.75-hinge, two basic radial sections carry the load, the side member of the trapezoid and the side member of the triangle (see Figure 6.3-36).

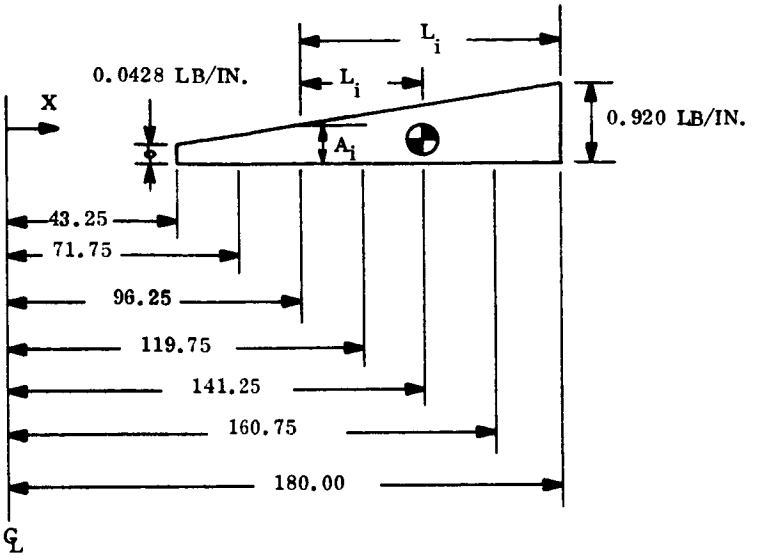


Figure 6.3-36. Folded Reflector Load Distribution and Geometry

Let

W_{Ri} = weight outboard of a given point

L_i = distance from point to center of gravity of weight

then, the ultimate load in each leg due to axial acceleration is

$$P'_{ci} = \frac{30\ W_{Ri}}{40}$$

$$= 0.75\ W_{Ri}$$

the maximum compression in the leg due to lateral acceleration is

$$P_{bi} = \frac{W_{Ri}\ (13.65)\ \bar{L}_i\ (43.25)}{\frac{40}{2}\ (43.25)^2}$$

$$= 0.0152\ \bar{L}_i\ W_{ri}$$

The basic section of the radial members is shown in Figure 6.3-37.

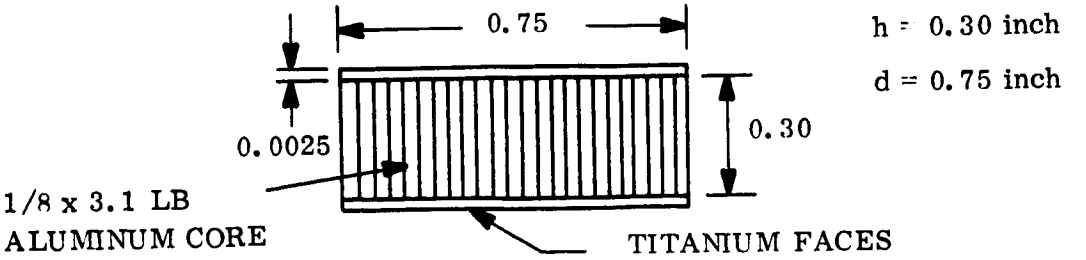


Figure 6.3-37. Typical Section - Radial Petal Member

Typical Section

$$A = 2(0.75)(.0025)$$
$$= 0.00375 \text{ in.}^2$$

$$I = \frac{(0.75)(0.0025)(0.30)^2}{2}$$
$$= 0.0000844 \text{ in.}^4$$

$$\rho 1 = \frac{h}{2}$$
$$= 0.15 \text{ in.}$$

$$\rho 2 = \frac{d}{3.46}$$
$$= \frac{0.75}{3.46}$$
$$= 0.217 \text{ in.}$$

Special Section

(0.0075 Doubler Each Face)

$$A = (4)(2)(0.75)(0.0025)$$
$$= 0.015 \text{ in.}^2$$

$$I = \frac{4(0.75)(0.0025)(0.30)^2}{2}$$
$$= .000338 \text{ in.}^4$$

$$\rho 1 = \frac{h}{2}$$
$$= 0.15 \text{ in.}$$

$$\rho 2 = \frac{d}{3.46}$$
$$= \frac{0.75}{3.46}$$
$$= 0.217 \text{ in.}$$

Considering packaging stresses, the folding of the reflector to the launch configuration straightens the hinge center lines inducing stresses in the petals. Complete redundant

solutions of prevous designs have shown that the maximum stress is approximately twice that required to change the local meridional radius of curvature to infinity. The local radius of curvature at the second petal-to-petal hinge from the center line of the paraboloid is used for this analysis. This hinge is at a radial distance of 96.25 inches from the center line. The meridional radius of curvature for a paraboloid having a focal length to diameter ratio of 4 is

$$r_m = 1.6\, R_o \left(1 + \frac{R^2}{2.56\, R_o^2}\right)^{3/2}$$

where r_m is the local meridional radius of curvature, R_o is the outside radius of the paraboloid, and R is the radius to the point.

For this analysis

$$r_m = 1.6 \left(\frac{30 \times 12}{2}\right) \left[1 + \frac{1}{256} \left(\frac{96.25}{180}\right)^2\right]^{3/2}$$

$$= 358 \text{ in.}$$

The moment required to change a circular arc to a straight line is,

$$M' = \frac{EI}{r}$$

where:

M' is the bending moment

E is Young's modulus of the material

I is the bending moment of inertia of structure

r is the arc radius

Since the estimated induced moment is twice the above moment, the maximum moment, M, on our section is

$$M = \frac{2 E I}{r_m}$$

The supporting members of the packaged reflector are beam columns. The maximum moment on a beam column is approximately

$$M_{max} = \frac{M}{1 - \frac{P}{P_{cR}}}$$

where:

M is the moment from transverse loads,

P is the axial load,

and P_{cR} is the critical column load.

If the total stress on a beam column remains below the proportional limit, the transverse forces will have a negligible effect on the allowable column load. Therefore, for preliminary analysis, the maximum limit stress will be equal to or less than the proportional limit of the material. The critical column load is

$$P_{cR} = C\pi^2 \frac{EI}{L^2}$$

where:

C is the end fixity coefficient, and

L is the column length.

C equals 1.0 for two pinned column ends; equals 2.0 for one fixed and one pinned end, and C equals 4.0 for two fixed column ends; therefore, for the first column, hub to first petal-to-petal hinge, C is 1.85 and for the remainder of the lengths a C of 3.75 is used. The hinges do not quite give complete fixity to the column ends.

The intercell buckling of the sandwich faces is given by

$$F_{ccR} = 0.9\ E\ \left(\frac{t}{b}\right)^{3/2}$$

where:

F_{ccR} is the face buckling stress,

t is the face thickness, and

b is the cell diameter.

Critical buckling stress of T_i faces:

Typical Section

$$F_{ccR} = 0.9\ (16)10^6 \left(\frac{0.0025}{0.125}\right)^{3/2}$$

$$= 14.4\ (10^6)(0.00282)$$

$$= 40600 \text{ psi}$$

F_{cy} = 70000 psi (Reference Mil 5 Hdbk).

Special Section

$$F_{ccR} = 0.9\ (16)10^6 \left(\frac{0.010}{0.125}\right)^{3/2}$$

$$= 14.4\ (10^6)\ (.026)$$

$$= 326,000 > 70000 \text{ psi}$$

The section of the petals between the hub and the first petal-to-petal hinge is critical for stress. This is the special section.

$$P_{cR} = 1.85\ \frac{16(10^6)\ (0.000338)\ \pi^2}{(71.75 - 43.25)^2}$$

$$= 111.4 \text{ lb}$$

$$M_{max} = \frac{M}{1 - \frac{86.9}{111.4}}$$

$$= 4.55\ M$$

$$M_{max} = 4.55\ \frac{2\ (16)\ (10^6)\ I}{r_m}$$

since

$$f_b = \frac{M_{Max.\ (c)}}{I}$$

where:

f_b = bending stress, and

c = distance from extreme edge to neutral axis

$$f_b = \frac{145.5 \times 10^6\ (\frac{0.30}{2})}{358}$$

$$= 61000\ \text{psi}$$

The maximum bending stress occurs near the first petal-to-petal hinge. The compressed load on the lower side of the hinge is estimated as

P_c 72.50- = 60.4 (Reference Table 6.3-7)

$$= 60.4\ \text{lb}$$

$$f_c = \frac{60.4}{0.015}$$

$$= 4020\ \text{psi}$$

$$f_b + f_c = 61000 + 4020$$

$$= 65020\ \text{psi (max. ult. comp. stress)}$$

$$\text{M.S.} = \frac{70000}{65020} - 1$$

$$= 0.075$$

For the column

$$M.S. = \frac{111.4}{(86,9)} - 1$$

$$= 0.285$$

b. Condition B - Spin-Up - The packaged antenna is rotated with an angular velocity of 71 rpm. Assuming each of the 40 legs resists the centrifugal force equally, the approximate loading of a beam is shown in Figure 6.3-38.

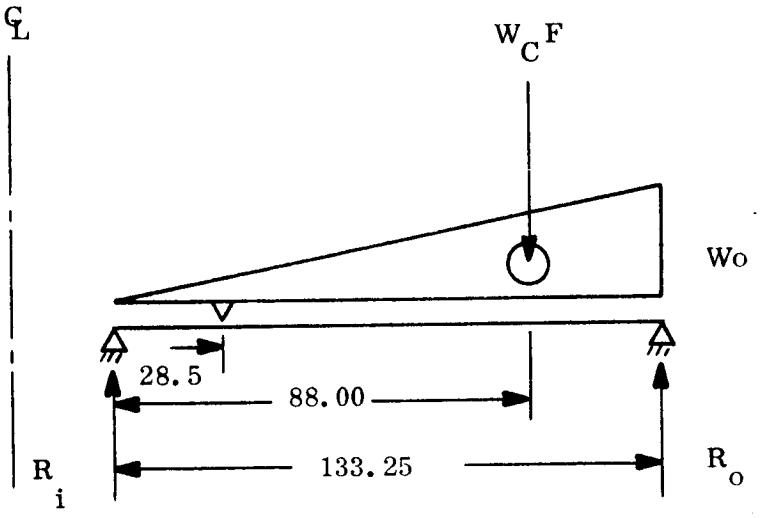


Figure 6.3-38. Approximate Loading of a Beam

$$W = \frac{2\pi(71)}{60}$$

$$= 7.45 \text{ rad sec}$$

$$W_{cF} = \frac{65}{40\,(386)} (0.70 \times 43.25)\,(7.45)^2$$

$$= 7.07 \text{ lb/leg}$$

$$R_i = \frac{133.25 - 88}{133.25}\ 7.07$$

$$= 2.45 \text{ lb}$$

$$M = 2.46 \times 28.50$$

$$= 67.8 \text{ in. lb}$$

$$\text{Acc (g)} = \frac{0.70(43.25)\,(7.45)^2}{386}$$

$$= 4.35 \text{ g}$$

$$f_b = \frac{67.8\ (0.15)}{.000338}$$

$$= 30,100 \text{ psi}$$

$$M.S. = \frac{40600}{30,100} - 1 = +.33$$

A circumferential band secures the outboard end of the petals. The tension in the band is:

$$T = \frac{n R_o}{2} \text{ lb}$$

$$R_o = 7.07 - 2.46$$

$$= 4.61 \text{ lb}$$

$$T = \frac{4.61\ (40)}{2\pi}$$

$$= 29.4 \text{ lb (for 4.35 g)}$$

$$T = \frac{13.65}{4.35}(29.4) = 92.3 \text{ lb (for 13.65 g)}$$

This is the ultimate design tension load for the securing band at the top of the antenna in the packaged condition based on antenna loading only.

6.3.3.2.2 Thermal Stress Analysis

Thermal stresses for the antenna were determined in conjunction with an analysis performed to determine deflections due to a thermal environment. A description of the analytical model of the antenna is shown in Figure 6.3-58 and discussed in detail in Section 6.3.4.3.2.

Thermal stresses were found to be generally low, except locally in the area of the hub structure. These stresses are conservative however, due to the modeling of a fully fixed (unyielding) hub. All stress levels are well below material allowables.

For the case of the fixed hub the maximum stresses occur in the first hoop members outboard of the hub. Computer loads printout, stress analysis, and margin of safety calculations are shown in Figure 6.3-39.

MEMBER 9 11 (CURVED BAR) FREQUENCY = 0

I JOINT, JOINT 9 = COORDINATES (6,9100 , 36,930 , 2,2400) - RESTRAINT CODE (0, 0, 0, 0, 0, 0)
J JOINT, JOINT 11 = COORDINATES (-6,9100 , 36,930 , 2,2400) - RESTRAINT CODE (0, 0, 0, 0, 0, 0)
O JOINT, REFERENCE = COORDINATES (0, 0, 2,2400)

REFERENCE TEMP	= 70,000	TOTAL MEMBER WEIGHT	= 0,1467-01	RADIUS OF CURVATURE	= 37,499
RATIO	= 0	ROTOR SPEED	= 0	INCLUDED ANGLE	= 19,995
YOUNGS MODULUS	= 0,1040+08	TORSIONAL CONSTANT	= 0,2420-03	DISTRIBUTED LOADS 1	= 0
SHEAR MODULUS	= 0,6300+07	SHEAR CONSTANT 1	= 0	2	= 0
THERMAL COEFFICIENT	= 0,3400-05	SHEAR CONSTANT 2	= 0	3	= 0
CROSS SECTIONAL AREA	= 0,3750-02	WEIGHT DENSITY	= 0,2990	4	= 0
MOMENT OF INERTIA 1	= 0,8150-04	TEMPERATURE GRAD 1	= 0	5	= 0
MOMENT OF INERTIA 2	= 0,1760-03	TEMPERATURE GRAD 2	= 0	6	= 0
ROTATION OF AXIS	= 173,14	TEMPERATURE AVERAGE	= -170,00		

• • • CALCULATIONS • • •

		DIRECTION 1	DIRECTION 2	DIRECTION 3	DIRECTION 4	DIRECTION 5	DIRECTION 6
MEMBER LOADS	JOINT 9 (I)	30,926	0,2265-04	-11,734	0,1110-05	-0,1536-02	0,1462-05
	JOINT 11 (J)	-30,926	-0,2277-04	11,733	-0,1110-05	0,1551-02	-0,1462-05
NORM: DEFLS,	JOINT 9 (I)	-0	-0	-0	-0	-0	-0
	JOINT 11 (J)	-0	-0	-0	-0	-0	-0
NORM: LOADS	JOINT 9 (I)	-5,3689	30,456	11,734	0,1508-02	0,2670-03	-0,1462-05
	JOINT 11 (J)	-5,3688	-30,456	-11,733	-0,1527-02	0,2681-03	0,1462-05

POTENTIAL ENERGY = 0 KINETIC ENERGY = 0



MATERIAL: 75A TITANIUM SHEET
t = .0025
F_{ty} = 70,000 LB/IN²
3.1 LB/FT³ x 1/8 x .0007 HONEYCOMB INTERCELLULAR BUCKLING = 40,600 LB/IN²

$$f_c = \frac{30.456}{.00375} - \frac{11.733 \times .375}{.000176}$$

$$= 8130 - 25000 = 16870 \text{ LB/IN}^2$$

$$f_t = 8130 + 25000 = 33130 \text{ LB/IN}^2$$

$$MS_t = \frac{70000}{33130} - 1 = +1.12$$

Figure 6.3-39. Computer Loads Printout, Stress Analysis, and Margin of Safety Calculations

The next most critical area concerns the members at a point where back up trusses are attached (joint 89). Computer loads printout, stress analysis, and margins of safety for the six members common to the truss point are shown in Figures 6.3-40 through 6.3-45. In addition, a summation of loads for this joint showing joint equilibrium and member and joint identification is shown in Figure 6.3-46.

a. Face Sheet - Bond - Core Thermal Compatibility Analysis - A conservative analysis was performed to establish the general magnitude of the stresses due to differences in thermal coefficients of expansion of the face sheets, bond, and core material. The analysis considers one of the radial members as a long composite beam subjected to a constant temperature of $-170^{\circ}F$ or a ΔT of $-240^{\circ}F$. It will be shown by analysis that the bond stresses are small but moderate compressive stresses are developed in the face sheet. The analysis conservatively neglects bond shear deformations, shear lag into adjacent petals via hinges, and considers the core to sustain tensile loads with transverse deflections restrained. Figure 6.3-47 shows the structural elements in their free thermally deflected shape along with the shear loads that are imposed to obtain compatibility at the free end. Note that one half of the cross section is considered as it is assumed that we have symmetry along with uniform face sheet thickness.

The mechanical deformation under the influence of the shear loads can be determined for each of the elements in the following manner:

External Work = Internal Work

$$1/2\ P\,\delta = 1/2 \int_0^{\ell} \frac{(qx)^2\,dx}{EA}$$

for q, EA = constant

$$1/2\ qL\delta = \frac{q^2}{2\ EA} \int_0^{\ell} x^2 dx = \frac{q^2}{2\ EA}\ \frac{\ell^3}{3}$$

$$\delta = (qL)\ L/3AE$$

MEMBER 88 89 (CURVED BAR) FREQUENCY = 0

I JOINT, JOINT 88 = COORDINATES (31,620 , 104,31 , 19,425) - RESTRAINT CODE (0, 0, 0, 1, 0, 0)
J JOINT, JOINT 89 = COORDINATES (18,930 , 107,34 , 19,425) - RESTRAINT CODE (0, 0, 0, 0, 0, 0)
O JOINT, REFERENCE = COORDINATES (0, 0, 19,425)

REFERENCE TEMP	= 70,000	TOTAL MEMBER WEIGHT	= 0,1464-01	RADIUS OF CURVATURE	= 109,00
RATIO	= 0	ROTOR SPEED	= 0	INCLUDED ANGLE	= 6,8623
YOUNGS MODULUS	= 0,1640+08	TORSIONAL CONSTANT	= 0,2420-03	DISTRIBUTED LOADS 1	= 0
SHEAR MODULUS	= 0,6300+07	SHEAR CONSTANT 1	= 0	2	= 0
THERMAL COEFFICIENT	= 0,3700-05	SHEAR CONSTANT 2	= 0	3	= 0
CROSS SECTIONAL AREA	= 0,3750-02	WEIGHT DENSITY	= 0,2990	4	= 0
MOMENT OF INERTIA 1	= 0,8150-04	TEMPERATURE GRAD 1	= 0	5	= 0
MOMENT OF INERTIA 2	= 0,1760-03	TEMPERATURE GRAD 2	= 0	6	= 0
ROTATION OF AXIS	= 158,91	TEMPERATURE AVERAGE	= -125,00		

• • • CALCULATIONS • • •

		DIRECTION 1	DIRECTION 2	DIRECTION 3	DIRECTION 4	DIRECTION 5	DIRECTION 6
MEMBER LOADS	JOINT 88 (I)	3,9216	-1,1840	0,6293	-0,1550	0,4690-01	0,7009-01
	JOINT 89 (J)	-3,9216	1,1840	2,5102	0,3674	0,8429	-0,7009-01
NORM: DEFLS,	JOINT 88 (I)	0,4545-01	-0,1435-0.	0,6716-03	0,4473-02	-0,4759-03	-0,4195-01
	JOINT 89 (J)	0,3624-01	0,2536-02	-0,2237-02	-0,3073-03	0,6790-03	-0,5857-04
NORM: LOADS	JOINT 88 (I)	-0,4540-02	4,0964	-0,6293	-0,9313-09	-0,1619	-0,7009-01
	JOINT 89 (J)	-0,4849	-4,0676	-2,5102	-0,8934	0,2157	0,7009-01

POTENTIAL ENERGY = -0,1267-01 KINETIC ENERGY = 0

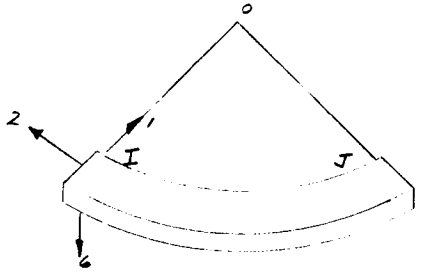
MATERIAL: 75A TITANIUM SHEET

$t = .0025$

$F_{ty} = 70000\ LB/IN^2$

$3.1\ LB/FT^2 \times 18 \times .0007$ HONEYCOMB

INTERCELLULAR BUCKLING = $40,600\ LB/IN^2$



$$f_c = \frac{4.068}{.00375} - \frac{2.510 \times .375}{.000176} - \frac{.893 \times .15}{.0000815}$$

$$1085 - 5350 - 1650 = 5915$$

$$MS_c = \frac{40600}{5915} - 1 = \underline{LARGE}$$

Figure 6.3-40. Computer Loads Printout, Stress Analysis, and Margin of Safety For One of Six Members Common to Truss Point 89

MEMBER 60 89 (CURVED BAR) FREQUENCY = 0

I JOINT, JOINT 60 - COORDINATES (12,850 , 72,580 , 5,8000) - RESTRAINT CODE (0, 0, 0, 0, 0, 0)
J JOINT, JOINT 89 - COORDINATES (18,930 , 107,34 , 19,425) - RESTRAINT CODE (0, 0, 0, 0, 0, 0)
O JOINT, REFERENCE - COORDINATES (0, 0, 315,50)

REFERENCE TEMP	= 70,000	TOTAL MEMBER WEIGHT	= 0,4103-01	RADIUS OF CURVATURE	= 315,50
RATIO	= 0	ROTOR SPEED	= 0	INCLUDED ANGLE	= 6,6449
YOUNGS MODULUS	= 0,1640+08	TORSIONAL CONSTANT	= 0,2420-03	DISTRIBUTED LOADS 1	= 0
SHEAR MODULUS	= 0,6300+07	SHEAR CONSTANT 1	= 0	2	= 0
THERMAL COEFFICIENT	= 0,3700-05	SHEAR CONSTANT 2	= 0	3	= 0
CROSS SECTIONAL AREA	= 0,3750-02	WEIGHT DENSITY	= 0,2990	4	= 0
MOMENT OF INERTIA 1	= 0,1760-03	TEMPERATURE GRAD 1	= 0	5	= 0
MOMENT OF INERTIA 2	= 0,8150-04	TEMPERATURE GRAD 2	= 0	6	= 0
ROTATION OF AXIS	= 0	TEMPERATURE AVERAGE	= -125,00		

* * * CALCULATIONS * * *

		DIRECTION 1	DIRECTION 2	DIRECTION 3	DIRECTION 4	DIRECTION 5	DIRECTION 6
MEMBER LOADS	JOINT 60 (I)	0,3997-02	0,1649	0,2988	0,3243	-0,4026-01	0,7330-01
	JOINT 89 (J)	-0,3997-02	-0,1649	0,5662	0,4497	-0,3625-01	-0,7330-01
NORM: DEFLS,	JOINT 60 (I)	0,1309	0,1419-01	0,3495-02	0,6246-04	-0,3102-02	-0,4055-02
	JOINT 89 (J)	0,1258-01	0,3399-01	-0,6797-03	0,1993-02	-0,1061-02	-0,2538-02
NORM: LOADS	JOINT 60 (I)	0,3300-01	-0,1757	-0,3263	0,2865	-0,8631-01	0,2472-01
	JOINT 89 (J)	-0,1244-01	0,1784	-0,5059	0,6278	0,6650-01	-0,2472-01

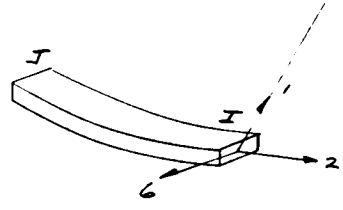
POTENTIAL ENERGY = 0.4183-02 KINETIC ENERGY = 0

,0

MATERIAL: .75A TITANIUM SHEET
$t = .0025$

$F_{ty} = 70000\ ^{LB}/_{IN^2}$

$3.1\ ^{LB}/_{FT^3} \times 1/8 \times .0007$ HONEYCOMB
INTERCELLULAR BUCKLING $= 40600\ ^{LB}/_{IN^2}$



$$f_c = \frac{.1784}{.00375} - \frac{.5059 \times .15}{.0000815} - \frac{.6278 \times .375}{.000176}$$

$$-47.7 - 932 - 1340 = 2320$$

$$MS_c = \frac{40600}{2320} - 1 = \underline{\text{LARGE}}$$

Figure 6.3-41. Computer Loads Printout, Stress Analysis, and Margin of Safety For One of Six Members Common to Truss Point 89

MEMBER 89 90 (CURVED BAR) FREQUENCY = 0

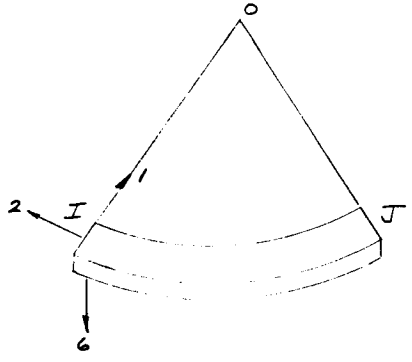
I JOINT, JOINT 89 - COORDINATES (18,930 , 107,34 , 19,425) - RESTRAINT CODE (0, 0, 0, 1, 0, 0)
J JOINT, JOINT 90 - COORDINATES (9,9800 , 108,84 , 19,425) - RESTRAINT CODE (0, 0, 0, 0, 0, 0)
O JOINT, REFERENCE - COORDINATES (0, 0, 19,425)

REFERENCE TEMP	= 70,000	TOTAL MEMBER WEIGHT	= 0,1463-01	RADIUS OF CURVATURE	= 109,00
RATIO	= 0	ROTOR SPEED	= 0	INCLUDED ANGLE	= 6,8567
YOUNGS MODULUS	= 0,1640+08	TORSIONAL CONSTANT	= 0,2420-03	DISTRIBUTED LOADS 1	= 0
SHEAR MODULUS	= 0,6300+07	SHEAR CONSTANT 1	= 0	2	= 0
THERMAL COEFFICIENT	= 0,3700-05	SHEAR CONSTANT 2	= 0	3	= 0
CROSS SECTIONAL AREA	= 0,3750-02	WEIGHT DENSITY	= 0,2990	4	= 0
MOMENT OF INERTIA 1	= 0,8150-04	TEMPERATURE GRAD 1	= 0	5	= 0
MOMENT OF INERTIA 2	= 0,1760-03	TEMPERATURE GRAD 2	= 0	6	= 0
ROTATION OF AXIS	= 158,91	TEMPERATURE AVERAGE	= -140,00		

* * * CALCULATIONS * * *

		DIRECTION 1	DIRECTION 2	DIRECTION 3	DIRECTION 4	DIRECTION 5	DIRECTION 6
MEMBER LOADS	JOINT 89 (I)	18,703	-1,8316	-4,7003	-0,6453-01	0,1136-01	-0,5872-01
	JOINT 90 (J)	-18,703	1,8316	0,5098	-0,2310-01	-0,7719	0,5872-01
NORM; DEFLS,	JOINT 89 (I)	0,3624-01	0,2536-02	-0,2237-02	-0,1153-01	0,6795-03	-0,5857-04
	JOINT 90 (J)	0,9189-01	0,7103-03	-0,2397-02	-0,8106-02	0,2429-02	-0,1440
NORM; LOADS	JOINT 89 (I)	-1,4445	18,737	4,7003	-0,3492-09	-0,6553-01	0,5872-01
	JOINT 90 (J)	-0,8028	-18,776	-0,5098	0,7720	0,1928-01	-0,5872-01

POTENTIAL ENERGY = -0,4952-01 KINETIC ENERGY = 0



MATERIAL: 75A TITANIUM SHEET

$t = .0025$

$F_{TY} = 70.000\ LB/IN^2$

$3.1\ LB/FT^3 \times 1/8 \times .0007$ HONEYCOMB
INTERCELLULAR BUCKLING = $40,600\ LB/IN^2$

$$f_c = \frac{18.737}{.00375} - \frac{4.700 \times .15}{.0000815}$$

$5000 - 8650 = 3650$

$$MS = \frac{40600}{3650} - 1 = \underline{\text{LARGE}}$$

Figure 6.3-42. Computer Loads Printout, Stress Analysis, and Margin of Safety For One of Six Members Common to Truss Point 89

MEMBER 89 117 (CURVED BAR) FREQUENCY = 0

T JOINT, JOINT 89 - COORDINATES (18,930 , 107,34 , 19,425) - RESTRAINT CODE (0, 0, 0, 0, 0, 0)
J JOINT, JOINT 117 - COORDINATES (25,010 , 141,61 , 34,780) - RESTRAINT CODE (0, 0, 0, 0, 0, 0)
0 JOINT, REFERENCE - COORDINATES (0, 0, 315,50)

REFERENCE TEMP	= 70,000	TOTAL MEMBER WEIGHT	= 0,4286-01	RADIUS OF CURVATURE	= 315,50
RATIO	= 0	ROTOR SPEED	= 0	INCLUDED ANGLE	= 6,9455
YOUNGS MODULUS	= 0,1640+08	TORSIONAL CONSTANT	= 0,2420-03	DISTRIBUTED LOADS 1	= 0
SHEAR MODULUS	= 0,6300+07	SHEAR CONSTANT 1	= 0	2	= 0
THERMAL COEFFICIENT	= 0,3700-05	SHEAR CONSTANT 2	= 0	3	= 0
CROSS SECTIONAL AREA	= 0,3750-02	WEIGHT DENSITY	= 0,2990	4	= 0
MOMENT OF INERTIA 1	= 0,1760-03	TEMPERATURE GRAD 1	= 0	5	= 0
MOMENT OF INERTIA 2	= 0,8150-04	TEMPERATURE GRAD 2	= 0	6	= 0
ROTATION OF AXIS	= 0	TEMPERATURE AVERAGE	= -125,00		

* * * CALCULATIONS * * *

		DIRECTION 1	DIRECTION 2	DIRECTION 3	DIRECTION 4	DIRECTION 5	DIRECTION 6
MEMBER LOADS	JOINT 89 (I)	-0,4957	-2,6974	0,4294	-1,4914	0,1970-01	-1,2277
	JOINT 117 (J)	0,4957	2,6974	0,2571	0,9831	-0,1652	1,2277
NORM: DEFLS.	JOINT 89 (I)	0,1258-01	0,3399-01	-0,6797-03	0,1993-02	-0,1061-02	-0,2537-02
	JOINT 117 (J)	0,5584-01	0,9167-01	0,2836-02	0,2439-03	-0,2658-02	0,9477-02
NORM: LOADS	JOINT 89 (I)	-0,2047	2,9978	1,4721	0,4857	0,7657-01	0,1961-01
	JOINT 117 (J)	-0,1593	-3,0005	-0,6030	0,2568	-0,6269-01	-0,1961-01

POTENTIAL ENERGY = -0,3322-01 KINETIC ENERGY = 0

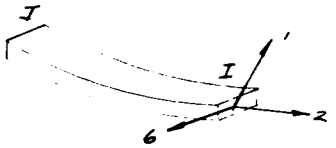
10

MATERIAL: 75A TITANIUM SHEET

$t = .0025$

$F_{ty} = 70000\ LB/IN^2$

$3.1\ LB/FT^3 \times 1/8 \times .0007$ HONEYCOMB
INTERCELLULAR BUCKLING = $40600\ LB/IN^2$



$$f_c = \frac{2.998}{.00375} - \frac{1.472 \times .15}{.0000815} - \frac{.4857 \times .375}{.000176}$$

$$= 800 - 2710 - 1038 = -2948$$

$$MS = \frac{40600}{2948} - 1 = \text{LARGE}$$

Figure 6.3-43. Computer Loads Printout, Stress Analysis, and Margin of Safety For One of Six Members Common to Truss Point 89

MEMBER 59 89 (STRAIGHT BAR) FREQUENCY = 0

I JOINT, JOINT 59 = COORDINATES (19,620 , 71,350 , 8,8000) - RESTRAINT CODE (0, 0, 1, 0, 1, 0)
J JOINT, JOINT 89 = COORDINATES (18,930 , 107,34 , 19,425) - RESTRAINT CODE (0, 0, 0, 0, 0, 0)
C JOINT, REFERENCE = COORDINATES (0, 0, 315,50)

REFERENCE TEMP	= 70,000	TOTAL MEMBER WEIGHT	= 0,4200-01	TOTAL MEMBER LENGTH	= 37,532
RATIO	= 0	ROTOR SPEED	= 0		
YOUNGS MODULUS	= 0.1640+08	TORSIONAL CONSTANT	= 0,2420-03	DISTRIBUTED LOADS 1	= 0
SHEAR MODULUS	= 0.6300+07	SHEAR CONSTANT 1	= 0	2	= 0
THERMAL COEFFICIENT	= 0.3700-05	SHEAR CONSTANT 2	= 0	3	= 0
CROSS SECTIONAL AREA	= 0,3750-02	WEIGHT DENSITY	= 0,2990	4	= 0
MOMENT OF INERTIA 1	= 0.1760-03	TEMPERATURE GRAD 1	= 0	5	= 0
MOMENT OF INERTIA 2	= 0.8150-04	TEMPERATURE GRAD 2	= 0	6	= 0
ROTATION OF AXIS	= 0	TEMPERATURE AVERAGE	= -120,00		

* * * CALCULATIONS * * *

		DIRECTION 1	DIRECTION 2	DIRECTION 3	DIRECTION 4	DIRECTION 5	DIRECTION 6
MEMBER LOADS	JOINT 59 (I)	-0,5602-01	1,8878	0,1708	-0,1092-01	-0,5064-01	0,5666
	JOINT 89 (J)	0,5602-01	-1,8878	0,5428	0,3428	-0,1537	-0,5666
NORM: DEFLS,	JOINT 59 (I)	0,1105	0,6972-02	0,4426-02	-0,3199-03	-0,7971-03	0,7373-03
	JOINT 89 (J)	0,1054-01	0,3456-01	-0,8644-03	0,2044-02	-0,7971-03	0,3795-02
NORM: LOADS	JOINT 59 (I)	0,1004-01	-1,9717	0,1955-09	0,1784	0,4657-09	0,1920-01
	JOINT 89 (J)	-0,1004-01	1,9717	-0,3768	0,5421	0,3729-08	-0,1920-01

POTENTIAL ENERGY = 0,2836-01 KINETIC ENERGY = 0

MATERIAL: 75A TITANIUM SHEET
$t = .0025$
$F_{tu} = 70000\ \#/IN^2$
$3.1\#/FT^3 \times 1/3 \times .0007$ HONEYCOMB
INTERCELLULAR BUCKLING = $40,000\ \#/IN^2$



$f_c = \frac{1972}{.00275} + \frac{.3763 \times .15}{.0000315} + \frac{.5421 \times .375}{.000176}$

$= 515 + 694 + 1155 = 2374$

$M.S. = \frac{40000}{2374} - 1 = \text{LARGE}$

Figure 6.3-44. Computer Loads Printout, Stress Analysis, and Margin of Safety For One of Six Members Common to Truss Point 89

MEMBER 61 89 (STRAIGHT BAR) FREQUENCY = 0

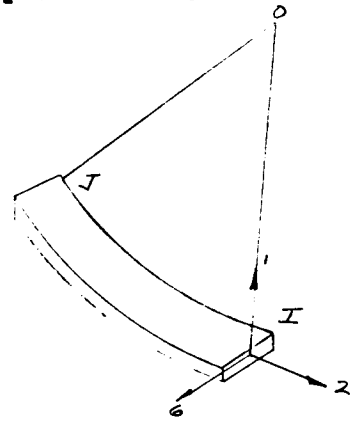
I JOINT, JOINT 61 = COORDINATES (5,9500 , 73,968 , 8,6080) - RESTRAINT CODE (0, 0, 1, 0, 1, 0)
J JOINT, JOINT 89 = COORDINATES (18,930 , 107,34 , 19,429) - RESTRAINT CODE (0, 0, 0, 0, 0, 0)
O JOINT, REFERENCE = COORDINATES (0, 0, 315,90)

REFERENCE TEMP	= 70,000	TOTAL MEMBER WEIGHT	= 0,4226-01	TOTAL MEMBER LENGTH	= 37,705
PATIO	= 0	ROTOR SPEED	= 0		
YOUNGS MODULUS	= 0,1640+08	TORSIONAL CONSTANT	= 0,2420-03	DISTRIBUTED LOADS 1	= 0
SHEAR MODULUS	= 0,6300+07	SHEAR CONSTANT 1	= 0	2	= 0
THERMAL COEFFICIENT	= 0,3700-05	SHEAR CONSTANT 2	= 0	3	= 0
CROSS SECTIONAL AREA	= 0,3750-02	WEIGHT DENSITY	= 0,2990	4	= 0
MOMENT OF INERTIA 1	= 0,1760-03	TEMPERATURE GRAD 1	= 0	5	= 0
MOMENT OF INERTIA 2	= 0,8150-04	TEMPERATURE GRAD 2	= 0	6	= 0
ROTATION OF AXIS	= 0	TEMPERATURE AVERAGE	= -140,00		

• • • CALCULATIONS • • •

		DIRECTION 1	DIRECTION 2	DIRECTION 3	DIRECTION 4	DIRECTION 5	DIRECTION 6
MEMBER LOADS	JOINT 61 (I)	-2,0998	-5,3979	0,3789	-0,1549-01	-0,1132	-1,6865
	JOINT 89 (J)	2,0998	5,3979	0,6517	0,1963	-0,1396	1,6865
NORM: DEFLS,	JOINT 61 (I)	0,1529	0,8059-02	0,5901-02	0,4796-05	-0,1041-02	-0,2247-02
	JOINT 89 (J)	0,1054-01	0,3366-01	-0,4741-03	0,2061-02	-0,1041-02	-0,8712-02
NORM: LOADS	JOINT 61 (I)	0,1199-01	6,0324	-0,9313-09	0,3958	0,2799-08	0,2934-01
	JOINT 89 (J)	-0,1199-01	-6,0324	-0,4520	0,7105	0,3727-08	-0,2934-01

POTENTIAL ENERGY = -0,7542-01 KINETIC ENERGY = 0



MATERIAL: 75A TITANIUM SHEET
$t = .0025$
$F_{TY} = 70000\ LB/IN^2$

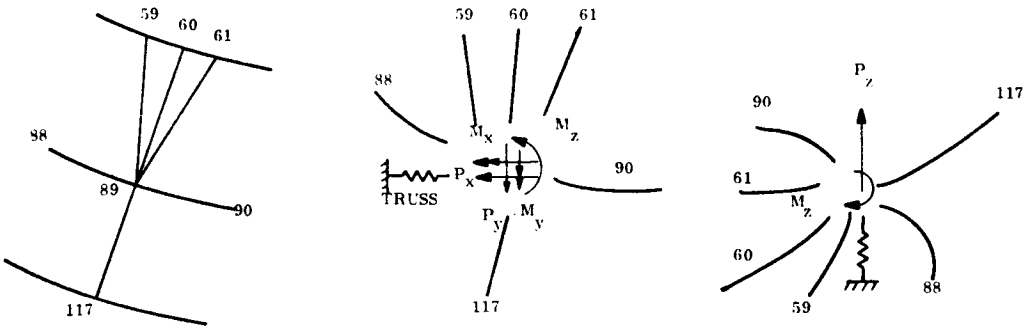
$3.1\ LB/FT^3 \times 1/8 \times .0007$ HONEYCOMB
INTERCELLULAR BUCKLING $= 40600\ LB/IN^2$

$$f_t = \frac{6.032}{.00375} + \frac{.452 \times .15}{.0000815} + \frac{.7105 \times .375}{.000176}$$

$$= 1685 + 831 + 1510 = 4026$$

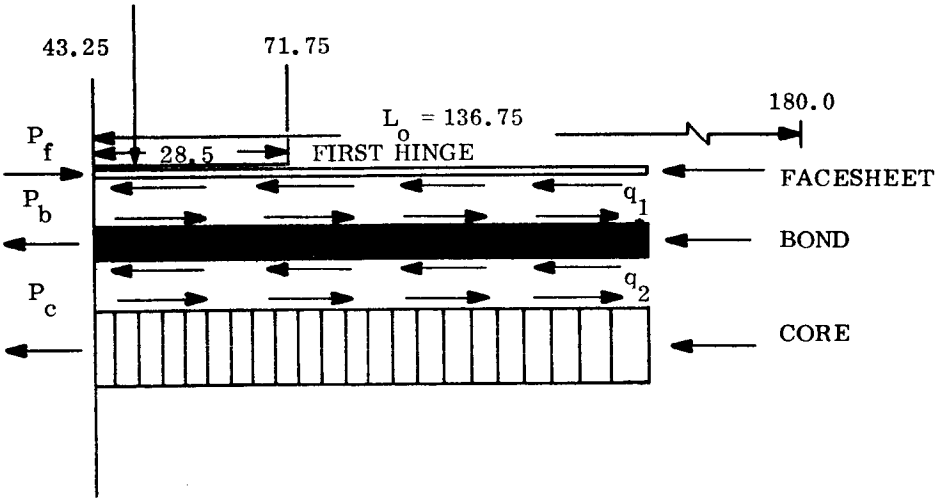
$$MS_T = \frac{20000}{4026} - 1 = \underline{\underline{LARGE}}$$

Figure 6.3-45. Computer Loads Printout, Stress Analysis, and Margin of Safety For One of Six Members Common to Truss Point 89



LOADS / MEMBERS	P_x	P_y	P_z	M_x	M_y	M_z
60-89	-0.004	-0.165	-0.073	0.450	-0.363	0.566
89-117	-0.496	-2.697	-1.228	-1.491	0.019	0.429
59-89	-0.056	-1.888	-0.567	0.343	-0.154	0.543
61-89	2.099	5.398	1.687	0.396	-0.357	0.652
88-89	-3.922	1.184	-0.070	0.367	0.842	2.510
89-90	18.703	-1.832	-0.059	-0.065	0.011	-4.700
TRUSS	-16.440 0	0	0.310 0	0	0	0

Figure 6.3-46. Member Loads at Joint 89



P_f = FACE SHEET AXIAL LOAD BUILD UP

P_b = BOND AXIAL LOAD BUILD UP

P_c = CORE AXIAL LOAD BUILD UP

Figure 6.3-47. Model Used for Face Sheet-Core Thermal Compatibility Analysis

We can now write the compatibility equations for the length of each of the elements. The subscripts f, b, c refer to the face sheet, bond, and core respectively.

$$L\alpha_c\Delta T + \frac{(q_2 L)\, L}{3\,(AE)_c} = L\alpha_b\Delta T + \frac{(q_1 - q_2)\, L^2}{3\,(AE)_b}$$

and

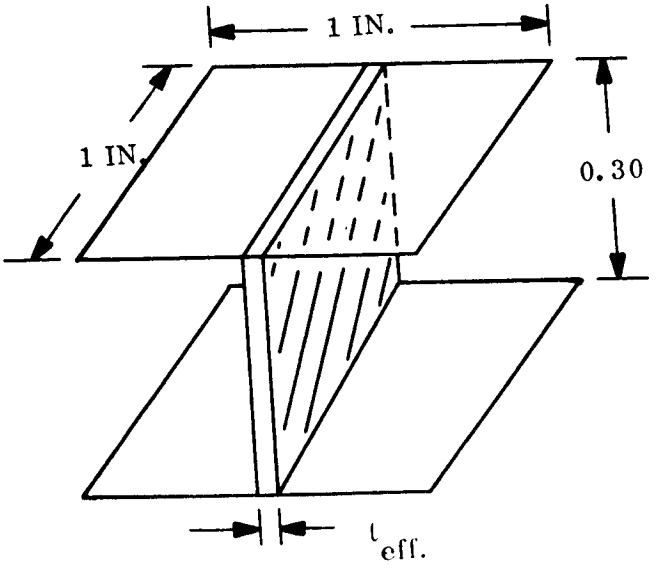
$$L\alpha_c\Delta T + \frac{(q_2 L)\, L}{3\,(AE)_c} = L\alpha_f\Delta T - \frac{q_1 L}{3\,(AE)_f}$$

Solving for q_1 and q_2 we get

$$q_1 = \frac{3\Delta T\,(AE)_f \left\{(AE)_b\,(\alpha_f - \alpha_b) + (\alpha_f - \alpha_c)\,(AE)_c\right\}}{L\,((AE)_f + (AE)_c + (AE)_b)}$$

$$q_2 = \frac{3\Delta T\,(AE)_c \left\{(AE)_f\,(\alpha_f - \alpha_c) + (AE)_b\,(\alpha_b - \alpha_c)\right\}}{L\,((AE)_f + (AE)_c + (AE)_b)}$$

The determination of the effective thickness and area of the core is accomplished in the following manner.



Weight of Honeycomb = $3.1\ lb/ft^3$

Density of aluminum = $0.1\ lb/in.^3$

Weight of 1 x 1 x 0.3 in. Cube shown = $\frac{(0.3)(3.1)}{1728} = 0.00054$ lb

b. Effective Thickness of Aluminum Core

$$t = \frac{0.00054}{(0.1)(0.3)} = \frac{0.0054}{0.3} = 0.018 \text{ in.}$$

c. Effective Cross-Sectional Area

$$A = (0.3)(0.018) = 0.0054 \text{ in.}^2$$

We now evaluate q_1 and q_2 using the following values:

$A_c = (1/2)(0.0054)(0.75) = 0.002 \text{ in.}^2$

$A_b = (0.004)(0.75) = 0.003 \text{ in.}^2/\text{in.}^2$

$A_f = (0.75)(0.0025) = 0.001875 \text{ in.}^2$

$E_c = 10 \times 10^6$ psi

$E_b = 212,000$ psi

$E_f = 16 \times 10^6$ psi

$\alpha c = 12.6 \times 10^{-6}$ in./in. ^oF

$\alpha b = 70 \times 10^{-6}$ in./in ^oF

$\alpha f = 4.8 \times 10^{-6}$ in./in. ^oF

$\Delta T = -270 - 70 = -240^oF$

$q_1 = 0.60$ lb/in.

$q_2 = 0.42$ lb/in.

$P_f = q_1 L = (0.6)(136.75) = 82$ pounds (Compression)

$P_b = (q_2 - q_1) L = (0.18)(136.75) = 25$ pounds (Tension)

$P_c = q_2 L = (0.42)(136.75) = 57$ pounds (Tension)

The bond shear stress will be the highest adjacent to the core as the effective thickness is only 0.018 inches in comparison to 0.75 inches between the bond and face sheet.

$$f_{s_b} = \frac{q}{t} = \frac{0.42}{0.018} = 23 \text{ psi (small)}$$

The face sheet compressive stress between the hub and first hinge (special section) is

$$f_{c_f} = \frac{P}{A} = \frac{82}{0.003750} = 21,800 \text{ psi}$$

$$\text{M.S.} = \frac{70,000}{21,800} - 1 = \underline{\underline{2.3}}$$

The face sheet compressive strength outboard of the first hoop (typical section) is

$$f_{c_f} = \frac{P}{A} = \frac{(82 - 0.42 \times 27.5)}{0.001875} = 37,000 \text{ psi}$$

$$\text{M.S.} = \frac{40,600}{37,000} - 1 = \underline{\underline{+0.10}}$$

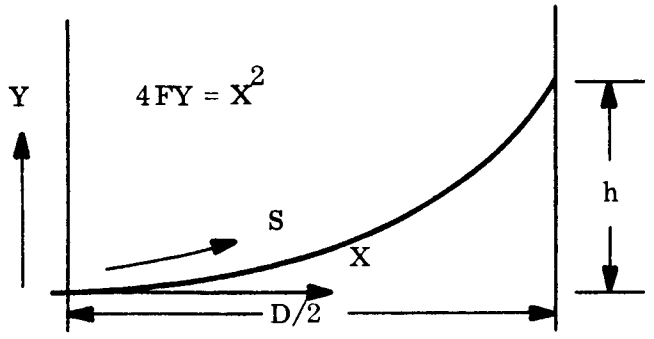
On the basis of this conservative analysis, we conclude that the bond shear stress is low (23 psi) and face sheet stress moderately high (37,000 psi). A more detailed analysis would show lower face sheet stresses as was discussed earlier in this section. More precise values can be obtained by proper modeling utilizing computer analysis of the complete antenna as was performed for thermal distortions.

6.3.3.3 Deployment Analysis

This section develops the deployment load required to snap-through the antenna to total deployment. It also provides the analysis of the capability of the deployment truss members to withstand the deployment loads. In addition, drive system requirements are specified.

6.3.3.3.1 Condition C - Deployment Load

The maximum load occurs near the end of the actuator stroke and is the force required to snap-through the petals. A derivation of this load is presented below:



Parabola geometry is

$$\frac{f}{D} = 0.4$$

$$D = 360 \text{ inches}$$

Therefore,

$$h = \frac{D^2}{16\,(0.40)}$$

$$= \frac{D^2}{6.4}$$

$$Y = \frac{x^2}{4\,F}$$

$$= \frac{x^2}{4\,D\,\frac{f}{D}}$$

$$= \frac{x^2}{576}$$

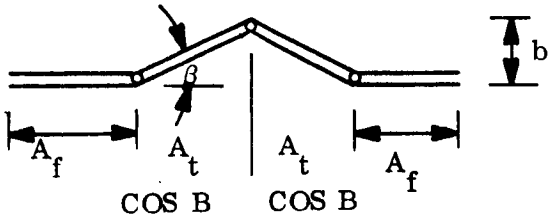
$$S = x\left[1 + \frac{2}{3}\left(\frac{Y}{x}\right)^2 - \frac{1}{10}\left(\frac{Y}{x}\right)^4 \ldots\right]$$

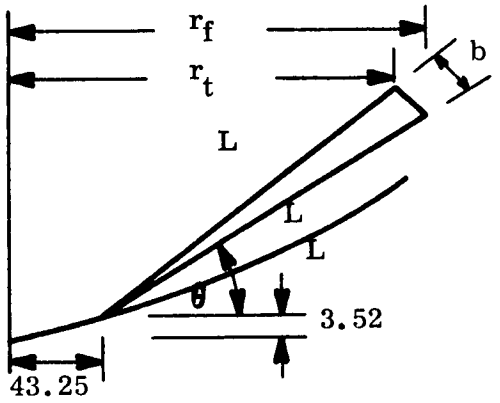
	x	y	s
Hub	43.25	3.52	45.18
Actuator	112.5	21.95	115.34
Rim	180	56.27	191.55

L_1=115.34-45.18=70.16

L =191.55-45.18=146.37

For Petal geometry at the snap-through position assume that the snap-through will occur when b = β = 0 at the rim.





For

n = 20 sectors

A_f = 6.15

A_t = 25.20

$2\pi r_f = n(A_f + 2A_t \cos\beta)$

$= (x_h + L\cos\theta)\,2\pi$

L = 146.37

X_h = 43.25 in.

Solving for β,

$$\cos\beta = \frac{\pi}{n A_t}(x_h + L\cos\theta) - \frac{A_f}{2 A_t}$$

Solving for θ,

$$\cos\theta = \frac{1}{L}\left[\frac{n\,A_t}{\pi}\left(\frac{A_f}{2\,A_t} + \cos\beta\right) - x_h\right]$$

at the rim for $\beta = 0$.

$$\cos\theta = \frac{1}{146.37}\left|\frac{20\,(25.20)}{\pi}\left(\frac{6.15}{2(25.70)} + 1\right) - 43.25\right|$$

$$= \frac{135.01992}{146.37}$$

$$= 0.92246$$

$$\theta = 22^{o}17'$$

at the actuator location.

$A_f = 8.34$ in. $\qquad L_1 = 70.16$ in.

$A_t = 13.50$ in.

$$\cos\beta = \frac{\pi}{20\,(13.50)}\,(45 + 70.16 \times 0.92246) - \frac{8.34}{2\,(13.50)}$$

$$= 0.96776$$

$$\beta = 14^{o}25'$$

$$b = A_t \sin\beta$$

$$= 13.50\,(0.25179)$$

$$= 3.40 \text{ in.}$$

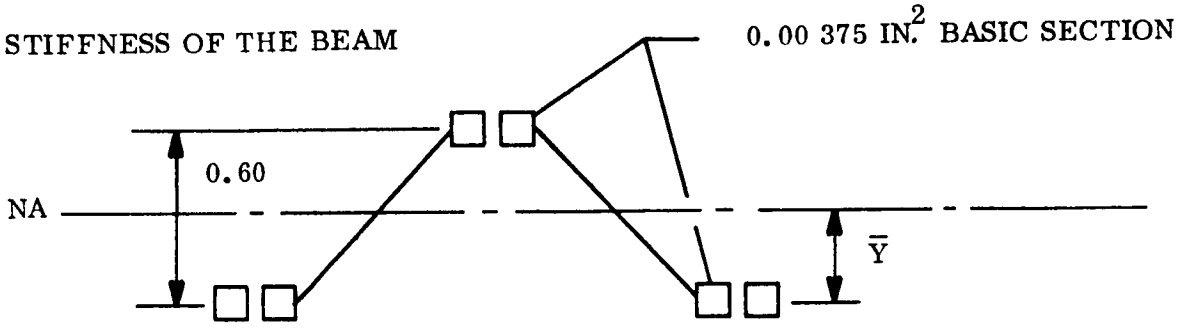
One repeating set of three petals is considered as a simply supported beam of variable bending moment of inertia with a concentrated load at the center, since the actuator is attached near midspan of the petal length. The load required to give a midspan deflection slightly greater than is assumed to be sufficient to snap-through the petals, say a deflection of 3.41 inches because (a) the moment of inertia of the beam will decrease as a squared function during the petal deflection, and (b) the moments of inertia vary spanwise

with a very small value at each end to a maximum near the center. An approximate typical constant moment of inertia is based on a reduced value of b as given below,

$$b_a = \text{(spanwise reduction) (deflection reduction) } b$$

$$= \frac{1}{2}\,\frac{1}{2\sqrt{2}} \quad (3.40)$$

$$= 0.60 \text{ in.}$$



$$\bar{Y} = \frac{1}{3}\,(0.60)$$

$$= 0.20 \text{ in.}$$

$$EI = (16)\,(10^6)(0.00375)\left[4\,(0.20)^2 + 2\,(0.40)^2\right]$$

$$= 0.288 \times 10^5 \text{ lb in.}^2$$

Using the standard simple beam deflection equation

$$\delta = \frac{P\,L^3}{48\,EI}$$

where:

δ = maximum deflection

P = beam load

L = beam length

The required load to produce the 3.41 in. deflection is

$$P = \frac{(3.41)\,(48)(0.288 \times 10^{5})}{146.37^{3}}$$

$$= 1.5 \text{ lb}$$

A factor of safety of 2 is used to increase the conservativeness of the calculation. The required design load is

$$P = 2\,(1.5)$$

$$= 3.0 \text{ lb}$$

The previous analysis was used to determine the preliminary design loads. The final design load will be based on tests.

6.3.3.3.2 Deployment Truss Analysis

Truss members are shown in Figure 6.3-48. Loads are presented in Table 6.3-8

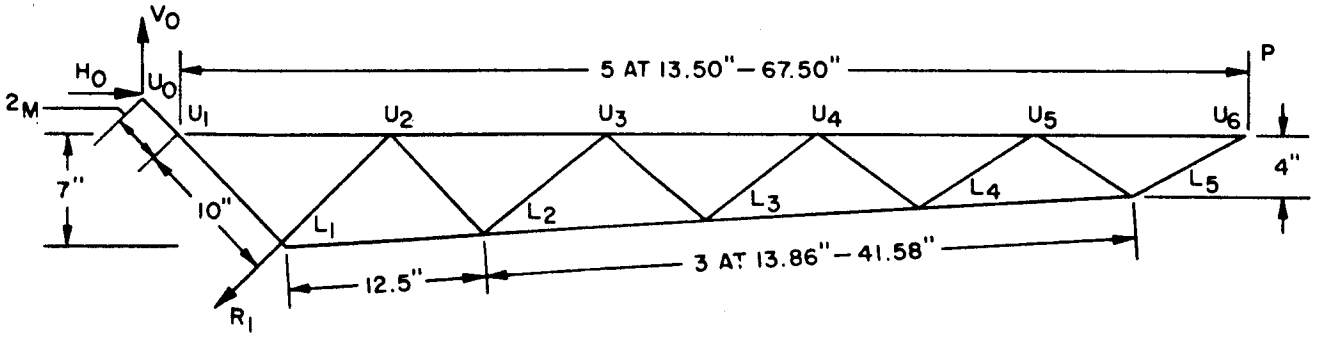


Figure 6.3-48. Truss Members

Table 6.3-8. Truss Member Loads

Member	Length	Force For P = 1 Lb (lb)	Force For P = 3 Lb (lb)
$U_0 U_1$	2.0	-0.683	- 2.05
$U_1 U_2$	13.5	-8.681	-26.04
$U_2 U_3$	13.5	-7.655	-22.97
$U_3 U_4$	13.5	-6.218	-18.65
$U_4 U_5$	13.5	-4.318	-12.95
$U_5 U_6$	13.5	-1.687	- 5.06
Σ	69.5		
$L_1 L_2$	12.5	8.167	24.53
$L_2 L_3$	13.86	6.907	20.72
$L_3 L_4$	13.86	5.280	15.84
$L_4 L_5$	13.86	3.095	9.29
Σ	54.08		
$U_1 L_1$	10.00	5.563	16.69
$U_2 L_2$	8.52	-0.741	- 2.22
$U_3 L_3$	8.52	-0.917	- 2.75
$U_4 L_4$	7.99	-1.188	- 3.56
$U_5 L_5$	7.86	-1.629	- 4.89
Σ	42.59		

Truss Member Loads (Cont'd)

Member	Length	Force For P = 1 Lb (lb)	Force For P = 3 Lb (lb)
$L_1 U_2$	10.00	0.760	2.28
$L_2 U_3$	10.01	0.978	2.93
$L_3 U_4$	9.27	1.182	3.55
$L_4 U_5$	8.55	1.481	4.44
$L_5 U_6$	7.85	1.962	5.89
Σ	45.68		

ΣM_{u_o} for P = 1 lb;

$$R_1 = \frac{67.5 + 2\,(0.72065)}{12}$$

$$= 5.745 \text{ lb}$$

ΣF_H and F_v at joint L_1 for P = 1 lb;

$$(0.69309)\,(5.745 - 0.760) - (0.99847)\,(8.167) - H_{U_1 L_1} = 0$$

$$(0.72065)\,(5.745 - 0.760) - (0.05539)\,(8.167) - V_{U_1 L_1} = 0$$

Therefore,

$$H_{U_1 L_1} = -4.70 \text{ lb}$$

$$V_{U_1 L_1} = -3.14 \text{ lb}$$

and from statics of member $U_O U_1 L_1$

$$H_O = F_{U_1 U_2} + H_{U_1 L_1}$$

$$= 3.98 \text{ lb}$$

$$V_O = V_{U_1L_1}$$

$$= 3.14 \text{ lb}$$

The member sizes required for either maximum stress or minimum section, whichever is greater, are determined. The truss is to be made of welded titanium tub. The mechanical properties of the welded material are assumed to be those of Mil-T-9046, class 5.

These properties are:

$$F_{tu} = 50 \times 10^3 \text{ psi}$$

$$F_{ty} = 40 \times 10^3 \text{ psi}$$

$$F_{cy} = 40 \times 10^3 \text{ psi}$$

$$E_c = 16 \times 10^6 \text{ psi}$$

The limit allowable stress is

$$F_{t\,(Lim)} = \frac{50}{1.5} \times 10^3$$

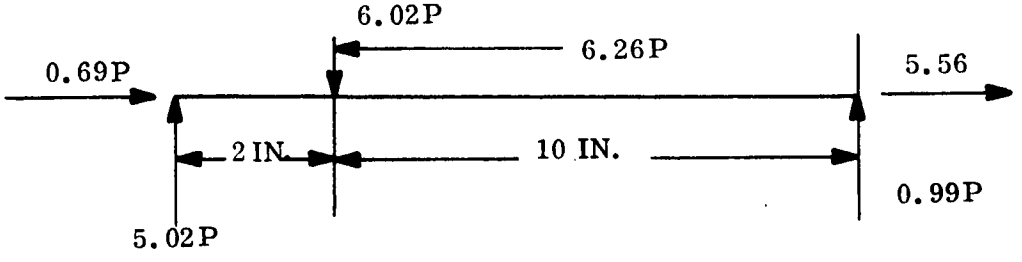
$$= 33300 \text{ psi}$$

$$F_{cy} = \frac{40}{1.5} \times 10^3$$

$$= 26600 \text{ psi}$$

Member $U_0U_1L_1$:

$$f_{t_{max}} = f_{b_t} + f_t$$



For round thin wall tubes $P_{Lim} = 3$ lb,

$$33300 = \left(\frac{2\,(5.02)}{2\pi d^2\, t} + \frac{5.56}{\pi\, d\, t} \right)^3$$

$$t_{min} = 0.028 \text{ in.}$$

therefore,

$$d^2 = \frac{3}{33000\ \pi\ 0.028}\ (5.02 + 5.56\ d)$$

$$d^2 = \frac{5.56}{11000\ \pi\ 0.028} = \frac{5.02}{11000\ \pi\ 0.028}$$

$$d = 0.093$$

$$d_{min} = 0.25 \text{ (0.25 x 0.028 tube minimum available size)}$$

Minimum tube is used for the member. The maximum tension in any member is 24.53 lb in member $L_1\ L_2$

$$A_{req} = \frac{2453}{33300}$$

$$= 0.766 \times 10^{-3} \text{ in.}^2$$

The area of the 0.25 x 0.028 tube is 19.5×10^{-3} in.^{2} The tube is more than adequate. Sizing of the compression members follows. Upper chord members, $U_1 U_6$ are treated as one member, because it is unsupported laterally. The entire length will be considered to be a pin-ended column. The limit column load is the average of the force in each of the top chord members. The allowable pin-ended column load is:

$$P_{cr} = \frac{\pi^2\ EI}{\ell^2}$$

Therefore,

$$I = \frac{P_{cr}\, \ell^2}{\pi^2 E}$$

since, $P_{cr} = 1.5\, P_{avg}$ and

$$I = \pi d^3 t_{min}$$

$$d^3 = \frac{1.5\, P_{avg}\, \ell^2}{\pi^3 E}$$

$$d = \frac{1}{\pi} \sqrt[3]{\frac{1.5 P_{avg}\, \ell^2}{E}}$$

$$= \frac{1}{\pi} \sqrt[3]{\frac{1.5\,(17.13)\,(67.5)^2}{16 \times 10^6}}$$

$$d = \frac{1}{10\pi} \sqrt[3]{1.084}$$

$$\approx \frac{1}{10\pi}$$

$$= 0.032 \text{ in} < 0.25 \text{ min. d.}$$

The entire truss can be made from the 0.25 x 0.028 C_p Ti tube with more than ample margins of safety. Different construction techniques may produce a weight saving, but for this analysis the weight is estimated for the welded tube truss design.

$$W_{truss} = (\Sigma L_i)\, A\, (0.16)\, (1.12)$$

where:

L_i = member length

A = member area

0.16 = density of C_p Titanium

1.12 = factor for joint material

$$W_{truss} = (69.5 + 54.08 + 42.59 + 45.68)\ (0.0195)\ (0.16)\ (1.12)$$

$$= 0.74 \text{ lb}$$

For 16 trusses required (other 4 trusses are solar array deployment trusses)

$$W = 16 \times 0.74$$

$$\cong 11.8 \text{ lb}$$

6.3.3.3.3 Drive System Requirements

The ball screw actuator is a purchased item that is required to meet the following specification:

Load = 5.75 x 3 (limit operating)

= 17.25 lb

Travel = 18 in.

6.3.3.4 Dynamic Analysis

6.3.3.4.1 Antenna Dynamic Modes and Frequencies

Simplified analytical methods of predicting natural frequencies and mode shapes have been developed based on model tests of both shell type and rib-ring type of antenna structural configurations. It has been observed from tests that the primary structural modes of dish type antennas with hub support have equally spaced diametrical node lines. The larger the number of diametrical node lines, the higher the frequency. Model tests reveal that the first primary mode of a shell type dish is the mode with two equally spaced diametrical node lines as show in Figure 6.3-49.

It has been found that the natural frequency of this mode may be analytically approximated by calculating the first mode natural frequency of an overhanging beam on two supports (hub and deployment strut).

A 45-degree sector of the antenna is chosen as representative of antenna stiffness and weight distribution. The 45-degree sector weight and stiffness distributions are projected to the overhanging beam on two supports and the first mode natural frequency is calculated using Rayleigh's static deflection method. The bending stiffness of the sector shown in Figure 6.3-50, ($EI = E \Sigma A Y^2$), is obtained through consideration of curvature effects of the antenna geometry.

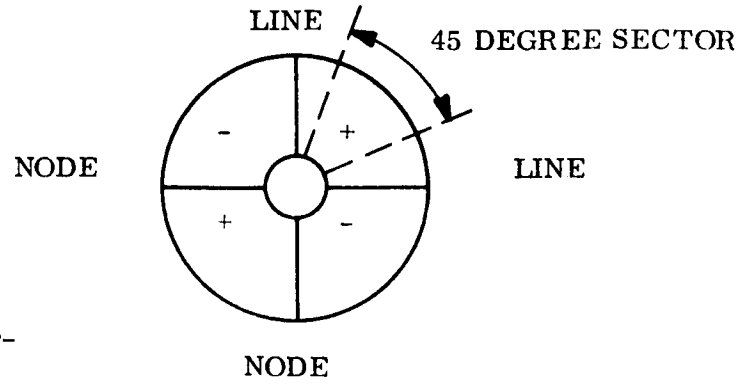


Figure 6.3-49. Two-Node Diameter Mode of Vibration

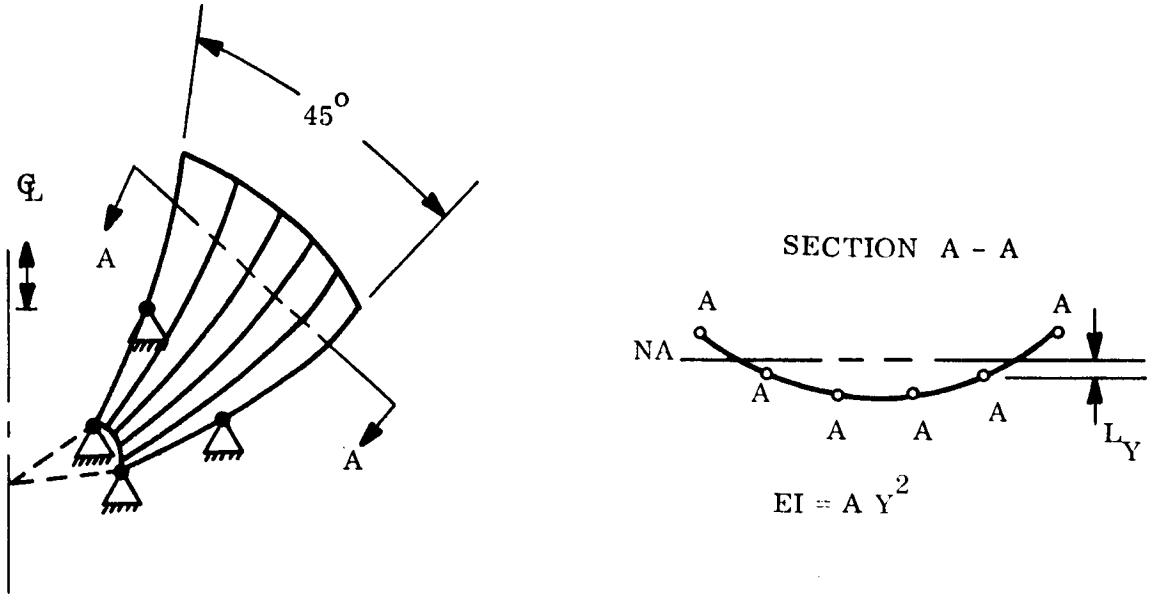


Figure 6.3-50. 45-Degree Sector of Antenna Representing Overhanging Beam on Two Supports

The natural frequency using the static deflection method is given by

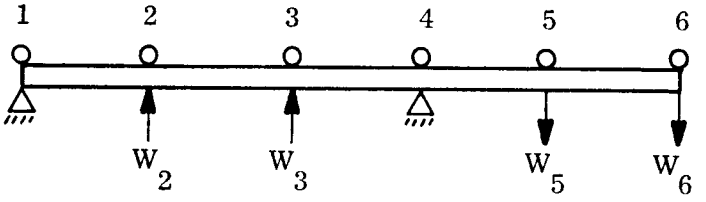
$$f = \frac{1}{2\pi}\sqrt{\frac{g\sum_{1}^{\delta} W_i \delta_i}{\sum_{1}^{\delta} W_i \delta_i^2}}$$

where

W_i = lumped weight at point i

δ_i = static deflection at point i

g = acceleration of gravity



Summarized below are the static deflections, δ_i, and point weights, W_i, for a titanium sandwich ATS-4 antenna. The ATS-4 two diametrical mode natural frequency is shown to be equal to 4.1 cps.

Point	δ (In.)	W (lb)	δ W	δ^2 W
1	0.00	——	——	——
2	0.413	0.738	0.305	0.126
3	0.288	0.961	0.277	0.080
4	0.00	——	——	——
5	0.360	1.430	0.515	0.185
6	0.724	2.640	1.910	1.380
			3.007	1.771

$$f = \frac{1}{2\pi}\sqrt{\frac{386\,(3.007)}{1.771}} = 4.1 \text{ cps}$$

The above frequency is considered as an upper bound of the actual antenna frequency. There are two reasons for this, in addition to the fact that the Rayleigh method yields a high estimate of the frequency. The first is that the antenna beam is considered as simply supported in the above calculation, while in reality it is supported on flexible members. The second is that the beam concept is not completely consistent with the truss type construction of the antenna.

An improved estimate of antenna frequency is obtained using the detailed structural model presented in Section 6.3.4.3.2. This model uses a discrete element approach to represent the individual members of the antenna. Stiffness matrices are obtained for each of the antenna elements and assembled into a total stiffness matrix representing the antenna in six degrees of freedom at each of its many nodes. The antenna is supported on 50 pound/inch springs, simulating the back deployment trusses.

The fundamental, lowest energy, mode occurs as the first non-extensional mode of the antenna as described previously. This mode shape has node lines separating the antenna into quadrants with the antenna contained in the first and third quadrants moving in-phase with each other and 180 degrees out-of-phase with the second and fourth quadrants.

The representative half of the symmetric antenna structure was solved, considering anti-symmetric boundary conditions, for the deflection due to a 1-g load acting upward in one quadrant and down in the other. The computer program used (MASS) calculates the potential energy term and yields the displacements of the loaded antenna.

The coefficient for the kinetic energy term is calculated from the deflection and weight components and the frequency determined for the condition of equal potential and kinetic energies.

The frequency thus obtained is 3.3 cps. This frequency is considered as a good estimate of the antenna fundamental frequency. Since a low antenna frequency is conservative for the control response problem, this frequency is reduced to 2.5 cps and incorporated into the orbital dynamic models.

6.3.4 THERMAL DISTORTION ANALYSIS

6.3.4.1 Introduction

The objective of the ATS-4 program is to orbit a 50-percent efficient paraboloid antenna with a minimum aperature diameter of 30 feet. These requirements impose a commitment to minimize all sources of rf losses. An important potential source of rf loss results from the distortion of the ideal paraboloid surface as a result of thermal gradients.

The following subsections present the thermal and structural analyses performed during this study. These analyses indicate that the selected antenna configuration will exhibit entirely acceptable thermal distortions and produce insignificant rf losses.

Four temperature effects have been considered:

a. Temperature gradients across the reflector.

b. Temperature gradients through the reflector.

c. Average reflector and feed support truss temperatures different from those which the antenna was accurately fabricated.

d. Thermal distortion of the antenna feed due to unequal temperatures of the truss support members.

6.3.4.2 Thermal Analysis

The final selected design exhibits an 80-percent open reflecting surface. Structural framing members are of sandwich construction, 0.3-inch thick, using an aluminum honeycomb core (0.0007 inch foil, 1/8 inch cell) and titanium face sheets (0.0025 inch thick). The main load carrying members are 3/4-inch wide, while the secondary members, designed to support the fine rf mesh, are only 3/8-inch wide. This final design was investigated for different coating combinations. The coating characteristics used for the selected configuration were $\alpha = 0.45$ and $\epsilon = 0.5$ for the reflector front surface (buffed titanium) and $\alpha = 0.12$ and $\epsilon = 0.04$ for the back surface (vapor-deposited aluminum).

Data for the worst orientation of the antenna with respect to the sun, that is, yaw axis normal to the sun's rays are given in Figure 6.3-51 for the selected design. These isotherms have been evaluated for structural distortion and have been found to have an insignificant effect on rf patterns. Preliminary isotherms for other sun-reflector orientations are shown in Figures 6.3-52 through 6.3-55.

Another case was investigated where both sides of the reflector are coated with vapor-deposited aluminum ($\alpha = 0.12$, $\epsilon = 0.04$). A slight improvement in the temperature distribution was noted. However, this case has not been analyzed for thermal distortions because the more severe Case No. 39 yielded very little rf degradation due to these distortions.

6.3.4.3 Structural Deformation

The potential severity of the thermal distortion problem was identified through preliminary analysis which indicated the need for a careful examination of the antenna design and material selection. Titanium was selected for the honeycomb face sheets in the design because of its lower coefficient of thermal expansion. It was recognized that other material and geometry combinations might result in a more nearly optimum design, but that the selected configuration represented a realistic and feasible design approach to the problem and that the results of subsequent analyses would be indicative of expected ATS-4 antenna performance. A major technical emphasis was then placed on a refined analysis of the parabolic antenna thermal distortion and resulting rf degradation conducted jointly by General Electric and Goodyear Aerospace. The analytical results revealed that the structural deformation was acceptably small and quite localized.

6.3.4.3.1 Preliminary Reflector Distortion Analysis

The initial calculations were made using a program for the thermal deflections of a shallow spherical shell. This program determined the fundamental thermal behavior of the antenna and formed the basis for preliminary tradeoff studies. The preliminary model was based on a continuous isotropic analysis which resulted in the following governing equations:

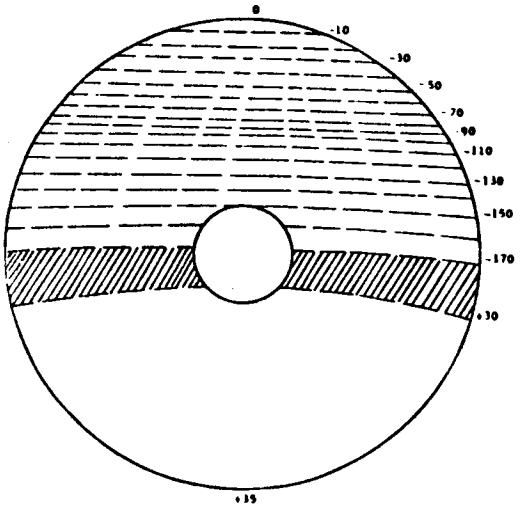


Figure 6.3-51. Antenna Isotherms 39-90

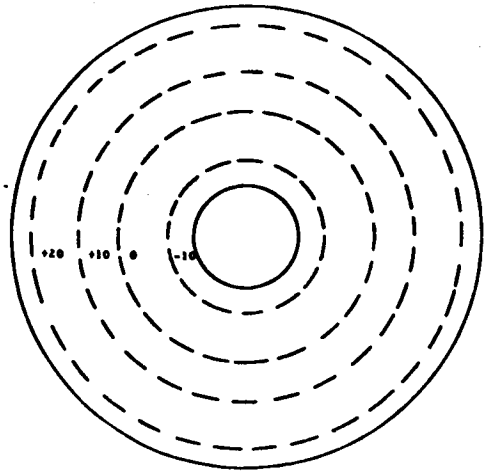


Figure 6.3-52. Antenna Isotherms 39-0

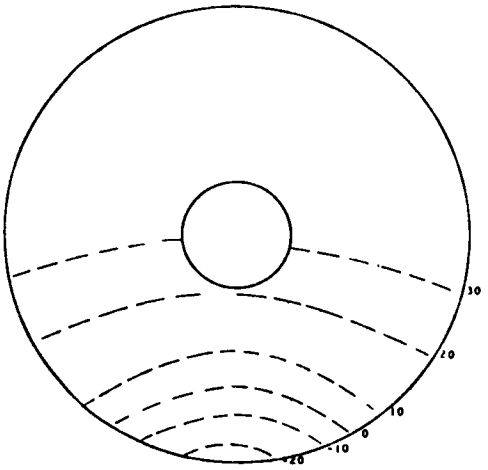


Figure 6.3-53. Antenna Isotherms 39-45

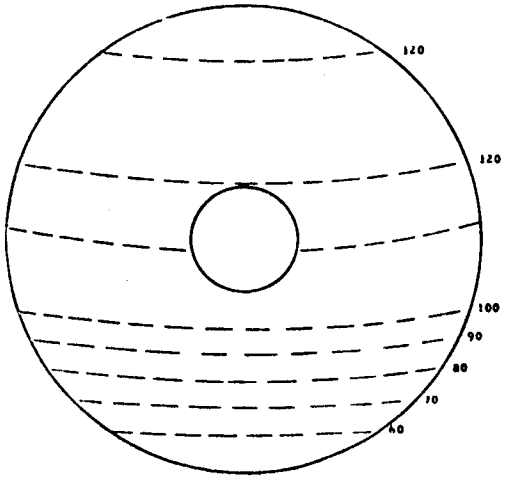


Figure 6.3-54. Antenna Isotherms 39-135

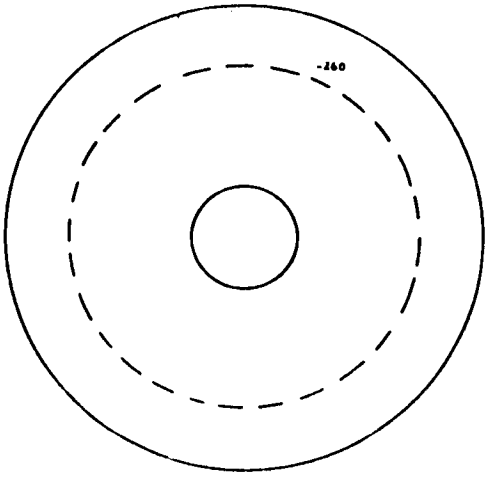


Figure 6.3-55. Antenna Isotherms 39-180

$$D \nabla^4 W - \frac{1}{a} \nabla^2 \phi = - \frac{E C_T}{1 - V} \nabla^2 T_M \qquad (6.3\text{-}1)$$

$$\frac{1}{E \delta} \nabla^4 \phi + \frac{1}{a} \nabla^2 W = - \frac{C_T}{\delta} \nabla^2 T_N \qquad (6.3\text{-}2)$$

W = Normal displacement

ϕ = Airy's stress function

E = Modulus of elasticity

V = Poisson ratio

D = Bending stiffness of the shell

a = Radius of the sphere

δ = Combined thickness of the two faces

C_T = Coefficient of thermal expansion

$T_N = T_i t_i + T_o t_o$

$T_M = \frac{1}{2} \left[T_i t_i (h - 2b - t_i) - T_o t_o (h + 2b - t_o) \right]$

T_i, T_o = Temperature of inner and outer faces, respectively

t_i, t_o = Thickness of inner and outer faces, respectively

h = Total thickness of the shell

$b = \frac{b}{2} \frac{(t_i - t_o)}{(t_i + t_o)} - \frac{(t_i - t_o)}{2}$

Equation (6.3-1) is an equilibrium equation and compares with the bending equation of a flat plate with the added influence of the membrane forces. Equation (6.3-2) is a compatibility equation and can be compared with the plane stress equation for a flat plate with the added influence of the transverse displacements.

By manipulating the equations and introducing a new dimensionless variable, α,

$$\alpha = r / \sqrt[4]{\frac{D \alpha^2}{E \delta}}$$

where r is the cylindrical polar radius, we have the equations

$$\nabla^6 W + \nabla^2 W = - \frac{a^2 C_T}{(1 - V)\,\delta r_o^2} \nabla^4 T_M - \frac{a\,C_T}{\delta} \nabla^2 T_N \qquad (6.3\text{-}3)$$

$$\nabla^2 \phi = \frac{E \delta r_o^2}{a} \nabla^4 W + \frac{a\,E\,C_T}{1 - V} \nabla^2 T_M \qquad (6.3\text{-}4)$$

By taking T_N and T_M in the form

$$T_M(\alpha, \theta) = \sum_{n=0}^{\infty} T_{M_n}(\alpha) \cos n\theta$$

$$T_N(\alpha, \theta) = \sum_{n=0}^{\infty} T_{N_n}(\alpha) \cos n\theta$$

where $T_{M_n}(\alpha)$ and $T_{N_n}(\alpha)$ are suitable polynomials in α, we can obtain the solutions of Equations 6.3-3 and 6.3-4 in the form

$$W(\alpha,\theta) = \sum_{n=0}^{\infty} W_n(\alpha) \cos n\theta$$

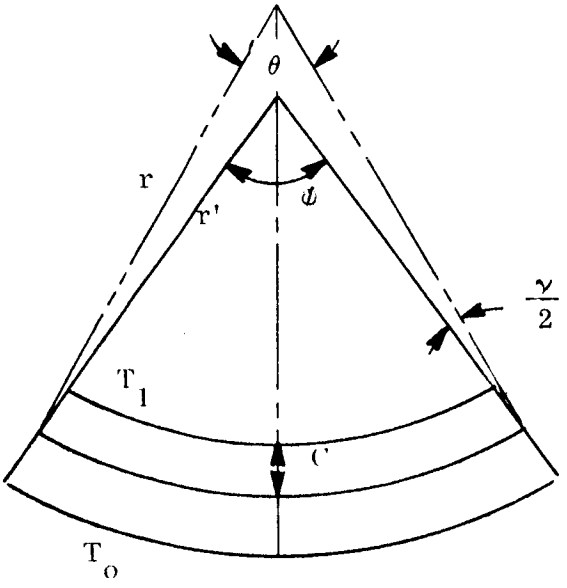
$$\phi(\alpha, \theta) = \sum_{n=0}^{\infty} \phi_n(\alpha) \cos n\theta$$

This form of the solution results in an ordinary differential equation to solve for each W_n and ϕ_n. The complementary solutions are in terms of harmonic functions and Kelvin functions. The particular solutions are expanded in series about some point other than the origin. (To ensure convergence of these series, the expansion point is taken as greater than half the maximum radius). By inserting the appropriate boundary conditions, we obtain the continuous solution of the boundary value problem. The entire analysis was programmed on the IBM 360 Model 40 digital computer.

To use this program to gain some insight into the action of the antenna when subjected to various temperature distributions, we made certain approximations to consider the fact that the antenna is a discrete structure and not a continuous shell. To do this, changes in the bending and membrane stiffness were made.

Because the continuous analysis assumes an isotropic material, any change in stiffness will apply to both directions. The circumferential axial stiffness and the radial bending stiffness were used because these appear to be the most significant. Thus, the initial model used for the antenna was a continuous shell. The membrane stiffness of this shell was set equal to the average distributed axial stiffness of the antenna in the circumferential direction. The bending stiffness was set equal to the average distributed bending stiffness of the antenna in the radial direction. Since accurate values for this substitution of stiffness are not easily determined, the results obtained from this study were only of value for gross estimations of antenna behavior. Several items of interest that were observed concerned the significance of different types of temperature distributions and different structural properties.

With regard to the different temperature distributions, it was found that the deflections due only to the temperature differences across the thickness were small in the range of temperature differences in this problem. This finding can easily be illustrated by considering the following model and computations as representative of a portion of the reflector.



r = Initial curvature

r' = Final curvature

$\gamma/2$ = Angular rotation of plane cross-section of surface

c = Distance from midplane to extreme fiber

T_i = Inner surface temperature

T_o = Outer surface temperature

α = Thermal coefficient of expansion

then

$$\frac{\gamma}{z} = -\frac{1}{2} \cdot \frac{\alpha\left(T_i - \frac{T_i + T_o}{2}\right)}{c}$$

$$\gamma = \frac{1}{2} \quad \frac{\alpha(T_i - T_o)}{c}$$

$$\phi = \theta + \gamma = \frac{1}{r'}$$

$$r' = \frac{1}{\theta + \gamma} = \frac{1}{\frac{1}{r} + \frac{1}{2} \quad \frac{\alpha}{c} \quad (T_i - T_o)}$$

Let $T_i - T_o = \Delta T$

$$r' = \frac{1}{\frac{1}{r} + \frac{\alpha \Delta T}{2c}}$$

For $\Delta T = 3^{\circ}F$ $\alpha = 4.8 \times 10^{-6}$ in./in./$^{\circ}$F, $r = 315.5$, $C = 0.15$ in.

$r' = 315.484$

or $\underline{\Delta r = 0.016 \text{ in.}}$

This shows in an elementary manner, that gradients through thickness have a relatively small effect on distortions for the range of temperature differences predicted for the orbital environment.

It was found that temperature gradients in the radial direction tend to set up large hoop forces, which in turn caused moderate normal deflections. From these initial studies, it appeared that the fixity of the hub had a significant effect on the stresses and deflections. If the hub were free to expand or contract, then a constant temperature distribution caused free thermal expansion or contraction. The deformed shape was simply a slightly different paraboloid as illustrated in Figure 6.3-56 for a constant temperature below ambient. If the hub were prevented from expanding or contracting, then large hoop forces tended to set up near the hub,

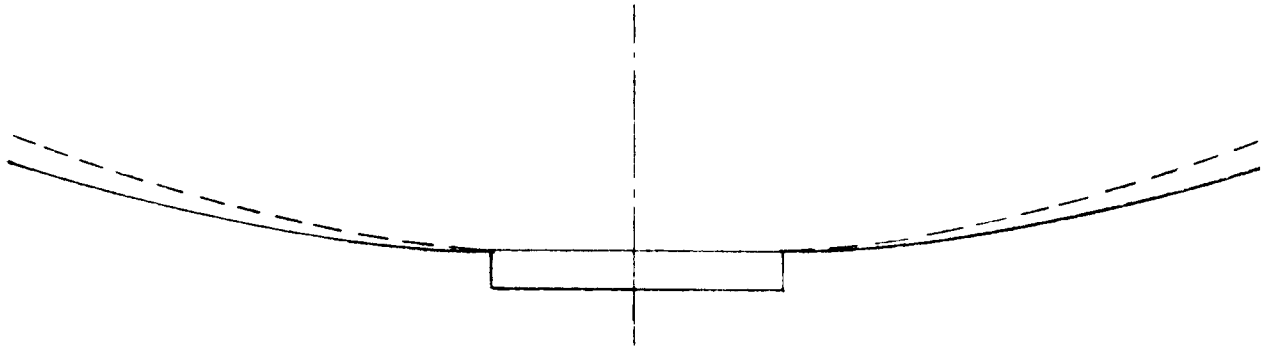


Figure 6.3-56. Deformed Shape at Below Ambient Temperatures
(Free Hub, No Deployment Trusses)

causing moderate normal deflections. A constant temperature distribution below ambient caused a deformed shape similar to Figure 6.3-57. From this preliminary model it was also

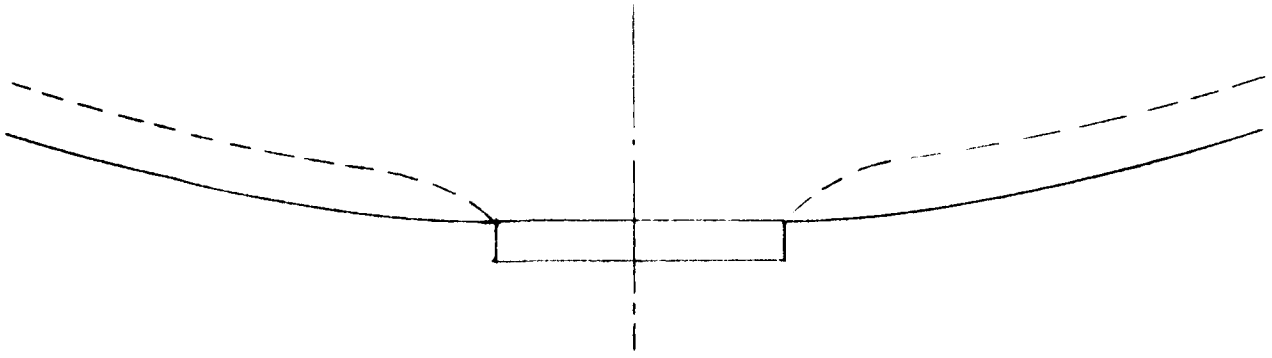


Figure 6.3-57. Deformed Shape at Below Ambient Temperatures
(Fixed Hub, No Deployment Trusses)

determined that the most detrimental type of temperature distribution was one that caused a deformation pattern which is doubly antisymmetric. This phenomenon stems from the fact that the structure is weaker in this mode than in any other.

Another important factor established is that the modulus of elasticity (E) of the antenna has no effect on the thermal deflections. It is the relative magnitude of the stiffness and geometry which are the controlling factors. This means that, if we increase all moduli in the same proportion, deflections due to thermal effects only will not change. However, thermal stresses will increase by that same proportion. This is true whether the structure is discrete or continuous. The theoretical basis for this will now be shown.

Using the matrix force method for the solution of redundant structural problems, the following expressions can be derived relating the member forces and joint displacements to externally applied loads and temperature distortions of the individual members.

$$|F| = \left[T - VG_{22}^{-1} G_{21}\right] |P| + \left[-VG_{22}^{-1} V^T\right] |\delta|^*$$

$$|D| = \left[G_{11} - G_{12} G_{22}^{-1} G_{21}\right] |P| + \left[-G_{12} G_{22}^{-1} V^T + T^T\right] |\delta|^*$$

$$|G| = \begin{vmatrix} T^T \\ V^T \end{vmatrix} |L| \, |TV|$$

Gij = Partioned submatrix of G

F = Member loads

P = Externally applied loads

D = Joint displacements in direction of P

$|\delta|^*$ = Thermal distortion of members

T, V = Relationships between internal force resultants and externally applied and redundant loads, respectively.

L = Member flexibility matrix

If there are no applied loads, the expressions become

$$|F| = \left[-VG_{22}^{-1} V^T\right] |\delta|^*$$

$$|D| = \left[-G_{12} G_{22}^{-1} V^T + T^T\right] |\delta|^*$$

If the modulus of elasticity is a constant throughout the structure, it can be factored out of the Gij matrix as a scalar. Consequently, when multiplying G_{12} times the inverse of G_{22} the value of the scalar in the result is unity. Therefore, it can be seen that the thermal distortions are independent of modulus, but are still functions of the other parameters that form the flexibility matrix, such as length, area, moment of inertias and torsional constant.

From the foregoing initial analysis, much was learned concerning cause and effect in thermal deflections. Results based up on the studies made using the simplified model indicated that the order of magnitude of expected deformations was such that they could not be neglected in establishing rf losses. A more representative model was required to capture the effects of discrete members, deployment trusses, and hinge lines; a major effort was initiated to attack the problem.

6.3.4.3.2 Final Reflector Distortion Analysis

The key to a realistic evaluation of antenna performance degradation is a sophisticated analytical modeling of the antenna structure. For this reason, both General Electric and Goodyear Aerospace Corporation approached this problem independently using different space-frame-work computer programs. These programs simulated each antenna structural member including hinge joints and deployment truss support constraints. Two final cases were evaluated by each contractor for the most severe thermal loading (Figure 6.3-51). The simplest case analyzed was that in which all hinges were assumed locked. The second case analyzed included all the moment releases at both the hub joints and the petal hinge lines (Both final cases were for a fixed hub titantum configuration). These four computer runs all indicated maximum deflections no greater than ± 0.25 inch with maximum deflections highly localized. The General Electric and Goodyear Aerospace Corporation computer

results were in excellent agreement concerning both the magnitude of the deflections and the mode shapes. Differences that did exist could be traced to the slightly different modeling approach particularly in the free hinge case. The description of the analysis used is explained in the the following paragraphs.

The final analysis is based on the discrete member stimulation of the antenna shown in Figure 6.3-58. Figure 6.3-59 shows a computer-generated drawing of the configuration used to debug the program and ensure there were no geometry errors or missing members which are normally difficult to detect in a large structure of this type. The structure was prepared for computer solution using a well established space-frame-work program. The program computes member stiffness from basic geometric and physical parameters. Then using a deflection technique, a total member stiffness matrix for the entire structure is generated. Force-deflection relationships are then established which are solved for internal loads and deflections. The program has been in use for several years and has proven accuracy in handling all types of loading conditions, including the dynamic, steady state and thermal environments. Structural parameters such as hinge lines, thermal gradients, temperatures,

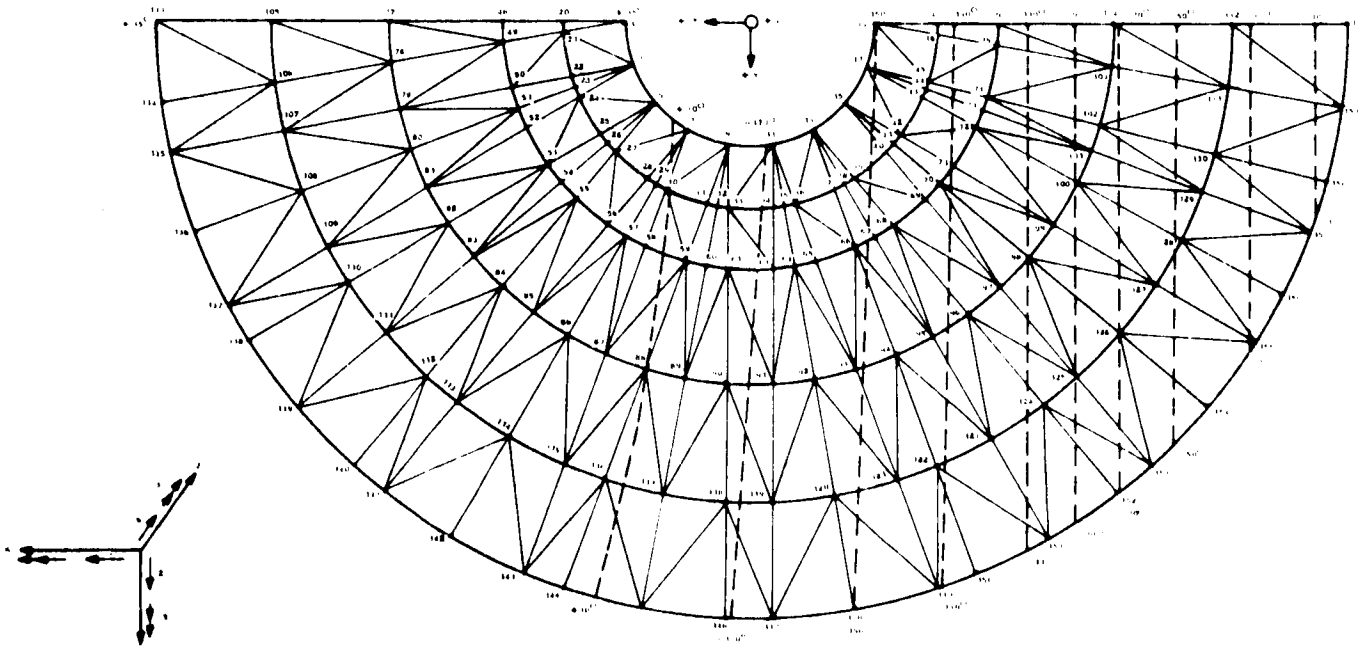
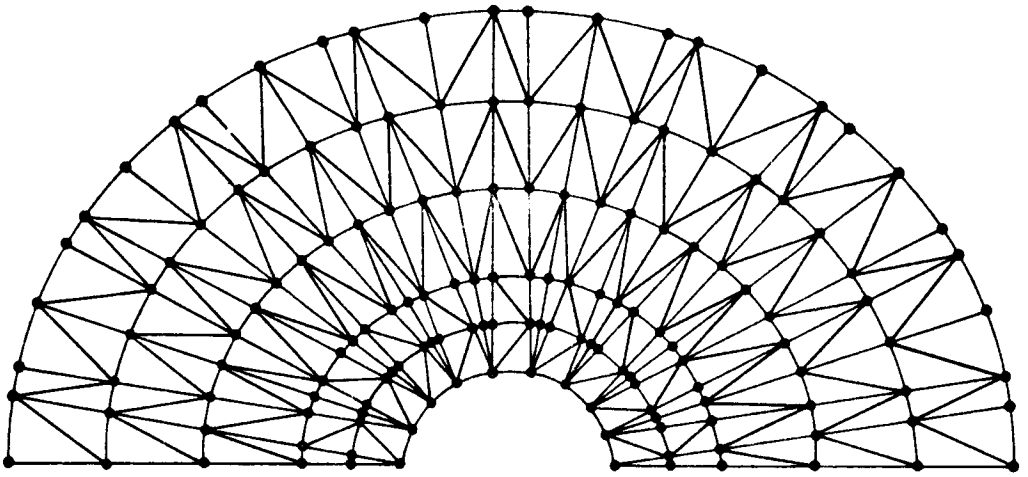
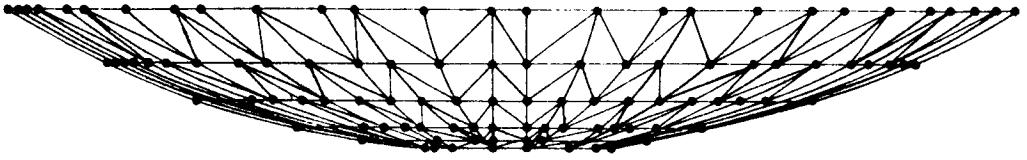


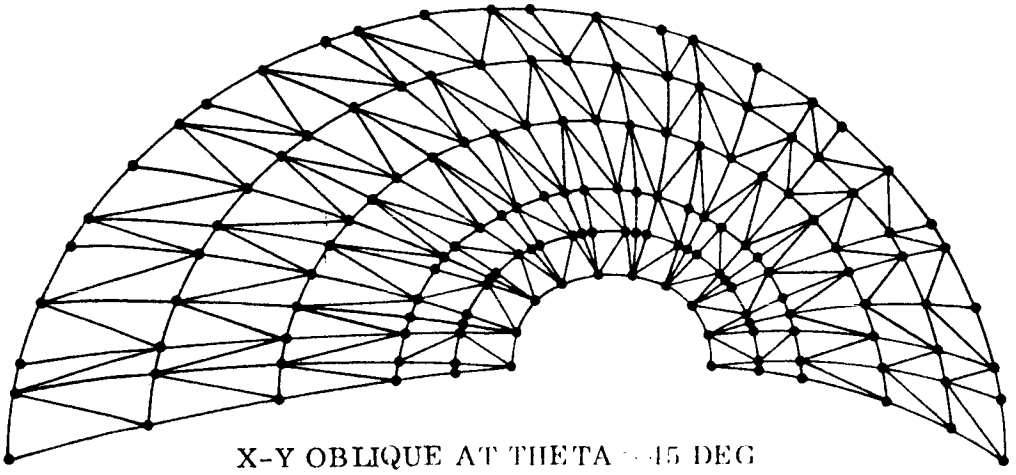
Figure 6.3-58. Structural Simulation for Digital Computer Program



X-Y PLANE



X-Z PLANE



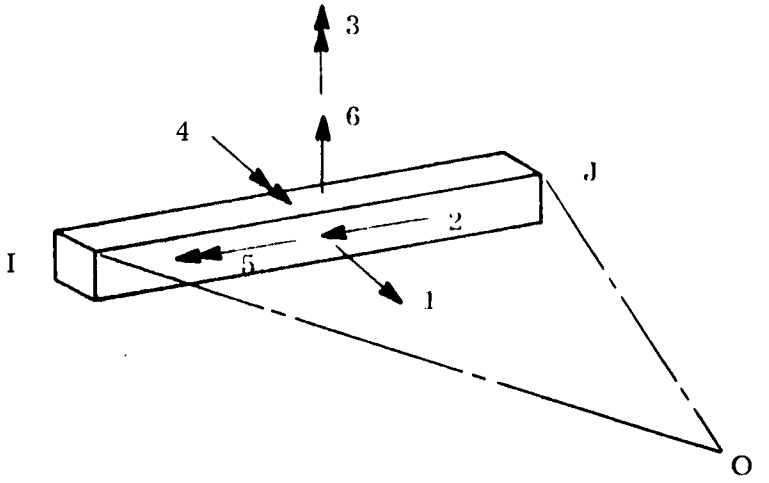
X-Y OBLIQUE AT THETA = 45 DEG

Figure 6.3-59. Computer-Drawn Schematic (or a Structural Antenna Simulation)

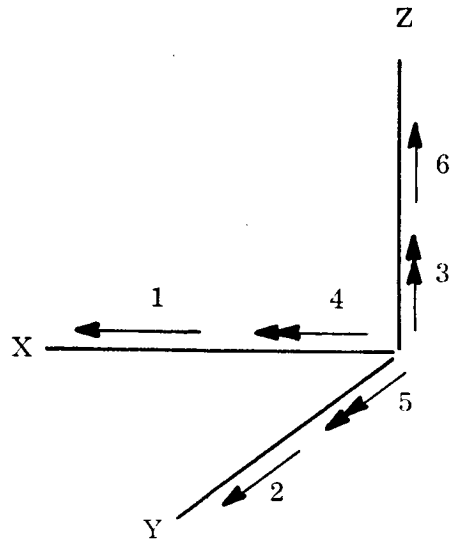
and support trusses are readily included in this representation. Only half the structure had to be programmed as the antenna structure and thermal pattern have a common plane of symmetry. The obvious advantage of this common plane of symmetry is the appreciable reduction in the amount of computer time (approximately 40 minutes) required to solve each case. Programming half the structure is accomplished by applying the approximate boundary conditions to each of the joints intersected by the plane of symmetry.

The significant items of input and the structure geometry, member elastic properties, and boundary conditions, include the member temperatures and associated thermal coefficients of expansion, and the back deployment solar array truss simulation. Upon determining elastic deflection properties of the trusses, we supplied this information to the computer in the form of spring constants acting at the truss attachment points. This joint incorporates a slotted hole oriented parallel to the length of the truss. The deployment truss was, therefore, modeled to only react vertical and transverse loads.

The restrained hub cases assumed a relatively rigid hub when compared with the reflector, and the hub temperature was considered to remain uniformly at ambient. This assumption invoked a condition of no shear displacements at the hub joints during the thermal environments. Computer output is given in three major sections: member information, joint deflections, and joint load summations. Member information consists of a repeat of all pertinent input data, member loads, normal deflections and normal loads. Each member is printed separately and is identified by the joint numbers at either end. Additionally a reference joint is specified to determine a plane that orients the member in space. This plane helps define the directions of a normalized sign convention. The positive sense of direction for loads and moments on the member in its plane are shown below.



The positive sense for deflections and rotations is identical to their respective forces and moments. The right hand rule applies for moments. In addition to the normalized coordinate system, the structure as a whole is referred to as a net of orthogonal axes. The structure roll, pitch and yaw axes are identically the x, y, z axes of this coordinate system shown below.



The 1, 2, and 6 vectors are loads or deflections in the positive x, y, and z directions, respectively; and 4, 5, and 3 vectors are moments or rotations about the x, y, and z axes, respectively. The computer solves for the normalized loads and deflections (orthogonal to member axis) together with the member and loads in the coordinate directions; i.e., parallel to the x, y, and z axes. The normalized loads are used to determine the number bending, axial, and shear stresses. After the member information is printed for all of the members, joint displacements in each of the six directions are printed for each structural joint in the x-y-z coordinate system. This printing is followed by a summation of forces and moments at each joint. This summation can be used to check joint equilibrium, because the total should be zero for all joints without boundary conditions.

As can be seen from Figure 6.3-58, the structure was set up in Quadrants I and II. The particular thermal pattern used is that shown in Figure 6.3-51. An overlay of this pattern was made to the same scale as the structural model and the average member temperatures were determined. The thermal coefficients of expansion were then specified for each member based up on the average thermal coefficient from room temperature to the temperature of

the member. This particular temperature distribution represents very high thermal gradients and a high temperature change (-240°F) from room temperature in the local area of the reflector surface, adjacent to the y axis of the model.

This particular model was used to run various cases to capture the effects of hub fixity, hinge lines, deployment trusses and face sheet material. The highest deflections were obtained from a model representing an aluminum face sheet-free-hub configuration. This particular case did not have hinges or deployment trusses; the resulting deflections were approximately one-half inch. Figures 6.3-60 and 6.3-61 are contour plots showing the effects of hub fixity

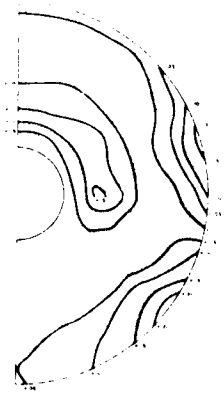


Figure 6.3-60. Contour Deflection for Fixed Hub

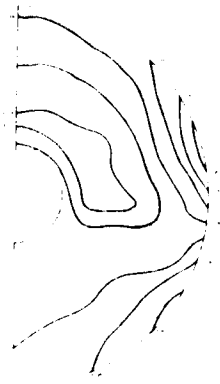
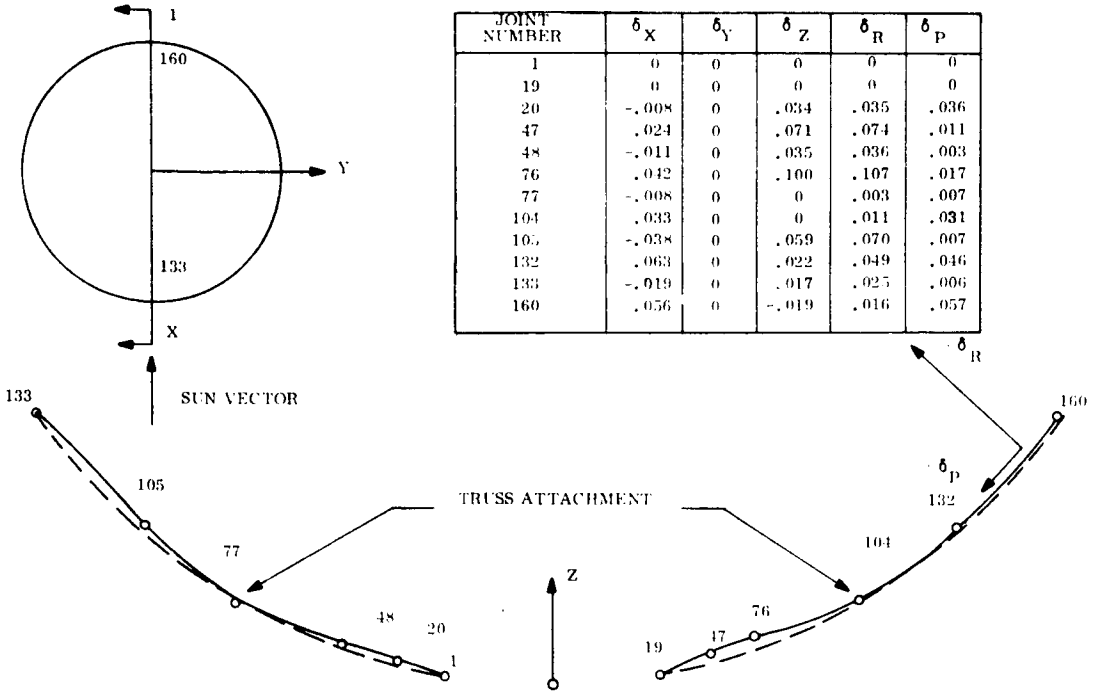


Figure 6.3-61. Contour Deflection for Free Hub

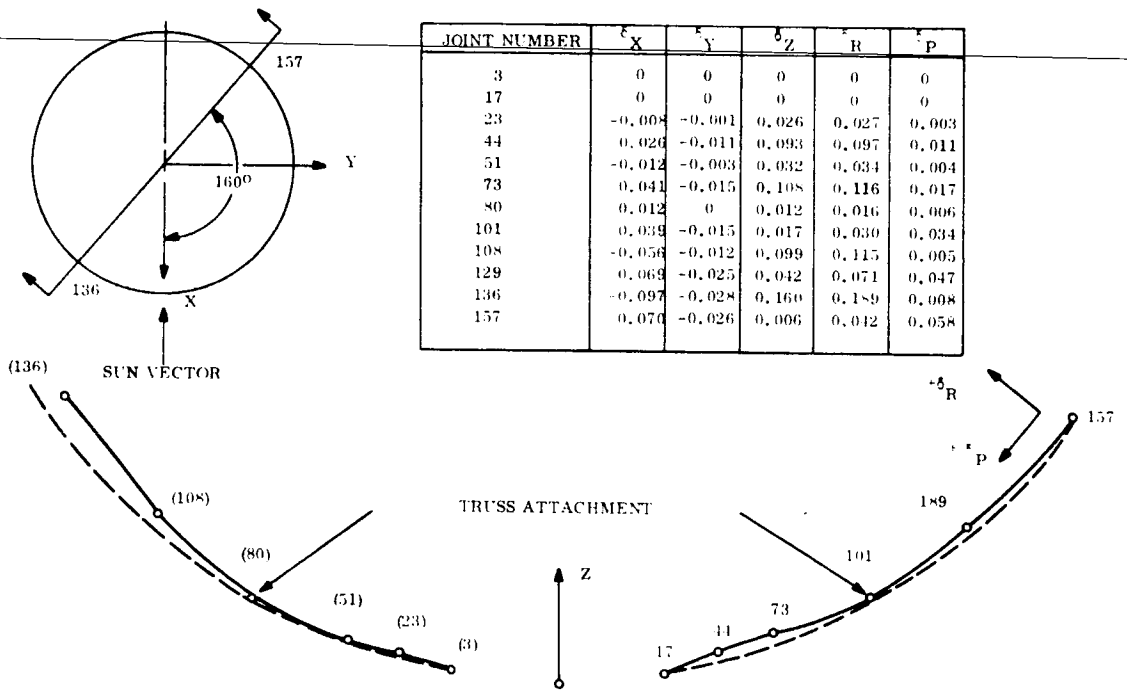
on distortions. Interestingly, the maximum deflections for the two cases are the same indicating that hub restraint is not a significant factor in determining the maximum excursions when the reflector is subjected to complex temperature distributions. The most significant effect of hub restraint was found to be in the stress distribution around the hub. As was discussed in Section 6.3.3.2.3, the stresses around the hub for a fixed hub become appreciable; whereas, it was found from computer results that corresponding stresses for a free hub are an order of magnitude less, as as predicted from earlier studies.

The results that are of most interest are those presented in Figures 6.3-62 to 6.3-66. These figures represent computer results for a fully hinged, fixed hub, titanium face sheet configuration. These results were used as a basis for thermal structural analysis as well as distortion analysis. Figures 6.3-39 to 6.3-45 of Section 6.3.3.2.3 show some of the computer



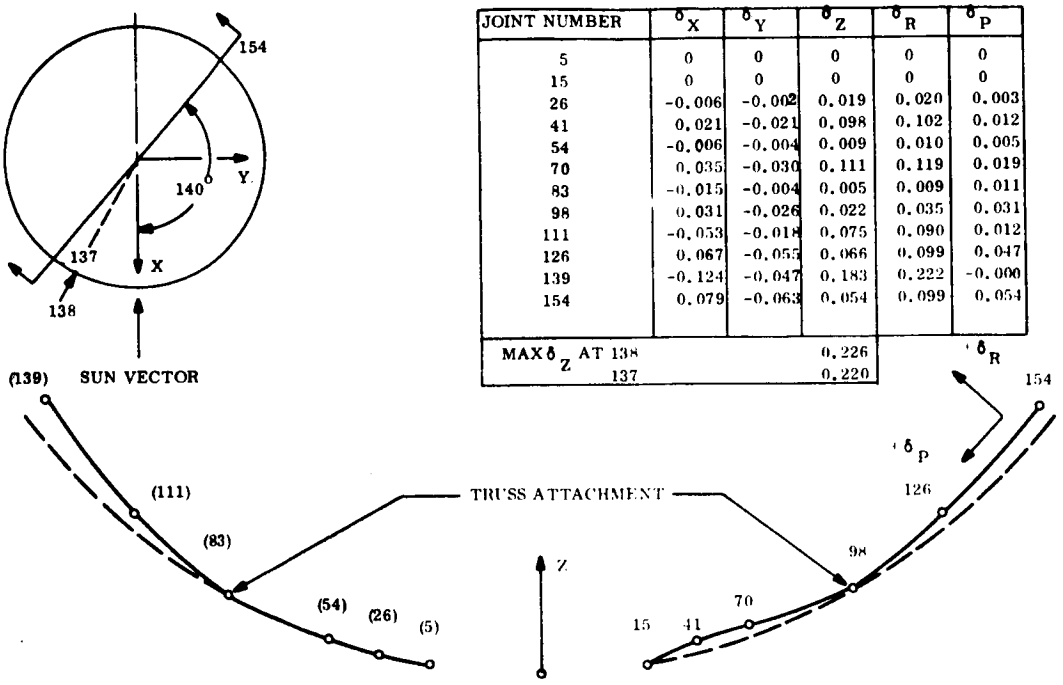
JOINT NUMBER	δ_X	δ_Y	δ_Z	δ_R	δ_P
1	0	0	0	0	0
19	0	0	0	0	0
20	-.008	0	.034	.035	.036
47	.024	0	.071	.074	.011
48	-.011	0	.035	.036	.003
76	.042	0	.100	.107	.017
77	-.008	0	0	.003	.007
104	.033	0	0	.011	.031
105	-.038	0	.059	.070	.007
132	.063	0	.022	.049	.046
133	-.019	0	.017	.025	.006
160	.056	0	-.019	.016	.057

Figure 6.3-62. Antenna Deflections Due to Temperature Gradients, Displacements of Radial Members θ=180 Degrees



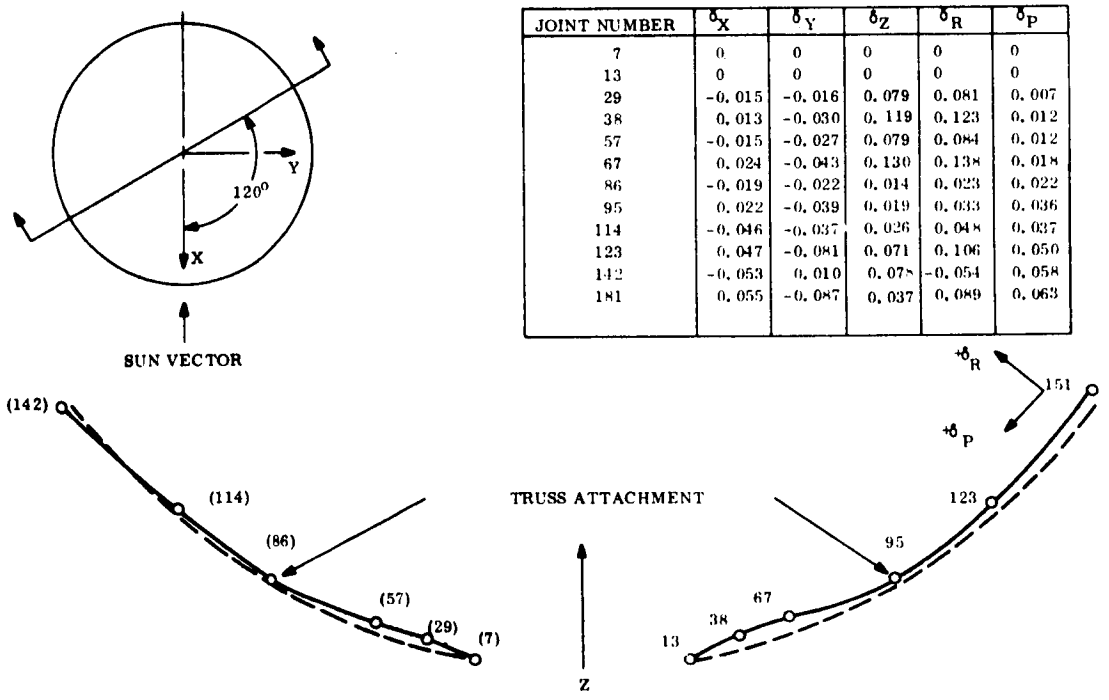
JOINT NUMBER	δ_X	δ_Y	δ_Z	δ_R	δ_P
3	0	0	0	0	0
17	0	0	0	0	0
23	-0.008	-0.001	0.026	0.027	0.003
44	0.026	-0.011	0.093	0.097	0.011
51	-0.012	-0.003	0.032	0.034	0.004
73	0.041	-0.015	0.108	0.116	0.017
80	0.012	0	0.012	0.016	0.006
101	0.039	-0.015	0.017	0.030	0.034
108	-0.056	-0.012	0.099	0.115	0.005
129	0.069	-0.025	0.042	0.071	0.047
136	-0.097	-0.028	0.160	0.189	0.008
157	0.070	-0.026	0.006	0.042	0.058

Figure 6.3-63. Antenna Deflections Due to Temperature Gradients, Displacements of Radial Members θ=160 Degrees



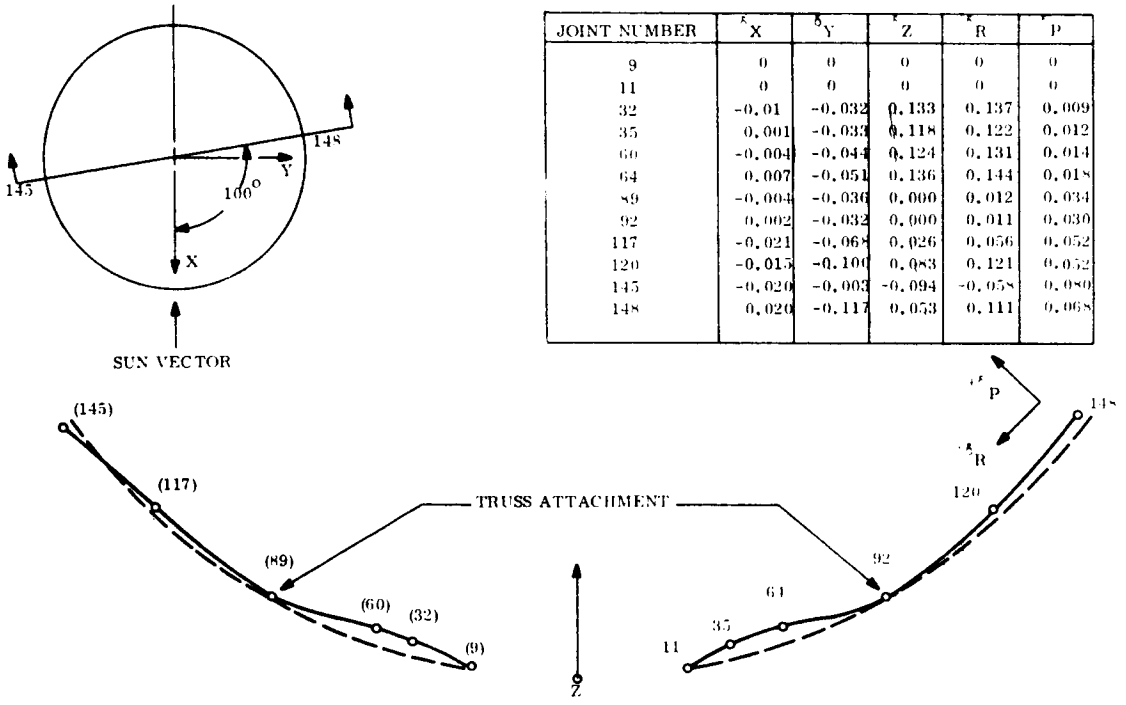
JOINT NUMBER	δ_X	δ_Y	δ_Z	δ_R	δ_P
5	0	0	0	0	0
15	0	0	0	0	0
26	-0.006	-0.002	0.019	0.020	0.003
41	0.021	-0.021	0.098	0.102	0.012
54	-0.006	-0.004	0.009	0.010	0.005
70	0.035	-0.030	0.111	0.119	0.019
83	-0.015	-0.004	0.005	0.009	0.011
98	0.031	-0.026	0.022	0.035	0.031
111	-0.053	-0.018	0.075	0.090	0.012
126	0.067	-0.055	0.066	0.099	0.047
139	-0.124	-0.047	0.183	0.222	-0.000
154	0.079	-0.063	0.054	0.099	0.054
MAX δ_Z AT 138			0.226		
137			0.220		

Figure 6.3-64. Antenna Deflections Due to Temperature Gradients, Displacements of Radial Members θ=140 Degrees



JOINT NUMBER	δ_X	δ_Y	δ_Z	δ_R	δ_P
7	0	0	0	0	0
13	0	0	0	0	0
29	-0.015	-0.016	0.079	0.081	0.007
38	0.013	-0.030	0.119	0.123	0.012
57	-0.015	-0.027	0.079	0.084	0.012
67	0.024	-0.043	0.130	0.138	0.018
86	-0.019	-0.022	0.014	0.023	0.022
95	0.022	-0.039	0.019	0.033	0.036
114	-0.046	-0.037	0.026	0.048	0.037
123	0.047	-0.081	0.071	0.106	0.050
142	-0.053	0.010	0.078	-0.054	0.058
181	0.055	-0.087	0.037	0.089	0.063

Figure 6.3-65. Antenna Deflections Due to Temperature Gradients, Displacements of Radial Members θ=120 Degrees



JOINT NUMBER	X	Y	Z	R	P
9	0	0	0	0	0
11	0	0	0	0	0
32	-0.01	-0.032	0.133	0.137	0.009
35	0.001	-0.033	0.118	0.122	0.012
60	-0.004	-0.044	0.124	0.131	0.014
64	0.007	-0.051	0.136	0.144	0.018
89	-0.004	-0.036	0.000	0.012	0.034
92	0.002	-0.032	0.000	0.011	0.030
117	-0.021	-0.068	0.026	0.056	0.052
120	-0.015	-0.100	0.083	0.121	0.052
145	-0.020	-0.003	-0.094	-0.058	0.080
148	0.020	-0.117	0.053	0.111	0.068

Figure 6.3-66. Antenna Deflections Due to Temperature Gradients, Displacements of Radial Members $\vartheta = 100$ Degrees

output sheets for this configuration that define individual member behavior. The particular members chosen were the set that intersect at a deployment truss connection because these were found to have the highest stresses, other than the sections of petals adjacent to the hub. Figures 6.3-62 to 6.3-66 contain a pictorial representation of the deflection profile of cross-sections cut by vertical planes at 20-degree increments of arc. When studied in sequence, they give the clearest insight into reflector behavior. The deflections are drawn to an exaggerated scale to separate the deflected shape from the original surface. Included on the figures, however, is a tabulation of the joint distortions, both in the x-y-z coordinate system and in the member coordinate system (normal to surface and meridianal). This tabulation may be used for quantitative evaluations. Of particular interest, aside from deflection magnitudes, is the deployment truss constraint. The ramifications of this constraint are readily apparent from these figures because a point of almost zero deflection (nodal point) is imposed at every truss connection. Thus is expected because the flexural rigidity of the truss is very

great in comparison with the reflectors and the thermal gradients through the truss itself are negligible. Because of the latter, no out-of-plane truss distortions are produced, and the trusses simply expand and contract with no accompanying changes in curvature. It is understandable from these pictorial representations of the reflector surface that high stresses are found over the deployment truss fittings because they represent structural discontinuities. The complete set of six directional displacements for every joint can be found in Table 6.3-9. Joints are located in Figure 6.3-58.

Generally, little difference was found between the deflections encountered between a hinged and non-hinged configuration. If it were desired, hinge lines could be locked after deployment. This locking could readily be accomplished by small preload springs, as moments at the hinge line for the fixed hinge line case did not exceed 4 inch-pounds. For the configuration chosen, the parameters that most affected the thermal distortions of the antenna were found to be the temperature distribution and the thermal expansion coefficient of the face sheet material. The conclusions drawn from this thermal distortion analysis of the reflector are that thermal distortions and stresses are relatively small for the worst case thermal distributions expected in the mission profile. The rf losses due to the reflector deflections are shown in Section 6.3.5.8 and are based on the displacements of Figure 6.3-67 which are believed conservative.

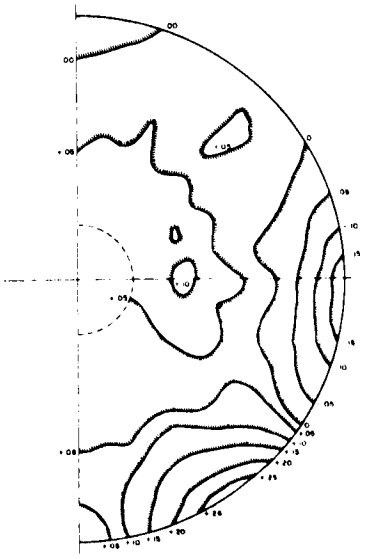


Figure 6.3-67. Case 39-90, Deviation Plot (Symmetrical about Centerline)

Table 6.3-9. Directional Displacements for Structural Joints (1 of 6)

	* * DEFLECTIONS * *					
JOINT	DIRECTION 1	DIRECTION 2	DIRECTION 3	DIRECTION 4	DIRECTION 5	DIRECTION 6
1	0.	0.	0.	0.	0.	0.
3	0.	0.	0.	0.	0.	0.
5	0.	0.	0.	0.	0.	0.
7	0.	0.	0.	0.	0.	0.
9	0.	0.	0.	0.	0.	0.
11	0.	0.	0.	0.	0.	0.
13	0.	0.	0.	0.	0.	0.
15	0.	0.	0.	0.	0.	0.
17	0.	0.	0.	0.	0.	0.
19	0.	0.	0.	0.	0.	0.
20	-8.2891-03	0.	0.	0.	-1.2814-03	3.4554-02
21	-9.0465-03	-3.6559-04	3.1865-04	3.4621-04	-1.3708-03	3.5308-02
22	-8.3204-03	-9.7264-04	-3.8286-04	-1.6940-04	-1.3844-03	3.1531-02
23	-7.5053-03	-1.0767-03	-4.5795-05	-8.0139-04	-1.4371-03	2.6175-02
24	-7.9757-03	-1.6465-03	3.9506-04	8.7417-04	-8.3810-04	2.7822-02
25	-7.2763-03	-1.7126-03	-4.4103-04	-1.6164-04	-1.0716-03	2.2992-02
26	-6.9234-03	-1.7914-03	2.7997-04	-4.8734-05	-1.1772-03	1.9064-02
27	-8.6620-03	-3.7240-03	8.3811-04	1.2444-03	-7.1594-04	1.9249-02
28	-1.4944-02	-1.4011-02	3.6846-04	4.1824-03	1.8396-03	6.0934-02
29	-1.4802-02	-1.6356-02	5.5457-04	2.1815-03	-1.5954-03	7.8808-02
30	-1.4875-02	-1.9952-02	8.9116-04	3.6886-03	-5.3054-04	8.2474-02
31	-1.2493-02	-2.9863-02	1.2935-04	4.2153-03	1.5995-03	1.3095-01
32	-1.0672-02	-3.2195-02	6.9025-04	4.3418-03	3.6045-05	1.3340-01
33	-8.7306-03	-3.6147-02	8.3922-04	5.3181-03	5.3892-04	1.3721-01
34	-1.1207-03	-3.4335-02	-6.6378-04	4.5746-03	-1.0172-03	1.2607-01

Table 6.3-9. Directional Displacements for Structural Joints (2 of 6)

	* * DEFLECTIONS * *					
JOINT	DIRECTION 1	DIRECTION 2	DIRECTION 3	DIRECTION 4	DIRECTION 5	DIRECTION 6
35	1.3729-03	-3.3143-02	1.3129-04	4.4685-03	-1.1778-03	1.1776-01
36	4.2777-03	-3.4422-02	6.1830-04	4.3842-03	1.5737-03	1.1944-01
37	1.0889-02	-3.1898-02	-4.1752-04	4.2488-03	1.6260-03	1.2486-01
38	1.3024-02	-3.0826-02	2.0824-04	4.5505-03	1.0071-03	1.1895-01
39	1.5938-02	-3.0571-02	3.9266-04	4.2288-03	2.2948-03	1.1662-01
40	2.0042-02	-2.4041-02	-6.7829-04	3.6722-03	1.8657-03	1.0608-01
41	2.0949-02	-2.1484-02	9.2758-05	3.7841-03	1.6683-03	9.8171-02
42	2.3759-02	-2.0613-02	5.0608-04	2.0069-03	3.5629-03	9.9879-02
43	2.4917-02	-1.3357-02	-5.3724-04	2.6594-03	2.6970-03	8.9091-02
44	2.5732-02	-1.1178-02	3.3738-04	3.8802-04	3.8374-03	9.3085-02
45	2.8103-02	-9.5555-03	3.7886-04	5.6164-04	4.1174-03	9.5631-02
46	2.4633-02	-2.2473-03	-6.2695-04	2.3031-03	3.2695-03	7.1843-02
47	2.3804-02	0.	0.	0.	3.2693-03	7.1247-02
48	-1.1158-02	0.	0.	0.	1.0505-03	3.4556-02
49	-1.1917-02	-9.5742-04	2.0721-04	7.1468-05	1.0905-03	3.3834-02
50	-1.2739-02	-2.5776-03	-9.5372-05	4.0182-05	2.1013-04	9.8029-02
51	-1.1513-02	-3.1556-03	-1.3277-04	-7.9623-04	-5.2775-04	9.1594-02
52	-1.1331-02	-4.0629-03	2.2894-05	2.5678-05	3.9093-04	9.1777-02
53	-7.1305-03	-3.3493-03	-2.9942-04	-1.7212-03	3.2015-04	1.0776-02
54	-6.4730-03	-4.0772-03	8.1863-05	-1.0168-03	9.2020-04	9.4301-03
55	-7.5817-03	-6.4367-03	5.1280-04	-1.1112-03	1.6483-03	9.4810-03
56	-1.3921-02	-1.9212-02	1.0514-03	1.3697-03	4.7460-03	8.2975-02
57	-1.5049-02	-2.6962-02	7.1829-04	4.7722-04	2.0556-03	7.8514-02
58	-1.4046-02	-3.3001-02	3.9040-04	-3.0535-04	2.2620-03	9.2132-02
59	-7.3679-03	-3.8022-02	3.2626-04	-2.0177-03	2.6635-03	1.0368-01

Table 6.3-9. Directional Displacements for Structural Joints (3 of 6)

	* * DEFLECTIONS * *					
JOINT	DIRECTION 1	DIRECTION 2	DIRECTION 3	DIRECTION 4	DIRECTION 5	DIRECTION 6
60	-3.7346-03	-4.4526-02	7.8849-04	-2.9201-03	3.5627-03	1.2394-01
61	-6.6441-03	-5.1740-02	8.6906-04	-3.7290-03	3.4011-03	1.4400-01
63	2.2365-03	-5.2375-02	-2.9262-04	-9.4110-04	-3.8769-04	1.4262-01
64	7.2704-03	-5.0682-02	-1.3842-04	7.4704-04	-1.1675-03	1.3553-01
65	1.2525-02	-5.0711-02	1.5292-04	-1.1321-03	3.0656-04	1.3697-01
66	1.9795-02	-4.6215-02	-1.2751-04	-2.0173-03	-6.1871-04	1.3236-01
67	2.3837-02	-4.3775-02	-2.2664-04	-1.6491-03	-1.5231-03	1.2979-01
68	2.7493-02	-4.0139-02	-5.3221-05	-1.7383-03	-1.9467-03	1.2256-01
69	3.3278-02	-3.4364-02	-2.4172-04	-5.7355-04	-8.4703-04	1.1924-01
70	3.5350-02	-3.0043-02	-1.7181-04	7.3844-04	-9.2374-04	1.1115-01
71	3.8866-02	-2.7049-02	1.1048-04	-1.0681-03	-3.7933-04	1.1480-01
72	3.9156-02	-1.8719-02	-3.0994-04	2.2575-04	-1.4194-03	9.8148-02
73	4.1009-02	-1.4881-02	1.4507-04	-1.6242-03	-8.2351-04	1.0838-01
74	4.3629-02	-1.1345-02	2.2587-04	-8.3356-04	-1.3358-03	1.1017-01
75	4.3303-02	-4.4718-03	-3.8079-04	9.8144-04	6.1197-06	1.0324-01
76	4.1707-02	0.	0.	0.	2.8975-04	1.0021-01
77	-7.7352-03	0.	0.	0.	-1.4054-03	1.9788-05
78	-2.3603-02	-2.0289-03	8.5548-04	2.6814-03	-1.3516-03	4.3426-02
79	-2.2430-02	-2.7069-03	-4.9660-04	-1.7236-04	-5.0153-04	4.4979-02
80	-1.1506-02	-8.5107-04	-1.5159-04	-1.4060-03	-5.8881-04	1.2649-02
81	-2.2453-02	-6.7948-03	7.6831-04	1.9556-03	9.2685-05	4.2816-02
82	-2.3712-02	-8.7254-03	-3.5747-04	2.0417-04	-2.1749-03	3.6690-02
83	-1.4900-02	-3.7896-03	-4.0313-04	-9.1465-04	-2.1140-03	4.5574-03
84	-1.7102-02	-7.9225-03	5.5436-04	7.6742-04	-6.8832-04	1.7260-03
85	-2.1021-02	-1.6656-02	6.5364-04	6.3317-04	1.4412-03	1.9430-02

Table 6.3-9. Directional Displacements for Structural Joints (4 of 6)

	* * DEFLECTIONS * *					
JOINT	DIRECTION 1	DIRECTION 2	DIRECTION 3	DIRECTION 4	DIRECTION 5	DIRECTION 6
86	-1.9263-02	-2.2048-02	6.3038-04	-1.2954-03	9.1769-04	1.4017-02
87	-2.0802-02	-3.8928-02	8.7399-04	-6.2545-04	2.3790-03	4.6206-02
88	-1.4560-02	-4.3084-02	-6.7158-04	-6.8957-04	-6.3612-04	4.1955-02
89	-3.7971-03	-3.6131-02	2.2373-03	7.2281-04	1.8459-04	5.8570-05
90	-4.3317-03	-9.1788-02	2.3972-03	2.8699-03	7.9610-03	1.4398-01
91	1.3318-03	-8.0477-02	-2.2973-03	-1.6020-03	-2.4859-03	1.2865-01
92	2.0304-03	-3.2325-02	-1.7679-03	-3.1158-03	-7.2923-03	2.0756-04
93	1.8515-02	-6.3092-02	2.2025-03	-2.9140-03	4.7868-03	8.3817-02
94	2.6929-02	-6.5355-02	-9.7603-04	1.2370-03	-2.7317-04	8.7583-02
95	2.2478-02	-3.9418-02	-5.5678-04	1.9842-03	-2.8556-03	1.8789-02
96	4.0833-02	-5.3787-02	1.2538-03	-9.3484-04	3.6454-03	7.8666-02
97	4.3553-02	-4.7898-02	-1.0203-03	-1.9831-04	-8.0956-04	8.5400-02
98	3.1265-02	-2.6274-02	-6.3156-04	1.0665-03	-3.6177-03	2.2049-02
99	5.1344-02	-3.2285-02	1.4564-03	-3.6476-03	8.5641-04	7.5432-02
100	6.1284-02	-3.1110-02	-6.9149-04	5.8785-04	4.5434-04	8.5536-02
101	3.9643-02	-1.4640-02	-7.1183-04	3.2516-03	-1.2573-03	1.6866-02
102	5.8256-02	-1.3512-02	8.5765-04	-2.5851-03	7.1176-04	8.4577-02
103	5.1733-02	-6.9806-03	-1.2072-03	1.3361-03	-1.9159-03	9.1798-02
104	3.2637-02	0.	0.	0.	-2.3361-03	8.0548-05
105	-3.8173-02	0.	0.	0.	2.4759-04	9.9489-02
106	-4.0649-02	-3.2914-03	3.6985-04	8.7538-04	-3.6196-04	6.7622-02
107	-4.5021-02	-6.0373-03	4.5534-04	1.0379-03	-1.4606-03	7.6380-02
108	-5.5839-02	-1.2460-02	4.4997-04	1.6492-03	-2.0107-03	9.9650-02
109	-5.9331-02	-1.7604-02	3.7947-04	1.8345-03	-2.5254-03	1.0679-01
110	-5.9781-02	-2.0089-02	1.6056-05	1.0720-03	-2.8174-03	1.0302-01

Table 6.3-9. Directional Displacements for Structural Joints (5 of 6)

	* * DEFLECTIONS * *					
JOINT	DIRECTION 1	DIRECTION 2	DIRECTION 3	DIRECTION 4	DIRECTION 5	DIRECTION 6
111	-5.2824-02	-1.8716-02	-5.7644-04	5.9384-05	-8.0665-03	7.5272-02
112	-4.3434-02	-1.4386-02	4.7694-05	2.6929-04	-8.5680-03	8.2657-02
113	-4.5578-02	-2.2289-02	6.1410-04	7.7918-04	-1.0811-03	2.7628-02
114	-4.6452-02	-3.7122-02	8.0635-05	-1.0244-03	-3.0798-04	2.5907-02
115	-3.4169-02	-3.4520-02	-2.3273-05	-1.6081-03	-6.3670-04	-1.2305-02
116	-2.8303-02	-4.0901-02	7.2604-04	-1.9741-03	1.1060-03	-6.6710-03
117	-2.1746-02	-6.8730-02	1.4301-03	-2.4017-03	2.7119-03	2.6104-02
118	-9.3599-03	-9.0858-02	1.2546-03	-7.3797-04	2.6439-03	6.8394-02
119	2.3479-04	-9.9650-02	2.2374-04	1.9478-03	2.7932-04	8.0345-02
120	1.5106-02	-1.0036-01	-3.7834-04	2.1338-03	-3.3170-04	8.3355-02
121	2.9016-02	-9.3497-02	1.6895-04	1.2035-03	9.2846-04	7.6700-02
122	3.6913-02	-8.8979-02	-1.7121-04	3.0104-04	-1.3894-04	7.6108-02
123	4.7243-02	-8.0560-02	-1.1185-04	-4.4258-04	-6.8034-04	7.1605-02
124	6.0170-02	-7.5812-02	5.2725-05	-3.5959-04	5.2628-04	8.4353-02
125	6.2764-02	-6.7198-02	-4.8653-04	1.3901-03	1.4669-04	7.6059-02
126	6.7276-02	-5.5244-02	-5.6416-04	1.2822-03	2.0209-04	8.6483-02
127	6.5703-02	-4.0609-02	6.0549-05	4.5724-04	7.3382-04	4.8142-02
128	7.0330-02	-3.6069-02	1.1691-04	-3.0709-04	-1.3826-04	5.3643-02
129	6.9274-02	-2.5139-02	-5.2970-04	6.0875-04	-1.3490-03	4.1684-02
130	6.4383-02	-1.4126-02	-1.8295-04	1.6389-04	-5.1401-04	2.8433-02
131	6.2674-02	-8.3766-03	-2.5604-04	7.9020-04	3.0797-04	2.1807-02
132	6.3330-02	0.	0.	0.	5.6787-04	2.2122-02
133	-1.9326-02	0.	0.	0.	1.6203-03	1.6793-02
134	-4.0973-02	-6.0739-03	1.2921-03	1.6787-03	7.5638-04	5.6836-02
135	-5.7069-02	-1.0941-02	1.3757-03	2.2460-03	2.4758-04	8.5434-02

Table 6.3-9. Directional Displacements for Structural Joints (6 of 6)

* * DEFLECTIONS * *

JOINT	DIRECTION 1	DIRECTION 2	DIRECTION 3	DIRECTION 4	DIRECTION 5	DIRECTION 6
136	-9.7037-02	-2.6784-02	1.7038-03	3.0159-03	-6.8532-04	1.5997-01
137	-1.3048-01	-4.6137-02	1.0268-03	2.8945-03	-2.2920-03	2.1976-01
138	-1.3596-01	-5.1565-02	2.3167-04	2.0189-03	-3.0467-03	2.2564-01
139	-1.2405-01	-4.7644-02	-8.7913-04	3.4512-04	-3.9190-03	1.8335-01
140	-9.8128-02	-2.8399-02	-1.2340-03	-1.8410-03	-3.5249-03	9.6070-02
141	-8.5788-02	-1.9082-02	-1.3530-03	-2.3493-03	-3.2801-03	4.1849-02
142	-5.3069-02	1.0497-02	-1.3020-03	-4.4689-03	-1.9427-03	-7.7712-02
143	-3.3149-02	2.0889-02	-1.5463-04	-4.2285-03	-1.2391-04	-1.4484-01
144	-2.6881-02	1.5225-02	7.1978-04	-3.6626-03	1.5666-03	-1.4470-01
145	-2.0804-02	-2.9968-02	2.3130-03	-2.8400-03	3.3944-03	-9.3527-02
146	-8.1414-03	-1.0031-01	2.1736-03	-1.1174-03	4.0952-03	2.2370-02
147	1.6502-03	-1.1824-01	7.9040-04	-7.0960-04	1.6749-03	4.9736-02
148	2.0231-02	-1.1705-01	-2.7457-04	-1.1854-03	-2.9507-04	5.2543-02
149	3.7275-02	-1.0790-01	-1.5543-04	-7.5605-04	-2.8984-04	4.8312-02
150	4.3784-02	-1.0155-01	-3.8504-04	-6.6813-04	-4.9487-04	4.6251-02
151	5.4502-02	-8.6789-02	-9.9518-05	-6.7745-04	-5.1191-04	3.7270-02
152	7.0989-02	-8.2638-02	2.6635-04	-8.5031-04	2.7984-04	5.8126-02
153	7.6328-02	-7.8747-02	-2.0419-04	-6.0937-05	-2.4179-04	5.8948-02
154	7.9546-02	-6.2795-02	-2.6595-04	1.9037-05	-5.0049-04	5.1443-02
155	8.4693-02	-5.0976-02	-2.1144-04	3.1926-04	2.7611-05	4.5356-02
156	8.3037-02	-4.3613-02	-5.3304-04	3.3013-04	-2.1532-04	4.1388-02
157	7.0463-02	-2.6019-02	-6.5897-04	8.3510-04	-1.1575-03	6.0602-03
158	6.3413-02	-1.3648-02	-2.6991-04	2.1675-04	-1.0223-03	-7.6471-03
159	6.0588-02	-8.6271-03	-3.3768-04	3.3048-04	-1.1226-03	-1.3488-02
160	5.6158-02	0.	0.	0.	-1.5453-03	-1.9119-02

6.3.4.3.3 Antenna Feed Distortion

Antenna feed distortions due to truss tube temperature variations are readily calculated using the theory previously discussed for antenna distortions. This case is simplified because the truss is statically determinate and the expression for deflection reduces to the following:

$$|D| = |T|^{T} |\delta| *$$

where

$|D|$ = (ζ, 1) Matrix of interface displacements

$|T|^{T}$ = is a (ζ, 6) matrix relating external loadings to internal loads

$|\delta|*$ = (ζ, 1) matrix of the individual member distortions due to temperature effects ($\delta = \alpha$ LΔT)

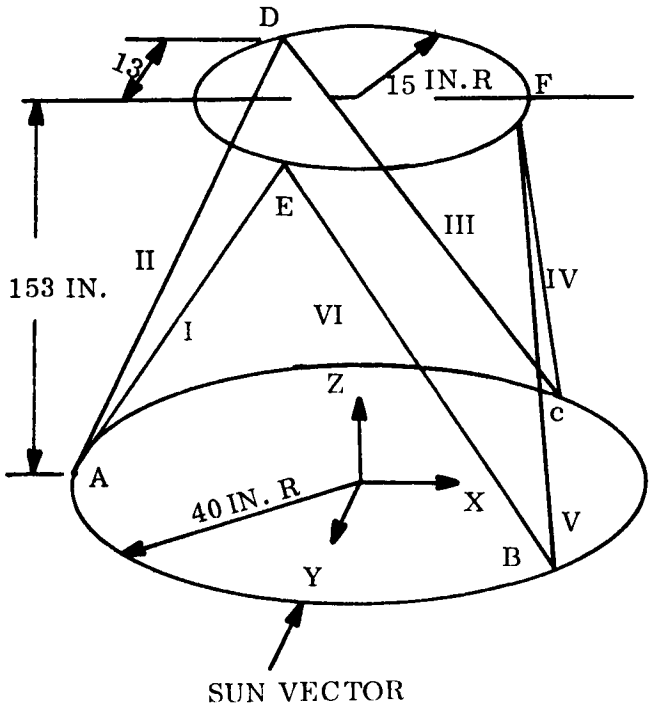
The solution of the problem used the truss geometry, nomenclature, and direction cosines shown in Figure 6.3-68. This information was incorporated into the following (ζ, 6) matrix 'A' which relates internal loads to external loads applied at the base of the feed:

$$\begin{vmatrix} \Sigma F_x \\ \Sigma F_y \\ \Sigma F_z \\ \Sigma M_x \\ \Sigma M_y \\ \Sigma M_z \end{vmatrix} = \begin{bmatrix} 0.207 & 0.207 & -0.175 & -0.032 & -0.032 & -0.175 \\ 0.083 & -0.083 & 0.138 & 0.220 & -0.220 & -0.138 \\ 0.975 & 0.975 & 0.975 & 0.975 & 0.975 & 0.975 \\ -12.68 & 12.68 & 12.68 & 0 & 0 & -12.68 \\ -7.31 & -7.31 & -7.31 & 14.62 & 14.62 & -7.31 \\ 3.31 & -3.31 & 3.30 & -3.30 & 3.31 & -3.31 \end{bmatrix} \begin{vmatrix} F_1 \\ F_2 \\ F_3 \\ F_4 \\ F_5 \\ F_6 \end{vmatrix}$$

a. Right hand rule for moments.

b. Positive sense of moments is same as for corresponding forces.

The problem was then programmed on the desk-side computer (linked to GE225) where the 'A' matrix was then inverted and transposed to establish T^{T}. The distortion matrices $|\delta|*$ were then read in and multiplied by T^{T} to yield interface displacements.



Member	X	Y	Z	L	X/L	Y/L	Z/L
I, AE	32.5	13.0	153	157	0.207	0.033	0.975
VI, BE	27.5	21.6	153	157	0.175	0.138	0.975
V, BF	5.0	34.6	153	157	0.032	0.220	0.975
IV, CF	5.0	34.6	153	157	0.032	0.220	0.975
III, CD	27.5	21.6	153	157	0.175	0.138	0.975
II, AD	32.5	13.0	153	159	0.207	0.083	0.975

Figure 6.3-68. Truss Geometry and Nomenclature used for Feed Distortion Analysis

The summary of maximum deflections for both the preferred ($\alpha/E = 2$) and the worst case is shown in Table 6.3-10 for two different orbital times.

Table 6.3-10. Feed Thermal Displacements

	$\alpha/E = 2$		$\alpha/E = 3$	
ΔX	-0.086	0.048	0	0.166
ΔY	0.049	0.028	0	0.096
ΔZ	0.009	0.043	0.12	0.0118
θX	-0.001	-0.0008	0	-0.0027
θY	-0.0006	-0.0005	0	0.0047
θZ	0.0033	0.0018	0	0.00639
Displacements in inches Rotations in radians				

The $|\delta|^*$ matrices were obtained using the predicted average truss temperatures as discussed in Section 5.9.6.4.5. The problem of feed motion due to temperature changes was handled in this analysis as dependent up on truss temperatures only. This is primarily true, however, secondary effects from distortions of the main structure and feed structure itself would have to be included for a more precise determination of displacements. For detailed analysis, the problem of establishing feed motions could be handled in the overall structural computer model.

6.3.5 RF PERFORMANCE ANALYSIS

6.3.5.1 Introduction

This section presents the detailed tradeoffs and design relationships used in arriving at the final feed configuration and in determining the overall rf system performance. A complete discussion of the various losses is given, and implementation of monopulse and beam steering operations is considered.

6.3.5.2 Feed Configuration Studies

6.3.5.2.1 General

The general requirements of the ATS-4 antenna were first examined through a baseline choice for geometry. Typical geometries for 0.3, 0.4 and 0.5 f/D are shown in Figures 6.3-69, 6.3-70, and 6.3-71 that include a preliminary design for Cassegrain geometry.

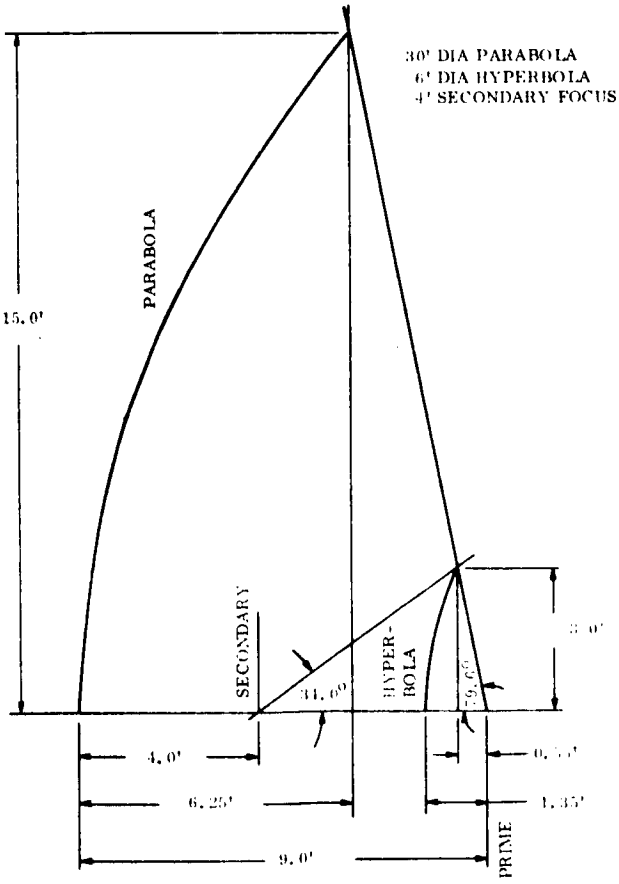


Figure 6.3-69. 0.3 f/D Geometry

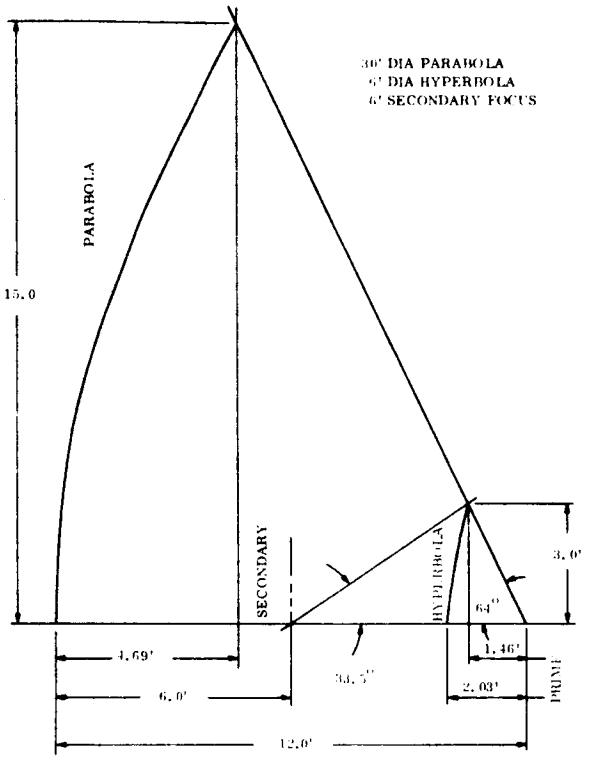


Figure 6.3-70. 0.4 f/D Geometry

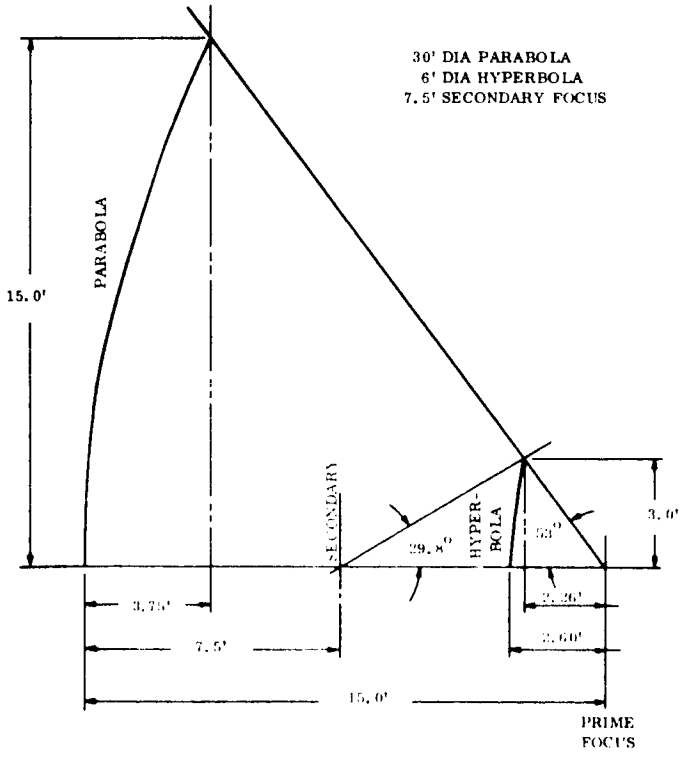


Figure 6.3-71. 0.5 f/D Geometry

The next step in the study of geometry choice involves tradeoff areas for alterations of the Cassegrain geometry. The nomenclature of the Cassegrain parameters is shown on Figure 6.3-72 and with the List of Symbols. These tradeoff areas are presented in Figures 6.3-73 through 6.3-77. The f/D ratios, subreflector size, and focal lengths were varied within limits that were considered to be practical. From these, the required feed horn size and lengths were found. Based upon geometrical relationships only, the curves contain inadmissible regions from the standpoint of operation in the near field of the horns. The dashed portion of the horn length curves indicate these regions, based upon a criterion of at least A^2/λ separation between the horn and the subreflector. The relationships and assumptions used to derive these data are included in the following geometry tradeoff notes.

a. Symbols and nomenclature are taken from Figure 6.3-72 and the List of Symbols.

b. The included half-angle of the main reflector, $\emptyset o$, was calculated from the relation:

$$\emptyset o = 2 \tan^{-1} \frac{1}{4\, f/D}$$

c. The subreflector focal lengths, f, were chosen so that $F/2 \leq f \leq F$.

d. The subreflector diameter, d, was varied between 6 feet, which approximately satisfies the minimum blocking criterion at 800 MHz, and 4 feet, which satisfies the minimum blocking criterion at about 1.9 GHz.

e. The included angle of the subreflector, α, was calculated from the relation,

$$\alpha = 2 \cot^{-1}\left(\frac{2f}{d} - \cot \emptyset o\right)$$

f. Feed diameters are for tradeoff illustration purposes. The feed system is assumed to consist of three coaxial conical horns. The diameters shown in Figures 6.3-75 through 6.3-77 are for the largest horn which operates at 0.8 GHz.

g. Feed size calculations were based on the following:

   1. 10 dB edge illumination of the subreflector

   2. The tenth-power beamwidth constant, $K_{1/10}$, equal to 132. This choice is based on measured conical horns having apertures of 3-4λ and phase errors Δ such that $\lambda/16 \leq \Delta \leq \lambda/4$.

h. Feed length calculations include only the tapered section of the horn when terminated in 8-inch diameter coax.

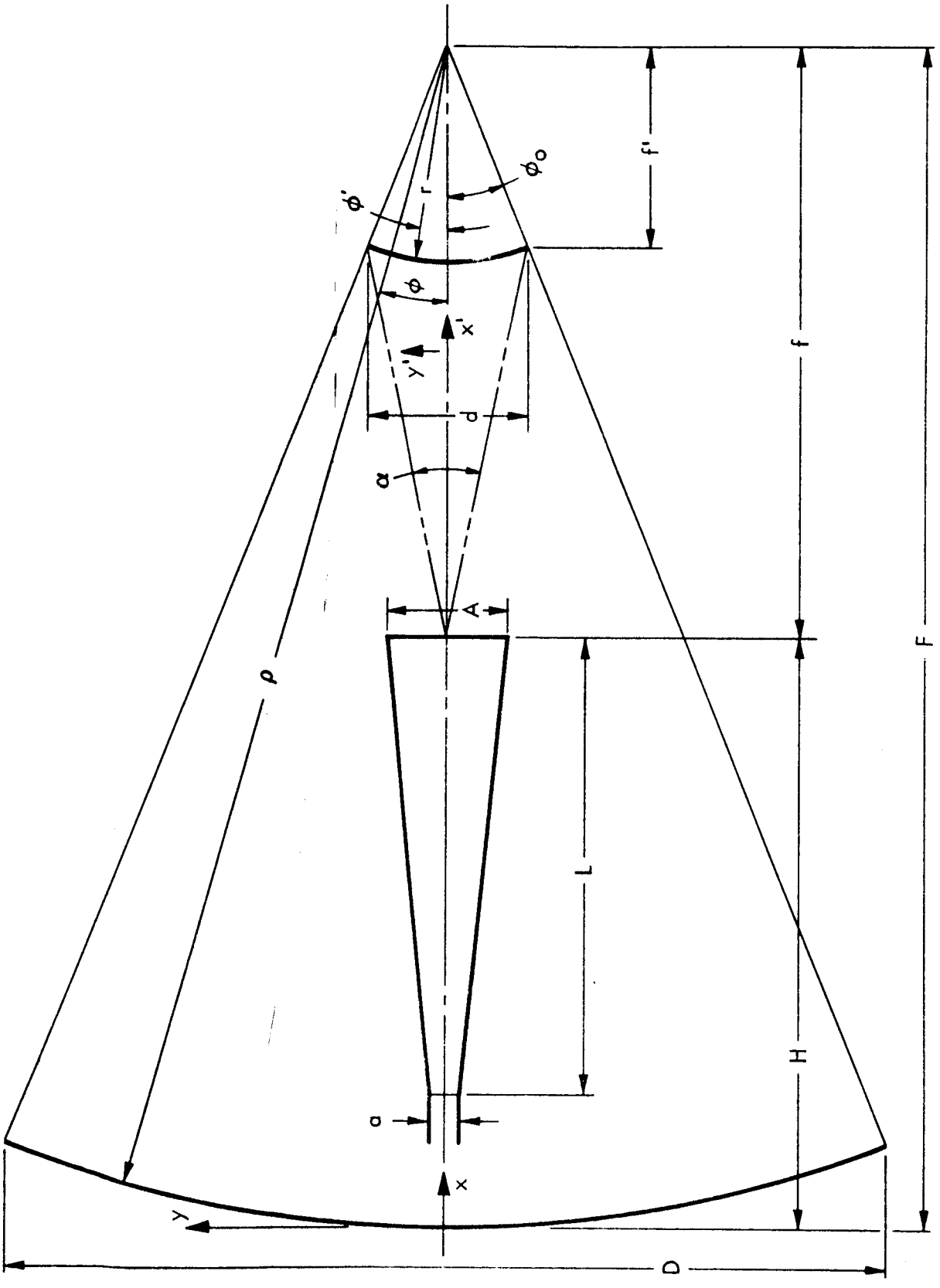


Figure 6.3-72. Cassegrain Antenna Nomenclature

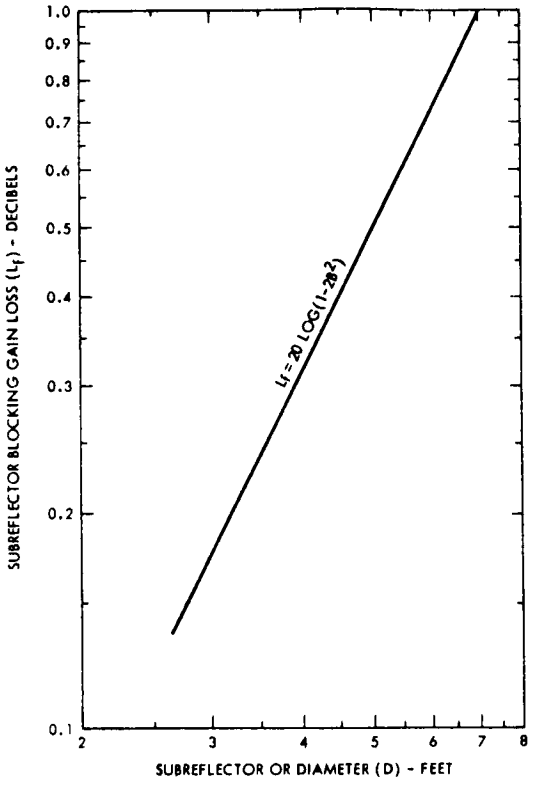


Figure 6.3-73. Subreflector Blocking Gain Loss

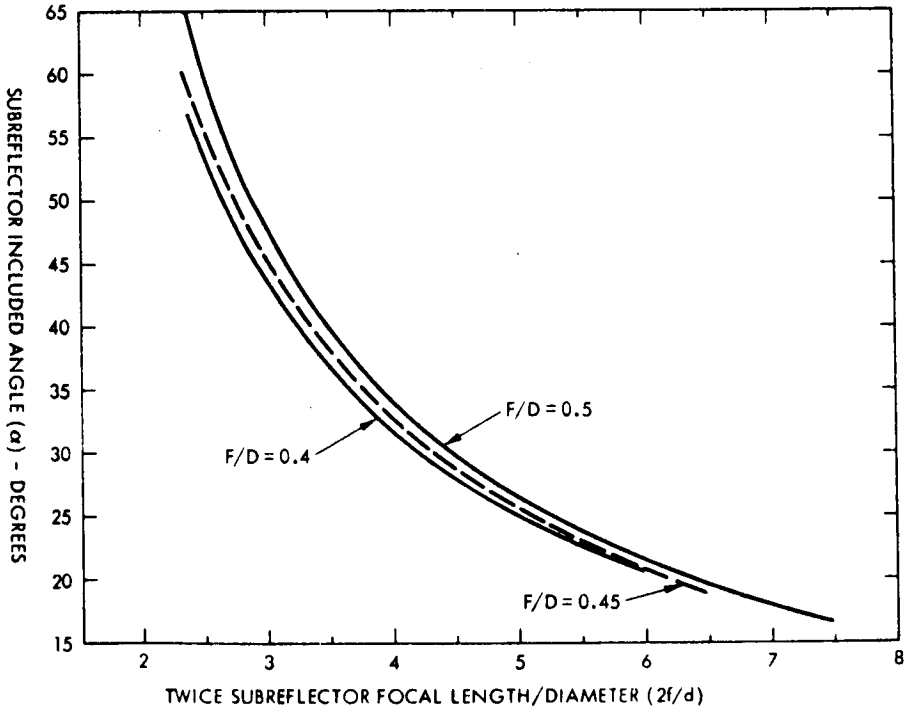


Figure 6.3-74. Subreflector Included Angle vs $\frac{2f}{d}$ for 30-foot Diameter Parabola

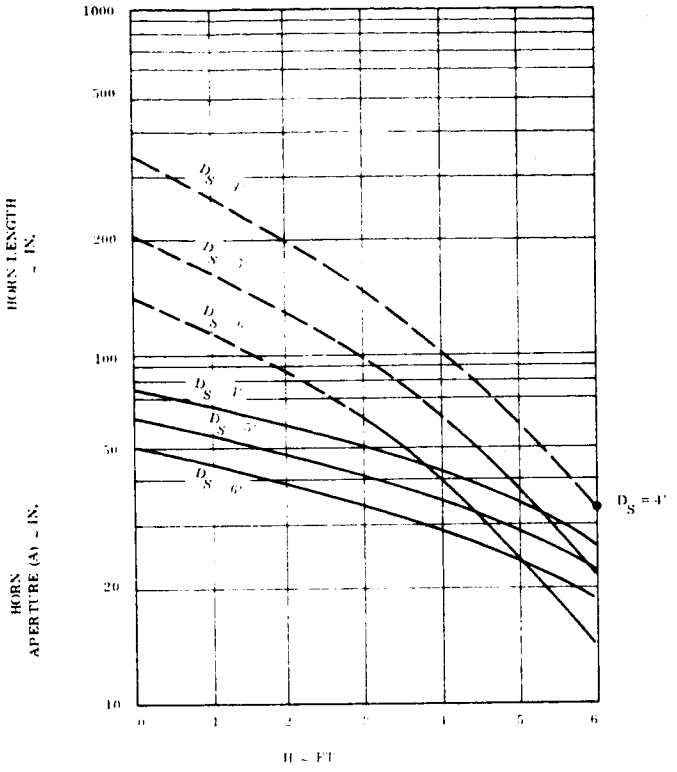


Figure 6.3-75. Horn Aperture and Length vs Secondary Focus H, f/D = 0.3

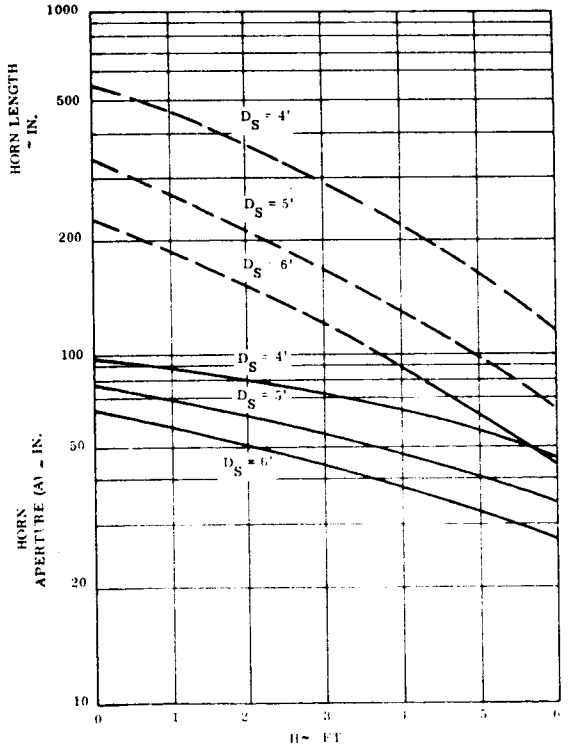


Figure 6.3-76. Horn Aperture and Length vs Secondary Focus H, f/D = 0.4

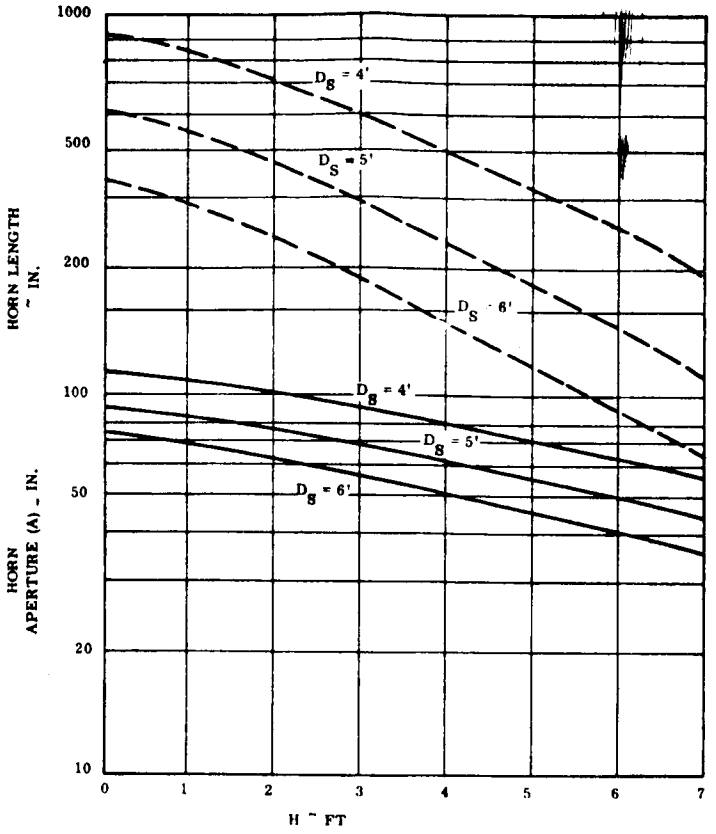


Figure 6.3-77. Horn Aperture and Length vs Secondary Focus H, f/D = 0.5

LIST OF SYMBOLS - FEED CONFIGURATION STUDIES

A	Feed H plane aperture
a	Width or height of waveguide at horn throat
B	Linear blocking ratio
b	Hyperbola constant
c	Hyperbola constant
D	Main dish diameter, inches
d	Subreflector diameter, inches
E_b	Maximum side-lobe level due to blockage, dB down
E_t	Theoretical side-lobe level, dB down
e	Base of natural logs
e_h	Subreflector blocking voltage
e_r	Reflector phase error voltage

e_s	Strut blocking voltage
e_t	Theoretical side-lobe voltage
F	Main dish focal length, inches
F_e	Equivalent parabola focal length, inches
f	Subreflector focal length, inches
f'	Distance from subreflector to parabola focal point, inches
G_a	Gain of main dish aperture with 100% efficiency, dB
G_L	Gain loss due to blocking, dB
H	Main dish vertex to feed aperture dimension, inches
k	Effective feed aperture to blocking diameter ratio
L	Feed horn length, inches
L_a	Feed attenuation loss, dB
L_f	Subreflector blocking loss, dB
L_h	Feed phase error loss, dB
L_i	Illumination taper loss, dB
L_l	Spillover loss, dB
L_n	Feed near field loss, dB
L_r	Reflector phase error loss, dB
L_s	Strut blocking loss, dB
M	Magnification ratio
n	Number of strut pairs
R	Resultant side-lobe level, dB
r	Radial coordinate of subreflector contour
S	Primary space attenuation, dB
S_o	Spillover fraction of feed energy
s	Strut diameter of width
T	Aperture illumination taper (edge illumination), dB
W	Length of package between feed horn and main dish, inches
x	Rectangular coordinate of main reflector contour
Δx	RMS surface error
x'	Rectangular coordinate of subreflector contour

y	Rectangular coordinate of main reflector contour
y'	Rectangular coordinate of subreflector contour
δ^2	Mean squared reflector phase error, $(\text{radians})^2$
ϵ	Hyperbola eccentricity
η	Antenna efficiency
η_a	Aperture efficiency
η_i	Illumination efficiency
Θ_{10}	Feed 10 dB beamwidth, degrees
Θ	Pattern far field angle, degrees
λ	Wavelength, inches
ϕ	Angular coordinate of main reflector contour, degrees
ϕ_{o_1}	Included half angle of main reflector, degrees
ϕ'	Angular coordinate of subreflector contour, degrees
ρ	Radial coordinate of main reflector contour

6.3.5.2.2 Configuration

The rf requirements for the ATS-4 antenna were analyzed in terms of various feeding schemes that could be used for the missions. Matrixes were prepared to permit preliminary selections of feed elements to be further considered. Charts were prepared for the following conditions:

a. 100 MHz (Transmit)

b. 800 MHz (Transmit)

c. 1.7 and 2.1 GHz (Receive), 2.3 GHz (Transmit)

d. 7.3 GHz (Transmit) 8.0 GHz (Receive)

e. 1.7 and 2.1 GHz (Receive) Monopulse

f. 8.0 GHz (Receive) Monopulse

Each matrix compares types of feeds for each tradeoff area as listed here:

a. Types (Prime Focus and Cassegrain)

1. Conical Spiral
2. Dielguide
3. Dipole
4. Helix
5. Horn
6. Log Periodic
7. Planar Spiral
8. Slot

b. Tradeoff Areas

1. Mechanical

(a) Height
(b) Width
(c) Depth
(d) Weight
(e) Precision
(f) Packaging
(g) Deployment
(h) Thermal

2. Auxiliary Electrical Circuitry

(a) Polarizers

(1) Type
(2) Physical size
(3) Availability

(b) Filters

(1) Type
(2) Physical size
(3) Availability

(c) Hybrids

(1) Type
(2) Physical size
(3) Availability

(d) Interconnecting Transmission Line

(1) Type
(2) Physical size

(e) Transmission Line to Interface

(1) Type
(2) Physical size

3. Auxiliary Mechanical Equipment

(a) Deployment

(1) Type
(2) Physical size

(b) Feed Movement

(1) Type
(2) Physical size

4. Performance Limitations

5. Development

(a) Requirements
(b) Risk

6. Feed Compatibility with other Feeds at Other Frequencies.

It was suggested during the study that a dielectric guiding scheme be used in a Cassegrain approach to lessen the spillover in the feed system. In examining a guiding scheme, total internal reflection at a dielectric free space interface must be used. Since total internal reflection occurs for incidence angles greater than the critical angle, typical critical angles are presented here for various dielectric constants, E.

E	Critical Angle (deg)
2.0	45
2.5	39
3.0	35
3.5	32
4.0	30

From f/D = 0.4 geometry for a Cassegrain $F' = \frac{F}{2}$, the critical angle can be no smaller than 43 degrees (by examining the ray to the edge of the subdish, 6-foot diameter). Then from Snell's law, the incidence angle is 28 degrees. For this Cassegrain and a relative dielectric constant of 2.0 the following points are observed:

a. Due to refractions, approximately 56 degrees of radiation from virtual feed cannot get past hyperbola without re-reflections, this would increase the effective subdish blocking diameter to:

$$\frac{1.56}{1.25} \times 6 \text{ feet} = 7.5 \text{ feet}$$

b. Within the 56 degree cone, the energy undergoes many reflections and refractions before re-entering the horn or leaving the feed system.

c. Due to refraction, the illumination taper (amplitude) of the virtual feed is compressed toward the center of the parabola's aperture.

d. The virtual focal point of the energy from the feed to the dish moves as a function of angle, this either provides various phase errors across the aperture or could require a new contour for the main reflector to correct these phase errors.

e. Using ray theory, the path lengths through the dielectric vary as a function of feed angle.

f. Phase errors are introduced as a function of feed angle at the dielectric space interface due to angle of incidence phase variations.

If it is assumed that the specific gravity of the dielectric is approximately 1.05, then the weight of this dielectric guide would be approximately 3,700 pounds.

The Parabolic Reflector Feed Selection Charts (see Appendix A) use a baseline design of a 0.4 f/D parabola, a 6-foot Cassegrain subdish diameter, and the Cassegrain feed is 6 feet from the parabola apex. Ten to 11 dB edge illuminations are used for maximum antenna efficiencies. Circular polarization is a baseline requirement. The following notes apply to the completed matrixes.

a. As soon as a particular feed was deemed unsuitable due to a particular rationale, the remainder of that row was left incomplete.

b. The broadband feeds were used for all frequencies (except 100 MHz) when axial interference with other feeds would result.

c. Under mechanical complexity, the structure is presented which uses maximum allowable tolerances for suitable electrical performance. More rigid structures may replace these if mechanically acceptable.

d. Mechanical equipment; this is any equipment necessary to position the feed after initial deployment of the antenna complements.

e. Under Performance Limitations and Feed Compatibility, the major difficulties are presented, even though other severe difficulties may exist.

f. Monopulse schemes in general are restricted to four feed, azimuth-elevation difference-type. For monopulse at X-band only, the use of dual modes in the inner horn of the three horn feed is possible.

Using acceptable and marginally acceptable feed members, six composite feed schemes were generated to be compared for suitability for the ATS-4 requirements. The log periodic structures were not included since the conical spiral will produce the same approximate results while not requiring a dual element structure. As may be noted under "Acceptability", the most suitable feed for a Cassegrain antenna is a multiple coaxial horn feed with a split subdish for 100 MHz. For the chosen prime focus configuration, the best feed is a multiple coaxial horn structure with a turnstile for 100 MHz.

6.3.5.3 Selected Feed Configuration

According to the results of the tradeoff study, a prime focus configuration is preferred on the basis of efficiency as shown in the loss budgets (Tables 6.3-11, -12, and -13). These were proposed to demonstrate the tradeoffs between prime focus and Cassegrain designs, and

are valid on this relative basis. The final loss budget reflects additional design effort on the preferred design and will therefore differ from the prime focus budget shown here.

Based on the selection of this concept, the f/D of 0.3 is discarded for the prime focus design since this would lead to undesirably small feed horn apertures. On the other hand, an f/D of 0.5 leads to undesirable structural dimensions. Therefore the selected configuration is developed for an f/D of 0.4.

The 100 MHz feed is a turnstile consisting of four quarter-wave rods projecting from the equipment module at 90 degree intervals around the horn cluster. The rods are inclined 30 degrees with respect to the mounting surface in order to realize satisfactory radiating performance. Since the parabola is only three wavelengths in diameter at 100 MHz, the 50 percent efficiency is not achieved since, at best, the small aperture is a poor collimator for rf energy.

The remaining frequencies are covered in three bands:

a. 800 MHz

b. 1.7, 2.1, 2.3 GHz

c. 7.3, 8.0 GHz

Each band covered by a conical horn which is coaxial with the other two. Although internal fins are shown for beamwidth control, external tabs could be used. The feed will have many properties similar to the feed for the ground-based 30 foot SYNCOM antenna.

This uses a circular waveguide through the center of the UHF feed. The UHF feed is operated in the coaxial TE_{11} mode. One of the major rf problems centered around the fact that two other modes can propagate in the UHF horn. On the SYNCOM antenna, several approaches and techniques were tried before good mode purity was achieved. Once achieved, however, this basically simple approach permits a very low noise temperature feed.

The bandwidths required for the ATS-4 feed are compatible with this triple coaxial horn design as evidenced by previous performance. The SYNCOM conical scan feed has a 12 percent bandwidth centered at 1800 MHz and the X-band transmitting feed has a 9-1/2 percent bandwidth centered at 7450 MHz.

Development schedules would be compatible with the ATS-4 program. The type of feed is conducive to good transmitter-receiver matches for the multifrequency requirement of ATS-4.

The pattern of each horn is affected by the presence of other horns. However, this effect is not severe. Figure 6.3-78 shows the SHF horn pattern with and without the UHF horn in position. Note that differences of one decibel occur only beyond the -10 dB points of the pattern.

The ATS-4, three-horn feed configuration is shown in Figure 6.3-79.

6.3.5.4 Monopulse

Monopulse operation may be achieved at 8 GHz by using an additional mode in the inner feed horn, the TM_{01}, in order to obtain the error signal. This produces a null on axis, and the phase and amplitude of the off-axis signal when referenced against the TE_{11} basic mode contain the desired information. Such a system requires a circularly polarized source having a good axial ratio; the ground equipment satisfies this condition. (For linear polarization the null point on axis degenerates into a null plane orthogonal to the axis of polarization since the radially symmetric field is not excited in this plane).

The inner horn of the feed configuration has an inside radius of 0.75 inch. With a slight flare to a 5/8 inch radius, the following cut off frequencies are realized:

Superscripts used in the following sections refer to the bibliography of 6.3.5.10.

TE_{11}	5500 MHz
TM_{01}	7200 MHz
TE_{01}	11500 MHz
TM_{11}	

The two desired modes will provide satisfactory operation at 8000 MHz; precautions must be taken to prevent excitation of the higher modes.

6.3.5.5 Beam Steering

6.3.5.5.1 General

During the course of this study program, the suggestion was made that the system be capable of pointing the rf beam anywhere in a 20 degree solid cone. This will produce serious effects at the higher frequencies.

Early work by Kelleher and Coleman indicates the loss of antenna gain as a function of the number of beamwidths scanned[8]. This work shows that for a $0.5\frac{f}{D}$ parabola, the beam may be scanned several beamwidths before a gain loss of a decibel is encountered. Displacement of the feed required to effect this beam tilt was studied in this project and later considered by Y. T. Lo[9]. Using the 30-foot SYNCOM ground-based antenna beamwidth constant where the dish illumination is similar to that desired here, half-power beamwidths at 7.3 and 8.0 GHz would be 0.32 and 0.29 degrees, respectively. Thus, at 8.0 GHz, a net beam displacement of approximately 35 beamwidths is required for 10 degrees of scan.

Figure 6.3-80 shows a net gain reduction of approximately 1.2 dB for two degrees of scan. Beyond this region, the gain falls off rapidly. Although more coverage is provided, it is obtained at a significant sacrifice of antenna gain. At the same time, the coma lobe can increase to an undesirably high level.

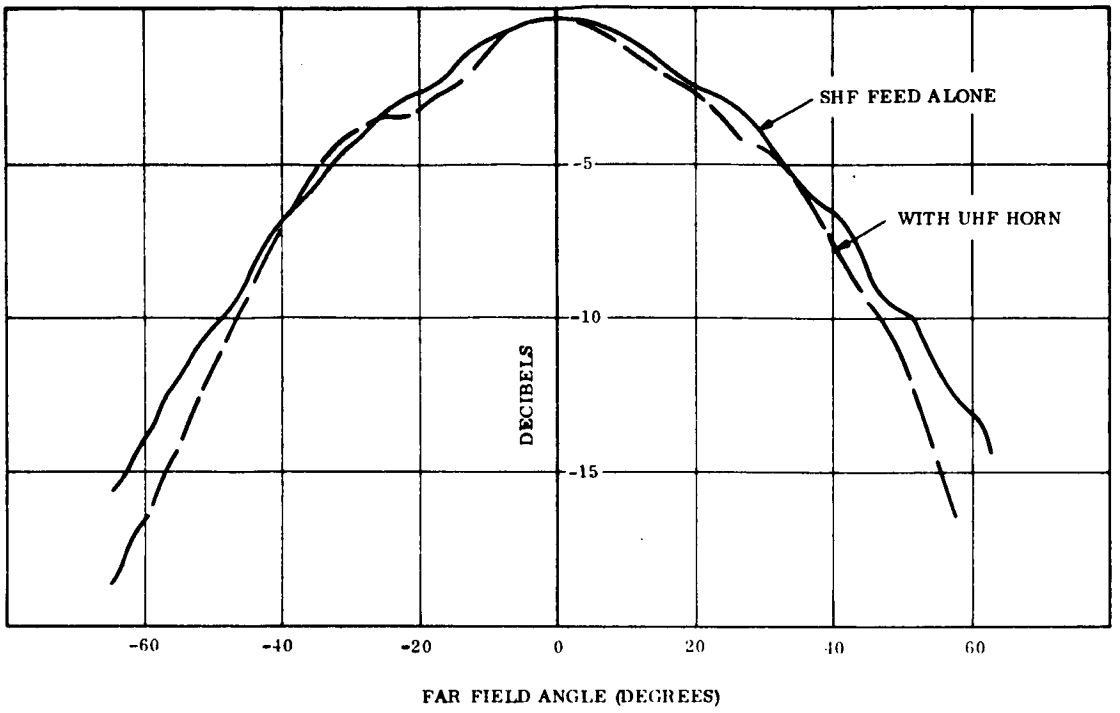


Figure 6.3-78. Syncom SHF Feed Patterns

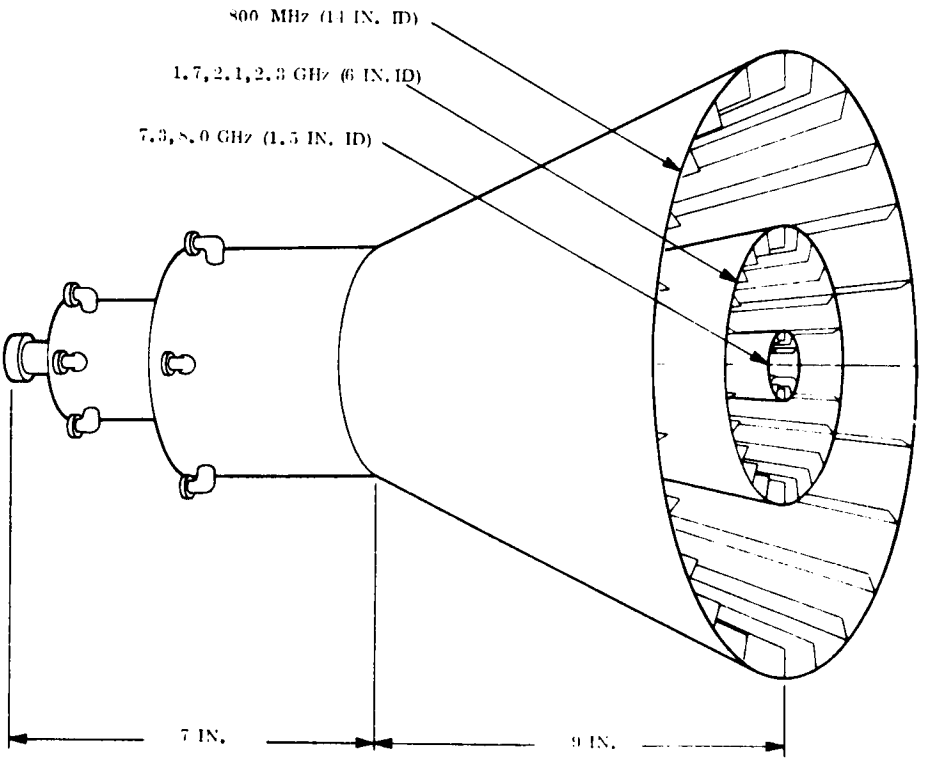


Figure 6.3-79. Feed Configuration

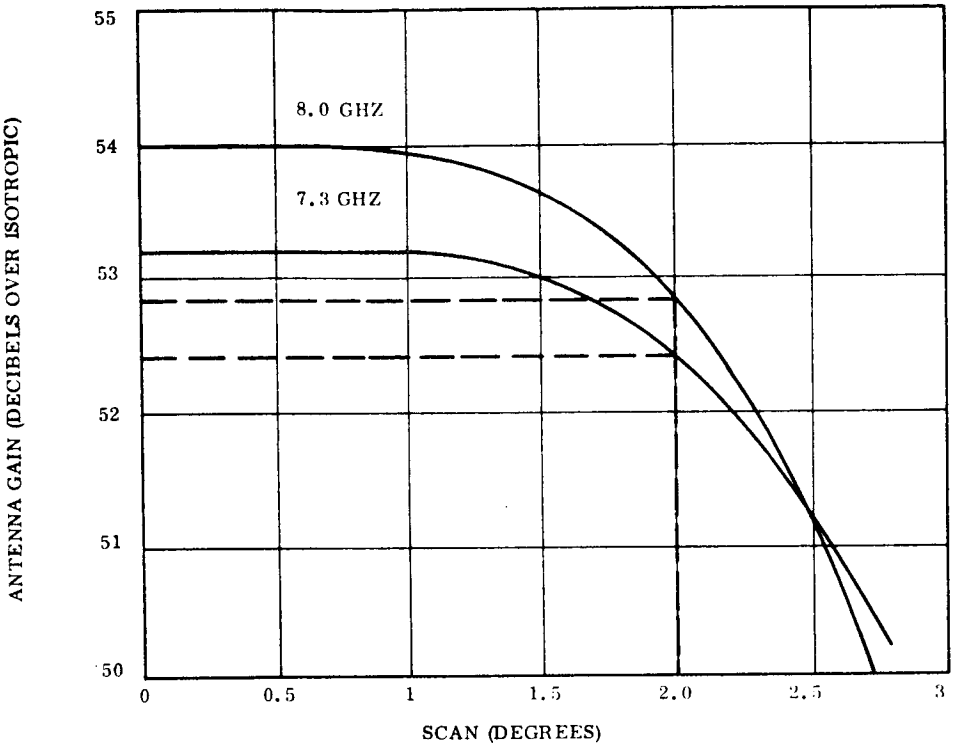


Figure 6.3-80. Gain Degradation vs Scan Angle

6.3.5.5.2 Suggested Scanning Scheme

Any scanning beyond a 4-degree solid cone reduces antenna efficiency to that of a poor antenna and creates rf interference problems with the resulting coma lobes. The side-lobe level with ± 2 degree scan capability would be as low as possible while optimizing gain and scanning performance.

A simple mechanical scheme could be used to produce reliable movement for accurate pointing of the beam. The method suggested is a simple movement of the feed around the apex of the parabolic reflector. Positioning the feed to one side, produces beam displacement to the opposite side of the reflector.

Because the reflector is parabolic rather than flat, there is a nonlinear correspondence between feed displacement and beam angle. For a 0.4 f/D parabola, the feed must be displaced approximately 2.3 degrees for a 2.0 degree beam displacement. The effect of these movements on the antenna efficiency is shown in Figure 6.3-81.

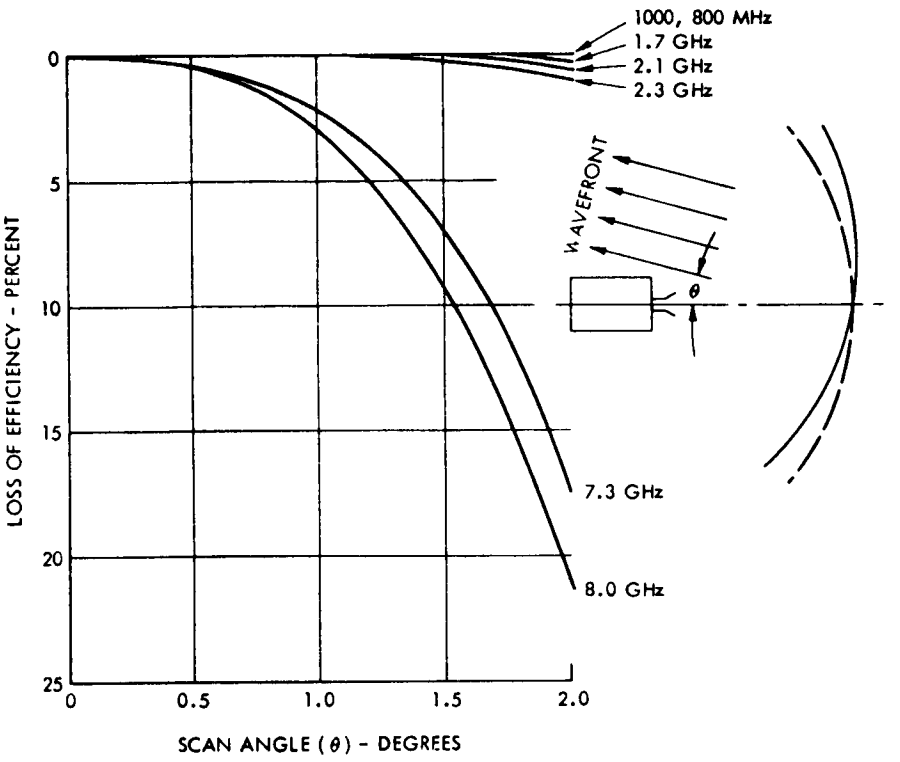


Figure 6.3-81. Gain Performance for Scanning Scheme

At 100 and 800 MHz, gain degradation is insignificant. This is expected because at 800 MHz the half-power beam width of the 30-foot diameter parabola is approximately 3 degrees.

6.3.5.5.3 Distributed Feed Alternate

Analysis of the image plane or focal plane for off-axis operation of a paraboloidal reflector has indicated the applicability of line-source and area-source feeds at the prime focus for beam steering.[12] [13] Results indicate that the area source is ultimately the best for beam scanning with a fixed paraboloid. Using shaped-area source feed with steering, phase, and amplitude control would give the greatest experimental flexibility. Not only steering but beam shaping could be accomplished with this feed. Figure 6.3-82 shows the loci of best azimuth focusing for three elevation angles. The loci are equivalent to a slice through a distributed feed surface. Figure 6.3-83 shows E-plane patterns using a small horn at Y_M of Figure 6.3-82 and a distributed line feed with beam steering of 15 degrees. Gain improvement is 4 dB and sidelobe reduction is 2 dB.

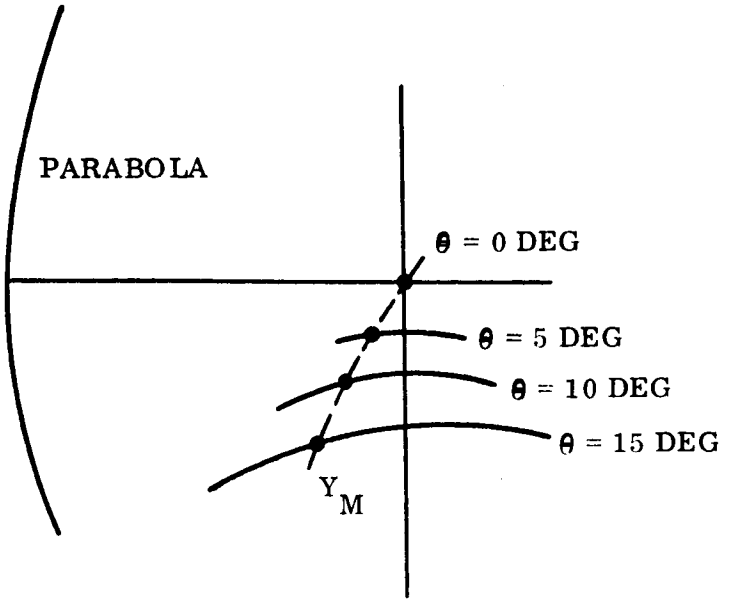


Figure 6.3-82. Loci of Best Azimuth Focus for Various Elevation Angles θ

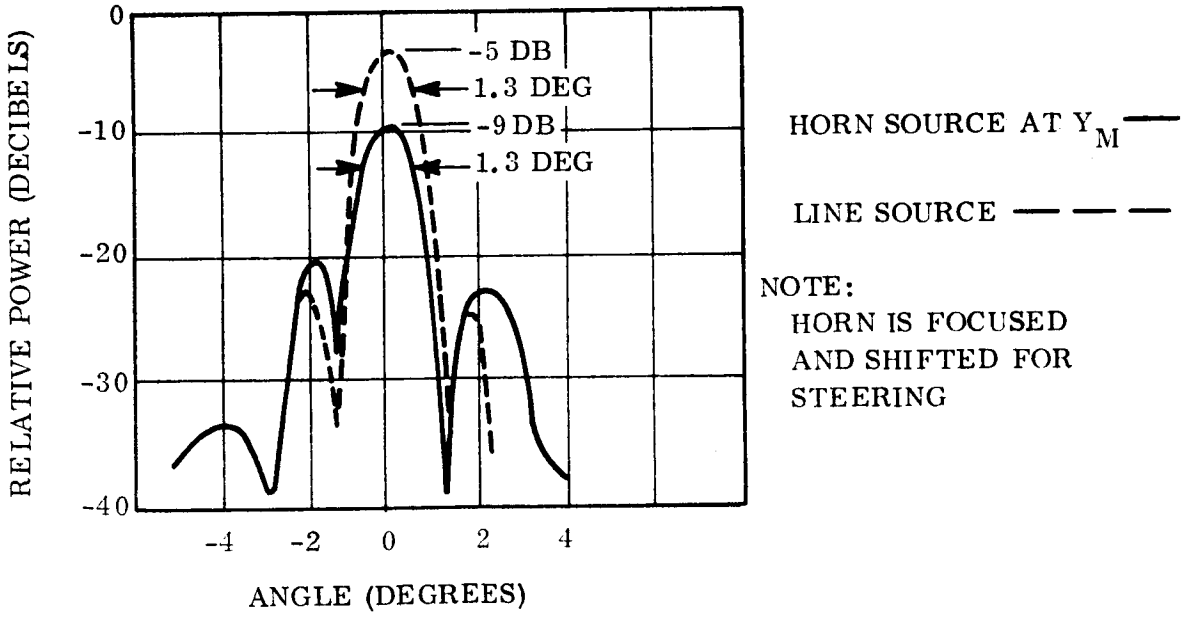


Figure 6.3-83. Comparison of Point Source and Line Source E-Plane Patterns, 15-Degree Steering

A distributed feed requires considerably more development than better known feeds. Analysis of parabolic reflector image planes for the desired angular range of scan would precede feed design. A series of orthogonal slices would be required to define a focal volume. A design enabling an array to fit the image-plane pattern then would be necessary. This design would include radiating elements and controls for phase and amplitude of each element. Mechanical steering of the distributed feed would accomplish basic beam-steering and focusing. Phase and amplitude control would permit control of focus refinement and astigmatism to produce a pencil beam or a shaped beam. If phase and amplitude control is derived from steering, the best pencil beam could be maintained automatically. If phase and amplitude are controlled independently, beam shaping may become an experimental variable.

Despite advantages of this feed, it is not proposed because it is estimated that the development of a spaceborne version of this feed would extend beyond the schedule of the ATS-4 program.

6.3.5.5.4 Main Reflector Modifications

An integrated approach to the ATS-4 large aperture antenna should consider modification of the main reflector. Because this is not properly within a practical feed design, this approach is not recommended. Benefits which might be gained using a Schwarzchild compensation or over-compensation is shown in Figure 6.3-84. The Schwarzchild compensated coma lobe is approximately 11.5 dB below the prime focus at five-degree scan angle.

With consideration restricted to the feed only, neither of the alternate approaches, area feed, or compensation of main reflector, can be recommended. However, a long term integrated program should consider the optimized combination of distributed feed and main reflector compensation, if beam steering with a wide field of view is found to be a must for a successful ATS-4 mission.

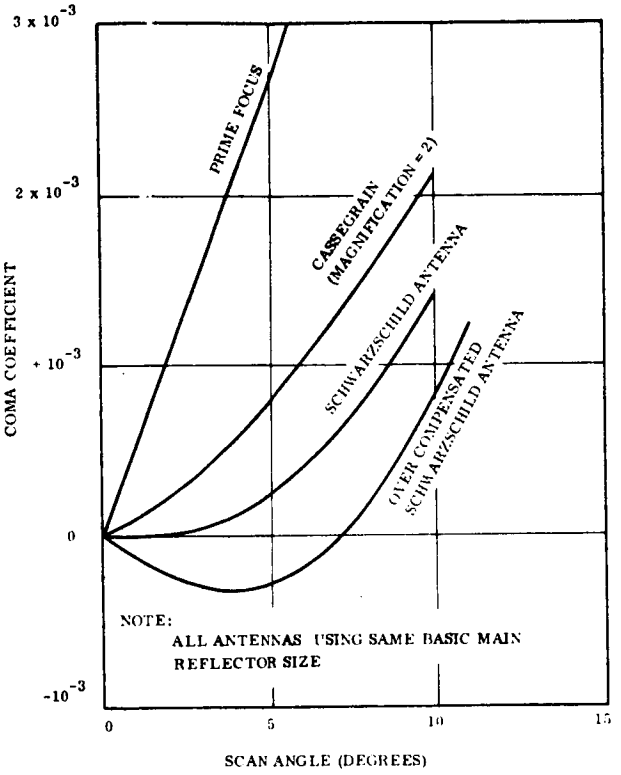


Figure 6.3-84. Coma Coefficient vs Scan Angle

6.3.5.6 RF Loss Budget Cassegrain vs Prime Focus

The preliminary selections of geometrics for the ATS-4 large aperture antenna were analyzed for electric performance. Each configuration was analyzed for gain reduction as compared to a uniformly illuminated perfect parabola with no blockage. The total losses may then be compared to 3 dB for the desired 50 percent efficiency. Loss budgets are presented in Tables 6.3-11, 6.3-12, and 6.3-13.

The illumination efficiency[15] is that efficiency of the aperture due to not having a uniform illumination[14]. The spillover efficiency is the fraction of energy from the feed that is not available for collimation by the parabola. Both efficiencies were obtained from measured horn data.

Blockage losses exist due to structures in the collimated wavefront of the parabola. The 6-foot diameter subreflector[17] of the Cassegrain causes a shadow similar to the feed[18] of a prime focus dish. The struts in the feed support structure also block the rf energy.[19][20]

Table 6.3-11. Antenna Loss Budget No. 1 (Prime Focus Feed)

Item	Frequency, GHz						
	0.1	0.8	1.7	2.1	2.3	7.3	8.0
Illumination Efficiency	1.2	0.72	0.22	0.80	1.10	0.58	0.90
Spillover Efficiency	1.12	0.66	1.70	0.58	0.40	0.82	0.50
Subreflector Blocking Loss	-	-	-	-	-	-	-
Feed Blocking Loss	0.10	0.08	0.08	0.08	0.08	0.08	0.08
Strut Blocking Loss	-	-	-	-	-	-	-
Umbrella Struts	-	-	-	-	-	-	-
Support Struts	0.53	0.53	0.53	0.53	0.53	0.53	0.53
Radial	-	-	-	-	-	-	-
Reflector Phase Error Loss	0.00	0.00	0.01	0.02	0.02	0.18	0.23
Feed Phase Error Loss And Feed Near Field Loss	0.05	0.01	0.04	0.04	0.04	0.04	0.04
Cross Polarized Loss	0.01	0.01	0.01	0.01	0.01	0.01	0.01
Feed Attenuation Loss (including circuitry)	0.2	0.2	0.2	0.2	0.2	0.2	0.2
Transmission Line Loss	0.08	0.24	0.10	0.08	0.07	0.28	0.25
	-	-	-	-	-	-	-
TOTALS (dB loss)	3.29	2.45	2.88	2.32	2.45	2.72	2.74

Table 6.3-12. Antenna Loss Budget No. 2 (Cassegrain Geometry Back Deploy)

Item	Frequency, GHz						
	0.1	0.8	1.7	2.1	2.3	7.3	8.0
Illumination Efficiency	1.2	0.48	0.21	0.63	1.04	0.38	0.60
Spillover Efficiency	1.12	0.45	1.15	0.37	0.20	0.60	0.38
Subreflector Blocking Loss	0.72	0.72	0.72	0.72	0.72	0.72	0.72
Feed Blocking Loss	-	-	-	-	-	-	-
Strut Blocking Loss	-	-	-	-	-	-	-
Umbrella Struts	-	-	-	-	-	-	-
Support Struts	-	-	-	-	-	-	-
Radial	0.18	0.18	0.18	0.18	0.18	0.18	0.18
Reflector Phase Error Loss	0.00	0.00	0.01	0.02	0.02	0.18	0.23
Feed Phase Error Loss and Feed Near Field Loss	0.05	0.03	0.06	0.07	0.08	0.06	0.06
Cross Polarized Loss	0.01	0.00	0.00	0.00	0.00	0.00	0.00
Feed Attenuation Loss (including circuitry)	0.2	0.2	0.2	0.2	0.2	0.2	0.2
Transmission Line Loss	0.04	0.11	0.05	0.04	0.03	0.13	0.12
TOTALS (dB loss)	3.52	2.17	2.58	2.23	2.47	2.45	2.49

Table 6.3-13. Antenna Loss Budget No. 3 (Cassegrain Geometry Front Deployment)

Item	Frequency, GHz						
	0.1	0.8	1.7	2.1	2.3	7.3	8.0
Illumination Efficiency	1.2	0.48	0.21	0.63	1.04	0.38	0.60
Spillover Efficiency	1.12	0.45	1.15	0.37	0.20	0.60	0.38
Subreflector Blocking Loss	0.72	0.72	0.72	0.72	0.72	0.72	0.72
Feed Blocking Loss	-	-	-	-	-	-	-
Strut Blocking Loss	-	-	-	-	-	-	-
Umbrella Struts	0.46	0.46	0.46	0.46	0.46	0.46	0.46
Support Struts	0.18	0.18	0.18	0.18	0.18	0.18	0.18
Radial	-	-	-	-	-	-	-
Reflector Phase Error Loss	0.00	0.00	0.01	0.02	0.02	0.18	0.23
Feed Phase Error Loss And Feed Near Field Loss	0.05	0.03	0.06	0.07	0.08	0.06	0.06
Cross Polarized Loss	0.01	0.00	0.00	0.00	0.00	0.00	0.00
Feed Attenuation Loss (including circuitry)	0.2	0.2	0.2	0.2	0.2	0.2	0.2
Transmission Line Loss	0.04	0.11	0.05	0.04	0.03	0.13	0.12
TOTALS (dB loss)	3.98	2.63	3.04	2.69	2.93	2.91	2.95

The shadows of the struts on the paraboloid were determined graphically using ray optics. The wedge-shaped shadows were weighted to account for the illumination tapes and the diameter of the equivalently weighted uniform strut was found. The blockage was then treated according to Gray[19].

The reflector phase error loss[21] was based on 0.030 inch rms error. The subdish of the Cassegrain was assumed to only add a negligible loss due to surface tolerance. The feed phase error loss and near field losses are reduced drastically during focusing but are not eliminated entirely. These losses were calculated[22], [23], [24] using the actual horn sizes. The cross polarized loss, being a function of f/D, [25] is a negligible loss.

The feed attenuation and transmission line loss uses standard loss values for appropriate size components.

Since the reflector must transmit as much optical energy as possible, wire mesh construction must be used where possible. The allowable wire sizes and spacings are shown in Figure 6.3-85. These are based on transmission properties at 8.0 GHz. Since the total volume of the wire should be a minimum to conserve weight the wire diameter should be as small as possible, yet be practical for mechanical integrity.

6.3.5.7 Additional Strut Loss

Subsequent to the selection of the prime focus design, the decision was made to use non-deployable support struts in order to ensure a higher degree of reliability. This required that the struts lie relatively close to the primary feed, thus affecting its pattern and consequently the secondary pattern characteristics. In order to determine the extent to which the antenna gain and sidelobes are changed by this design procedure, a measurement program was carried out as detailed below.

6.3.5.7.1 Antenna Test Configurations

The antenna under consideration, at full scale, is a 30-foot reflector having a f/D ratio of 0.4. The feed support struts lie on a circle of 8-foot diameter around the hub, and connect to a disc which supports the circularly polarized primary feed. Three disc

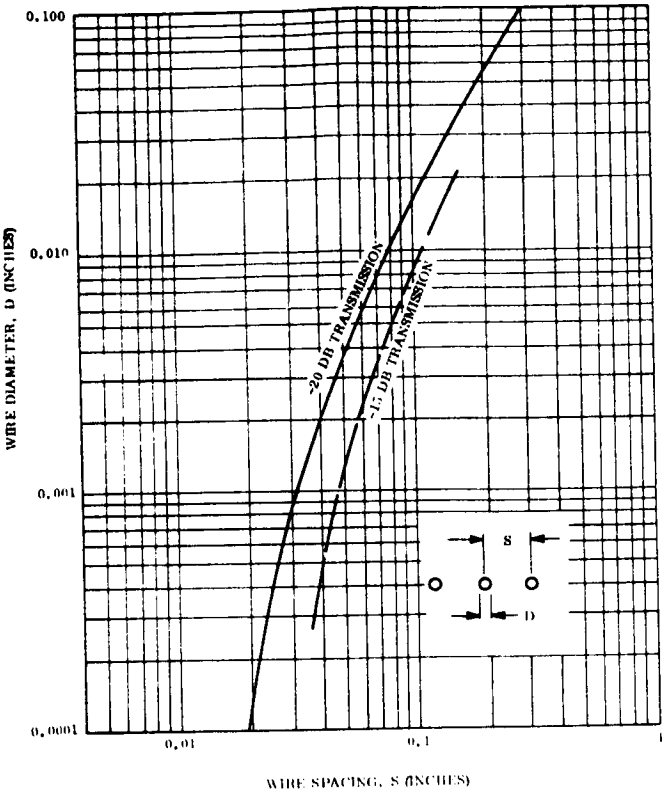


Figure 6.3-85. Subreflector Grid Sizes

arrangements were used for this investigation in conjunction with two basic types of strut. The first type consists of four 6-inch diameter struts with 1/4-inch crosswire bracing on each side forming an X between the dish and feed. This configuration was used with a 4-foot diameter feed disc. The second type consists of three 4-inch diameter V struts arranged to attach to both the dish and the disc at three points. A 54-inch disc was used in this instance, with attachment points at the rim and alternatively on a 2-foot diameter circle.

6.3.5.7.2 Scale Model Antenna

The combination of a close simulation of the antenna together with readily available pattern range facilities to measure its performance was found at the Martin Company in Baltimore. A 39-inch dish having a f/D ratio of 0.385 was fitted with a linearly polarized feed horn designed for this measurement, as well as the necessary feed support structures. The primary feed was designed for 13 dB edge illumination. A full scale frequency of 800 MHz was chosen for this investigation; the scale frequency was 7400 MHz. Figures 6.3-86

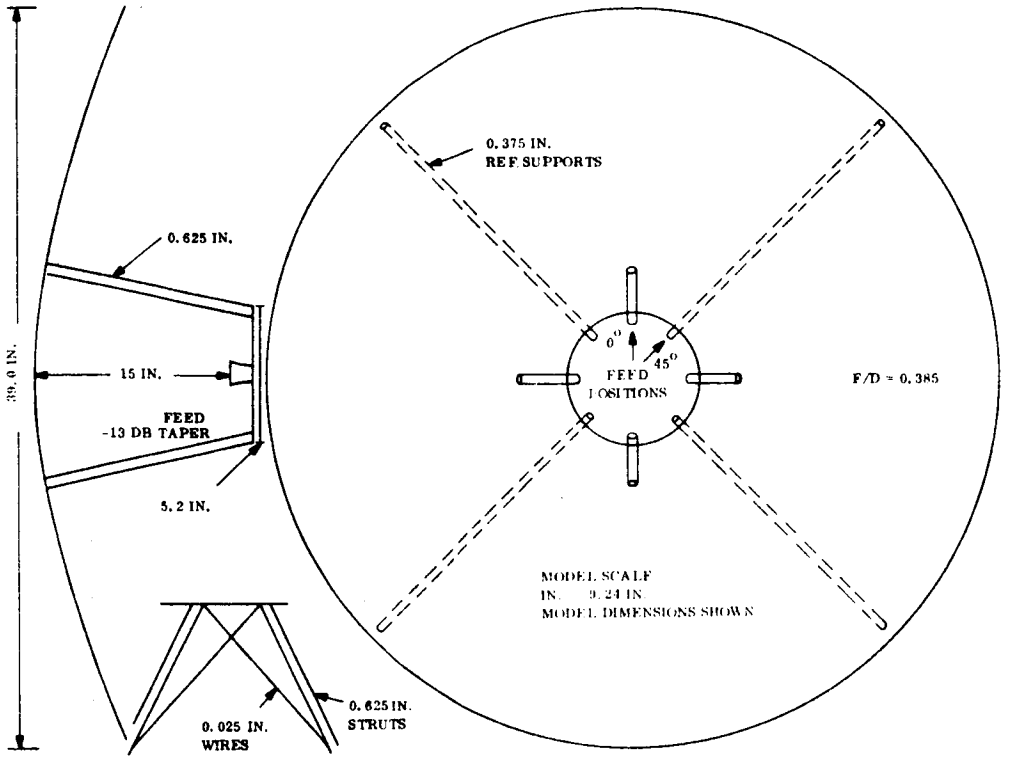


Figure 6.3-86. Strut Model Configuration

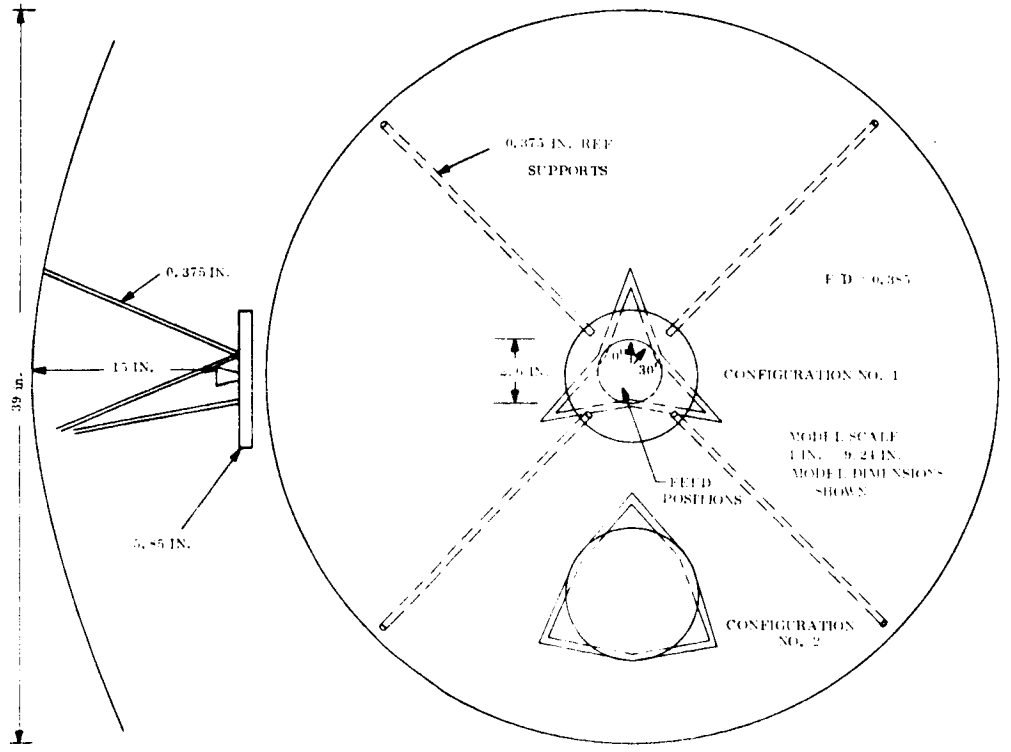


Figure 6.3-87. Three-V Strut Model Configuration

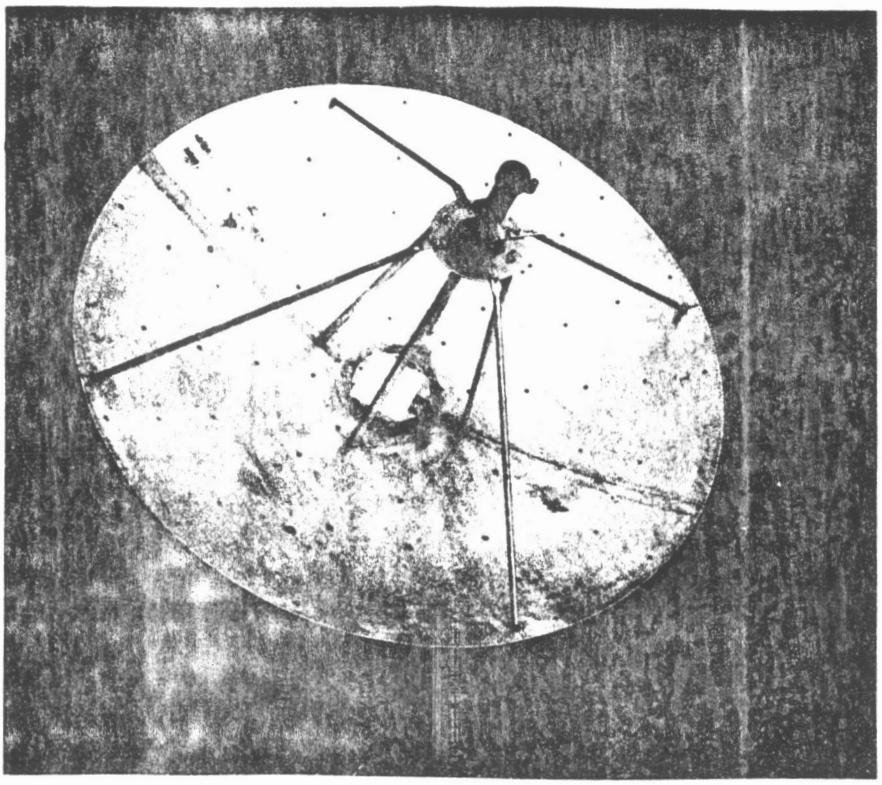


Figure 6.3-88. Four-Strut Model

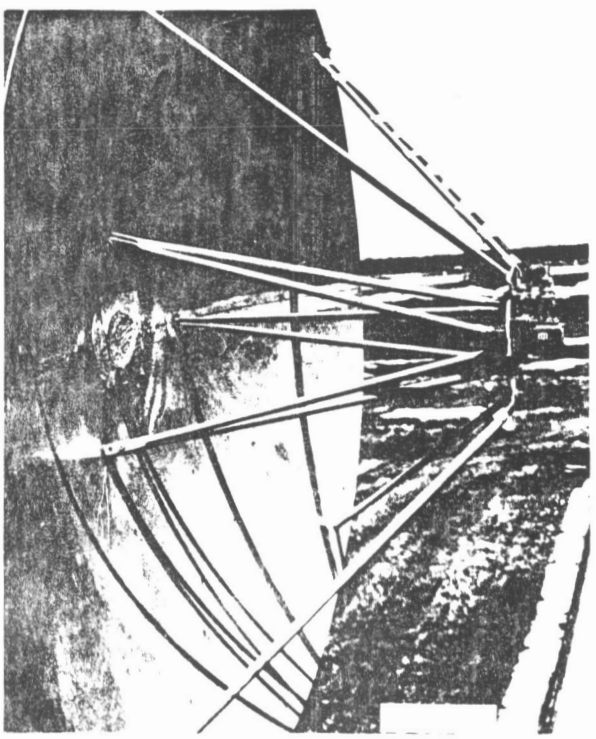


Figure 6.3-89. Three V Struts on 2-Foot Diameter Circle

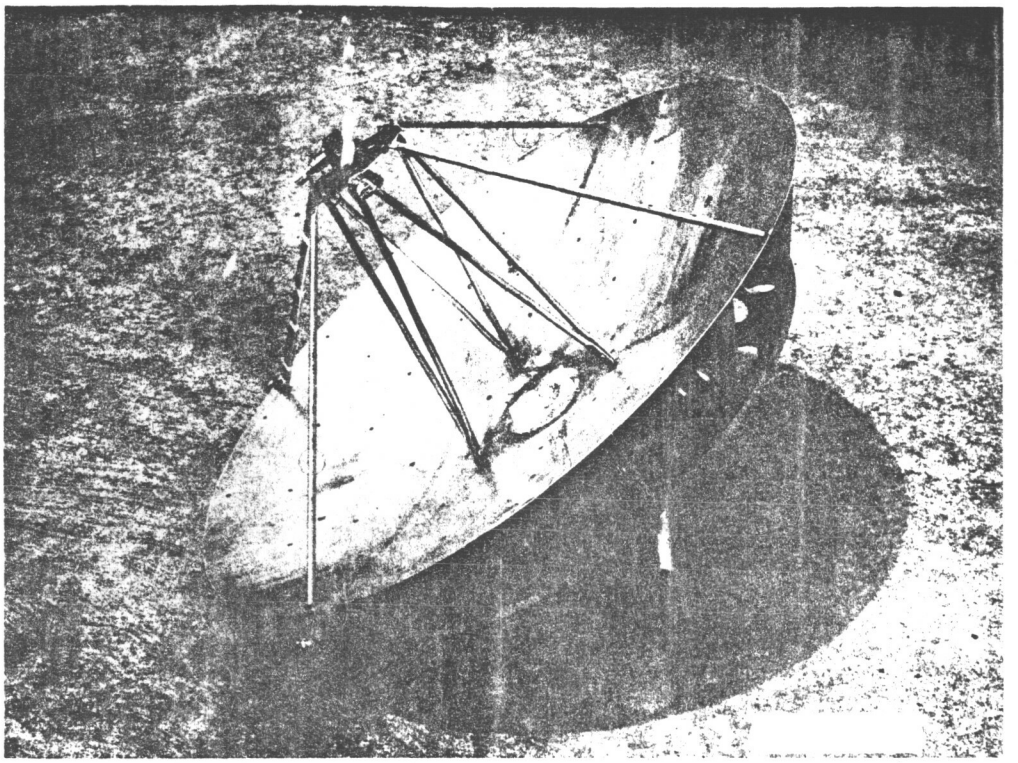


Figure 6.3-90. Three V Struts on 54-Inch Diameter Feed Circle

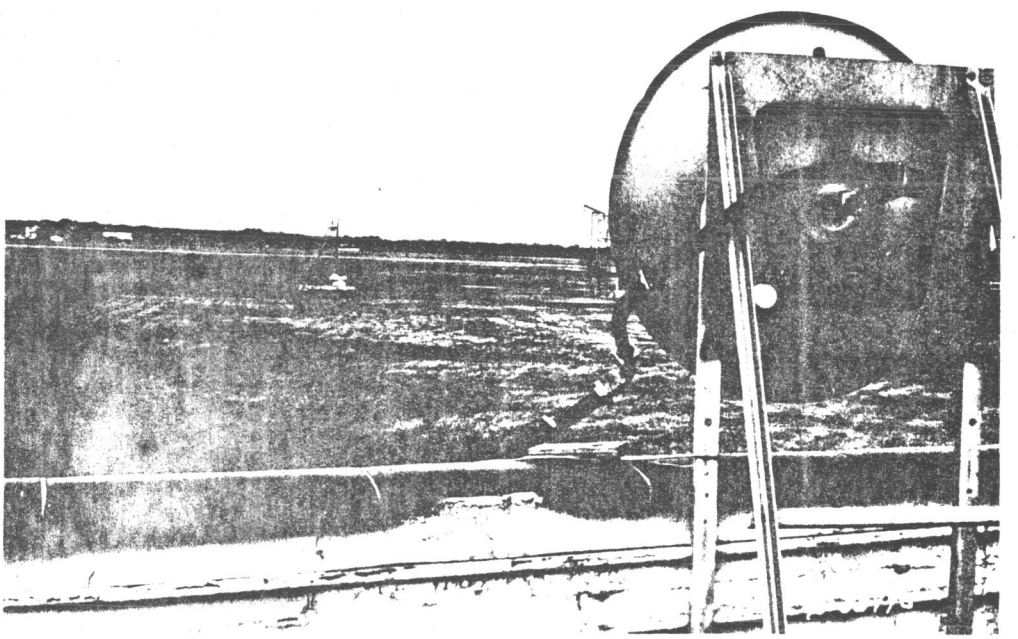


Figure 6.3-91. 450-Foot Test Range, From Source

and 6.3-87 are sketches of the two basic arrangements. Two polarizations were used with each; the directions of the corresponding E vector are noted. In all cases the reference feed supports, attaching to the rim of the dish, were left in place throughout the measurement series. Figure 6.3-88 shows the four strut configuration without crosswire bracing. Figure 6.3-89 shows the V struts on the simulated 2-foot diameter feed circle; the 54-inch diameter case is shown in Figure 6.3-90.

6.3.5.7.3 Antenna Range Facilities

The measurements were made on the 450-foot range at the Martin Antenna Laboratory. Figure 6.3-91 is a view taken from the source antenna looking toward the test tower on the left. A HP 618 signal generator with HP 491 traveling wave tube amplifier were used as a signal source, the stability of which was monitored throughout the series by means of a monitor horn and HP 415-B indicator.

6.3.5.7.4 Test Data

The 26 patterns shown in (a) through (z) of Figure 6.3-92 indicate the measured properties of the various configurations. The central abscissa scale is used; each small division represents 0.5 degree. Since the source fluctuation was negligible, the various gain degradations may be read by direct comparison with the reference patterns, using the decibel scale. This data is summarized below for convenience.

Four Strut Configuration		
Polarization (Deg)	No Wires (dB)	With Wires (dB)
0	-2.2	-2.6
45	-2.5	-3.6

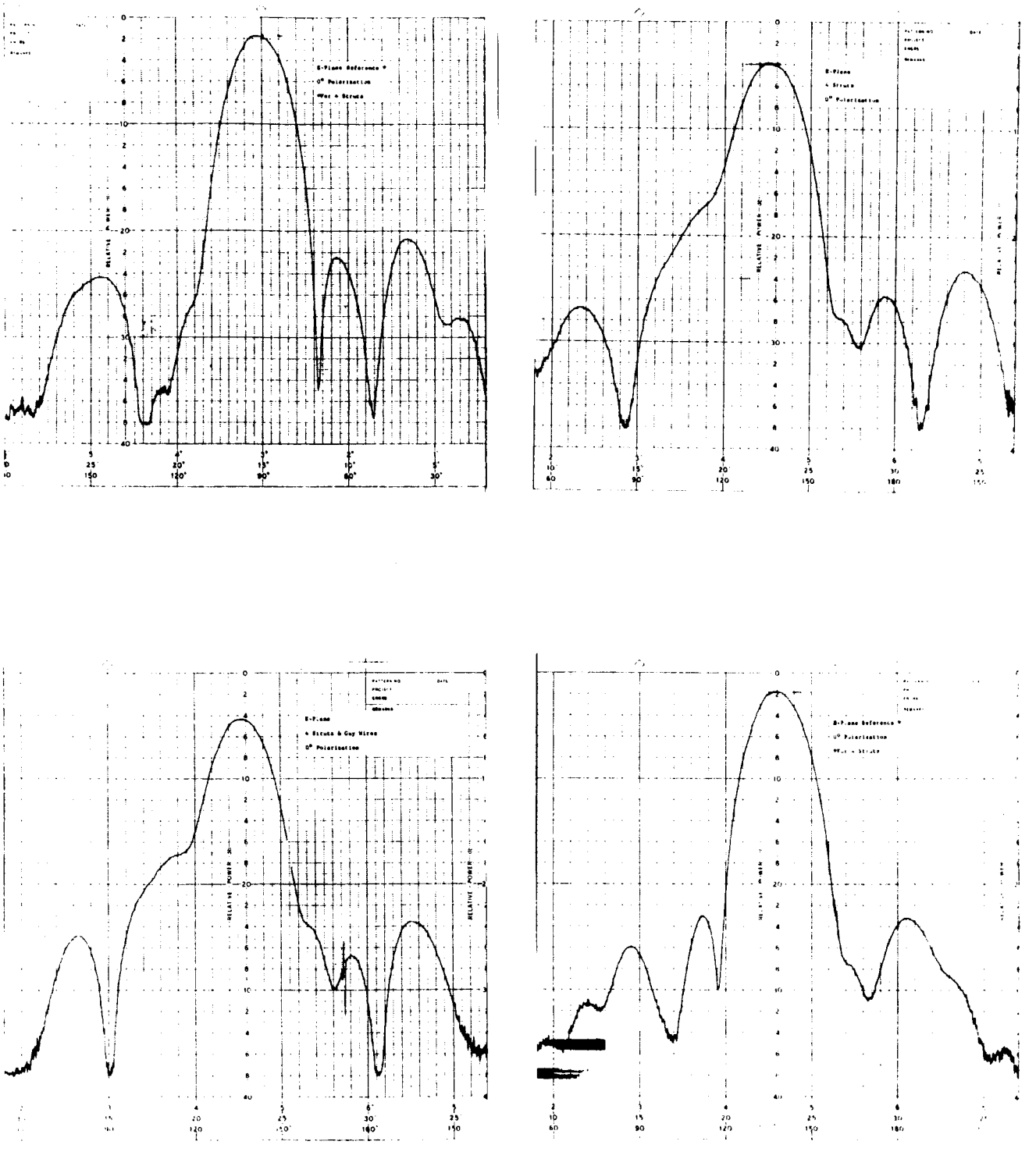


Figure 6.3-92. Measured Patterns
(Sheet 1 of 7)

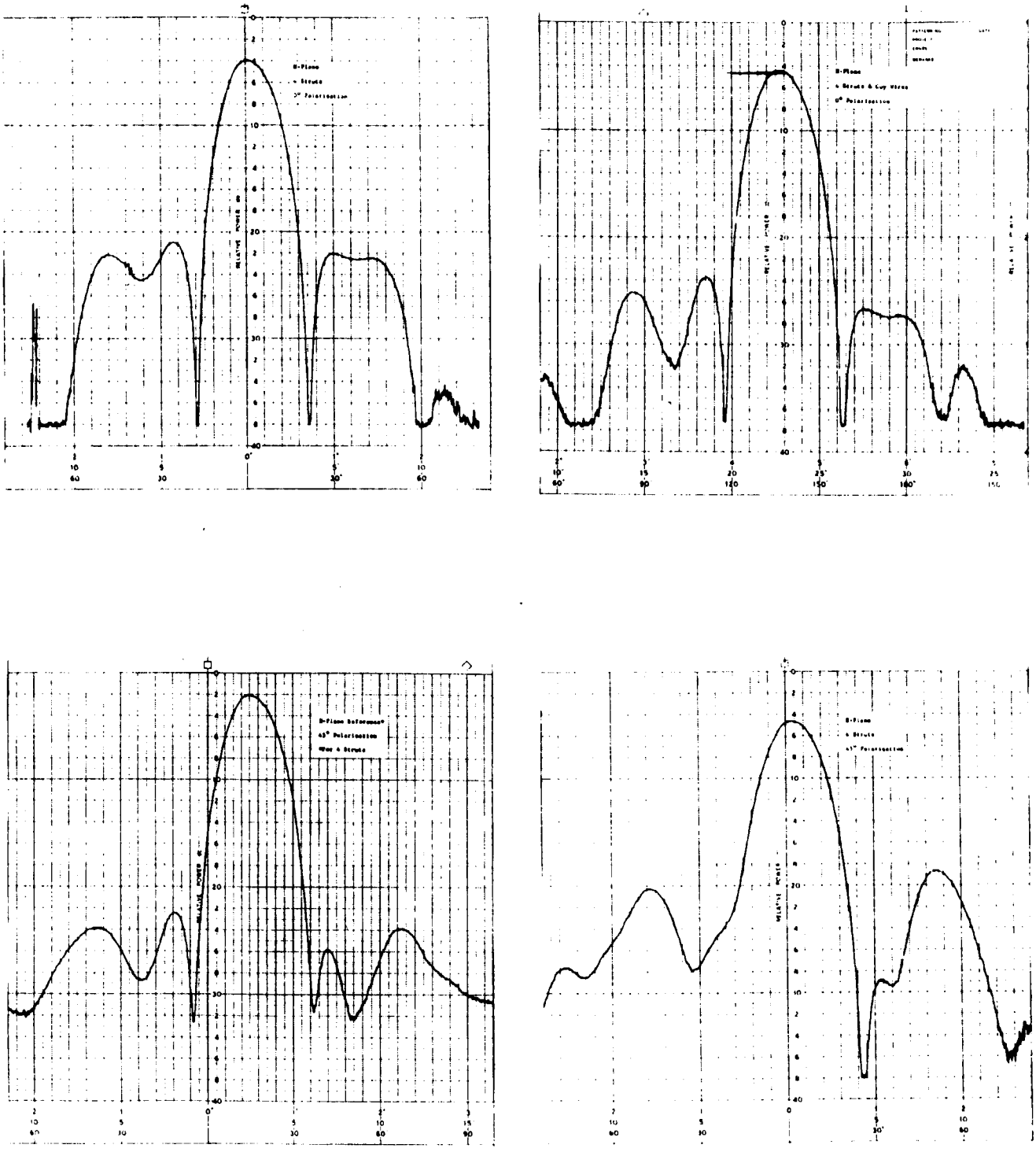


Figure 6.3-92. Measured Patterns

(Sheet 2 of 7)

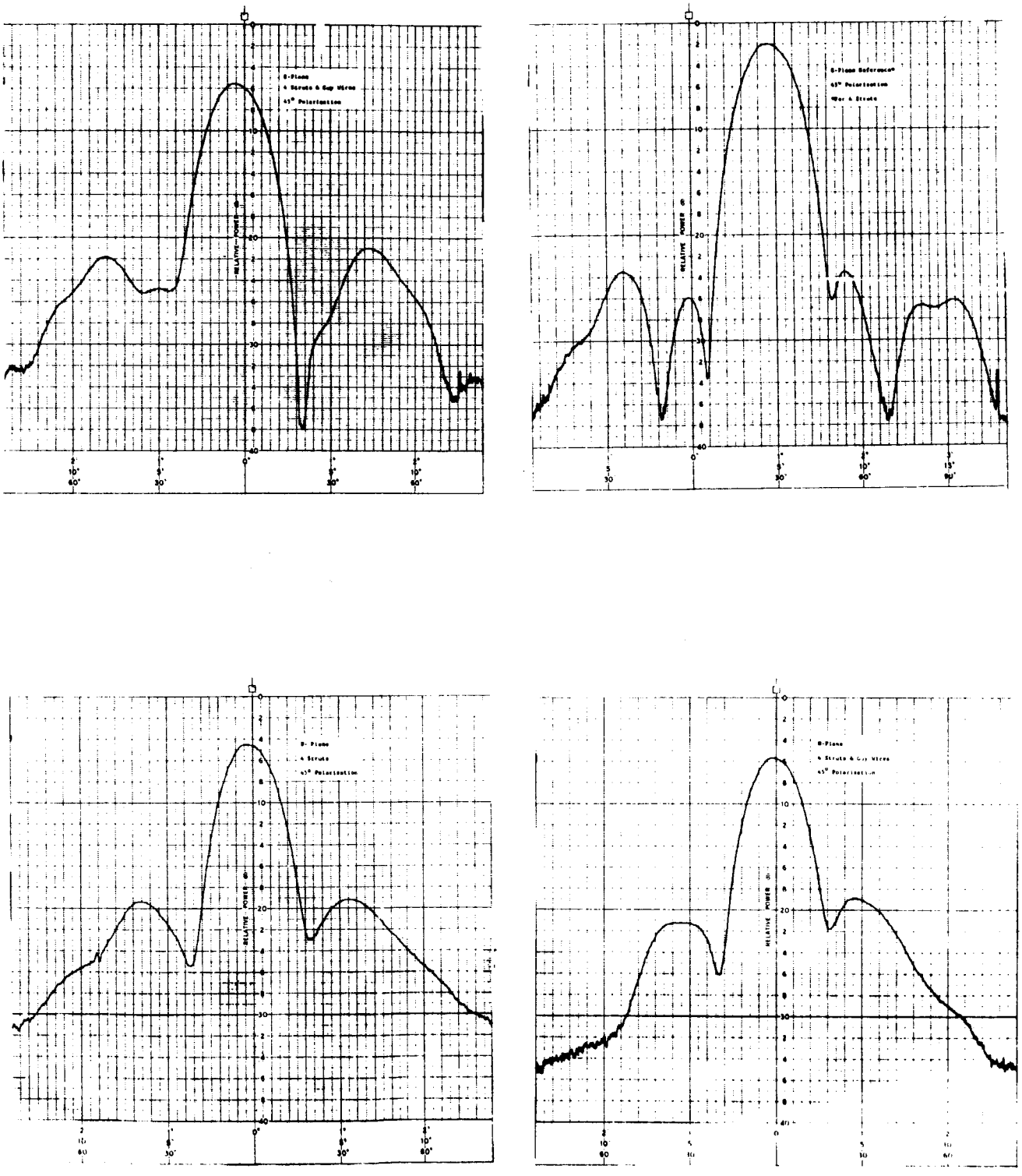


Figure 6.3-92. Measured Patterns
(Sheet 3 of 7)

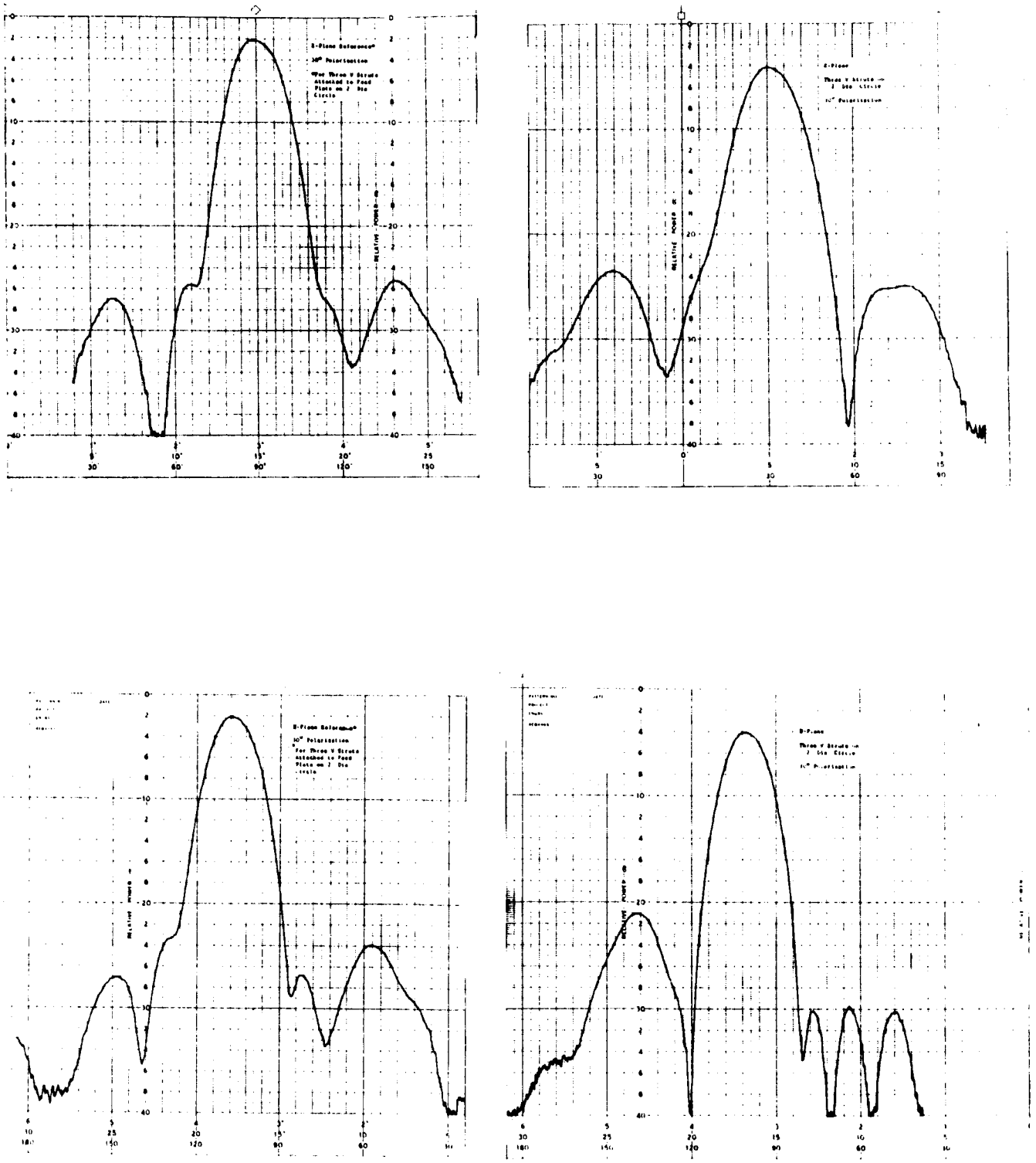


Figure 6.3-92. Measured Patterns
(Sheet 4 of 7)

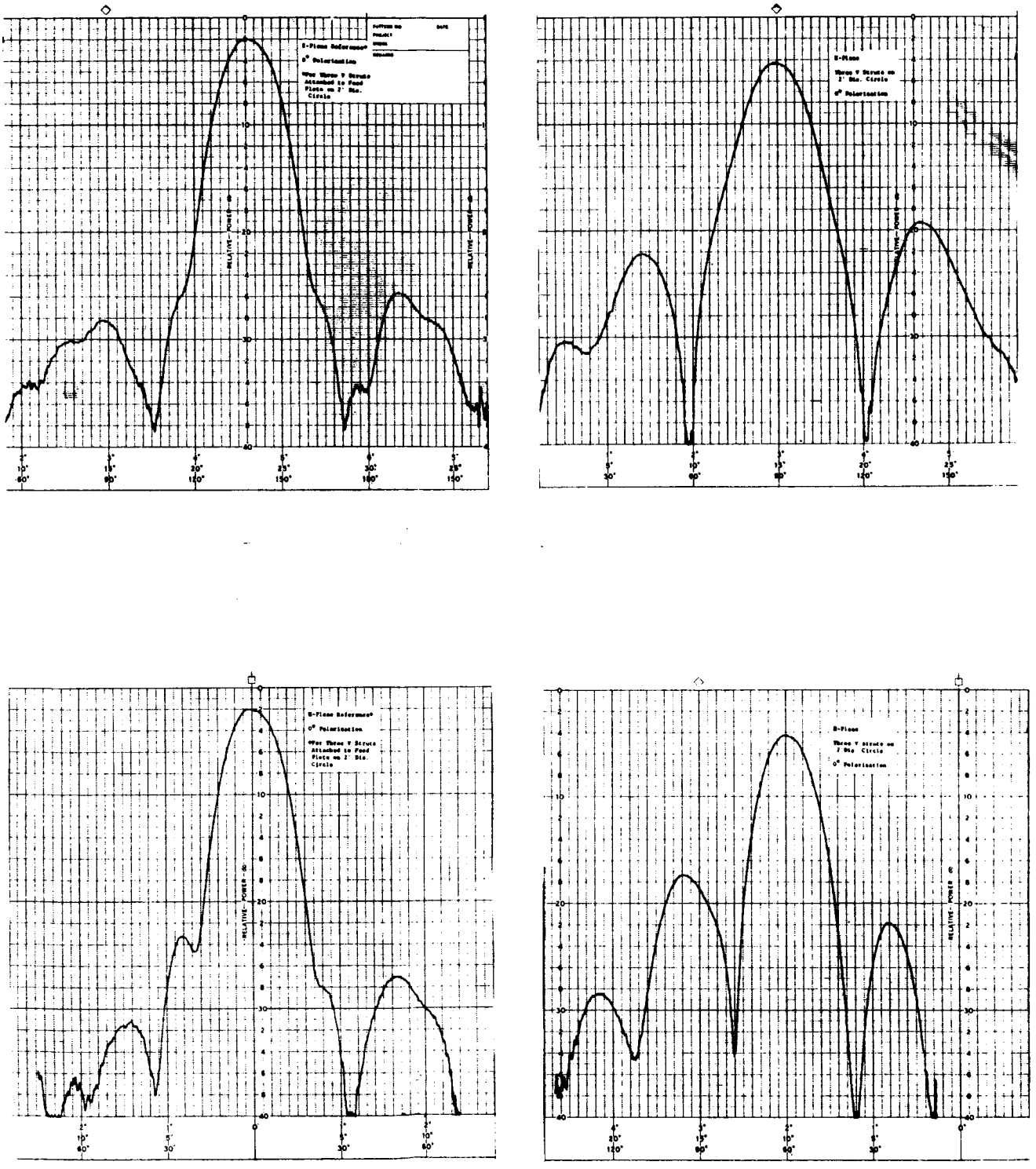


Figure 6.3-92. Measured Patterns
(Sheet 5 of 7)

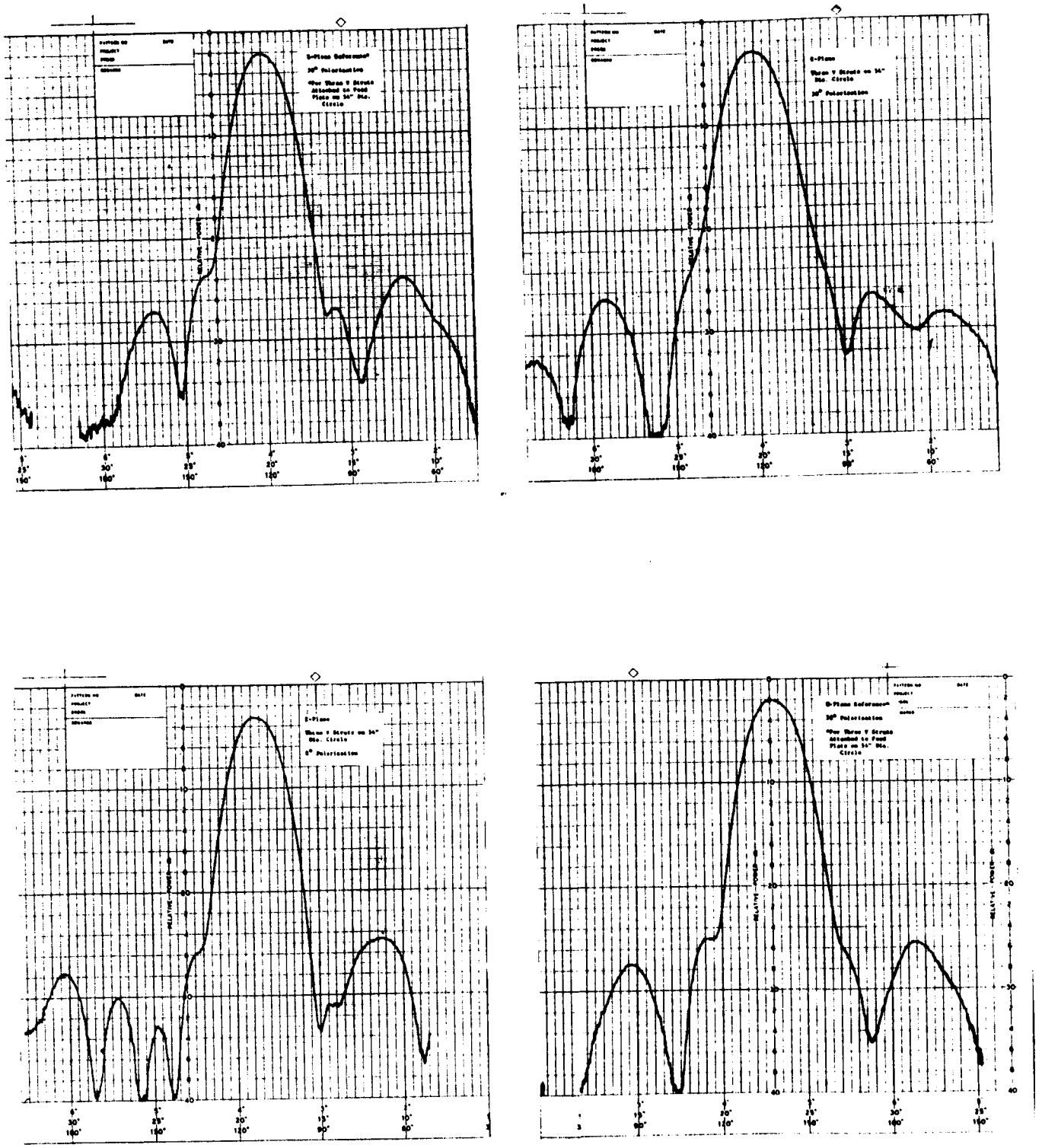


Figure 6.3-92. Measured Patterns

(Sheet 6 of 7)

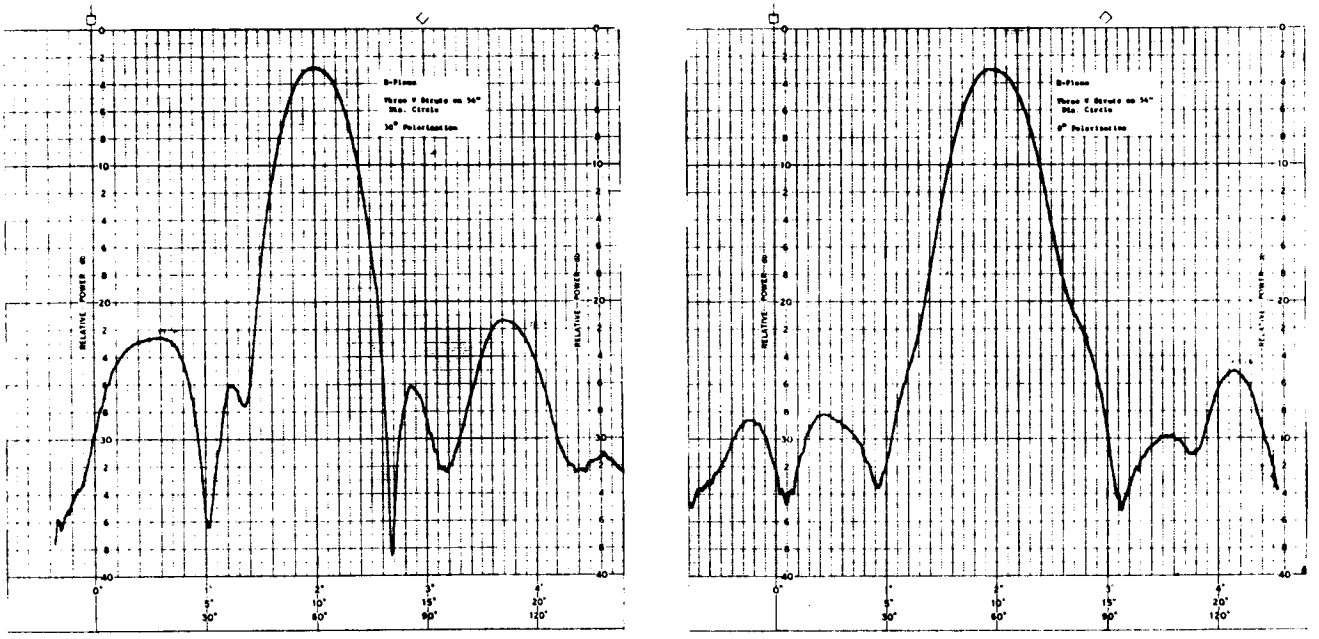


Figure 6.3-92. Measured Patterns
(Sheet 7 of 7)

Three V Strut Configuration		
Polarization (Deg)	2-foot Diameter (dB)	54-inch Diameter (dB)
0	-2.2	1.0
30	-2.0	1.0

It should be mentioned that approximately 0.5 dB improvement over the number shown for the 2-foot diameter attachment was noted when the feed horn was surrounded with absorbing material out to the edge of the disc. This would appear to be a worthwhile design feature.

The configuration selected for ATS-4 is closely simulated by the Three-V strut model with 54-inch diameter disc. The 1 dB figure shown for this case has accordingly been reflected into the final loss budget shown below and in Section 5.4.3. Since this value also includes blockage loss, the calculated value of the latter is presented separately; the total is 1 dB.

This is shown as an estimated value at all frequencies, since the actual measurement was made at only one frequency as described above.

6.3.5.8 Thermal Distortion Loss

Degradation of gain was calculated for thermal distortions of the paraboloid in the 90 degree orbit position presented as a worst case design. These distortions are shown in Figure 6.3-93. The errors were then analyzed according to Anderson's[28] treatment. At each radius, the weighted phase deviation was calculated at each point "k" in ring "i" from:

$$\Delta = \left\{ \sum_n \left[\Sigma \Delta d_k \ (1 + \cos \alpha) \right]^2 \ \frac{F_i}{n_i} \right\}^{1/2}$$

where Δd_k = axial surface deviation at point, k

α = feed angle to ring "i"

F_i = normalized weighting factor for illumination and geometry at ring "i"

$$F_i = \frac{V^2 \ r_i}{\Sigma V^2 \ r_i}$$

r_i = radius at "i"

V = feed voltage at reflector at radius "i"

From this it was determined that the rms phase length for the distorted reflector is 0.051 inches. Thus the loss of gain at each frequency in decibels is given by:

$$\text{dB loss} = 171 \left(\frac{0.051}{\lambda} \right)^2$$

where λ = wavelength in inches

Thermal distortion calculations have indicated that the worst case feed deflection is 0.14 inch in the axial direction, which produces a negligible amount of defocusing. For the 0.4 f/D antenna, an edge phase error of $\lambda/16$ decreases the gain by 2 percent. This criterion permits a focusing tolerance of $(\lambda/16) \sec \Psi$ where, Ψ is half the maximum subtended feed

angle, 65 degrees in this case. Thus for a 2 percent gain decrease (0.1 dB) the permissible focusing error at 8 GHz is 0.22 inches.

There is also a worst angular case in which the feed is displaced 0.001 radian as well as 0.10 inch axially. For the f/D ratio 0.4, the beam would be offset by 0.000875 radian, or 0.05 degree, which is negligible in comparison to the smallest beamwidth to be encountered, which is 0.29 degree at 8 GHz.

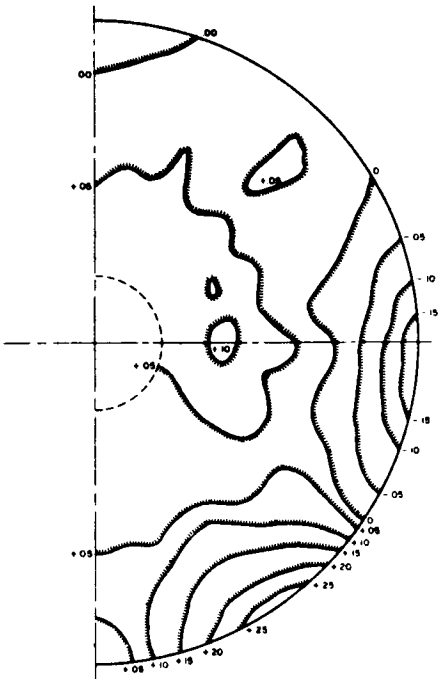


Figure 6.3-93. Case 39-90 Deviation (Symmetrical About Centerline)

6.3.5.9 RF Loss Budget - Final

Taking all factors into account, the final rf loss budget for the chosen prime focus configuration, with f/D = 0.4, is given in Table 6.3-14. It is seen that the losses range from 4.14 dB (38.5%) at 100 MHz to 3.11 dB (49%) at 2.1 GHz, where the optimum illumination-spillover combination is achieved.

Table 6.3-14. Final Configuration Loss Budget

Item	Frequency, GH_z						
	0.1	0.8	1.7	2.1	2.3	7.3	8.0
Illumination Efficiency	1.20	0.72	0.22	0.80	1.10	0.58	0.90
Spillover Efficiency	1.12	0.66	1.70	0.58	0.40	0.82	0.50
Equip. Module Blockage	0.40	0.40	0.40	0.40	0.40	0.40	0.40
Strut Blockage	0.24	0.24	0.24	0.24	0.24	0.24	0.24
Strut Reflection Loss*	0.76	0.76	0.76	0.76	0.76	0.76	0.76
Reflection Tolerance Loss	0.00	0.00	0.01	0.02	0.02	0.18	0.23
Loss Thru Wire Mesh Reflector	0.00	0.00	0.00	0.00	0.00	0.03	0.04
Feed Phase Error Loss	0.05	0.01	0.04	0.04	0.04	0.04	0.04
Cross Polarized Loss	0.01	0.01	0.01	0.01	0.01	0.01	0.01
Feed Attenuation Loss (Including Circuitry)	0.20	0.20	0.20	0.20	0.20	0.20	0.20
Transmission Line Loss	0.01	0.03	0.01	0.01	0.01	0.05	0.05
VSWR Reflection Loss	0.15	0.10	0.05	0.03	0.05	0.03	0.03
39-90° Thermal Distortion Loss	0.00	0.00	0.01	0.02	0.02	0.17	0.03
TOTALS (dB LOSS)	4.14	3.13	3.65	3.11	3.25	3.51	3.70

* Estimated

6.3.5.10 References

1. Bracewell, R. N., Tolerance Theory of Large Antennas, I.E.E.E. Trans. on Antennas and Propagation, January 1961, p. 54.

2. Anderson, L. J., Reflector Surface Deviations in Large Parabolic Reflectors, I.E.E.E. Trans. on Antennas and Propagation, March 1963, p. 148.

3. Gray, C. L., Estimating the Effect of Feed Support Member Blocking on Antenna Gain and Sidelobe Level, Microwave Journal, March 1964.

4. Wested, J. H., Shadow and Diffraction Effect of Spars in a Cassegrainian System, Danish Academy of Technical Sciences, 1 March 1966.

5. Rusch, W. V. T., Phase Error and Associated Cross Polarization Effects in Cassegrain-Fed Microwave Antennas, I.E.E.E. Trans. on Antennas and Propagation, May 1966, p. 266.

6. Putter, P. D., A Simple Beamshaping Device for Cassegrain Antennas, JPL Technical Report 32-214, 31 January 1962.

7. Haylett, J. W., High Gain Spacecraft Antenna, Modification Program, Goodyear Engineering Report 12856, 1 October 1966.

8. Kelleher, K. S., and Coleman, H. P., Off-Axis Characteristics of the Paraboloidal Reflector, Rep 4088, Washington, D.C., National Research Laboratory, December 1952.

9. Lo, Y. T., On the Beam Deviation Factor of a Parabolic Reflector, IRE Transactions on Antenna and Propagation, May 1960, p. 374.

10. Hannan, P. W., Microwave Antennas Derived from the Cassegrain Telescope, IRE Transactions on Antenna and Propagation, March 1961, p. 150.

11. Gronlund, M. P. S., et al., Nutating Subreflector and Cassegrainian Antenna System, Copenhagen, Denmark, Danish Academy of Technical Sciences, 1 March 1966; p. 2114.

12. Slettin, C. J., et. al., Corrective Line Sources for Paraboloids, IRE Transactions on Antennas and Propagation, July 1958, Vol AP-6. p. 239-251.

13. Kay, I. W. and Goldberg, M., Investigation of Electromagnetic Fields in the Focal Region of a Paraboloid Reviewing Off-Axis, AFCRL-66-461, Ann Arbor, Michigan, Conductron Corp., 24 June 1966.

14. Aperture Gain - Uniform Illumination, Silver, Microwave Antenna Theory and Design, Rad. Lab Series, Vol. 12, p. 177

15. Illumination Efficiency - Jasik, Antenna Engineering Handbook, p. 2-30.

16. Not used.

17. Hannan, Microwave Antennas Derived from the Cassegrain Telescope, IRE Transactions on Antennas and Propagation, March 1961, p. 146.

18. Cutler, Parabolic-Antenna Design for Microwaves, Proceedings IRE, November 1947, p. 1288.

19. Gray, Estimating the Effect of Feed Support Member Blocking on Antenna Gain and Side-Lobe Level, The Microwave Journal, March 1964.

20. Godwin, Surface Tolerance and Strut Blockage Studies for Very High Performance Parabolic Reflector Antennas, GER-10961, 30 December 1963.

21. Reflector Phase Error Loss, Ruse, Physical Limitations on Antennas, MIT Technical Report 248, 30 October 1952.

22. Kelleher, Microwave Optics at Naval Research Laboratory, Proceeding Symposium on Microwave Optics. McGill University, Montreal, Canada, Vol. 2 Paper 34, June 1953.

23. Viggh, Cassegrain Antennas, Elteknik, Vol. 5, May 1962, p. 83-87.

24. Folder and Komlos, Theoretical and Experimental Study of Wide-Band Paraboloidal Antennas with Central Reflector Feed, RCA Review Vol XXI, March 1960, p. 94-116.

25. Potter, The Aperture Efficiency of Large Paraboloidal Antennas as a Function of Their Feed-System Radiation Characteristics, JPL Technical Report 32-149, 25 September 1961.

26. Moreno, Microwave Transmission Design Data, Dover, 1948.

27. High-Gain, Self-Steering Antenna System (Contract NAS 5-10101) Engineering Model Design Report, R.A. Birgenheier and C. Lew, March 1966.

28. Anderson, L. J., Grath, L. H., Reflector Surface Deviations in Large Parabolic Antennas, I.E.E.E. GAP, March 1963, p. 148.

29. Bowman, B. M., Broadband Compensator for Conical Electromagnetic Horns, GER-12754, Goodyear Aerospace, 25 July 1966.

6.4 GUIDANCE AND CONTROL

6.4.1 SUMMARY

Presented in this section are the tradeoff studies and design analyses made during the course of the study to arrive at a design which will meet the performance requirements. A number of tradeoff studies were made in the process of arriving at the preferred design. The most significant perhaps, with regard to impact on the overall design of the guidance and control subsystem, was the selection of spin stabilization for the station acquisition phase and the selection of an earth sensor for the primary orientation control sensor. Two other major influences on the total design were the use of a single mass expulsion system to perform the coning control, precession control, vernier thrusting, and despin functions and the use of a single mass expulsion subsystem to perform all the on-station attitude control and stationkeeping functions. The following is a tabulation of the more important tradeoffs giving the selected approach.

a. Spacecraft Configuration Considerations - The primary considerations were as follows:

   1. Minimize the distance between the center of pressure and center of mass to minimize disturbance torques. (This was a major factor in the rejection of the tandem configuration. The preferred spacecraft configuration is excellent in this respect.)

   2. Locate sensors to minimize field of view restrictions imposed by the spacecraft appendages but without having low natural frequency structure between the sensors and the torquers. (This was a major factor in eliminating the star tracker approach early in the study.)

   3. Provide a compatible situation between the minimum natural frequency of the structure and the bandwidth of the control system to avoid low system damping due to the structural dynamics. (A minimum natural frequency of the structure of about one cps was set as a design goal. The minimum frequency of the preferred spacecraft design is nearly two cps.)

b. Earth Sensor/Star Trackers - Initially it appeared that the 0.1 degree accuracy requirement could only be met using a three-axis star tracker system. Further investigation of the earth sensor accuracy and the weight, power and field of view problems led to the selection of the earth sensor as the primary pointing mode sensor.

c. Three Axis Control/Spin Stabilization During the Station Acquisition Phase - Spin stabilization was selected primarily because of the tradeoff of providing coning and precession control rather than providing a three axis control subsystem and an apogee motor with thrust vector control.

d. Polaris Star Sensor/Gyrocompassing - The Polaris star sensor was selected primarily on the basis that the required star sensor could be a modification of an existing Canopus star tracker whereas significant development appeared necessary to acquire a gyrocompass subsystem with sufficiently low drift rate.

e. Momentum Storage Device - The mechanical flywheel was selected over the fluid flywheel and control moment gyro because of advantages in weight, power and simplicity.

f. On-Off/Proportional Flywheel Control - Proportional control was selected over an on-off type flywheel control because the reduction in control electronics offered by the approach is minimal and the on-off approach introduces a potential problem with regard to exciting of flexible structural members.

g. Spacecraft Orientation During Vernier Thrusting - Vernier thrusting with the same spacecraft spin axis attitude used during apogee motor burn and with the spacecraft spin axis normal to the orbit plane were considered. The apogee burn attitude was selected for vernier thrusting because it avoids the need to precess the approximately 70 degrees that would be required to get the spin axis attitude perpendicular to the orbit plane. With the selected attitude, rf Polang measurements are limited to approximately three hours every 12 hours, whereas continuous measurements are possible with the spin axis perpendicular to the orbit plane.

h. Yaw/Roll Axis Stabilization to the Sun - Prior to initiating earth stabilization, it is necessary to establish controlled attitude and rate conditions. The sun is used to establish the initial attitude from which to transfer to earth sensor control. Earth sensor control could be initiated with either the yaw or the roll axis controlled to the sun. Control of the yaw axis to the sun was selected primarily because roll axis stabilization would require earth acquisition from a dynamic rather than a static control condition, and an additional high thrust thruster would be required to remove the rate existing about the roll axis. Yaw axis stabilization to the sun required an additional sun sensor.

i. Orientation Control and Stationkeeping Mass Expulsion Subsystem - The General Electric resistance jet, AVCO resistojet and ion engines were considered. Other mass expulsion approaches were eliminated on the basis of incompatibility with the required thrust level. Either the resistance jet or resistojet approach would be capable of meeting all attitude control and stationkeeping requirements. The ion engine would be suitable for only a portion of the requirements, thus requiring a hybird approach. This would not be competitive with the other two approaches. The GE resistance jet was selected because it provided a weight advantage.

j. Accelerometer/Gyro for Coning Control - The use of an angular accelerometer was selected on the basis that it provides a design where the crosscoupling effects of the spacecraft spin rate are minimal. It also offers a weight advantage.

k. Station Acquisition and Despin Mass Expulsion Subsystem - Monopropellant and bipropellant systems were investigated. After the initial tradeoff of the monopropellant and bipropellant design candidates, in which an approximate weight equivalence was shown, advantages noted for the monopropellant system in terms of system complexity, reliability, and development cost, resulted in selection of a monopropellant hydrazine system design.

l. Spinup Motor - Information was compiled on available solid propellant motor suitable for spacecraft spinup. The spacecraft spin speed was then selected to use an available spin motor. The use of an available motor did not compromise the required design spin speed.

Design analyses were conducted to define the disturbance torques acting on the spacecraft throughout the mission after separation from the booster. This was necessary to define the precession caused by the disturbance torques during the transfer orbit and during the vernier thrusting period. The on-station disturbance torques were analyzed and computer programs were written to determine the disturbance torque as a function of time for a 24-hour period. These disturbance torque profiles were then used to determine the flywheel momentum requirements and the mass expulsion required for flywheel unloading. Study of the flywheel momentum profiles resulted in the selection of a 2 ft-lb-sec flywheel and verification that the flywheel unloading mass expulsion requirements are small relative to the stationkeeping requirements. Design analyses were conducted for the coning and precession control subsystem including the effect of center of mass migration and jet damping during apogee motor burn. Digital computer runs were made to determine the nature of the coning. In addition, analog computer studies were made for the various on-station control modes of sun stabilization, earth stabilization, pointing, reorientations for changing the pointing location, and tracking in response to ground commanded, time programmed changes in pointing direction. These computer studies were used to select design parameters to obtain satisfactory dynamic performance and to demonstrate that the control system will meet the specified pointing, reorientation and tracking requirements. The effect of structural dynamics of the spacecraft and its flexible appendages were included in this analysis for damping factors down to 0.001. These studies showed that the control system can meet the orientation control requirements as set forth for the ATS-4 mission.

6.4.2 TRADEOFF ANALYSIS

During the course of this study a number of specific tradeoff studies were made to arrive at the preferred design. The significant tradeoff areas listed below are discussed in detail in this section. Basic generic tradeoff considerations such as reliability, weight and power are not included as specific tradeoff areas as these were continuously factored into the design approach and hardware considerations.

a. Spacecraft Configuration Considerations

b. Earth Sensor/Star Trackers

c. Three Axis Control/Spin Stabilization During the Station Acquisition Phase

d. Polaris Star Sensor/Gyrocompassing

e. Momentum Storage Devices

f. On-Off/Proportional Flywheel Control

g. Spacecraft Orientation During Vernier Thrusting

h. Yaw/Roll Axis Stabilization to the Sun

i. Orientation Control and Stationkeeping Mass Expulsion Subsystem

j. Accelerometer/Gyro for Coning Control

k. Station Acquisition and Despin Mass Expulsion Subsystem

l. Spinup Motor

6.4.2.1 Spacecraft Configuration Considerations

The final choice of sensors and thrusters, the magnitude of disturbance torques, and the complexity of sensor signal processing are all factors influenced by the choice, or affecting the design, of spacecraft configuration. It is desirable to attain as small a separation of the spacecraft center of mass and center of pressure as possible, since the magnitude of the disturbance torques are directly related to this separation. Increased disturbance torques necessitate the use of higher capacity momentum storage devices, with resulting higher weight, power and volume penalties. Larger torques also increase the mass expulsion subsystem fuel requirements.

A second important consideration in the spacecraft design is the desirability of locating the sensors and torquers in the same compartment. If separation of the sensors and torquers is necessary, possible penalties in signal processing and performance are incurred. To be able to separate the sensors and torquers requires that the modal characteristic of the separation structure be of a high frequency (10 times higher than controller cross over) and low modal mass (1/10 rigid body) nature. If the lowest characteristic frequency of the structure approaches controller crossover and modal mass approaches rigid body, a possible control system instability is sustained, resulting in eventual destruction of the structure. To curtail the possibility of this occurrence, a complex sensor signal filtering scheme is necessary to remove the effects of structural coupling. Filtering schemes, however, usually result in a degradation of controller performance, both dynamic and static. Thus, it is undesirable to separate the sensors and torquers unless the separation structure is sufficiently rigid.

The spacecraft configuration may dictate the type of sensor that can be used. Sensors requiring large unobstructed fields of view such as star trackers (requiring approximately a 70 degree half-cone angle clear field) are not easily adaptable to a spacecraft configuration composed in part of several protruding appendages. This was a major consideration for discarding the three axis star tracker approach early in the program. Difficulties are presently being encountered, however, in meeting a 40-degree half-cone angle clear field for the Polaris star sensor. The present clear field of view is 29 degrees. This requires additional effort to design a sophisticated sun shield to prohibit sunlight reflections from entering the optics of the star sensor.

Location of the thrusters on the spacecraft must include provisions for clearance of the exhaust plume. If the thrusters are located such that significant impingement with the spacecraft structure occurs, the efficiency of the thruster is decreased. Also, possible deterioration of the spacecraft surface may result from chemical reaction with the exhausting gases. It is also desirable to locate the thrusters on portions of the spacecraft body that are not subject to deployment to avoid flexible joints in the thruster supply lines.

6.4.2.2 Earth Sensor/Star Trackers

The basic requirement of a sensor system for this mission is to orient the beam of the parabolic antenna to within 0.1 degree of the commanded position. The star tracker system provides the highest accuracy pointing (error analyses predict a 3σ pointing accuracy of 0.07 degree compared to a 0.09 degree accuracy for the Earth Sensor/Polaris Sensor approach). However, other considerations such as weight, power, complexity, field of view, etc., strongly influenced the final choice of a sensor subsystem.

Theoretically, only two star trackers are necessary for three-axis control, but field of view restrictions made it necessary to consider an additional tracker. Figure 6.4-1 depicts the spacecraft with the star trackers. The motion of the optical axis of the star tracker is shown for local vertical and offset pointing. The total clear field of view required is also shown. The total clear field of view is determined by adding 30 degrees to the maximum excursion of optical axis motion. (The closest angle to the sun line that the OAO star tracker can operate is 30 degrees.) The 30 degree value was used for ATS-4 to avoid the effects from solar reflections from the appendages. Because of the problem of obtaining the required clear field of view, Polaris would be used as one of the two stars. An improved sun shield would be used to allow tracking to within 6 degrees of the reflected sunlight. The second star would be α^1Cru with a declination of 62.9 degrees. Two star trackers would be required for tracking this star, one on each of the two compartments. Each star tracker would track the star for approximately 12 hours with some overlap between switching from one tracker to the other.

The Earth Sensor and The Polaris Sensor (22.7 lb) weigh less than one-sixth that of the three axis star tracker subsystem (135 lb) and use about one-third the power (15 watts to 54 watts). The star tracker subsystem also requires continual gimbal command updating at a high data rate (up to every 1.5 seconds) to maintain an earth pointing orientation. The complexity of the required signal processing and difficulty of control analysis of the star tracker approach are also disadvantages. Control stability and the variation of system accuracy with the star tracker approach are discussed in Appendix F. Since the Earth Sensor/Polaris Sensor approach is much lighter, uses less power, and is much less complex

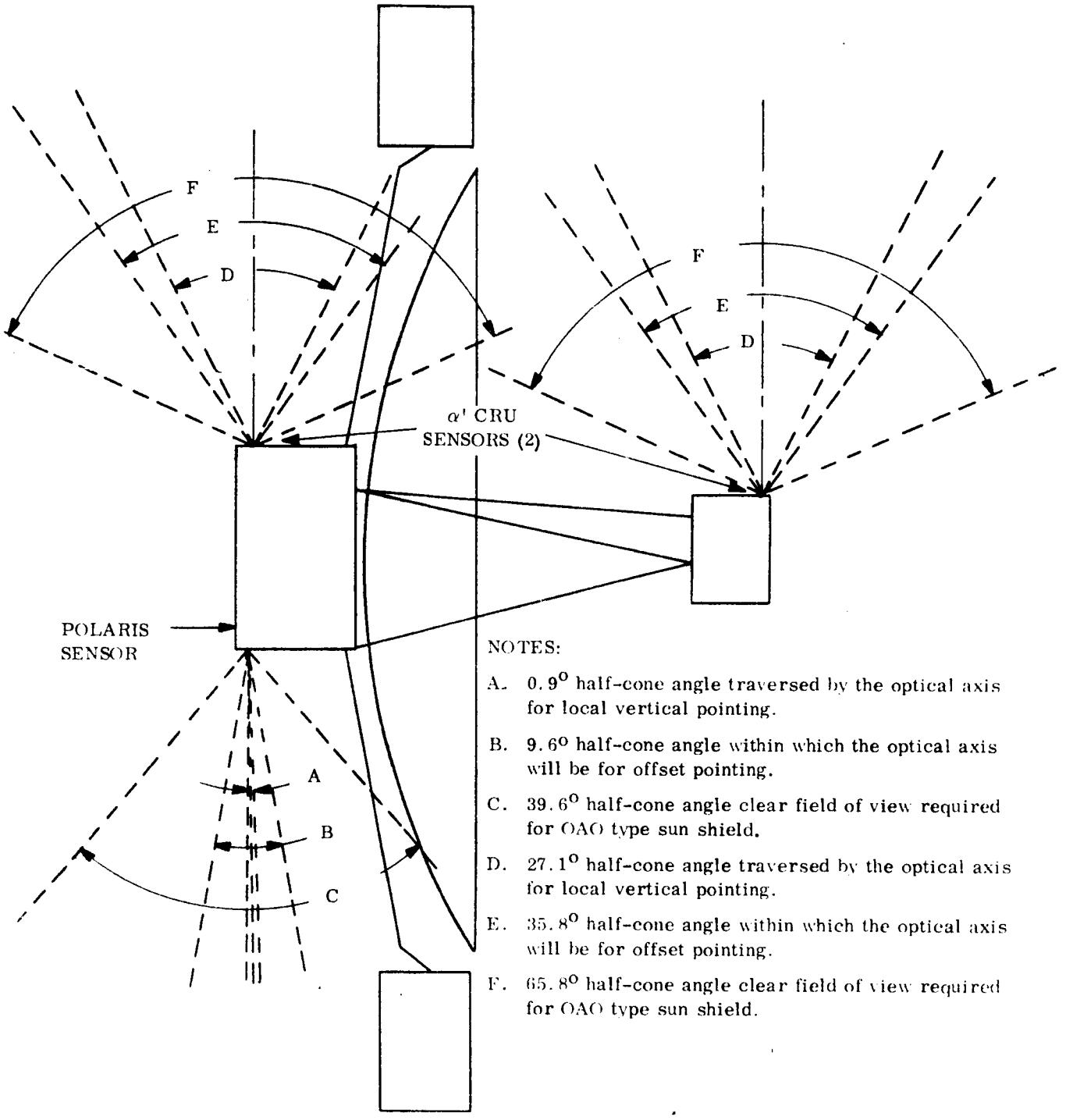


Figure 6.4-1. Star Tracker Field of View Requirements

than the three axis star tracker approach, and provides pointing accuracy within requirements, it became the selected approach.

6.4.2.3 Three Axis Control/Spin Stabilization During Station Acquisition Sequence

The feasibility of using the three axis orientation control and stationkeeping system during station acquisition was studied. This approach was not considered feasible for the following reasons:

a. In the apogee burn attitude, the orientation control earth sensor would not see the earth (the sensor field of view is a +20 degrees square around the $+Z_5$ axis, and the angle between the $+Z_5$ axis and the local vertical is 90 degrees for apogee burn). Also, the star tracker would not see Polaris (the sensor field of view is ±2 degrees around the $-Y_5$ axis, and the minimum angle between Polaris and the $-Y_5$ axis is 19.4 degrees for apogee burn).

b. The aerodynamic disturbance torque at perigee of the transfer orbit is greater than 0.5 lb-ft. The torque capacity of the momentum wheels and mass expulsion jets is 0.01 lb-ft (2 oz-in. and 1.6 oz-in., respectively). Thus, additional actuators would be required.

A separate three axis control system would be required for the station acquisition phase. A comparison of this type of system with spin stabilization follows:

Item	3 Axis Control	Spin Stabilization
Sensors	1. Earth sensor, star tracker or earth sensor, sun sensor or sun sensor, star tracker 2. 3 axis gyro package	1. Angular accelerometer 2. Sun sensor 3. rf polarized antenna
Actuators	Nine 0.1 lb thrusters for transfer orbit attitude control and vernier thrusting and four 50 lb thrusters (or development of thrust vector control) for apogee motor thrust misalignment	Eight 1 lb thrusters and one 10 lb thruster for transfer orbit attitude control, vernier thrusting and despin (no control required during apogee burn), two spin-up motors.

Since spin stabilization is considered to offer advantages in equipment weight and simplicity, it has been selected for the ATS-4.

6.4.2.4 Polaris Star Sensor/Gyrocompassing

Two approaches appeared reasonable for yaw axis attitude control: (1) use of a Polaris star sensor or (2) use of a gyrocompass gyro. Yaw axis attitude must be maintained to an accuracy determined by the maximum crosscoupling error allowable in the pitch and roll channels. Analysis of the pitch and roll axis error sources has shown that the maximum allowable yaw crosscoupling error is 0.03 degree (3σ). If the crosscoupling error were to exceed this, the pointing requirements of 0.1 degree would not be met.

Yaw axis attitude accuracy is related to crosscoupling error by the following equations:

$$\theta_c \text{ Sin } \Delta\psi = \Delta\phi_{cc}$$

$$\phi_c \text{ Sin } \Delta\psi = \Delta\theta_{cc}$$

where θ_c and ϕ_c are commanded pitch and roll attitude, $\Delta\theta_{cc}$ and $\Delta\phi_{cc}$ are the induced pitch and roll crosscoupling errors, and $\Delta\psi$ is the yaw attitude error.

As is shown by the above equations, maximum crosscoupling error occurs at maximum commanded offsets. Since the crosscoupling error may not exceed 0.03 degree, and the maximum offset is limited to +8.7 degrees, it is possible to calculate the required yaw axis attitude accuracy. Substition of these quantities into the above equations yields:

$$8.7 \text{ Sin } \Delta\psi = 0.03$$

or

$$\text{Sin } \Delta\psi = 3.44 \times 10^{-3}$$

and

$$\Delta\psi \approx (3.44 \times 10^{-3})\,(5.73 \times 10^{1})^{o}$$

$$\Delta\psi \approx 0.197^{o}$$

If 0.06 degree is allocated as the basic sensor error, the required gyrocompass gyro total uncertainty may be calculated. The gyro will be mounted with its input axis along the spacecraft velocity vector (roll axis). Thus, for a yaw error $\Delta\psi = 0.06$ degree, the rate uncertainty limit of the gyro is:

$$\dot{\theta}_{um} = (15)\ \text{Sin}\ (0.06\ \text{deg})$$

$$\dot{\theta}_{um} = \frac{15 \times 6 \times 10^{-2}}{5.73 \times 10^{1}}\ \text{degree/hour}$$

$$\dot{\theta}_{um} = 0.0157\ \text{deg/hour}$$

where

$\dot{\theta}_{um}$ = maximum gyro uncertainity

W_o = orbit rate (15 deg/hr)

To meet the two year orbital life capability, a gas bearing gyro would be utilized with the necessary electronics provided for a closed loop, rate mode of operation. Several leading gyro vendors were contacted to establish state-of-the-art gyro capabilities. Estimates from two vendors of the smallest total uncertainty possible in a gyro to be produced in the near future (1969-70) were 0.05^{o}/hr and 0.15^{o}/hr. Both estimates are based on a gyro that would be kept running following the last trim of bias drift.

The field of view of the Polaris star sensor is required to be about 4 degrees by 4 degrees with an electronic offset capability of ± 9 degrees about the spacecraft roll axis. The ± 9

degree offset is required to maintain Polaris within the sensor field of view during roll offset pointing from the local vertical. The 4 degree view is necessary to maintain Polaris within the field of view throughout the complete orbit without the need to update command angles to account for the apparent 0.9 degree radius circular movement of Polaris, and to allow for initial acquisition. Since the fields of view of existing Canopus trackers closely approximate the above requirements, modifications to these trackers were considered. The JPL/Barnes Canopus tracker would require the following modifications:

a. Shorter aperture in the image dissector tube

b. Change in threshold settings

c. Change in power supply design

Although Canopus is approximately 12 times as bright as Polaris, the required sensitivity of the present optics is considered to be adequate.

Since the best estimate of gyro total uncertainty available on a gyro to be utilized in the 1969-70 period was approximately a factor of three greater than that required, and because of special handling of the gyro with regard to drift trim prior to installation on the vehicle, the Polaris star sensor was selected over the gyrocompass approach.

6.4.2.5 Momentum Storage Devices

Discussed in this section are the results of investigation and comparison of some of the important properties (weight, power, etc.) of various momentum storage devices. This study was conducted prior to selecting the final design and, as such, the momentum values are greater than the preferred design values. The results, however, are applicable to the preferred design. The devices considered were:

a. Mechanical Flywheel (MFW)

b. Control Moment Gyro (CMG)

c. Fluid Flywheel (FFW)

Each of the above devices is compared on the basis of providing the following angular momentum storage capability:

a. Pitch: 10 ft-lb-sec

b. Roll: 6 ft-lb-sec

c. Yaw: 6 ft-lb-sec

6.4.2.5.1 Mechanical Flywheel

A weight and power breakdown for the three MFW axes is presented below:

Axis	Momentum Storage Capability (ft-lb-sec)	Weight (lb)	Power (watts)
Pitch	10	30	8
Roll	6	21	6
Yaw	6	21	6
Total	22	72	20

6.4.2.5.2 Control Moment Gyro

The CMG differs from the mechanical flywheel in that it produces torques by changing its angular momentum vector in direction, rather than in magnitude. However, because of this, a single CMG per axis introduces a crosscoupling torque in an axis orthogonal to that axis about which control is desired. Thus, to avoid crosscoupling, it is necessary to use two CMG's per axis, mounted such that the components of torque orthogonal to the controlled axis cancel. To accomplish the cancellation, the gyro gimbals must be driven in opposite directions with the drives required to be in close synchronization. On this basis, the following weight and power figures were derived:

Axis	Momentum Storage Capability (ft-lb-sec)	Weight (pounds)	Power (watts)
Pitch	10	29	12
Roll	6	22	7
Yaw	6	22	7
Total	22	73	26

6.4.2.5.3 Fluid Flywheel

The angular momentum capability of a fluid flywheel is proportional to the area enclosed by the fluid loop. For a given angular momentum, the larger the area enclosed, the lower the weight of the system. The following formula relates the weight, power, radius of enclosed area, and angular momentum of a fluid flywheel momentum device:

$$H^{2.84} = P\ Eff\ R^{2.26}\ W_{hg}{}^{2.42}/717$$

where:

H = angular momentum (ft-lb-sec)

R = radius of enclosed area (ft)

W_{hg} = weight of mercury fluid (lb)

P = power (watts)

Eff = system efficiency, assumed to be (Eff pump) times (Eff controller)
= 0.06

For a rectangular area, the following formula is used to derive an effective radius for use in the above formula:

$$R_{eff} = 2A/L$$

where:

R_{eff} = effective radius

A = area of rectangle

L = length of the periphery of the rectangle

(All weights listed below include 15 percent of the weight of the mercury as the weight of the pump necessary to circulate it.)

Axis	Momentum Storage Capability (ft-lb-sec)	Weight (pounds)	Power (watts)
Pitch	10	103	35
		77	70
		58.5	140
Roll	6	57.5	35
		43.6	70
		33.4	140
Yaw	6	51.7	35
		39.1	70
		28.8	140
Totals			
Minimum Weight	22	120.7	420
Minimum Power	22	212.2	105

Fluid flywheel systems have an inherent time constant of approximately one second. Since it is desired to have an orientation control system time constant on the order of several hundred seconds (to minimize the effects of structural/control system elastic coupling), it will be necessary to provide means of increasing the FFW system time constant. The increase in time constant can be obtained mechanically, but a severe weight penalty occurs.

Increasing it electrically adds further complexity and weight to the system. Presented below is a tabulation of the total weight and power of each of the momentum devices considered:

System	Weight (pounds)	Power (watts)
Mechanical Flywheel	72	20
Control Moment Gyro	73	26
Fluid Flywheel	121	420

The mechanical flywheel is thus the lightest and requires the least power. The fluid flywheel would require further work to reduce the inherent 1-second time constant or to add electrical networks. This modification would probably result in increased weight and reduced reliability. The CMG appears to be a more complex device requiring a highly synchronized gimbal drive. This, and the fact that CMG gyros run continuously at high speed, tends toward lower reliability than that of a mechanical flywheel. Also, the CMG time constant is normally small which would require additional electronics. Thus, since the mechanical flywheel weighs slightly less than the CMG, is less complex, and will provide the long time constant desired without additional modification, the three axis mechanical flywheel control was selected as the optimum momentum storage device for this mission.

6.4.2.6 On-Off/Proportional Flywheel Control

The technique of on-off control of the flywheels was recently investigated on another program. The results of the investigation are applicable to ATS-4. Tnis technique was considered because it offered possibilities of low power operation and simplicity of circuit design. However, following an analysis of this method, it was rejected in favor of proportional flywheel control for the following reasons:

a. Logic circuitry required for flywheel unloading of the on-off system caused the circuit complexity to increase to the point where it was approximately equal to that for proportional control.

b. Gating operation had to be accomplished in small increments compared to proportional control (approximately 10:1 ratio). This increased the number of solenoid operations.

c. The difference in power requirements was small compared to total subsystem power.

d. Proportional control allows the direct use of existing electronic controller designs.

e. Torquer cycling can give rise to considerable energy in the higher frequency spectrum, thus potentially creating undesirable excitation of flexible appendages.

6.4.2.7 Spacecraft Orientation During Vernier Thrusting

Two alternatives for the spacecraft orientation during vernier thrusting were considered: (1) precession of the spacecraft spin axis normal to the orbit plane, and (2) no precession other than that required for correction for attitude errors. These alternatives are compared below:

(a) Precession Perpendicular to Orbit Plane	(b) No Precession
Requires additional precession sequence - precession through 70.6 degrees (535 lb-sec), followed by attitude correction.	Attitude correction only required.
Thrusting at apse, and trade radial velocity for altitude error.	Thrusting at apogee burn point and 180^{o} point.
Requires six 1-lb thrusters and one 10-lb thruster	Requires eight 1-lb thrusters and one 10-lb thruster
After precession, there is continuous POLANG coverage.	Intermittent POLANG coverage.

Approach (a) has a slight weight advantage since the extra fuel weight required for precession by (a) is counter balanced by the weight of two additional 1-lb thrusters for (b), and a small (10 lb/ sec) reduction in vernier velocity requirement is obtained with (a) by trading radial velocity for altitude error. However, approach (a) requires an additional precession sequence, and the intermittent POLANG coverage of approach (b) is not considered to be a

serious disadvantage (POLANG coverage from Rosman is about three hours twice a day (Figure 6.4-2). Since the attitude corrections required in approach (b) are relatively small (of the order of 10 degrees), vernier thrusting without attitude correction would be feasible as a backup mode. Thus, approach (b) has been selected for the ATS-4.

6.4.2.8 Yaw/Roll Axis Stabilization to the Sun

Prior to attempting to establish yaw axis pointing to the earth using an earth sensor, it is desirable to establish well defined spacecraft attitude and rate conditions for the initiation of control with the earth sensor. The sun is used to establish the spacecraft attitude and a gyro is employed to establish rate control. Two schemes were considered with regard to the manner of transferring from sun/gyro control to earth control. One method was to point the negative yaw axis to the sun with the rate about the yaw axis controlled to nominally zero and transferring to earth sensor control around high noon. The second scheme was to align the roll axis to the sun with a rate of about 0.2 degree/ second around the roll axis until the earth entered the field of view of the earth sensor, at which time the roll rate bias would be removed and earth stabilization would occur. In this case earth control would

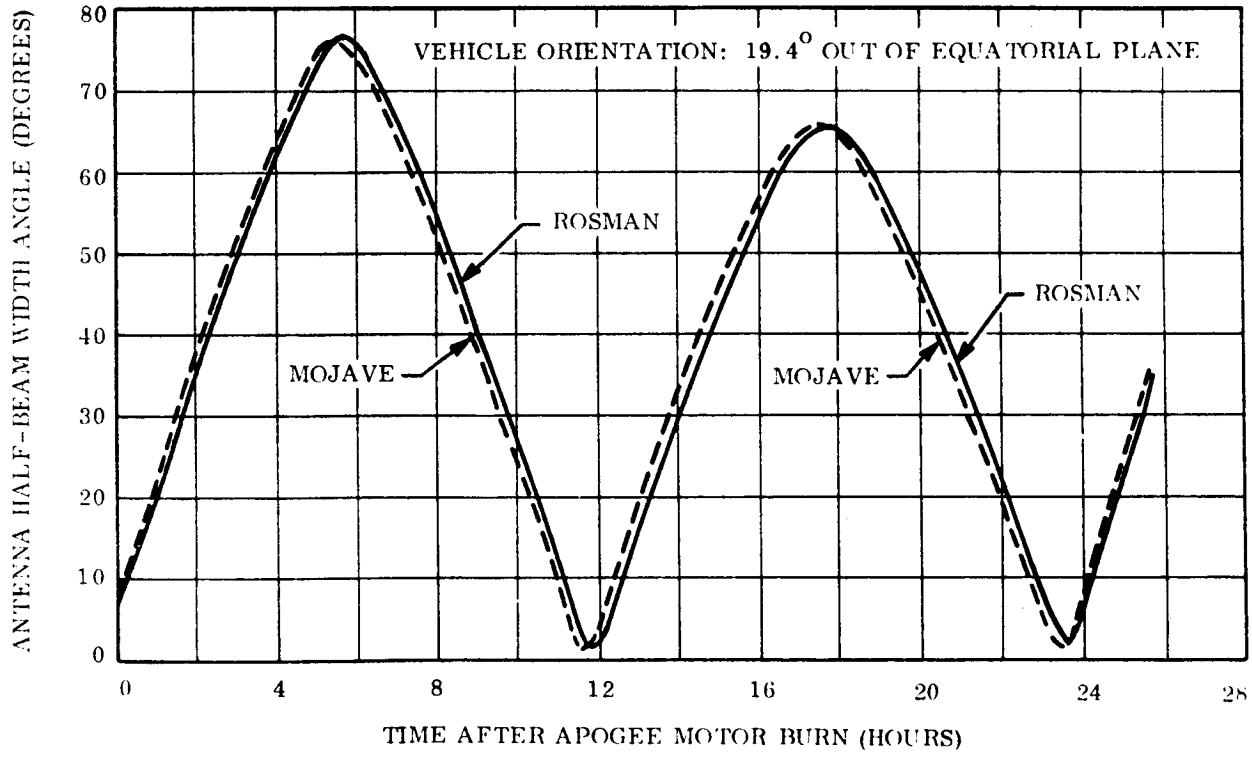


Figure 6.4-2. Antenna Half-Beam Angle During Vernier Maneuvers During Synchronous Orbit

occur around 6 am or 6 pm. Listed below are the significant considerations for each approach:

Roll Axis to Sun Concept	Yaw Axis to Sun Concept
a. Requires roll rate bias to insure that FOV of the earth sensor intersects the earth (rates of 0.2 deg/sec).	a. Requires an additional sun sensor set and associated control electronics (2.5 lb).
b. Requires dynamic acquisition of earth.	b. Allows passive earth acquisition and confirmation, interpretation and control by ground if desired.
c. Requires an additional thruster producing 8 times (0.007 lb) the thrust of the normal thrusters to remove roll rate bias within the FOV of the earth sensor.	c. Allows the possibility of restabilization without the use of gyros.
d. Requires 25 watts of power and 4 lb for additional thruster for removing roll rate bias.	d. Provides a more desirable attitude for solar power collection after deployment.
e. Difficult to provide continuous communications contact during roll search and earth acquisition.	e. Provides an improved command telemetry antenna configuration and continuous communications contact with the earth during earth stabilization.
f. If the advantage of saving one sun sensor is to be realized, then the spacecraft axis about which the roll search is made varies with the time of year which will result in undesirable crosscoupling between axes due to gyros and thrusters being on the control axes and due to cross-products of inertia.	

6.4.2.9 Orientation Control/Stationkeeping Mass Expulsion Subsystem

This subsystem provides the impulse required to perform station capture, east/west and north/south stationkeeping and east/west station change. In addition, it provides the control torques for orientation control after despin which involves the stabilization modes

and flywheel unloading. Preliminary requirements for this subsystem indicated that the thrust level would be about 0.001 pound and the impulse requirement would be about 17,750 pounds/second and that a configuration using 12 thrusters was indicated. A resistance jet propulsion approach was selected since the 0.001 pound thrust range is too low for higher energy liquid propellants and requires too much power for the use of ion engines. Ion engines were investigated and were found feasible for performing a portion of the total orientation control/stationkeeping function because of the high power requirement for functions such as N-S Stationkeeping, E-W station changing, and sun stabilization. The power required is about 250 watts per 0.001 pound of thrust. It was found that the attitude stabilization and east/west station change functions particularly are not feasibly accomplished with ion engines, and that a single resistance jet subsystem to perform all of the functions presents the optimum approach.

Two resistance jets were studied for the stationkeeping mission, one using ammonia (NH_3) as the propellant and the other using nitrogren (N_2) as the propellant. The following parameters were used in the calculations:

	NH_3	N_2
Density (70°F)	38 lb/ft^3 (liquid)	9.7 lb/ft^3 (gas at p = 4000 psi)
Specific Impulse	210 sec	$\approx$ 125 sec

The total impulse (I_T) required is 17,750 lb-sec, then the weights and volumes of the two propellants are:

	Weight	Volume
NH_3	84.5 lb	2.22 ft^3
N_2	142 lb	14.7 ft^3

As can be seen from the above data, the ammonia system is lighter and requires less volume than the nitrogen system. In addition, the reliability of the ammonia system is higher due to

the lower operating pressure required and the fact that the N_2 system needs a complicated regulator system to control the 4000 psi N_2 to approximately 10 psi. For these reasons, the ammonia resistance jet was chosen to accomplish the stationkeeping mission.

Having selected the NH_3 resistance jet approach, a tradeoff was made between the General Electric (Evendale) resistance jet and the AVCO resistojet. The General Electric resistance jet was selected because of a weight advantage. These tradeoffs are discussed below.

6.4.2.9.1 General Electric Resistance Jet

To start the study, the optimum operating temperature of the thruster must be determined. Figure 6.4-3 shows the weight for a typical system for various operating temperatures at a total impulse of 17,750 pound-second. It was assumed that existing Airite tanks would be used. This total impulse was chosen because the study was done before the final total impulse was decided upon and 17,750 pound-seconds was in the general range expected. A typical system configuration is shown in Figure 6.4-4. An operating temperature of 1800°F was chosen to realize a high specific impulse and to make use of an existing 2000°F thruster design while limiting warmup time. Characteristics for various temperatures are listed below:

Operating Temperature (°F)	1200	1400	1600	1800	2000
Average I_{sp} $\left(\frac{\text{lbf-sec}}{\text{lbm}}\right)$	150	170	190	210	240
Thruster Weights (lb)					
Single	1.67	1.67	1.67	1.67	1.67
Dual	1.60	1.60	1.60	1.60	1.60
Power (watts at 28 vdc)					
Single nozzle	8	12	16	20	25
Dual nozzle	10	14	18	24	30
Triple nozzle	13	17	21	27	33

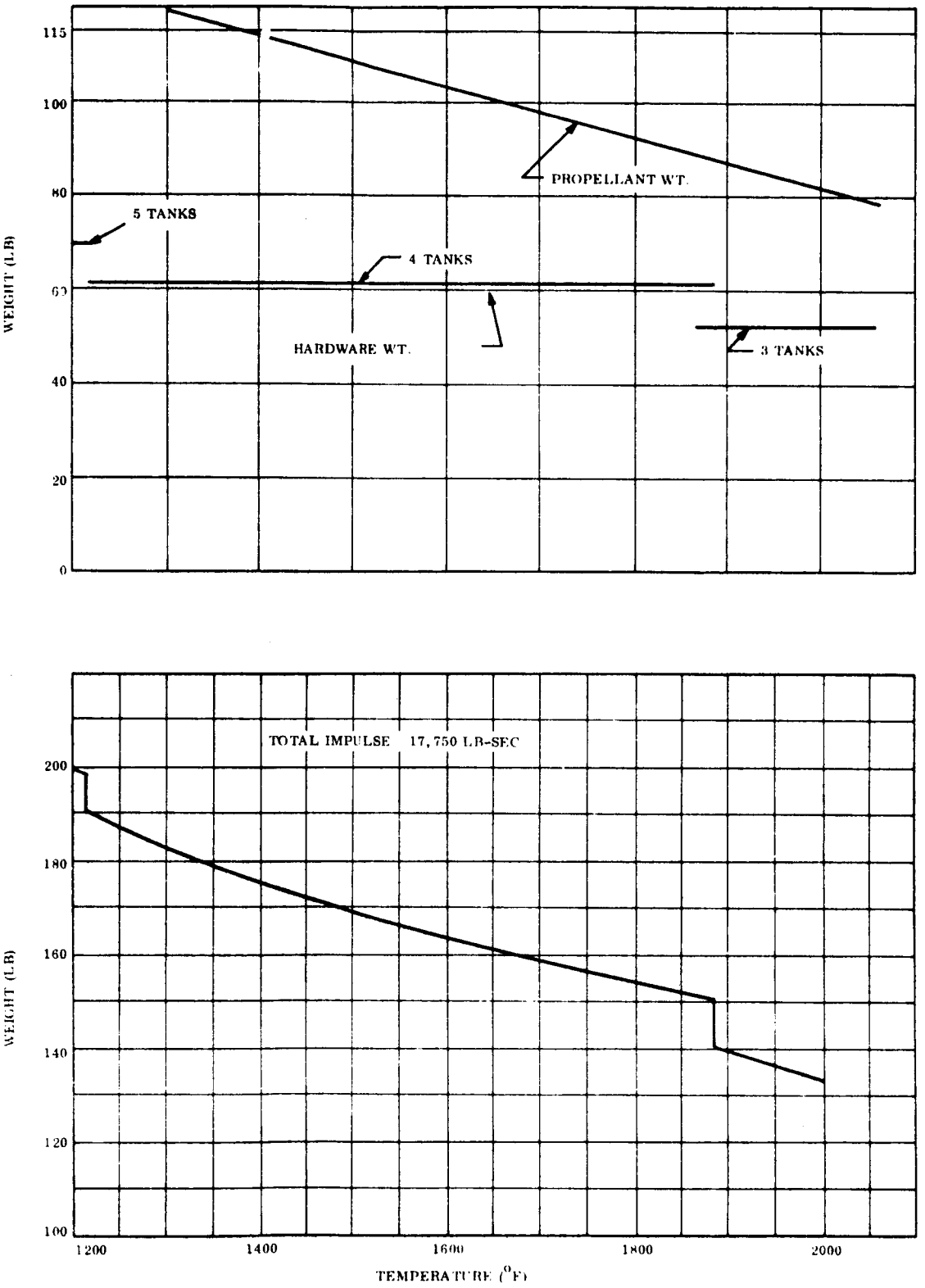


Figure 6.4-3. Data for GE Resistance Jet

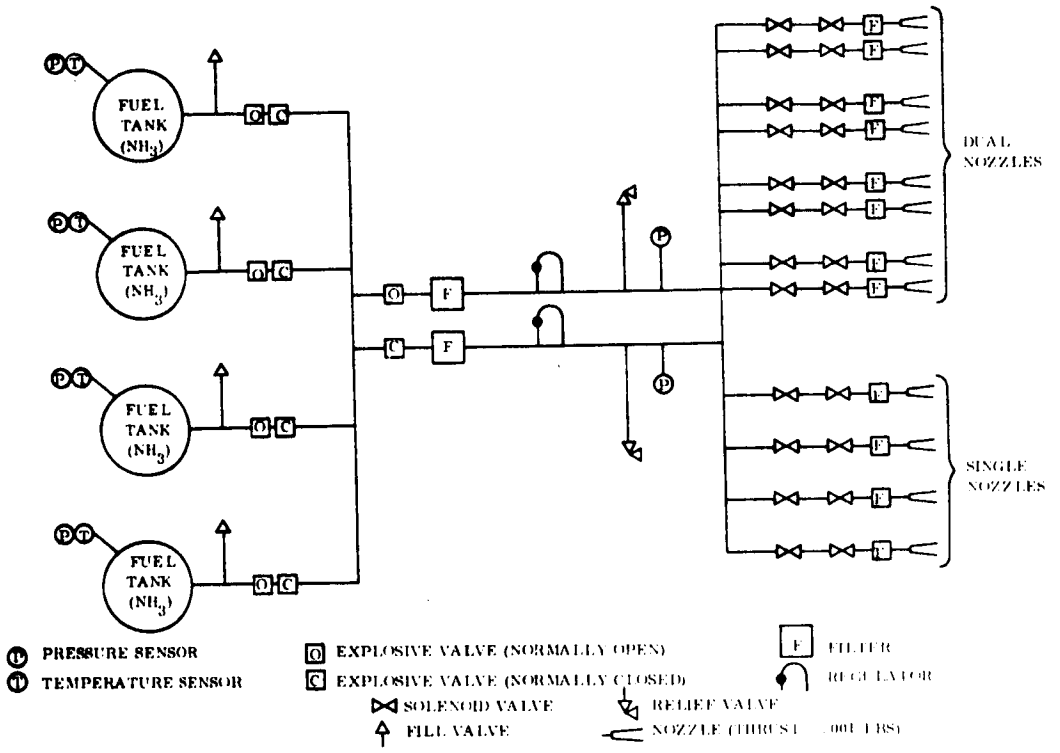


Figure 6.4-4. Resistance Jet Stationkeeping/Orientation Control Subsystem (GE)

Once the operating temperature was determined, different system weights were determined for various total impulses. Figures 6.4-5 and 6.4-6 show these system weights. The propellant for the system is ammonia (NH_3). Between the properties of NH_3 and the system hardware considerations, the environmental temperature range is limited. The free vaporization principle is used along with a capillary action on internal wicking in the propellant tanks to deliver gaseous ammonia to the regulator which regulates the pressure downstream to 10 psi. This means that the regulator must be fed at least a pressure of 10 psi. If the free vaporization principle is to be used, the temperature of the ammonia in the tanks must be at least $-35^{\circ}F$ to produce 10 psi vapor pressure. Once vaporization occurs, the propellant must not be allowed to change back to a liquid since this might damage the regulator and possibly the valves. To be certain liquification does not occur, the environmental temperature should be $0^{\circ}F$ or greater. The upper limit on the temperature range is $120^{\circ}F$. This upper limit is imposed by the vaporization pressure in the propellant tank. The pressure should not exceed the design pressure of the tank which

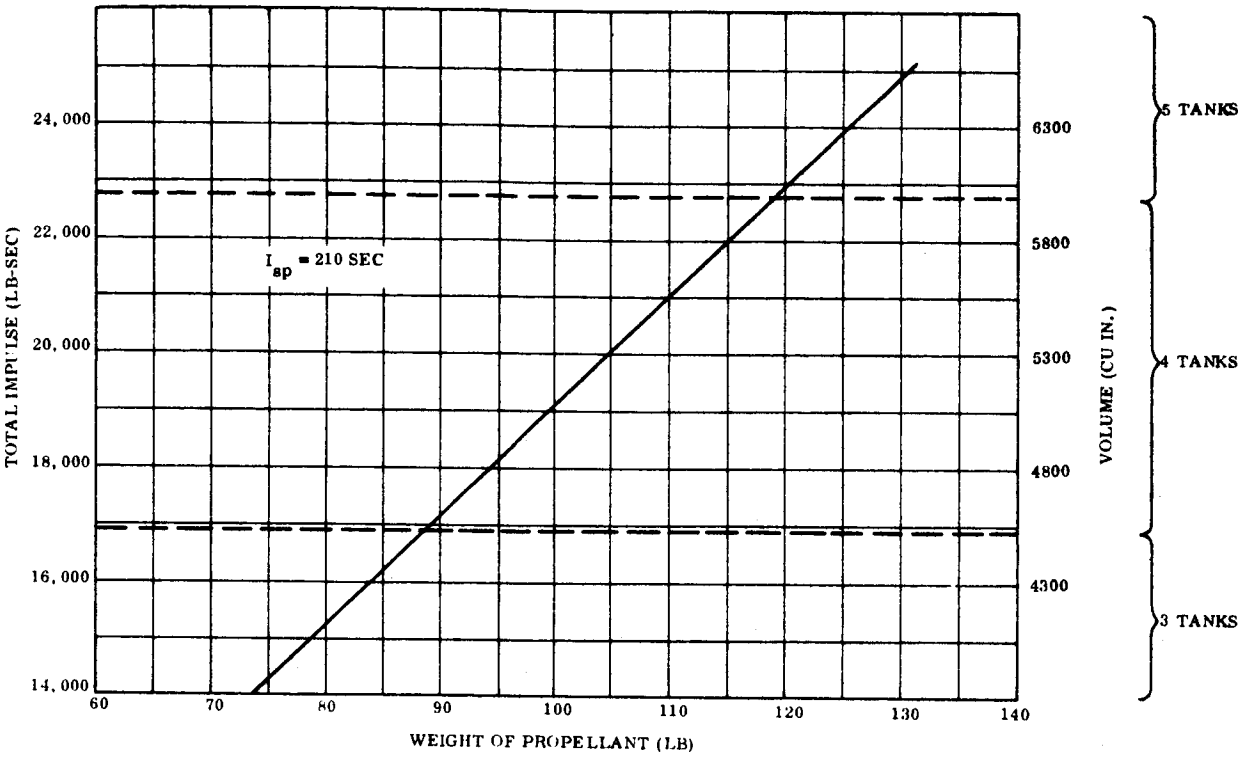


Figure 6.4-5. Propellant Weight vs Total Impulse at 1800°F (GE System)

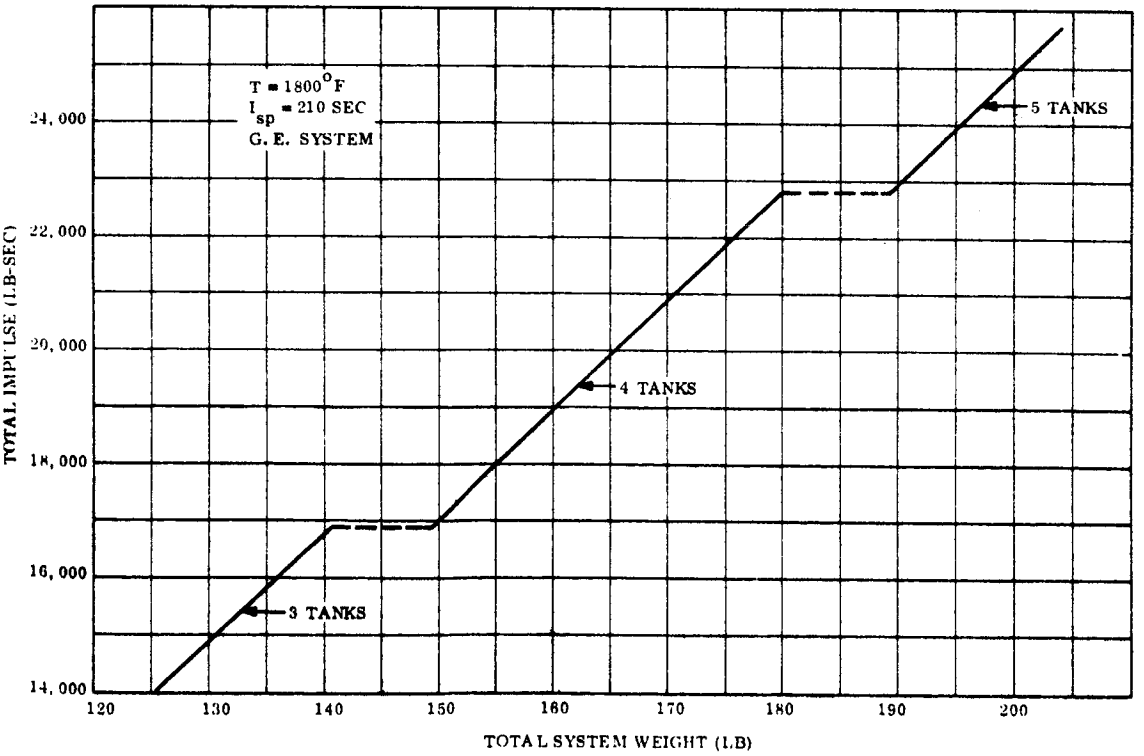


Figure 6.4-6. Total System Weight vs Total Impulse (GE System)

is approximately 300 psi for this system. Figure 6.4-7 is a trace of the propellant on a pressure-enthalpy curve. Point A is propellant at 20°F in the propellant tank. Point B is propellant after it leaves the regulator. From B to C is the heating of the propellant in the thruster. From C onward is the gaseous propellant expanding in the exit nozzle.

6.4.2.9.2 AVCO Resistojet

The AVCO system does not have a range of operating temperatures; therefore, the specific impulse is fairly constant at 150 seconds. In order to compare this system further with the GE system, a typical AVCO system (Figure 6.4-8) to meet the same requirements was chosen for analysis. Figures 6.4-9 and 6.4-10 give the total weight of the system for various total impulses. The AVCO system requires power only during thrusting; however, the power required is 40 watts for each thruster at one volt. The AVCO Resistojet also uses ammonia as a propellant. The temperature range of the system is limited by the properties of ammonia and the system hardware, the first being the more critical. This system uses the free vaporization principle. The propellant tank delivers a mixture of vapor and liquid ammonia to the first plenum chamber. Due to increase in volume experienced by this mixture of vapor and liquid ammonia, the pressure drops. This induces more vaporization which in turn reduces the amount of liquid in the first plenum chamber. The same process continues in the second plenum chamber to eliminate all liquid ammonia before the propellant (vaporous ammonia) proceeds to the thrusters. The plenum chambers are controlled by a pressure switch which keeps a downstream pressure of 10 psi to the thrusters. To provide 10 psi, the ammonia vapor pressure must be at least 10 psi which requires a temperature of -35°F. To be certain the desired pressure is obtained and liquification does not occur, a lower temperature limit of 0°F is recommended. The upper temperature limit is 120°F due to design pressure of the propellant tank and plenum chambers.

6.4.2.9.3 GE and AVCO Approaches

The following comments can be made regarding the GE and AVCO approaches:

a. Both systems operate with a 10 psi pressure in the propellant lines upstream of the thruster. The propellant tanks for both systems operate from 50 to 300 psi

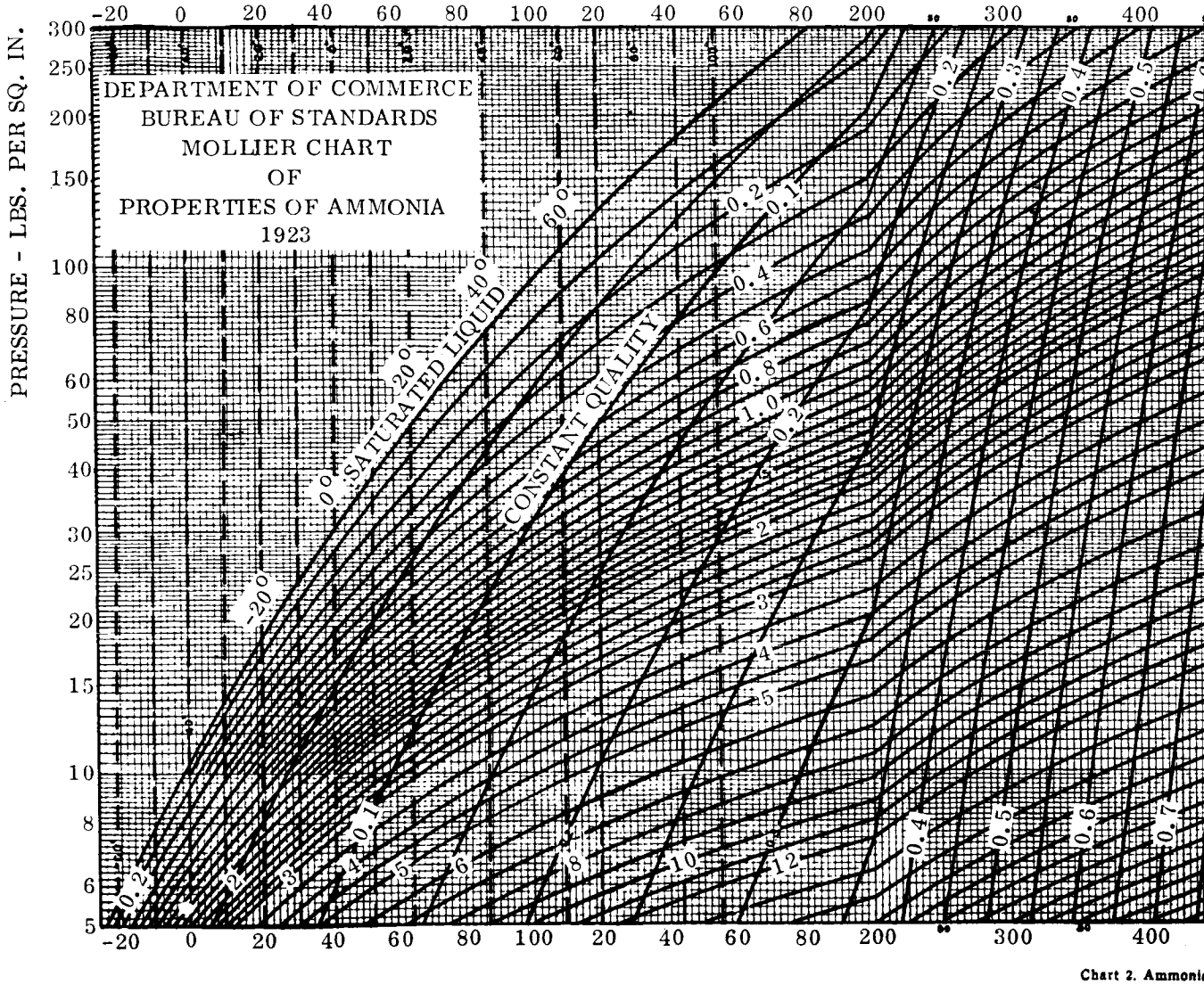
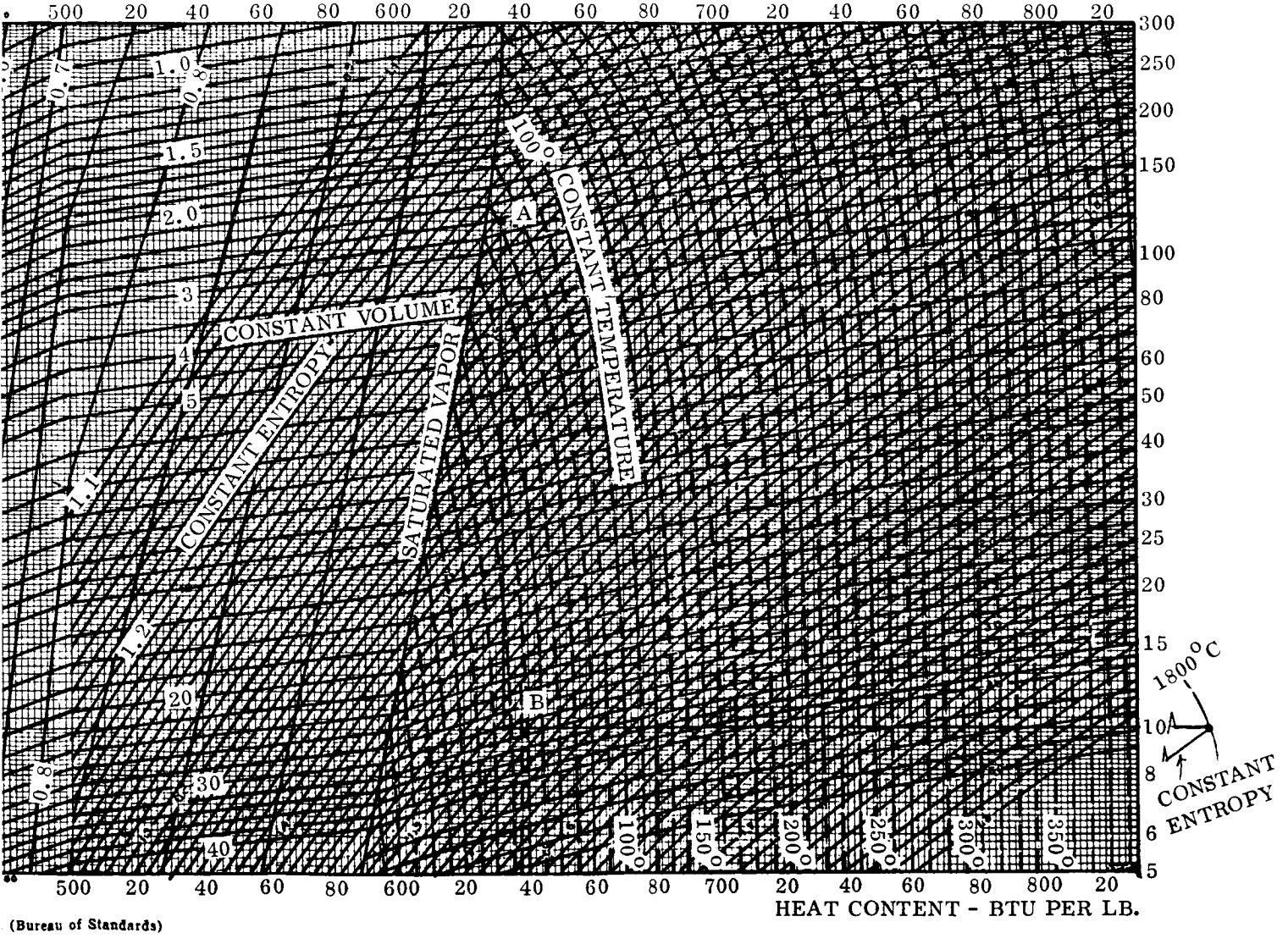


Chart 2. Ammoni

6.9-25



(Bureau of Standards)

Figure 6.4-7. Mollier Chart of Properties of Ammonia

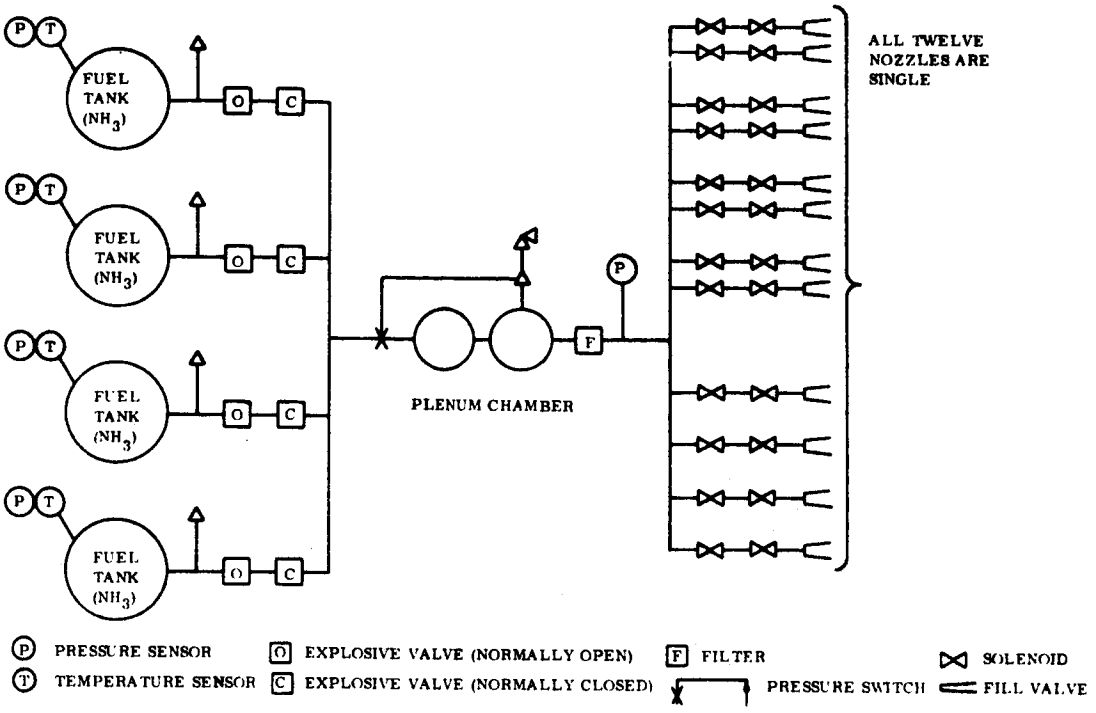


Figure 6.4-8. AVCO Resistance Jet Subsystem

depending on the environmental temperature. Therefore, both systems are basically low pressure systems.

b. With the duty cycles that are being considered for the propulsion system of the ATS-4 program, the AVCO system uses somewhat less average power. For a typical duty cycle of thrusting 2.5 hours/day N-A and 0.05 hours for orientation control and stationkeeping, the General Electric Resistance Jet requires 439.6 watt-hours per day and the AVCO Resistojet requires 412.8 watts-hours per day. This includes warmup time for the General Electric system.

	Total Watts/Day	Average Watts/Hour
GE	439.6	18.3
AVCO	412.8	17.15

c. Both use the same solenoid valve made by Carleton.

d. There are two ways to heat the propellant to obtain a high Isp. One is the thermal storage technique which the General Electric (Evendale) system uses. This method uses a heater constructed of a platinum resistance wire surrounded by magnesium oxide and boron nitride insulation material in an Inconal 600 cylindrical sheath.

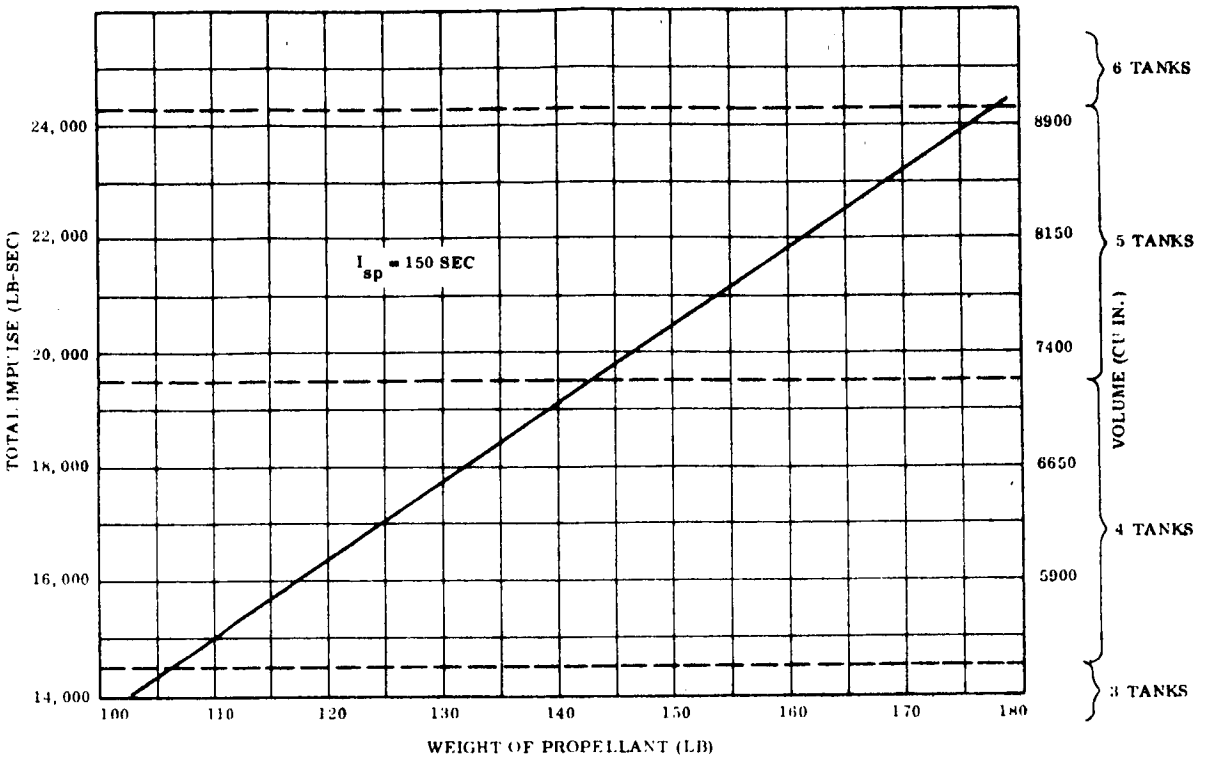


Figure 6.4-9. Propellant Weight vs Total Impulse (I_{sp} = 150 sec), AVCO System

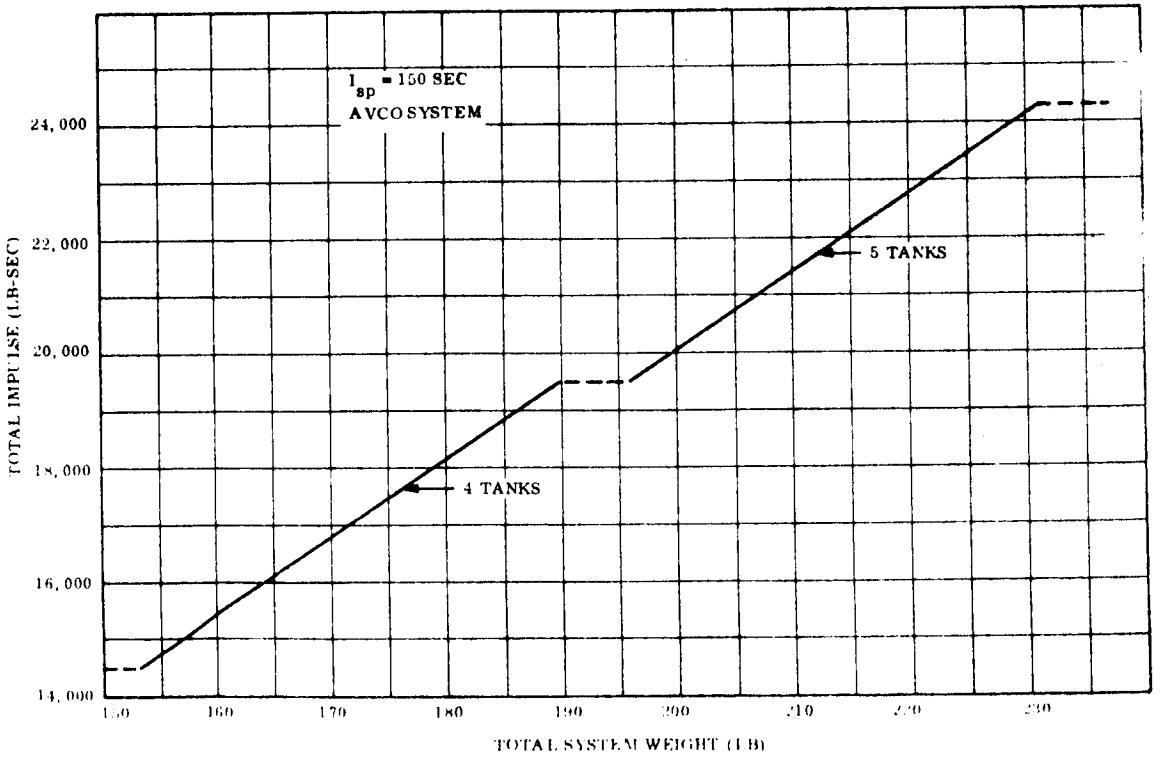


Figure 6.4-10. Total System Weight vs Total Impulse (AVCO System)

This technique requires a 1-hour warmup time. The second method uses a fast heat-up technique in which the power and the thruster are turned on simultaneously. The heater is a coiled heater through which the flow passes. AVCO uses the fast warmup technique which has the advantage of no warmup time. The thruster temperature and percent of warmup as a functional time are shown in Figure 6.4-11.

Figure 6.4-11 also shows the temperature drop for the AVCO and General Electric (Evendale) units over a period of time. This temperature drop directly affects the Isp of the unit. The General Electric unit (thermal storage) temperature does not drop because a 2000°F heater is used. When the propellant is allowed to flow after a 1-hour warmup, the temperature still increases due to the 2000°F heater, but not as fast and not to 2000°F because of the heat going out in the propellant.

e. General Electric uses free vaporization with tank wicking and a pressure regulator while AVCO uses free vaporization with two plenum chambers and a pressure switch.

f. General Electric Company has developed a dual and a single thruster. AVCO has only a single thruster.

g. The AVCO system has a much lower specific impulse than the General Electric system. Isp = 150 seconds for AVCO and 210 seconds for General Electric. Because of this difference in specific impulse, the AVCO system requires a greater amount of propellant than the General Electric system. The weight for a system having a total impulse of 17,750 lb-sec is 152 pounds for the GE system and 175 pounds for the AVCO system. The preceding weights were obtained from the following table.

Part	AVCO		GE	
Propellant tanks	(4)*	24.60	(4)	7.6
Explosive Valve	(8)	3.04	(10)	3.8
Filters	(10)	2.22	(11)	2.40
2 regulators, 2 pressure transducers				1.8
2 relief valves				
1 pressure switch, 4 temperature sensors		3.00		
Solenoid valves (Carleton)	(24)	4.80	(24)	4.8
Thrusters	(12)	1.20	(12)	13.8
Tank internal parts (wicking, etc.)				2.4
Pressure transducer	(5)	2.25	(4)	1.8
Plenum tank	(2)	0.80		
		41.91		38.40
Supports, tubing etc.				8.5
Propellant weight		124.86		93.0
		175.00 lb		**139.9 lb

* Numbers in parantheses are quantity of parts.

** This weight is less than that shown in Figure 6.4-7 because of refinement of the weight values.

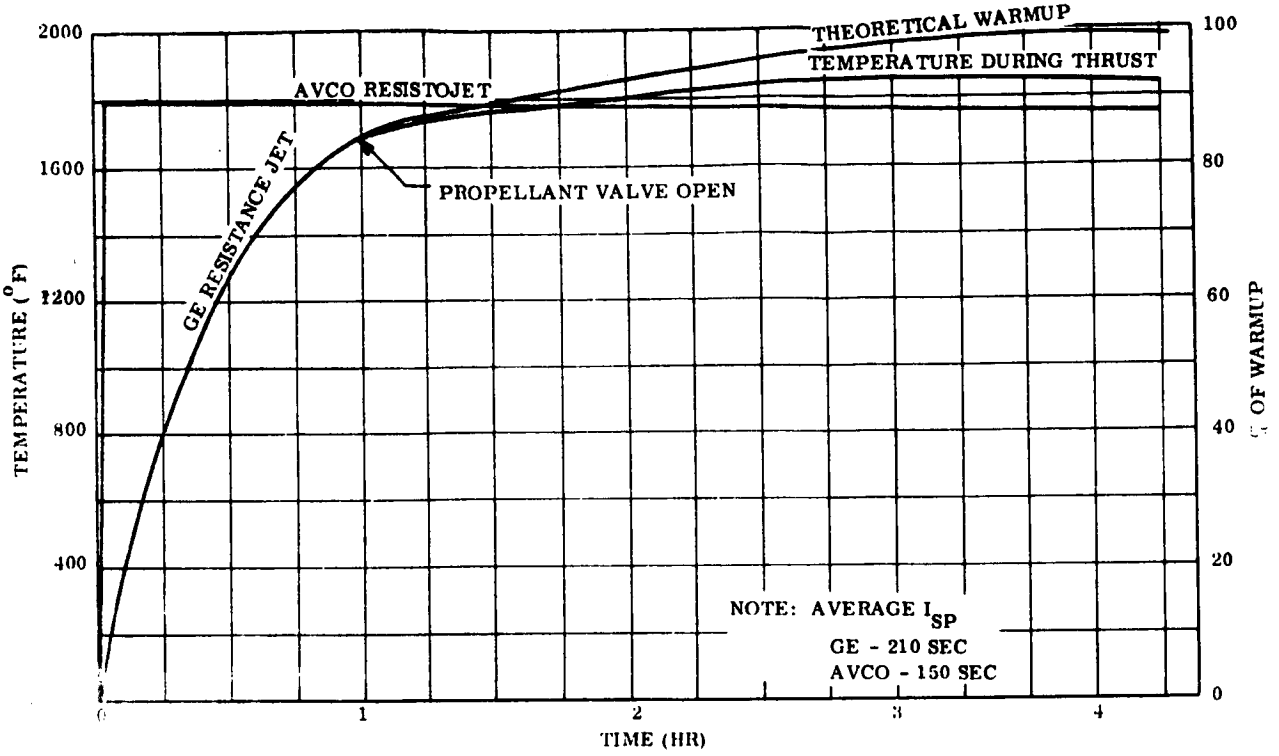


Figure 6.4-11. GE Resistance Jet and AVCO Resistojet Operating Temperatures

h. Both GE and AVCO have experience in the micropound thrust level range; therefore, both companies are capable of producing a thrust level of approximately 1000 micropounds. Previous experience is as follows:

General Electric

10 Micropound thruster for NRL
300 Micropound thruster demonstrated for Goddard
20 Millipound thruster for NRL to be flown early in 1967

AVCO

Thrusters in the range of 1000 micropounds have been demonstrated for NASA Lewis.

i. Both GE and AVCO systems have thrusters which require gaseous ammonia at approximately 10 psi; therefore the feed systems can be interchanged. By doing this the optimum thruster unit can be used with the optimum feed system. Following is a table of the weights of the GE thruster with the AVCO feed system and the GE feed system with the AVCO thruster.

Component	AVCO Feed System with GE Thruster		GE Feed System with AVCO Thruster	
Propellant tank	(3)	18.15	(4)	8.80
Explosive valves	(6)	2.28	(8)	2.72
Filter	(13)	2.86	(13)	2.86
1 pressure switch, 4 temperature sensors		3.00		
2 regulators, 2 relief valves				1.8
Solenoid valve (Carleton)	(24)	4.8	(24)	4.8
Thruster	(12)	13.8	(12)	1.2
Pressure transducer	(4)	1.8	(6)	2.7
Plenum tank	(2)	0.8		
Tank internal parts				2.4
		47.49		27.28
Supports, tubing, etc.		8.0		4.00
Propellant weight		93.00		124.86
Total weight		148.49		156.14

Propellant tank weight for the GE system is based on a design input from GE Evendale. No information was obtained from AVCO on the tanks; therefore, an existing tank was assumed for use (Airite Tank 6431-3).

The above comparisons are as complete as possible considering the limited information available relative to the AVCO system.

6.4.2.10 Accelerometer/Gyro for Coning Control

When the spacecraft is spun up about its Z axis, initial body rates and disturbance moments about the X and Y areas will cause a coning motion of the spin axis in inertial space. At the outset of the study, a coning damper was considered necessary for two reasons:

a. The ratios of moments of inertia I_z/I_x and I_z/I_y are less than 1 for the ATS-4. spacecraft, so that structural damping and propellant sloshing would cause the cone angle to increase. Since the rate of increase of the cone angle is proportional to the cone angle, it is necesaary to reduce the cone angle to a small value immediately after spinup.

b. A coning motion with a 10 degree amplitude (possible without a coning damper) would cause a sinusoidal variation of the attitude sensor signals corresponding to an attitude variation of $\pm$ 10 degrees. The frequency would be about 0.1 cps. This would increase the difficulty of obtaining accurate attitude information.

Coning may be reduced by applying a control torque (T_x) about the body x-axis in phase with the body x-axis angular rate ($-W_x$) or by applying T_x in phase with the body y-axis angular acceleration ($\dot{W}_y$). Thus, W_x could be sensed by a rate gyro, or alternatively, $\dot{W}_y$ could be sensed by a linear accelerometer or an angular accelerometer. Location of the three sensor types in the spacecraft is shown in Figure 6.4-12.

The sensors are required to have a threshold level corresponding to a coning amplitude of less than 0.25 degree, and a saturation level of greater than 2.5 degrees coning. Body rates and acceleration amplitudes for practical sensor locations in the ATS-4 spacecraft are summarized in Table 6.4-1. The rates W_x, W_y and acceleration $\dot{W}_y$ have a frequency of about 1 cps, while W_z is constant.

For the rate gyro, the range of signal rates to be measured is between 0.17 degree/sec and 2.0 degree/sec. However, the spin rate of 430 degree/sec may be about an axis displaced by an angle E_i due to the I_{xz} cross product of inertia:

$$E_i = I_{xz}/(I_x - I_z)$$

Thus, if I_{xz} is 0.25 percent of I_x, E_i = 9.5 arc min. Additionally, misalignment of the sensor input axis by 6 arc minutes may be present. Thus, a dc bias level corresponding to 430 sin (15.5 arc min.) = 1.94 degree/sec may appear to the gyro output signal. This signal must be attenuated by 21 dB in order that the threshold switches will operate properly. Since the signal frequency is less than 1 cps, satisfactory operation of the system may be difficult to achieve.

In the case of a linear accelerometer, the signal range is 0.00191 g to 0.0214 g, and the dc bias level, assuming alignment as above, is 5.25 sin (15.5 arc min.) = 0.0237 g. Again, attenuation of this signal by 22 dB is required.

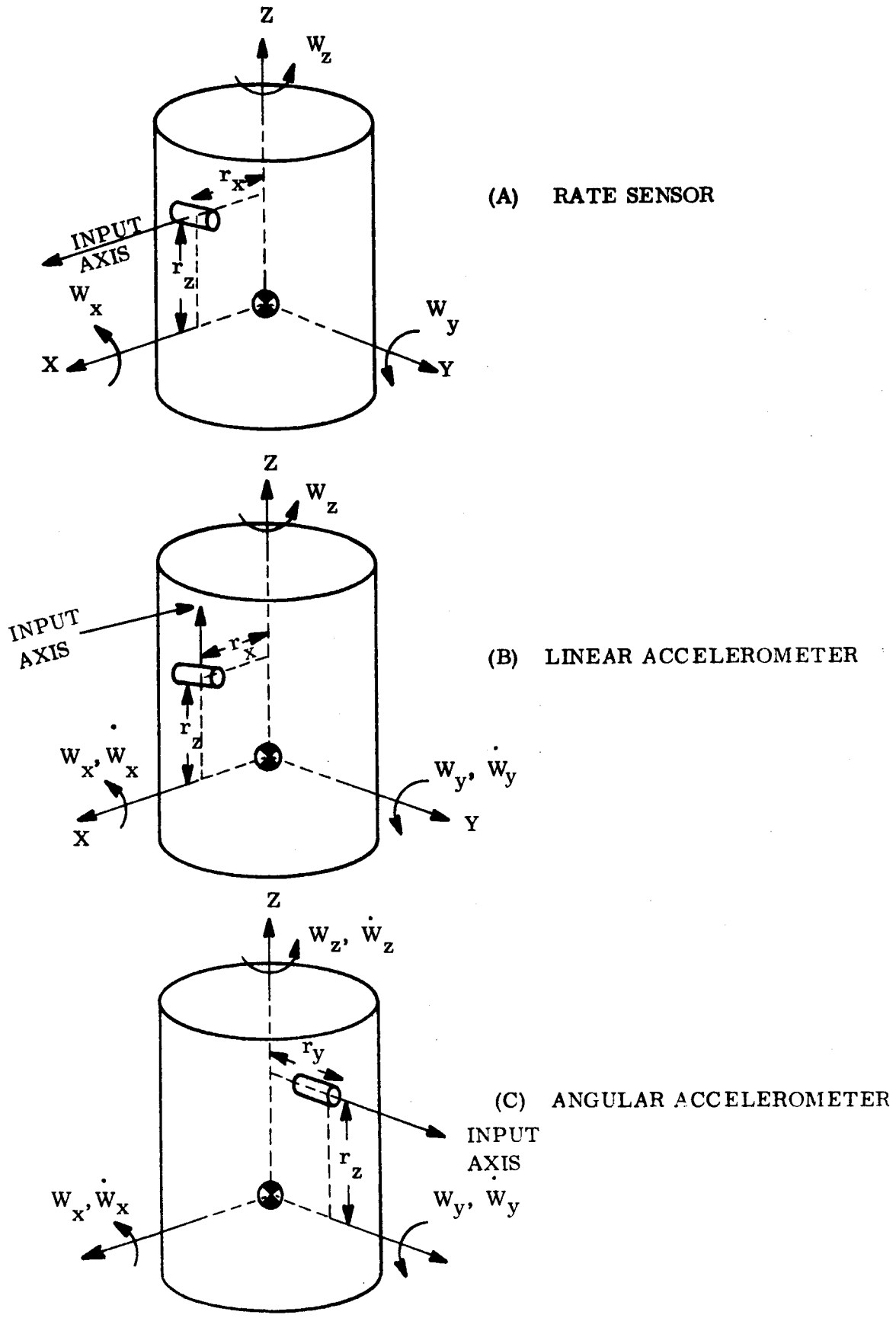


Figure 6.4-12. Coning Control Sensor Location

In the case of the angular accelerometer, the sensor sensitivity to cross axis forces is 0.001 radian/sec^2/g. The centrifugal force of 5.25 g is along the sensor input axis, and the cross axis force would be 5.25 sin (15.5 arc min.) = 0.0237 g, which would produce a sensor error of 0.0002 radian/sec^2 compared to the threshold level of 0.02 radian/sec^2.

On the basis of the above considerations, the angular accelerometer has been selected. However, both the gyro and linear accelerometer approaches are feasible providing that the bias levels can be sufficiently attenuated.

6.4.2.11 Station Acquisition and Despin Mass Expulsion Subsystem

The tradeoff study between candidate station acquisition and despin mass expulsion subsystems was made prior to finalizing the spacecraft system design. Thus, a value of about 30,000 lb-sec was used for the total impulse, or approximately twice the final value of the total impulse (Section 5.5.3.6). The lower total impulse enhances the selection of the monopropellant system.

6.4.2.11.1 System Requirements (Nominal Design)

The vernier thrusting system is required to provide correction of injection errors, torques for coning and precession control, and despin. It is required that the system provide injection error and positioning velocity increments of 350 ft/second. This ΔV was apportioned 100 ft/ sec axial and 250 ft/ sec radial, using two rocket engines nominally, although additional engines may be required if mounting problems prevent pointing the radial engine at the spacecraft center of gravity or if redundancy is required. A spin rate of 60 to 100 rpm on a spacecraft with a roll moment of inertia of 1000 lb-sec^2-ft initially and 800 lb-sec^2-ft after apogee firing was assumed. A velocity of 100 ft/ second is the largest and 2 feet/ second the smallest velocity increment required. A radial thrusting angle of 60 degrees per spin revolution may be employed for thrusting in those mission tasks requiring this firing mode. All axial and radial thrusting should be accomplished within 1 to 2 hours (proximity time at a node in the orbit). A 4-foot radius arm was assumed for thruster moment calculations about the roll axis.

Table 6.4-1. Body Rates and Acceleration Amplitudes for Practical Sensor Locations

Item	Units	Prior to Apogee Burn	After Apogee Burn
r_x, r_y	ft	3.0	3.0
r_z	ft	2.0	5.0
1. Rate Gyro			
a. Signal (W_x)			
W_x threshold	deg/sec	0.17	0.20
W_x saturation	deg/sec	1.7	2.0
b. Cross axis rates			
W_y threshold	deg/sec	0.17	0.20
W_y saturation	deg/sec	1.7	2.0
W_z	deg/sec	430	430
2. Linear Accelerometer			
a. Signal ($r_x\dot{W}_y$)			
$r_x\dot{W}_y$ threshold	g	0.00191	0.00214
$r_x\dot{W}_y$ saturation	g	0.0191	0.0214
b. W_x Centrifugal force			
$r_z W_x^2$ threshold	g	0.00001	0.00004
$r_z W_x^2$ saturation	g	0.0001	0.0004
c. Cross axis force			
$r_x W_z^2$	g	5.25	5.25
3. Angular Accelerometer			
a. Signal ($\dot{W}_y$)			
$\dot{W}_y$ threshold	radian/sec^2	0.0203	0.0230
$\dot{W}_y$ saturation	radian/sec^2	0.203	0.230
b. Centrifugal force			
$r_x W_z^2$	g	5.25	5.25

6.4.2.11.2 General Tradeoff Considerations

A very basic tradeoff may be made between use of storeable hypergolic bipropellants, monopropellant hydrazine, and a water electrolysis rocket engine system. Total impulse and thrust requirements are high enough to permit elimination of cold and heated gases, cap pistol, subliming solids, ion engines, resistojets, solid propellant electrical thrusters, etc., after a cursory examination. The water electrolysis system designed by Hughes Aircraft Company for ATS is most suited to a spun spacecraft under existing state-of-the-art, since separation of water and electrolyzed gases is simply and reliably accomplished. The consideration of this system then centers on the despin function and the comparison of terms of weight, system complexity, and reliability between use of a single monopropellant or bipropellant system for vernier thrusting and despin. At this juncture it appeared that the weight saving and reliability enhancement in the use of the electrolysis rocket was overshadowed by a subsequent degradation of each parameter when a separate spin system was considered. Therefore, the electrolysis rocket was not considered further.

A tradeoff between monopropellant hydrazine and bipropellants was made. This tradeoff was influenced by whether "blowdown" design could be used for the hydrazine system. (In this approach, the pressurant is contained in the same tank with the hydrazine and, as the fuel is expended, the pressure decays, creating a corresponding but nonlinear decay in the thrust level.) A bipropellant system is not suited to this approach since the oxidizer-to-fuel balance in the injector is critical to chamber life. Since a calibration of tank pressure-to-engine thrust is achievable, and firing times may be adjusted thereby, no apparent mission impediment to the blowdown design was found. The blowdown system eliminates a separate propellant tank, pressurant regulator, explosive valve, pressure transducer, filter, etc. Figure 6.4-13 displays typical system designs for regulated and blowdown systems. The inherent advantages of the blowdown system in terms of weight, reliability, and developmental simplicity are apparent. However, prior studies have shown that a weight saving over the regulated system may only be realized at ullage fractions of 0.5 to 0.6 and total impulses of less than 16000 lb-sec for a minimum pressure of 100 psi. Since the total impulse of the system studied was higher, a 2 to 3 lb (order of magnitude) weight penalty was required to realize the reliability advantages.

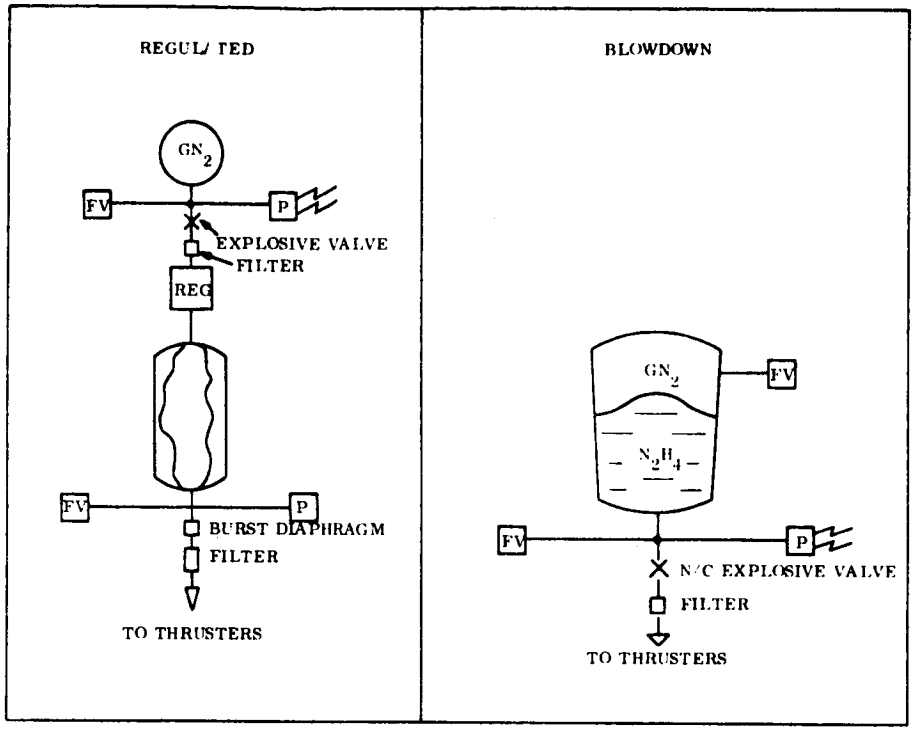


Figure 6.4-13. Regulated and Blowdown Monopropellant System

Other general considerations indicate the need for a pair of solid propellant spin rockets with less than a 2-sec burn time and high thrust to meet the impulse-time restrictions placed on the spinup maneuver. The liquid system was, therefore, not suitable for spinup.

6.4.2.11.3 System Sizing Requirement (Nominal Design)

a. Monopropellant Hydrazine - For 350 feet/second imparted to a 2245-lb vehicle, approximately 100 lb N_2H_4 (23000 lb-sec) are required. An additional 2700 lb-sec was allocated to precession of the spin axis. Approximately 132 lb of N_2H_4 are required , including a 2 percent inefficiency in expulsion. These numbers were based on an I_{sp} of 230 seconds, and it was realized that they would require modification when more detailed information on pulse widths and thruster performance became available. (An I_{sp} of 230 is consistent with steady-state performances currently being realized). However, the propellant loading also required further analysis after precession requirements were known and compensation effects on propellant weight were anticipated in this analysis.

b. Bipropellants - For 350 feet/second on a 2245 pound vehicle, 80 pounds of nitrogen tetroxide and 50 percent anhydrous hydrazine 50 percent unsymmetrical dimethyl hydrazine (23200 lb-sec) are required. For the remaining 6600 lb-sec another 23 pounds of propellant are required. The total propellant loading is therefore 105 pounds including 2 percent expulsion inefficiency. These propellant allocations were based on an I_{sp} of 290 seconds and were to be modified when more information on pulsing duty cycles and engine performances became available. (I_{sp} of 290 is conservatively consistent with steady-state performances currently being realized).

6.4.2.11.4 Sizing Calculations (Nominal Design)

a. Monopropellant System

$132 \text{ lb} \times \frac{\text{ft}^3}{60 \text{ lb}} = 2.20 \text{ ft}^3$

ullage fraction = 0.5

total tank volume = $4.4 \text{ ft}^3 = 7550 \text{ in.}^3$

minimum pressure = 100 psi

initial pressure = 200 to 250 psi

tank working pressure capability = 300 psi

proof = 450 psi

burst = 600 psi

tank material = Ti 6 Al 4V (light weight, high strength, compatibility)

tensile strength = 160,000 psi at 120°

$7550 \text{ in.}^3 = 0.5236 \text{ d}^3$

$d = 24.3$ in.

$r = 12.15$ in.

(no existing tank of correct size) $s = \frac{pr}{2t}$

$$t = \frac{pr}{2s} = 600 \times 12.15 \times 0.5 \times \frac{1}{160,000}$$

$t = 0.023$ in.

weight = $3.1416 \text{ d}^2 \times t \times 0.16 \times 1.05$ + bladder + fittings =

7.17 + bladder + fittings

bladder material = butyl rubber

total tank weight including fittings = 12.0 lb

pressurant weight (Gaseous Nitrogen)

$$Wg = \frac{PV}{RT}\ (1.03 = \frac{250 \mid 144 \mid 2.185 \mid 1.03}{55.2 \mid 520 \mid}$$

$$Wg = 2.83$$

Since 50 feet/ second is the maximum anticipated portion of the Δ V to be expended at a single orbit node, $\frac{150}{350}$ x 23000 lb-sec = 9850 lb-sec must be expended in 1 to 2 hours

$$\frac{9850 \text{ lb-sec}}{3600 \text{ sec/hr } 0.167 \text{ duty cycle}} = 16.4 \text{ lb thrust}$$

For two hours thrusting time, an 8.2-pound thruster would be adequate. Therefore, 15-pound thrusters (initially) decaying with blowdown to approximately 10 pounds were assumed. Use of lower thrusts would be advantageous in areas of response and specific impulse in pulsing operation. It was recommended, therefore, that consideration be given to increasing allowable thrusting time. Use of the same thrust level for despin was assumed since no requirements to the contrary were known.

Weight Tabulation (Monopropellant System)

propellant tank	12.0 lb
fill valves (2) at 0.5	1.0
pressure XDCR	0.4
N/C explosive valve	0.5
filter	0.3
tubing, fittings (15% of dry weight)	3.5
six 15 lb thrusters	15.0
hydrazine propellant	132.0
gaseous nitrogen	2.9
TOTAL WEIGHT	167.6 lb

b. Bipropellant System (Figure 6.4-14)

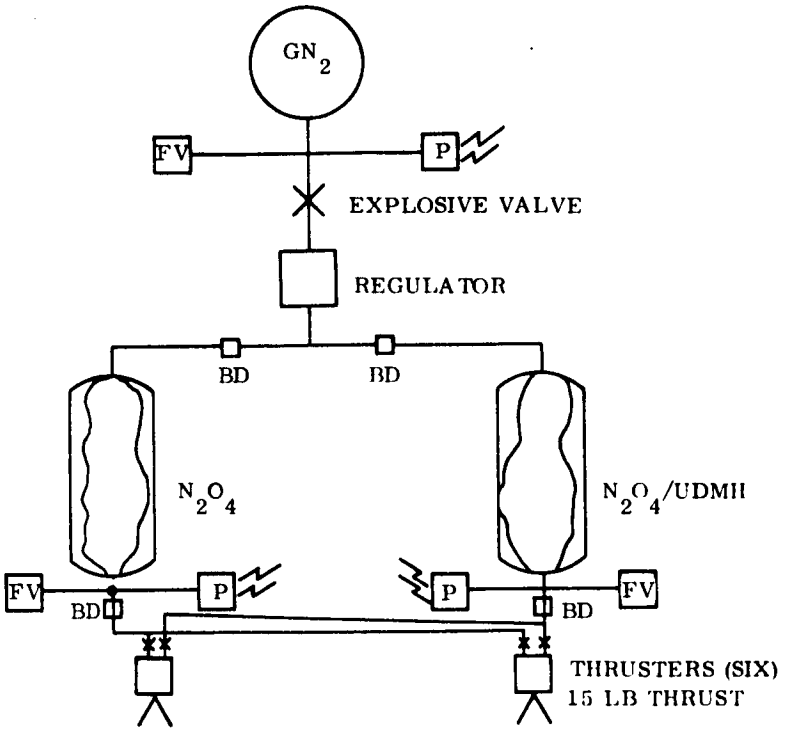


Figure 6.4-14. Bipropellant System Schematic

Fuel: $34.9 \text{ lb} \times \frac{\text{ft}^3}{90 \text{ lb}} = 0.382 \text{ ft}^3 \ (1000 \text{ in.}^3)$

Oxidizer: $70.1 \text{ lb} \times \frac{\text{ft}^3}{90 \text{ lb}} = 0.780 \text{ ft}^3 \ (1350 \text{ in.}^3)$

TOTAL VOLUME = 1.362 ft^3

1.362×1.05 (ullage) = 1.43 ft^3

Weight pressurant = $\frac{Pp\ Vp}{RTo} \left| \frac{K}{1-Pg'Po} \right|$ (Sutton)

$$= \frac{250 \times 144 \times 1.44}{55.2 \times 520} \left[\frac{1.4}{1-\frac{350}{4500}} \right]$$

Weight = 2.73 lb stored at 4500 psi

Volume pressurant = $\frac{WRT}{P} = \frac{2.73 \mid 55.2 \mid 520 \mid 1.05}{4500 \mid 144 \mid \quad \mid \quad}$ (leak allowance)

0.127 ft^3 (220 $in.^3$ at 4500 psi)

(275 $in.^3$ at 3600 psi)

pressurant tank selection (AIRITE Part No. 6363) = 252 $in.^3$

3600 psi working pressure

7.4 lb weight

propellant tank selection - use two existing transtage (Rocketdyne) tanks.

14.2 in. dia. sphere = 1487 $in.^3$

7.5 lb weight (each)

Weight Summary (Bipropellant System)	
pressurant tank	7.4 lb
fill valves (3) at 0.5	1.5
pressure XDCR (3) at 0.4	1.2
explosive valve	0.7
regulator	2.6
burst dia. (4) at 0.5	2.0
prop. tanks (2) at 7.5	15.0
15 lb thrusters (6) at 3.5	21.0
tubing, fittings (15%)	6.8
fuel	34.9
oxidizer	70.1
pressurant	2.8
TOTAL SYSTEM WEIGHT	166.0 lb

6.4.2.11.5 System Design Selection

After the initial tradeoff of the monopropellant and bipropellant design candidates, in which an approximate weight equivalence was shown, advantages noted for the monopropellant system in terms of system complexity, reliability, and development cost resulted in selection of the monopropellant hydrazine system.

6.4.2.12 Spinup Motor

Since spinup is a "one shot" function requiring rapid operation to minimize attitude errors, solid propellant motors were selected. A number of solid propellant motors having characteristics typical of those required for spinup are available. Since it is desirable to use existing hardware wherever possible, the characteristics of candidate motors were investigated which placed the spinup time at 1 to 2 seconds for a spin speed between 40 and 80 rpm for a spacecraft moment of inertia about the spin axis of 300 to 400 slug-ft^2 and a moment arm of about four feet. Four motors developed by Atlantic Research Corporation were considered. These are presented in Table 6.4-2.

Table 6.4-2. Atlantic Research Corporation Spinup Motor Data

Motor Designation	Propellant Wt. (lb)	Total Impulse (lb-sec)	Max. Thrust (lb)	Action Time (sec)	Motor Dimen. (in)	Motor (Wt (lb)
1-KS-210 (MK6A)	1.020	222	206.0	1.50	3.06 x 10.19	3.38
1-KS-210 (MK6B1)	1.060	236	177.5	1.59	3.06 x 10.90	3.65
1.35-KS-300	2.13	402.7	404.1	1.36	2.90 x 14.70	5.8
1-KS-380	2.13	489	498	1.36	2.90 x 14.88	5.16

The total impulse range was based on the following calculations:

$$I_r \dot{W} = I_r \frac{W}{t} Fr$$

$$Ft = \frac{I_r W}{r}$$

$$\text{Total Impulse} = Ft = \frac{0.1047\, I_r W}{r}$$

Using the following typical values for Ir, r, and w:

$$I_r = 377 \text{ slug ft}^2$$

$$r = 42 \text{ in.} = 3.5 \text{ ft}$$

$$W = 70 \text{ rpm}$$

$$I_{tot} = \frac{0.1047\ (377)\ (70)}{3.5} = 792.0 \text{ lb-sec}$$

for two motors, the total impulse of each equals 396.0 lb-second. Figure 6.4.15 shows the total impulse needed for various W and $\frac{I_r}{r}$ values. Once the final spacecraft design is decided, the $\frac{I_r}{r}$ term will be fixed. This, along with the desired spin rate, will specify the total impulse needed per motor. By using Figure 6.4-15 (use of two motors assumed), and trading off spin requirements against motor availability indicated that a readily available spin capability could be obtained.

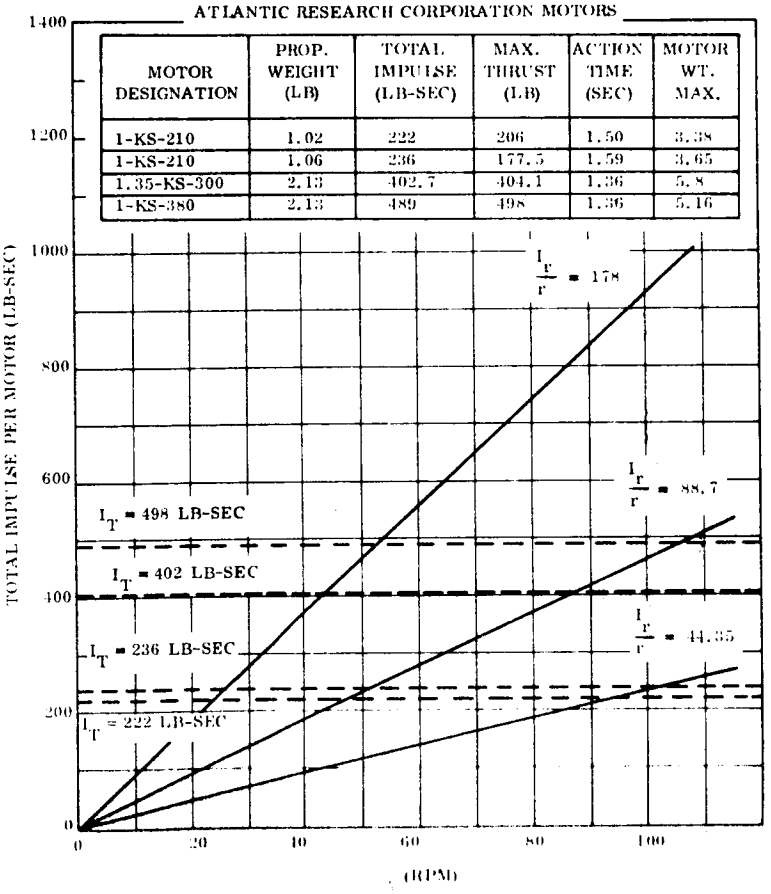


Figure 6.4-15. Total Impulse for Various Spin Rates and I_r/r

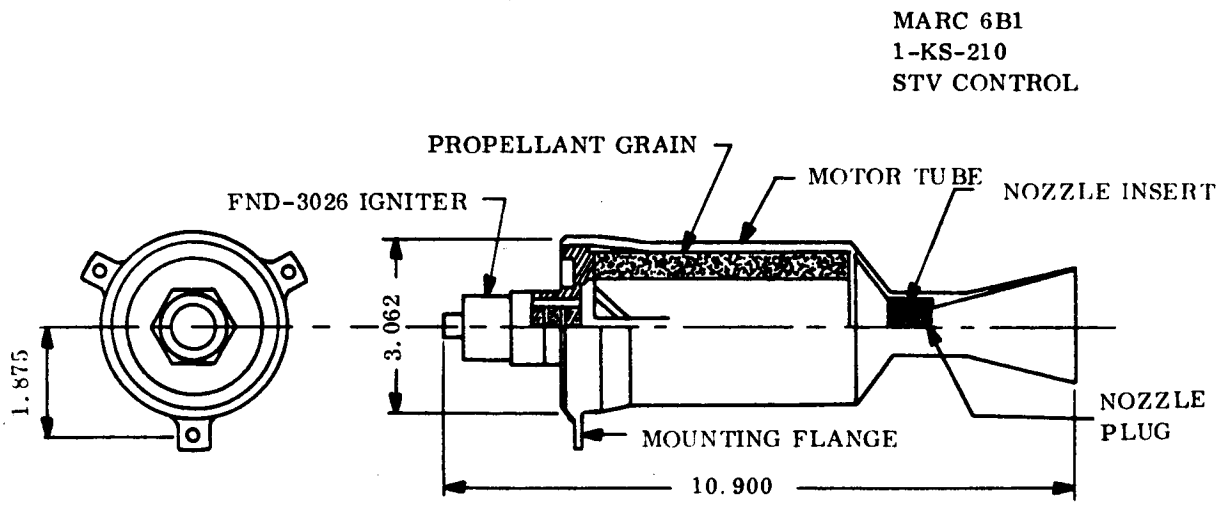
Two examples for the final choice for the spinup rockets are two Atlantic Research Corporation 1-KS-210 (MK6B1) and two ARC .. 35 KS-300 (MK7E1) based primarily on total impulse and the fact that they are available and compatible with nominal spin impulse requirements and thrust levels. Table 6.4-3 summarizes data for the ARC MK6B1 (I-KS-210) and the Marc 7E1 (1.35KS-300) motors.

Table 6.4-3. Atlantic Research Corporation Motor Data

Parameter	Units	Motor	
		1-KS-210	1.35-KS-300
I_{sp}	sec	223	190
Average Thrust	lbf.	177.5	296
Burn Time	sec.	1.243	1.002
Total Impulse	lb-sec	236	402.7
Propellant Weight	lb	1.10	2.13
Inert Weight	lb	2.55	3.67
Burnout Weight	lb	2.55	3.67
Total Weight	lb	3.65	5.80
Motor Length	in.	10.900	14.7
Motor Diameter	in.	3.062	2.9
Nozzle Diameter	in.	4.0	
Throat Diameter	in.	0.380	0.464
Operating Limits	^{o}F	-40 to 160	-40 to 200
Average Chamber Pressure During Burn	psi	325	1220

These motors are typical of several similar units available. The MK 6 B1 is a solid propellant (ARCITE 377A) motor developed by Atlantic Research Corporation for Avco Corporation and the USAF. The development for a special test vehicle was completed in 1963. Qualification testing which included 15 units was completed in July, 1963. By 1 January 1964, over 150 units had been produced. Figure 6.4-16 presents the motor design. The Marc 7 El

is a solid propellant (ARCITE 377A) motor developed by Atlantic Research Corporation for the Air Force. The Marc 7 series started in 1958 as a retro motor for the Atlas ICBM. To date there have been 20 firings. ARC has delivered 296 units.



ATLANTIC RESEARCH CORPORATION

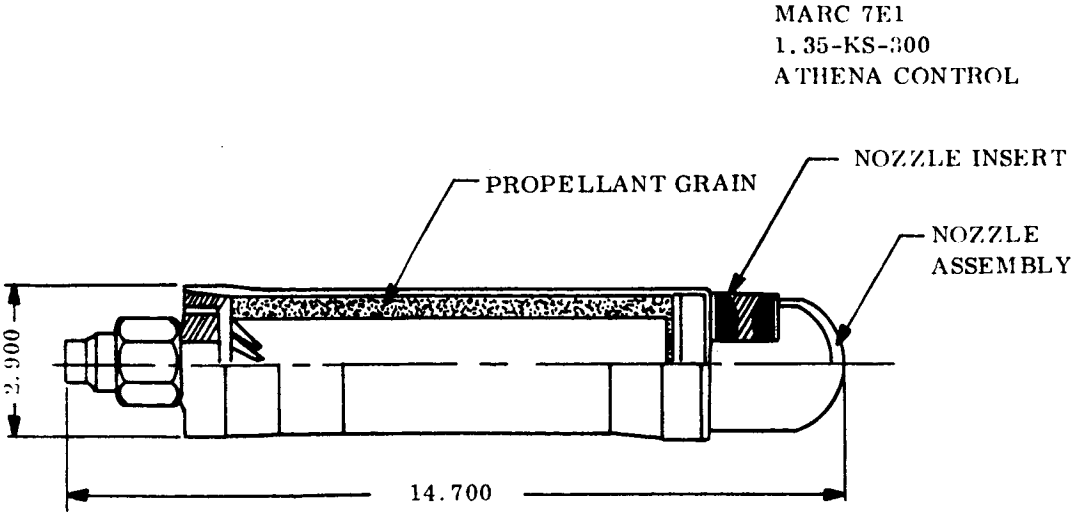


Figure 6.4-16. Candidate Spinup Motors

6.4.3 DESIGN ANALYSIS

During the course of this study significant analysis was performed in support of defining the preferred design and to define control parameters to meet the specified performance requirements for the orientation control subsystem. Early in the study primary emphasis was placed on investigating the control system requirements necessary to obtain satisfactory control dynamic performance with the spacecraft and its flexible appendages having structural damping factors down to 0.001. It was found that spacecraft attitude would be satisfactorily controlled provided that the bandwidth of the control system was significantly below the lowest natural frequency of the structure and its appendages.

Considerable emphasis was also placed on error analysis of the pointing mode early in the study. Initially it appeared as if the 0.1 degree accuracy requirement could be met only if a three axis star tracker approach was used. However, associated with the star tracker approach was higher weight and power, increased control system complexity and field of view and solar impingement problems. Concerted effort on accuracy resulted in an apparent ability to meet the 0.1 degree accuracy requirement with an earth sensor.

In-orbit disturbance torques were computed early in the study using a simplified model of the spacecraft. This resulted in defining the flywheel momentum requirements as 10, 6, and 6 ft-lb-sec for pitch, roll, and yaw, respectively. A more sophisticated spacecraft model was then defined and a digital computer program was written for generating disturbance torque-time profiles for a 24 hour period. Because of the transfer of momentum between roll and yaw as the spacecraft orientation changes in inertial space, an additional computer program was written to compute the flywheel momentum-time profiles for a 24 hour period. The result was that it was possible for the preferred spacecraft design to use the 2 ft-lb-sec Orbiting Astronomical Observatory (OAO) flywheel in pitch, roll, and yaw affording a considerable weight and power saving.

The dynamic performance of the orientation control system was analyzed using a simplified model for the sensors, torquers, and spacecraft. As the design progressed, more sophisticated models were used for the analog computer study. The study terminated with analog

computer runs for the sun stabilization, earth stabilization, pointing, reorientation and tracking modes using sensor models which included noise, the nonlinear characteristic of the flywheel, structural dynamics and the parameter values associated with the preferred design with regard to thruster torque levels, spacecraft inertias, etc.

In addition to the dynamic performance analysis of the control system after injection into orbit, the dynamic performance during separation and spinup, coning control after spinup and as the result of apogee motor burn, and precession control were investigated.

Specifically, the following analyses are discussed in this section.

a. Transfer Orbit Disturbance Torques

b. On-Station Disturbance Torques

c. Control Static and Dynamic Performance Analysis

d. Earth Pointing Error Analysis.

6.4.3.1 Transfer Orbit Disturbance Torques

Presented here is a discussion of the disturbance torque-time profiles resulting during the transfer orbit. The assumed spacecraft model and the orbital data which influence these torques are defined in Appendix C. The disturbance torques include gravity gradient, solar radiation pressure, aerodynamic pressure and magnetic torques. By integrating the disturbance torque over the transfer orbit time of 15.75 hours the magnitude of the precession of the spacecraft can be determined. In this analysis it was found that the aerodynamic pressure is the predominant disturbance torque.

6.4.3.1.1 Solar Radiation Pressure Torque

The ATS-4 spacecraft is considered to be a cylinder (Figure 6.4-17). The $X_B Y_B Z_B$ axis system is an inertially fixed system determined by the spacecraft attitude at perigee. $\bar{Z}_B$ corresponds to the spin axis, $\bar{X}_B$ coincides with the local vertical at perigee, and $\bar{Y}_B$ forms a right-handed system.

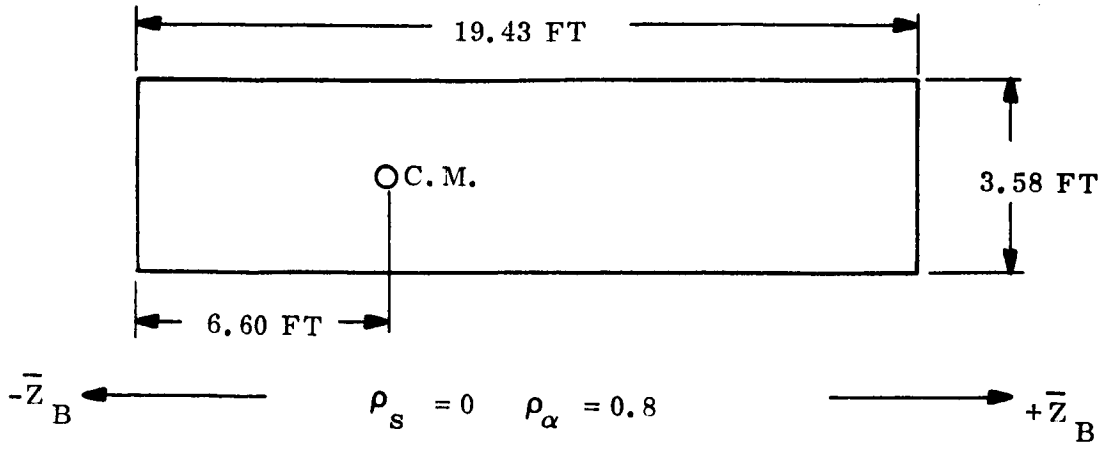


Figure 6.4-17. ATS-4 Spacecraft Configuration

The magnitude of the solar torque on the cylindrical surface (Appendix C) is 29.4×10^{-6} foot-pounds. The solar torque on the end surface is much smaller.

At the autumnal equinox the solar unit vector $\bar{S}$ lies along $\bar{X}_B$ and the solar torque is

$$\bar{T}_S = -\bar{S} \times \bar{Z}_B \, T_S = +\bar{Y}_B \, T_S$$

At the summer solstice, the solar unit vector is

$$\bar{S} = \bar{X}_B \cos 23.45^\circ + \sin 23.45^\circ \, (-\bar{Y}_B \cos 19.4^\circ + \bar{Z}_B \sin 19.4^\circ)$$

and the solar torque is

$$\bar{T}_S = 29.4 \times 10^{-6} \, (\bar{X}_B \sin 23.45^\circ \cos 19.4^\circ + \bar{Y}_B \cos 23.45^\circ)$$

6.4.3.1.2 Aerodynamic Pressure Torques

The $\bar{X}_B$ and $\bar{Y}_B$ components of the aerodynamic pressure torque are plotted in Figure 6.4-18 for the spacecraft configuration model shown in Figure 6.4-17. These curves apply to both the autumnal equinox and the summer solstice. The $\bar{Z}_B$ component of this torque is always zero. Only values near perigee are plotted, because there is a rapid decrease in the density of the atmosphere at higher altitudes. Therefore, the aerodynamic pressure torque decreases rapidly at higher altitudes, so that the contribution to the torque impulse is negligible. Only half of one orbit is plotted. The plots for the approach to perigee near the end of the first orbit would look the same except that the sign of the $\bar{Y}_B$ component is reversed. The third half-orbit looks exactly like the first half-orbit.

6.4.3.1.3 Magnetic Torques

The magnetic disturbance torques all arise from interaction of the spacecraft magnetic properties with the geomagnetic field. These properties include hysteretic material, spinning conductive material, and residual magnetic moment. No analysis of magnetic hystersis effects is yet available for the ATS-4 spacecraft.

The eddy-current torque is less than 4.77×10^{-6} foot-pounds. The upper limit is based on the assumption of maximum values of the pertinent variables, such as 0.6 oersted for the geomagnetic field, and 100 rpm for the spin rate. The limit is also based on the assumption that the skin is 0.02 inch aluminum. For other materials and thicknesses, the eddy-current torque is proportional to the conductivity and thickness of the material. Because the spacecraft will be at higher altitudes during most of the orbit, the eddy-current torque impulse will be two or three orders of magnitude less than the value obtained by multiplying the upper limit of the torque by the elapsed time. The effect is, therefore, negligible in comparison with the other disturbances.

The residual magnetic moment of the spacecraft is unknown. Its magnitude is assumed to be 4 pole-centimeters per pound of spacecraft weight. The weight of the metallic portion of the ATS spacecraft was assumed to be 2000 pounds. The magnetic moment is resolved into equal components along each spacecraft axis. Each component is then

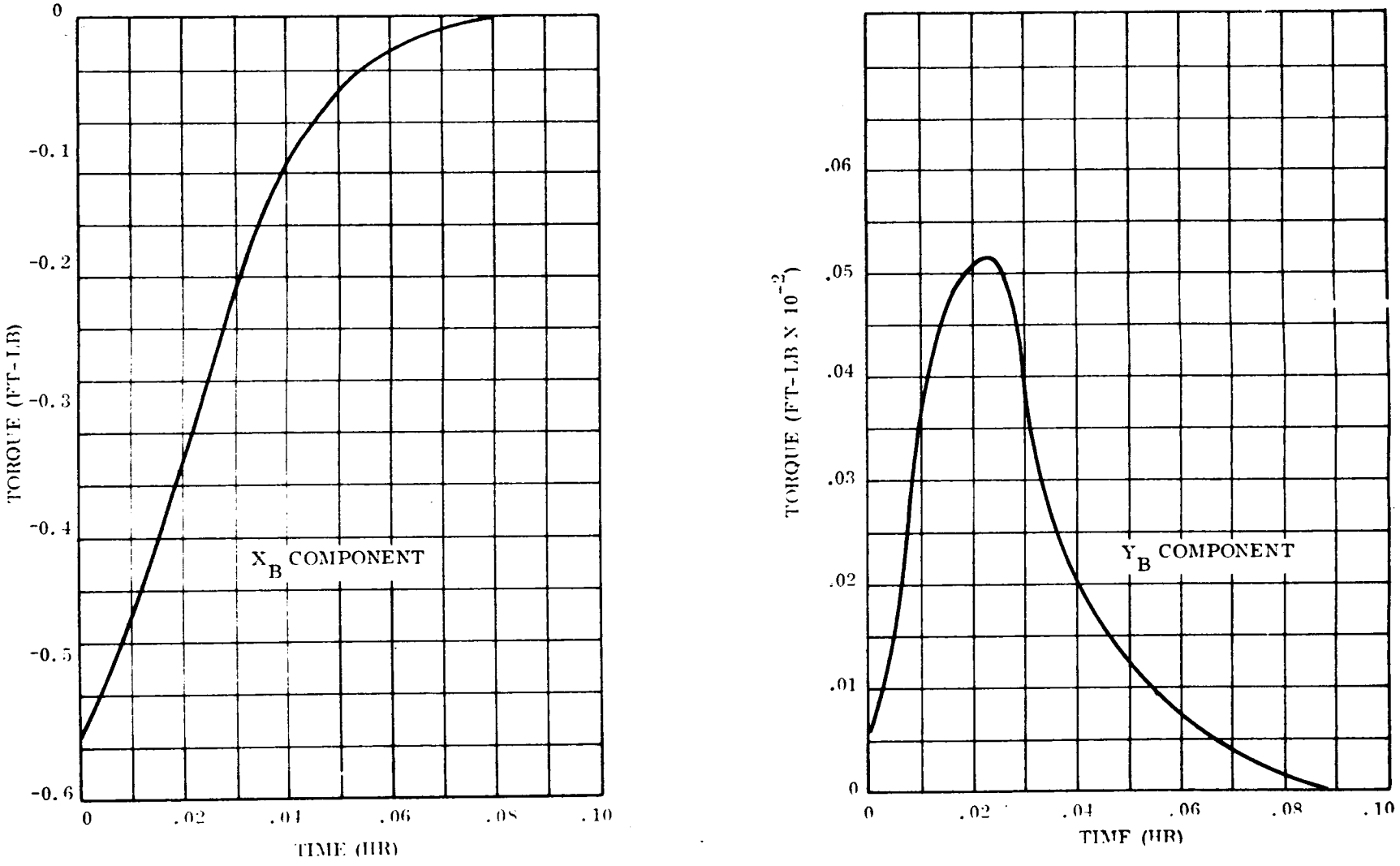


Figure 6.4-18. X_B and Y_B Components of Aerodynamic Torque

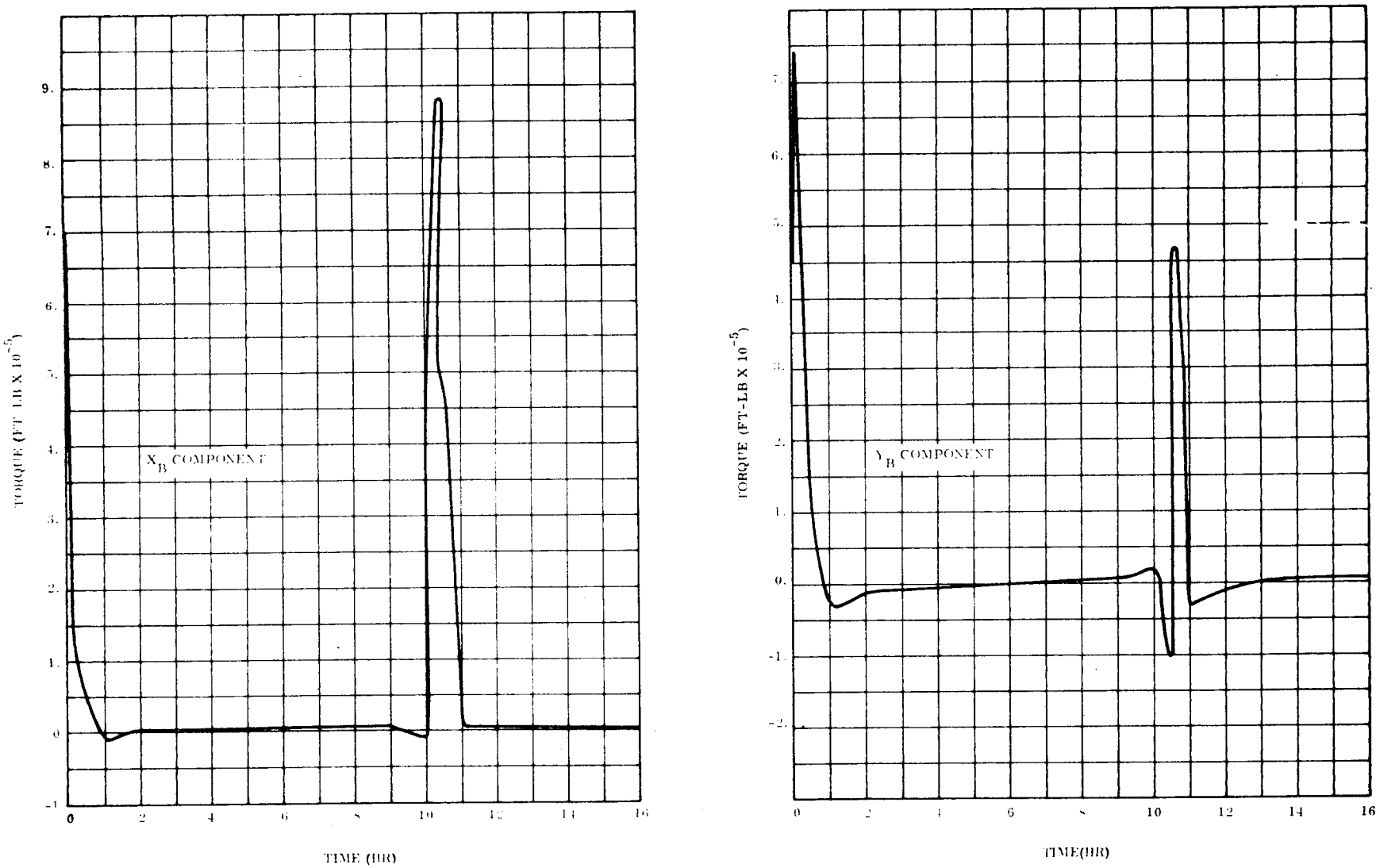


Figure 6.4-19. X_B and Y_B Components of Magnetic Torque

3.4×10^{-4} foot-pounds per oersted. Appreciable torque impulse is produced only by the axial component. Consequently, the transverse components were set equal to zero in the digital computer run which calculated the torque. The $\bar{X}_B$ and $\bar{Y}_B$ components of the magnetic torque are plotted in Figure 6.4-19 which applies to both the autumnal equinox and the winter solstice. The $\bar{Z}_B$ component of the torque has no secular component. Sinusoidal torques, at spacecraft spin rate, occur about all three axes, but these have only negligible effects.

6.4.3.1.4 Gravity Gradient Torques

The $\bar{X}_B$ and $\bar{Y}_B$ components of the gravity gradient torque are plotted in Figure 6.4-20 which applies to both the autumnal equinox and the summer solstice. The $\bar{Z}_B$ component of the gravity gradient torque is always zero, because of the assumption of equal moments of inertia about the transverse axes. The torque data were obtain from the digital computer run which was used for the magnetic torque. The axial moment of inertia was taken as 535 slug-ft^2 and the transverse moment of inertia as 4523 slug-ft^2.

6.4.3.1.5 Total Disturbance Torques

The total disturbance torques are not plotted, because the plots would appear identical to those of the aerodynamic pressure torques.

6.4.3.2 On-Station Disturbance Torques

The results of computation of the disturbance torques acting on the ATS-4 spacecraft in its synchronous orbit are presented in this section. Also included are the spacecraft characteristics which influence these torques. The disturbances include gravity gradient and solar radiation pressure torques. The magnetic disturbance torque was considered negligible at synchronous altitude. The results are presented in the form of plots showing the disturbance torque as a function of the time for a 24 hour period. The disturbance torque profiles provide design information for sizing the momentum wheels and mass expulsion system, as well as inputs for the analog computer simulation of the spacecraft attitude control dynamics. The graphs are the results of IBM 7094 digital computer runs. A detailed description of the method of calculation of the torques is given in Appendix D.

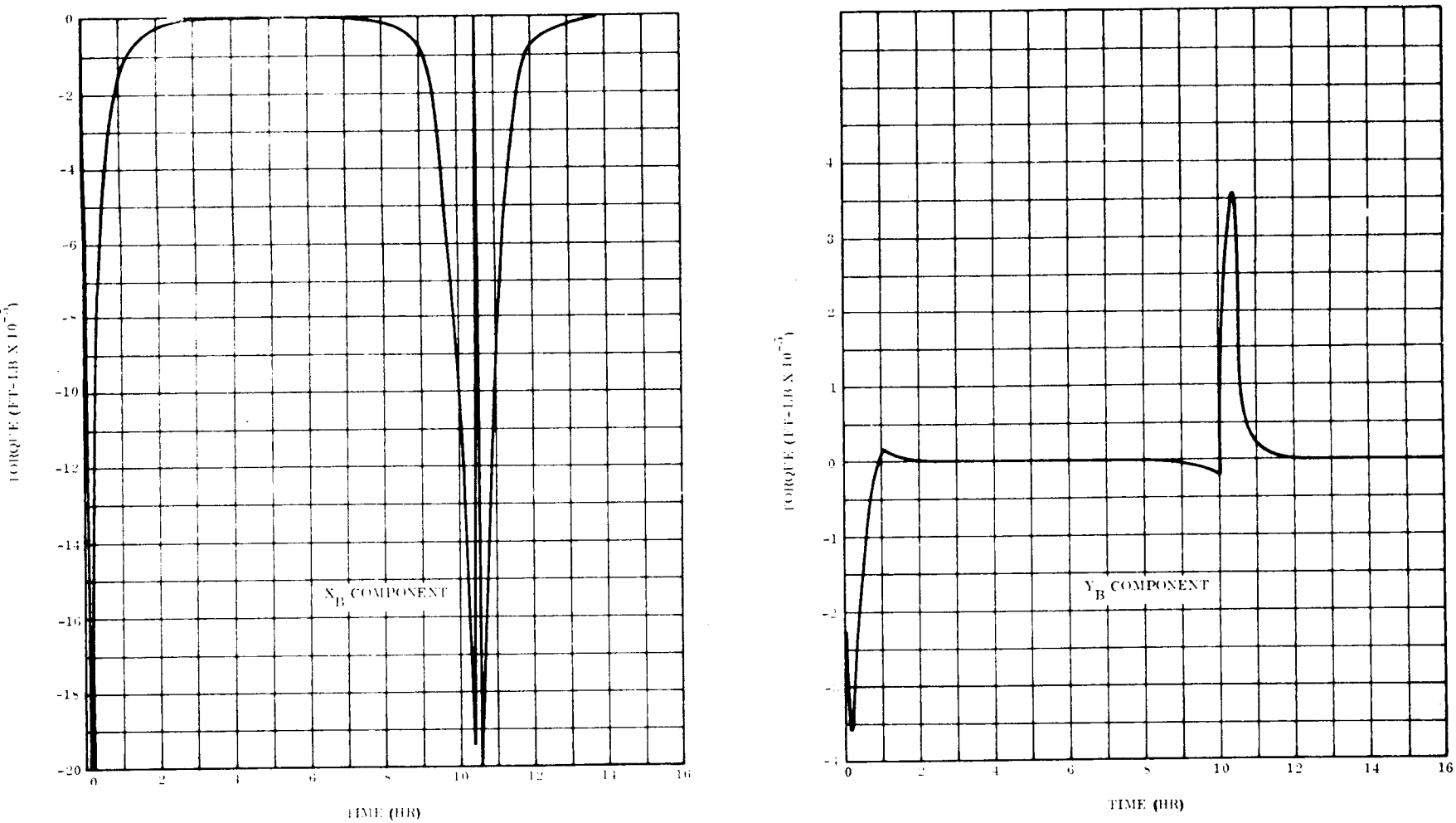


Figure 6.4-20. X_B and Y_B Components of Gravity Gradient Torque

The satellite orientation relative to the local vertical reference frame is expressed in terms of three Euler angles: (1) θ_P about the nominal pitch axis, (2) θ_R about the roll axis, and (3) θ_Y about the yaw axis. The spacecraft attitude angles used in the computer runs were:

Run Number	Time of Year	Attitude Angles (Degrees)			
		Pitch (θ_P)	Roll (θ_R)	Yaw (θ_Y)	
1	Fall	0	0	0	(Local Vertical)
2	Summer	0	0	0	(Local Vertical)
3	Fall	0	-8.7	0	
4	Summer	0	-8.7	0	
5	Fall	0.689	3.4	0	(Rosman)
6	Summer	0.689	3.4	0	(Rosman)
7	Fall	-2.6	3.41	0	(Mojave)
8	Summer	-2.6	3.41	0	(Mojave)

The results are based on the selected spacecraft configuration defined on Figure 5.3-2. For the purpose of computing the disturbance torques, a simpler configuration was used, consisting of two cylindrical equipment modules, four flat solar paddles, and one large antenna. The antenna shape is a paraboloid, but it is approximated as a spherical cap.

All of the dimensions and characteristics which affect the computed disturbance torques are shown in Table 6.4-4 and Figure 6.4-21. The disturbance torque profiles for the conditions listed above are shown in Figure 6.4-22 through 6.4-25.

For an inertially oriented spacecraft the flywheel momentum and mass expulsion requirements can be determined directly from the disturbance torque profiles by computing the area under the curve. For ATS-4, which is earth oriented, there is a continual momentum transfer between the yaw and roll flywheels. The Euler vector equation relating torque and momentum reduces to the set

Table 6.4-4. Spacecraft Parameters Associated with On-Station Disturbance Torque Computation

Spacecraft Mass	52.39 slugs
Moments of inertia	
Roll axis	3538 slug-feet^2
Pitch axis	2940 slug-feet^2
Yaw axis	1727 slug-feet^2
Solar Paddles	
Specular reflectance	0.0
Diffuse reflectance	0.3
Antenna	
Specular reflectance	0.0
Diffuse reflectance of inside surface	0.5
Diffuse reflectance of outside surface	0.9
Fraction of closed area (effective area)	0.2
Cylinders	
Specular reflectance	0.0
Diffuse reflectance	0.7

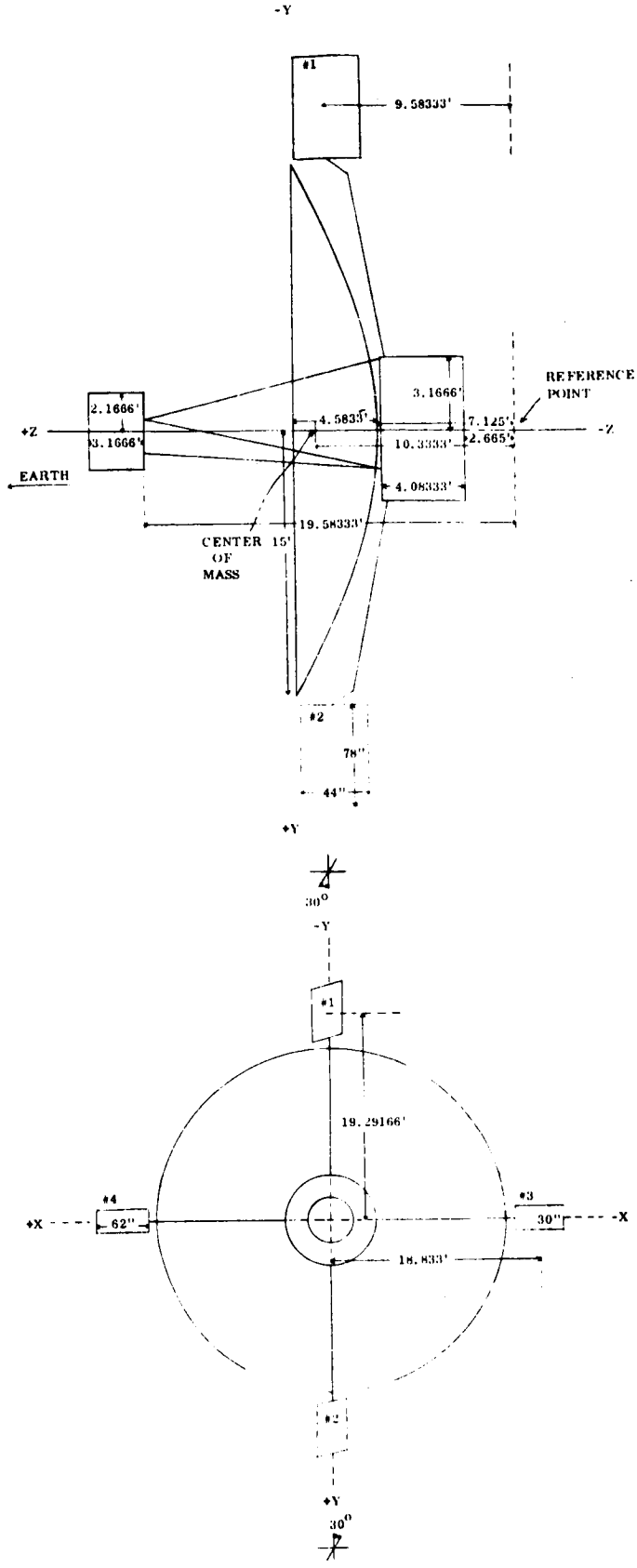
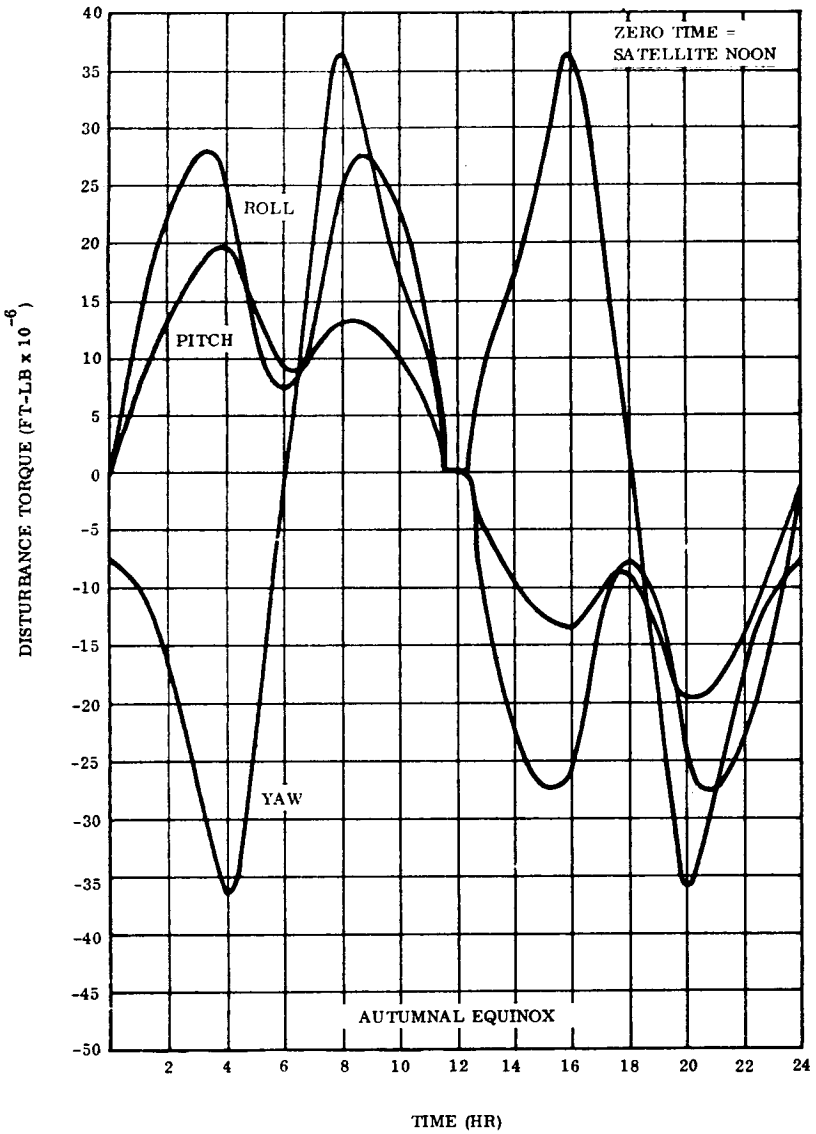


Figure 6.4-21. Assumed Configuration for Disturbance Torques



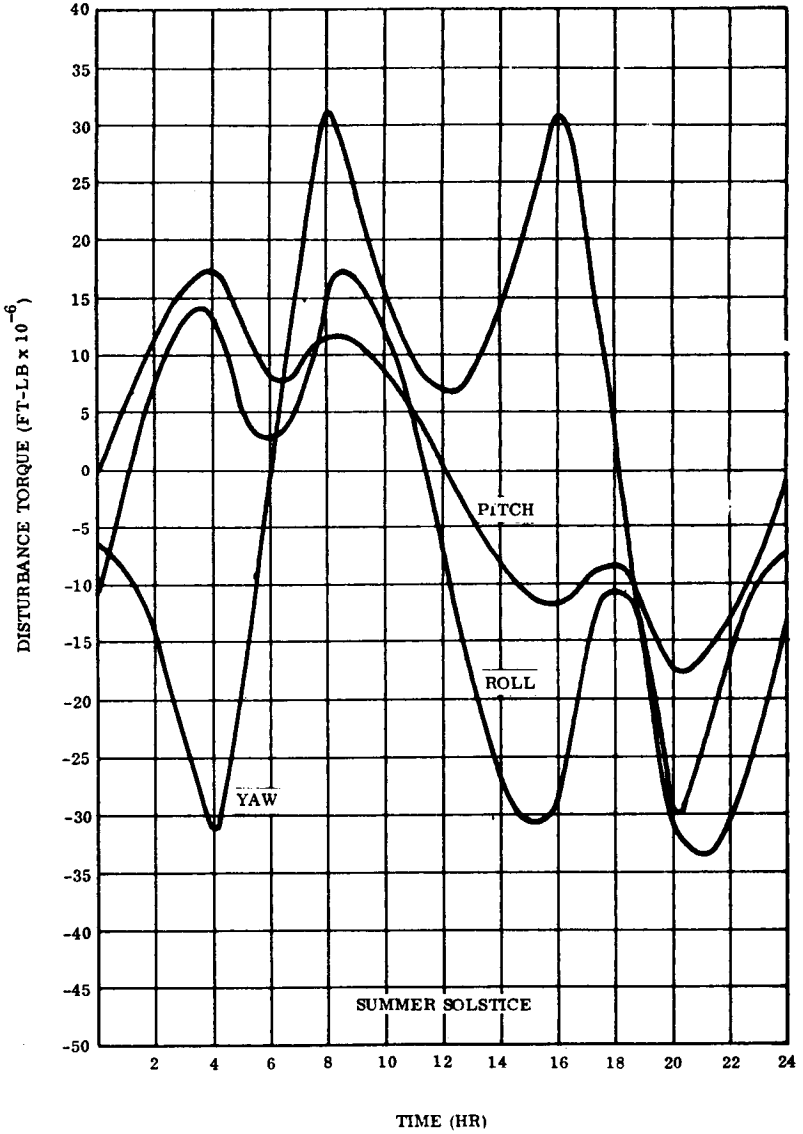


Figure 6.4-22. Disturbance Torque Profile (Yaw Axis Pointed to Local Vertical)

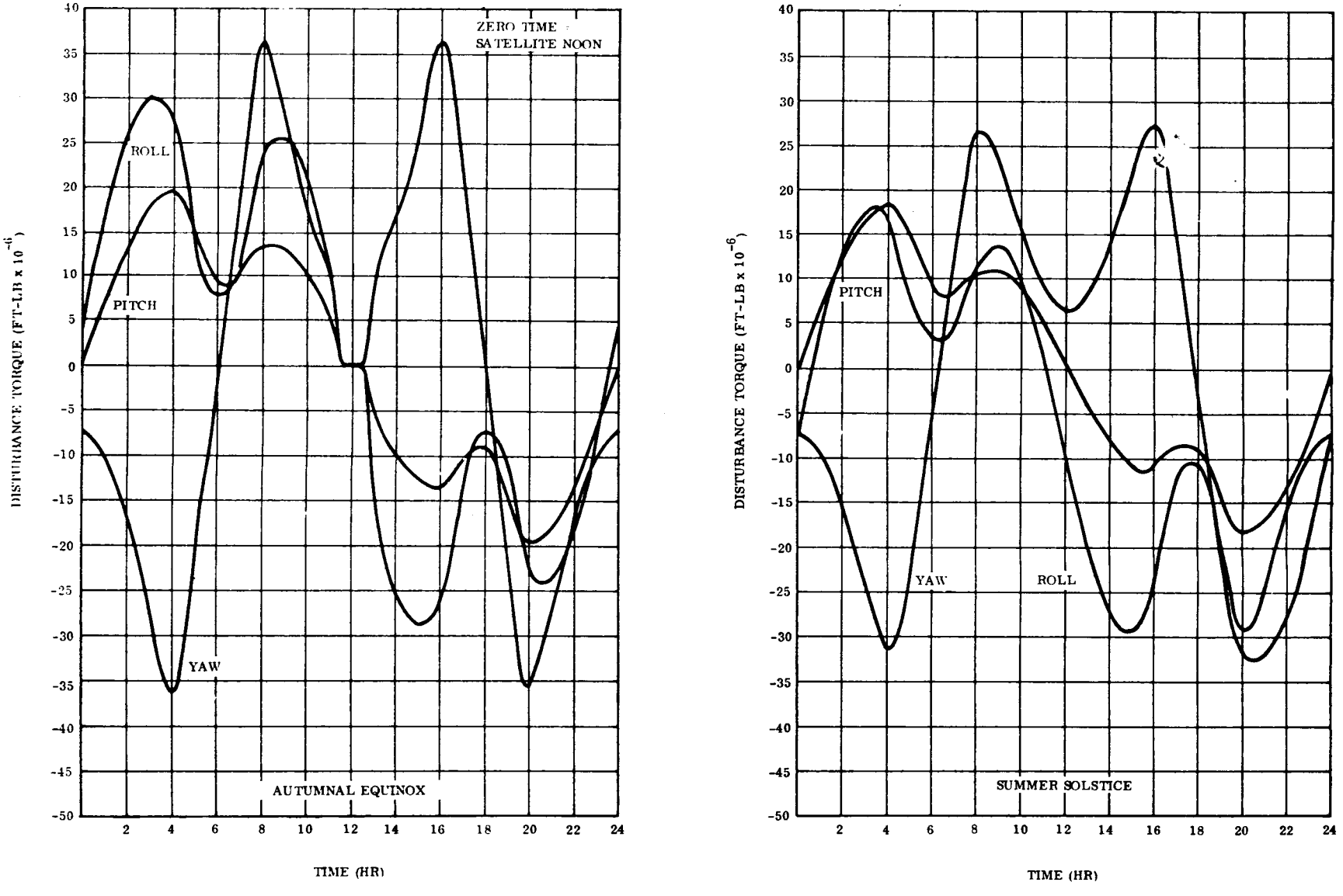


Figure 6.4-23. Disturbance Torque Profile (Yaw Axis Pointed to 0^{o} Pitch, 8.7^{o} Roll)

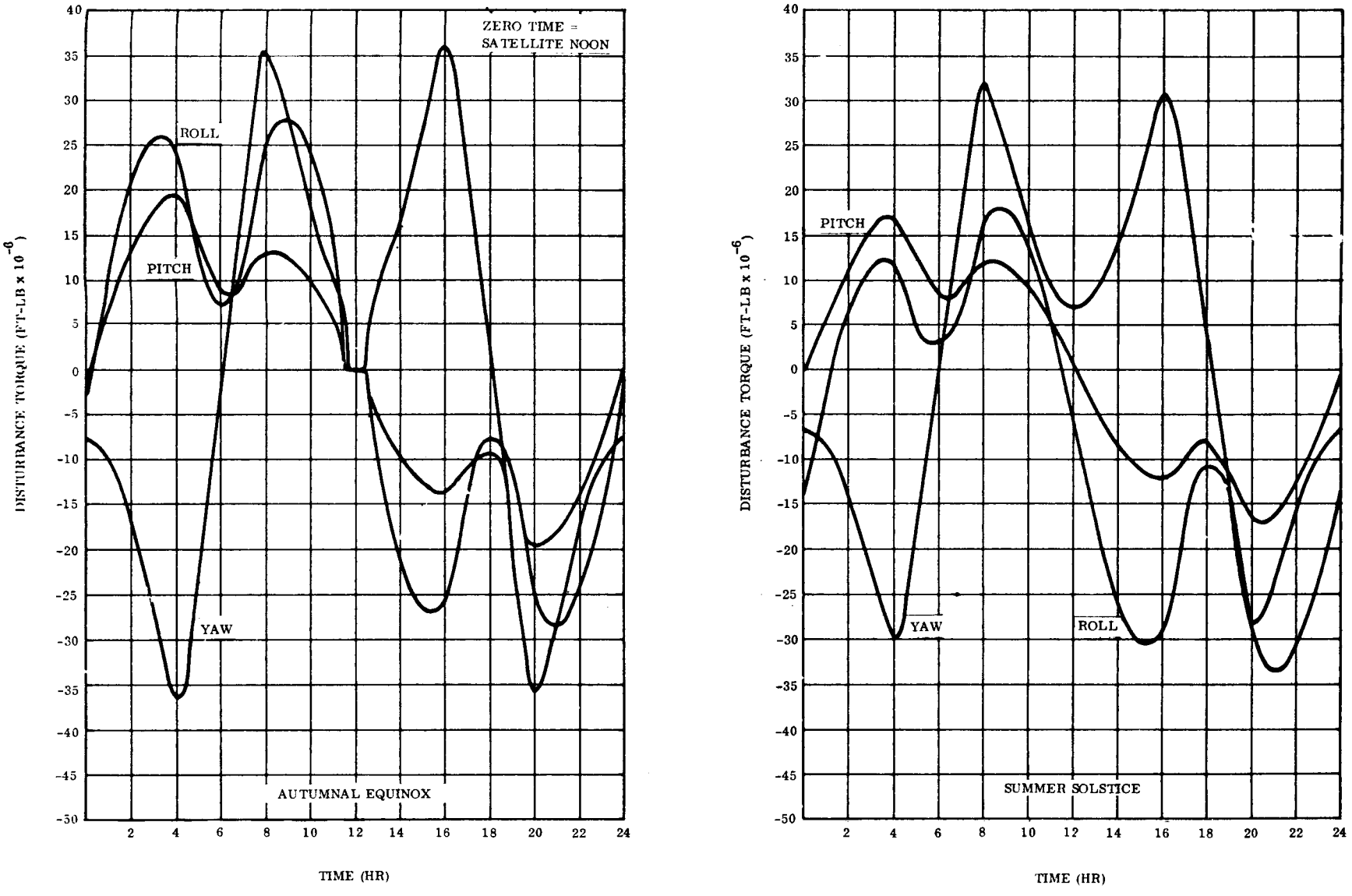


Figure 6.4-24. Disturbance Torque Profile (Yaw Axis Pointed to Rosman Station)

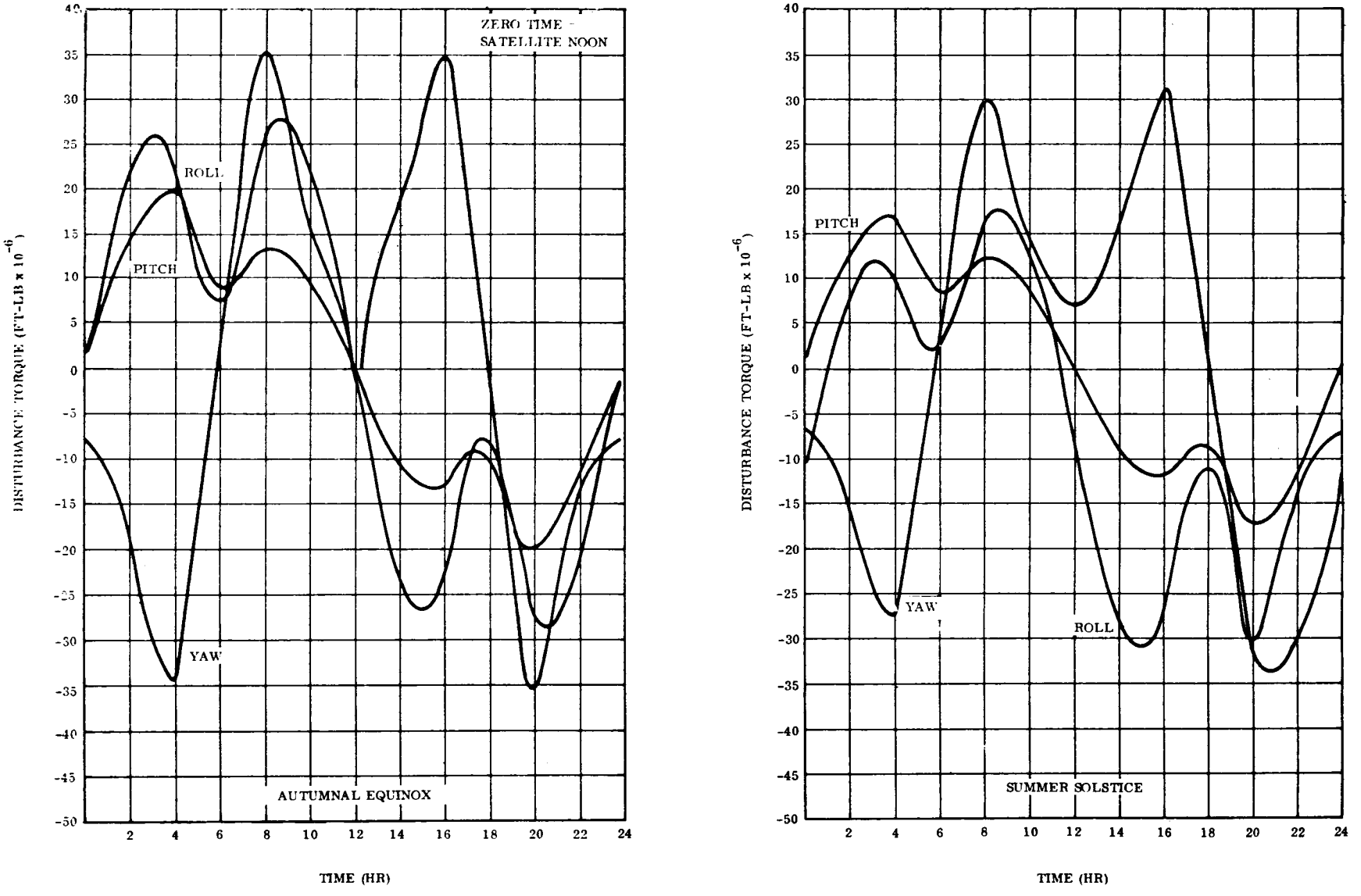


Figure 6.4-25. Disturbance Torque Profile (Yaw Axis Pointed to Mojave Station)

$$L_x = \dot{h}_x - W_o h_z$$

$$L_y = \dot{h}_y$$

$$L_z = \dot{h}_z + W_o h_x$$

since there is only one spacecraft frame rate (W_o) in the negative pitch direction (L = torque, h = momentum). It was assumed that the yaw axis is pointed to the local vertical. Then:

$$\dot{h}_x = L_x + W_o h_z$$

$$\dot{h}_y = L_y$$

$$\dot{h}_z = L_z - W_o h_x$$

The solution of this set represents the time history of the angular momentum of the flywheels. The pitch axis is uncoupled and requires only integration of the pitch disturbance torque history. The coupled equations for roll and yaw are:

$$h_x(i) = h_x(i-1) + W_o \Delta T\, h_z(i-1) + \Delta T\, h_x(i)$$

$$h_z(i) = h_z(i-1) - W_o \Delta T\, h_x(i-1) + \Delta T\, h_z(i)$$

where $W_o = \frac{2\pi}{24\ (3600)}$ radian/second. A ΔT of 20 minutes was used for computing the time history of the momentum. Thus i takes on values from 0 to 72 for a 24 hour period.

A computer program was set up to compute the momentum which would be stored on each of the flywheels. The results are presented in Figures 6.4-26 through 6.4-29 for the 8 cases listed above, with the integration beginning at Satellite noon (i. e. assuming flywheel unloading at noon). Also shown on Figures 6.4-27 and 6.4-28 are the momentum profiles

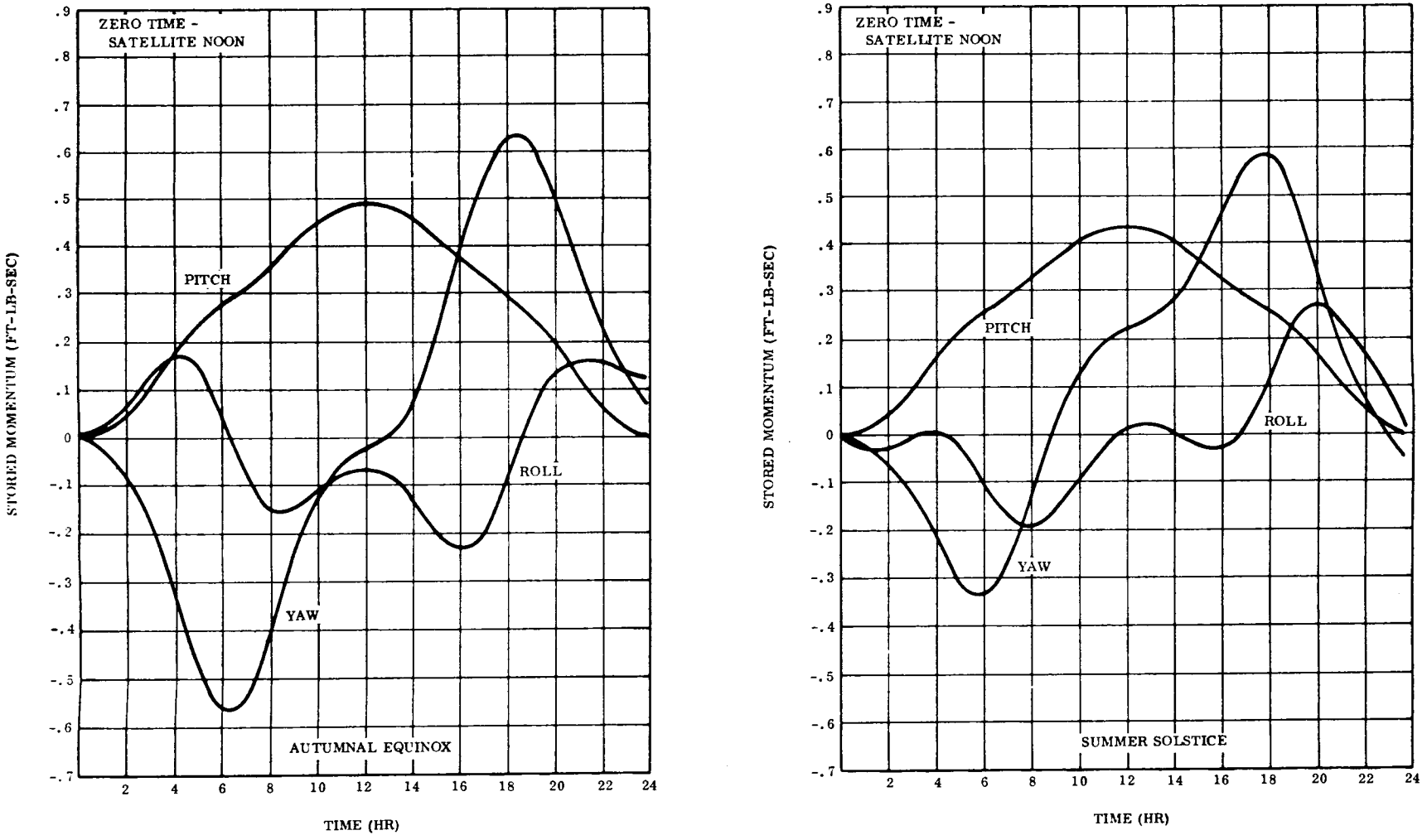
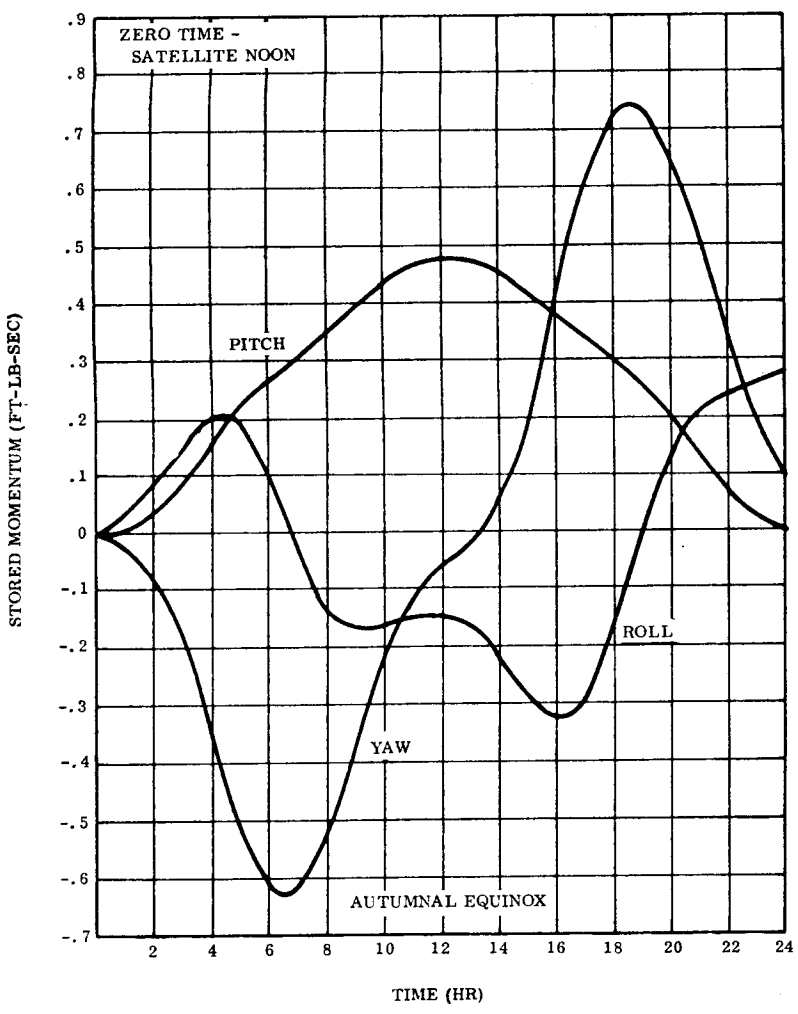


Figure 6.4-26. Flywheel Momentum Profile (Yaw Axis Pointed to Local Vertical)



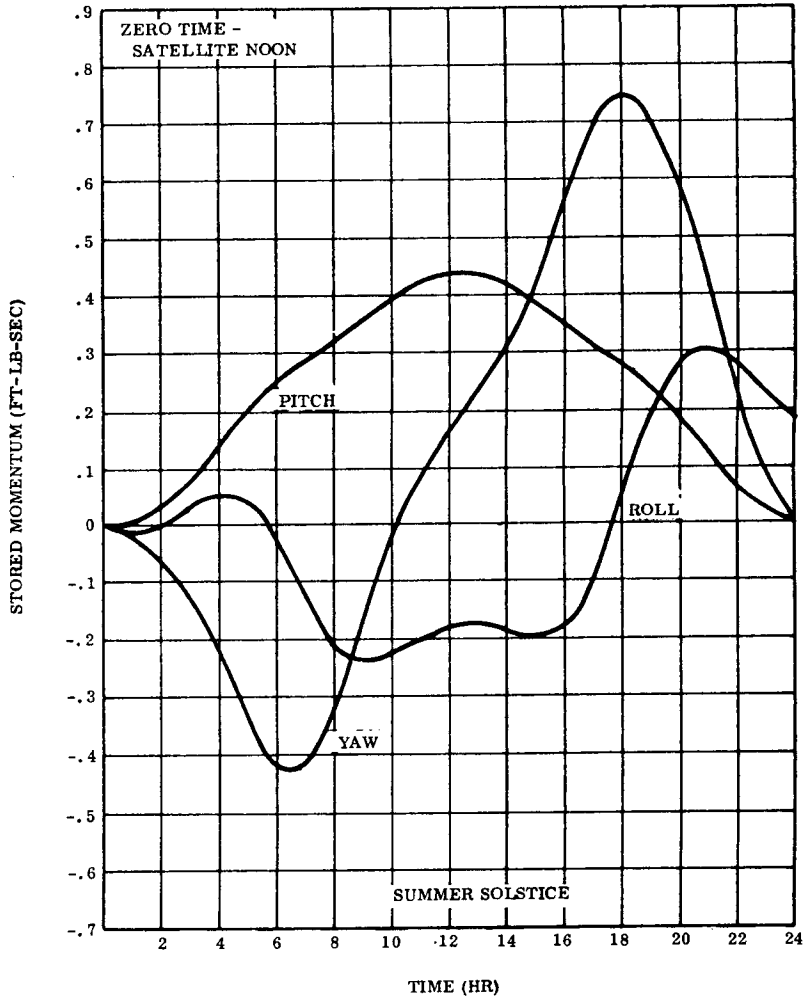


Figure 6.4-27. Flywheel Momentum Profile (Yaw Axis Pointed to 0^{o} Pitch, 8.7^{o} Roll)
(Sheet 1 of 2)

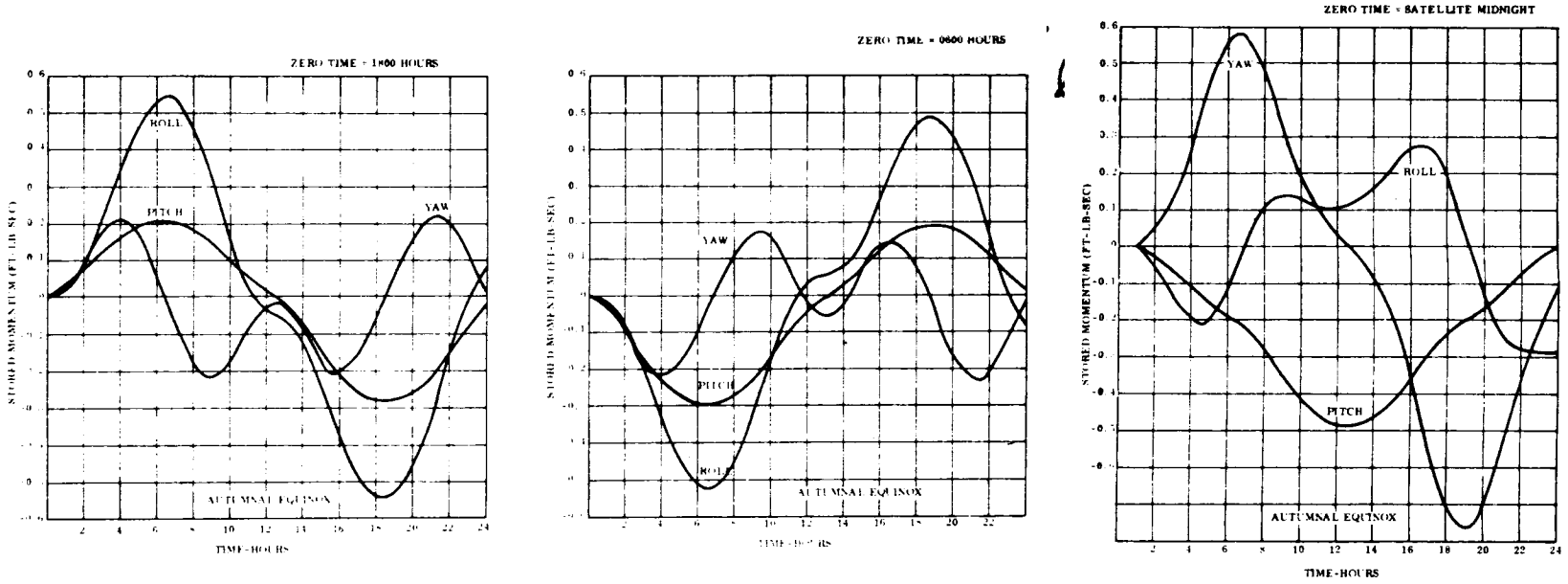
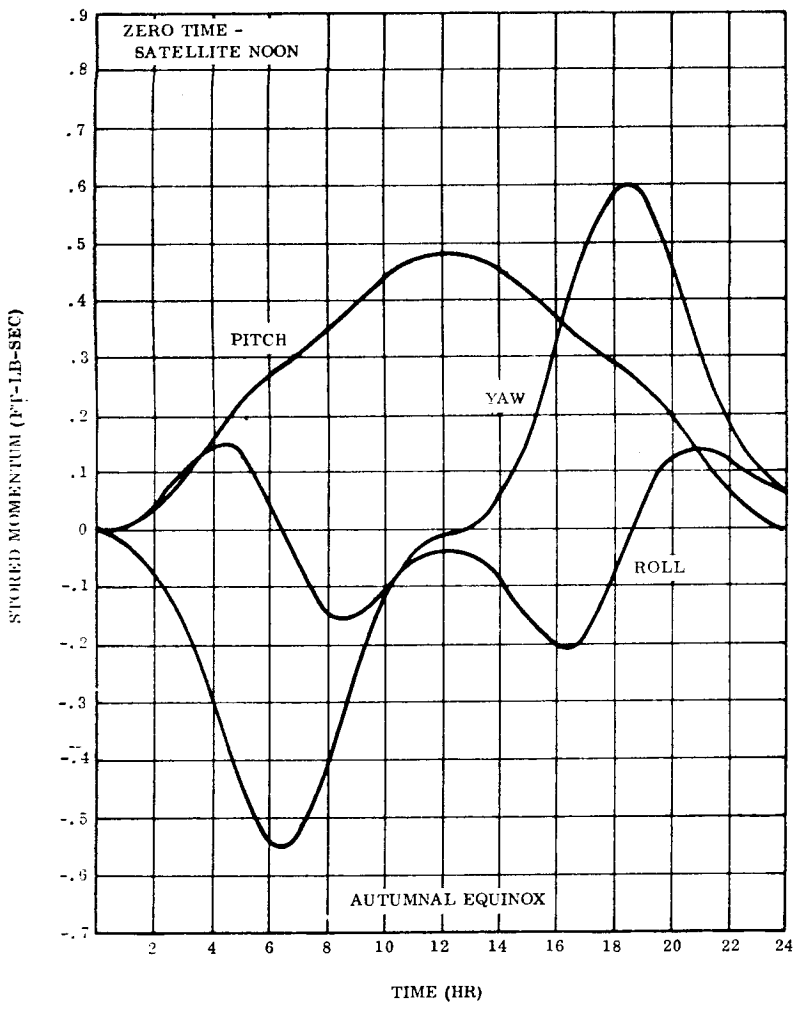


Figure 6.4-27. Flywheel Momentum Profile (Yaw Axis Pointed to 0^{o} Pitch, 8.7^{o} Roll)
(Sheet 2 of 2)



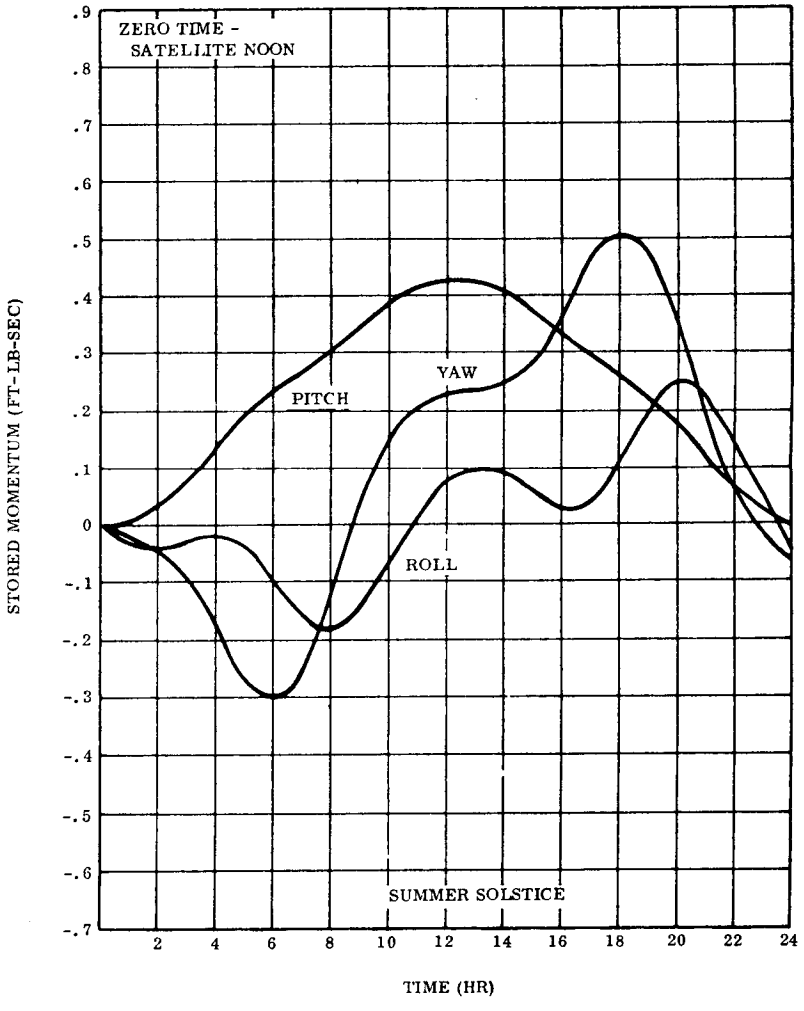


Figure 6.4-28. Flywheel Momentum Profile, Autumnal Equinox, (Yaw Axis Pointed to Rosman Station)
(Sheet 1 of 2)

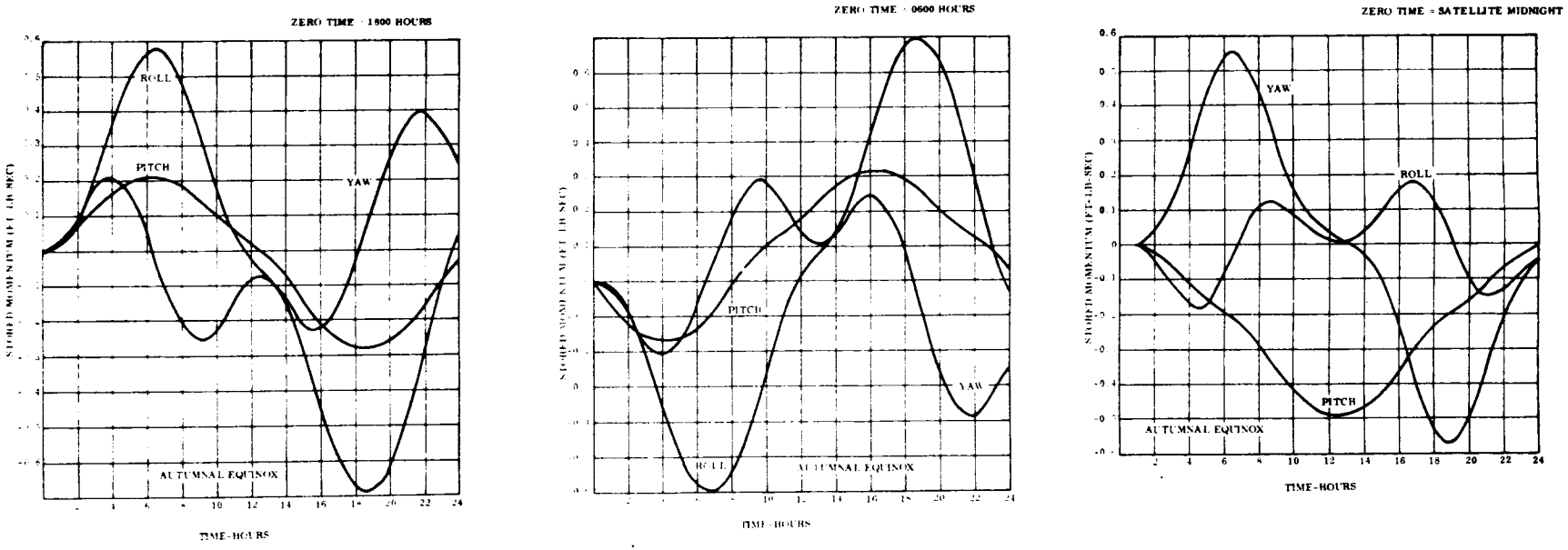
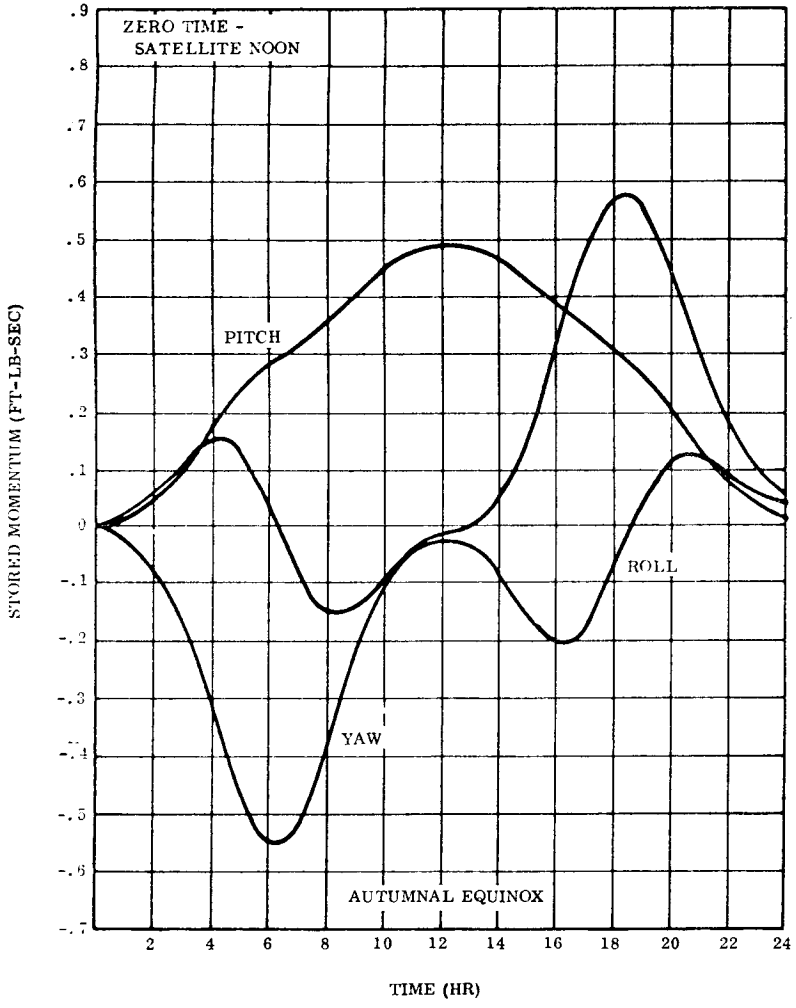


Figure 6.4-28. Flywheel Momentum Profile, Autumnal Equinox, (Yaw Axis Pointed to Rosman Station)
(Sheet 2 of 2)



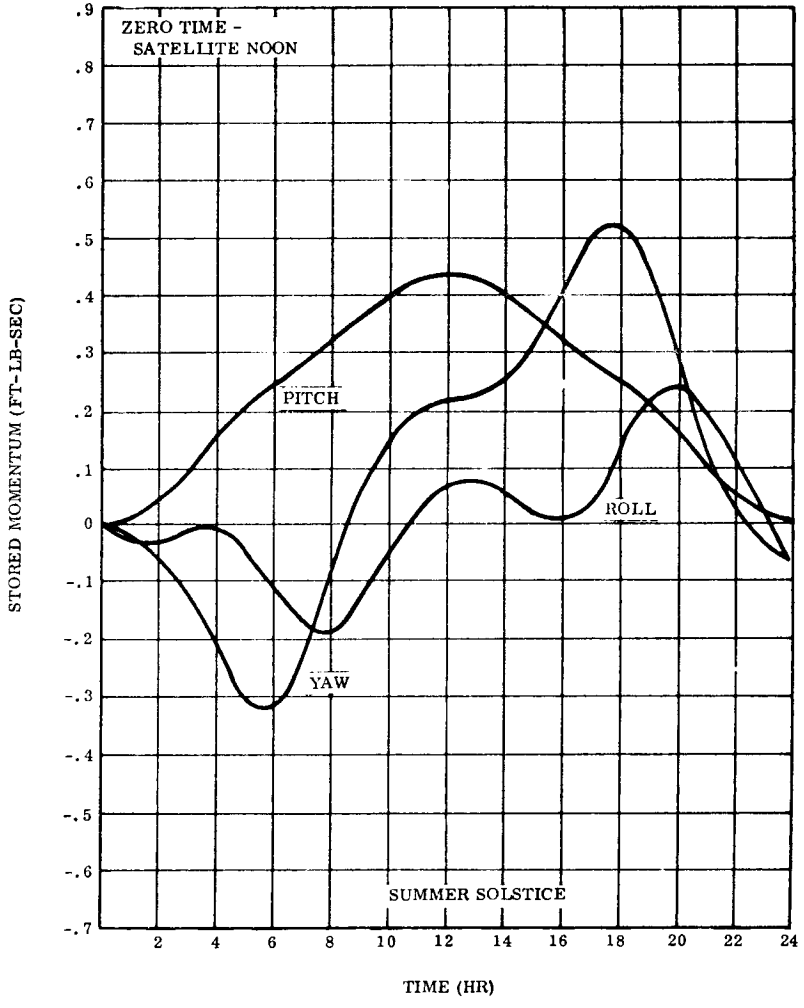


Figure 6.4-29. Flywheel Momentum Profile (Yaw Axis Pointed to Mojave Station)

for flywheel unloading at 1800 hours, midnight and 0600 hours. These curves do not represent more severe flywheel loading conditions than the curves for noon. The peak value of momentum storage required is readily determined from these figures (e.g., from Figure 6.4-26, the peak momentum required for the yaw flywheel for pointing to the local vertical in the Fall is 1.18 ft-lb-second). The residual momentum after 24 hours shows the mass expulsion required for unloading the flywheels. The use of the OAO flywheels having a stored momentum of 2 ft-lb-sec at 100 percent speed appears to be appropriate for use on ATS-4. The mass expulsion required for a particular pointing attitude can be determined by multiplying the momentum existing after 24 hours by 730 to obtain the ft-lb-sec required from the mass expulsion subsystem for the 2-year spacecraft lifetime.

6.4.3.3 Control Static and Dynamic Performance Analysis

This section describes the performance analysis carried out during the design of the ATS-4 station acquisition and orientation control systems. The following are discussed:

a. Spinup, coning control, precession control and spin rate.

b. Sun stabilization.

c. Earth stabilization.

d. Star stabilization.

e. Pointing.

f. Re-orientation.

g. Tracking.

h. Restabilization.

6.4.3.3.1 Spinup, Coning Control, Precession Control and Spin Rate

The Euler equations are used for the analysis of body rates, and the moments of inertia I_x and I_y are considered to be equal ($I_x = I_y = I$) to simplify the discussion. Euler's equations are:

$$T_x = I\dot{W}_x - (I-I_z)\, W_y W_z$$

$$T_y = I\dot{W}_y + (I-I_z)\, W_x W_z$$

$$T_z = I_z \dot{W}_z$$

To represent the spin axis attitude in inertial space, the Euler angles (ξ, ζ, ψ) are used, and the angles ξ and $\zeta_1 = (\zeta - \pi/2)$ are taken to be small. Thus:

$$\dot{\xi} = W_x \sin\psi + W_y \cos\psi$$

$$\dot{\zeta} = W_x \cos\psi - W_y \sin\psi$$

$$\dot{\psi} = W_z$$

6.4.3.3.1.1 Spinup - If a spinup moment (T_z) is applied about the z-axis at t=0, then assuming $W_z \simeq 0$ at t=0

$$\dot{W}_x = f t\, W_y + T_x/I$$

$$\dot{W}_y = f t\, W_x + T_y/I \qquad \text{where } f = \frac{T_z (I-I_z)}{I I_z}$$

$$\dot{W}_z = T_z/I_z$$

The first two equations may be combined by considering the complex angular velocity $W_r = (W_x + jW_y)$ in the x-y body plane. The combined equation is:

$$\dot{W}_r = -j\, f t\, W_r + T/I$$

where $T = (T_x + j\, T_y)$. The solution of this equation is:

$$W_r = e^{-j\, ft^2/2} \left(W_o + \frac{T}{I} \int e^{j\, ft^2/2}\, dt\right).$$

The first term represents a pure rotation, since the exponent is imaginary. The integral is a Fresnel integral (ref. Jahnke, et al, "Tables of Higher Functions", McGraw Hill, 1960) and has been evaluated for the values of f and t_b (40 sec burn time) used in the ATS-4. The resulting expression for W_r is

$$W_r = e^{-j\ ft^2/2} \left(W_o + 0.50\ \frac{Te}{I}\ ^{j\beta}\right)$$

where the phase angle β is given as 60 degrees in the Fresnel integral table for the specific conditions. In the case of the ATS-4, a pair of spin rockets are used whose mean thrust level (and hence burn time) may vary by $\pm$ 5 percent. If the motors are at opposite ends of the tolerance band, a malalignment moment + T corresponding to a thrust level of 10 percent of the motor thrust will exist for the burn time t_b of the high thrust motor, followed by a moment of -9T for 0.11 t_b. The above analysis is relevant to the first moment +T. Since the spacecraft spin rate changes only slightly during the period 0.11 t_b for which -9T acts, this moment may be regarded as being impulsive (for the ATS-4, 0.11 t_b is about 0.14 sec., corresponding to 42 degrees of a revolution at 71.7 rpm).

Thus, W_r is increased by

$$W_r = \frac{-9T\ (0.11\ t_b)}{I} = \frac{-T\ t_b}{I} = 1.34\ T/I$$

A number of digital computer iterations of the body motion during spinup have been made, and it has been found that adding the contributions of W_o, T and -9T to the value of W_r gives a conservative estimate for the value of W_r after spinup. Thus:

$$\left|W_r\right| = \left|W_o\right| + \left|0.5T/I\right| + \left|1.34\ T/I\right|$$

and the cone angle C_s is given by:

$$C_s = \tan^{-1}\ (I\ \left|W_r\right|\ /\ I_z W_s)$$

where W_s is the final value of the spin rate. A plot of the spin axis motion for a typical case is shown in Figure 6.4-43.

It has also been found that for the short spin motor burn time used for the spinup, an estimate of the precession of the spin axis in inertial space between separation and completion of spin up may be obtained by taking the RSS value of C_s and the angle through which the spin axis moves between separation and spin motor ignition. Thus:

$$P_s = (t_s^2 W_o^2 + C_s^2)^{1/2}$$

6.4.3.3.1.2 Coning Control - After spinup, the solution of the Euler equations for zero applied torques is

$$W_x = W_o \text{ Sin } (gt + \alpha)$$

$$W_y = W_o \text{ Cos } (gt + \alpha)$$

$$W_z = W_s$$

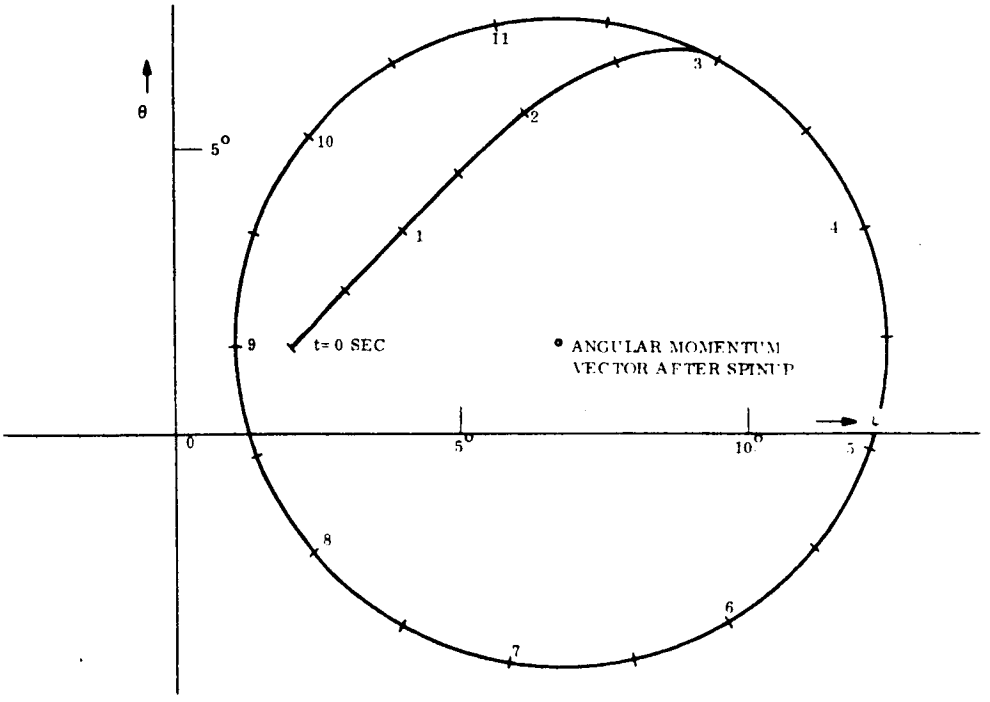


Figure 6.4-30. Locus of Spin Axis After Booster Separation

where the initial conditions are $W_o = (W_{xo}^2 + W_{yo}^2)^{1/2}$, $\alpha = \tan^{-1}(W_{xo}/W_{yo})$ and where $g = \frac{(I-I_z)W_s}{I}$. The first harmonic representation of the control torque produced about the x-axis by a coning damper of the type shown in Figure 6.4-31 (a) is, neglecting threshold effects,

$$T_x = -I \left| a+b \sin (gt + \alpha) \right|$$

$$T_y = 0$$

where a = 0, b = T/I for a bidirectional control torque of magnitude $\pm$ T, and a=b=T/21 for a monodirectional control torque +T. Inserting these torques into the Euler equations and solving, the resulting expressions for W_x and W_y are:

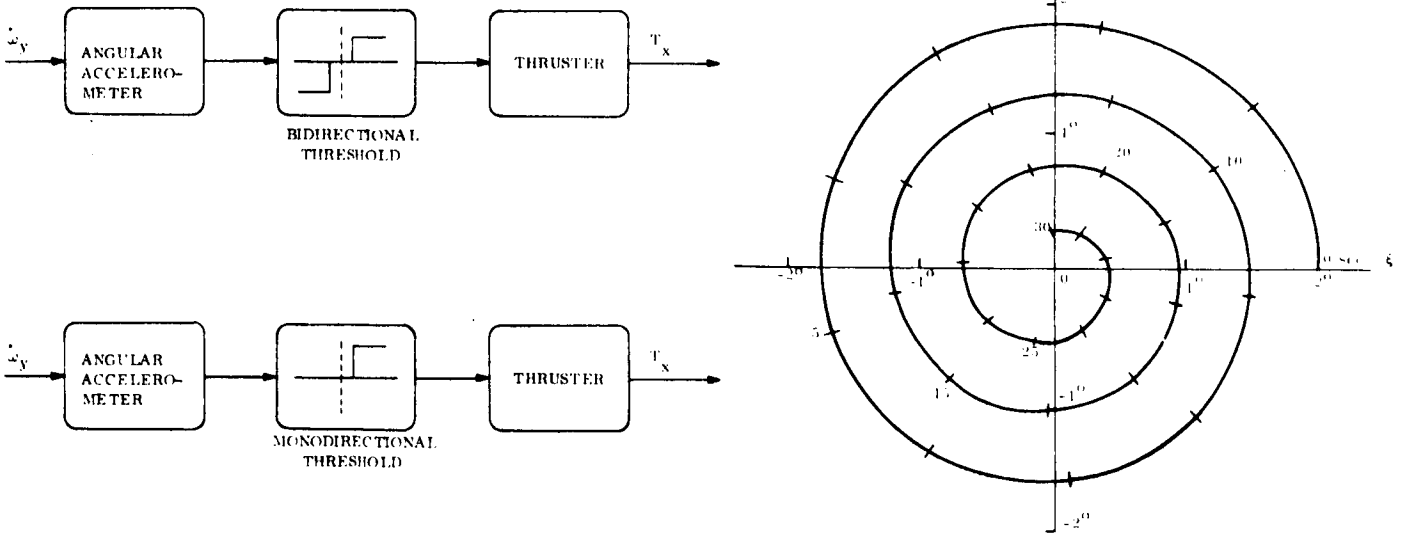


Figure 6.4-31. Coning Damper

$$W_x = (W_o - \frac{bt}{2}) \sin(gt + \alpha) - \frac{a}{g}(\sin gt) - \frac{b}{2g} \sin gt \sin \alpha$$

$$W_y = (W_o - \frac{bt}{2} \cos(gt + \alpha) + \frac{a}{g}(1 - \cos gt) + \frac{b}{2g} \sin gt \cos \alpha$$

Thus $\left|W_r\right| = (W_x^2 + W_y^2)^{1/2}$ is reduced at a rate given by b/2. The rate of change of the cone angle C is given by:

$$\text{Sec}^2 C \frac{dc}{dt} = \frac{d}{dt}\left\{\frac{(I\left|W_r\right|}{I_z W_s}\right\} = \frac{-Ib}{2I_z W_s}$$

$$\frac{dc}{dt} = -\cos^2 C \quad T/4I_z W_s \simeq -T/4I_z W_s$$

where the last result quoted refers to the monodirectional damper with the cone angle less than 10 degrees. The second and third terms on the right of the above equation for W_x and W_y represent a residual coning which is introduced by the finite pulse width of the coning damper; the magnitude of this coning is given for the monodirection d amper by ($\sin \alpha = 1$, $\cos g\, t = -1$)

$$C_{r_{max}} = \frac{3aI}{gI_z W_s}$$

This equals 0.08 degree before apogee burn and 0.16 degree after apogee burn. It is necessary to keep this level below the 0.5 degree threshold level, or the coning damper would continue operation indefinitely.

Extension of the first harmonic approxima tion used above to a more exact approximation of the square wave control torque introduces terms which contribute a residual coning of the order of 0.05 degree. For the bidirectional control system the rate of reduction of cone angle, and the rate of fuel consumption, is double that of the monodirectional system, so that the two systems are equally efficient.

Solving the inertial equations for ξ and ζ_1, and putting $W_n = (W_s - g)$

$$\xi = \xi_0 + \sin(W_n t - \alpha)\,(W_o - bt/2)/W_n + b\,|\cos\alpha - \cos(W_n t - \alpha)|/2W_n^2 + \xi_r$$

$$\zeta_1 = \zeta_{10} + \cos(W_n t - \alpha)\,(W_o - bt/2)/W_n + b\,|\sin\alpha + \sin(W_n t - \alpha)|/2W_n^2 + \zeta_r$$

Where ξ_0 and ζ_{10} are the initial conditions and ξ_r and ξ_{1r} contain terms an order of magnitude smaller than the terms written in full. The precession of the angular momentum vector is given by $|b \sin(W_n t/2)|\ /W_n^2$. Thus the maximum value of the precession for the case considered above, is 0.45 degree for the bidirectional damper and 0.23 degree for the monodirectional damper. Since the monodirectional damper uses two thrusters, compared to four for the bidirectional damper, it has been selected for use in the ATS-4. The coning damper reduces the energy of the system; however, the angular momentum is also reduced (since W_s remains constant). Thus, the coning damper does not violate the commonly used rule that energy must be added to a body with $I > I_z$, since this rule applies only to the case where the body angular momentum remains constant. A plot of the spin axis motion during operation of a monodirectional coning damper with a threshold corresponding to a cone angle of 0.25 degree is shown in Figure 6.4-31(b).

6.4.3.3.1.3 Structural Damping - Since the ATS-4 spacecraft spins about its axis of least moment of inertia, structural damping causes an increase in the coning amplitude which is given by the relation

$$\frac{dc}{dt} = K\,\zeta_d \sin c$$

The factor K has been estimated to be 2.98 degrees/hr (Section 6.7) for $W_s = 2\pi$ radian/second, and K is proportional to $(W_s)^4$. Taking a worst case value for ξ_d of 0.12 and c = 10 degrees

$$\frac{dc}{dt} = 0.062 \left(\frac{Ws}{2\pi}\right)^4 \text{ degrees/hour}$$

Since the coning control reduces the cone angle to less than one degree shortly after spinup, the rate of increase in cone-angle would be about 0.01 degree/hour for a spin rate of 71.7 rpm, and the increase in coning during the 15 hour transfer orbit or the first two days of synchronous orbit would not be significant.

6.4.3.3.1.4 Precession Control - The inertial equations with body-fixed moments included are:

$$\ddot{\xi} - W_n \dot{\zeta}_1 = \frac{T_x}{I} \sin \psi + \frac{T_y}{I} \cos \psi$$

$$\ddot{\zeta}_1 + W_n \dot{\xi} = \frac{T_x}{I} \cos \psi + \frac{T_y}{I} \sin \psi$$

A simplified model of the precession control consists of a torque impulse ($T_x \Delta t$) applied at a phase angle of ψ_i . The Laplace transforms of the inertial equations with zero initial conditions are then:

$$s^2 \xi - W_n s \zeta_1 = \frac{T_x \Delta t \sin \psi_i}{I} e^{-\psi_i s/W_s}$$

$$s^2 \zeta_1 + W_n s \xi = \frac{T_x \Delta t \cos \psi_i}{I} e^{-\psi_i s/W_s}$$

and the time solution is, with the time scale shifted by ψ_i/W_s:

$$\xi = \frac{T_x \Delta t}{I W_n} \left| \cos \psi_i - \cos (W_n t + \psi_i) \right|$$

$$\zeta_1 = \frac{T_x \Delta t}{I W_n} \left| \sin \psi_i - \sin (W_n t + \psi_i) \right|$$

This motion is a step shift in the angular momentum vector by an amount

$$\Delta s = \frac{T_x \Delta t}{} = \frac{T_x \Delta t}{I_z W_s}$$

and a coning motion with an amplitude Δs. The direction of the precession Δs is given by:

$$\tan \psi_p = \frac{\Delta \xi}{\Delta \zeta_1} = -\cot \psi_i$$

Thus, to produce rhumb line precession, the phase angle ψ_i is equal to $(\pi/2 + \psi_p)$, where ψ_p is the calculated rhumb line angle.

A train of impulses produces precession at constant rhumb line angle ψ_p, and also a buildup of coning. It can be shown that the maximum cone half angle is given by the relation:

$$C = \Delta s \sum_{m=o}^{\infty} e^{jw_n (t + 2\pi m/W_s)} = \frac{\Delta s \, e^{jw_n t}}{\left(1 - e^{j2\pi W_n/W_s}\right)}$$

$$\therefore |C| = \frac{\Delta s}{\left|2 (1-\cos 2\pi W_n/W_s)\right|^{1/2}}$$

For the ATS-4, $|C| = 1.77 \Delta s$ before apogee burn and $1.5 \Delta s$ after apogee burn. Thus, the coning introduced by the rhumb line precession is small, since Δs is less than 0.1 degree.

The effect of using T_x pulses of finite width rather than impulses is primarily a reduction in efficiency of the precession. The ratio between the precession produced by a pulse of width ψ_w and that produced by an impulse of the same magnitude is:

$$\frac{\sin(\psi_w/2)}{(\psi_w/2)}$$

If the variation in specific impulse of the thruster with pulse on-time is taken into account, a curve can be drawn of efficiency versus pulse width ψ_w, where efficiency is defined as:

$$(\text{eff}) = \frac{\sin(\psi_w/2)}{(\psi_w/2)} \cdot \frac{\text{Isp}}{\text{Isp}(\infty)}$$

Where Isp is the specific impulse at pulse width ψ_w and Isp (∞) is that for continuous thrusting, Figure 6.4-32 shows the efficiency for various spin rates. At 71.7 rpm the maximum efficiency is obtain for a pulse width of 175 msec ($\psi_w = 75^o$).

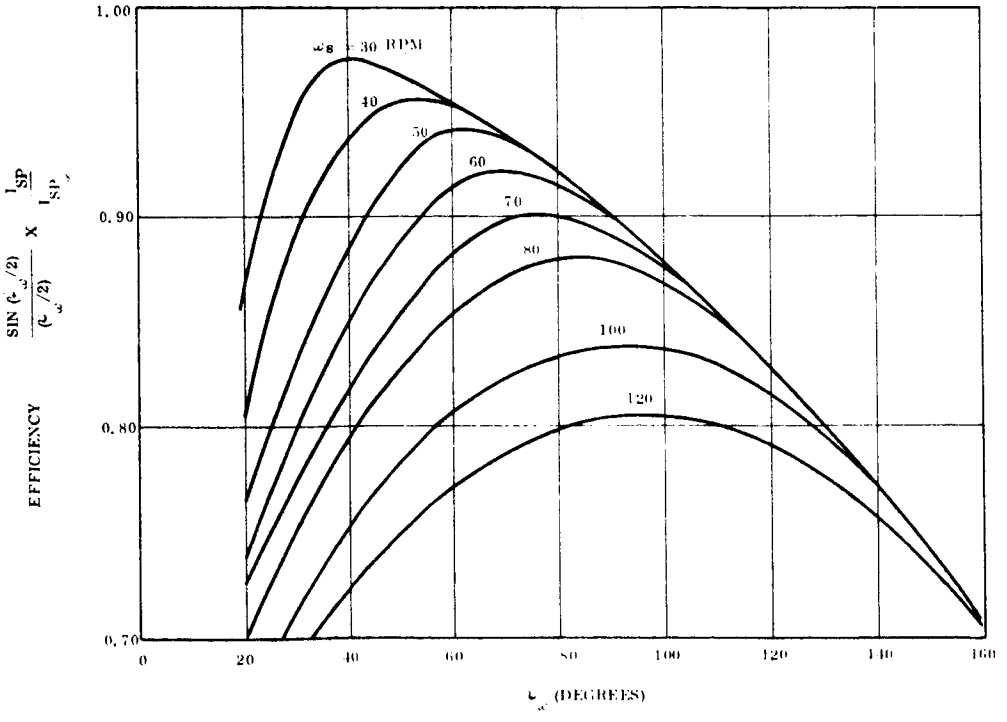


Figure 6.4-32. Thruster Efficiency vs Pulse Width

Launch window restrictions imposed by the precession control sun sensors are discussed in Appendix B. The sun sensor and rf POLANG measurement used for determining the required precession are discussed in Section 5. 5.

6.4.3.3.1.5 Apogee Motor Burn - For the simple case of body-fixed moments M_x and M_y due to thrust malalignment, it can be shown that the solution of the Euler equations for zero initial rates is:

$$W_x = \frac{M_x}{Ig} \sin gt + \frac{M_y}{Ig} (1 - \cos gt)$$

$$W_y = \frac{-M_x}{Ig} (1 - \cos gt) + \frac{M_y}{Ig} \sin gt$$

and the Euler angles, ξ and ζ_1, are given by:

$$\xi = \frac{-M_x}{IgW_s} \sin W_s t + \frac{M_x}{IgW_n} \sin W_n t + \frac{M_y}{IgW_s} (1 - \cos W_s t) - \frac{M_y}{IgW_n} (1 - \cos W_n t)$$

$$\zeta_1 = \frac{M_x}{IgW_s} (1 - \cos W_s t) - \frac{M_x}{IgW_n} (1 - \cos W_n t) + \frac{M_y}{IgW_s} \sin W_s t - \frac{M_y}{IgW_n} \sin W_n t$$

Where W_n is the coning frequency ($W_n = W_s - g$).

The pattern of variation of ξ and ζ_1 consists of a net shift of the angular momentum vector given by:

$$(\xi_s^2 + \zeta_{1s}^2)^{1/2} = (M_x^2 + M_y^2)^{1/2} \frac{W_s - W_n}{IgW_sW_n} \approx (M_x^2 + M_y^2)^{1/2} \frac{1}{I_z W_s^2}$$

and a complex coning motion whose mean amplitude is equal to the angular momentum migration.

A more detailed model of the spacecraft dynamics has been programmed for digital computer solution using equations listed below (W. T. Thomson and G. S. Reiter, AIAA Journal, Vol. 3, March 1965, p. 413, "Jet Damping of a Solid Rocket: Theory and Flight Results").

$$I_x \dot{W}_x = T_x + (I_y - I_z) W_y W_z + \ell^2 m W_x - MZ (W_y W_z - \dot{W}_x) - 2zW_x)$$

$$I_y \dot{W}_y = T_y + (I_z - I_x) W_x W_z + \ell^2 m W_y + MZ (Z(W_x W_z + \dot{W}_y) + 2zW_y)$$

$$I_z \dot{W}_z = T_z + (I_x - I_y) W_x W_y$$

Where ℓ is a parameter related to the mean distance between the spacecraft center of mass and the nozzle throat, m is the mass rate, M is the spacecraft mass, Z is the shift of the center of mass from the initial position and z is the rate of change of Z. The third terms of the first two equations ($\ell^2 m$) represent jet damping, and the last terms (MZ) represent center of mass shift.

Computer solutions have been obtained for the case where a linear time variation has been assumed for the center of gravity position and the inertias I_x, I_y, I_z, and the thrust has been assumed to be of the form

$$F = F_o (1 - e^{-at})$$

Where a = 10 sec^{-1} (100 msec rise time). It has been found that for the ATS-4, little effect on the coning motion is caused by the jet damping, inertia variation and center of mass shift, and that the simple expression noted above is a good approximation. At motor burnout, a second shift of the angular momentum vector occurs in a direction not related to the initial shift. The maximum coning amplitude after apogee burn is given by:

$$\tan C = \frac{(M_x^2 + M_y^2)^{1/2}}{I_z W_s g}$$

where the values of M_x, M_y, I_z and g are those at burnout.

Typical plots of ξ versus ζ_1, are shown in Figure 6.4-33. The apogee motor thrust vector malalignment was 0.25^o, (at the nozzle). Figure 6.4-33 (top) shows the case of no coning at motor ignition, and Figure 6.4-33 (bottom) shows the case of 0.5 degree coning amplitude at motor ignition, with the initial coning approximately in phase with the coning produced by the motor thrust malalignment (if the initial coning were out of phase, the coning during apogee motor burn would have a much smaller amplitude). In both situations, the coning after apogee burn is close to the maximum value (if burnout occurs while the ξ-ζ_1 curve is at a cusp, the coning after apogee burn is small).

6.4.3.3.1.6 Spin Rate Tradeoff - Factors influenced by the spin rate of the ATS-4 spacecraft are:

a. Apogee motor thrust vector migration and coning (vary as $1/W_s^2$ and affect vernier velocity requirement).

b. Thruster efficiency in pulsed mode (decreases linearly with increasing W_s).

c. Impulse required for coning and precession control, and spindown (proportional to W_s).

d. Coning caused by structural damping (found to be negligible for the range of spin rates of interest).

e. Component g-level caused by centrifugal force (proportional to W_s^2).

A tradeoff can be made between items a, b, and c. The vernier velocity requirement has been calculated as a function of spin rate for the case in which the spacecraft is not precessed perpendicular to the orbit plane after apogee burn. The following are the error sources and propulsion requirements (the apogee burn velocity increment is 5498 ft/sec:

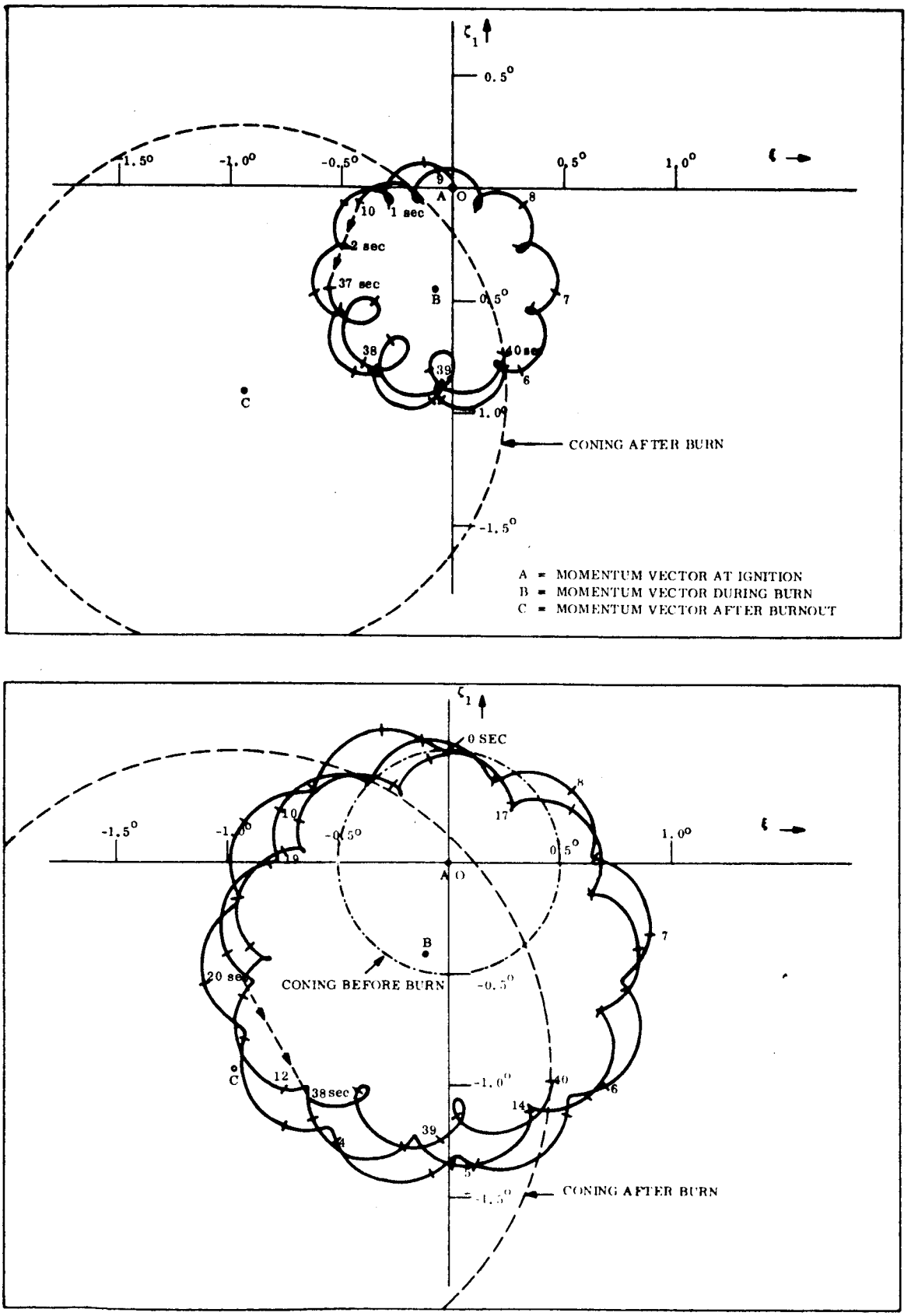


Figure 6.4-33. Apogee Motor Burn

Error Source	Spacecraft Alignment Error (Deg)	ΔV_r ft/sec Radial	ΔV_a ft/sec Axial
Perigee burn	--	$\pm$ 12	$\pm$ 34
Apogee motor total impulse (1.5%)	--	--	--
Sun Sensor error	0.5	$\pm$ 48.0	0
RF sensor error	1.0	$\pm$ 96.0	- 0.8
Residual coning	1.0	--	- 0.8
Apogee motor migration	ϵ_a	$\pm$ 5498 sin ϵ_a	- 5498 (1-cos ϵ_a)
Apogee motor coning	ϵ_a	--	- 5498 (1-cos ϵ_a)

The total impulse required to correct the spacecraft attitude after apogee burn was calculated by multiplying the RRS values of ΔV_r (normal to the spacecraft spin axis) and ΔV_a (parallel to the spin axis) by the spacecraft mass. ΔV_r was also adjusted to allow for the thruster efficiency, since this vernier component is removed by pulsed-mode thrusting. The impulse requirements for coning control, precession control and despin were calculated. The curve of total impulse requirement versus spin rate shows a broad minimum between 70 and 80 rpm (Figure 5.5-8, Section 5.5.2.1.4).

For the design spin rate of 71.7 rpm, ϵ_a = 0.55 degree. The apogee motor migration contributes 52.8 ft/sec to ΔV_r, and a negligible amount to ΔV_a. The RSS values of ΔV_r and ΔV_a are 123 ft/sec and 89.2 ft/sec, respectively.

6.4.3.3.2 Sun Stabilization

6.4.3.3.2.1 Summary - An analog computer simulation was used to verify satisfactory stability and response time of the proposed ATS-4 sun stabilization system. For current values of spacecraft inertia and jet torque, simulated rate stabilization and solar orientation computer runs for a 180 degree pointing error and 0.15 degree/second rate were conducted. Sun stabilization was completed in approximately one hour as shown on

Figure 6.4-34. A model of the sun stabilization system as simulated on the analog computer is summarized in Figures 6.4-42, 6.4-43 and 6.4-44 and Table 6.4-5 and 6.4-6.

6.4.3.3.2.2 Rate Stabilization and Solar Orientation - The operation of the sun stabilization and solar orientation system is described in terms of the phase plane diagram of Figure 6.4-45. The switching lines shown are determined by the attitude deadband or threshold detector level (θ_d), the rate gyro gain (K_g), and the sensor signal limiting level (θ_r). For the negative jet, the switching line equations are as follows:

$$\theta + K_g\omega = \theta_d \qquad -\theta_r < \theta < \theta_r$$

$$\omega = -(\theta_r - \theta_d) / K_g \qquad \theta \geq \theta_r$$

$$\omega = (\theta_r + \theta_r) / K_g \qquad \theta \leq \theta_r$$

The switching line equations for the positive jet are:

$$\theta = K_g\omega = -\theta_d \qquad -\theta_r < \theta < \theta_r$$

$$\omega = -(\theta_r + \theta_d) / K_g \qquad \theta \geq \theta_r$$

$$\omega = (\theta_r - \theta_d) / K_g \qquad \theta \leq -\theta_r$$

For some initial rate and attitude error, ω_o and θ_o, as shown in Figure 6.4-45, the error signal actuates the negative jet. The resultant torque drives the vehicle as shown to the switching line at Point 2. The error signal at this point falls below the threshold and the jet is de-energized with the result that the attitude error continues to decrease at some constant rate. Note that were it not for the sun sensor signal limiter, the jet would have remained on until the rate had reached that at Point 2. For this reason the sensor signal limit is often called a "rate limit" even though the position rather than rate

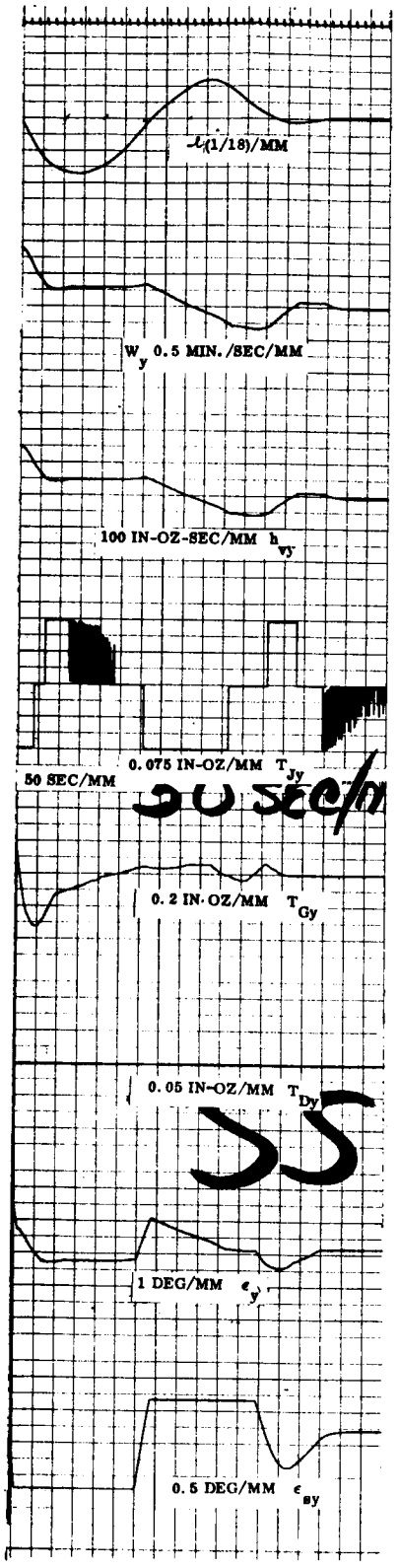


Figure 6.4-34. Initial Stabilization Pitch Axis

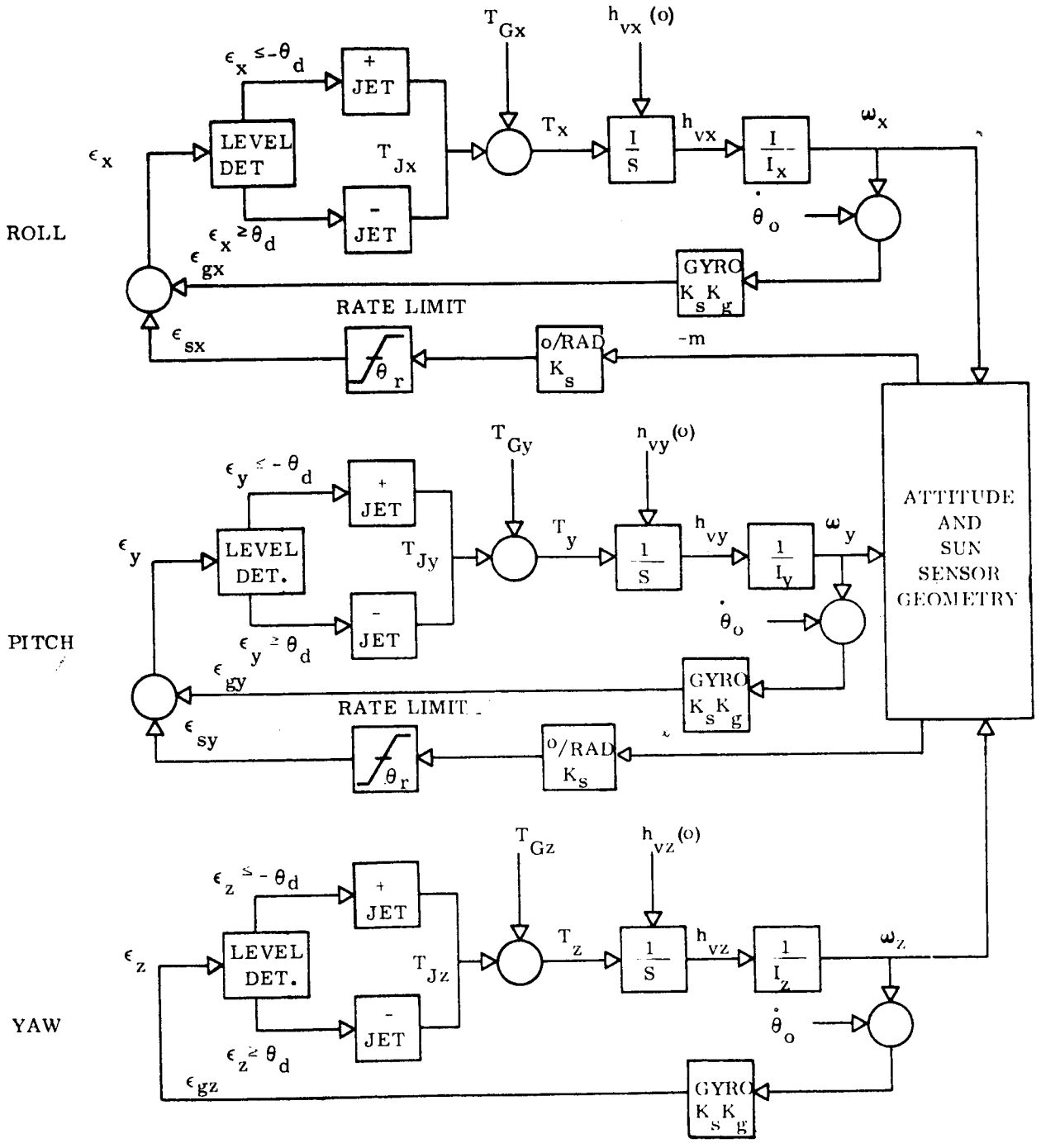


Figure 6.4-35. Sun Stabilization System, Block Diagram

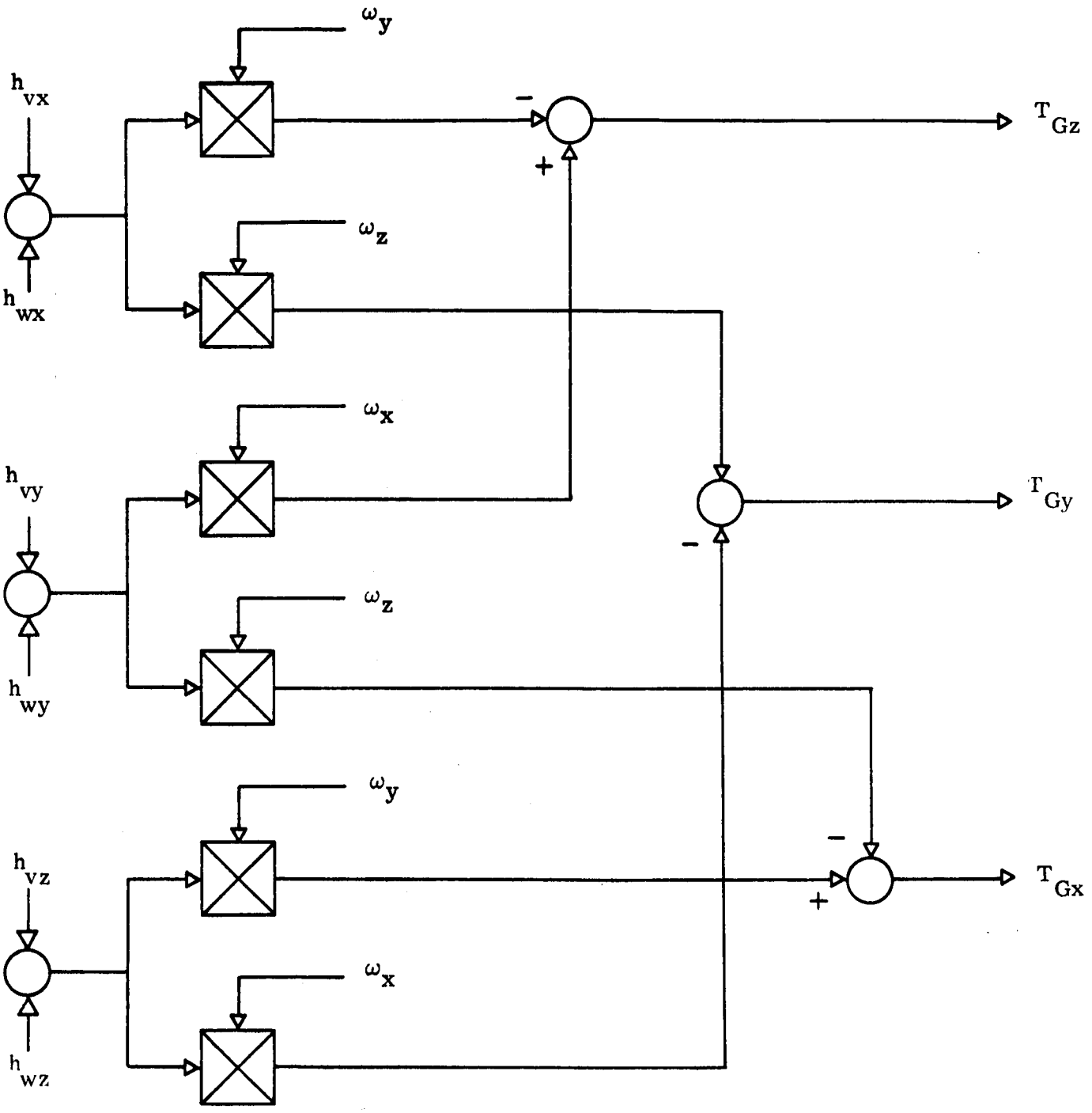


Figure 6.4-36. Gyroscopic Torques

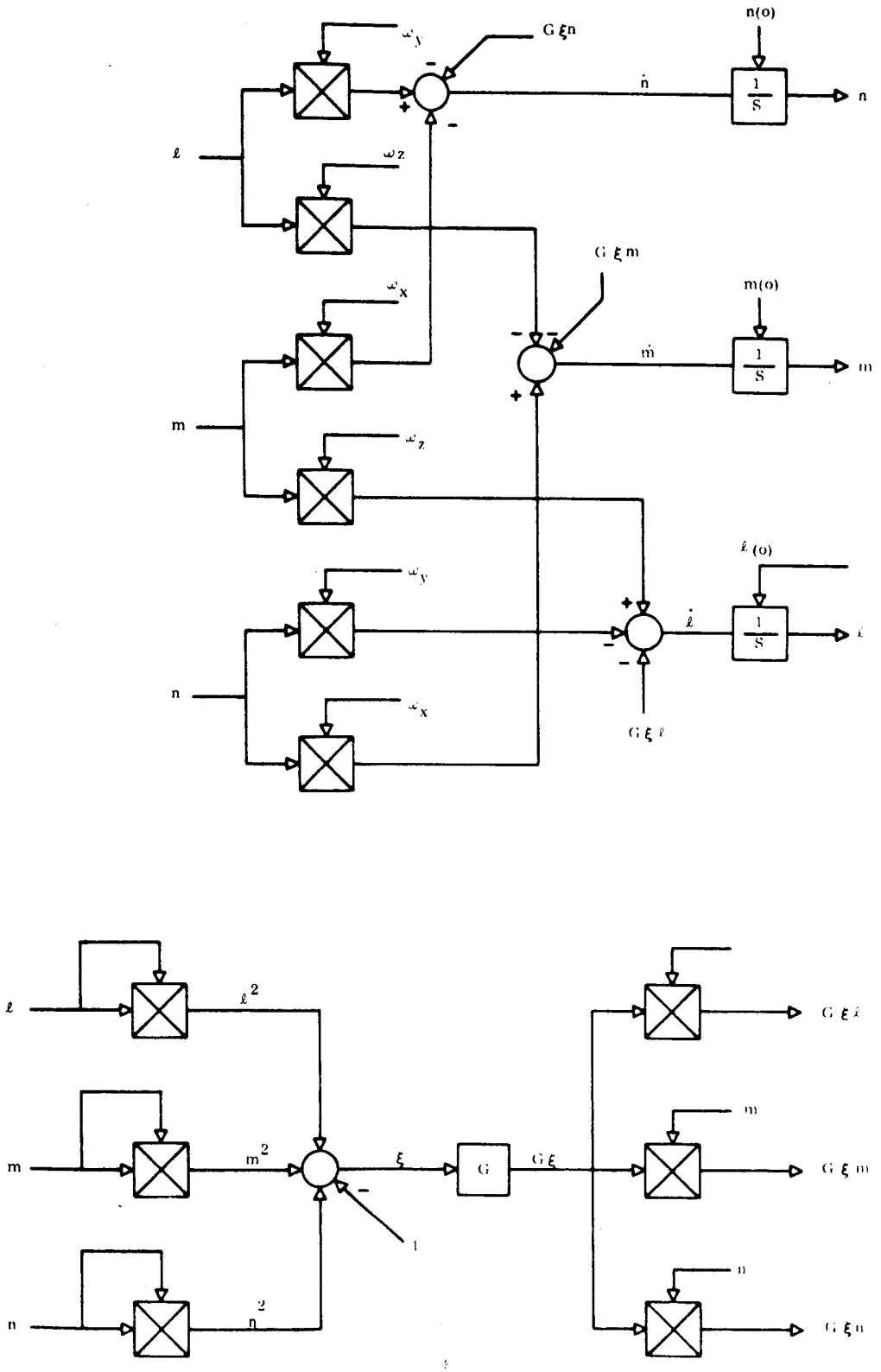


Figure 6.4-37. Attitude and Sun Sensor Geometry

Table 6.4-5. Sun Stabilization System Nomenclature

Symbol	Nomenclature
x	Roll Axis
y	Pitch Axis
z	Yaw Axis
ℓ	Direction cosines of angular displacements between roll, pitch, and yaw axes, respectively, and sunline.
m	
n	
I_x	Moments of inertia
I_y	
I_z	
ϵ_x	Control axis
ϵ_y	Error
ϵ_z	Signals
ϵ_{gx}	Rate
ϵ_{gy}	Gyro
ϵ_{gz}	Signals
ϵ_{sx}	Sun
ϵ_{sy}	Sensor
ϵ_{sz}	Signals
θ_r	Sensor signal saturation (rate limit)
K_s	Sensor gain
θ_d	Threshold detector level
h_s	Threshold detector hysteresis
ϕ_c	Rate gyro uncertainty
T_{Jx}	Jet Torque
T_{Jy}	
T_{Jz}	
T_{Gx}	Gyroscopic Torque
T_{Gy}	
T_{Gz}	
h_{vx}	Vehicle momentum
h_{vy}	
h_{vz}	

Symbol	Nomenclature
ω_x	Vehicle angular velocity
ω_y	
ω_z	
T_x	Vehicle torque
T_y	
T_z	
ℓ_c	Direction cosines of angular displacements between roll, pitch, and yaw axes, respectively, and local vertical.
m_c	
n_c	
e_1	Euler Parameters
e_2	
e_3	
e_4	
γ_r	Earth Scanner Signals
γ_p	
A_{ijk}	Momentum/velocity transfer function coefficient i=x, y, z; j=x, y, z; k = 1, 2...N
ω_{jk}	Natural frequency - flexible appendages j=x, y, z, k = 1, 2...N
ζ_{jk}	Damping ratio - flexible appendages j=x, y, z, k = 1, 2...N
h_m	Wheel momentum capacity
T_s	Wheel stall torque
V_r	Rated voltage of wheel
T_1	Flywheel controller lead time constant
T_2	Flywheel controller lag time constant
h_{wx}	Wheel momentum
h_{wy}	
h_{wz}	
θ_x	Attitude error
θ_y	
θ_z	

Symbol	Nomenclature
Ω	Orbital velocity
$\bar{x}_S$	Unit vectors along body axes
$\bar{y}_S$	
$\bar{z}_S$	
Y_{ij}	Elements of structural admittance matrix
$\bar{x}_3$	Unit vectors along the axes of the geocentric coordinate system
$\bar{y}_3$	
$\bar{z}_3$	
$\bar{s}$	Unit vector along the sunline
A_{ij}	Direction cosines i=1, 2, 3; j=1, 2, 3
ω_x	Angular velocity of an arbitrary coordinate system
ω_y	
ω_z	
ϕ	Body axis rotations similar to Euler Angles
θ	
ψ	
V_x	Wheel voltage
V_y	
V_z	
μ	Desired angular displacement between sunline and roll axis for star stabilization
α	Sun sensor mounting angles for star stabilization
β	
α_1	Sun sensor mounting angles for sun stabilization
α_2	
β_1	
β_2	
$\dot{A}$	$\dot{A}_x\bar{x} + \dot{A}_y\bar{y} + \dot{A}_z\bar{z}$
K_A	Loop gain
V_s	Power amplifier saturation voltage
$\bar{T}_E$	External Torque
$\bar{T}_D$	Disturbance Torque
ℓ_s	Direction cosines of angular displacements
m_s	Between roll, pitch, and yaw axes, respectively, and local vertical
n_s	
K_g	Rate gyro gain

Table 6.4-6. Sun Stabilization System Parameter Values

Symbol	Value	Symbol	Value
I_x	2737 (no appendages) slug feet^2	K_A	15 volts/arc minute
I_y	2663 (no appendages) slug feet^2	V_S	26 volts
I_z	300 (no appendages) slug feet^2	K_G	100 sec
θ_R	7^o	A_{xx}	$1.47.10^{-6}$ (in. oz-sec^2)$^{-1}$
K_S	57.3 deg/rad	A_{yy}	$1.77.10^{-6}$ (in. oz-sec^2)$^{-1}$
θ_D	2^o	A_{zz}	$3.02.10^{-6}$ (in. oz-sec^2)$^{-1}$
h_S	0.15^o	A_{yy1}	$6.25.10^{-7}$ (in. oz-sec^2)$^{-1}$
$\dot{\theta}_o$	0.003 deg/sec	A_{zz1}	$1.52.10^{-6}$ (in. oz-sec^2)$^{-1}$
T_{jx}	1.5 in. oz	A_{xx2}	$5.13.10^{-7}$ (in. oz-sec^2)$^{-1}$
T_{jy}	1.5 in. oz	A_{yy2}	$5.53.10^{-7}$ (in. oz-sec^2)$^{-1}$
T_{jz}	0.8 in. oz	A_{ij}	0(1 / j)
h_m	2 foot-lb-sec	ω_{x1}	5.54 rad/sec
T_S	2 in. oz	ω_{y1}	5.54 rad/sec
V_R	32 volts	ω_{x2}	17.76 rad/sec
T_1	200/11 sec	ω_{y2}	17.76 rad/sec
T_2	20/11 sec	ω_{z1}	11.75 rad/sec
Ω	7.27×10^{-5} radians/second	ξ_{x1}	$\xi_{x2} - \xi_{y1} \quad \xi_{y2} \quad \xi_{z1} = 0.001$

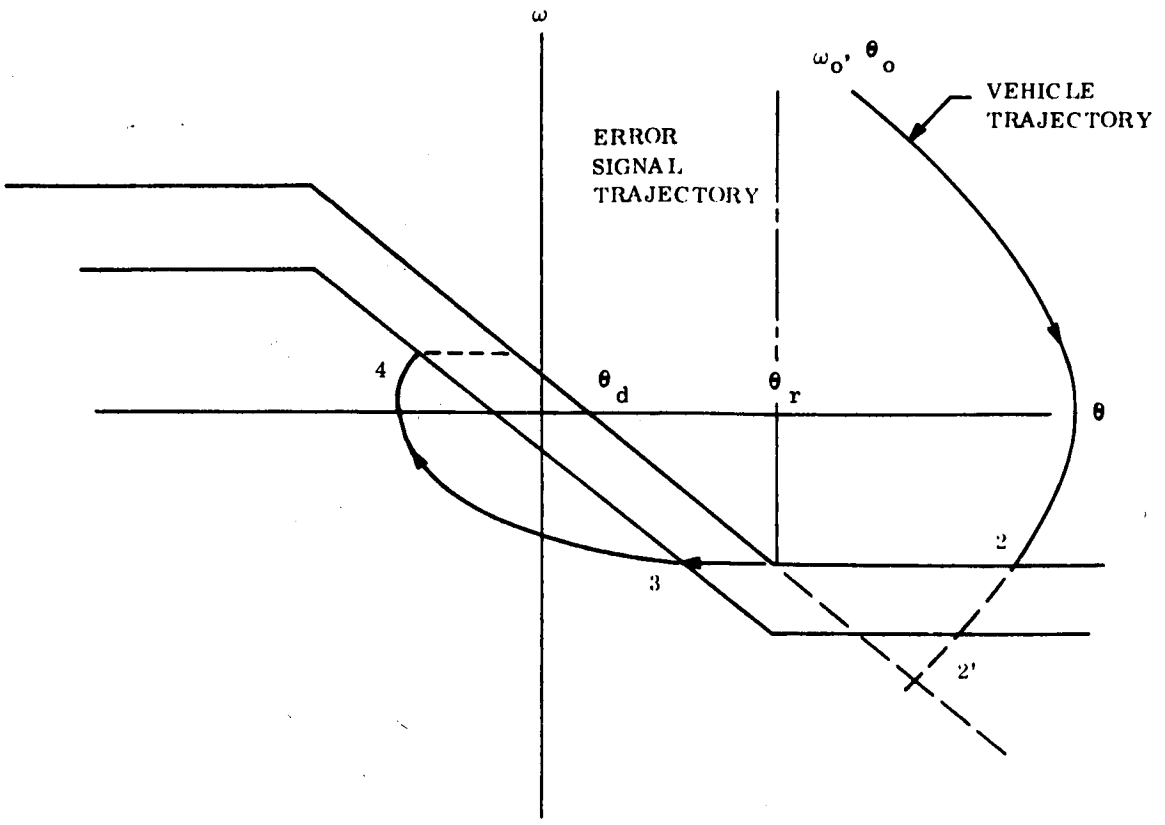


Figure 6.4-38. Phase Plane Diagram

signal is being limited. Eventually, the error signal trajectory reaches the positive jet switching line at Point 3 and the spacecraft is torqued along the trajectory shown to Point 4 where the positive jet is turned off. The vehicle continues this cycle until hardware limitations such as the rate gyro uncertainty, threshold detector hysteresis, solenoid valve pickup and dropout time delays, and sun sensor errors prevent further reduction of the rate and attitude errors. The rate limit discussed above, since it does limit the vehicle rate, reduces the amount of gas required to effect stabilization and increases the settling time.

The satisfactory stability and settling time of the sun stabilization system for ATS-4 parameters (Table 6.4-6) are demonstrated on Figure 6.4-34, depicting simulated stabilization from a 180 degree pointing error and body axis rates of 0.15 degree/second. The time required for stabilization is 66 minutes. Much shorter stabilization times could be achieved using jets of greater thrust or moment arm. The stabilization time would be increased to approximately two hours for an initial rate below zero.

The features of system operation discussed in terms of the phase plane plot of Figure 6.4-38 are illustrated to a limited extent in the strip chart recording. The rate limiting is very much in evidence. However, the rate/position trajectory is obscured somewhat because the direction cosine ℓ is equal to rotation about the pitch body axis only for relatively small errors (10 degrees at most). Furthermore, the constant jet torque is supplemented by a varying gyroscopic torque of the same order of magnitude.

6.4.3.3.2.3 Sun Pointing - The sun stabilization system must reduce the initial body axis rates to within the 0.03 degree/second capacity of the mechanical flywheels for a spacecraft with deployed appendages (to insure restabilization capability). For a rate gyro uncertainty ($\dot{\theta}_o$), a threshold detector hysteresis (h_s), solenoid valve pickup time delay (t_n), and solenoid dropout time delay (t_f), the peak limit cycle rate of the sun stabilization system can be calculated from the approximation:

$$\omega_{MAX} = \frac{h_s + \frac{T_J}{I} t_f (K_G - t_{f/2})}{2K_G - t_f - t_n} + \dot{\theta}_o$$

For anticipated values of these parameters,

$\dot{\theta}_o$ = 0.003 degree/second

h_s = 0.15 degree

t_f = 0.03 second

t_n = 0.02 second

the peak limit cycle rate becomes 0.004 degree/second allowing a comfortable margin of wheel capacity.

Achieving this low peak limit cycle rate is contingent upon use of a rate gyro of sufficient quality to allow a gyro gain as high as 100 seconds without noise saturation and an uncertainty as low as 0.003 degree/second.

Limit cycling does not show on Figure 6.4-34 because gyro uncertainty, threshold detector hysteresis and solenoid valve time delay were not included in the simulation on the computer, nor were simulated disturbance torques applied to the spacecraft. The principal objective of simulating the sun stabilization system was to demonstrate stability and adequate settling time given jets of relatively low torque.

6.4.3.3.3 Earth Stabilization

6.4.3.3.3.1 Summary - An analog computer simulation was used to verify satisfactory stability, response time and wheel capacity of the proposed ATS-4 earth stabilization system. For current values of spacecraft inertia and flywheel parameters (Table 6.4-6), simulated earth stabilization from a 25 degree roll error, a 5-degree pitch error and body axis rate errors of 0.02 degree/second was successfully completed in 27 minutes as illustrated on Figures 6.4-39 and 6.4-40. A more favorable polarity combination of rate and attitude errors resulted in a much lower settling time of 10 minutes (Figures 6.4-41 and 6.4-42).

A model of the earth stabilization system has been summarized in Figures 6.4-43 through 6.4-50.

6.4.3.3.3.2 Earth Stabilization System Performance - The principal performance features of the earth stabilization system are illustrated in Figures 6.4-39 through 6.4-42. These features include:

a. The satisfactory stability of the system given nonlinear components and gyroscopic torques.

b. The ability of the flywheels to remove the anticipated worst case rate and attitude errors in a suitably brief period of time.

The initial roll and pitch errors of 25 and 5 degrees respectively, are the anticipated maximums. The initial rates of 0.02 degree/second are substantially more than the anticipated maximum rates (0.004 degree/second at the end of sun stabilization and appendage deployment.

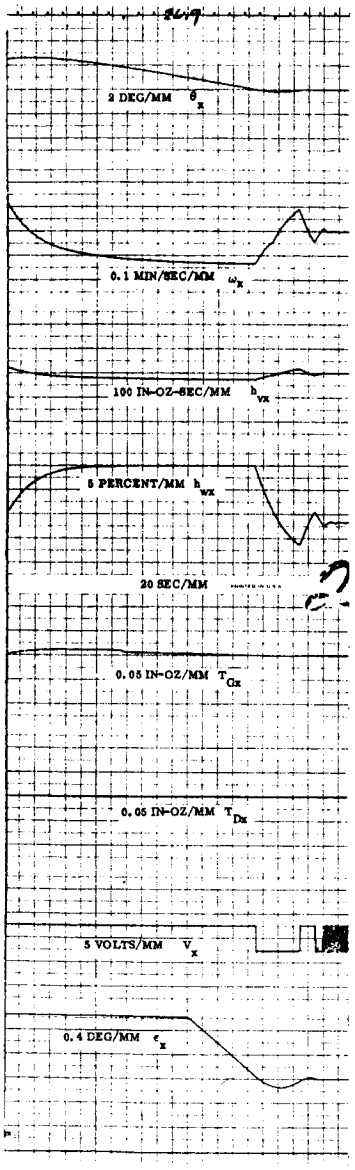


Figure 6.4-39.
Earth Stabilization
Roll Axis, E1

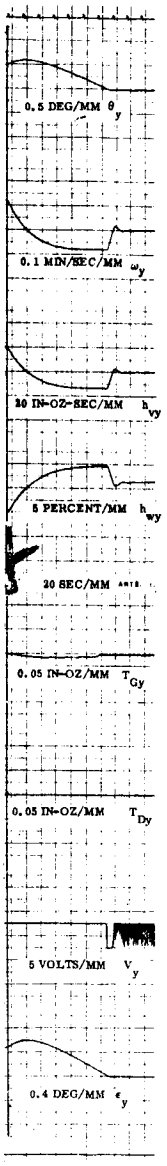


Figure 6.4-40.
Earth Stabilization
Pitch Axis, E2

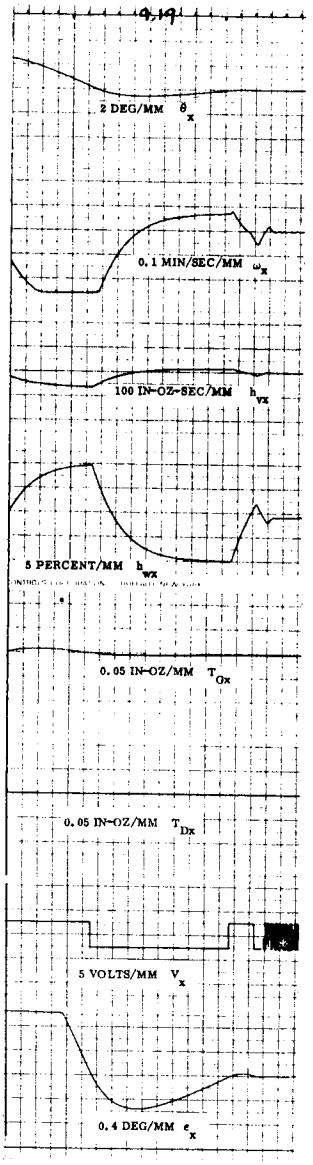


Figure 6.4-41.
Earth Stabilization
Roll Axis, E3

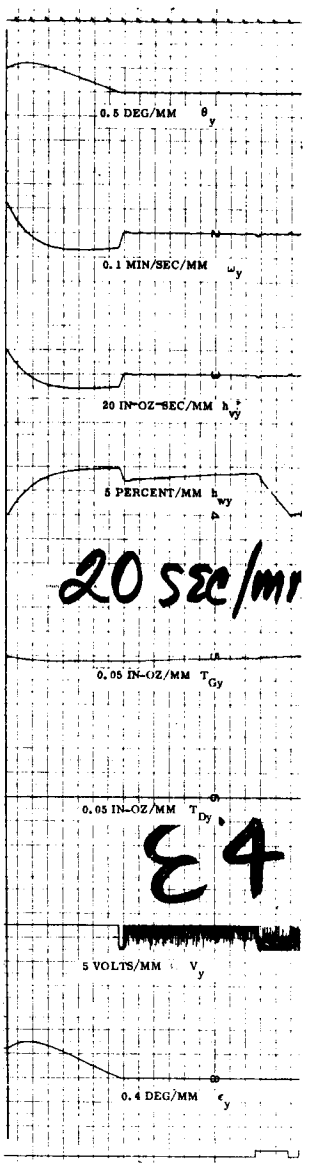


Figure 6.4-42.
Earth Stabilization
Pitch Axis, E4

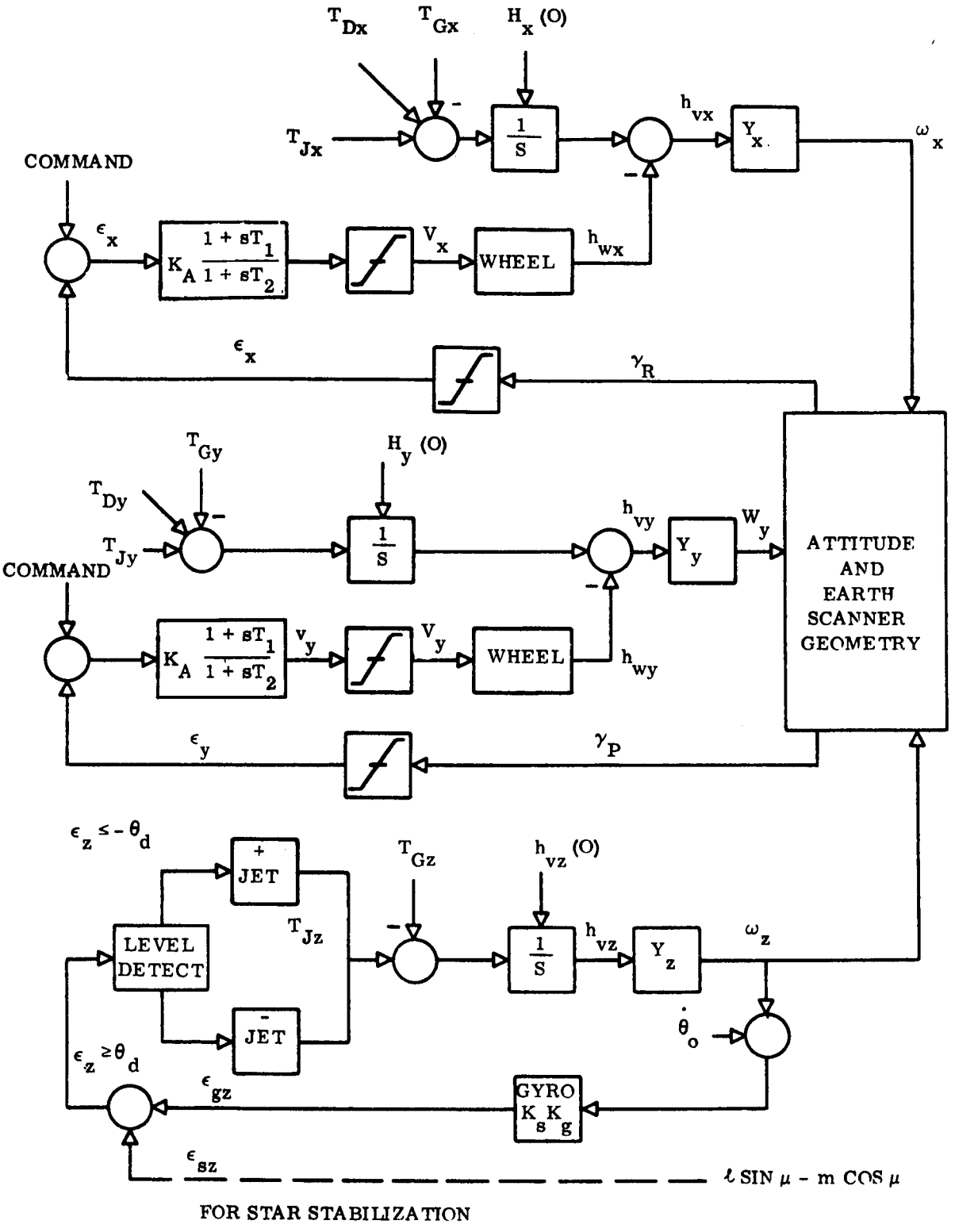


Figure 6.4-43. Earth and Star Stabilization System

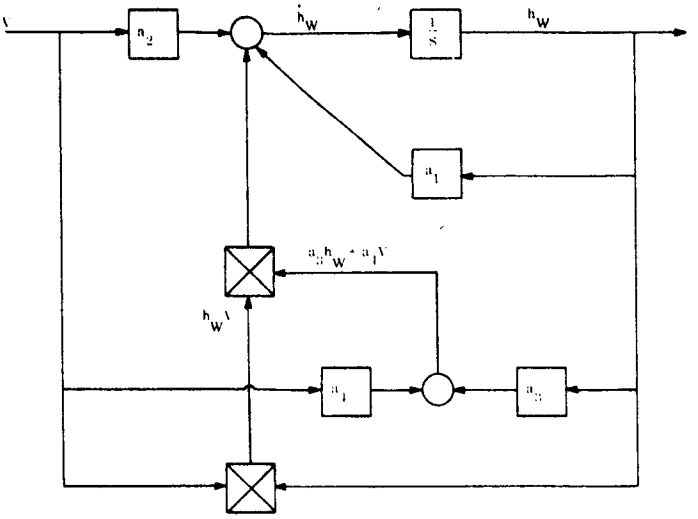


Figure 6.4-44. Nonlinear Flywheel

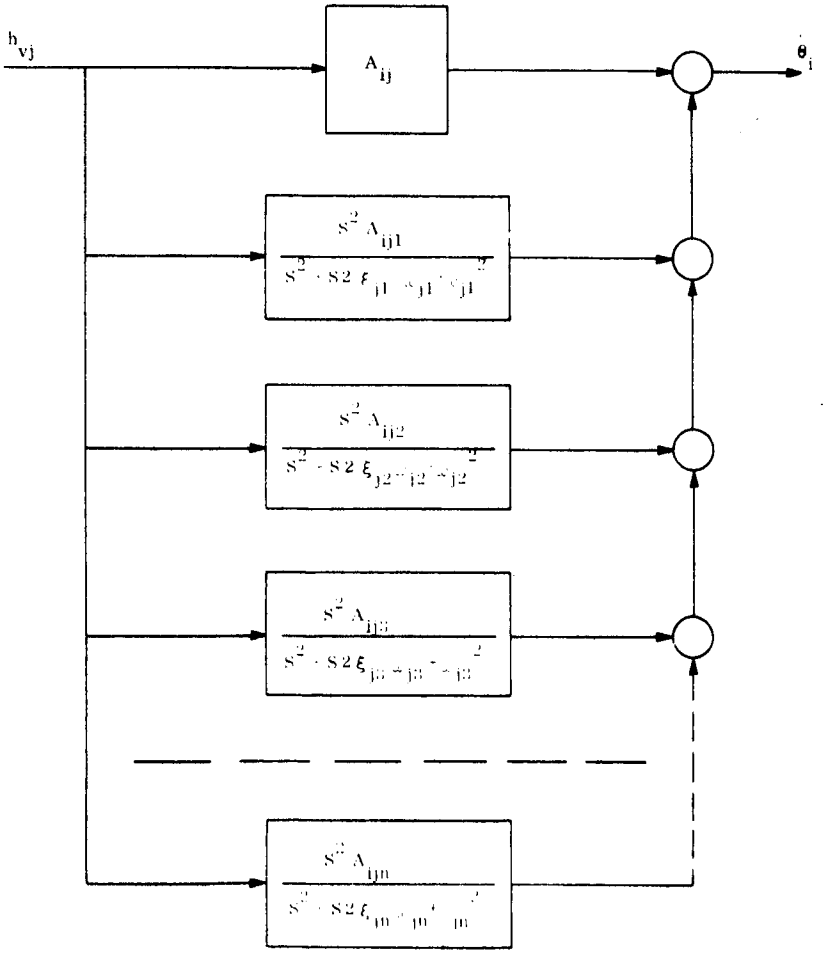
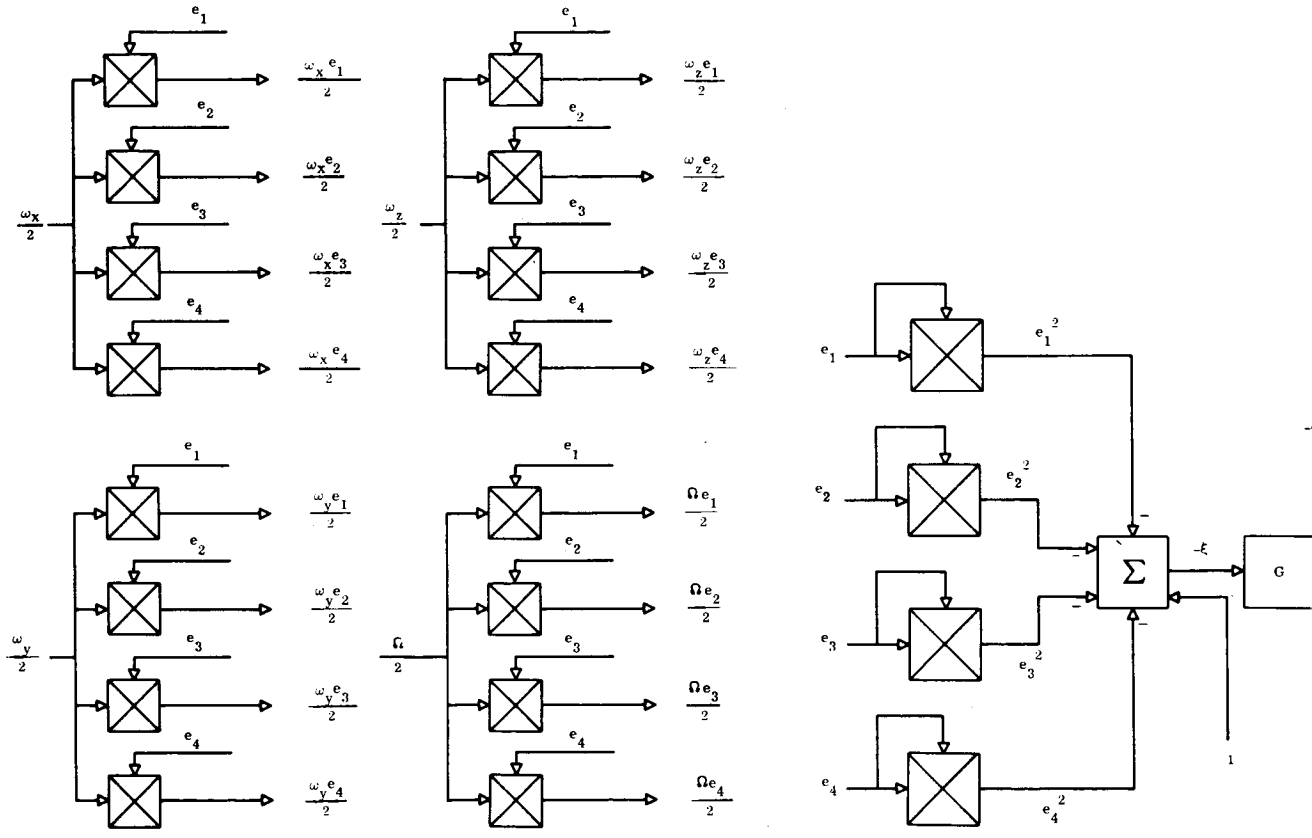


Figure 6.4-45. Velocity-Momentum Transfer Function for Rigid Vehicles with Flexible Appendages


$\frac{\omega_x}{2}$
e_1
e_2
e_3
e_4
$\frac{\omega_x e_1}{2}$
$\frac{\omega_x e_2}{2}$
$\frac{\omega_x e_3}{2}$
$\frac{\omega_x e_4}{2}$
$\frac{\omega_z}{2}$
$\frac{\omega_z e_1}{2}$
$\frac{\omega_z e_2}{2}$
$\frac{\omega_z e_3}{2}$
$\frac{\omega_z e_4}{2}$
$\frac{\omega_y}{2}$
$\frac{\omega_y e_1}{2}$
$\frac{\omega_y e_2}{2}$
$\frac{\omega_y e_3}{2}$
$\frac{\omega_y e_4}{2}$
$\frac{\Omega}{2}$
$\frac{\Omega e_1}{2}$
$\frac{\Omega e_2}{2}$
$\frac{\Omega e_3}{2}$
$\frac{\Omega e_4}{2}$
e_1^2
e_2^2
e_3^2
e_4^2
Σ
$-\xi$
G
1

6.4-97

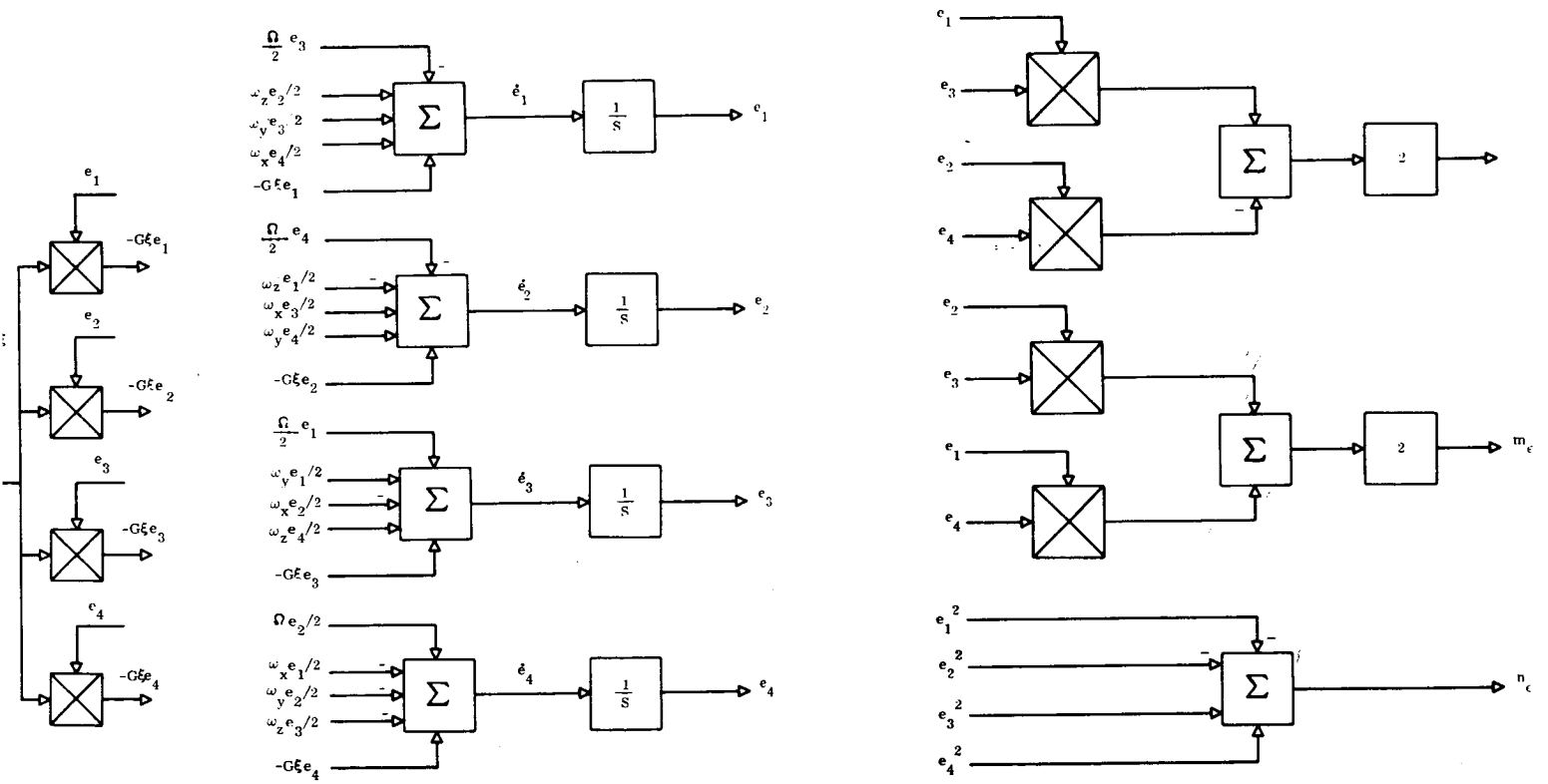


Figure 6.4-46. Attitude Geometry

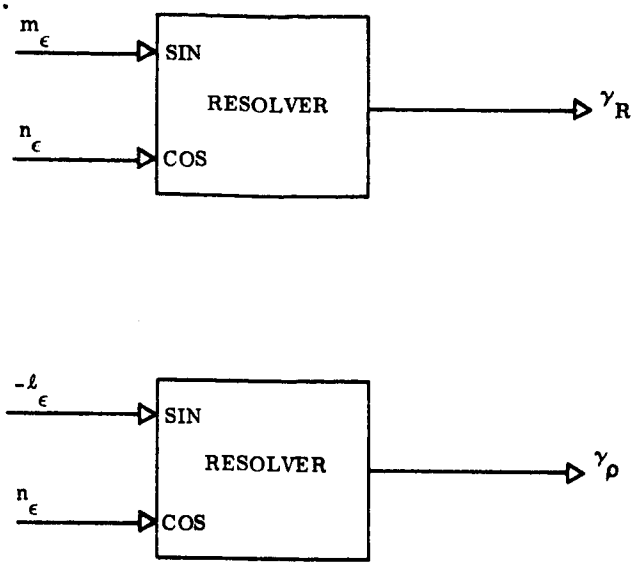


Figure 6.4-47. Earth Scanner Geometry

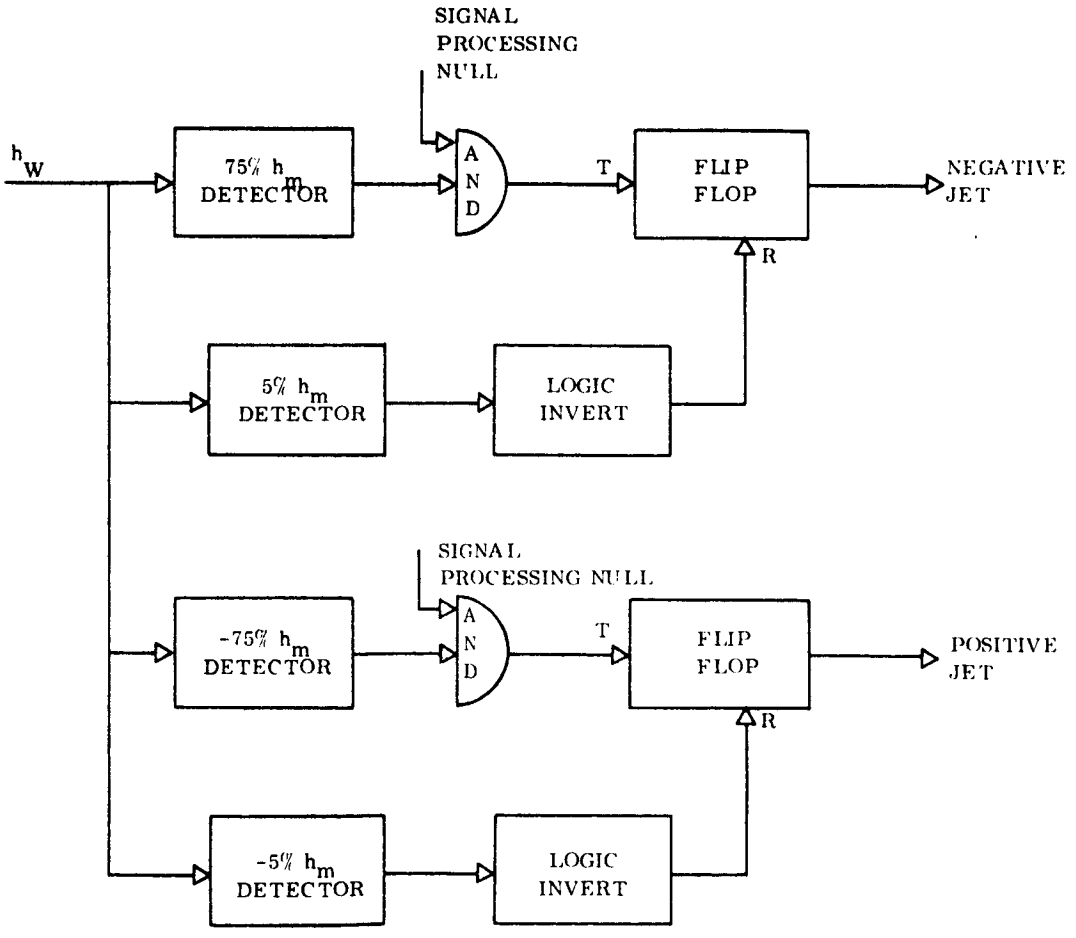


Figure 6.4-48. Flywheel Unloading Jet Controller

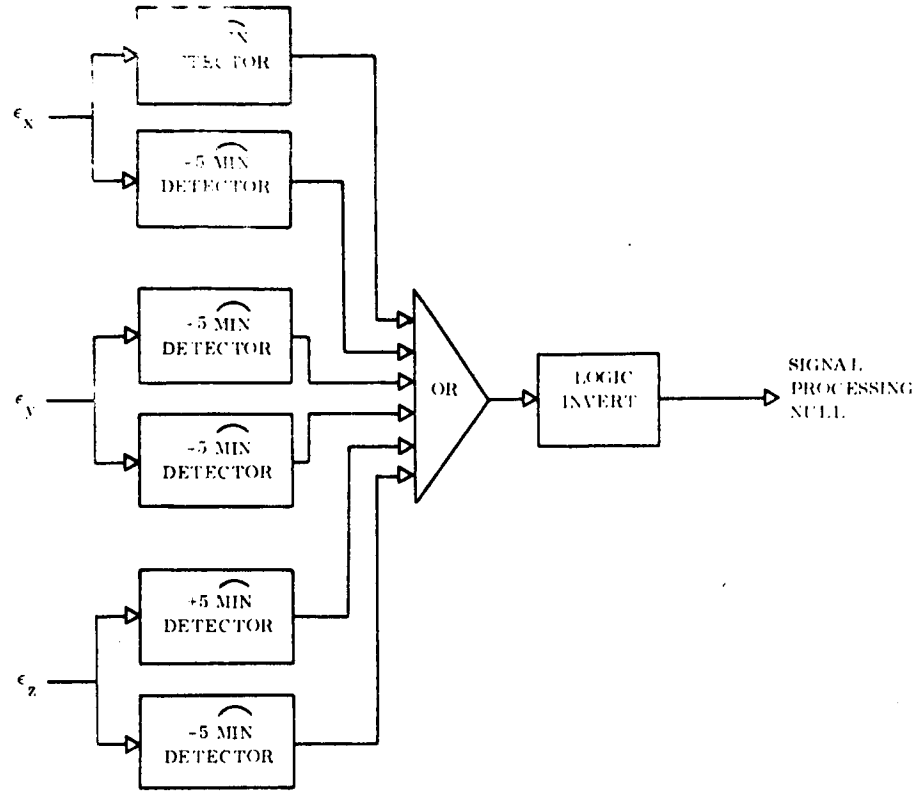


Figure 6.4-49. Signal Processing Null

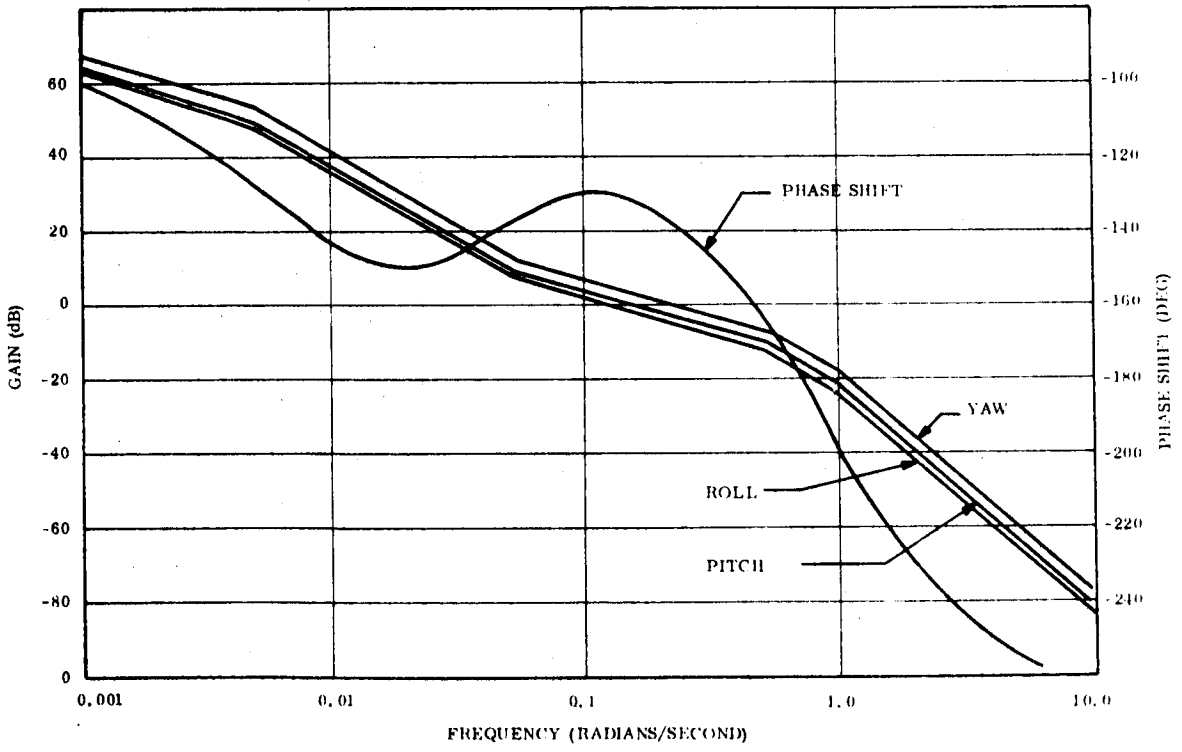


Figure 6.4-50. Open Loop Frequency Response

In the absence of a position sensor, the rate stabilized yaw axis is expected to have a rate as large as 0.01 degree/second at the end of sun stabilization. This rate can be reduced considerably during earth stabilization by the action of gyroscopic torques generated by the roll and pitch axis momenta. If an appreciable yaw rate does exist at the end of earth stabilization, as is typically the case, the roll and pitch wheel momenta continue to change beyond the conclusion of stabilization under the influence of the resultant gyroscopic torques (see Figures 6.4-41 and 6.4-42). This change in wheel momentum is, in addition of course, to that produced by disturbance torques or, for the roll axis, in addition to the torque associated with a rotating attitude reference (the local vertical).

The analog computer runs were completed with a simplified model of vehicle attitude. Rather than generating Euler parameters, direction cosines, and then the sensor signals γ_R and γ_P as shown in the figures, sensor cross coupling was neglected and γ_R and γ_P approximated by θ_x and θ_y, the integrals of the roll and pitch axis rates. The more complex model is expected to yield results differing only in form and detail. The stability, for example, is not expected to show any significant degradation. The settling time may be expected to change by as much as ± 20 percent. The wheel capability remains unaffected.

6.4.3.3.4 Star Stabilization System

The star stabilization system is to point the negative pitch axis in the direction of the star Polaris to within the ± 2 degree square field of view of the Polaris star sensor mounted on the pitch axis. The model for the star stabilization system differs from that for the earth stabilization system only in the addition (for star acquisition) of a yaw axis position signal as shown in Figure 6.4-37.

In addition to accurately positioning the pitch axis, the position signal, derived from sun sensors as described in Appendix E, reduces the yaw axis rate from the ± 0.01 degree/second deadband of the rate stabilization system to less than 0.004 degree/second. This rate is well within the momentum capacity of the yaw axis flywheel which is enabled at the conclusion of star acquisition. A model of the sun sensor geometry is shown in Figure 6.4-51.

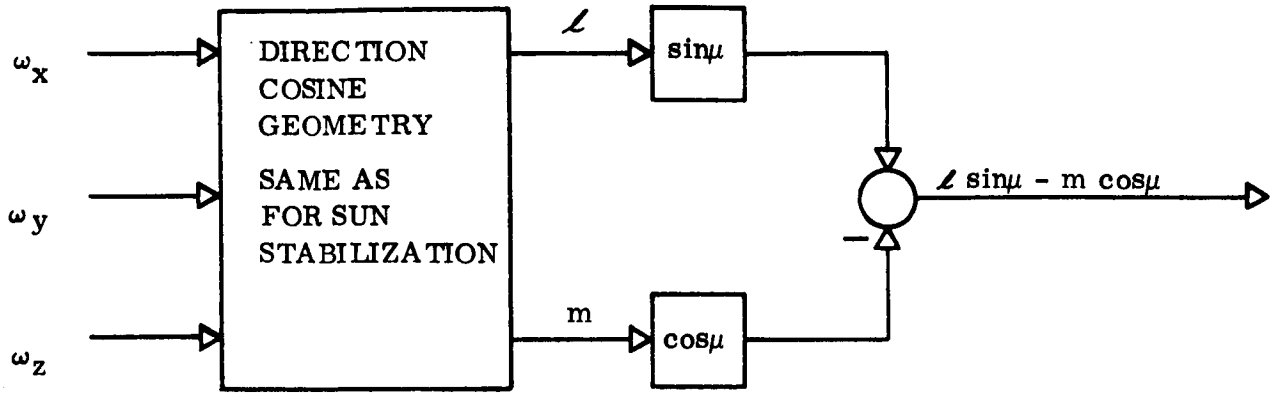


Figure 6.4-51. Sun Sensor Geometry for Star Stabilization

6.4.3.3.5 Pointing

An analog computer simulation of the primary pointing system was used to verify satisfactory pointing accuracy. For specified rms noise levels of 0.42 arc-minutes for the roll and pitch sensors and 0.6 arc-minutes for the yaw axis sensor (Polaris star sensor), the roll and pitch attitude errors of 0.026 degree meet the desired error budget of 0.03 degree at the wheel unloading speed. The yaw axis error of 0.042 degree is within the desired error budget of 0.05 degree. The errors of 0.03 and 0.05 degree, budgeted to driving the wheel, represent only one source of error, of course. The overall pointing error of the system is discussed in Section 6.4.3.4.

A model of the primary pointing system is shown in Figure 6.4-52. The primary pointing system differs from the earth stabilization and star stabilization systems only with respect to yaw axis sensor, torquer, and controller equipment. As for the earth and star stabilization system models, sensor cross coupling has been neglected. Sensor cross coupling does not degrade pointing accuracy when the yaw axis is aligned to the local vertical. For other pointing directions, errors on the yaw axis are expected to increase roll and pitch pointing errors up to 0.03 degree - the budgeted error for off local vertical pointing. If yaw axis errors (due to noise, for example) were eliminated, roll and pitch errors due to sensor cross coupling would be eliminated.

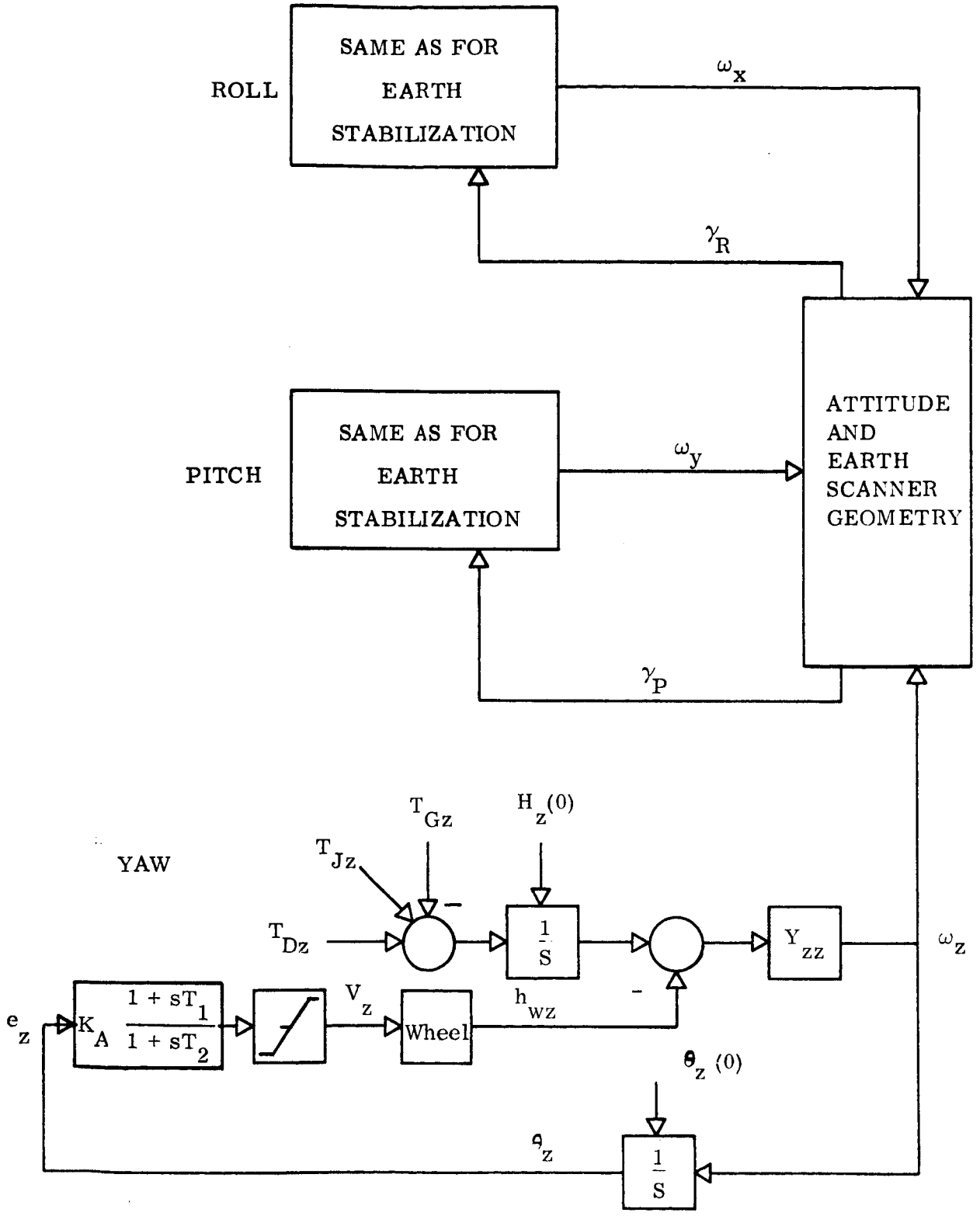


Figure 6.4-52. Primary Pointing System, Block Diagram

The results in previous paragraphs are illustrated on Figures 6.4-53, 6.4-54 and 6.4-55. Figures 6.4-56, 6.4-57 and 6.4-58 illustrate pointing accuracy in the absense of noise. Figures 6.4-59 and 6.4-60 illustrate the resultant pointing accuracy prior to having added sensor noise filtering.

6.4.3.3.6 Reorientation

The analog computer simulation of the primary pointing system was used to demonstrate the ability of the proposed system to complete a horizon to horizon reorientation in less than 30 minutes. As shown in Figures 6.4-61 through 6.4-66, reorientation from one horizon to another can be completed in less than 23 minutes with initial flywheel speeds up to 40 percent (see Figure 6.4-62). Reorientation can be made by slewing roll and pitch (step command) simultaneously (see Figures 6.4-63 and 6.4-64). The slewing time could of course, be reduced by increasing the wheel momentum capacity or the wheel torque. The lengthy slewing time of 40 minutes with the gravity gradient rod (Figure 6.4-65) results from too small a wheel.

6.4.3.3.7 Tracking

The analog computer simulation of the primary pointing system was used to demonstrate the ability of the proposed design to track a 10 milliradian per minute (0.01 degree/second) ground commanded slew with an error of less than 0.5 degree. The error was less than 0.5 degree for initial wheel speeds of up to 40 percent. The tracking maneuver can be divided into three parts:

a. Initial transient

b. Tracking

c. Terminal transient

The initial transient occurs as the wheel transfers to the spacecraft the velocity required to track the command. During the finite amount of time required to do this the tracking error reaches a peak of 0.15 degree. If the initial wheel speed is 40 percent rather

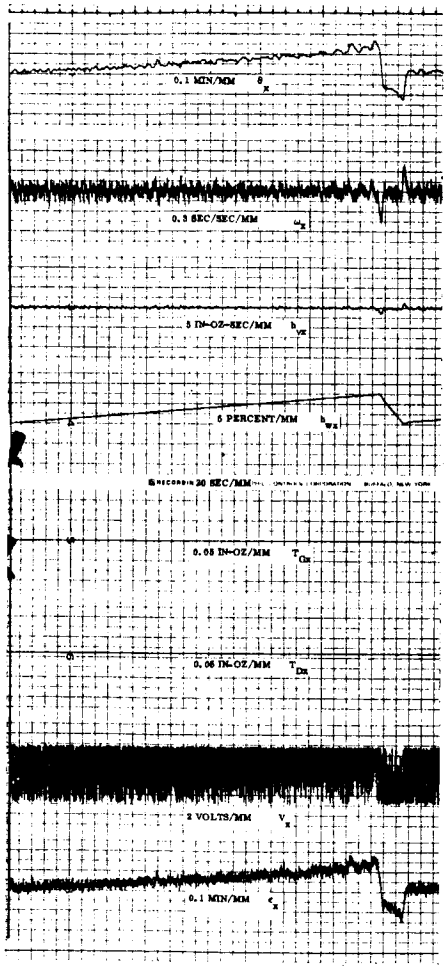


Figure 6.4-53. Roll Axis Pointing, P2

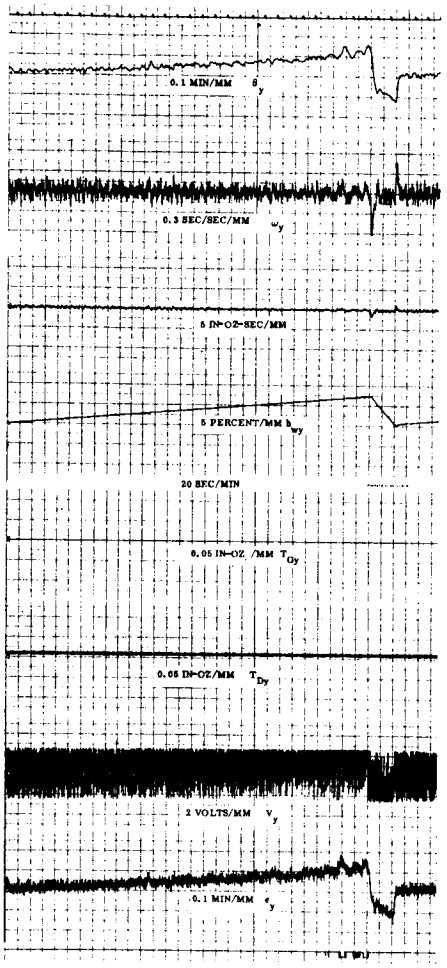


Figure 6.4-54. Pitch Axis Pointing, P5

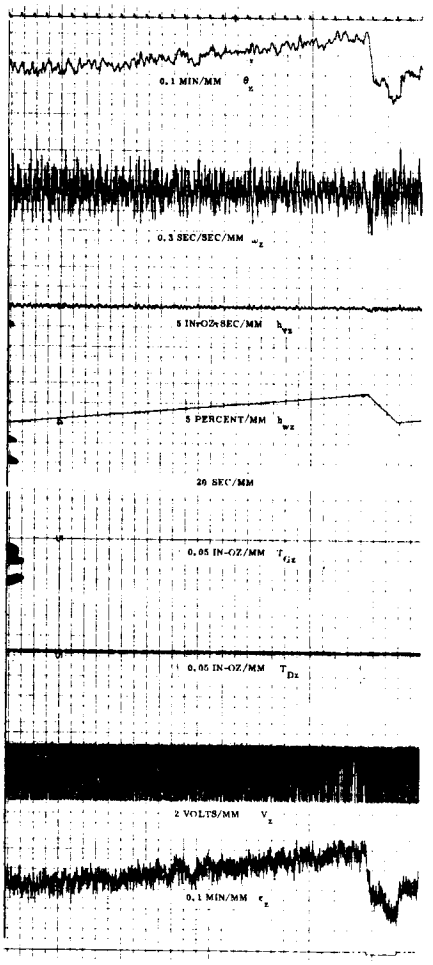


Figure 6.4-55. Yaw Axis Pointing, P8

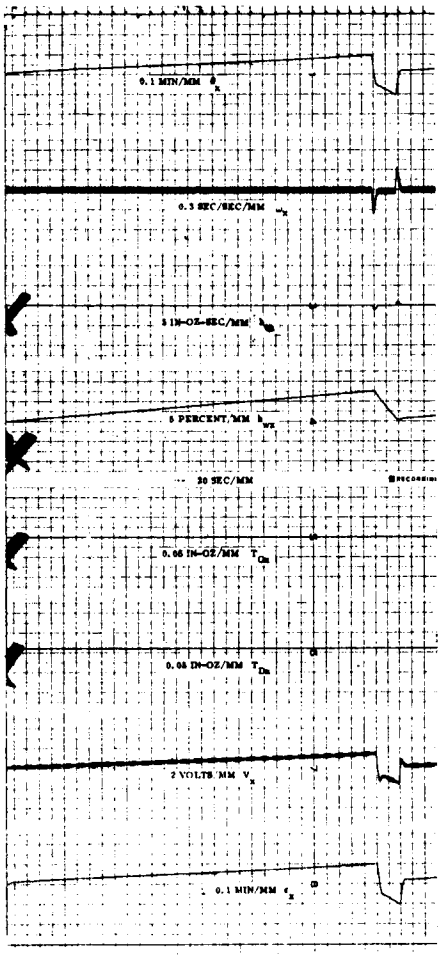


Figure 6.4-56. Roll Axis Pointing, P1

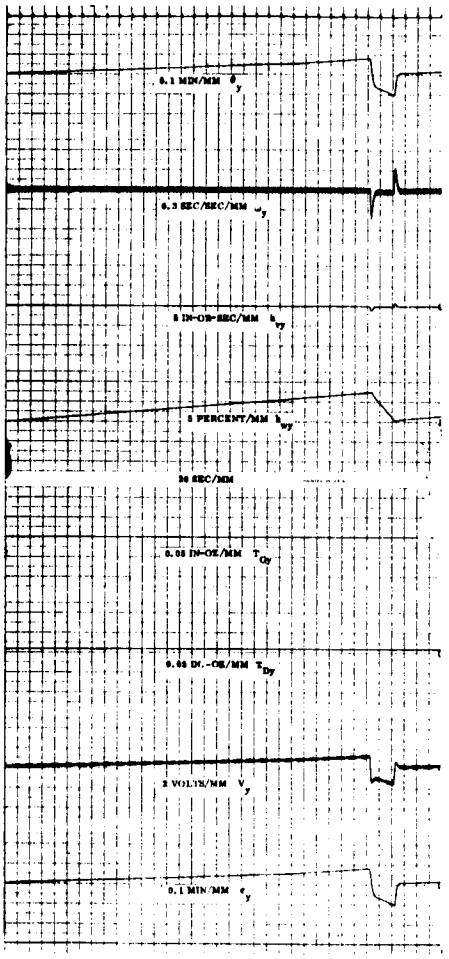


Figure 6.4-57. Pitch Axis Pointing, P4

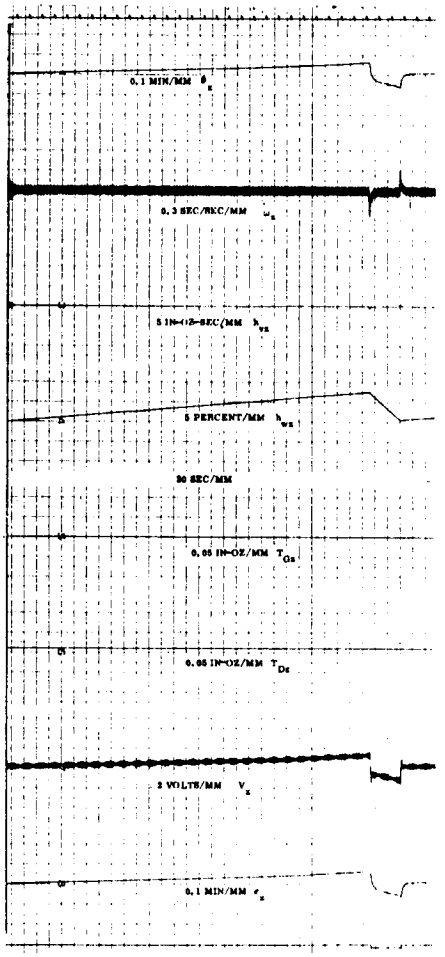


Figure 6.4-58. Yaw Axis Pointing, P7

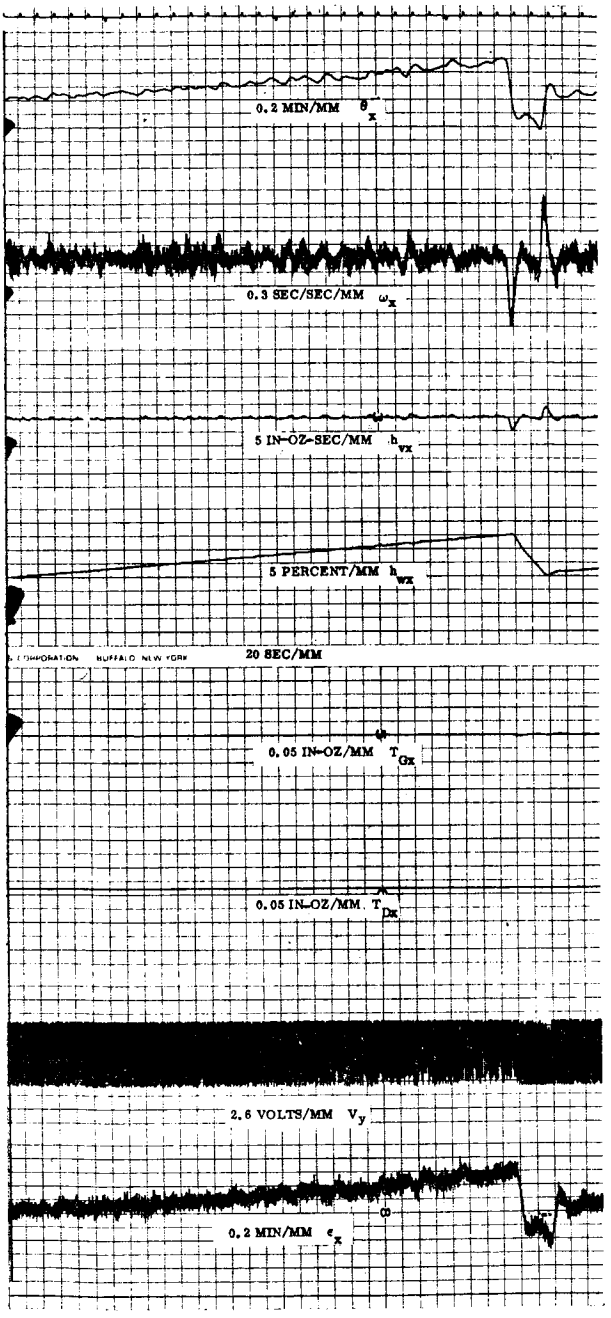


Figure 6.4-59. Roll Axis Pointing, P3

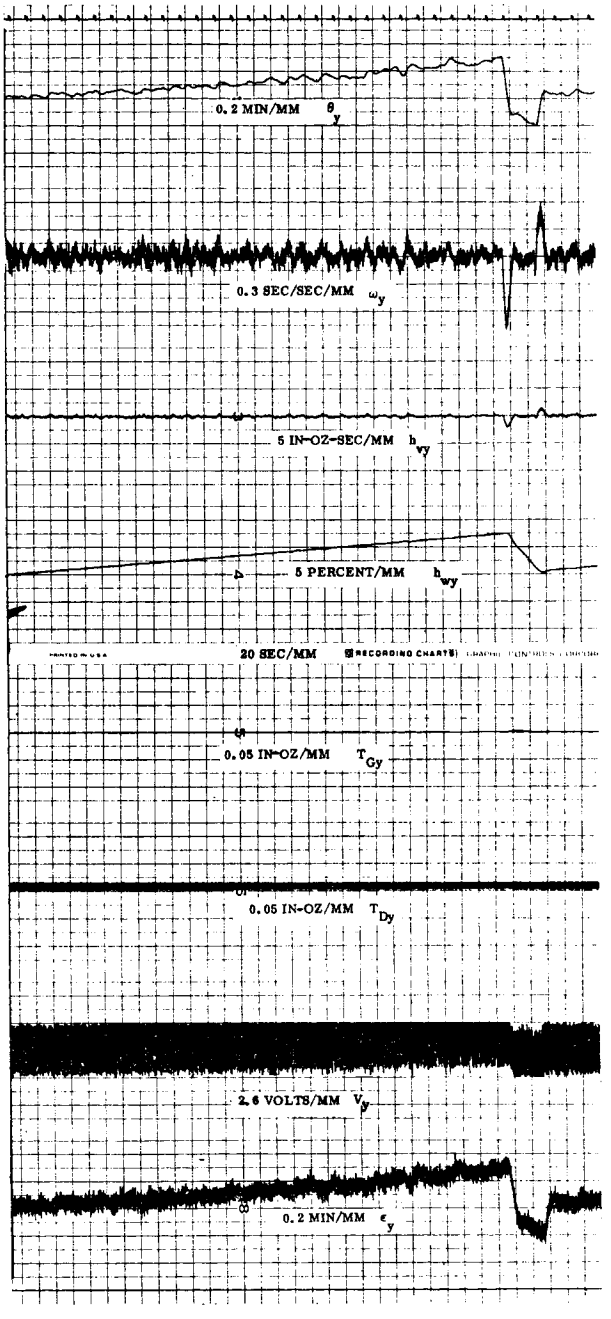


Figure 6.4-60. Pitch Axis Pointing, P6

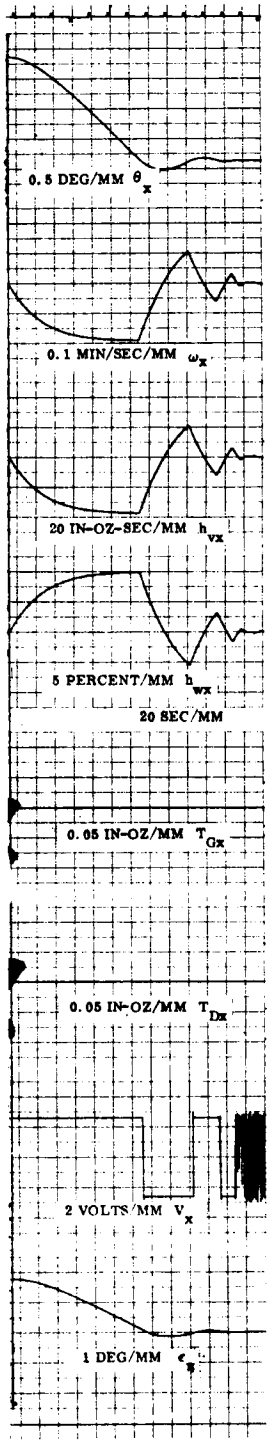


Figure 6.4-61.
Roll Axis Slew, S1

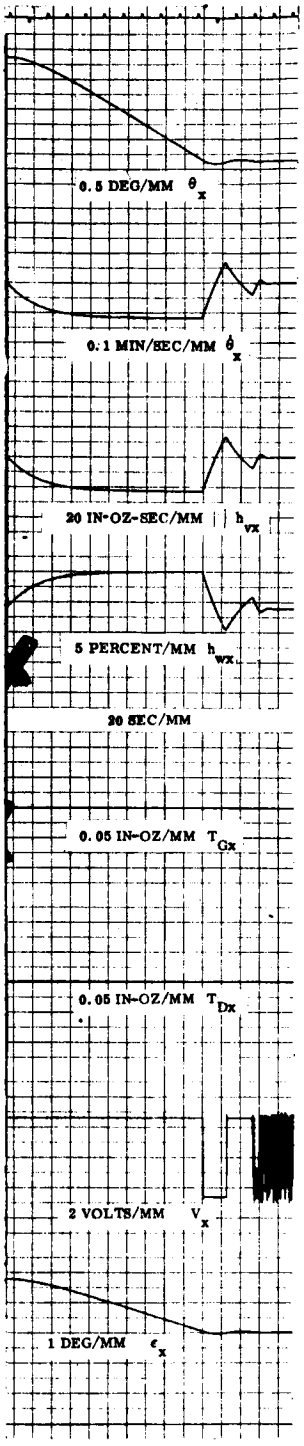


Figure 6.4-62.
Roll Axis Slew, S2

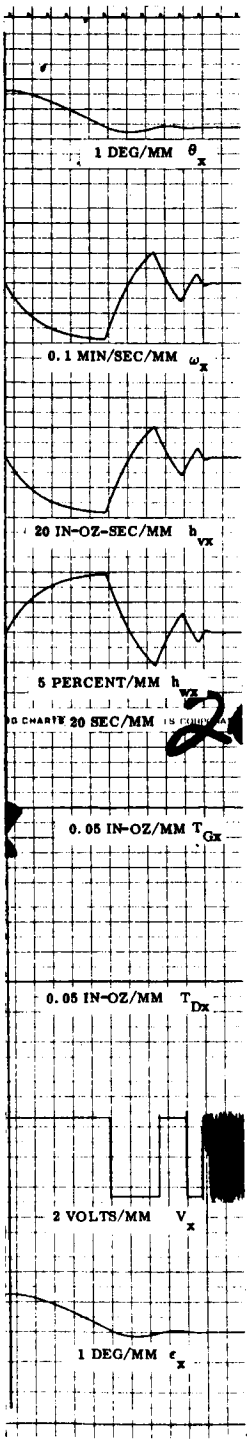


Figure 6.4-63.
Roll Axis Slew, S3

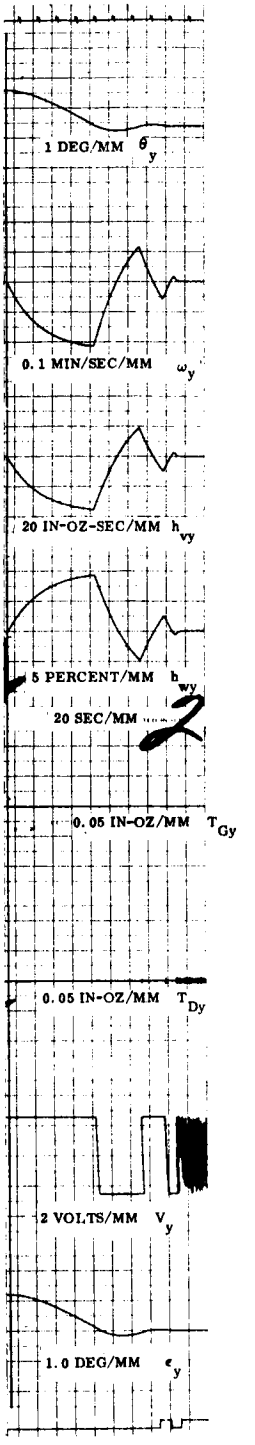


Figure 6.4-64.
Pitch Axis Slew, S4

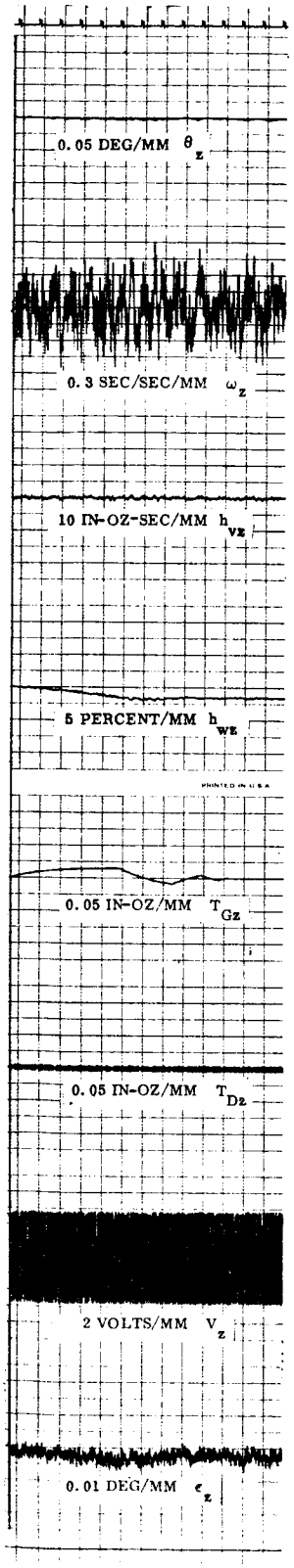


Figure 6.4-65. Roll/Pitch Axis Slew, Yaw Axis, S5

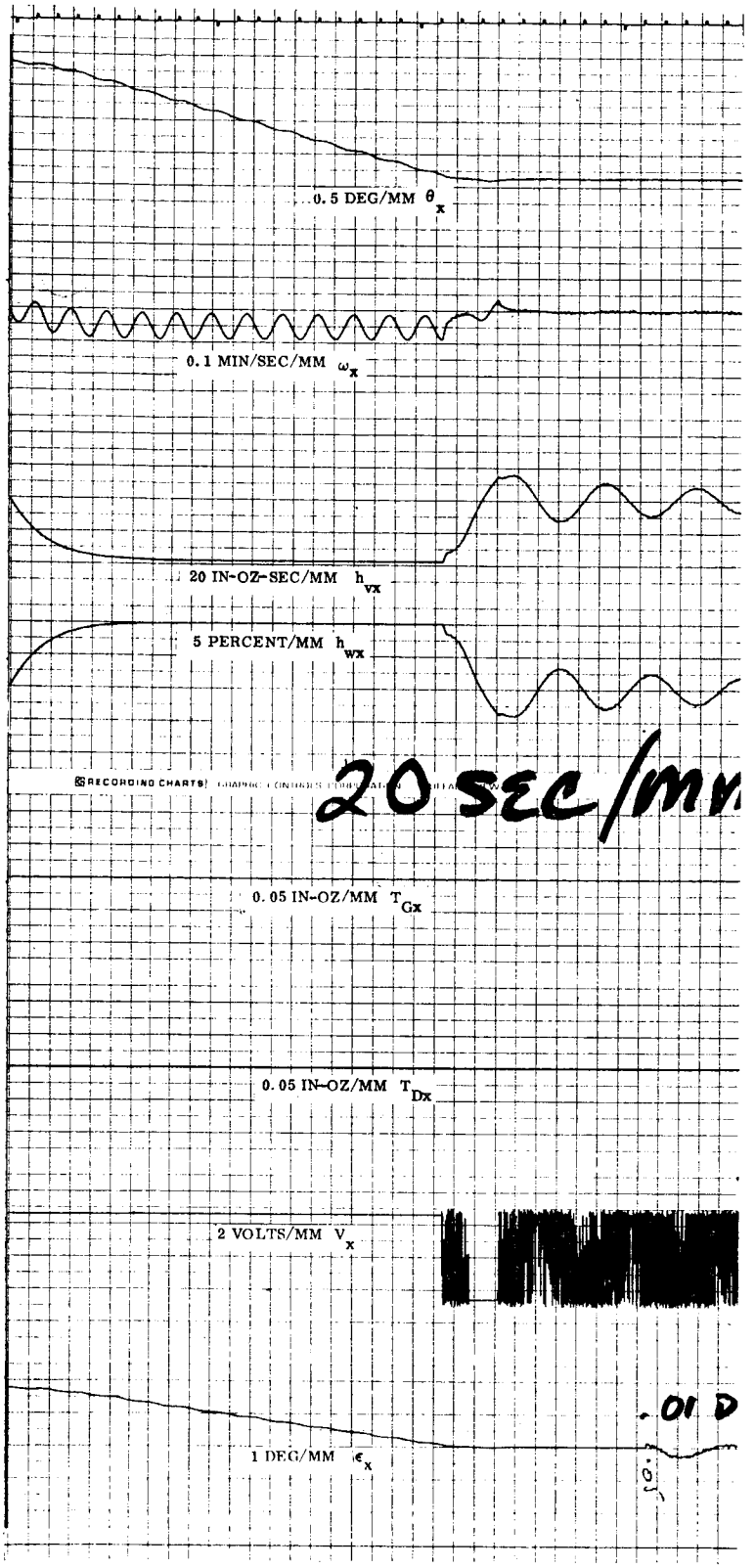


Figure 6.4-66. Gravity Gradient Rod, Roll Axis Slew, S6

than 0 percent of maximum, the initial error reaches a peak of 0.28 degree, since the wheel requires a greater amount of time to bring the spacecraft up to tracking speed. During the principal part of the tracking maneuver, the error is less than 0.03 degree.

When the ramp or tracking command is removed, a terminal transient results during the period of time required for the wheel to absorb the vehicle tracking speed. For an initial wheel speed of 0 percent, the terminal transient is approximately the same as the initial transient except in the opposite direction. For an initial wheel speed of 40 percent, the terminal error is approximately 0.1 degree. The lower error of the latter results from the favorable polarity combination of the wheel speed and wheel voltage resulting in a higher flywheel torque. These results are illustrated on Figures 6.4-67 through 6.4-72 as follows:

6.4-67	0.01 deg/sec roll axis track with gravity gradient rod.
6.4-68	0.01 deg/sec roll axis track zero initial wheel speed.
6.4-69	0.01 deg/sec roll axis track 40% initial wheel speed.
6.4-70	0.01 deg/sec roll/pitch track zero initial wheel speed (roll axis)
6.4-71	0.01 deg/sec roll/pitch track zero initial wheel speed (pitch axis)
6.4-72	0.02 deg/sec roll axis track zero initial wheel speed

Referring to Figure 6.4-72, the large error results from the difficulty the wheel has in accelerating the spacecraft to the required tracking velocity. The error shown can be reduced as necessary by using a wheel of larger capacity or a wheel of greater torque or both. The large tracking error for a vehicle with gravity gradient rod continues to increase as shown in Figure 6.4-66 simply because the wheel capacity, in terms of spacecraft velocity, is less than 0.01 degree/second. The addition of the rod greatly increases the inertia of the spacecraft.

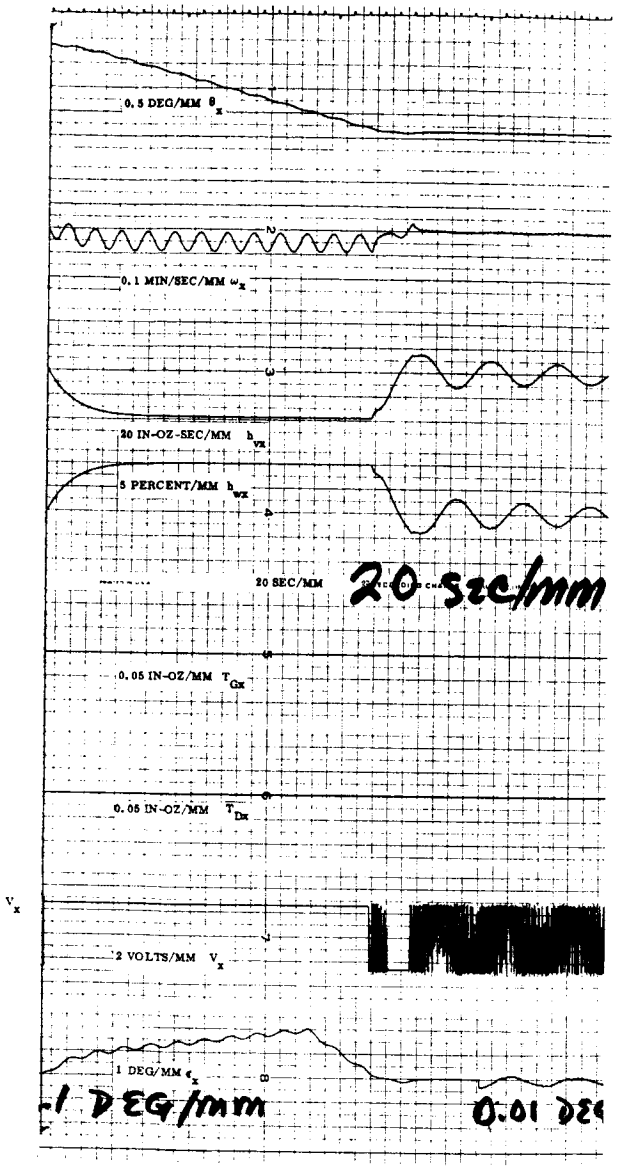


Figure 6.4-67. Roll Axis Track, T6

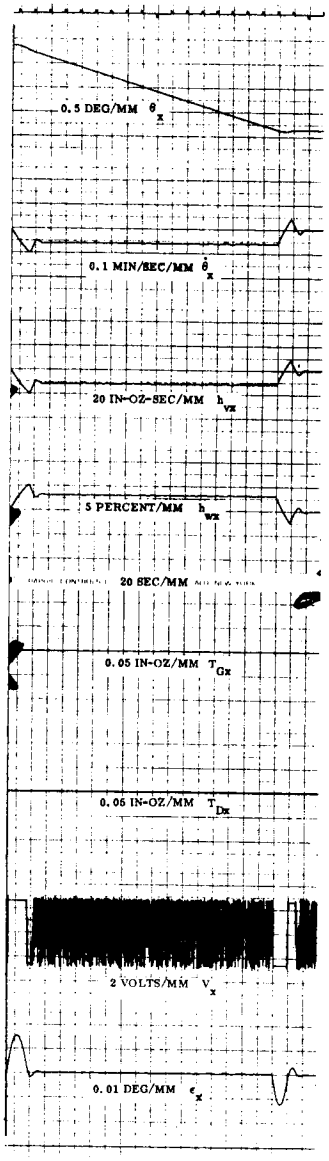


Figure 6.4-68. Roll Axis Track, T1

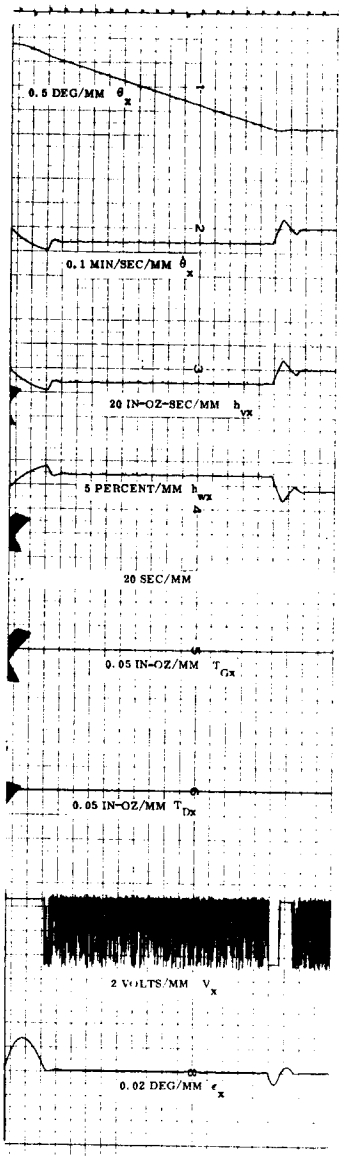


Figure 6.4-69. Roll Axis Track, T2

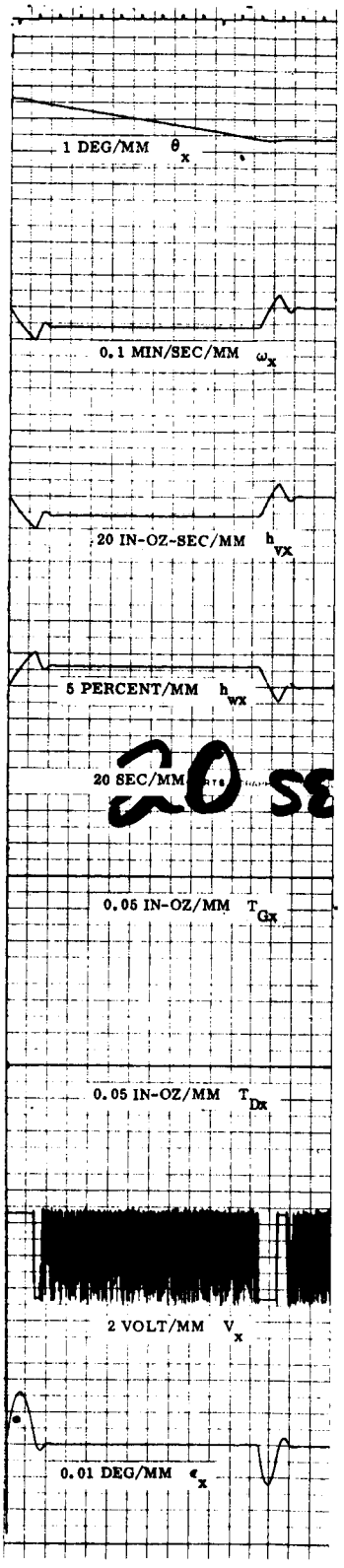


Figure 6.4-70. Roll Axis Track, T3

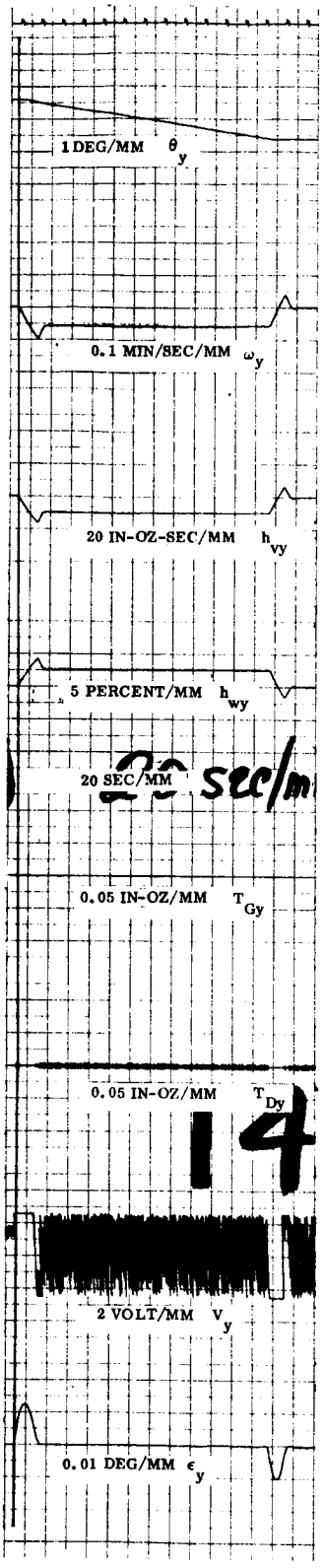


Figure 6.4-71. Pitch Axis Track, T4

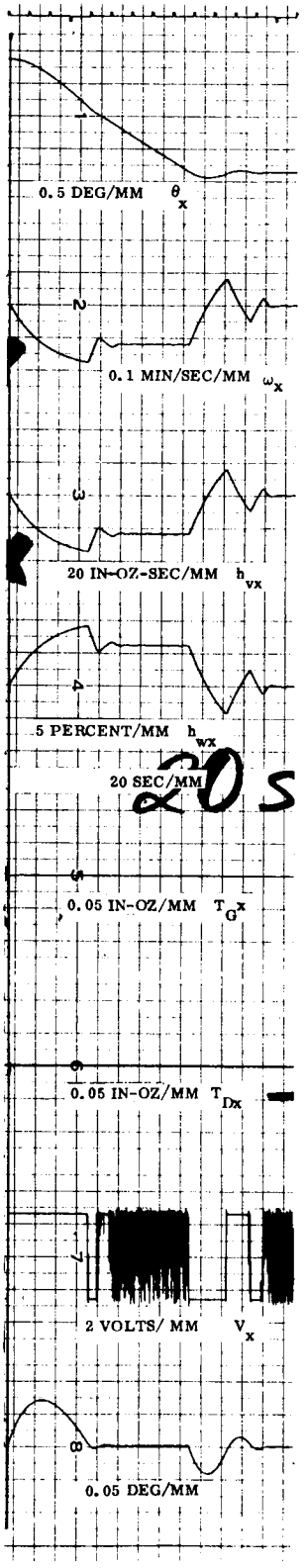


Figure 6.7-72. Roll Axis Track, T5

6.4.3.3.8 Restabilization

The analog computer simulation of the sun stabilization system was used to verify restabilization capability. The performance of the system with deployed appendages and the resulting higher inertias is similar to the performance recorded for the spacecraft with undeployed appendages.

6.4.3.4 Earth Pointing Error Analysis

6.4.3.4.1 Three Sigma Error

Presented in Table 6.4-7 are the three-sigma (3σ) error sources for each of the control axes. The error sources are assumed independent, thus allowing the calculation of the standard deviation of their sum by the root sum square method. That is:

$$\sigma(\Sigma_1 + \Sigma_2 + \ldots \Sigma_n) = (\sigma_{\Sigma 1}^2 + \sigma_{\Sigma 2}^2 + \ldots \sigma_{\Sigma n}^2)^{1/2}$$

where $\Sigma_1, \Sigma_2 \ldots\ldots \Sigma_n$ represent the various error sources and $\sigma^2_{\Sigma_1}, \sigma^2_{\Sigma_2} \ldots\ldots \sigma^2_{\Sigma_\eta}$ the variances of these sources. The 3σ control accuracy for the pitch and roll axes is expected to be 0.08 degree, for yaw, 0.07 degree.

6.4.3.4.2 Absolute Pointing Accuracy

The ability of the control system to point the spacecraft yaw axis is governed by the statistical distribution of errors in the pitch and roll axes. Assuming errors $\Delta\theta$ and $\Delta\phi$ in the pitch and roll axes respectively, at any given instance the absolute pointing error would be determined as follows:

$$R = (\Delta\theta^2 + \Delta\phi^2)^{1/2}$$

where R is the radial absolute pointing error in degrees. To be able to attach some significance to the radial error, its statistical properties must be computed. Computation of the statistical properties of the radial error can be accomplished by standard calculus of random variable techniques and knowledge of the statistical properties of $\Delta\theta$ and $\Delta\phi$.

Table 6.4.7. Three-Sigma Error Budget Data

Error Source	Error Allocation	
	Pitch/Roll	Yaw
Basic Sensor Error	0.05	0.02
Commanded Angle Resolution	0.02	0.003
Star Tracker Gimbal Offset	--	0.03
Earth Horizon Anomalies	0.004	--
Sensor Control Axis Misalign.	--	--
1. Prior to Launch	0.02 (incl. Cal.)	0.003
2. Due to Launch Effects	0.01	0.01
3. Orbit Environment	0.01	0.01
Sensor Output Noise	0.02	0.03
Control Electronics Error	0.01	0.01
Momentum Storage Offset	0.03	0.05
Timing Error ST Gimbal Comm.	0.005	0.005
Spacecraft Angular Pos. Uncert.	0.03	--
Spacecraft Drift	0.02	--
Target Location Uncertainty	0.0003	0.0003
Yaw Cross Coupling Error	0.01	--
Earth Sensor Readout	0.01	--
3σ Accuracy Per Axis	0.08	0.07
3σ Absolute Pointing Accuracy	0.09	

The probability density of each of the error sources contributing to the total error per axis may reasonably be assumed to be zero mean Gaussian. Thus the probability density function of their sum is a zero mean Gaussian distribution with standard deviation equal to the root of the sum of the squares. That is:

$$P(\Delta\phi) = P(\Delta\theta) = \exp\left(-\frac{1}{2}\frac{\Delta\phi^2}{\sigma^2}\right) \Big/ \sqrt{2\pi}\,\sigma$$

$\Delta\phi$ = Roll axis error

where:

$\Delta\theta$ = Pitch axis error

σ = Roll and pitch error standard deviation

Assuming independence of the pitch and roll errors, the probability density of R is easily computed.

$$F(R) = P(rSR) = \int_{-R}^{+R} - \int_{-(R^2-\Delta\phi^2)^{1/2}}^{+(R^2-\Delta\phi^2)^{1/2}} P(\Delta\phi, \Delta\theta)\, d\Delta\theta\ d\Delta\phi$$

where F(R) is the cumulative distribution of the radial error. Since $\Delta\theta$ and $\Delta\phi$ are assumed independent the following holds:

$$P(\Delta\phi, \Delta\theta) = P(\Delta\phi\ P(\Delta\theta)$$

$$F(R) = \int_{-R}^{R} \int_{-(R^2-\Delta\phi^2)^{1/2}}^{+(R^2-\Delta\phi^2)^{1/2}} P(\Delta\theta)\, P(\Delta\phi)\, d\Delta\theta\, d\Delta$$

Substituting for P ($\Delta\phi$) and P ($\Delta\theta$)

$$F(R) = \int_{-R}^{R} \int_{-(R^2 - \Delta\phi^2)^{1/2}}^{+(R^2 - \Delta\phi^2)^{1/2}} \frac{\exp\left\{-\frac{(\Delta\phi^2 + \Delta\theta^2)}{2\sigma^2}\right\}}{2\pi\sigma^2} d\Delta\theta\, d\Delta\phi$$

Changing to polar coordinates:

$$F(R) = \int_{0}^{2\pi} \int_{0}^{R} \frac{r\, e^{-r^2/2\sigma^2}}{2\pi\sigma^2} dr\, d\theta$$

Integration yields:

$$F(R) = 1 - e^{-R^2/2\sigma^2}$$

The probability density may now be obtained by differentiating F(R). That is:

$$f(R) = \frac{d}{dR} \left[F(R)\right]$$

or

$$f(R) = \frac{R}{\sigma^2} e^{-R^2/2\sigma^2} \qquad R > 0$$

This probability density function is a chi-square distribution with two degrees of freedom. It is better known as a Rayleigh distribution.

It is now desired to find the value R_1 that satisfies the following:

$$\int_0^R \frac{R}{\sigma^2} e^{-R^2/2\sigma^2} \, dR = 0.9974$$

(The value of the right hand side of the preceding equation is equal to the value of the integral of a normal or Gaussian probability density function between plus and minus three sigma.)

Defining the following:

$$R^2/2\sigma^2 = X; \; dR = \frac{\sigma^2}{R} dX$$

Substituting these relations into the above integral yields:

$$\int_0^{R_1^2/2\sigma^2} e^{-X} \, dX = 0.9974$$

Integration of the above yields:

$$-e^{-x} \Big|_0^{R_1^2/2\sigma^2} = 0.9974; \; e^{-R_1^2/2\sigma^2} = 0.0026$$

Taking the $\log_e$ of both sides results in:

$$-R_1^2/\sigma^2 = 2(-5.95) \text{ or } R_1 = \sqrt{2} \; (2.44\sigma)$$

Utilizing the above results for the circulated pitch and roll standard deviation ($\sigma = \frac{0.08}{3}$) results in the following 3σ absolute pointing accuracy figure:

$$R_1 = 0.09^{o}$$

It should be noted that the error budget of Table 6.4-8 does not include such factors as mechanical misalignment between antenna and control axes, electrical (rf) misalignment, and rf distortion between the spacecraft and ground.

It is assumed these errors would be calibrated out of the system in orbit by various test procedures.

6.5 TT&C SUBSYSTEM TRADEOFFS AND ANALYSIS

This section summarizes the analysis and tradeoffs made in selecting the reference design of the TT&C subsystem. A tradeoff between a VHF and a S-Band TT&C subsystem was performed to determine which system would best meet the system requirements. An antenna configuration tradeoff was performed to determine the system ramifications of the various configurations. An analysis of the tracking accuracy which could be achieved by using the Goddard Range and Range-Rate system and an analysis to determine requirements of a memory for updating the star tracker gimbal angle were made. The details of these tradeoffs and analyses are given in the following paragraphs.

6.5.1 VHF VERSUS S-BAND COMMUNICATION LINK

Since the ATS ground stations are equipped for command transmission at 150 MHz and telemetry reception at 136 MHz, it would be desirable to make use of this equipment if possible. For telemetry operating at 136 MHz a vehicle transmitter power of from 2 to 5 watts would be required (see margin calculations in Table 6.5-1). Since transmitters at this frequency are about 25 percent efficient, approximately the same amount of primary power is required by the 136 MHz and S-Band transmitters (1W S-Band transmitter assumed 6 percent efficient). Therefore, in power, weight, and size the systems would be comparable. However, if the 136/150 MHz system were used additional equipment including antennas,would have to be implemented for tracking and for polarization angle measurements. Also, since the 136/150 MHz antennas are relatively large, they would cause considerable interference problems with the parabolic reflector. Discussions with NASA personnel indicated that no foreseeable problems existed in implementing the S-Band capability at the ground stations. (This capability is required for the experiment subsystem anyway.) Therefore, the S-Band system appeared to be a better system approach and was selected for the reference configuration.

Table 6.5-1. 136 MHz Telemetry

	Gain (dB)	Loss (dB)	Power (dBm)
CARRIER			
Transmitter Power (5W)			37
Modulation Loss (±65 deg)		7.48	
Line Losses		4	
Diplexer and Switch Losses		1	
Vehicle Antenna Gain		3	
Space Loss (19,500 mm, 136 MHz)		166.34	
Ground Station Antenna Gain*	20		
Power Available at Receiver			-124.82
Required Power at Receiver			-134
Margin	9.2		
DATA			
Transmitter Power (5W)			37
Modulation Loss (±65 deg)		1.77	
Line Losses		4	
Diplexer and Switch Losses		1	
Vehicle Antenna Gain		3	
Space Loss (19,500 mm, 136 MHz)		166.34	
Ground Antenna Gain*	20		
Power at Receiver			-119.11
Receiver Noise Density (NF = 5 dB, galactic noise temp. 1000°K, Te = 1725°K)			-166.3 Hz
Data Rate (500 bps)		27	
Required S/N (10^{-5} band error rate)		9.6	
Detection Loss		1.5	
Required Receiver Power			-128.2
Margin	9.1		

*ATS Telemetry Antenna

6.5.2 TRACKING ANALYSIS

An analysis was undertaken to determine the tracking accuracy which could be achieved using the Goddard Range and Range Rate System. The analysis was limited to the use of only the Rosman and Mojave tracking stations. Only the synchronous orbit case was considered. The tracking accuracy which can be achieved determines the requirements for stationkeeping.

The following data was used in the analysis:

a. Vehicle Parameters

	Position	Drift in an Hour
Latitude	0^{o}	0.0001^{o}
Longitude	80^{o} West	0.001^{o}
Geocentric distance	1.38402472×10^{8} ft	1.4×10^{4} ft

b. Random Measurement Error

Range - 50 feet
Range rate 0.33 feet/sec
Azimuth and Elevation angle 0.1^{o}

c. Station Location Error

A value of 60 feet in each coordinate is assumed. This value reflects expected state-of-the-art by 1969-70.

d. External Error Sources

Geopotential model - thirteen errored co-efficients; speed of light error.

e. Tracking Geometry to Satellite

Mojave	Azimuth	127.57^{o}
	Elevation	33.49^{o}
Rosman	Azimuth	$175.^{o}$
	Elevation	49.04^{o}

f. Bias Errors

Three variations in measurement bias were considered:

Case	Range bias	Range rate bias	Angle bias
1.	55 ft	0.06 ft/sec	5 min
2.	20 ft (optimistic)	0.06 ft/sec	5 min
3.	4.6 ft (unrealistic)	0.02 ft/sec	0.4 min (unrealistic)

It was assumed that both stations would be used simultaneously. The result of the analysis is shown in Figure 6.5-1. The bar graphs vary due to the difference in bias errors assumed and the duration of the measurements. The results indicate that a large portion of the bias error is eliminated when the duration of the measurement is greater than 1/2 hour. The in-track error is small and the random measurement error is the dominant contributor of cross-track errors. The contribution of each of the errors to the total error is tabulated in Table 6.5-2. All random errors are significant contributors with the elevation angle random error being the largest contributor. The results indicate that, for the stated capabilities of the Goddard Range and Range Rate System (case 2), a 1-hour tracking period by the Rosman and Mojave ground stations will provide knowledge of the position of the vehicle to the desired accuracy ($\pm$0.02 deg), 3σ.

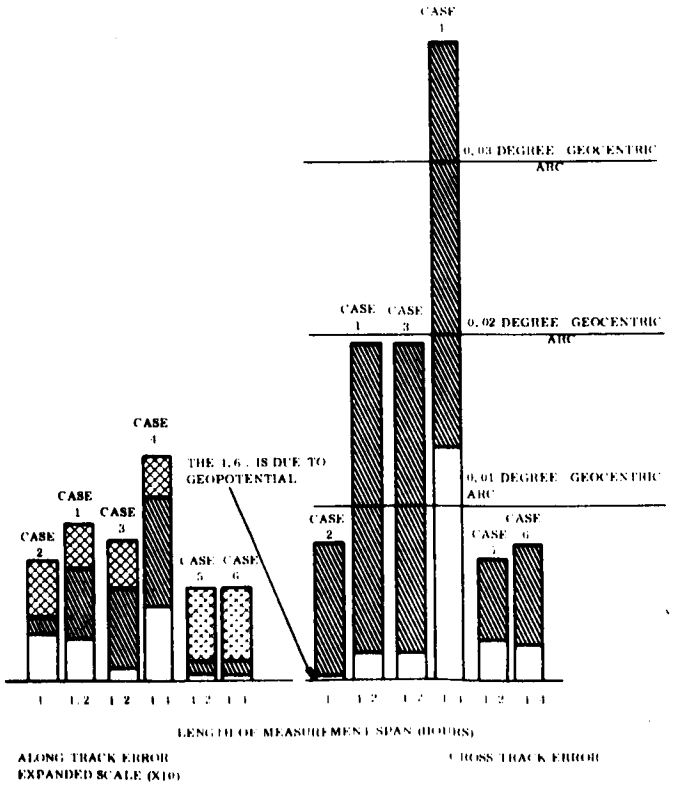


Figure 6.5-1. Results of Tracking Analysis

Table 6.5-2. Position and Velocity Errors

		Position Error			Velocity Error		
		Along Track	Cross Track	Radial	Along Track	Cross Track	Radial
No.							
1	σ (ft)	0.0219 + 5	0.471 + 5	0.0467 + 5 (ft/sec)	0.283	13.300	1.440
	σ (1)(ft)	0.0333 + 5	0.701 + 5	0.0698 + 5 (1) (ft/sec)	0.450	17.700	1.500
	Br	0.262	0.078	0.078	0.065	0.071	0.074
	Rr	0.470	0.415	0.915	0.920	0.929	0.922
	Sr	0.265					0.003
	Gr	0.003	0.006	0.006	0.015		
2	σ (ft)	0.0167 + 5	0.191 + 5	0.0189 + 5 (ft/sec)	0.120	4.14	0.476
	σ (1-1/4)	0.0179 + 5	0.226 + 5	0.0225 + 5	0.146	4.04	0.486
	σ (1-1/2)	0.0196 + 5	0.261 + 5	0.0260 + 5	0.172	3.93	0.499
	σ (1-3/4)	0.0218 + 5	0.295 + 5	0.0295 + 5	0.197	3.80	0.513
	σ (2)	0.0248 + 5	0.328 + 5	0.0329 + 5	0.222	3.65	0.528
	σ (2-1/4)	0.0283 + 5	0.359 + 5	0.0362 + 5	0.246	3.49	0.546
	σ (2-1/2)	0.0324 + 5	0.389 + 5	0.0393 + 5	0.269	3.32	0.565
	σ (2-3/4)	0.0370 + 5	0.418 + 5	0.0423 + 5	0.291	3.13	0.585
	σ (3)	0.0421 + 5	0.445 + 5	0.0452 + 5	0.312	2.92	0.607
	σ (3-1/4)	0.0476 + 5	0.470 + 5	0.0479 + 5	0.332	2.71	0.630
	σ (3-1/2)	0.0536 + 5	0.493 + 5	0.0504 + 5	0.350	2.48	0.654
	σ (3-3/4)	0.0599 + 5	0.513 + 5	0.0527 + 5	0.367	2.25	0.680
	σ (4)	0.0666 + 5	0.532 + 5	0.0548 + 5	0.383	2.01	0.706
	Br	0.381	0.009	0.009	0.006	0.007	0.032
	Rr	0.161	0.944	0.945	0.922	0.993	0.937
	Sr	0.452	0.001				0.030
	Gr	0.006	0.046	0.046	0.072		
3	σ (ft)	0.0196 + 5	0.471 + 5	0.0467 + 5	0.283	13.3	1.44
	σ (1) (ft)	0.0319 + 5	0.701 + 5	0.0698 + 5	0.450	12.7	1.50
	Br	0.085	0.078	0.078	0.066	0.071	0.072
	Rr	0.582	0.915	0.915	0.920	0.929	0.925
	Sr	0.329					0.003
	Gr	0.004	0.007	0.007	0.014		
4	σ (ft)	0.0311 + 5	0.892 + 5	0.088 +5	0.522	29.56	3.14
	σ (1) (ft)	0.0754 + 5	1.646 + 5	0.164 +5	1.096	27.79	3.34
	Br	0.325	0.364	0.364	0.247	0.314	0.321
	Rr	0.543	0.635	0.635	0.748	0.686	0.678
	Sr	0.131					0.001
	Gr				0.005		

Table 6.5-2. Position and Velocity Errors (Cont'd)

		Position Error			Velocity Error		
		Along Track	Cross Track	Radial	Along Track	Cross Track	Radial
No.							
5	σ (ft)	0.0127 + 5	0.169 + 5	0.0168 + 5	0.147	6.06	0.639
	σ (1) (ft)	0.016 + 5	0.267 + 5	0.0265 + 5	0.216	5.87	0.659
	Br	0.074	0.339	0.338	0.134	0.194	0.206
	Rr	0.135	0.659	0.657	0.705	0.753	0.721
	Sr	0.791		0.003		0.001	0.024
	Gr	0.001		0.002	0.161	0.052	0.048
	Cr			0.001			
6	σ (ft)	0.0129 +5	0.189 + 5	0.187 + 5	0.328	12.3	1.23
	σ (1) (ft)	0.0244 + 5	0.474 + 5	0.046 + 5	0.524	11.9	1.24
	Br	0.062	0.252	0.252	0.021	0.066	0.073
	Rr	0.171	0.747	0.745	0.949	0.918	0.905
	Sr	0.766		0.002			0.007
	Gr		0.001	0.001	0.028	0.015	0.015
	Cr			0.001			

Case 1 - 1/2 hour measurement period; case 1 bias errors

Case 2 - 1 hour measurement period; case 1 bias errors

Case 3 - 1/2 hour measurement period; case 2 bias errors

Case 4 - 1/4 hour measurement period; case 2 bias errors

Case 5 - 1/2 hour measurement period; case 3 bias errors

Case 6 - 1/4 hour measurement period; case 3 bias errors

σ = Standard deviation

σ (x) = Standard deviation propagated from end of measurement phase to x hours after beginning of measurement phase.

Br = ratio of the measurement bias variance to the total variance

Rr = ratio of the random measurement error to the total variance

Sr = ratio of the station location error to the total error.

Gr = ratio of the geopotential error to the total error.

Cr = ratio of the speed of light error to the total error.

6.5.3 ANTENNA CONFIGURATION TRADEOFF

An antenna configuration tradeoff was performed to determine the best antenna patterns and mounting locations available to meet the desired telemetry, tracking and command coverage. It is desirable to have as high an antenna gain as possible for all modes of operation so that the transmitter power can be minimized. Factors which were considered in the tradeoff were antenna patterns, number of antennas, number of switches required, mounting locations and mechanical constraints. The alternate system configuration was first considered for the antenna tradeoff study. This is because at the initiation of the TT&C antenna study this system configuration was being given primary consideration for the reference design. The alternate system configuration is the case where the solar panels are folded toward the positive yaw axis. The difference between the alternate and reference design is that the alternate configuration would not become stabilized immediately after despinning because the primary orientation control sensors and nozzles would be blocked by the solar panels. The vehicle will therefore be tumbling at a rate of about 0.5 deg/sec.

The angle from the spacecraft pitch-roll plane to the Rosman and Mojave ground stations during the transfer orbit and prior to despinning has been described in Section 5.7.6. It was pointed out that a half angle of about 20 degrees is sufficient for the transfer orbit and a half angle of from 70 to 80 degrees is required for full coverage during the spin stabilized/synchronous orbit modes to realize 100 percent coverage. Once the vehicle is despun, the parabolic reflector will be commanded to unfold. It is required that telemetry be received during this unfolding so that sufficient data is available to evaluate the unfolding procedure.

The antenna configuration tradeoff for the alternate design configuration is summarized in Table 6.5-3. The percentages stated for coverage is for the telemetry system assuming the vehicle is not tumbling. The numbers given for the switches is based on the implementation of the redundant subsystem as discussed in Section 5.7.8. The trade-off study indicated that total coverage could not be guaranteed for the system configuration especially because the tumbling would cause loss of receiver lock at the ground stations each time the system passed through nulls in the transmitting pattern. In fact, it is possible that the tumbling inherent after the despinning could be about such an axis as to prohibit the reception of commands from the ground station. Also, with the vehicle not stabilized during the un-

Table 6.5-3. Summary, Antenna Configuration Tradeoff For Alternate Design Configuration

Antenna Configuration	No. 1	No. 2	No. 3	No. 4	No. 5
No. of Antennas	5	5	4	3	4
Antenna Mounting	Two on edge of solar paddle Two on rear of vehicle High gain on + yaw axis	One on boom extended from equipment pod One on edge of paddle Two on rear of vehicle High gain on +yaw axis	Two on edge of solar paddle One in rear High gain on + yaw axis	One on boom extended from equipment pod One on rear High gain on +yaw axis	One on boom extending from equipment pod Two in rear High gain on + yaw axis
Antenna Patterns	a. Two toroids about yaw axis both 60 deg wide, one squinted 30 deg. one squinted -20 deg b. Two cardioids, one on +yaw one on -yaw axis. c. High gain, 20-30 deg beamwidth antenna	a. Two toroids about yaw axis both 60 deg wide, one squinted +30 deg, one squinted -20 deg Two cardioids, one on + yaw axis, one on -yaw axis c. High gain, 20-30 deg beamwidth antenna	a. Two toroids about yaw axis both 60 deg wide, one squinted +30 deg b. Cardioid on solar panel axis tilted 20 to 25 deg towards yaw axis c. High gain, 20 -30 deg beamwidth antenna	a. Cardioid in + yaw direction b. Cardioid in - yaw c. High gain. 20 -30 deg beamwidth antenna	a. Toroid about yaw axis 40 deg beamwidth b. Cardioid in + yaw direction. c. Cardioid in - yaw direction. d. High gain, 20 -30 deg beamwidth antenna
Coverage during transfer orbit	Full coverage switching required	Full coverage switching required	Full coverage switching required	May have marginal coverage in pitch-roll plane	Full coverage
Coverage during spin mode synchronous orbit	Switching required: 100% if cardioid also used	Switching required: 100% if cardioid also used	Two 3-1/2 hour dead periods i.e. 75% coverage; switching required	Lose about 6 hr, i.e, marginal coverage at apogee and perigee; Switching required	Full coverage 6 hr or about 25%
Coverage during unfold mode	Depends on vehicle attitude about 75% coverage 80-90% if no motion of vehicle	Depends on vehicle attitude about 85% coverage 95-100% if no vehicle motion	Depends on vehicle attitude: about 40%	Depends on vehicle attitude: 95-100% coverage if attitude doesn't change during unfolding	Depends on vehicle attitude: 95-100% coverage if attitude doesn't change during unfolding
Coverage during operating mode	75%	100%	75%	100%	100%
No. of SPDT SW	5	5	3	1	2
No. of XFER SW	2	2	2	2	2
No. of Diplexers	4	4	3	2	2
Disadvantages	Receiver nulls in P-R Plane Long cable run for antennas on paddle	Receiver nulls in P-R plane Long cable run for antenna on paddle and boom Boom required.	No omni coverage for command; long cable for antennas on paddles; low probability of TLM during unfolding	Marginal coverage during early phases Requires boom	Requires boom and long cable

Table 6.5-3. Summary, Antenna Configuration Tradeoff For Alternate Design Configuration (Cont'd.)

Antenna Configuration	No. 6	No. 7	No. 8	No. 9	No. 10	No. 11
No. of Antennas	4	4	3	3	4	5
Antenna Mounting	One on boom extending from equipment pod Two in rear High gain, on + yaw axis	One mounted on paddle Two in rear High gain, on +yaw axis	One mounded on paddle One in rear High gain, on +yaw axis	One mounted on paddle One in rear High gain, on +yaw axis	One mounted on paddle Two in rear High gain, on +yaw axis	Two on edge of solar paddle Two on rear of vehicle High gain on + yaw axis
Antenna Patterns	a. Toroid about yaw axis, 40 deg beamwidth b. Cardioid in + yaw c. Cardioid in - yaw direction d. High gain + yaw	a. Toroid about yaw axis, 40 deg beamwidth b. Cardioid on solar paddle axis tilted 20 deg to 25 deg towards yaw axis c. Cardioid in -yaw axis direction d. High gain + yaw	a. Cardioid in + yaw direction b. Cardioid in +yaw direction c. High gain, 20-30 deg beamwidth antenna	a. Cardioid on solar paddle axis tilted 20 to 25 deg toward yaw axis b. Cardioid in -yaw axis direction c. High gain, 20-30 deg beamwidth antenna	a. Toroid about yaw axis 40 deg beam b. Cardioid on solar paddle axis tilted 20 to 25 deg towards yaw axis c. High gain	a. Two toroids about yaw axis both 60 deg wide, one squinted 30 deg one squinted 20 deg b. Cardioid on solar paddle axis tilted 20 to 25 deg towards yaw axis c. Cardioid on -yaw axis d. High gain, 20-30 deg beamwidth antenna
Coverage during transfer orbit	Full coverage	Full coverage	Full coverage at lowest margin; switching required	50% coverage	Full coverage	Full coverage Switching required
Coverage during spin mode synchronous orbit	Full coverage	Full coverage	Full coverage at lowest margin; switching required	50% coverage	Full coverage	Two 3-1/2 hour dead periods i.e. 75% coverage
Coverage during unfold mode	95-100% if attitude doesn't change during unfolding	75%	75%	75%	85%	100% if no motion of vehicle
Coverage during operating mode	100%	85%	75%	1	2	2
No. of SPDT SW	2	2	1	2	2	3
No. of XFER SW	2	2	2	2	2	3
No. of Diplexers	2	2	2	No omni command & TLM coverage	Requires spin axis orbital phase	No omni command coverage
Disadvantages	Requires boom Requires spin axis and orbital plane	Long cable run to antenna or paddle Only 75% command & TLM coverage Requires spin axis orbital plane	No omni directional command & TLM coverage Long cable run to antenna on paddle.	Long cable run to antenna on paddle	Requires stabilization about yaw axis	Long cable runs for antenna on paddle

folding of the parabolic reflector, realistic coverage during this mode could not be obtained. This problem was one of the factors in selecting the solar panels towards the negative yaw axis as the reference configuration. Based on the tradeoff analysis on the alternate configuration, an antenna configuration which meets all of the requirements for the reference configuration immediately involved. This was the configuration discussed in Section 5.7.6.

The following constraints were placed on the telemetry and command antenna system:

a. Full coverage during transfer orbit and before despinning

b. Full coverage while parabolic reflector is unfolding

c. Full coverage while on station

d. No erectible booms

e. Minus three dB gain minimum within beamwidth for 500 bps data rate

f. Two to five dB gain when earth stabilized

The attitude of the vehicle in the various modes are as follows:

a. Reference Configuration

1. Vehicle spin stabilized during transfer orbit

2. Vehicle spin stabilized, inclined 19.4 degrees to the orbital plane prior to despinning

3. Vehicle stabilized while reflector is unfolding

4. Vehicle stabilized during normal mode of operation

b. Alternate Configuration

1. Vehicle spin stabilized during transfer orbit

2. Vehicle spin stabilized either perpendicular to the orbital plane or inclined 19.4 degrees to the orbital plane prior to despinning

3. Random vehicle attitude during reflector unfolding

4. Attitude of vehicle can change while reflector is unfolding

5. Three axis stabilized during normal mode of operation

6.5.4 ANALYSIS OF MEMORY REQUIREMENTS

In order to stabilize the vehicle to the desired accuracy, the Polaris star tracker gimbal angle offset must be continually updated with a command accuracy of 20 arc-seconds. The required gimbal angle command as described in Section 5.6.3 is as follows:

$$\text{Gimbal angle command} = \theta \text{ off} + (90 \text{ deg} - \delta) \sin (w_e t + \phi)$$

The period of the sine wave is 24 hours. As a starting point, consider the sine wave as shown in Figure 6.5-2 with a peak amplitude of 0.9 degree. Twenty arc-seconds would correspond to 0.005 of the peak signal. If the zero to peak amplitude were resolved to 8 bits, then the 0.9 degree would be divided into 256 quantization levels; one level corresponding to 0.39 percent of the peak amplitude or a resolution of 12.65 arc-seconds. Let $\epsilon = 0.0039$ and Δ be the smallest angle such that $\sin \Delta = \epsilon$ or $\Delta \approx 0.004$ radians which corresponds to 6.37×10^{-4} days. This means that the smallest time interval between increments of the sine wave function is 6.37×10^{-4} days or 54.2 seconds. It is desirable to select this time interval to within at least a 10 percent accuracy or 5 seconds.

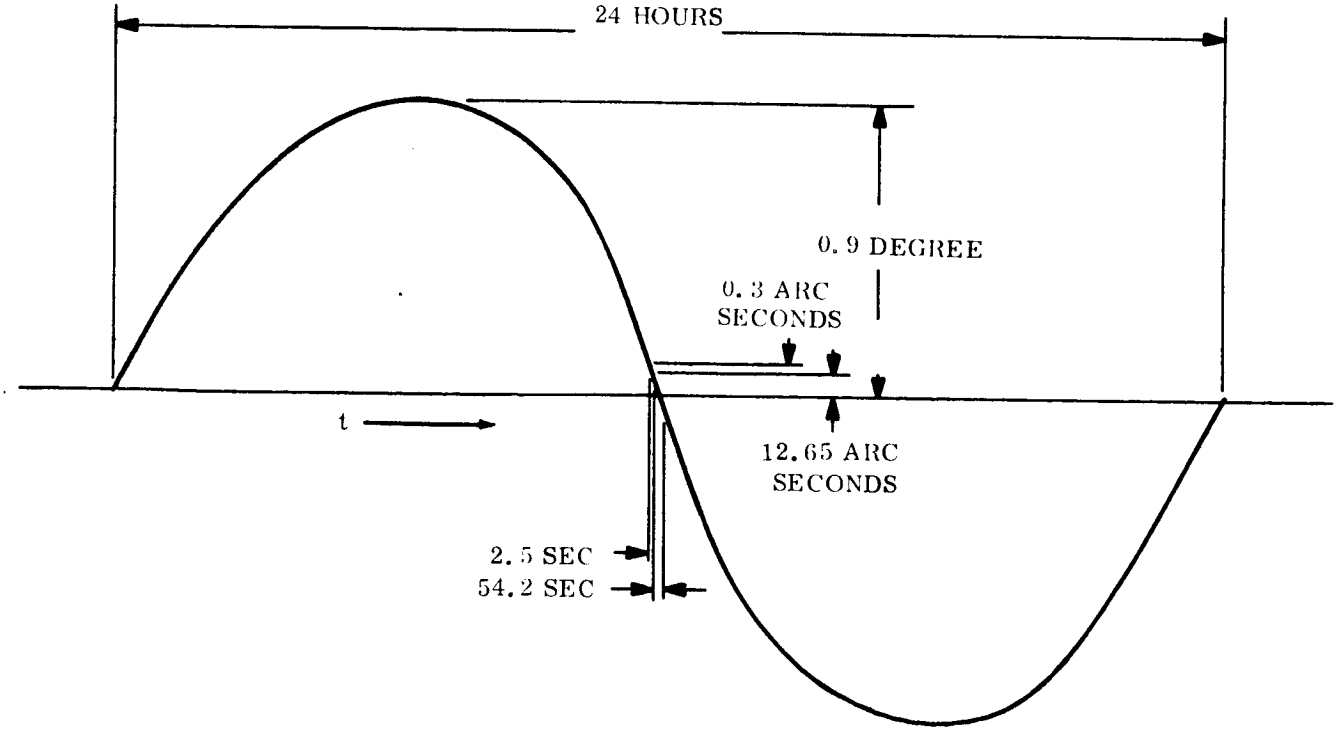


Figure 6.5-2. Minimum Δt for Memory

With a 5-second resolution in the time base we can select a time increment to within ±2.5 seconds. Factoring the plus 2.5 seconds back into the total error increases the smallest Δ by 1.8×10^{-4} radians or $\Delta_1 = 0.00418$ radians. This gives an amplitude resolution, including the timing error, of 12.92 arc-seconds. Therefore, with a 5-second timing accuracy a command accuracy of roughly 13 arc-seconds is achieved. The 5-second timing accuracy over a 6-hour period requires 13 bits with each amplitude increment being approximately 0.4 percent of peak amplitude. Two hundred and fifty-six incremental steps are necessary per quarter cycle or a total of 1024 steps. The sine wave is therefore approximated by a combination of unit step functions. The remainder of the allowed errors will be allocated to the commanding of θ off. This angle varies ±8.7 degrees with a 7 arc-second resolution now being required or 8.95×10^{3} resolvable elements. This requires 15 data bits.

There are several ways in which the storage of the sine wave function can be implemented. Two approaches will be discussed. First, storage of 250 thirteen-bit words could be implemented.

The data in each word would consist of a time label corresponding to one of the increments of the amplitude of the sine wave. Each word would be sequentially compared to the reference clock. When a valid comparison occurs a pulse would be generated providing either a positive or negative increment to the star tracker gimbal angle. Internal control logic would be used to define the quarter of the cycle in which the memory is to be working. This requires a total storage capacity of 3250 bits.

A second approach would be to store only the time difference between each amplitude increment. In this approach, only one word would be compared to the clock reference. The clock reference would be the time since the last increment. When the stored increment and the clock reference compare, an output pulse would be generated to increment the star tracker gimbal angle, the clock reference would be reset and the comparison would be made to the next stored word. The stored word length in this case is 11 bits since the maximum time between increments is 1080 seconds (occurring near the peak of the sine wave). See Figure 6.5-3 for a summary of this analysis.

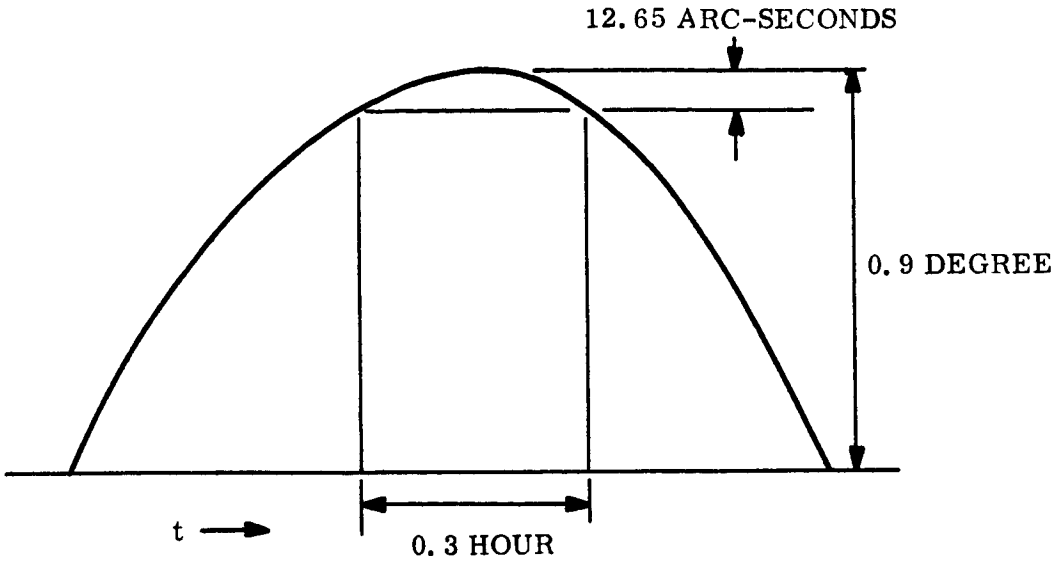


Figure 6.5-3. Maximum Δt for Memory

This requires a storage capacity of 2750 bits. This approach appears to be more efficient. However, a comparison of the control logic required for the two has not been made, therefore a valid tradeoff cannot be made. The reference design has been sized based on the first approach.

The timing signal is to be initiated by ground command. The inaccuracy associated with the time of generation of the command should be in the millisecond range and contributes an insignificant error. Command capability will be provided to initiate the clock at one of 12 phases of the total cycle (30 degrees apart). This limits the maximum waiting time, before an updating via ground command is transmitted, to 2 hours.

6.6 POWER

6.6.1 RADIATION ENVIRONMENT REQUIREMENTS

The components of the natural charged particle radiation environment that the spacecraft will encounter at synchronous orbital altitude are as follows:

a. Trapped radiation-electrons and protons

b. Solar cosmic radiation

c. Primary galactic cosmic rays

This section defines the magnitude of each of these components that have been utilized in the present study.

6.6.1.1 Trapped Radiation

The geomagnetically trapped radiation environment that the spacecraft will encounter consists of electrons and protons. For the most part, the electrons will constitute the primary penetrating component of the trapped particles because the magnetic field at this altitude is not capable of trapping protons of energy greater than about 5 Mev[1]. However, large quantities of low energy protons, less than about 5 Mev, can be expected. These low energy protons are readily absorbed in the external spacecraft surface and are only of concern to components and materials mounted on the exterior spacecraft surfaces.

The penetrating radiation in the so-called "outer radiation zone" has been the subject of numerous investigations in the past.[1, 2, 3, 4, 5, 6, 7] It is well known, for example, that the particle energy spectrum tends to soften with increasing altitude. Also, the particle intensity in the outer zone varies considerably with solar activity. For the synchronous orbit, this temporal variation can be as much as a factor ten above that for quiet solar periods. Because the orbital time period of interest (1969-1972) corresponds to a period of expected high solar activity (see below), the estimates for the trapped radiation environment for the present study include a factor of ten increase over that for quiet solar periods.

This increase is consistent with the estimates of others for the synchronous orbit during periods of increased solar activity. (8)

The expected electron environment, in terms of yearly, integrated, isotropic dose, used in the present study is shown in Figure 6.6-1. As will be shown later, this component of the environment will significantly affect the solar cell power supply, particularly for thinly shielded cells. The low energy proton flux is taken to be 1.6×10^{15} protons/cm^2/year with energies between 0.1 Mev and 5 Mev. (1) This high flux, although not very penetrating, can deliver a significant dose to the spacecraft surface.

6.6.1.2 Solar Cosmic Radiation

6.6.1.2.1 Solar Flares

The time period of interest for the system operation corresponds to the next maximum period in the 11-year solar sunspot cycle. During this time period, sporadic, intense

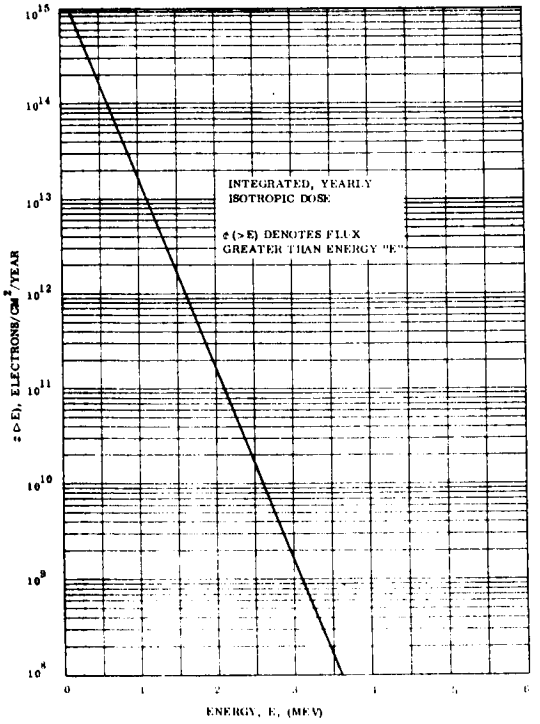


Figure 6.6-1. Trapped Electron Environment

solar activity is expected which will result in the spacecraft receiving a significant radiation dose due to solar flare protons. An estimate of the integrated yearly isotropic dose due to the solar flares is shown in Figure 6.6-2. This estimate is obtained by considering the data obtained during the last maximum in the solar sunspot cycle (1956 to 1961 time period). Table 6.6-1 shows a summary of the yearly integrated particle doses for energies greater than 30 Mev and 100 Mev, respectively, for the years of the last solar maximum period.[9,10] For the present estimate, the average yearly particle doses above 30 Mev and 100 Mev averaged over the last maximum period, as shown in Table 6.6-1, are assumed to apply for the 2 year time period of interest. This gives a 2 year particle dose as follows:

$$E> 30 \text{ Mev}, \quad \phi = 8 \times 10^{9} \text{ protons/cm}^2$$

$$E>100 \text{ Mev}, \quad \phi = 6 \times 10^{8} \text{ protons/cm}^2$$

The particle energy spectrum can vary significantly from one flare to another and also during the time duration of any given flare. The spectrum shape of Figure 6.6-2 represents the integrated spectrum shape of a number of flares such as that which would occur over a 1 to 2 year time interval.[9, 10]

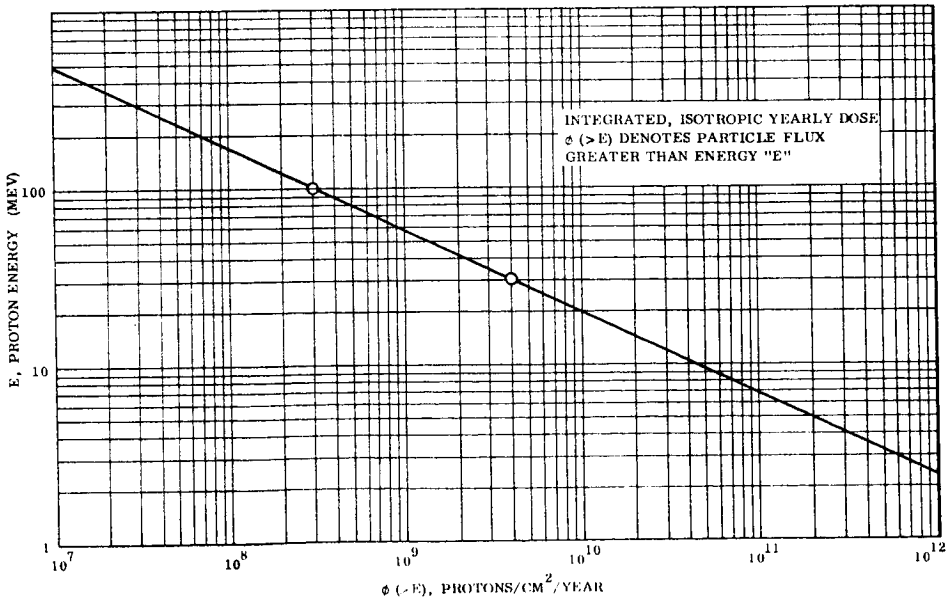


Figure 6.6-2. Solar Flare Environment

Table 6.6-1. Yearly Integrated Intensities Of Solar Cosmic Rays

Year	Number of Events	Solar Cosmic Rays Integrated Intensity (particles/cm^2)	
		> 30 Mev	> 100 Mev
1956	2	8×10^9	8×10^8
1957	4 or 5	4×10^8	1.5×10^7
1958	6	1×10^9	1.4×10^7
1959	4	7×10^9	5.2×10^8
1960	8	5×10^9	4.1×10^8
1961	5	2.7×10^9	3.3×10^7
Avg.		4×10^9	3×10^8

6.6.1.2.2 Solar Wind

In addition to the energetic particles that are periodically emitted (solar flares), the sun also continually releases a flux of very low energy particles into the solar system. This flux is referred to as the "solar wind." It consists primarily of low-energy protons and electrons. In the vicinity of the earth, the protons have energies of several Kev and a density of approximately five protons/cm^3. (11) Similarly, the electron density is approximately 1000 electrons/cm^3 with energies on the order of several electron volts. The mean velocity of the solar wind is approximately 500 Km/second. This gives a proton flux of about 2×10^8 particles/cm^2/sec. Although this flux is not very penetrating, it will constitute a significant ionization dose on the spacecraft surface.

6.6.1.3 Primary Galactic Cosmic Rays

Primary galactic cosmic rays consist primarily of various atoms stripped of their electrons, with high energy electrons amounting to a few percent of the primary flux. The majority, however, are hydrogen atoms. Table 6.6-2 gives the relative abundance of the elements

Table 6.6-2. Abundance Of Cosmic Rays

ATOMS	PERCENT
Hydrogen	85
Helium	13
Light Nuclei (Li, Be, B)	0.2
Medium Nuclei (C, N, O, F)	1.0
Heavy Nuclei (Z>10)	0.8

in cosmic ray fluxes. [12] The average energy of these particles is four Bev, with the energy varying from less than 100 Mev to 10^{10} Bev.

The average free-space isotropic flux is two particles/cm^2/sec. This intensity is modulated somewhat by the 11-year solar cycle, being about a factor of two less at solar maximum than at solar minimum. This is apparently due to the injection of large magnetic clouds into the entire solar system by the sun during maximum sunspot years, which in turn deflect away some of the galactic particles. This component of the radiation environment, although very penetrating, will not consitutue a significant radiation dose to the spacecraft systems.

6.6.2 ENERGY SOURCE SELECTION

Silicon solar cells for conversion of solar to electrical energy are the primary energy source used on long-life (one year or more) spacecraft today, and apparently they will continue to be the only reliable source available for the time period of the ATS-4 vehicle. Therefore, they were selected for the ATS-4 vehicle.

Similarly, nickel-cadmium batteries are the only energy storage system that have proven capability for durations such as the 2-year mission of the ATS-4. Therefore, they were selected as the energy storage device for the ATS-4 vehicle.

6.6.3 ARRAY CONFIGURATION SELECTION

6.6.3.1 Array Location on Vehicle

The major considerations involved in selecting the location of the solar array on the vehicle were to find a location with minimum sun-shadowing effects of the vehicle throughout an orbit while meeting the following other system constraints:

a. The array panels must be located so as not to interfere with the rf pattern of the parabolic reflector,

b. the panels must be stowable for launch, and

c. deployable for orbit operation with a minimum of mechanical complexity.

Without considering vehicle shadows, the simplest approach, body-mounted cells, would appear to meet constraints (a), (b), and (c). However, considering the size of the equipment modules which evolved for the vehicle, together with the priority of the active thermal control system for the available equipment module surface space, it became clearly evident that all body-mounted solar array was impractical and that addition structure would have to be created especially for mounting the array (array panels) and that this structure would have to be deployed away from the equipment modules. The simplest approach for deployment of such panels, compatible with the constraint of not interfering with the rf pattern of the parabolic reflector, would be to hinge the panels as directly as possible to the aft equipment module above the antenna reflector. However, this arrangement obviously requires the panels to operate in the shadow of the parabolic reflector for large portions of the orbit, and deployment to a location near the periphery of the reflector to avoid the shadows becomes the next logical consideration. In particular, deployment beyond the reflector along the Y-axis would eliminate all array shadowing.

However, because deployment to the fully illuminated ideal location at the reflector periphery has a structural and mechanical complexity associated with it, and because the parabolic reflector maximum porosity of close to 77 percent (when viewed perpendicular to the reflector surface) made consideration of operation in the shadow of the antenna appear feasible, detail studies were carried out to establish the tradeoffs involved. The feasibility of operating an array in the shadow of the parabolic reflector is discussed in Section 6.6.3.1.1.

An obvious result of shadows on a solar array is that solar energy is thereby prevented from reaching the array for conversion to electrical power and that the potential power output of the array will be at least reduced in proportion to the solar energy cutoff. However, depending on the distribution of the shadows, the temperature of the shadowed panel at the time of shadow occurrence relative to the panel design temperature, the operating voltage of the array and whether or not by-pass diodes are being used, the effect of the shadows on array power output can be either much greater or even less than the proportional amount of the area shaded. These aspects of array shading will be discussed below both for arrays without bypass diodes and for arrays with bypass diodes.

6.6.3.1.1 Shadow Effects on Arrays Without By-Pass Diodes

A typical array panel consists of several strings of series-connected elements, each element consisting of several solar cells connected in parallel. When uniform illumination is assumed, the available voltage from a string of such series-parallel connected solar cells is determined by the number of series-connected elements in the string and the operating temperature of the elements. The available current is determined by the number of cells connected in parallel in each of the elements and the intensity of the solar energy that impinges on the elements. Therefore, in the design of the array, the total number of series elements in each string is selected on the basis of the desired minimum operating voltage for the array in conjunction with the minimum peak-power cell voltage, which will correspond to the maximum operating temperature of the cells. The number of strings and cells in parallel for each element is then selected on the basis of the desired minimum current required of the array at the design voltage level, which will correspond

to the minimum effective solar intensity condition of the array. The major variables affecting the effective solar intensity on the array throughout an orbit are angles of solar incidence on the various panels of the array and/or extent of the shadows.

Consider one of the above series strings of cells partially shadowed. To the extent that solar energy is thereby prevented from reaching any element of the string, regardless of the distribution of the illuminated and shadowed portions on that element, the effective intensity of illumination on that element will be reduced proportionately. Therefore, if each element of the string is equally shadowed, such as by a shadow with edges lying parallel to the direction of the string, the current output of each element of the string will be decreased equally in proportion to the area of the element shaded.

However, if the shadow deviates from the above ideal pattern such that even only one series element of the string is shadowed more than the others, the more greatly shaded element presents such a high impedance to the other elements of the string for currents greater than its short-circuit current capability under its partially illuminated condition,that the current output of the entire string is limited to the short-circuit current capability of the shadowed element. (Also, the voltage contribution of the short-circuited element is lost at this current level.) Thus, it is the percent of shadowing on the most severely shaded single element of a series string that determines the current output of that string---not the overall percent shadowing of the entire string. In the extreme, only one element of the series string needs to be completely shaded to lose the output of the entire string due to the current restriction of this one element.

Effects of Antenna Reflector Shadows. When the above considerations are applied to evaluate the effects of vehicle shadows on arrays, the following observations are evident:

a. If the shadowing structure is solid such that the array panel is divided into a totally shaded section and a totally illuminated section, the analysis is relatively simple. That is, if the direction of the series strings on the panel are parallel to the edge of the shadow, each string is either fully illuminated, not illuminated, or each element of the string is equally partially illuminated, and the current output of the panel will therefore be proportional to the total illuminated area.

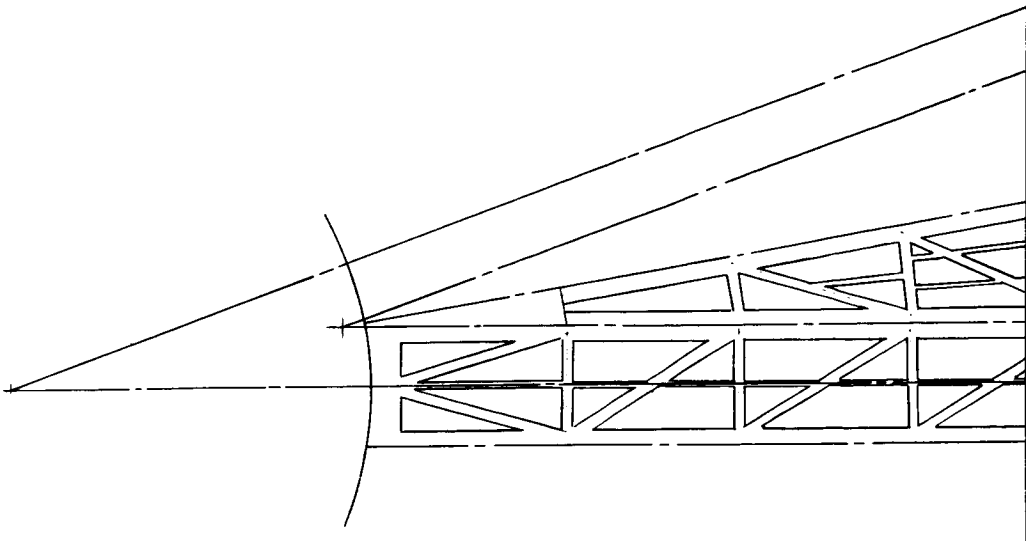
(This principle was used in evaluating the effects of vehicle shadows on the X-axis panels and center-beam shadows on the longitudinal strings of the Y-axis panels for the preferred vehicle configuration). However, if the direction of the series strings is perpendicular to the shadow edge and some elements of each string are thereby completely shaded, then the output of each string and the total panel output will be zero because of the current-restricting effect of the shaded elements.

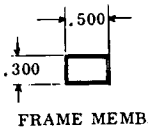
b. If the shadowing structure is "porous" such that the array panel is subjected to a striped or checkered pattern of alternate shadows and illuminated areas, such as the shadows that the antenna reflectors illustrated in Figures 6.6-3 and 6.6-4 would cast, then the analysis of the panel for power output is more complex than described above. In accordance with the principle discussed above, the current output of any string will be limited to the short-circuit current capability of the most severely shaded single element of that string. Therefore, each series string of the panel must be examined for the percentage shade on the most severely shaded element to establish the upper limit of current (and thus power) for that string. Thus, it is the width and direction of the largest shadowing members of a porous structure, as they relate to the maximum percent of a single series element of each string that they can shade, that determines the maximum power output of the shaded panel, not the overall percent blockage of solar energy by the structural members.

(NOTE: If the temperature of the panel is near the design-operating temperature so that voltage capability is critical, then the number of elements with the maximum degree of shading also must be considered because the voltage of these elements is lost when they are forced by the other elements to operate at their short-circuit current levels. Should the string voltage thus be inadequate at the short-circuit current level of the shaded elements, the string will operate at a lower current to achieve the design operating voltage. However, near the peak power current of the shaded element, which is approximately 10 percent less than the short-circuit current of the shaded element, this is the maximum additional decrease required.)

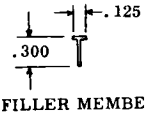
Because at the earth's distance from the sun, some of the solar flux has an angularity of approximately 1/2 degree to any point, it is theoretically possible to get far enough behind the reflector shading members so that the harsh shadows become diffuse and the average solar intensity over the shadowed area will be the intensity that results from considering the overall percentage blockage of the shadowing members. However, this distance appears to be impractically far behind the reflector for the reflector shadowing members being considered. This can be seen from the following analysis.

As shown in Figure 6.6-5, the width of a harsh shadow behind a shadowing member decreases to zero at a distance of approximately 107 times the diameter of the shadowing member. However, at this distance, the average solar intensity over a distance the same width as the shadowing member is still only 25 percent of the

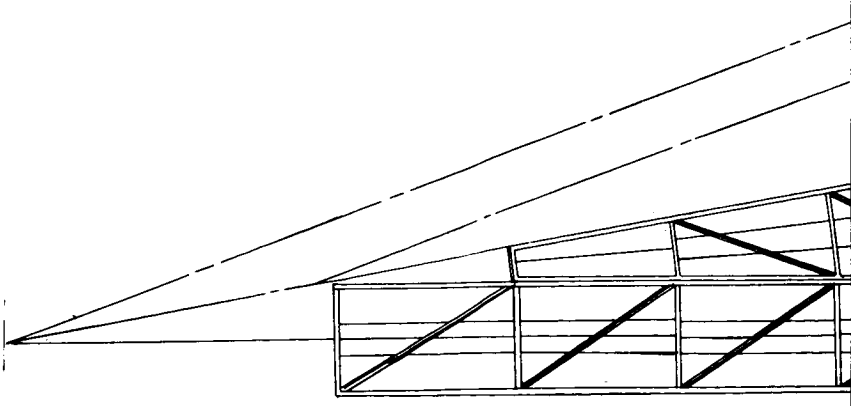




FRAME MEMBERS



FILLER MEMBERS



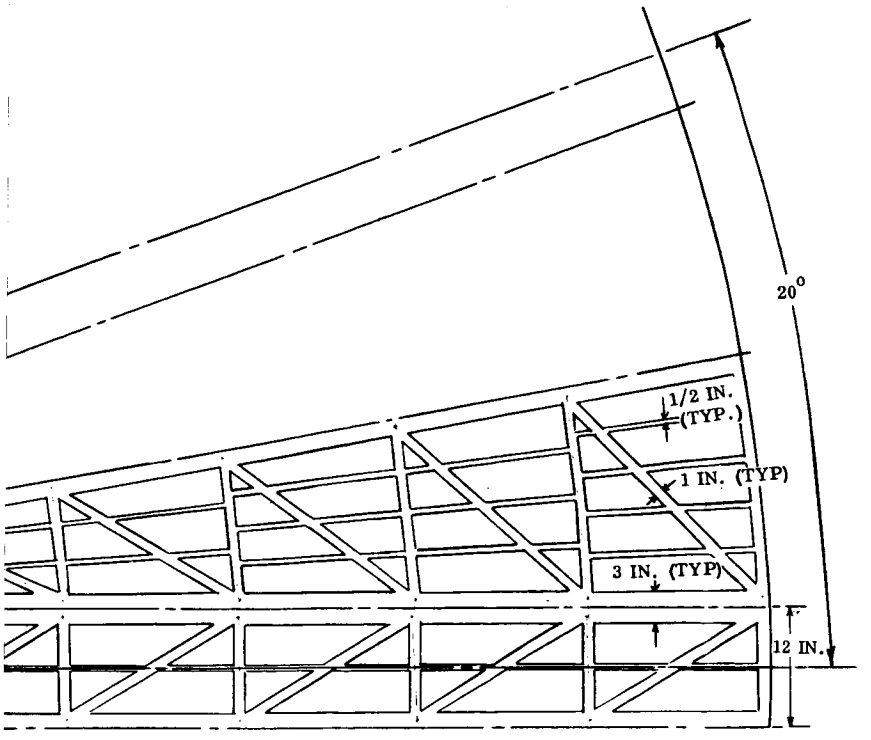


Figure 6.6-3. Segment of 30-Foot Diameter Petal Antenna Reflector

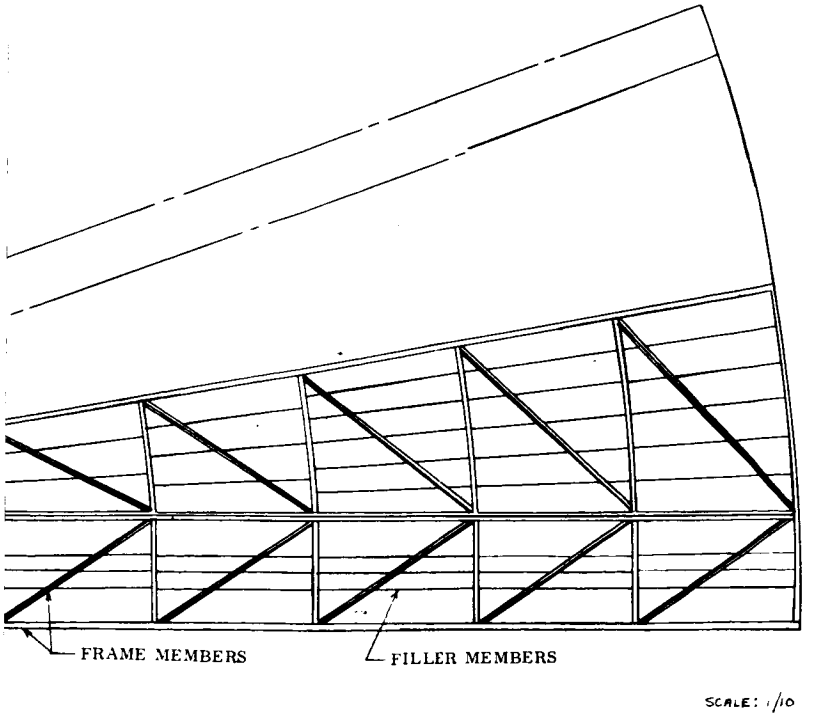


Figure 6.6-4. Segment of 30-Foot Diameter Petal Antenna Reflector

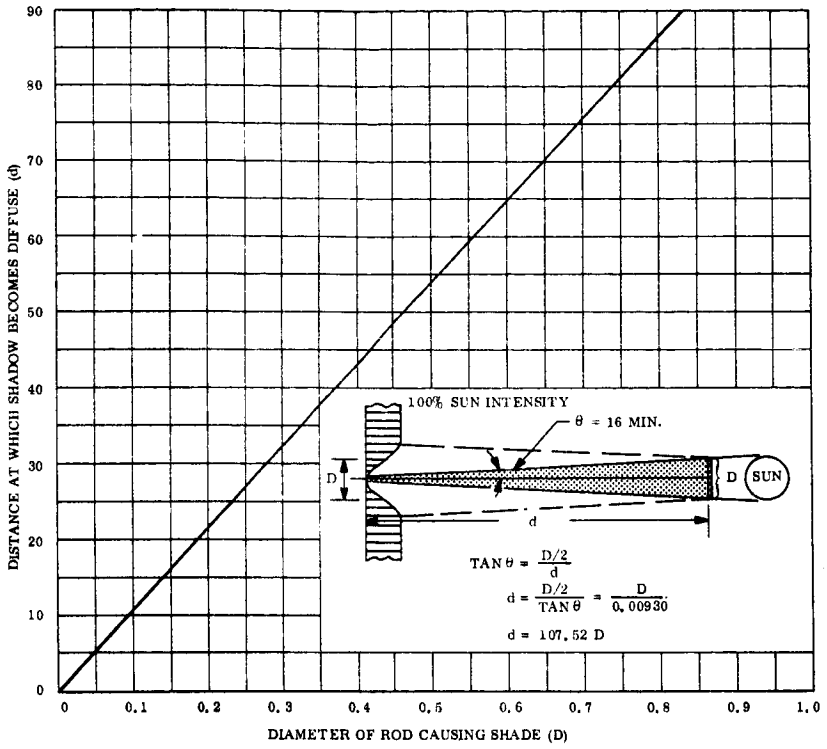


Figure 6.6-5. Sun Shadow Distribution

unshaded intensity (See Figure 6.6-5) and the full width of the shadowing member is therefore still 75 percent as effective on a single element as a harsh shadow.

When the antenna reflector structure (Figure 6.6-3) which has 1-and 3-inch wide members at approximately right angles to each other is considered, it can be seen that some of the 0.75-inch-long elements (active length of 2 x 2 cm cell) of each series string being shadowed by this reflector would be fully, or nearly fully shadowed, no matter what direction the strings were placed on the panel, even if the panels were 100 inches away from the reflector and the sun was perpendicular to the reflector and panel. And it is evident that angularities of the sun and/or panel and structural member thicknesses could serve to increase the width of these shadows. Therefore, the output of each series string and the entire panel would be nearly zero.

Similarly, the 1/2-inch shadowing members of the antenna reflector, which represent 67 percent of an element active length, would represent a large degradation of the panel output for series strings oriented in a direction perpendicular to these members. If the strings are reoriented parallel to these 1/2-inch members, the elements of the string would be subjected to widthwise shadows from the 1-inch members, which, being wider than a series element, would reduce the

output of the panel to practically zero.

In view of the above considerations, it appears that the output of arrays without bypass diodes will be reduced practically to zero by antenna reflector shadows of the type considered in Figures 6.6-3 and 6.6-4. The possibility of overcoming this effect by use of bypass diodes will be considered next.

6.6.3.1.2 Shadow Effects on Arrays with Bypass Diodes

The effects of shading on an array can be significantly reduced using bypass diodes around each series element. The electrical interconnection of the bypass diodes is shown in Figure 6.6-6, where, as described in Section 6.6.3.1.1, the series element consists of a number of cells in parallel. In this arrangement, when a series element is shaded and becomes a high impedance to the current flow of the entire series string, the current generated by the unshaded cells flows around the shaded cells through the bypass diode. Thus, instead of losing current (and thus power) from each element of the entire string in proportion to the percent that this one-series element is shaded for arrays without bypass diodes, the loss consists of the voltage of the shaded series element plus the voltage drop of the bypass diode, which is about twice the voltage output of a solar cell (approximately 0.8 volt) in a typical application. A normalized V-I curve illustrating the above principles is presented in Figure 6.6-7. (The incorporation of bypass diodes into an array is a fully developed and qualified item at GE-MSD, and such array panels manufactured by GE-MSD have been used for the Gravity Gradient Test Satellite recently successfully orbited.)

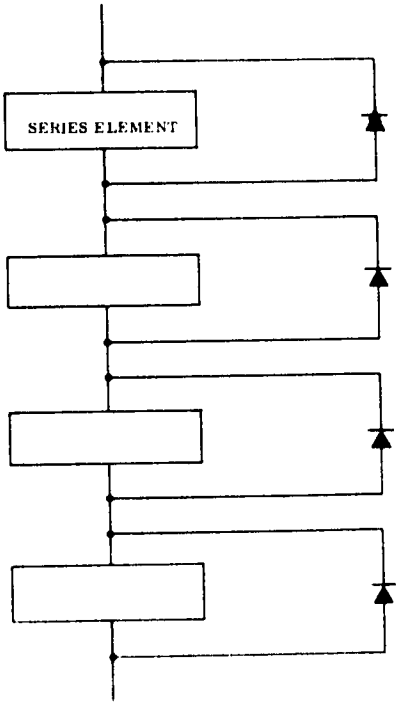


Figure 6.6-6. Bypass Diode Functional Arrangement

It should be noted that for the example V-I curve illustrated, when only one of the 80 series elements is considered shaded, the resulting voltage drop did not significantly affect the current output at the array operating voltage. However, at the voltage loss

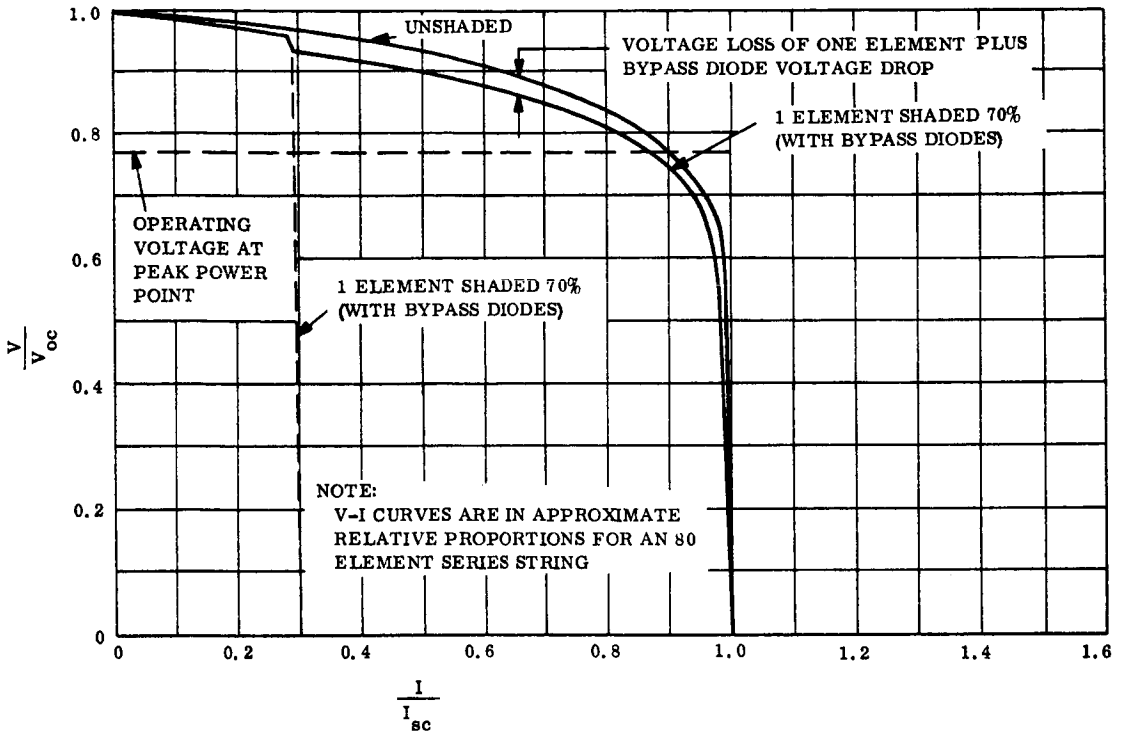


Figure 6.6-7. Comparison of V-I Curves for a Partially Shaded Array Series String, With and Without Bypass Diodes

ratio of 3:1, it is apparent that only a limited number of elements can be shaded before the current at the operating voltage is reduced back to that which would be obtained from an array without the diode protection. Thus, for a diode-protected array, the number of elements shaded as well as the severity of the shade is important---not just the one element most severely shaded, as for an unprotected array. Also, the temperature of the array at the time the shadows occur is important. This is illustrated in Figures 6.6-8 and 6.6-9 for an array operating at approximately a constant voltage.

In Figure 6.6-8, a normalized V-I curve for an array operating in an ideal end-of-life condition at its design point maximum temperature is illustrated both unshaded and shaded. The shaded curves show how many shaded elements in each string of an assumed 80-element array can be tolerated before the voltage drops so low that the current maintained by the

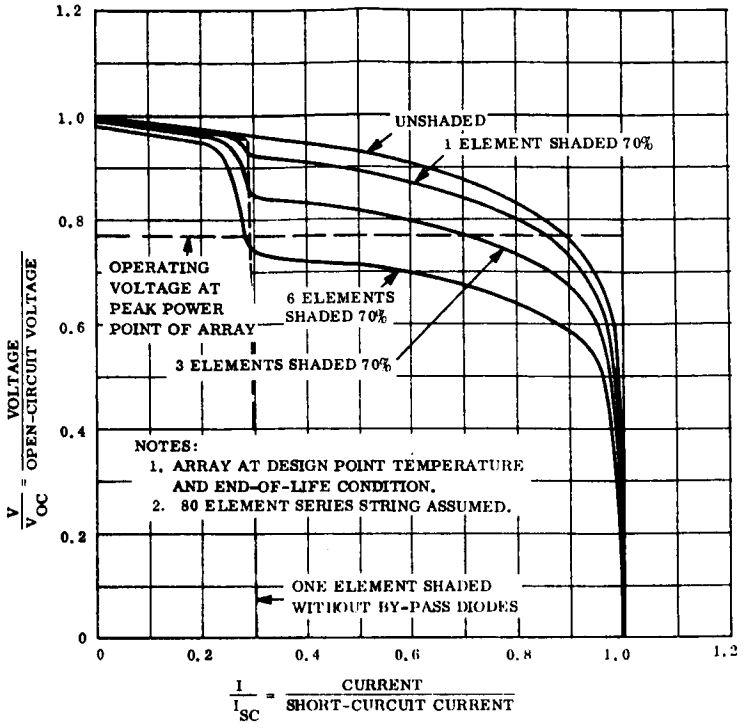


Figure 6.6-8. Illustration of Effects of Number of Elements Shaded on Degradation of an Array Series String Operating at String Peak Power Voltage

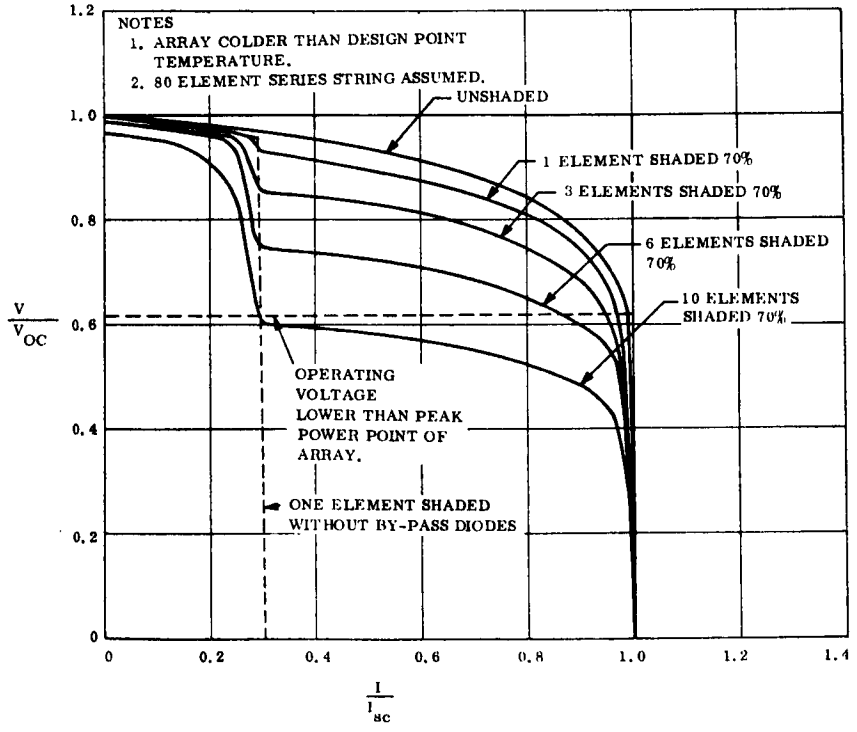


Figure 6.6-9. Illustration of Effects of Number of Elements Shaded on Degradation of an Array Series String When Operating Voltage is Off Peak Power Point of Array

bypass diodes is not available at the operating voltage. It can be seen that the shading of 6 elements in each string eventually nullifies the protection obtained from the bypass diodes.

In Figure 6.6-9, the same array is illustrated operating at a solar angle of incidence which results in a 30^{o} F colder array so that the assumed constant array operating voltage is low relative to the total voltage capability of the array. In this condition, the array can tolerate a larger number of elements of each string being shaded before the protection offered by the diodes is nullified. It can be seen, however, that the array can still only tolerate 8 to 18 shaded elements without degradation to the array.

Effects of Antenna Reflector Shadows. To establish the extent of the shadows cast by the antenna reflector structures of Figures 6.6-3 and 6.6-4 on array panels for evaluation in light of the above principles, the configuration of Figure 6.6-10 was selected as representative of a potential panel location for operation in the shadow of the array. A scaled layout of the antenna reflector structure of Figure 6.6-4 in proper relationship to the above panel arrangement for panels sized to a 300-watt minimum power output was made. The size and locations of the shadows cast by the antenna reflector structure onto the panels was then determined semigraphically. It was found that the 0.125-inch and 0.500-inch antenna structural members can cast shadows onto the panels as wide as 0.6 and 1.1 inches, respectively, for any sun angle within ± 45 degrees of orbit on each side of the eclipse period. Furthermore, this analysis showed that these shadows occur at such angles relative to possible layouts of array series string elements on the panels that many elements are shaded 30 to 50 percent and some up to 100 percent. Also, the shadows producing the 30- to 50-percent range of shading of an element occur often enough over the panel area to shade more than enough elements (more than 8-10) of any series string on the order of 80 in length to nullify the effectiveness of bypass diodes in preventing this degradation at the power point (Figures 6.6-8 and 6.6-9).

From the above analysis, it is apparent that degradations of array power on the order of 30 to 50 percent would occur during shadowing by the most open antenna reflector structure under consideration (Figure 6.6-4), approximately 77 percent open.

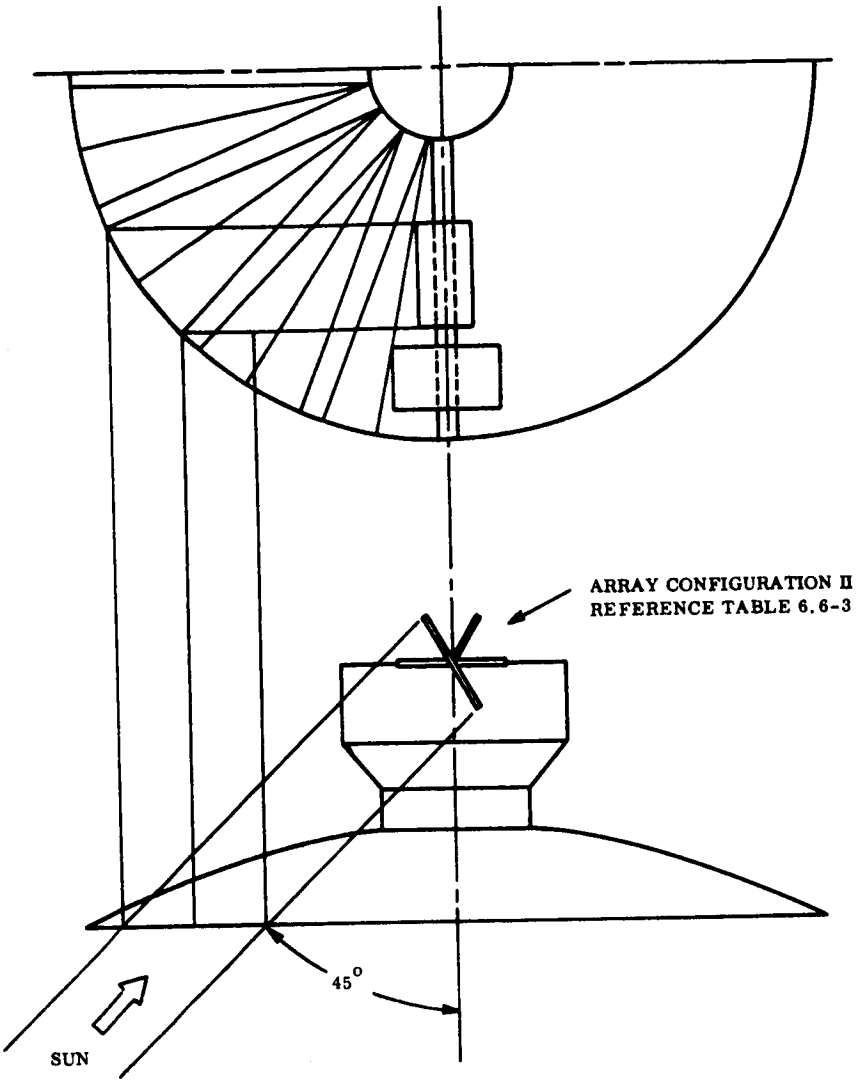


Figure 6.6-10. Array Located in Shadow of Antenna Reflector Structure

From Figure 5.8-10, it is apparent that a severe weight penalty would result to tolerate this loss by means of battery supplementary power. For example, a decrease in array power of 30 percent would mean an array capability without battery supplement of about 160 watts, which would require the battery to supplement all the loads above about 130 watts (reduced array capability during battery supplement) for about 6 hours (about 90 degrees of orbit); i.e., provide 558 watt hours of energy to the loads. (Consistent with the assumption made throughout this report---that the loads of Figure 5.8-3 can occur at any time---the decreased array power was assumed to occur in conjunction with the 223 watt level of loads.) At the batteries, this represents $\frac{558}{(0.90)(0.97)} = 640$ watt-hours (reference Section 5.8.3.2) of increased capacity at the batteries. And maintaining the 30-percent depth of

discharge limitation, this would require the battery to be increased in size by $\frac{640}{0.30} = 2160$ watt-hours. At 10 watt-hours/lb, this represents 216 pounds increase in battery weight. In comparison, the weight of structure required to deploy the array panels to the periphery of the antenna structure is approximately 31 pounds (reference Section 5.9).

6.6.3.1.3 Conclusions

a. Antenna reflector shadows would reduce the output of arrays without series element bypass diode protection to practically zero.

b. Antenna reflector shadows would reduce the output of arrays with series element bypass diode protection by 30 to 50 percent.

c. Use of batteries to supplement array power during antenna shadowing periods would involve large weight penalties compared with weight of structure required to deploy panels beyond shadows of antenna reflector structure.

6.6.3.2 Array Configuration Studies

A fully oriented array was not selected based on the fact that the additional system complexity involved was not desirable for the ATS-4 vehicle. Therefore, the most efficient arrangement of fixed solar array panels became the major consideration. Only conventional rigid panels were considered because flexible roll-up type arrays were judged not sufficiently developed for application during the ATS-4 time period. Since the total energy output of any set of unshadowed array panels of equal size would be the same throughout an orbit (assuming each panel is oriented perpendicular to the orbital plane, does not shadow another panel of the array, and have locations on the vehicle which do not affect the array temperatures), an arrangement was sought which would provide the most uniform power distribution yet keep the mechanical complexity of launch-stowage and deployment to a minimum. Uniformity of power output was deemed desirable to avoid the inefficiencies of introducing battery sharing of even nominal loads, as well as considerations of the effects of the increased power source fluctuations on the power conditioning equipment. The analyses of the various configurations compared are presented below.

6.6.3.2.1 Basic Array Power Equations

For the purpose of configuration comparisons, the following simplified equation for the power output of an array was utilized:

$$P = (S)(F_D)(\eta)(A_T)(F_P)(K_G)(K_I)(F_T)(F_1)(F_2)(F_3)(F_4)(F_5)(F_6)(F_R)(F_S)$$

where

S = solar intensity of sun at the earth's mean distance from sun (130 watts/ ft^2)

F_D = factor to account for variation in sun flux intensity with distance from sun

η = solar power to electrical power conversion efficiency of cells at air mass zero (AMO) under standard test conditions (generally 85^oF)

A_T = total gross surface area of array panels

F_P = factor to account for cell packing efficiency; ratio of active cell area to gross panel area.

K_G = geometry factor for total array; factor to account for variation in sun flux intensity on array cells with variations in solar angle of incidence on cells due to variation in sun flux intercepted by cell area

= ratio of the projected area of the active solar cell area of the illuminated portion of the array in the solar vector direction to the total active cell area of the array.

$$= \frac{1}{A_t} \int_A \cos \varphi \, dA \qquad (6.6\text{-}1)$$

where

A_t = total active solar cell area of array

$= A_T F_P$

A = active solar cell area of the illuminated portion of the array

φ = solar angle of incidence on the element of active solar cell area dA

$$= \frac{1}{A_t} \sum_{j=1}^{n} A_j (\cos \varphi)_j F_{P_j} \qquad (6.6\text{-}2)$$

for arrays consisting of flat panels

where,

A_j = gross surface area of illuminated panel "j."

F_{P_j} = packing factor for panel "j."

K_I = solar incidence factor for total array; factor to account for the variation in power output of array cells with variations in solar angle of incidence exclusive of the variations due to the geometry factor (sun flux interception). These additional variations in the power output of array cells with variations in solar angle of incidence on the cells is due to (a) variation in sun flux intensity resulting from changes in front-face reflectivity of the cells, (b) variations in sun flux intensity resulting from band-pass shifts of the cell filter, and (c) fact that the peak power point current of a solar cell decreases more rapidly with decreases in flux intensity than the short circuit current.

= ratio of actual array output at solar angle of incidence to array output if only the geometry effect on total flux intercepted is considered

$$= \frac{\frac{1}{A_t} \int_A K_i \cos \varphi \, dA}{\frac{1}{A_t} \int_A \cos \varphi \, dA} \qquad 6.6\text{-}3$$

where K_i = solar incidence factor for cell with a solar angle of incidence φ.

A plot of $K_i \cos \varphi$ together with a plot of $\cos \varphi$ is presented in Figure 6.6-11. The effects of changes in angle of incidence on the relative short circuit current is also shown.

$$\frac{\sum_{j=1}^{n} A_j (K_i \cos \varphi)_j F_{P_j}}{\sum_{j=1}^{n} A_j (\cos \varphi)_j F_{P_j}} \qquad (6.6\text{-}4)$$

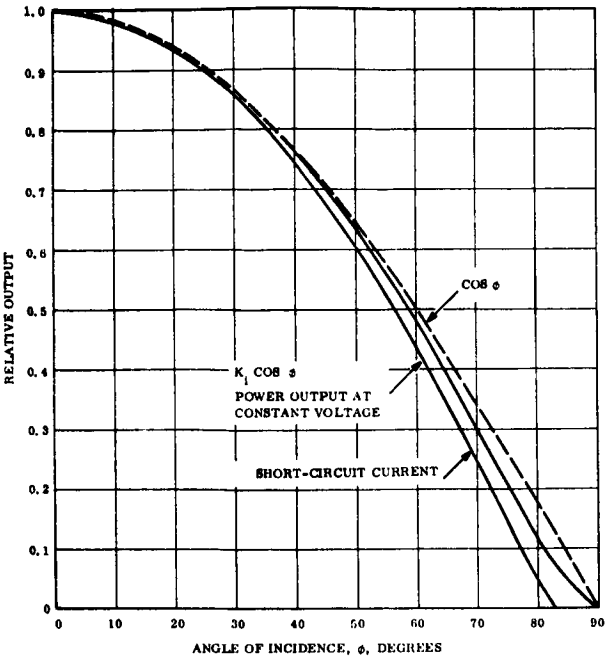


Figure 6.6-11. Dependence of Solar Cell Output on Angle of Incidence

F_T = factor to account for temperature change from cell efficiency standard test conditions temperature

$$= 1 - (T_C - T_S)C_T \qquad (6.6\text{-}5)$$

where

T_C = cell operating temperature

T_S = cell standard test condition temperature

C_T = cell efficiency temperature coefficient

F_1 = factor to account for degradation of cell output due to filter losses

F_2 = factor to account for solder degradation losses

F_3 = factor to account for measurement uncertainties (e.g., sun intensity constant, cell output measurements, etc.)

F_4 = factor to account for calculation uncertainties

F_5 = factor to account for environmental degradations in addition to radiation damage (micrometeorite damage, tab interconnection failures due to thermal effects, etc.)

F_6 = factor to account for blocking diode losses

F_R = factor to account for radiation degradation of cells

F_S = factor to account for effects of shadows on cells

Or, the uncertainty factors may be combined into a composite RMS factor as follows:

$$F_{RMS} = 1 - \sqrt{(1 - F_3)^2 + (1 - F_4)^2} \qquad (6.6\text{-}6)$$

For comparison of different array configurations, it is convenient to write the power equation in the following form:

$$P = K\,(A_T)\,(K_G)\,(K_I)\,(F_T)\,(F_S) \qquad (6.6\text{-}7)$$

where, A_T, K_G, K_I, F_T and F_S are the predominant variables in configuration selection and K is a combination of the factors which are relatively constant.

$$K = (S)\,(F_D)\,(\eta)\,(F_P)\,(F_1)\,(F_2)\,(F_3)\,(F_4)\,(F_5)\,(F_6)\,(F_R) \qquad (6.6\text{-}8)$$

or,

$$K = (S)\,(F_D)\,(\eta)\,(F_P)\,(F_1)\,(F_2)\,(F_5)\,(F_6)\,(F_R)\left[1 - \sqrt{(1 - F_3)^2 + (1 - F_4)^2}\right] \qquad (6.6\text{-}9)$$

6.6.3.2.2 Value of K for Array Configuration Studies

To establish representative sizes of the various array configurations being compared, the following typical values of the various factors included in the parameter K of Equation (6.6-7) are assumed.

S	=	130 watts/ft^2	F_1	=	0.92	F_5 = 1.00
F_D	=	0.966	F_2	=	0.98	F_6 = 0.97
η	=	11% AMO @ 85^{o}F	F_3	=	0.96	F_R = 0.90
F_P	=	0.90	F_4	=	0.95	(end of 2 years of 10 Ω - cm cells)

Using Equation 6.6-9:

$$K = (130)(0.966)\ (0.11)\ (0.90)\ (0.92)\ (0.98)\ (0.97)\ (0.90)\ (0.936)$$

where

$$1 - \sqrt{(1 - 0.96)^2 + (1 - 0.95)^2} = 0.936$$

$$K = 9.16\ W/ft^2$$

6.6.3.2.3 Array Geometry Factors (K_G) for Various Configurations

Using Equation (6.6-2)

$$K_G = \frac{1}{A_t} \sum_{j=1}^{n} A_j \ (\cos \varphi)_j \qquad (6.6\text{-}10)$$

For a flat panel in an equatorial orbit, with the normal vector of the panel lying in the plane of the orbit, the cosine of the solar angle of incidence to the panel is given by the following relationship:

$$\cos \varphi = \cos \psi \sin \theta \qquad (6.6\text{-}11)$$

where

θ = orbital angular position of panel, with $\theta = 0$ when the normal vector of the panel is perpendicular to the sun line.

ψ = angle between sun-line and equatorial plane (varying between ± 23.5 degrees during a year but constant for any one orbital variation of θ).

For a multi-panel array, with all normal vectors of the panels lying in the orbital plane, the above equation for K_G becomes

$$K_G = \frac{1}{A_T} \sum_{j=1}^{n} A_j \cos \psi \sin (\theta + \beta_j) \qquad (6.6\text{-}12)$$

where

β_j = angle between normal vector of plane i and plane j, measured in positive direction of rotation angle θ.

Or, for panels of equal areas,

$$\frac{K_G}{\cos \psi} = \frac{A}{A_T} \sum_{j=1}^{n} \text{Sin} (\theta + \beta_j) \qquad (6.6\text{-}13)$$

The value of $\frac{K_G}{\cos \psi}$ for various array configurations, evaluated using equation (6.6-4), are presented in Table 6.6-3.

As an example, for configuration I of Table 6.6-3 this equation becomes

$$\frac{K_G}{\cos \psi} = 1/4 \, (\sin \theta + \cos \theta) \quad \text{for } 0 \leq \theta \leq 90^o$$

From symmetry it can be seen that a similar equation will result for the other quadrants of the angle θ although different panel surfaces will be illuminated. The variation of $\frac{K_G}{\cos \psi}$ for 90^o of orbit is presented in Figure 6.6-12.

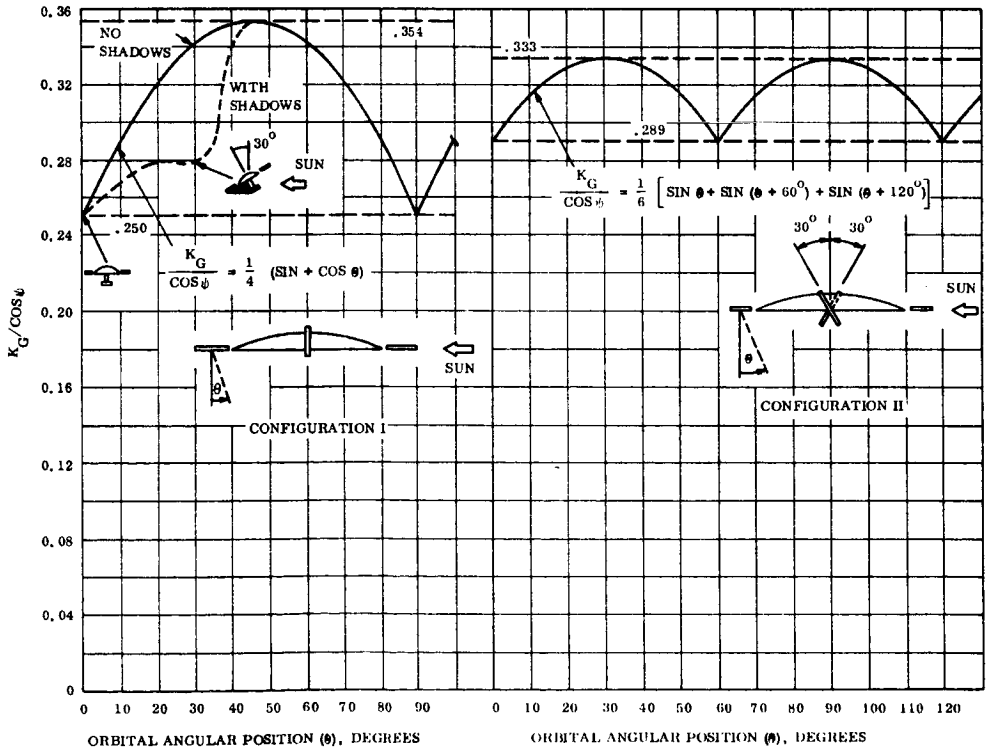
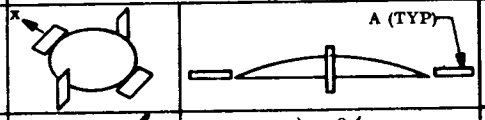
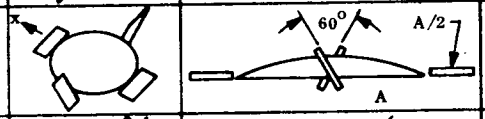
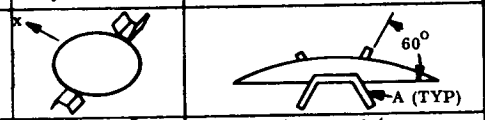
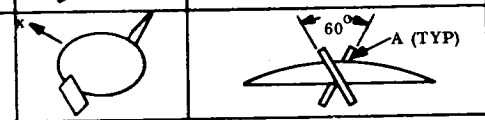
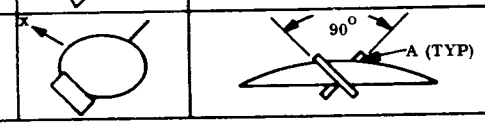


Figure 6.6-12. Orbital Variations of Geometry Factor $K_G/\cos \psi$

Table 6.6-3. Power Equation Factors for Various Array Configurations $\left[P = K (A_T) (K_G) F_T F_S\right]$

CONFIGURATION				(1)		(2)		(3)	(4)	(5)	(6)
				$\frac{K_G}{\cos\phi}$		$F_{T_{MIN}}$		$\left(\frac{K_G}{\cos\phi}\right) F_T$	$F_{S_{MIN}}$	(RIPPLE) $\frac{K_{G_{MAX}}}{K_{G_{MIN}}}$	R^b
	CELL REQUIREMENTS		PANEL ARRANGEMENT	MIN	MAX	MAX TEMP (°F)	F_T	$_{MIN}$			
	ONE SIDE	BOTH SIDES									
I		✓		0.250	0.354	120	0.909	0.227	1.00	1.416	0.863
II		✓		0.289	0.333	120	0.909	0.263	1.00	1.152	1.000
III		✓		0.177	0.354	125	0.896	0.159	(1.00)[a]	2.000	0.605
IV		✓		0.217	0.250	125	0.896	0.194	(1.00)[a]	1.152	0.738
V	✓			0.289	0.333	130	0.883	0.255	(1.00)	1.152	0.970
VI	✓			0.289	0.333	140	0.857	0.248	(1.00)	1.152	0.943
VII		✓		0.217	0.250 0.433	120	0.909	0.197	1.00	2.000 1.152	0.749
VIII		✓		0.250	0.354	120	0.909	0.227	1.00	1.416	0.863

a. FOR P = 1.00, RESTRAINT THAT SERIES STRINGS OF CELLS BE PARALLEL TO EDGE OF SELF-INDUCED SHADOWS IS INTRODUCED.

b. $R = \frac{\text{COLUMN (3)}}{\text{COLUMN (3)}}$ FOR CONFIGURATION II

Similarly, the equation for configuration II is

$$\frac{K_G}{\cos \psi} = 1/6 \left[\sin \theta + \sin (\theta + 60^o) + \sin (\theta + 120^o) \right] \text{ for } 0 \leq \theta \leq 0^o$$

By symmetry, a similar equation results for each additional 60 degrees. The variation of $\frac{K_G}{\cos \psi}$ for 120^o of orbit is presented in Figure 6.6-12.

6.6.3.2.4 Array Solar Incidence Factors (K_I) for Various Configurations

For the present initial configuration studies, where the solar angle of incidences will be relatively large for the points of interest, the effects of K_I will be neglected and K_I will be assumed equal to 1.00.

6.6.3.2.5 Array Solar Incidence Factors (F_T) for Various Configurations

Values of F_T for the various configurations are presented in Table 6.6-3. These values were obtained from Equation (6.6-5), using

$$T_S = 85^o F$$

$$C_T = 0.0026$$

and values of T_C from independent thermal studies. The temperature of the panels corresponding to the maximum temperature of a panel during an orbit was used and are also presented in Table 6.6-3. (Note: For a power subsystem in which power is extracted from the array at a constant voltage, this temperature and resulting value of F_T can also be assumed for other array orientations. Under these conditions the increased power theoretically available from the array as the panel temperature decreases with larger incidence angles will not be available for use because the primary effect of the lowered temperature is increased array voltage. Actually, some power increase will be available with decreased temperatures due to current increases at the fixed voltage, but as this correction becomes significant, the output of the panel has become small due to the large angle of incident and the total effect is therefore negligible.)

6.6.3.2.6 Array Shadow Factors (F_S)

For the configurations presented in Table 6.6-3, the panels are assumed to be mounted near the periphery of the antenna such that the panels are not shadowed by the antenna. When a panel is partially shadowed by another panel, the illuminated portion of the panel is assumed to be effective by making the assumption that the series strings of cells are parallel to the edge of the shadows and that the cells of that string are thereby effective to the extent they are illuminated.

The panels located on the X-axis are subjected to shadows from the Aft Equipment Module and the Earth Viewing Equipment Module, but these shadows occur at low solar angles of incidence when the power contribution of the shadowed panels would be small and the total array power is, therefore, not reduced below the value for minimum array orientation. An example of this is shown in Figure 6.6-12 for Configuration I.

6.6.3.2.7 Array Areas for Various Configurations

Using the array power Equation (6.6-7) of Section 6.6.3.2.1, with the K value obtained in Section 6.6.3.2.2, the array area may be found from the following equation:

$$A_T = \frac{P}{9.16\ (K_G)\ (K_I)\ (F_T)\ (F_S)}$$

Assuming a minimum array power of 300 watts is required, the values of A_T for the values of the other parameters tabulated in Table 6.6-3 were calculated from the above equation for the highest angle of orbital inclination ($\psi = 23.5^{o}$) and are tabulated in Table 6.6-4.

6.6.3.2.8 Discussion of Results

Comparison of the geometry factors ($K_G / \cos \psi$) in Table 6.6-3 for the various array configurations shows that Configurations II, V and VI have the same minimum value of 0.289. However, due to the blockage for radiation cooling of adjacent panels on Configurations V and VI, Configuration II has the highest temperature factor, F_T, and therefore the highest product value. Therefore, based on sizing the array for the minimum output power, Configuration II will require the smallest array area, as can be seen in Table 6.6-4.

Table 6.6-4. Array Area Requirements for Various Configurations (300 watt minimum array)

Configuration (Ref. Table 6.6-3)	Total Array Area A_T	Area Per Structural Panel A	No. of Structural Panels N_S	No. of Array Surfaces on Structural Panels N_A	No. of Support Trusses If Body Mounted N_T
I	157.2	19.7	4	8	4
II	135.9	22.7	3	6	4
III	225.2	28.2	4	8	2
IV	183.7	23.0	4	8	2
V	144.3	24.1	6	6	2
VI	144.2	24.0	6	6	2
VII	181.1	45.3	2	4	2
VIII	157.3	39.3	2	4	2

With battery energy storage capability as part of the power subsystem, the total energy (or average) output of the array over an orbit is another criterion for evaluating the various array configurations because the battery integrates the variations in array power over the orbit. However, a wide variation in array power can increase the battery supplemental power required and impose more severe requirements on the power conditioning equipment. Also, should the battery fail, in order to maintain continuous load daytime operation, it is desirable to maintain the minimum array output higher than the continuous load. Table 6.6-3 shows that the variations in array power (ripple) is the same for Configurations II, IV, V and VI, but substantially larger for Configurations I and III.

Other considerations in comparing the arrays are: fabricability relative to cells on one side versus two sides (Table 6.6-3); the number of structural panels and separate support structures involved (as indicated in Table 6.6-4); and, the restraint introduced on the direction of the series strings of cells on array configurations which produce self-shadowing. The results tabulated in Tables 6.6-3 and 6.6-4 are applicable to any location of the particular configuration which does not introduce shadowing beyond the amounts discussed.

6.6.3.3 Comparison of Four-Panel Configuration With Two-Panel Configuration

The four-panel configuration (Configuration II of Table 6.6-3) produced the most uniform power output at minimum size, and for the simplified analysis used, the X-axis location for two panels (one-half the size of the two Y-axis panels) did not result in excessive shadowing effects (due to the generally low angles of incidence on these panels when shadowing occurs). However, since two panels offered potential advantages of

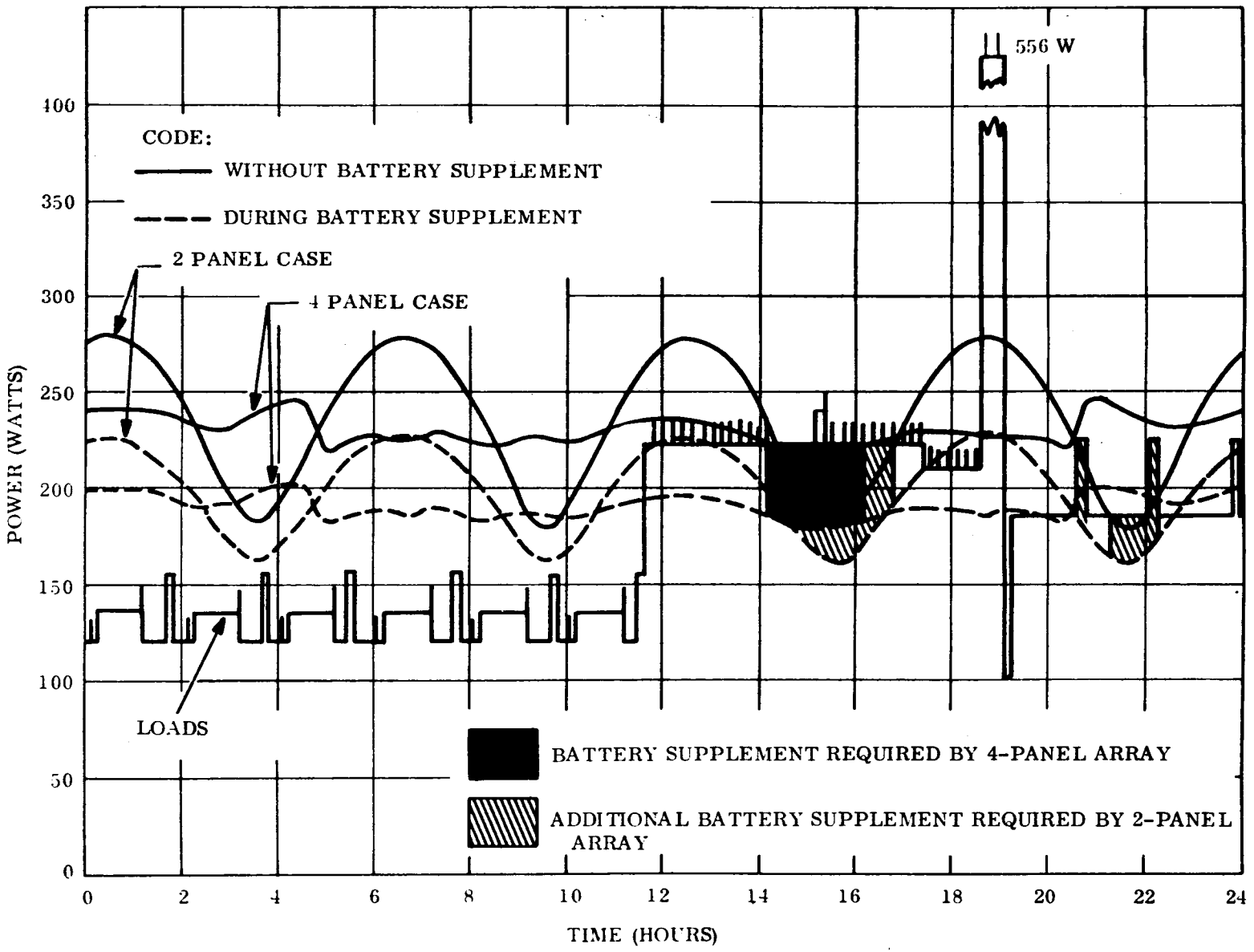
a. Eliminating two of the four solar array trusses required,

b. Eliminating two panel deployment mechanisms, and

c. Eliminating the effects of X-axis vehicle shadows,

a more detailed comparison was made of two panels versus four.

Two panels, containing the same number of cells as for the four-panel array, were assumed to be located on the X-axis and oriented 90 degrees apart (Configuration VIII of Table 6.6-3). The array output, obtained using the same computer program as for the four-panel configuration (Figure 6.6-13), is interpreted at the 28-volt dc bus and superposed on the design load requirements. No shadowing effects of the parabolic reflector or centerbeam are included, however. For comparison, the capability of the four-panel array, with shadow effects included, is shown. Inspection of the figure shows that at the peak load of 556 watts, the two-panel array requires less supplement than the four-panel array. Flexibility in timing of this peak load is desirable and since it may occur at a time when the two-panel array would show an approximately equal disadvantage (e.g., at time 21.3 to 21.9 hours), this peak load requirement will be considered to have an equal effect in the following comparison. For the other loads of the design load profile, the two-panel array requires more battery supplement than the four-panel array (approximately 160 watt-hours compared to 79 watt-hours, an increase of 81 watt-hours). This represents an increase of energy requirements at the batteries of $\frac{8}{(0.90)(0.97)} = 92.8$ watt-hours (see Table 6.6-6). If the 30-percent depth of discharge design limitation were maintained, an increase in battery capacity of $\frac{92.8}{0.30} = 309$ watt-hours would be required. At 10 watt-hours/lb, this represents approximately 31 lb of additional batteries, or an increase of $\frac{31}{103} = 30$ percent. Therefore, the more uniform array power output of the four-panel array provides a weight saving of approximately 23 percent in batteries over the two-panel array for the design power profile and for the array size compared. (This saving would likely be more if shadowing effects were accounted for on the two-panel array as they were on the four-panel array.) Apparently the comparison being made is dependent on the size of the arrays being compared. For example, if the arrays were larger, so that the bus capability was increased by about 50 watts and only the peak load of 556 watts required battery supplement in either case, then the trade-off on battery weight would approach insignificance relative to the other major considerations; namely, ease of launch-stowage and complexities of deployment. These latter considerations are predominantly in favor of the four-panel approach and become the dominant consideration for selecting four panels for the preferred design.



Fgirue 6.6-13. Comparison of Four-Panel and Two-Panel Solar Arrays Power Capability at Loads

6.6.4 ARRAY DESIGN

6.6.4.1 Array Sizing and Performance

A review of the load profile of Figure 5.8-3 shows that there is one peak load of 556 watts lasting 30 mintues which far exceeds the next level of loads of 223 watts which last for many hours. A simple weight tradeoff study between the array and battery relative to sizing for these peak loads shows a weight saving by decreasing the array size until it requires supplementation for the long-duration 223-watt-load level. At this point the battery weight increases faster than the array weight. Because for this array size there is also adequate power available for recharging the batteries during the periods of lower loads, the array was sized to this optimum point. That is, the array was sized so that at the end of two years, in the summer solstice orbit, the array has degraded to the point where the supplementation required from the battery is working the battery to its design limit (30 percent depth of discharge), for a battery which was sized to this array for an equinox orbit. The average power capability over an orbit for this 2-year design point is 272 watts (see Table 5.8-1).

The array solar cells were connected electrically to provide this power after two years at a peak power voltage of 41 volts. This is the minimum voltage required to charge the batteries when they approach an end-of-life, nearly full-charged, high-voltage condition.

The array performance was calculated using the computer program described in detail in Appendix G.

6.6.4.2 Solar Cell Selection

Silicon solar cells appear to be the most economical, reliable type cell available for the ATS-4 time period. Although other types of cells are under development that may offer advantages such as greater radiation resistance or lighter weights, it does not appear now that such cells will be proven and in production in time for ATS-4. Therefore, the most advanced N/P silicon cells presently in production were selected.

Recent test experience at GE-SD with ,NP ' silicon solar cells indicates representative economical efficiencies of 10.5 percent for 10-ohm-cm resistivity cells and 11.3 percent for 1-ohm-cm cells. However, the 10-ohm-cm cells are more radiation resistant than the 1-ohm-cm cells, therefore the choice depends on the efficiency at the end-of-life design point following exposure to the radiation environment. Estimates of the amount of radiation flux to degrade 10-ohm-cm cells vary from two to three times the amount producing the same degradation in 1-ohm-cm cells (see Section 6.6.4.5). For the radiation environment of Section 6.6.1, Figure 6.6-14 shows the efficiency versus time in orbit for 1-ohm-cm cells, 10-ohm-cm cells with twice the radiation resistance, and 10-ohm-cm cells with three times the radiation resistance of the 1-ohm-cm cell. After two years in orbit, the efficiency of the 10-ohm-cm cells is greater than that of the 1-ohm-cm cells if the radiation resistance factor is 3. If the factor of 2 is used, the 10-ohm-cm cells are slightly less efficient after 2 years. The 1-ohm-cm cells produce more power than the 10-ohm-cm cells the first six months of the mission, but unless efficient operational management of the available array power is exercised, this increased power is of little value because of the excess power available over the end-of-life power in either case.

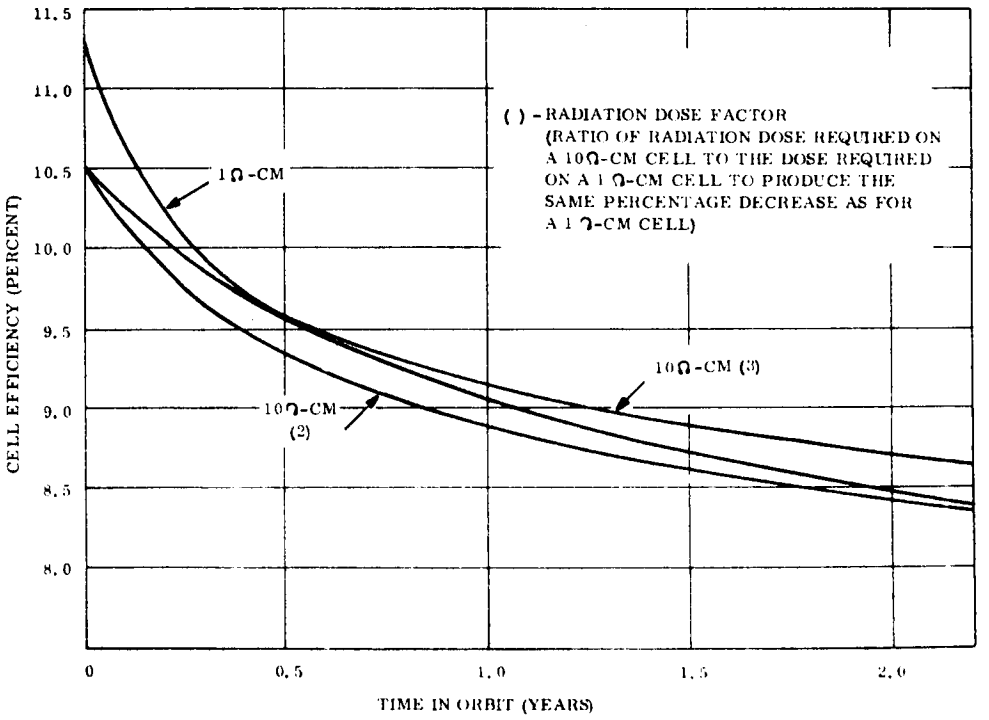


Figure 6.6-14. Efficiencies of 1-ohm-Centimeter and 10-ohm-Centimeter Cells Subjected to Radiation Degradation

It even causes some disadvantages in the form of increased thermal load to be dissipated. The 10-ohm-cm cells were chosen because of their potential advantage over 1-ohm-cm cells at the two-year-design point. For purposes of sizing the array, the efficiency of the less resistant of the 10-ohm-cm cells was used.

6.6.4.3 Solar Cell Characteristics

6.6.4.3.1 Basic Cell V-I Characteristics

The voltage-current characteristics used in the computer program as the basis for predicting the solar array output were derived from V-I measurements made at GE-SD on a large group of solar cells under simulated air mass zero illumination over -200^{o}F to $+200^{o}$F. The general temperature efficiency coefficient for these cells is -0.26 percent/^{o}F referenced to 85^{o}F.

6.6.4.3.2 Intensity Dependence

The solar intensity and the solar cell short circuit current vary simultaneously. In the normal range of solar intensity, the variation of short circuit current is proportioned to the variation in solar intensity. The characteristics of a solar cell are such that a decrease in short circuit current causes a linear shift of the V-I curve to lower current values; i.e., a differential current is subtracted from the entire V-I curve. Thus, because of the shape of the V-I curve, the power output of the array at a fixed voltage will decrease faster than the solar intensity (at a fixed temperature). A second effect must also be included. Because of the series resistance of the solar cell a small increase in the voltage values of the V-I curve will accompany the decrease in cell output current. These same effects occur in reverse when an increase in short circuit current occur. The computer program takes these effects into account.

6.6.4.4 Solar Cell Loss Analysis

Certain losses and output uncertainties must be considered to determine solar array output. These factors are tabulated in paragraph 5.8.2.4. A discussion of each of these loss factors follows.

6.6.4.4.1 Filter Transmission Loss

When solar cell covers with filters are bonded to solar cells, a loss in cell current output occurs from the imperfect transmission of the filter. This loss is estimated to be less than eight percent. The exact amount of loss will depend upon the spectral reflectance and the index of refraction of the solar cell cover antireflection coating and the index of refraction of the cover glass bond. Average values of less than one percent loss have been reported by others for filters on polished N/P cells. However, GE-SD experience shows loss to be up to eight percent.

6.6.4.4.2 Soldering Process Degradation

Soldering operations usually degrade the V-I characteristic by a small amount. GE-SD experience shows this degradation to be up to two percent.

6.6.4.4.3 Radiation Degradation

The analysis of the radiation degradation of the solar cell output is detailed in Section 6.6.4.5. The optimum fused silica cover thickness was determined on a tradeoff of array unit weight and radiation degradation protection; 10 mil was selected for the cover thickness. Thus, the 2-year radiation degradation factor used in sizing the array, expressed as the fraction of original power remaining at the end of the mission, was 0.802. Separation of the radiation damage effects on cell short-circuit current and open-circuit voltage shows the results to be (1) residual I_{sc} = 0.850 and (2) residual V_{oc} = 0.950. Examining the effects of the short-circuit current reduction shows that the I_{sc} reduction will result in a V_{oc} reduction of about 0.975 due just to the V-I characteristic of the cell. Therefore, the reduction in cell voltage characteristics due to radiation is 0.975 and the two radiation damage V-I coefficients are (1) current - 0.850 and (2) voltage - 0.975.

6.6.4.4.4 Micrometeoroid and Random Cell Failures Effects

Measurements made at General Electric on solar cell cover composites indicate the maximum power degradation from micrometeoroid erosion to be 5 percent, for the case of complete surface "sandblasting." There are, however, large uncertainties in the

micrometeoroid environment, but the fraction of surface area erosion is expected to be much less than 100 percent.

There are expected random failures of individual cells both from meteoriod punctures and from solar cell contact and wiring failures due to thermal cycling. A degradation factor of 0.970 was used to allow for erosion, puncture and random cell failures.

6.6.4.4.5 Measurement Uncertainty

The mean solar radiation external to the earth's atmosphere has been determined by deductions based primarily on earth surface observations. Many values of the solar constant have been reported by different investigators, the values reported having an aggregate 3σ tolerance of ± 3 percent about a nominal 140 mw/cm^2. The tolerance accounts for the uncertainty in the actual value of the solar constant due to measurement limitations.

Measurements of solar cell output on earth are subjected to many errors - uncertainty in establishing the spectrum and intensity of the light sources used during testing, instrumentation errors, tolerance due to thermal fluctuations, etc.

For sizing calculations a 4 percent allowance (rms) is made for "measurement uncertainty," which includes the uncertainty in the solar constant as well as the instrumentation errors associated with solar cell measurements.

6.6.4.4.6 Calculation Uncertainty

Since the mathematical modeling of the V-I characteristics of a solar cell for a computer program, which accounts for all the factors affecting the performance of the cells as detailed in Appendix G, is likely to have some uncertainty associated with its accuracy, a calculation uncertainty factor was included in the computations. Also, this factor is included to allow for such uncertainties as the ultraviolet effects discussed below.

6.6.4.4.7 Ultraviolet Effects

Much testing of composite assemblies of filters, fused silica covers, adhesives, and silicon solar cells has led to confidence in the use of organic (silicon) cover glass adhesives. The filter (blue or blue-red) reduces the damaging ultraviolet radiation impinging on the organic bond material so that it does not experience discoloration and therefore reduce transmission. However, experimental results have shown a decrease of about 5 percent in the transmission properties of the filter itself due to ultraviolet exposure. Subsequent work has cast doubt on the original findings. Until fully resolved, allowance is made for this factor only in the form of the above calculation uncertainty factor.

6.6.4.5 Solar Cell Radiation Degradation Analysis

Utilizing the radiation environment estimates given in section 6.6.1 and the calculational techniques given in Appendix H, the N/P, 1-ohm-cm, silicon solar cell degradation expected at the end of the 2-year mission has been determined. These results are given in Figure 6.6-15 as a function of front shield thickness. The back side shielding for

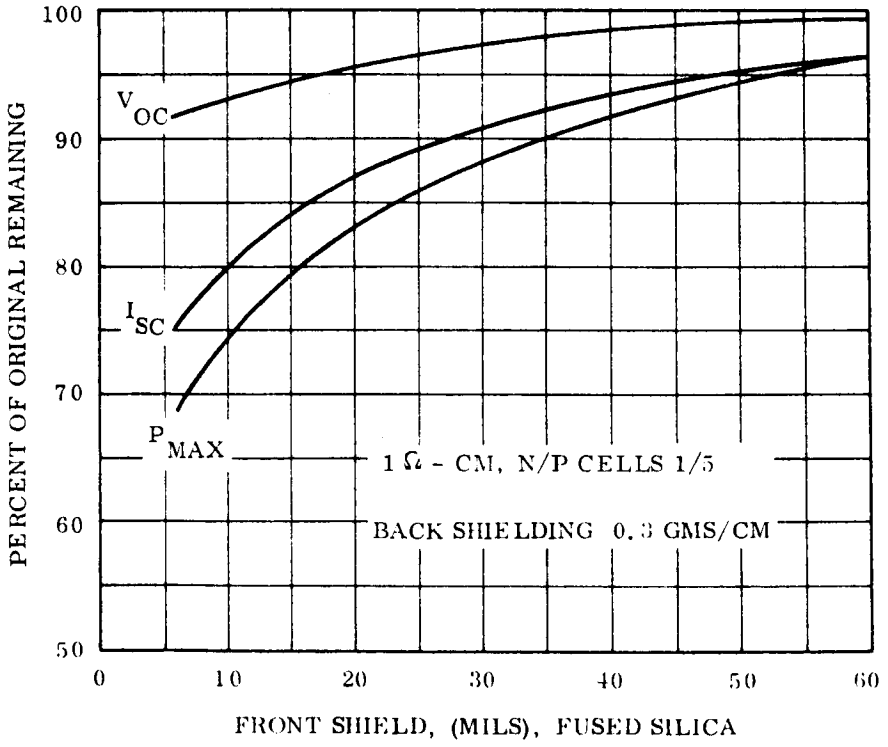


Figure 6.6-15. Solar Cell Degradation After Two Years

the cells in all cases is taken as 0.3 gms/cm^2. For front shield thicknesses less than about 40 mils, the trapped electron component of the radiation environment constitutes the main damaging component. Figure 6.6-16 shows the 1-ohm-cm cell degradation as a function of time in orbit for a 10-mil front shield.

The advantage of nominally 10-ohm-cm resistivity cells over 1-ohm-cm cells is a function of both the initial cell efficiencies and their relative radiation resistance. It has been shown that 10-ohm-cm cells can vary from a factor of 2 to a factor of 5 in radiation resistance over that for 1-ohm-cm cells based upon degradation of short circuit current or damage constant value (References 13, 14, 15, and 16). In other words, it takes from a factor of 2 to 5 more radiation dose in a 10-ohm-cm cell to produce the same percentage decrease as that in a 1-ohm-cm cell. Figure 6.6-17 shows the percentage of maximum power remaining as a function of orbit time for a 10-mil front shield for cells with a factor of 2, 3, and 5 times more radiation resistance than the 1-ohm-cm cell.

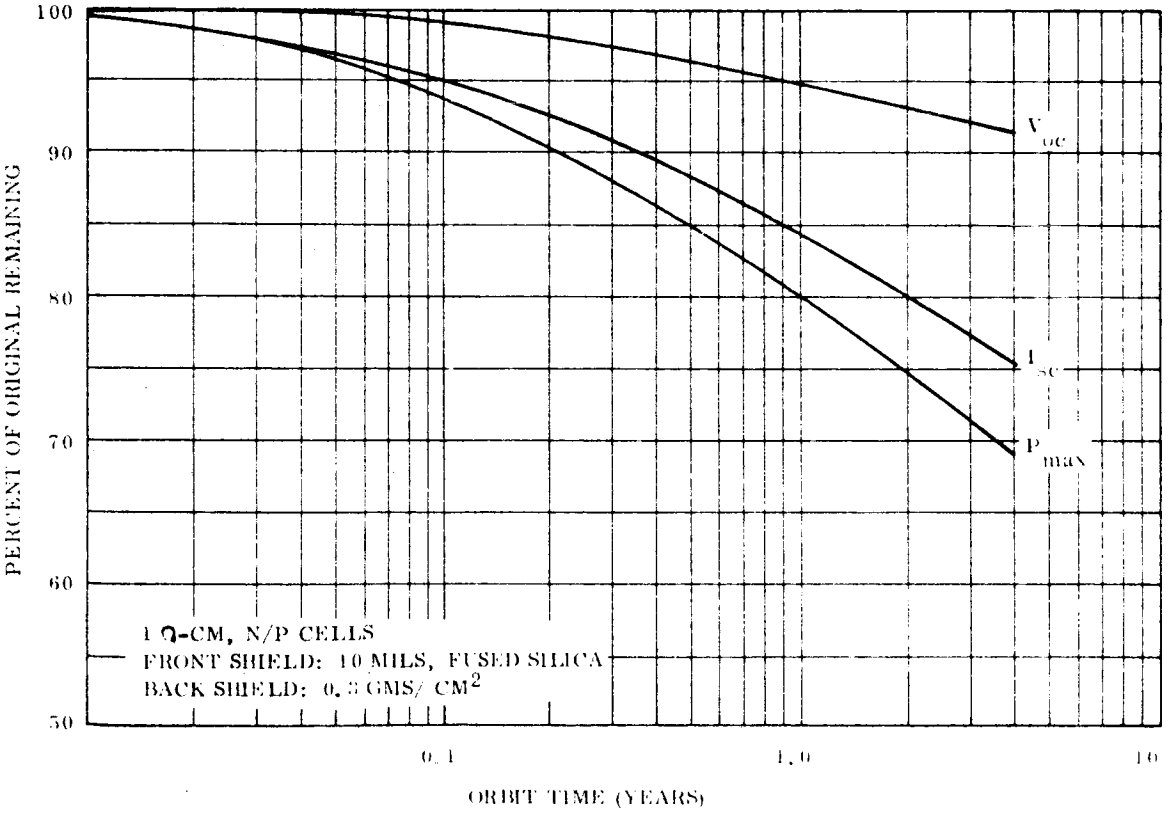


Figure 6.6-16. One Ohm-Centimeter Solar Cell Degradation vs Orbit Time

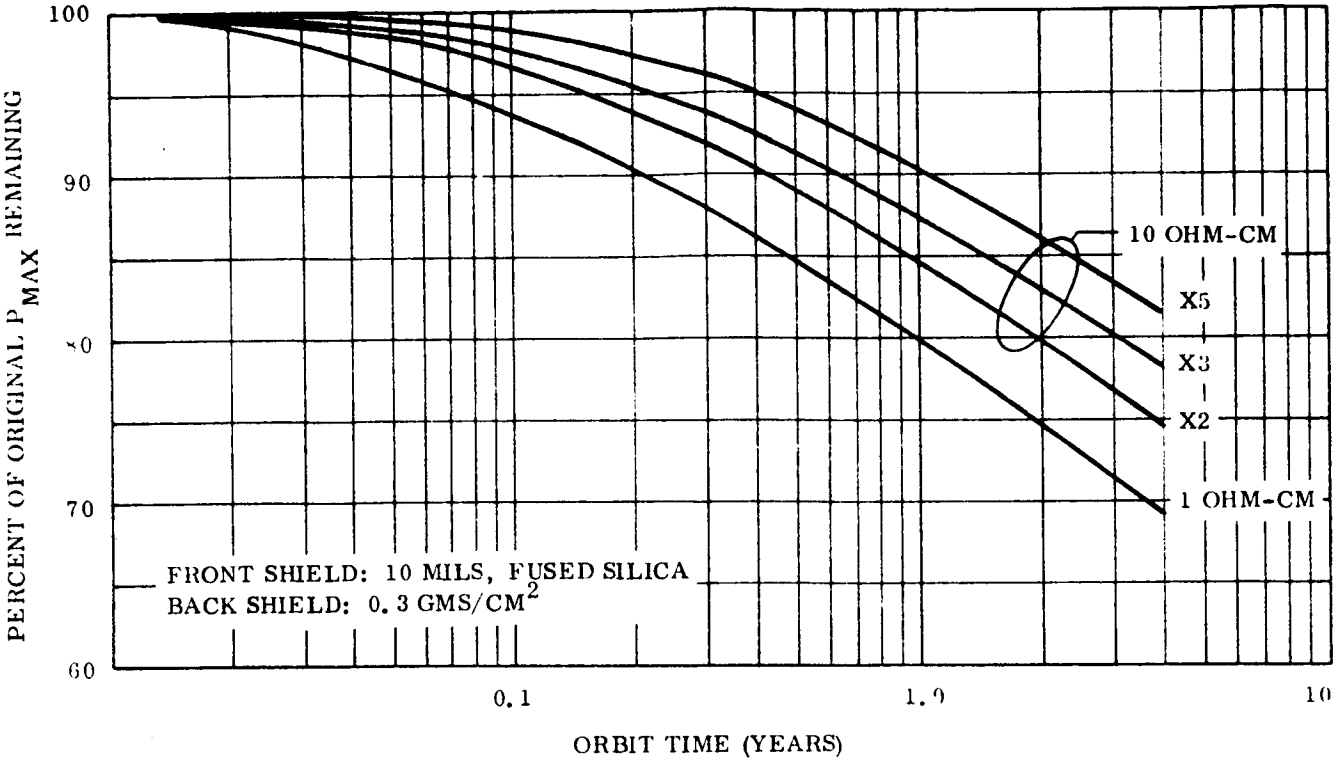


Figure 6.6-17. Maximum Power Degradation vs Orbit Time

For the most part, however, this factor usually has a value between 2 and 3 with respect to the 1-ohm-cm cells (References 13 and 16). The results of past flight experiments has also shown this to be the case (Reference 15). Thus, for the present study, a factor of 2 increase in radiation resistance for the 10-ohm-cm cells over the 1-ohm-cm cells is taken to be representative of present 10-ohm-cm cells. Figure 6.6-18 shows the degradation characteristics of 10-ohm-cm cells, so defined, as a function of orbit time and with a 10-mil front shield.

6.6.4.6 Cover Thickness Selection

Protective transparent covers are required to protect the solar cells from radiation and micrometeoroid damage. The cover thickness may be weight-optimized for a given life in orbit. If the covers are thick, the array for a given power is heavy because of the weight of the covers. If the covers are thin, the array weight for a given power is heavy because of the large array area required due to the solar cell degradation. The

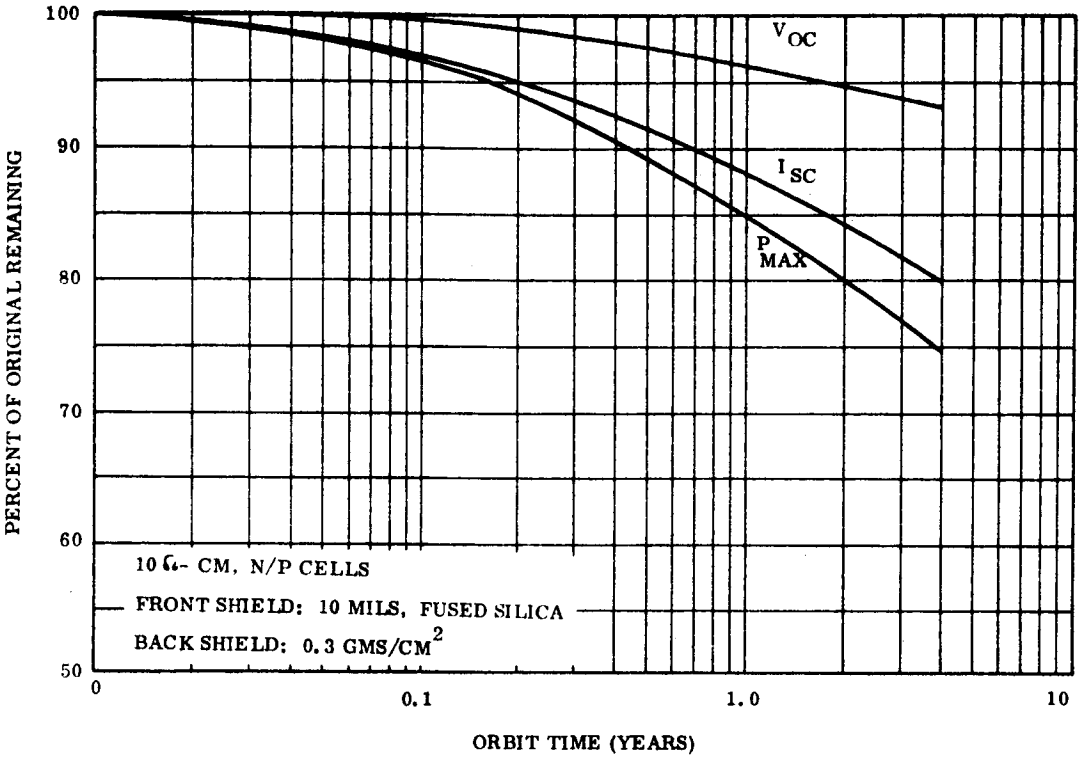


Figure 6.6-18. Ten Ohm-Centimeter Solar Cell Degradation vs Orbit Time

optimum thickness is determined by calculating the relative array power per unit array weight. The relative power per unit area is obtained from the P_{max} radiation degradation curve for 2 years in orbit (See Figure 6.6-18). The array weight per unit area is the sum of the following:

$$\text{Array structure weight per ft}^2 = 0.40 \text{ lb/ft}^2 \text{ for } t \leq 10$$
$$= 0.38 + 0.002t \text{ lb/ft}^2 \text{ for } t > 10$$
$$\text{Array (cells, covers, etc.) weight per ft}^2 = 0.772 + 0.0194t \text{ lb/ft}^2$$
$$\text{where } t = \text{cover thickness in mils}$$

This data is used to obtain the curve in Figure 6.6-19, which gives the normalized relative power per unit weight of array. The weight optimized thickness is 9 mils. It is advantageous to be slightly thicker than optimum so as to avoid the sharp decrease which occurs for very thin covers.

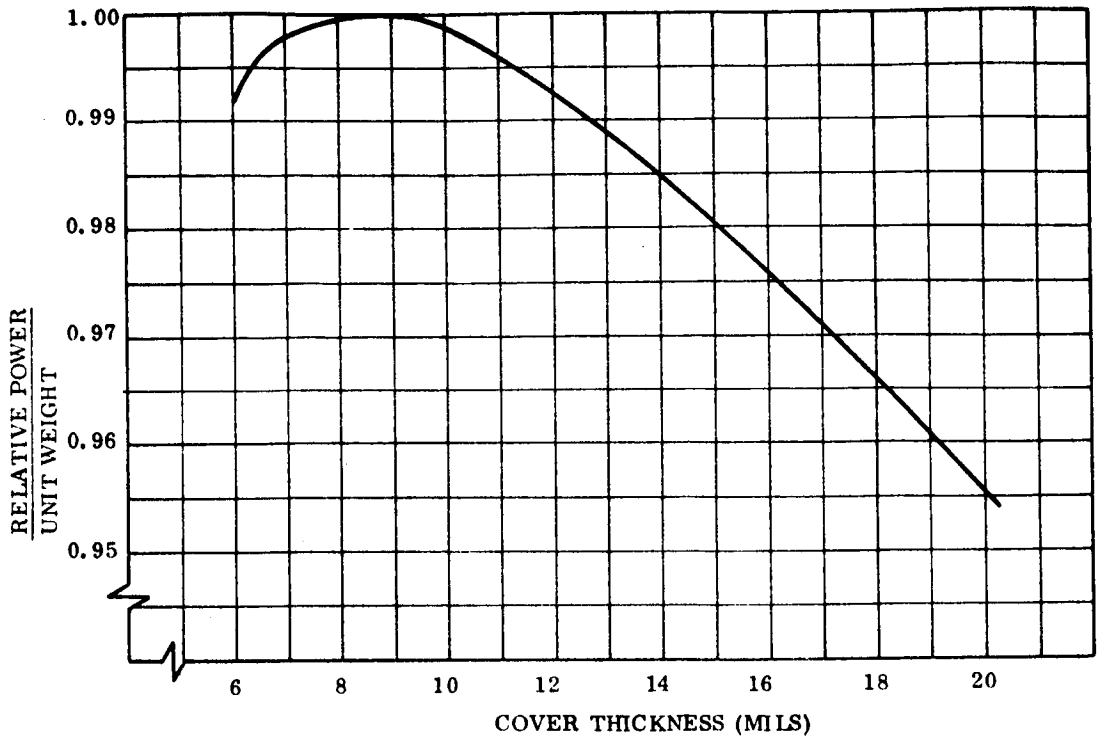


Figure 6.6-19. Solar Cell Cover Thickness Optimization

6.6.4.7 Launch Array Power Analysis

Power is required from the stowed solar array during the transfer orbit. The four solar array paddles are stowed 90 degrees apart, parallel to the yaw axis, around the collapsed parabolic antenna. The outer array surface (half the total array area) has a clear view of space. During the transfer mode the spacecraft is spinning about the yaw axis. It is evident that maximum array power is obtained if the spin axis is normal to the sun direction. However, other considerations result in the following spin axis directions.

a. It may be as much as 25 degrees out of the equatorial (orbital) plane.

b. The angle between the normal-to-the-spin axis and the sun direction in the ecliptic plane may be 15 degrees.

c. Depending on the time of year, the sun can be 23-1/2 degrees from the equatorial plane. The worst-case combination of these angles can be used to calculate the worst-case solar array power output during this period. Since the vehicle is spinning, the array is relatively cool, 60°F. The array output assuming this temperature, worst-case angles and a spin rate of approximately 72 rpm is given in Figure 5.8-12.

6.6.5 BATTERIES

6.6.5.1 Requirements

There are two basic requirements which must be met by the battery. The battery must supply all electrical power during the eclipse periods and it must also supply power for peak loads during noneclipse periods. This power must be provided throughout the mission, which has a design goal of 2 years.

The power subsystem load requirements for the orbit phase of operation are presented in Figure 5.8-3. These loads are repetitive every 24 hours, and, therefore, the battery will be required to supply peak loads on a 24-hour cycle. In addition, the vehicle will experience various periods of eclipse for approximately 80 days out of every year, and consequently the battery will be required to provide additional power for eclipse operation on a 24-hour cycle. For design purposes, time for occurence of the eclipse is as shown in Figure 5.8-3, whereas the peak load may occur at any time, including the eclipse period.

Since the array power degrades as a function of time, the actual load to be supplied by the battery varies and increases with time. Table 6.6-5 is a convenient summary of the resultant battery requirements. It shows the relationship of maximum power required initially and after 2 years in orbit, and also how power requirements vary as the angle of inclination, ψ, of the vehicle to the sun varies. Since less power is provided by the array at maximum inclination, $\psi = 23.5$ degrees, more power must be delivered by the batteries for the peak load demand. However, the maximum power requirement results from the orbit for which $\psi = 0$, when the battery must supply loads for both the maximum eclipse period and the peak load.

6.6.5.2 Selection of Battery Type

In order to fulfill the 2-year life requirement for the vehicle, the only electrochemical power system which can be considered is the sealed nickel cadmium cell. Of all the energy storage devices, this is the only one capable of repetitive use, charge and discharge, over a 2-year period. All long-life satellites now in orbit use this type of battery. Although other battery

Table 6.6-5. Maximum Power Required From Battery(Watt Hours)

Time	$\psi = 0^{o}$ (80 orbits/yr)		$\psi = 23.5^{o}$ (285 orbits/yr)	
	Accumulated Occurrences	Umbra & Peak Loads	Accumulated Occurrences	Peak Loads
1 Day	1	474	1	179
2 Years	160	506	570	305

systems, such as silver cadmium batteries, have a higher energy-to-weight ratio, they have not demonstrated the required life capability.

A considerable amount of interest has lately been shown toward third electrode cells and other exotic methods of charge controls, but these cells are still in the development stages and have not been flown as operational power supplies. In addition, these devices are useful primarily when the maximum charge rate controls the size of the battery, as is often the case of low orbit vehicles. In the case of the ATS-4 battery, size is not determined by the maximum allowable charge rate, but rather the maximum allowable depth of discharge.

6.6.5.3 Method of Sizing

Battery sizing was done assuming worst-case conditions for the amount of power provided by the array during maximum load requirements. Referring to the load profile of Figure 5.8-3, it was assumed that minimum array power output occurs during the peak loads. For a new array, only the 542-watt load must be shared by the battery, but for an old array it can be seen from Figure 5.8-10 that it is sometimes necessary for the battery to share the 222-watt load during the summer solstice and near-summer solstice orbits. In addition, as shown in Figure 5.8-9, the load between the hours of 12 and 13.2 must be completely carried by the battery during maximum eclipse periods. Therefore, the maximum power requirement for the battery would be the sum of a maximum eclipse and the battery share of peak loads. Additionally, power is required from the battery every orbit for peak load

conditions, regardless of the eclipse. This peak load requirement reaches its maximum at maximum sun-array inclination, 23.5 degrees, when array output is lowest. Also, the power required from the batteries increases as the array ages, since array output decreases with time in orbit.

Although there is very little battery test data which is applicable to a 24-hour orbit, some work has been done at the Naval Ammunition Depot at Crane, Ind. with a 24-hour cycle (Reference 17). Two groups of cells were cycled at a 50 percent depth of discharge, one at 25°C. The one at 25°C lasted for 545 cycles, while the one at 40°C failed after 349 cycles. On this basis, it was decided to use as guidelines for battery sizing a maximum 30 percent depth of discharge for a 24-hour noneclipse cycle and a maximum 50 percent depth of discharge for the eclipse loads which occur about 80 times per year. These calculations were based on end-of-life conditions when the array output is lowest.

A summary of sizing calculations is presented in Table 6.6-6.

6.6.5.4 Effect of Two Paddles Versus Four Paddles

One of the considerations in deciding to use four array paddles rather than two paddles was the additional size of the battery which would be required to support a two-paddle vehicle. It was calculated that about 12 pounds more of batteries would be required to sustain similar depths of discharge with a two-paddle system compared to a four-paddle system for array bus capabilities that exceeded the 223-watt level of loads. (See section 6.6.3.3 for additional discussion). This was because of the lower values to which the array output could drop using two paddles and the greater loads the battery would be required to support. It would have been possible to keep the maximum loads from occurring at minimum array output by careful power management, but this would tend to destroy the flexibility of the system.

6.6.5.5 Effects of Load Timing on Batteries

The battery has been sized to provide for eclipse loads and the maximum loads to follow immediately afterward, with the array at minimum power output and without time for recharging of the batteries between loads on any one cycle. For the design load profile,

Table 6.6-6. Battery Sizing And Performance

Item	Notes (Reference Figs. 5.8-9 & -10)	New Array		Old Array (2 years)	
		$\psi = 0^{o}$	$\psi = 23.5^{o}$	$\psi = 0^{o}$	$\psi = 23.5^{o}$
Max. eclipse (watt-hours)	222.3W x 1.2 hr	267	-	267	-
No. 1 peak load (watt-hours)	(222.3-183) 2 hr	-	-	-	79
No. 2 peak load (watt-hours)	(542-bus) 0.5	147	156	175	187
Total load (watt-hours)		414	15€	442	266
Battery energy required	$C_L = \frac{\text{Load}}{(0.90)(0.97)}$	474	179	506	305
Battery capacity required	$C_T = \frac{C_L -}{0.50}$	-	-	1010*	-
Depth of discharge	*Design point	47%	17.7%	50%*	30.2%
Battery capacity (ampere-hours)	Assuming 31.2V 26 Cells	-	-	32*	-
Battery weight (lb)	10 watt-hr/lb	-	-	103	-
Time required to recharge	Assuming minimum array power with 136-watt load			< 8.8 hr	<7.3 hr

it can be seen from Figures 5.8-5, 5.8-9, and 5.8-10, recharging will be accomplished during the first 12 hours of the cycle when load requirements are the lowest. By careful power management, and insuring that the 542-watt load occurs at a time when the array power is at a maximum, the total battery requirements could be reduced by a few pounds. However, it is believed that this savings in battery weight would be more than offset by the loss of flexibility in system performance due to a necessity to accurately program load-time occurrences.

It is useful to know that should a battery failure occur, mission life could possibly be extended by this load-timing principle.

6.6.5.6 Battery Description

Three nickel cadmium batteries are proposed to supply the electrical energy storage requirements of the mission. Each battery is composed of 26 series-connected sealed nickel cadmium cells of 11 ampere-hours nominal capacity. The cells are sealed in stainless cans, with a ceramic bushing being used to isolate the positive terminal from the can. The battery box is not sealed but is designed to physically restrain the cells, supporting them against the internal pressure which develops as a result of normal operation. The battery boxes will be of aluminum construction.

Each battery is provided with a separate charger so that it may be charged independently. Under normal operation, all three batteries will be discharged in parallel so that they may share the loads equally. Should failure of one of the batteries or chargers occur, it is possible to remove the set (battery/charger) from the circuit by command.

6.6.5.7 Battery Performance Summary

A summary of battery performance is shown in Table 6.6-6, where four separate operating conditions are considered: new array at minimum inclination to the sun (with maximum eclipse), new array at maximum inclination (no eclipse), 2-year-old array at minimum inclination (with maximum eclipse), and old array at maximum inclination (no eclipse). Also, in order to estimate worst-case conditions it was assumed that the load profile was oriented such that minimum array output would occur on each cycle at maximum load conditions.

In order to determine if the battery was charge limited, an analysis was made of the power required for recharge at various depths of discharge. This data is shown in Table 6.6-7. A comparison of the charging power requirements of Table 6.6-7 with the power available from the array at end of life. (see Figure 5.8-5) shows that more than sufficient power is available during the first 12-hour period of every 24-hour cycle to completely recharge the batteries to full capacity. That is, conservatively assuming minimum array output at all times (274 watts) and a constant 136-watt load, (160 watts at the array), 114 watts are available for battery charging. It can then be seen from Table 6.6-7 that the batteries can be fully recharged from a 50 percent depth of discharge (maximum eclipse cycle conditions) in less than 8.8 hours of the first 12 hours of each orbit. Similarly the batteries may be fully recharged in less than 7.3 hours from a 30 percent D.O.D. for the end of life, achieved at maximum array inclination conditions. The above recharges can be accomplished with a maximum battery charge current limit set at a C/8 rate. This rate was selected beacuse it is a conservative overcharge rate which will do a minimum of harm to the battery over long periods of time and provide a maximum of system flexibility.

The effect of the initial launch phase loads on battery power was also evaluated. Here the undeployed array is rotating at $\sim$ 72 rpm.

In Figure 5.8-13, the array bus capability at the loads is shown superposed on the maximum load requirements of 109 watts (see Figure 5.8-2). It can be seen that during part of each cycle the battery is required to supply power. Analysis shows, however, that the charging energy available from the array, represented by the area between the unsupplemented array bus and the load line, far exceeds the recharge energy requirements of the battery, represented by the approximate area below the load line amplified by the appropriate inefficiencies of Table 6.6-6 and 6.6-7. Therefore, there will be no net discharge of the battery.

To ensure optimum operating conditions and battery life, it is proposed to operate the battery 0^{o}C and 25^{o}C. A voltage limit will be imposed on the charge regulator to limit the charge rate to an acceptable value at the lower temperatures and prevent an excessive voltage rise which might lead to hydrogen evolution. Hydrogen cannot be tolerated in a

Table 6.6-7. Time and Power Required to Recharge Batteries (33 A-HR)

Charge Rate (B)	Amp-Hr Effic. (A)	Time* Req'd to Recharge from 50% D.O.D. (hr)	Time* Req'd to Recharge from 30% D.O.D. (hr)	Charge Current Req'd $I = \frac{33}{\text{Rate}}$ (amp)	Charge Pwr Req'd $P = \frac{39 \times I}{0.95} = 41\ I$ (watts)	Charge Energy Req'd $E = P \times T$	
						50% D.O.D. (watt-hr)	30% D.O.D. (watt-hr)
7	0.800	4.4	2.62	4.71	193	849	506
8	0.770	5.2	3.13	4.13	169	879	529
9	0.754	6.0	3.57	3.67	150	900	536
10	0.731	6.8	4.10	3.30	135	918	554
11	0.708	7.76	4.57	3.00	123	954	562
12	0.685	8.75	5.25	2.75	113	989	593
13	0.662	9.82	5.88	2.54	104	1021	612
14	0.639	10.95	6.60	2.36	97	1062	640
15	0.616	12.18	7.31	2.20	90	1096	658
16	0.593	13.49	8.10	2.06	84	1133	804
17	0.570	14.91	8.95	1.94	80	1193	716
18	0.547	16.45	9.90	1.83	75	1234	425
19	0.524	18.13	10.85	1.74	71	1287	704
20	0.500	20.00	12.00	1.65	68	1360	816

* Time = $\frac{\text{Charge Rate x D.O.D.}}{\text{Amp-Hr Efficiency}}$

(A) Efficiency assumed linear between 0.80 at C/7 and 0.50 and C/20

(B) Hours required to charge from 0 to 100% capacity if charge efficiency is 100%.

sealed nickel cadmium cell, for it will not recombine as will oxygen and therefore its continued generation results in cell rupture.

6.6.6 POWER SUBSYSTEM ANALYSIS

Having selected a solar array for the primary energy source and a Ni-Cd battery for the secondary energy source, the selection of a power subsystem involving power conditioning equipment is required. The primary considerations affecting the selection are:

a. Power subsystem efficiency - power available at the load compared to power available at the power source

b. Weight of power subsystem

c. Complexity of operation - related reliability

The first selection made was the method of power distribution to the loads, i.e., regulated dc voltage distribution or regulated ac voltage distribution. The regulated dc voltage distribution was selected, and the follow-on effort consisted of comparing three methods of obtaining the dc power distribution. The three methods compared were as follows:

a. Series-switching regulator

b. Series-switching regulator with a voltage limiter

c. Shunt regulator with a battery boost regulator

The selection is the series-switching regulator with a voltage limiter. The power system analysis in the following sections is the basis for the selection.

6.6.6.1 Power Distribution Selection (Dc versus Ac)

The two methods of power distribution compared are regulated dc voltage and regulated square wave ac voltage. The ac voltage is provided through a PWM regulator. The ac voltage is provided through a PWM pre-regulator and a dc-ac inverter. The two representative methods are shown in Figure 6.6-20, Power Distribution Comparison. The efficiencies

indentified in each block are based on analyses carried out in Appendix I, Basic Design Data for Subsystem Comparison. For purposes of comparison, 50 percent of the total load is assumed to require added power conditioning and the remaining 50 percent is assumed useable to the provided dc level. The 50 percent of total power assumption, along with an assumption that five loads are serviced, provides a basis for weight comparison. If the number of loads are more, or the percentage requiring ac is larger, the weight difference increases.

The efficiency comparison is based on the product of the individual component efficiencies required beyond the PWM regulator. The ac distribution efficiency is

$$\eta = \frac{P_{out}}{P_{in}} = (0.98)\ (0.97)\ (0.96)\ (0.89) = 0.812$$

Filter, Rectifier, Transformer, Inverter

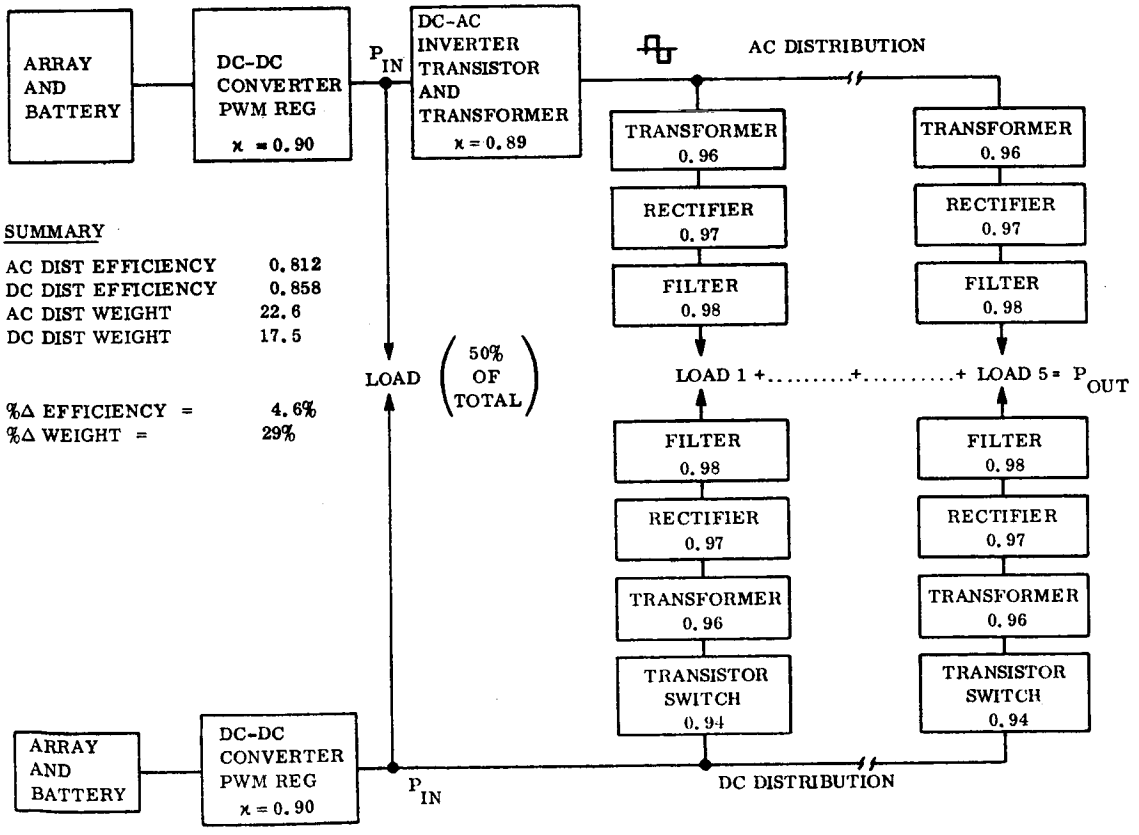


Figure 6.6-20. Power Distribution Comparison

The dc distribution efficiency is,

$$\eta = \frac{P_{out}}{P_{in}} = (0.98)\ (0.97)\ (0.96)\ (0.94) = 0.858$$

Filter, Rectifier, Transformer, Transistor Switch

The difference in efficiency is 4.6 percent. The major cause for the 4.6 percent difference is the added loss credited to the requirement for two power transformers in the ac distribution case. One power transformer is required in the ac inverter, and one is required at the load. The additional transformer also accounts for the added 29 percent in weight for the ac distribution method. The weight breakdown is tabulated in Table 6.6-8.

Table 6.6-8. Power Distribution Weight Comparison

Component	DC Distribution	AC Distribution
DC-DC Converter	12.0	12.0
DC-AC Inverter	0.0	6.6
Load Power Conditioner	1.1 lb / Unit 5.5	0.8 lb / Unit 4.0
Total Weight (Pounds)	17.5	22.6

The dc distribution method was selected based on the weight and efficiency advantage over the ac distribution system.

6.6.6.2 Power Conditioning Equipment Selection

Having selected the approach of providing a regulated dc voltage for spacecraft operational loads and experiment loads, a nominal 28-volt level was selected for this study for purposes of possible utilization of existing equipments. A second requirement on the power conditioning equipment is to provide charging current to the batteries at a maximum rate of C/8.

The three methods compared for providing the regulated 28-volt dc bus and charging the batteries are shown in Figures 6.6-21, 6.6-22, and 6.6-23. The subsystem differences are primarily in the configuration of the following basic components: the solar array, battery, battery charge regulator, and voltage regulator. (For purposes of discussion and comparison, the power control unit and dc-ac inverter are considered part of the load, since the power dissipation in each is constant.) The three systems compared are:

a. Series Regulator, Figure 6.6-21

b. Series Regulator with Voltage Limiter, Figure 6.6-22

c. Shunt Regulator with Boost Regulator, Figure 6.6-23

Due to the various combinations of the basic power system components, the additional components noted are required to assure high efficiency and reliable operation. The added components or functions will be discussed with the description of each power system.

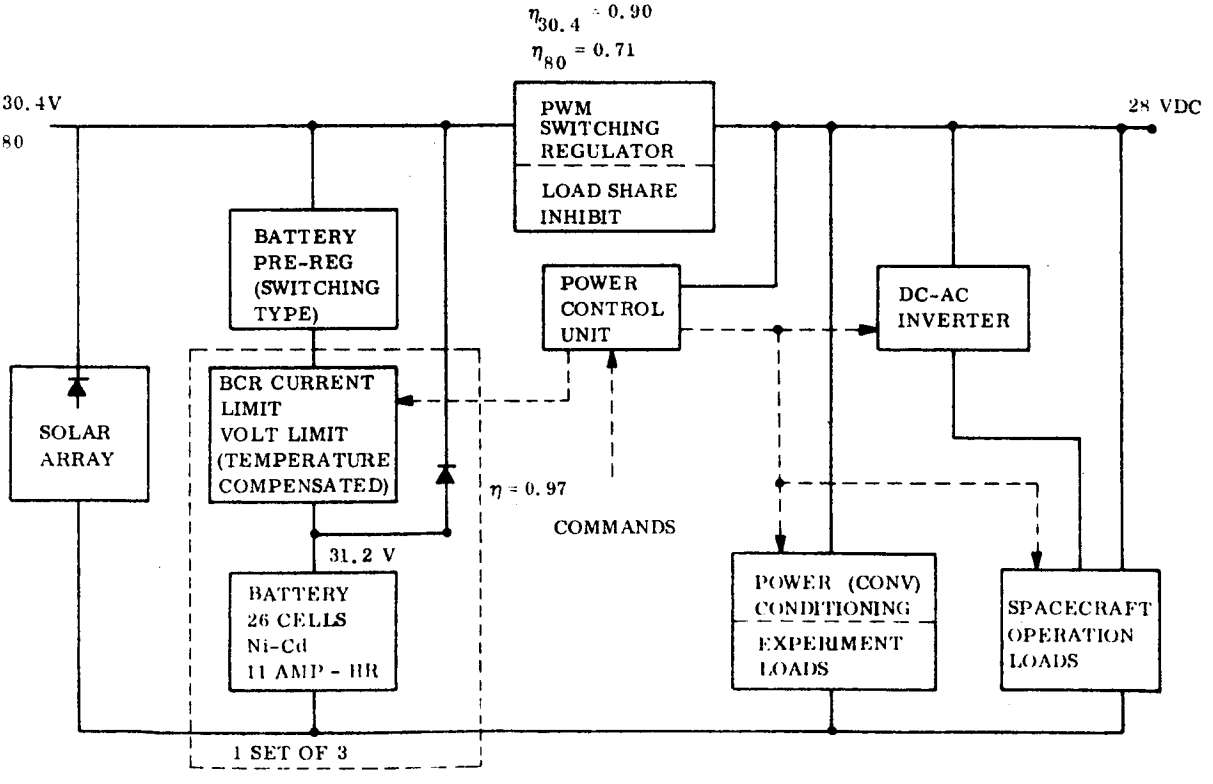


Figure 6.6-21. Power System Block Diagram, Series Regulator

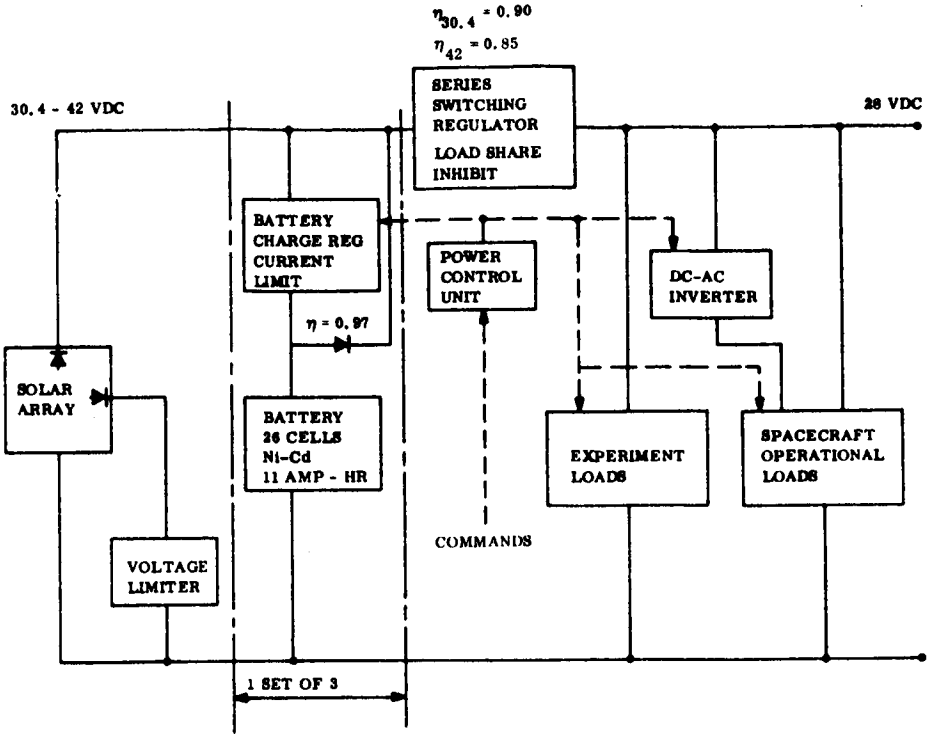


Figure 6.6-22. Power System Block Diagram, Series Regulator with Voltage Limiter

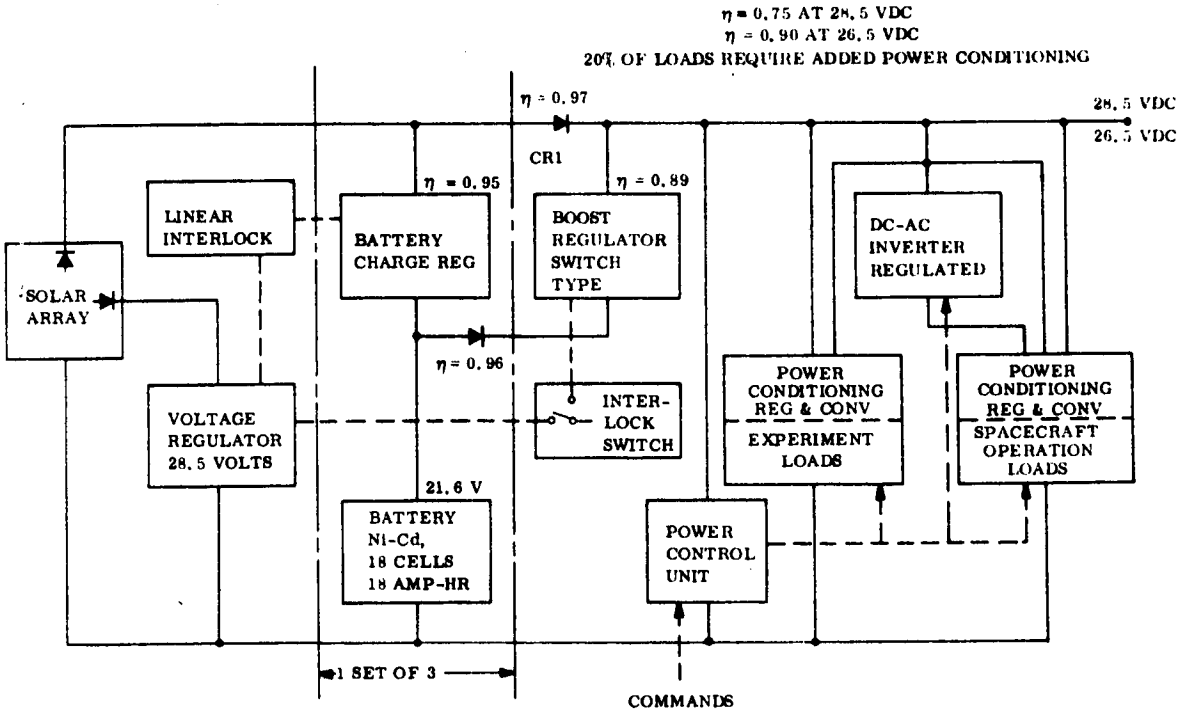


Figure 6.6-23. Power System Block Diagram, Shunt Regulator

6.6.6.2.1 Series Regulator System (Figure 6.6-21)

The series regulator system initially contains only the essential system components. These are:

a. Solar array

b. Battery

c. Battery charge regulator

d. Switching series regulator

This series regulator system was considered because it contains the minimum components to satisfy the output requirements. The regulator input voltage variation is determined by the solar array and battery voltages. From the solar array V-I curve of Figure 5.8-11, for the post-eclipse condition, a maximum array voltage of about 80 volts will result from minimum loads on the array. The battery discharge voltage will be 30.4 volts. The series regulator will dissipate minimum power at the low-input voltage and maximum power at the high-input voltage for any given loads. The efficiency derivation is shown in Appendix I for the minimum input voltage (90 percent at 30.4 volts). An efficiency correction factor of 0.4 percent per volt rise above the minimum is used to estimate the efficiency change as a function of input voltage change. Thus, for the series regulator operating from 30.4 to 80 volts the efficiency at 80 volts is

$$90 - (80.0 - 30.4) \text{ volts} \times \frac{0.4 \text{ percent}}{\text{volt}} = 71.2 \text{ percent}$$

At the post-eclipse array peak power point of about 70 volts, the efficiency would be

$$90 - (70.0 - 30.4) \text{ volts} \times \frac{0.4 \text{ percent}}{\text{volts}} = 75.2 \text{ percent}$$

The lower efficiency at high-input voltages represents added thermal dissipation for any given load. Therefore, the regulator must be designed not only for wide input voltage range but also for a wide thermal variation. The wide input voltage range requires larger input

and output filter components than would a narrow voltage range, and the wide thermal variation results in added weight and complexity for thermal design.

For the battery charge regulator, the efficiency is based on the ratio of battery charge voltage to the source voltage. This efficiency may be from 50 to 95 percent. With this efficiency range, power management as well as thermal control is very difficult. Therefore, a preregulator is provided having an efficiency range similar to the load series regulator. With the use of a preregulator, the battery charge regulator including the preregulator, efficiency range becomes 68 to 85 percent. The charge regulator efficiency has thus increased at the higher voltages with the addition of the preregulator and the thermal dissipation problem is thereby reduced. Therefore, a battery charge preregulator is included as part of the power subsystem. The component weights are tabulated in Table 6.6-9.

Table 6.6-9. Power Conditioning Equipment Weight Summary

Component	Power Conditioning Equipment Weight		
	Series Regulator	Series Reg. with Voltage Limit	Shunt Reg. with Boost Regulator
Power Control Unit	4	4	4
DC-AC Inverter	5	5	5
Battery Charge Regulators	6	6	6
PWM Regulator	15	12	8
Voltage Limiter			5
Control Unit	--	3	3
Resistor Ass'y	--	4	5
Battery Charge Pre-Regulator	5	--	--
Battery	100	100	107
Total Weight (pounds)	135	134	138

6.6.6.2.2 Series Regulator with Voltage Limiter System (Figure 6.6-22)
Since permitting the source voltage to vary from 30.4 volts to 80 volts required an added component (battery charge preregulator) and imposed high heat dissipation requirements on the regulators, a power system providing a voltage limiter was considered.

The voltage limiter selected is a partial shunt regulator selected over a full shunt regulator for the thermal advantage of dissipating only about one half of the maximum available dissipative power. The voltage power tap on the array is about 0.6 of full array voltage.

With a voltage limiter, the series regulator efficiency during the array power period is a minimum of 85 percent and, no thermal post-eclipse transient is generated in the series regulator. In addition, the weight of the series regulator is lighter due to the smaller input and output filter components resulting from the smaller range to input voltage. The battery charge regulator minimum efficiency is 95 percent; therefore, power management is easily predicted. The component weights are tabulated in Table 6.6-9.

For both the series regulator system and the series voltage regulator with a voltage limiter system, solar array/battery load sharing is possible even though adequate solar array power is available to supply full load. This mode of operation is undesirable. An acceptable method of transferring from the load sharing mode is by reducing loads. However, reducing loads restricts spacecraft operation, and since operational restrictions are considered undesirable, a function was added to the regulators for automatically inhibiting a load share mode without interrupting the load (see Section 6.6.6.3). Weight estimates include the inhibit function.

6.6.6.2.3 Shunt Regulator with Boost Regulator System (Figure 6.6-23)
The shunt regulator system was considered for evaluation for the possible advantage of providing 100 percent array power directly to the load without the losses of intermediate series regulation. The shunt regulator power system contains all the basic components discussed for the previous two power systems. The regulators for this system are the partial shunt regulator and the boost regulator. When power is provided to the load from

the solar array directly, the shunt regulator controls the bus voltage. When power is provided to the load from the battery, the boost regulator controls the bus voltage. The boost regulator is required to raise the battery discharge voltage up to the regulated bus voltage. The voltage levels are identified in Figure 6.6-23.

The bus voltage variation is established by the range of regulation of the two regulators required; the shunt regulator regulates from 27.5 to 28.5 volts, and the boost regulator regulates from 26.5 volts to 27.5 volts. Proper load sharing by the array and battery is a design implementation problem which is satisfied by the output voltage range of each regulator and the addition of three interlocks. One interlock is required to assure that the shunt regulator is not dissipating power from the array when the boost regulator is taking energy from the battery. The second interlock is required to gradually remove battery charge current according to load requirements after the shunt regulator has opened, thereby maintaining the bus voltage within required limits. The third interlock, provided by the diode, (CR1), is required to prevent the boost regulator from dissipating energy in the battery charge regulator.

As a result of assuring proper load sharing by the array and battery, a wide voltage variation is established at the bus, which results in the requirement for additional voltage regulation for some loads. From a load analysis, about 20 percent of the loads will require additional regulation. The effect of added regulation for 20 percent of the loads and the diode, CR1, results in an array discharge efficiency of 92 percent. Therefore, the concept of providing of array power to the loads without intermediate losses has been revised.

The component weights are tabulated in Table 6.6-9.

6.6.6.2.4 Selection

A comparison summary of the design factors for each of the three power subsystems considered in the previous paragraphs is presented in Table 6.6-10. The series regulator with a voltage limiter system was selected as the preferred design. This system was selected

as the preferred design primarily for the simplicity of operation (and the reliability) it offered relative to the other two approaches. Weight and efficiency differences of the three subsystems proved to be negligible.

The series regulator with a voltage limiter system is selected over the series regulator system for the following reasons:

a. The greater input voltage variation of the series regulator system increases heat dissipation problems with the series regulator and battery charge regulator due to post-eclipse thermal transients. In comparison, the voltage limiter minimizes heat dissipation in the series regulator and battery charge regulator and allows dissipation of a lesser amount of heat in an especially designed heat-dissipating component located in a select location.

b. The battery charge regulator efficiency of the series regulator system is lower at the array peak power voltage due to the addition of the pre-regulator, necessitated by the need to minimize heat dissipation problems associated with the higher range of input voltages. Therefore, a longer time or more array power is required to charge the battery.

c. Relative complexity is greater for the series regulator system when comparing the complexity of voltage limiter circuitry to efficient battery pre-regulator circuit system.

d. Negligible weight difference.

The series regulator with a voltage limiter system is selected over the shunt regulator with a boost regulator for the following reasons:

a. The objective of a high array to load efficiency for the shunt regulator with a boost regulator system was not fully achieved because the load bus voltage tolerance is greater and requires added voltage regulation for some of the loads, which negated a large portion of the potential gain in efficiency (Table 6.6-10). When the additional inefficiency of the battery boost regulator and its effect on the battery energy requirements is considered, the overall effective array-to-load efficiency is further reduced and only a net gain of about 1.6 percent results.

b. Complexity due to interlocks of the shunt regulator system.

c. Negligible weight difference.

Table 6.6-10. Power Systems Comparison Summary

	Series Regulator	Series Regulator wtih Voltage Limiter	Shunt Regulator with Boost Regulator	Notes
Array Voltage (volts)	30.4 80.0	30.4 42.0	27.0, -0.5 28.0, +0.5	
Loads Voltage (volts)	28 ± 0.5	28 ± 0.5	26.5 28.5	
Loads Voltage Tolerance (percent)	±1.8	±1.8	±3.7	
Required Load Voltage Tolerance (percent)	±2.0	±2.0	*1 ±2.0	*1 2% for approx 20% of loads
Efficiency of Array to Load (percent)	90 @ 30.4 v 71 @ 80.0 v	90 @ 30.4 v 85 @ 42.0 v	92 @ 28 v	v → volts input
Efficiency of Battery to Load (percent)	87.4	87.4	83.8	Non Load Share Mode
Efficiency of Array to Battery (percent)	85 @ 41 v 75 @ 56 v 65 @ 80 v	95 @ 41 v	95 @ 28 v	v → volts input
Complexity, relative	Lowest (No voltage limiter)	--------	Highest Due to interlocks	
Reliability, relative	High	High	*1 High	*1 Lowest due to additional regulation of loads
Day Thermal Dissipation (watts)	33 - 72 100 post eclipse transient	33 - 72	0 - 34	Only Regulator
Eclipse Thermal Dissipation (watts)	24 - 30	24 - 30	28 - 37	Only Regulator
Weight (pounds)	135	134	138	Includes all Power Conditioning Equip.

The efficiency difference of (a) is considered a small gain relative to the complexity of the shunt regulator system interlocks. The operation of the selected system is discussed in Section 5.8.2.3 and Section 6.6.6.3.

6.6.6.3 Selected Power Subsystem Performance

Power system performance is described most easily in terms of load requirements. Load requirements are shown in Figure 5.8-3. The time duration at four power levels are significantly long to consider the power system at steady state. These load power levels are:

a. Load 109 watts

b. Load 246 watts

c. One load between 109 and 246 watts

d. Load 522 watts

e. Reduced load from 522 to 246 watts

The selected power subsystem consists of solar array, battery and battery charge regulator, voltage limiter, and regulator and is shown in Figure 6.6-22. The voltage limiter, battery and battery charge regulator, and regulator and loads are shunt loads on the array bus. The solar array peak power voltage is 41 volts. The voltage limiter is a shunt regulator designed to present a load to the array such that the array voltage will not rise above 43 volts maximum and to present no-load to the array at and below 41 volts. The battery and battery charge regulator present a constant current load to the array from 39 to 43 volts. Below 39 volts, the battery charge regulator reduces the charge according to available array power and load demands. The regulator and load present a near constant power to the array for any of the numerous fixed loads regardless of input voltage between 30.4 and 43 volts. Thus, an analysis of system performance is a summary of solar array power, load requirements and component dissipation. For the analysis presented at each load, only the peak array power at start of performance life is presented, since all possible modes of operation are described through the use of the maximum available peak power.

6.6.6.3.1 Load 109 watts

The analysis for load 109 watts follows.

	Watts		
Solar array peak power-new array	416		
Load requirements		109	
Regulator dissipation		33	
Battery charge - C/8 charge		185	
Total	416	327	
Difference			89
Voltage limiter effective dissipation		89	
	416	416	

The voltage limiter operates at 0.6 array voltage, therefore, dissipates about one-half total available dissipation power. Therefore, the voltage limiter will dissipate 45 to 50 watts.

With the batteries fully charged, the following analysis applies:

	Watts		
Solar array peak power	416		
Load requirements		109	
Regulation dissipation		33	
Battery charge - C/20 charge		72	
Total	416	214	
Difference			202
Voltage limiter effecive dissipation		202	
	416	416	

The voltage limiter will dissipate 100 to 105 watts and be designed such that the major portion of power is dissipated in resistors. The power identified here is the maximum power to be dissipated by the voltage limiter.

6.6.6.3.2 Load 246 watts

The analysis for load 246 watts follows.

	Watts	
Solar array power	416	
Load requirements		246
Regulator dissipation		40
Battery charge		185
Total	416	471
Voltage limiter		0

Load requirements and losses result in a source power deficit; therefore, the array voltage falls below 41 volts resulting in about a 2-percent array power decrease and less charge power is available for the battery. The corrected summary is as follows where the voltage limiter dissipation is negligible and the battery accepts all excess power available.

	Watts	
Solar array power	408	
Load requirements		246
Regulator dissipation (efficiency increased)		33
Battery charge - available excess power		129
Total	408	408

6.6.6.3.3 One load between 109 and 246 watts

This load is considered for discussion because it represents an operational mode related to the voltage limiter design. The voltage limiter consists of a control assembly (transistors power and control) and a resistor assembly. For safe thermal design, the identification of maximum power dissipation is required, and the maximum power dissipation in the voltage limiter control assembly occurs at some load between 109 and 246 watts. The maximum power occurs when the voltage drop across the control assembly equals the voltage drop across the resistor assembly. The maximum control power dissipation is $1/4\ P_{max}$, 26 watts.

6.6.6.3.4 Load 522 watts

To satisfy 522 watt load requirement, the battery is required to supplement the array power, and during solar array/battery load share mode, solar array power is reduced by the voltage ratio 30.4/41.0. Solar array end-of-life minimum power is used here rather than new array maximum power to identify the maximum battery power requirement.

	Watts	
Solar array power-end of life	200	
Battery power	404	
Load requirement		522
Regulator Dissipation		72
Battery discharge diode dissipation		10
Battery charge regulator		0
Voltage limiter		0
	604	604

Battery power requirement is 404 watts.

Battery charge regulator is reverse bias and voltage limiter power is detector power only and considered negligible.

6.6.6.3.5 Reduced Load from 522 to 246 watts

Decreasing the load from 522 watts to 246 watts is a decrease from the load share mode to a mode which should be described in Section 6.6.6.3.2. However, load sharing continues, because the array power capability at 30.4 volts is only 200 watts while the load is 246 watts. If the array voltage could be raised from the 30.4-volt level to 41-volt level, then load share would be inhibited and the dissipation of Section 6.6.6.3.2 applies, or if the load were reduced below the unlock load power of 200 watts, then the load share would be inhibited and the description of Section 6.6.6.3.2 applies. To prevent load sharing under the conditions described above, a function is added to the regulator which inhibits load share without interrupting load power when adequate array power is available. The load share problem is discussed further in Section 6.6.6.3.6.

6.6.6.3.6 Load-Sharing Problem

A potential load-sharing problem exists. Within certain load ranges, the battery may unnecessarily share the load. Figure 6.6-24 shows a V-I curve of the available power (the voltage limiter above 42 volts, the solar array between 42 and 30.4 volts, and the battery below 30.4 volts) with a nominal battery discharge voltage, minus the diode drop, of 30.4 volts. The dashed curves, P_1, and P_2, represent two constant power loads which are generated by the use of a PWM regulator. Assume that the load is initially P_1 and that it gradually increases. The operating point will follow the V-I curve from point A to point B, the approximate peak power point of the array. With an increase above P_2, the operating point will shift from point B, the solar array alone, to point D, the battery and solar array load share mode. A further increase in power will move the operating point further out on the battery curve. Now if the load is decreased to P_1, the operating point will move through D to C with a shift from point C to A. Therefore, the undesirable load sharing occurs from point D to C even though the array is capable of providing all the power in this range. To avoid this unnecessary battery drain and loss of battery charge time, a method is needed to cause the operating point to effectively shift from point D to B. This may be accomplished by momentarily reducing the load supplied

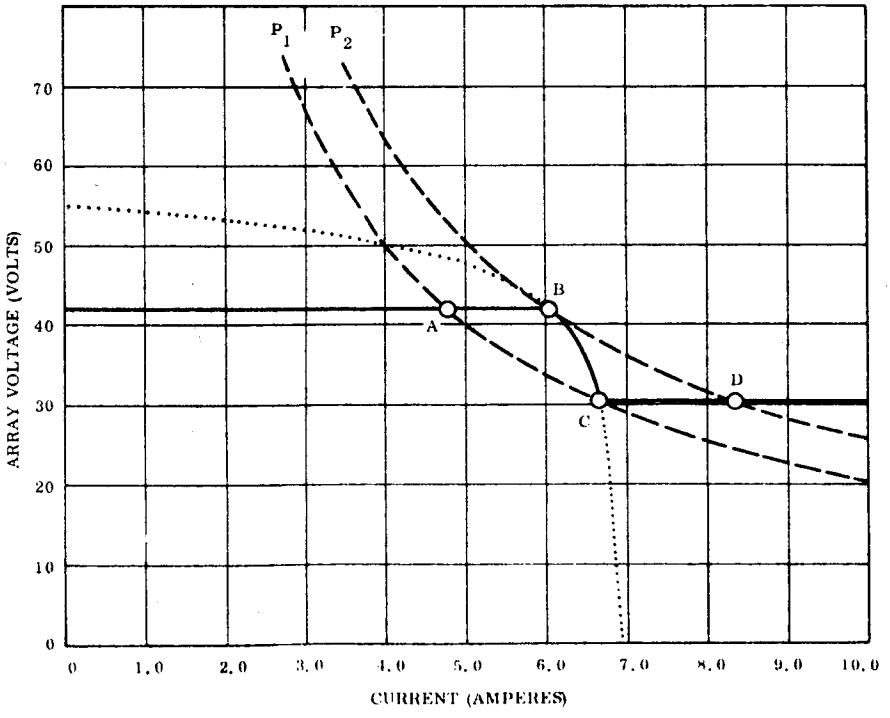


Figure 6.6-24. Load Sharing Problems

from point D to B. This may be accomplished by momentarily reducing the load supplied by the array and battery below the P_1 level. A switching regulator with a partially unfiltered input will produce this effect. However, this will result in increased noise and regulator inefficiency. The load supplied by the array and battery can also be effectively reduced by momentarily supplying the load from another source, such as a charged capacitor. This method consists of discharging a capacitor to the bus at regular intervals during load sharing conditions. The discharge interval will be at a relatively slow rate (once every 15 seconds) so the time averaged noise level will be low, and the PWM regulator prevents transfer of high voltage pulse to loads. The input filter to the switching regulator may be designed for maximum efficiency and minimum noise generation. For these reasons, the latter method has been chosen as the preferred method to inhibit load sharing.

6.6.7 REFERENCES

1. Galbraith, T.L., A Model For The Protons Trapped In The Magnetic Field Of The Earth, presented at the meeting of the American Geophysical Union, Dallas, Texas, September 1-3, 1965.

2. Frank, L.A., "A Survey of Electrons E > 40 kev Beyond 5 Earth Radii with Explorer 14," J. Geo. Res., 70, (7), 1965.

3. Freeman, J.W., "The Geomagnetically Trapped Radiation," presented at 2nd Symposium on Protection Against Radiation in Space, Gatlinburg, Tenn. October 12-14, 1964.

4. Hess, W.N., "Radiation Belts," Trans of Amer Geo Union, 44, (2), 1963.

5. O'Brien, B.J., "The Trapped Radiation Zones," Space Physics, edited by D.P. LeGalley, Wiley & Sons, New York, 1964.

6. Rosen, A., "The Dynamics of the Outer Radiation Zone," Space Physics, edited by D.P. LeGalley, Wiley & Sons, New York, 1964.

7. Vette, J.I., Aerospace Corporation, Correspondence of January 31, 1966.

8. Steiner, H.A., The Natural Environment At The Synchronous Orbital Altitude, Special Technical Report, Office of the Staff Meteorologist, AFSC, Washington, June, 1966.

9. McDonald, F.B., Editor, Solar Proton Manual, NASA X-611-62-122, January, 1963, National Aeronautics and Space Administration, Washington, D.C.

10. Webber, W.R., "Solar Proton Data," Nucleonics, Vol. 21, No. 8, August, 1963.

11. Scherb, F., Velocity Distribution of Interplanetary Plasma Detected by Explorer-X, Proceedings of the Fourth International Space Science Symposium, Warsaw, June, 4-10, 1963.

12. Foelsche, T., Current Estimates of Radiation Doses In Space, NASA-TN-D-1267, July, 1962, National Aeronautics and Space Administration, Washington, D.C.

13. Cunningham, B.T., and Moss, E., Post-Irradiation, Room Temperature, Electrical Characteristics On N/P Silicon Solar Cells, NASA/GSFC Report, August, 1964.

14. Statler, R.L., "Status of Silicon Solar Cell Radiation Damage, "Proceedings of the Fifth Photovoltaic Specialists Conference, Vol. II, 19 October 1965, AD-477120.

15. Slifer, L.W., Jr., "Preliminary Results of the Explorer XXVI Solar Cell Experiment," Proceedings Of The Fifth Photovoltaic Specialists Conference, Vol. II, 19 October 1965, AD-477120.

16. Downing, R.G., "The Energy Dependence Of Electron Damage In Silicon," Proceedings Of The Fourth Photovoltaic Specialists Conference, Vol. I, 2 June 1964, AD-444112.

17. Reference "Evaluation Program for Secondary Spacecraft Cells", Second Annual Report, QI/C 66-304, 13 May 1966, prepared for Goddard Space Flight Center, Contract W11, 252B.

6.7 SPACECRAFT DESIGN

The selected design, and its evolution from initial conceptional studies, has been based on a firm analytical foundation.

The analysis of the major experimental power, and TT&C subsystems has been presented in previous paragraphs. This section groups together the analysis and trade-off rationale for the remaining spacecraft subsystems which have been performed to insure that the overall integration of experimental subsystems has been accomplished in the most efficient manner.

For convenience, these spacecraft subsystems studies are discussed in individual paragraphs, despite their close inter-relation and their significance to the complete system.

These paragraphs are delineated as follows:

a. 6.7.1 Structural Analysis
b. 6.7.2 Separation and Deployment
c. 6.7.3 Dynamic Analysis
d. 6.7.4 Electronic Packaging

The majority of the thermal analysis has been performed on the electronic packaging arrangement and the antenna selected for the final design. This has been discussed in Subsections 5.4, 5.9, and 6.3 and is not repeated here.

6.7.1 STRUCTURAL ANALYSIS

A preliminary structural analysis has been performed for all components of major mass or with functional structural significance, together with a computerized load and stress analysis of the primary structure supporting such components. The related environmental criteria and dynamic response analysis are presented in Paragraph 5.9.2 and Paragraph 6.7.3, respectively.

6.7.1.1 Critical Loading Conditions

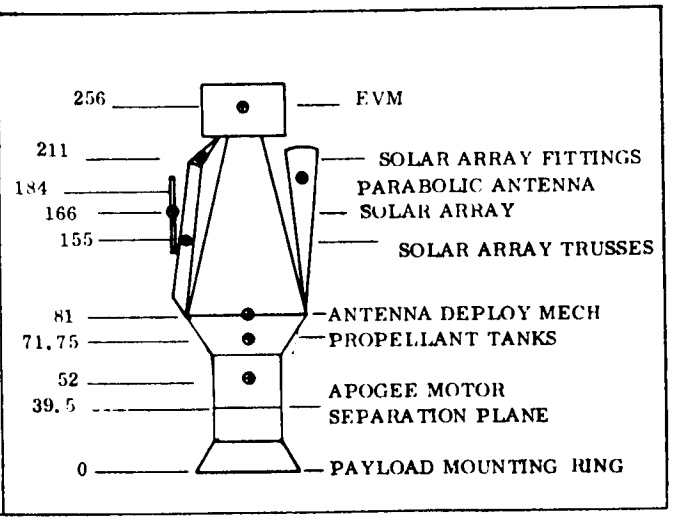
It may be generally stated that the primary structure such as the feed support truss, the aft equipment module, and the spacecraft adapter is critical for the lateral launch environment; and that major components such as the EVM, the equipment bays, the solar array panels and support trusses are critical for both the axial and lateral launch environments.

6.7.1.1.1 Ultimate Launch Loads

Ultimate launch loads in g's presented below in Table 6.7-1 are obtained by multiplying the dynamic response (Reference Paragraph 6.7.3) for the critical mode at the applicable vehicle station by the inputs at the base of the adapter; namely, 1.5 g lateral and 3.0 g axial. In the case of lateral loads acting on components whose centers of gravity lie between the antenna interface ring and the base of the EVM, it was necessary to use a straight line interpolation of the response values quoted at these two stations in order to realistically approximate the loads on the intermediate components. These tabulated loads are used to size structure in all subsequent analyses and are assumed to act individually; that is, there is no combining of axial and lateral loads.

Table 6.7-1. Ultimate Launch Loads (g)

Station	11 cps G_x or G_y (Lateral)	32 cps G_x or G_y (Lateral)	50 cps G_z (Axial)
256	18	↑	30
211	15.9		30
184	13.65	Not	
166	12.15	Critical	30
155	11.40	↓	30
81	5.4	12.3	33
71.75	5.4	12.3	33
52	5.4	12.3	33
39.5	5.4	12.3	33



6.7.1.2 Preliminary Design Philosophy

The objective of the structural analysis is to prove the feasibility of the overall concept and to provide a basis for a reasonable estimate of the structural weight involved. As such, it was not the intent to attempt anything more than a rough cut at structural optimization and it should be recognized that certain areas will require a more detailed analysis and refinement to achieve the desired stress levels and stiffnesses. This objective can be achieved within the present limitations of structural weight.

The extremely complex characteristics of the spacecraft structure, as a single entity, dictated the following basic preliminary design philosophy:

a. Major components such as the EVM, the aft equipment bays, the parabolic antenna, the solar array trusses, and the propellant tank support beams were analyzed independently of the primary structure (feed support truss and aft equipment module).

b. The component loads were applied to the prime structure as mass item loads in relation to their estimated dynamic responses, centers of gravity, and mechanical nature of attaching to the primary structure.

c. No interaction between components or component mounting structure with the primary structure was assumed.

The last facet of the design philosophy is directly applicable to the solar array strusses, the EVM, and the equipment bays due to the non-redundant nature of their reactions on the prime structure; however, a degree of conservatism is introduced into the prime structural analysis by neglecting the interaction of the propellant tank beams with the structure of the aft equiment module. This is particularly true with regard to the antenna interface ring whose large in-plane kick loads at the juncture of the feed support truss can be reduced by the consideration of the propellant tank beam network to partially resist these loads.

6.7.1.3 Methods of Analysis

Methods of analysis were selected in keeping with the design philosophy to be sufficient to determine the validity of the structural concept and establish the structural weight.

6.7.1.3.1 Component Analysis

Component structures such as the EVM, the solar array panels and trusses, the equipment bays and the propellant tank support beams were analyzed by routine methods with standard conservative assumptions occasionally employed to reduce structural elements to statical determinacy.

6.7.1.3.2 Primary Structure Analysis

The complex structural characteristics of the primary structure necessitated the employment of computerized internal loads analysis to assure a reasonable degree of refinement and accuracy in member sizing. Of the several structural programs available, the MASS digital computer program was selected on the basis of proven reliability, versatility, and capacity. This routine is capable of analyzing any three dimensional structure comprised of, or approximated by, straight and curved members, tubes, and panel elements for both static and dynamic effects. The program computes member stiffnesses from basic geometric and physical parameters. Using a deflection technique, a total stiffness matrix for the entire space structure is obtained. Substructures may also be used to build up the total system to enable the routine to handle very large structures. The routine sets up the force-deflection relationships, which are then solved for internal loads, stresses (if desired), and deflections. Included, is the capability to account for pinned and sliding connections anywhere in the structure, unsymmetrical bending, distributed mass, rotary inertia effects, rigid eccentric connections, shear distortion, variable section properties and loadings, thermal gradients, and flexible supports.

Component loads for the critical lateral condition were applied to the spacecraft primary structure by elementary theory in relation to the centers of gravity of the components involved. Additionally, the weight of primary structure was included, thereby obtaining a truly representative condition of lateral loading.

A feature of the primary structural analysis presented here is the inclusion of the computer output sheets for selected critical members. The print-out for all straight and curved members initially repeats all input data such as joint coordinates, section, and material parameters. Member loads and moments are given both with respect to the X, Y, and Z coor-

dinates of the entire structure and also the actual plane of the member itself (normalized sign convention). Normal deflections and load calculations are also applicable to the actual plane of the member. The coordinate sign convention and the normalized sign convention are illustrated in Figure 6.7-1.

The structural representation of the primary structure is given in Figure 6.7-2 which defines the member and joint locations and the rectilinear system of coordinate axes.

6.7.1.4 Selected Configuration Design Rationale and Tradeoffs

The major objectives of the overall structural design were:

a. To provide a minimum weight, state-of-the-art, structural configuration capable of supporting all components at their various exacting locations under the design ultimate loadings.

b. To provide a structure with such an overall inherent stiffness as to meet the stipulated natural frequency requirements during both boost and orbital phases.

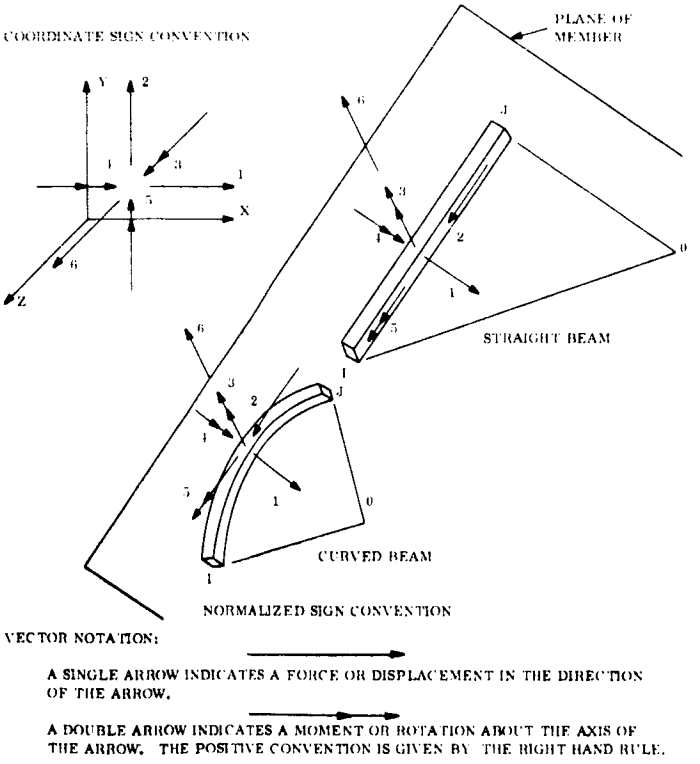


Figure 6.7-1. Coordinate and Normalized Sign Conventions

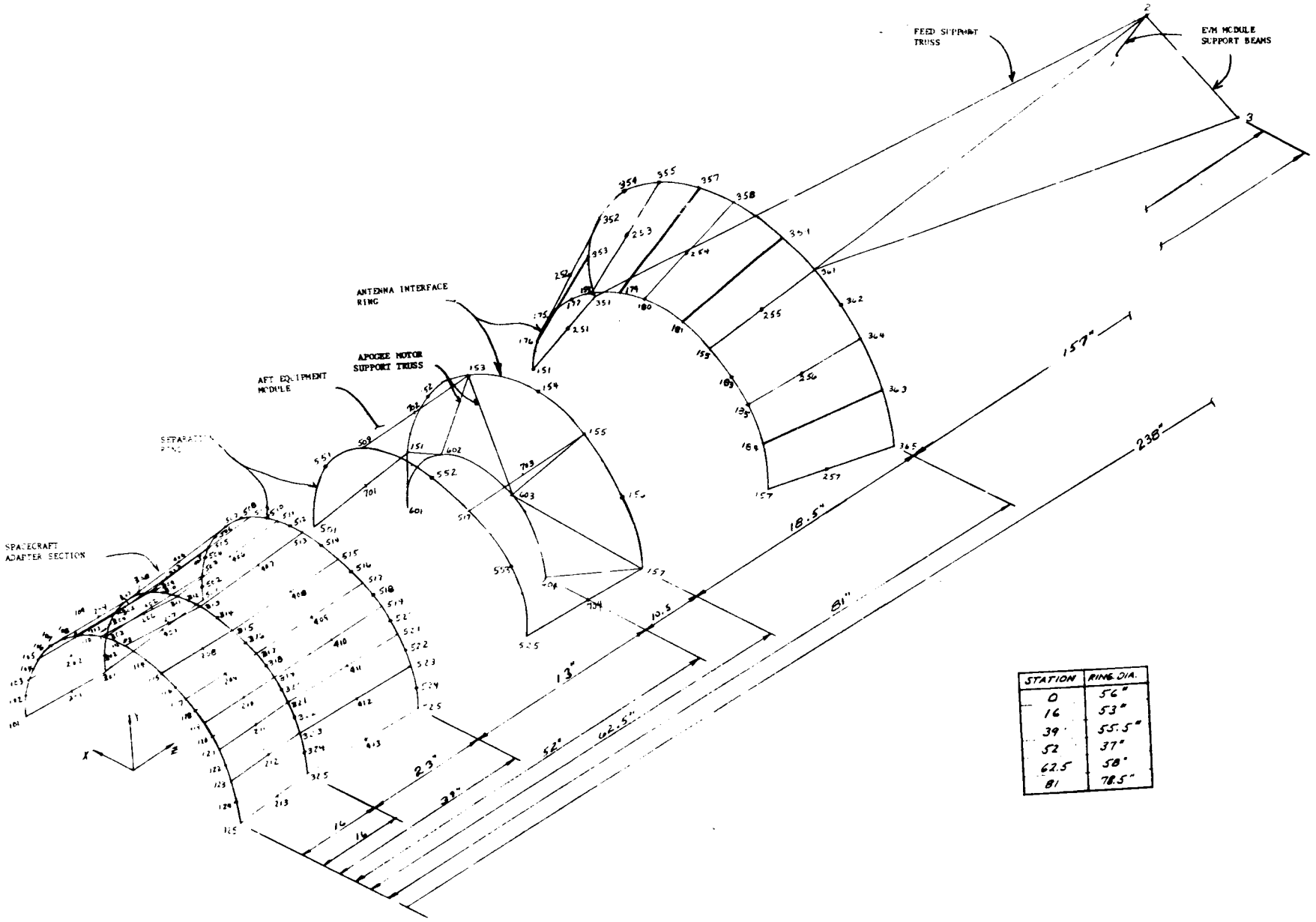


Figure 6.7-2. Primary Structure Model

Such requirements presented a structural paradox in that in many areas it was necessary to provide structure for stiffness requirements that was not required solely on the basis of strength to resist the ultimate loading conditions. This is particularly true in areas such as the spacecraft adapter and the solar array trusses where stiffness is the governing design parameter. It was also necessary to resort to a non-optimum structure for the antenna feed and EVM support truss in order to limit the degradation of the rf performance characteristics of the parabolic antenna.

Other important factors having a pronounced effect on the selected structural configuration were:

a. The necessarily large mass of equipment located or reacting upon the Earth Viewing Equipment Module.

b. The small diameter of spacecraft adapter permitted by the Centaur payload mounting ring.

The significance of the above stated design constraints is apparent when one considers the spacecraft as a long cantilever beam with a large tip mass, a narrow root at the fixed end (the Centaur payload mounting ring) and a rather flexible structural link (the feed support truss) in between. The resulting primary structure is rather soft laterally and therefore critical for the significant launch lateral load conditions and lateral natural frequency requirements (10 cps).

The approach to the structural design as discussed below was to optimize the feed support truss with regard to stiffness and strength as much as possible within rf performance limitations and then to tailor the aft equipment module to obtain the overall strength and stiffness requirements.

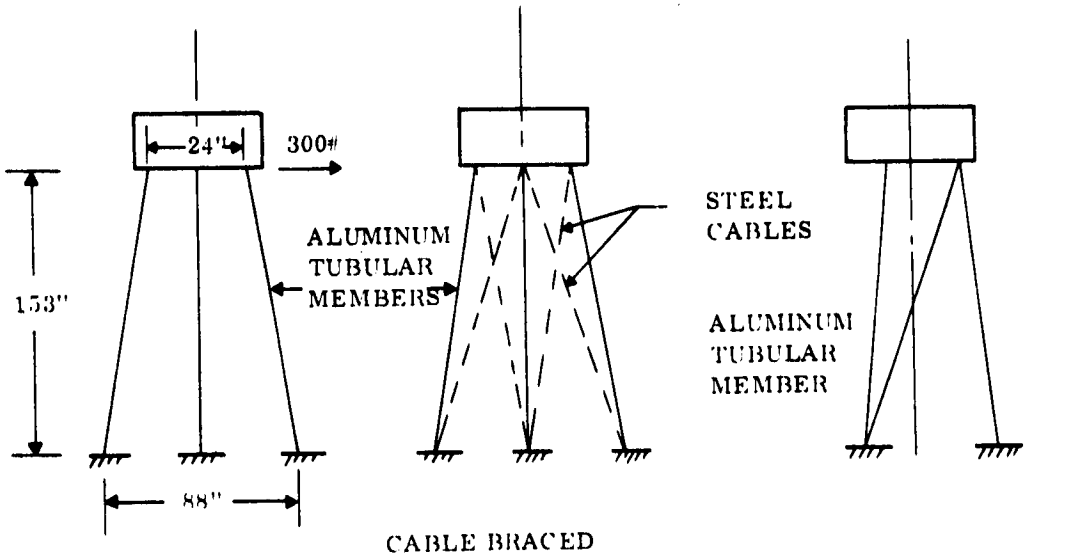
6.7.1.4.1 Feed Support Truss Optimization

A parametric tradeoff study was conducted to determine the optimum feed and support structure (consistent with antenna performance requirements) with the tip mass assumed to be 300 pounds. The structures were sized to achieve a minimum lateral natural frequency of 10 cps

and considered to be hard mounted at the base. The basis of comparison was solely upon the structural weight involved.

Among the concepts investigated were a four-legged tubular aluminum rigid frame (quad-pod), a "quad-pod" with diagonal bracing of steel cables, and a six diagonal member pinned-end aluminum tubular truss similar to that currently being utilized on Nimbus. Presented below in Figure 6.7-3 are the results of the tradeoff study. The weights quoted are for the tubular members (and cables) alone and include no allowances for end fittings or top cross bracing. Envelope dimensions for each concept are identical.

It is evident that the truss tube concept is optimum from stiffness considerations and being pinned-ended, allows for precise adjustment of the feed and EVM with respect to the parabolic antenna.



QUAD - POD

Tube Dia	Wt
8"	205
10"	131
12"	91
14"	67

CABLE BRACED
QUAD - POD
(TUBE DIA 8" ALL CASES)

Tube Wall Thickness (in.)	Cable Dia (in.)	Wt.
0.015	0.435	80.3
0.020	0.395	78.1
0.032	0.348	86.8
0.050	0.305	106.5

DIAGONAL TRUSS

Tube Dia	Wt
4"	25.8

Figure 6.7-3. Results of Feed Support Truss Trade-Off Study

At the point in time of this investigation, the tube buckling strength was adequate to resist anticipated lateral loads; however, a subsequent revision of lateral loads to a shaker-type environment markedly increased the axial tube loads. As such, a truss arrangement would prove even more superior to the rigid frames, comparatively, but would require a substantial increase in buckling stiffness to withstand the higher loads. It was determined that tapered aluminum alloy tubes of 5-inch maximum diameter and weighing a total of 83 pounds would suffice for this condition of lateral loading; but, through the use of non-tapered extruded beryllium tubes, the diameter could be reduced to 3.25 inch and the attendant tube weight to 36.3 pounds thus enhancing the antenna performance characteristics and improving the overall weight picture. This tradeoff is presented in the first computer print-out sheet in the analysis proper.

6.7.1.4.2 Optimization of the Aft Equipment Module and Adapter

a. Module and Spacecraft Adapter - In order to obtain a spacecraft with an overall lateral natural frequency of vibration of 10 cps per second and recognizing the flexibility of the feed support truss, it was necessary to establish a stiffness criteria for the aft structure (Aft Equipment Module and Spacecraft Adapter) acting independently of the feed support truss. From preliminary dynamic analysis, it was determined that the required lateral spring constant of this aft structure must be a minimum of 357,000 pounds-per-inch (deflection at Station 81) to achieve the desired overall lateral frequency in combination with the feed support tubes chosen. This spring constant requirement can be expressed by the following equation:

$$E\delta = \int_0^{18.5} \frac{M x dx}{I_1} + \int_{18.5}^{42} \frac{M x dx}{I_2} + \int_{42}^{65} \frac{M x dx}{I_3}$$

$$+ \int_{65}^{81} \frac{M x dx}{I_4}$$

where

$$E = 10 \times 10^6 \text{ psi}$$

$$\delta = 1 \text{ inch}$$

$$M = 357{,}000\ x$$

$$I_1 = \pi t_1 (39.25 - .5545x)^3$$

$$I_2 = \pi t_2 (29.99456 - .05376x)^3$$

$$I_3 = \pi t_3 (29.99456 - .05376x)^3$$

$$I_4 = \pi t_4 (20.40625 - .09375x)^3$$

Reference to the geometry of the aft structure shown below, this equation reduces to:

$$85.99971 = \frac{0.06868}{t_1} + \frac{1.09338}{t_2} + \frac{3.34580}{t_3} + \frac{4.22346}{t_4}$$

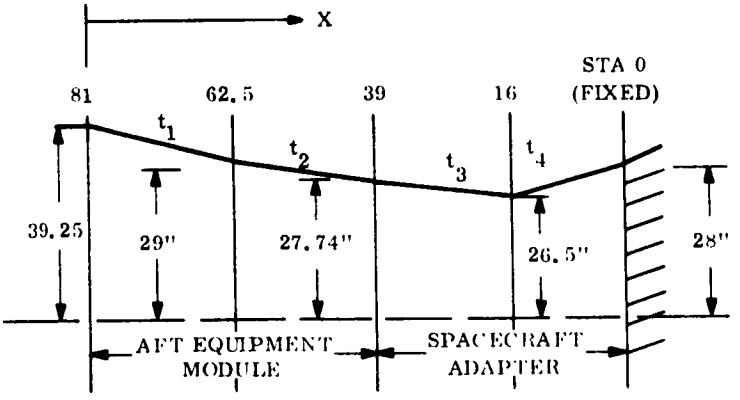


Figure 6.7-4. Geometry of the Aft Structure

Thicknesses t_1, t_2, etc., refer to effective thicknesses of aluminum structure. The optimization procedure was then based on the desire to provide the required thicknesses in such a manner as to minimize the orbital weight of the spacecraft (Aft Equipment Module) and still maintain the required strength to resist the lateral bending loads. As such, the aft equipment module is sized from strength considerations and the spacecraft adapter supplies the bulk of the stiffness required to achieve the desired lateral spring constant. The effective thicknesses of aluminum skin are then calculated by an iterative process as the following:

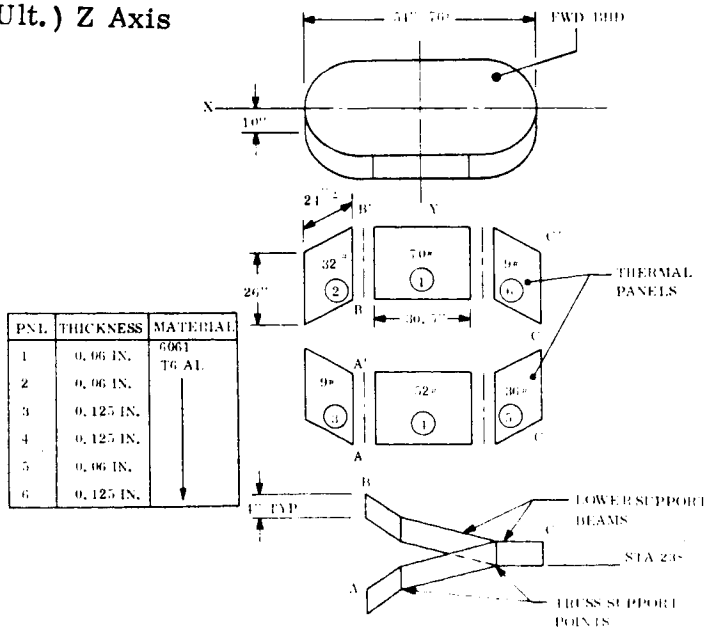
$$t_1 = 0.0297 \text{ inch}$$
$$t_2 = 0.0389 \text{ inch}$$
$$t_3 = 0.1146 \text{ inch}$$
$$t_4 = 0.1600 \text{ inch}$$

These thicknesses include all axial members and related effective skin acting with these members.

In an effort to achieve unbuckled skins in the adapter section, hence a more effective utilization of skin for stiffness, magnesium skin of equivalent stiffness was substituted for the originally contemplated aluminum skin. A similar material change in the Aft Equipment Module would have little benefit inasmuch as the bolted connections at the separation plane (Station 39) prohibit the development of significant direct skin stresses.

b. Earth Viewing Module.

Critical Load Condition
Lateral: 18 g (Ult.)
Axial: 30 g (Ult.) Z Axis



PNL	THICKNESS	MATERIAL
1	0.06 IN.	6061 T6 AL
2	0.06 IN.	
3	0.125 IN.	
4	0.125 IN.	
5	0.06 IN.	
6	0.125 IN.	

Exploded View
(Bhds. Sta. 242 and 268 Omitted for Clarity)

Fwd. Bhd. - Axial Load

Assume circular plate uniformly loaded with no stiffening from modules

Max. face sheet bending stress

$$f_b = \frac{K_1 W}{t_e^2} \quad \text{(Ref. 3)}$$

$K_1 = 0.398$

$W = 76 \times 30 = 2280$ lb

t_e is the thickness of isotropic plate with bending stiffness equivalent to that of the fwd. honeycomb bhd.

$$\frac{t_e^3}{12} = \frac{t_f h^2}{2}$$

$$t_e = \sqrt[3]{6\, t_f h^2}$$

t_f = Face sheet thickness

h = Distance between facing centroids

$$f_b = \frac{0.398 \times 2280}{\left|6\, t_f h^2\right|^{2/3}}$$

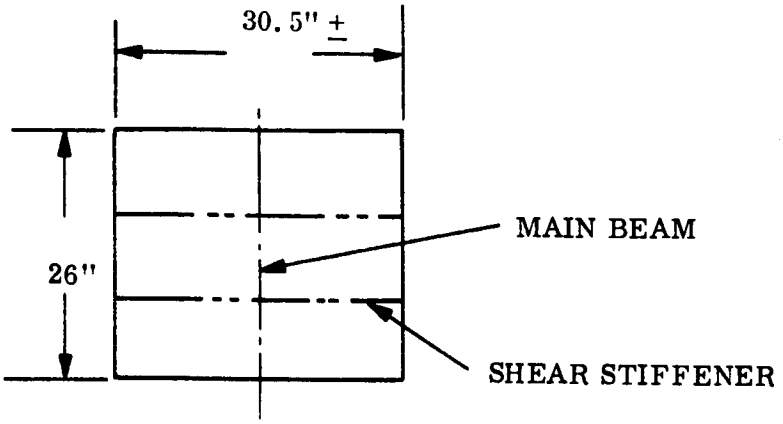
For 5052 aluminum core @ 1.6 lb/ft^3
and 0.005 - inch - 5052 H38 aluminum alloy face sheets (F_{cy} = 29,000 psi) the face sheet dimpling stress is 19,870 psi (Ref. solar array structural analysis which follows).
The minimum allowable for "h " is then .571"

Use 0.625 inch thick core, h = 0.625 + 0.005 = 0.63 inch

$$f_b = \frac{0.398 \times 2280}{\left|6 \times 0.005 \times 0.63^2\right|^{2/3}} = 17,450 \text{ psi}$$

$$MS = \frac{19870}{17450} - 1 = +0.14 \text{ face sheet dimpling}$$

Thermal Panel No. 1 - Lateral Load



Maximum beam moment

$$M_m = \frac{70 \times 18}{2 \times 26} \times \frac{26^2}{8} = 2050$$

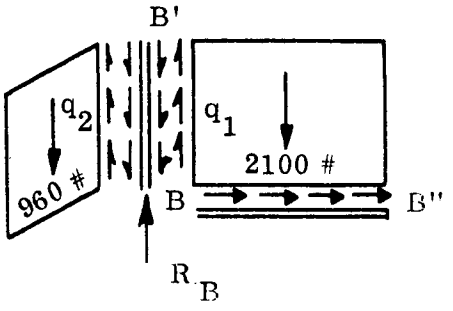
Moment capability of 2 x 3/4 x 0.040 | - 7075 T6 Aluminum alloy is 3000 in.lb (Ref. 2)

$$MS = \frac{3000}{2050} - 1 = +0.46 \text{ crippling}$$

A similar amount of bracing is required for panels No. 2, 3, and 4.

Thermal Panel No. 1 - Axial Load

Assume Panel No. 1 and 2 loads taken entirely by member BB'



$$q_1 = \frac{2100}{26} = 80.7 \text{ ppi}$$

$a = 15.25$

$b = 26/2 = 13$

$\frac{b}{a} = 0.853$

$k = 8.8$

$$q_{cr} = \frac{8.8 \times 10 \times 10^6 \times 0.06^3}{13^2} = 112.5 \text{ (Ref. 2)}$$

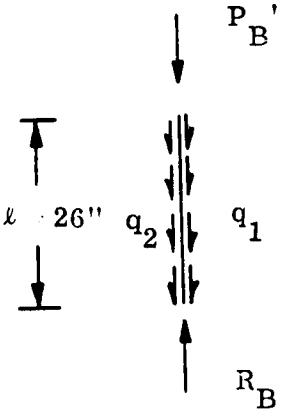
MS = + 0.39 shear buckling

Required $I_s = 1.64 \times 15.25 \times 0.06^3 = 0.0054$

$1 \times \frac{1}{2} \times 0.040$ inch < adequate

typical for Panels No. 2 and 3

Typical Longeron BB', Axial Load



$$q_1 + q_2 = \frac{2100 + 960}{26} = 117.8 \text{ ppi}$$

$P_B' = 810$ Load due to unaccounted for weight such as structure, wiring, misc. equipment.

Min. Required $I = \frac{\ell^2}{\pi^2 E} \left| 810 + 117.8 \frac{\ell}{2} \right|$ (Ref. 5)

$$= \frac{26^2 \times 2340}{\pi^2 \times 10.6 \times 10^6} = 0.0151$$

For members BB' and AA' use $1\frac{1}{8}$ x $1\frac{1}{8}$ x .035 $\sqcap$ 7075 -T6 Aluminum alloy

$I = 0.0275$

$A = 0.1435$ $\quad \frac{\ell}{\rho} = 60$ use long column formula

$\rho = 0.434$

$$f_c = \frac{810 + 26 \times 117.8}{0.1435} = 27,000 \text{ psi}$$

$$F_c = \frac{\pi^2 E}{(\ell/\rho)^2} = 28,600 \text{ psi}$$

MS = + 0.06 buckling (O.K. for crippling)

Longeron CC'

Use $1\frac{1}{4}$ x 7/8 x 0.04 I - 7075 -T6 Aluminum alloy

$I = 0.0290$

$\rho = 0.509$ $\qquad \frac{\ell}{\rho} = 51.1$ use long column formula

$A = 0.112$

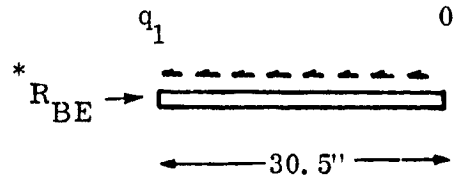
$$f_c = \frac{3870}{0.112} = 34,600 \text{ psi}$$

$$F_c = \frac{\pi^2 \times 10.4 \times 10^6}{51.1^2} = 39,300 \text{ psi}$$

$\frac{b}{t} = \frac{0.4375}{0.04} = 11$ $\qquad F_{cc} = 46,000$ psi (Ref. 2)

M.S. = + 0.14 buckling

Typical thermal panel framing member BB''



$$R_{BE} = \frac{q_1}{2} \times 30.5 = 1230 \text{ lb}$$

*Kick loads are taken by aft bhd.

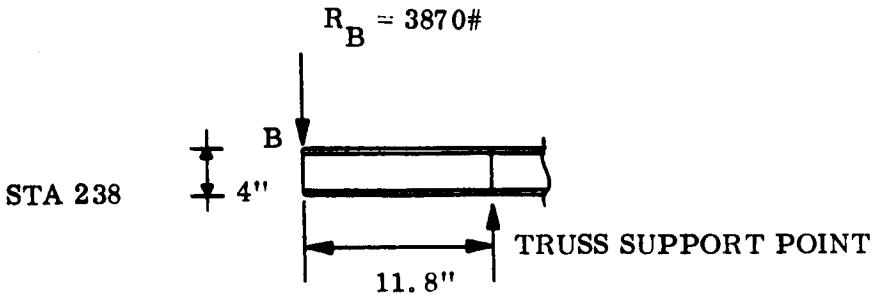
Buckling is prevented by thermal panel and aft Bhd.

Use 1 x 1 x 0.040 ∠ 7075 T6 Alum. Alloy F_{cy} = 71,000

$$f_c = \frac{1230}{0.076} = 16200 \text{ psi}$$

M.S. High

Lower support beams - Axial Load



Moment at truss support point

M = 3870 x 11.8 = 45,600 inch pound

Use AND10140 - 4003 - 7075 T6 Aluminum Alloy

I = 2.424

A = 0.969

$$f_B = \frac{45,600 \times 2}{2.424} = 37,600$$

$$\frac{b}{t} = \frac{1}{0.125} = 8 \qquad F_{cc} = 58,000 \qquad \text{(Ref. 2)}$$

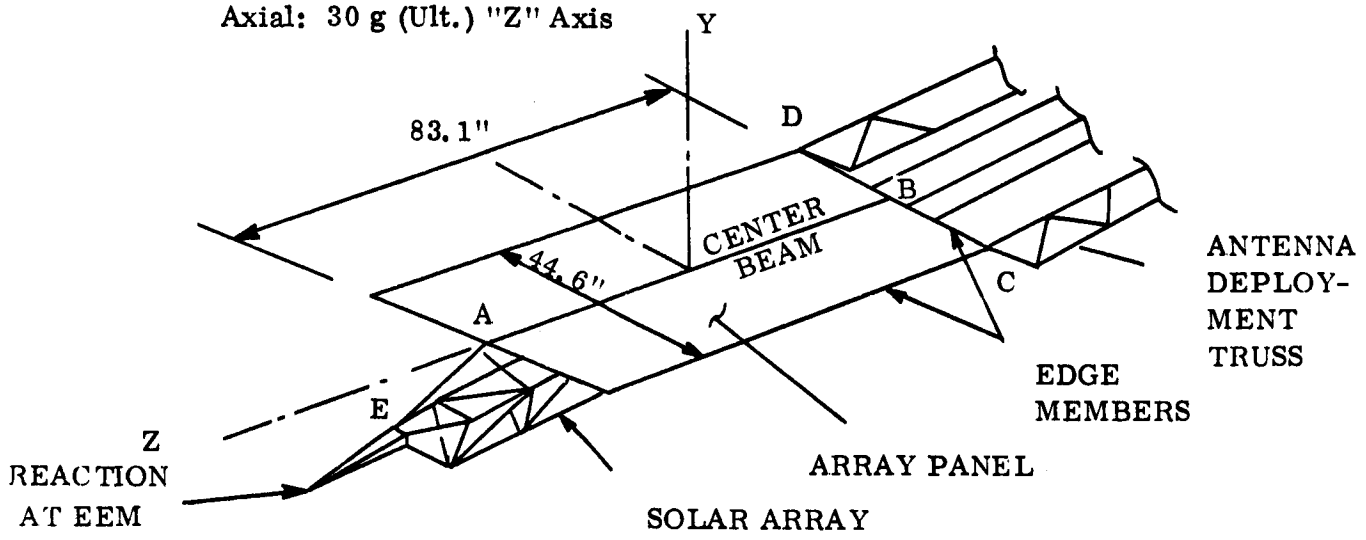
M.S = + 0.54

Pitch Axis Solar Array Panels

Critical Load Condition (Boost Phase)

Lateral: 12.15 g (Ult.) "X" or "Y" Axis

Axial: 30 g (Ult.) "Z" Axis



Panel loaded in "Y" direction

Panel is assumed to be cantilevered from center beam

Assumed weight/square foot of panel, solar cells, wiring, edge members, etc. is 1.3 lb/ft^2

Panel face sheets

0.005 inch thick 5052-H38 aluminum alloy, F_{cy} = 29,000 psi

0.3 inch thick core 5052 aluminum alloy @ 1.6 lb/ft^3

G_c' = 12,800 psi effective shear modulus

t_s^c = 0.0007 inch cell wall thickness

s = 0.25 inch cell size

F_s' = 90 psi core shear strength

Pitch Axis Solar Array Panels

Face sheet wrinkling stress

$$\frac{F_{cw}}{\eta_2} = 0.43 \sqrt[3]{E_f E_c' G_c'} \qquad \text{(Ref. 4)}$$

For $s/t_s = 357$

$$\frac{F_{cw}}{\eta_2} = 40{,}000 \text{ psi} \quad \text{Ref. 4 Fig. 12.5.7a}$$

$$\frac{F_{cy}}{F_{cw}/\eta_2} = \frac{29000}{40000} = .725$$

$$F_{cw}/F_{cy} = 0.98 \qquad \text{(Ref. 4 Fig. 12.5.7b)}$$

$$F_{cy} = 28,400 \text{ psi}$$

Face sheet dimpling

$$\frac{F_{ci}}{\eta} = 0.75 E_f \left(\frac{t_f}{s}\right)^{3/2} \qquad \text{(Ref. 4)}$$

For $\frac{s}{t_f} = 50$

$$\frac{F_{ci}}{\eta} = 21,000 \qquad \text{(Ref. 4 Fig. C12.5.2a)}$$

$$\frac{F_{cy}}{F_{ci}/\eta} = 1.38$$

$$\frac{F_{ci}}{F_{cy}} = 0.685 \qquad \text{(Ref. 4 Fig C12.5.2b)}$$

$$F_{ci} = 19,870 \text{ psi critical}$$

Max face sheet stress due to panel bending

$$f_b = \frac{M_m \frac{h}{2} \times 2(1-\mu^2)}{t_f h^2}$$

Pitch Axis Solar Array Panels

Where M_m is the max panel bending moment at center beam

t_f is the face sheet thickness

h is the distance between centroids of face sheets

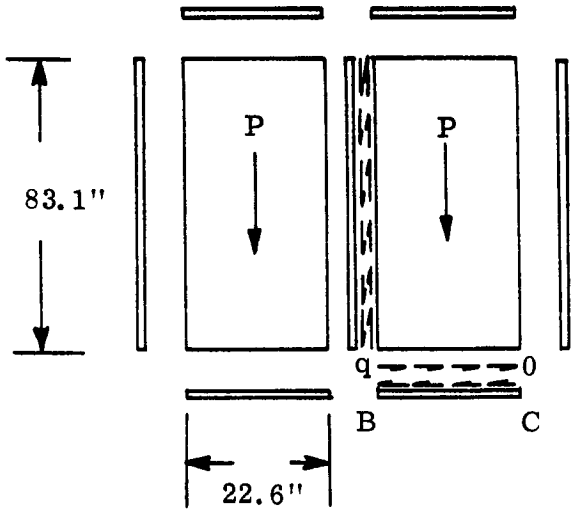
μ is Poisson's ratio for face sheet material

$$M_m = \frac{1.3}{144} \times 12.15 \times \frac{22.3^2}{2} = 27.3 \text{ in lb per inch of panel length}$$

$$f_b = \frac{27.3 \times 0.91}{0.005 \times 0.305} = 16300 \text{ psi}$$

$$\text{M.S.} = \frac{19870}{16300} - 1 = +0.22 \text{ dimpling}$$

Short edge members, load in Z direction



$$P = \frac{83.1 \times 22.6}{144} \times 1.3 \times 30 \text{ g}$$

$$= 508 \text{ pounds}$$

$$q = \frac{508}{83.1} = 6.11 \text{ ppi}^*$$

Buckling of member BC

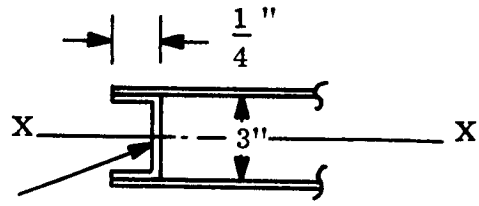
$$\frac{1}{2}(q_{av}\ell)_{cr} = \frac{\pi^2 EIxx}{\ell^2} \qquad \text{(Ref. 5)}$$

$$\text{Required } I_{xx} = \frac{22.6^2 \times 6.11 \times 22.6}{4 \times \pi^2 \times 10 \times 10^6} = 0.00018 \text{ in.}^4 \text{ (6061-T6 Alum. Alloy)}$$

* Face sheet shear stress $f_s = \frac{6.11}{2 \times 0.005} = 611$ psi

Panel good for shear by inspection

Solar Array Edge Member

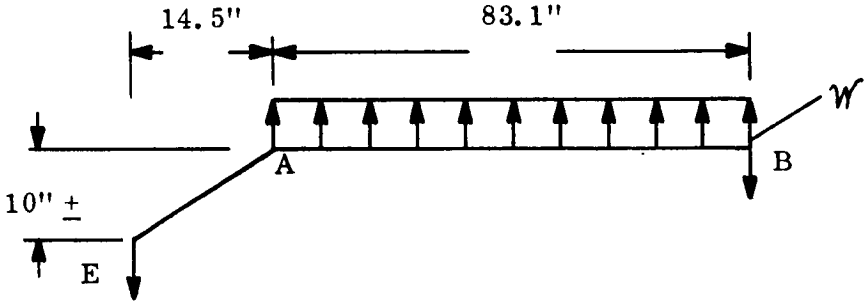


t = 0.015 TYP

$$I_{xx} = \frac{0.015 \times 0.27^3}{12} + 2 \times 0.25 \times 0.015 \times 0.1425^2 = 0.00018 \text{ conservative}$$

Typical for long edge members

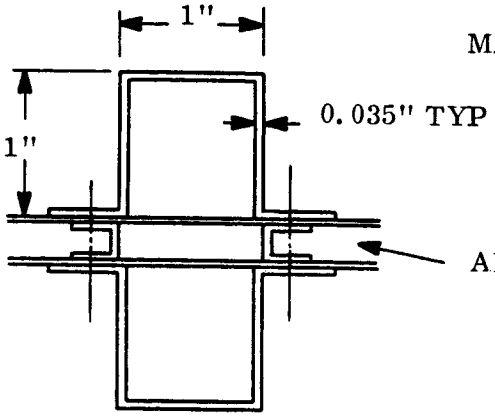
Solar Array Center Beam - Load in "Y" Direction
Assume all loads are reacted at "B" and "E"



$$W = \frac{1.3 \times 44.6}{144} \times 12.15 \text{ g} = 4.9 \text{ lb/inch}$$

$$M_{max} = \frac{4.9 \times 83.1 \times 56.05}{97.6} \left(\frac{83.1 \times 56.05}{2 \times 97.6}\right) = 5590 \text{ inch-pound}$$

Solar Array Center Beam



MATL 7075 T6 ALUM AL

Neglect shear tie in array

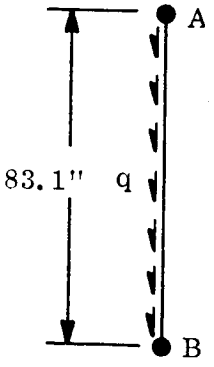
$$I = 2 \times 0.0190 + 2 \times 0.1271 \times 0.65^2 = 0.1453$$

$$f_b = \frac{5590 \times 1.15}{0.1453} = 44,200 \text{ psi}$$

$$\frac{b}{t} = \frac{1}{0.035} = 28.6 \qquad F_{cc} = 50,000 \text{ psi} \quad \text{(Ref. 2)}$$

M.S. = + 0.13 crippling

Load in "Z" direction



$$q = \frac{83.1 \times 44.6 \times 1.3}{83.1 \times 144} \times 30 \text{ g}$$

$$= 12.08 \text{ ppi}$$

$$q_{cr} = \frac{\pi^2 EI}{1/2\, \ell^3} = \frac{\pi^2 \times 10.4 \times 10^6 \times 0.1453}{0.5 \times 83.1^3} = 52 \text{ ppi}$$

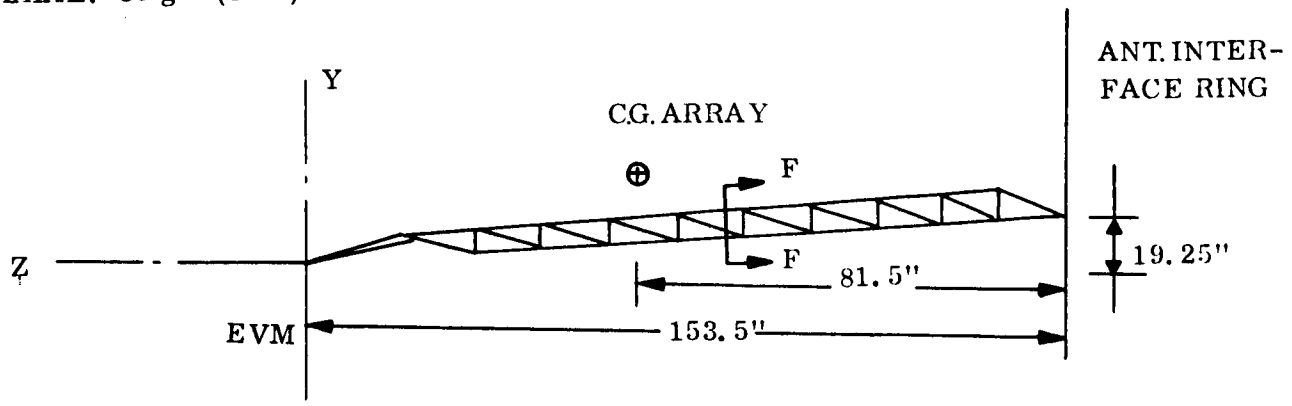
M. S. High for buckling

Solar Array Trusses

CRITICAL LOAD CONDITION ON ARRAY

LATERAL: 12.15 g (ULT) "X" OR "Y" AXIS

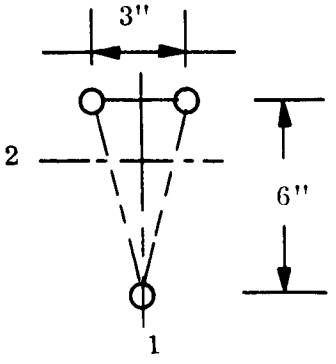
AXIAL: 30 g (ULT) "Z" AXIS



Axial buckling - load in "Z" direction

Load along axis of truss

$$P_A = \frac{83.1 \times 44.6}{144} \times 1.3 \times 30\ g \times \frac{154.7}{153.5} = 1010 \text{ pounds}$$



SECT FF

Orbital natural frequency criteria requires minimum cap areas of 0.134 square inch (Aluminum)

Solar Array Trusses

For buckling about weak axis 1-1

$$P_{cr} = \frac{\pi^2 K E I_1}{L^2} \qquad \text{(Ref. 6)}$$

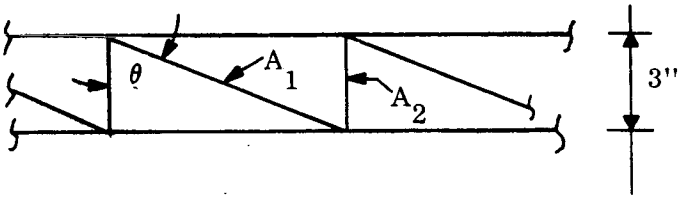
where

$L = 154.7$ inches

$I_1 = 2 \times 0.134 \times 1.5^2 = 0.603$ in.^{4}

$E = 10.1 \times 10^6$ psi (6061 T6 Aluminum Alloy)

$$K = \frac{1}{1 + \frac{4.93\, I_1}{A_1 L^2 \cos^2\theta \sin\theta} + \frac{4.93\, I}{A_2 L^2 \tan\theta}}$$



Top plane of truss

Assume panels 15.875 inches long

$A_1 = A_2 = 0.0503$ (3/4 inch O.D. x 0.022 inch W.T. tubing)

$\tan\theta = 5.292$

$\sin\theta = 0.98261$

$\cos\theta = 0.18567$

$$K = \frac{1}{1 + 0.07290 + 0.0047} = 0.93071$$

$P_{cr} = 2338$

M.S. = +1.31 overall buckling

Similar side wall bracing will be adequate for buckling about 2-2 axis

Solar Array Trusses

Caps are critical for local buckling under lateral load in "Y" direction. Bending load in "X" direction is greatly reduced by reaction of array with antenna deployment trusses

$$R_{EVM} = \frac{83.1 \times 44.6}{144} \times 1.3 \times 12.15\ g \times \frac{81.5}{153.5} = 216 \text{ pounds}$$

$$R_{ANT.\ INT.} = 191 \text{ pounds}$$

Max. bending moment about 2-2 axis

$$M_M = 81.5 \times 191 = 15,570 \text{ inch-pound}$$

$$\text{Max cap load} = \frac{15570}{6} = 2595 \text{ pounds}$$

Use 3/4 inch O. D. x 0.065 inch W. T. tubing - 6061T6 Aluminum Alloy

$$A = 0.1399$$

$$\rho = 0.2433$$

$$f_c = \frac{2595}{0.1399} = 18550 \text{ psi}$$

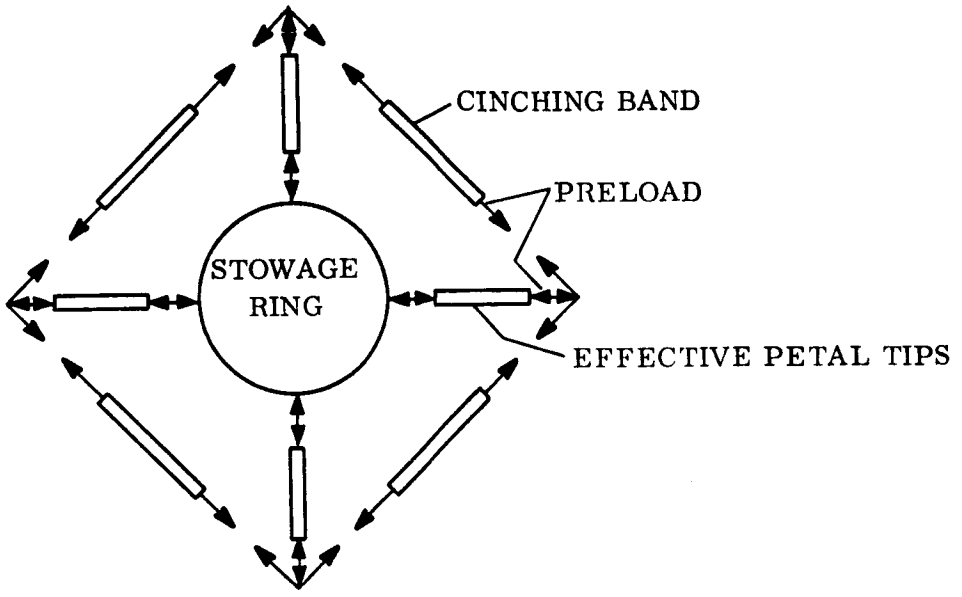
$$\frac{L}{\rho} = \frac{15.875}{0.2433} = 65.2$$

$$F_{cc} = 20,000 \qquad \text{(Ref. 1)}$$

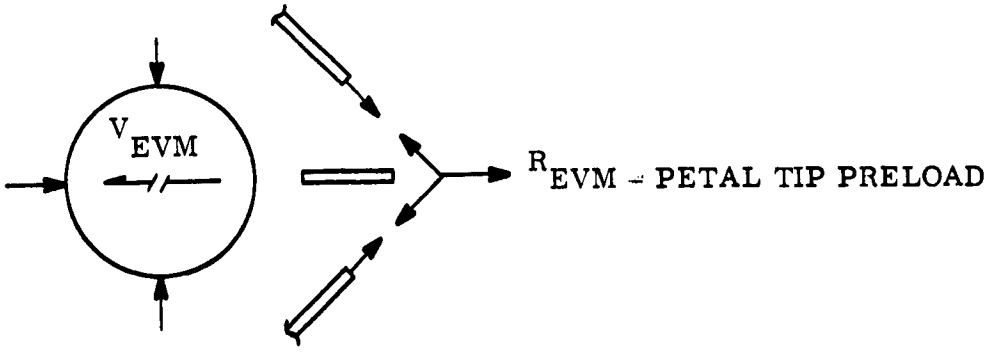
M.S. = + 0.08 buckling

Solar Array Truss Reacting Upon Antenna Cinching Band

Under lateral loading, the clevis type device on the EVM will react the forward loads of three of the solar array trusses. The fourth truss load must be resisted by transferring this load through a rigid link to the antenna cinching band and thence through the petal tips to the antenna stowage ring mounted on the EVM. Presented below are simplified free bodies of the system under cinching band preload and under the lateral truss load.



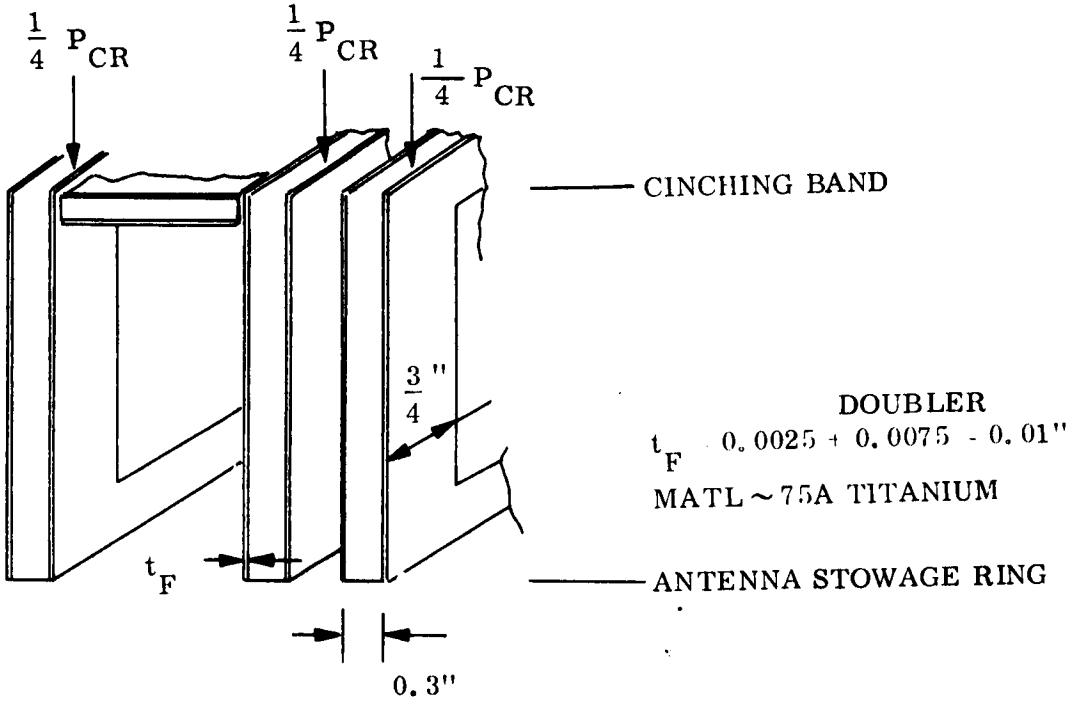
PRELOAD FREE BODY



LATERAL LOAD FREE BODY

Solar Array Truss Reacting Upon Antenna Cinching Band

The preload free body is essentially unchanged as long as R_{EVM} does not exceed the compressive preload in the effective petal tips. Assume four petal tips act together under preloading.



$$P_{cr} = \frac{4\pi^2 EI}{L^2}$$

where

$E = 16 \times 10^6$ psi

$I = 2 \times 0.75 \times 0.01 + 0.15^2 = 0.000338$ in.^{4}

$L = 24$ inches

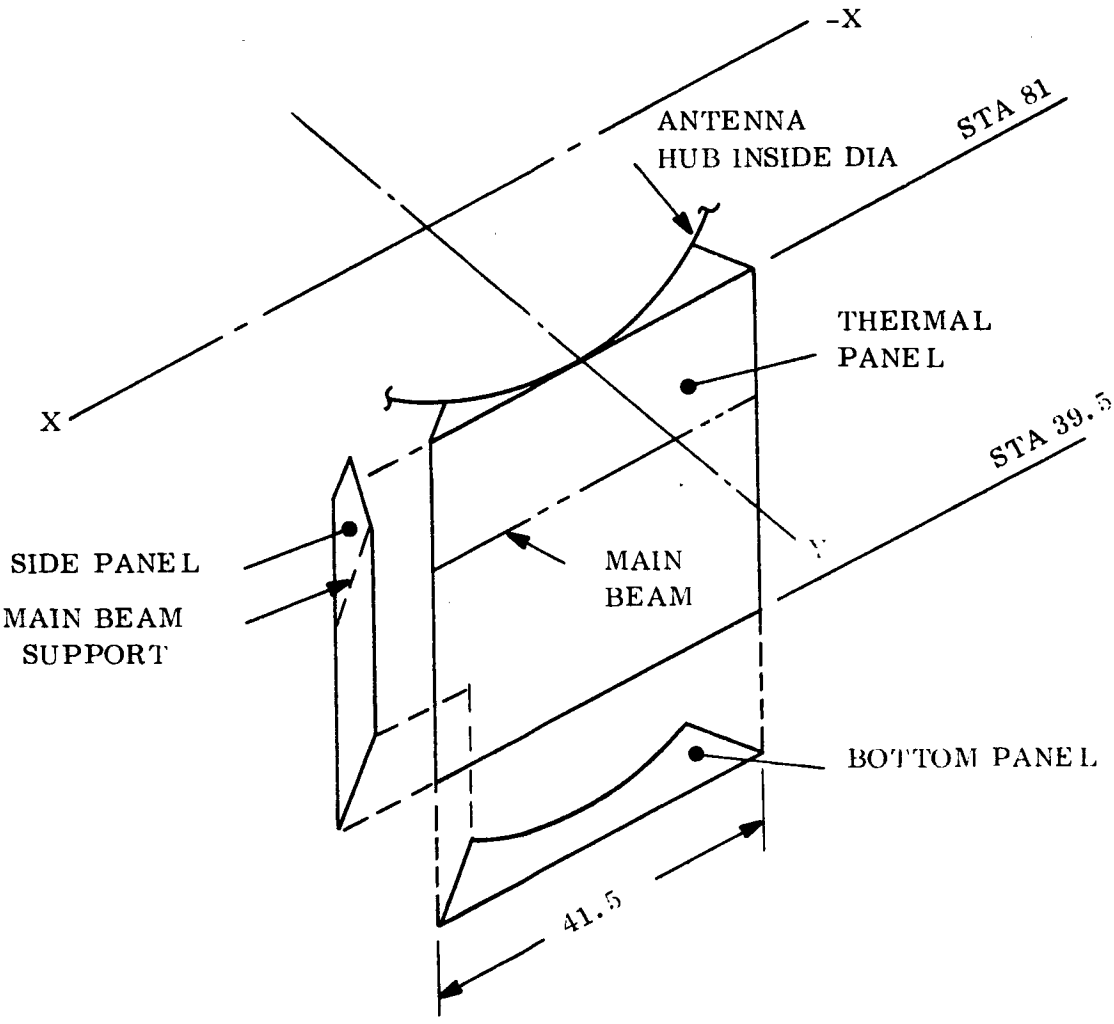
$P_{cr} = 370.6$ pounds

Total preload for 4 effective petal tips = R_{EVM} = 216 pounds

M.S. $\frac{370.6}{216}$ - 1 + 0.71 petal tip buckling

Equipment Bay

Critical Load Condition
Lateral: 12.3 g (Ult.) "X" or "Y" Axis
Axial: 33 g (Ult.) "Z" Axis

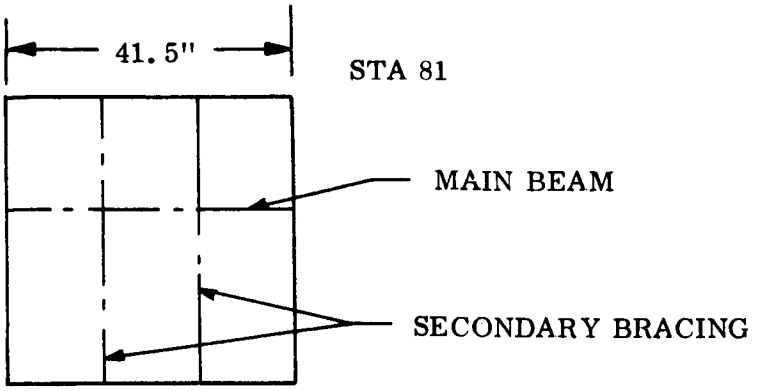


EXPLODED VIEW

1 g thermal panel load
134 pounds equipment
18 pounds panel and shutters
152 pounds
total = 0.0883 pounds/inch^2

Equipment Bay

Thermal panel - lateral load, "Y" axis

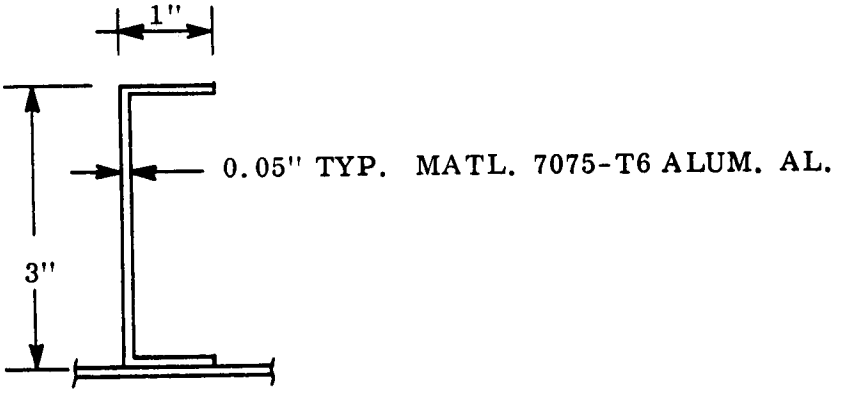


Max. moment main beam (beam column effect due to angle of side panel is negligible)

$W = 0.0883 \times 20.75 \times 12.3 = 22.53$ pounds/inch

$$M_M = \frac{w \times 41.5^2}{8}$$

$= 4850$ inch/pounds



Main beam sect.

$$I = 2 \times 1 \times 0.05 \times 1.475^2 + \frac{0.05 \times 2.90^3}{12} = 0.320 \text{ in.}^4$$

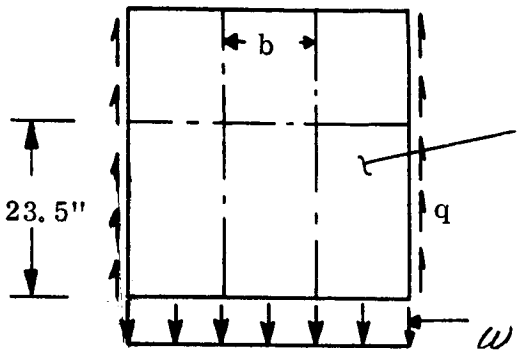
$$f_b = \frac{4850 \times 1.5}{0.320} = 22,750$$

$\frac{b}{t} = 20$ $F_{cc} = 28000$ (Ref. 2) M.S. = + 0.23 crippling

Equipment Bay

Thermal panel - Axial load, "Z" direction

Secondary bracing carries equipment kick loads and shear stabilizes thermal panel



MATL 6061 T6 ALUM

t = 0.06"

E = 10.0×10^6

$$W = \frac{152 \times 33}{41.5} = 120.8 \text{ pounds/inch}$$

$$q = \frac{120.8 \times 41.5}{2 \times 41.5} = 60.4 \text{ ppi}$$

Shear buckling

a = 23.50

b = 13.83

$\frac{b}{a} = 0.589$

k = 6.7

$$q_{cr} = \frac{K E t^3}{b^2} = \frac{6.7 \times 10.0 \times 10^6 \times 0.06^3}{191.2} = 75.6 \text{ ppi} \quad \text{(Ref. 2)}$$

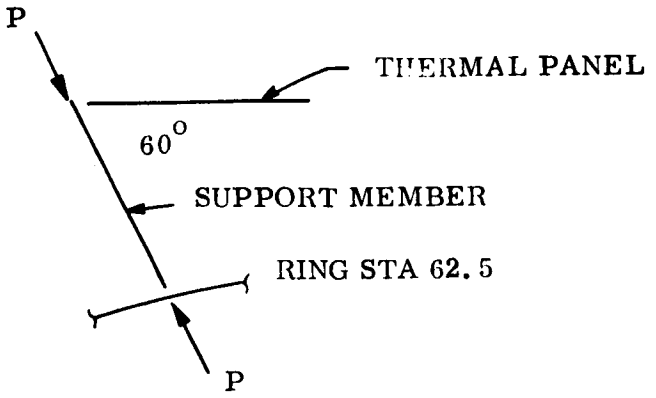
$$MS = \frac{75.6}{60.4} - 1 = +0.25 \text{ shear buckling}$$

Required I of stiffeners = $2.8 \times 23.50 \times 0.06^3 = 0.0142 \text{ in.}^4$ (Ref. 2)

$1\frac{1}{4} \times \frac{3}{4} \times 0.040$ adequate

Equipment Bay

Main beam support members - lateral load, "Y" axis



$$P = \frac{22.53 \times 20.75}{\cos 30^{o}} = 540 \text{ pounds}$$

Use AND10133 - 0401 ∠ 7075 T6 Aluminum Alloy

Min $\rho = 0.147$

$A = 0.582$

$$f_c = \frac{540}{0.0582} = 9270 \text{ psi}$$

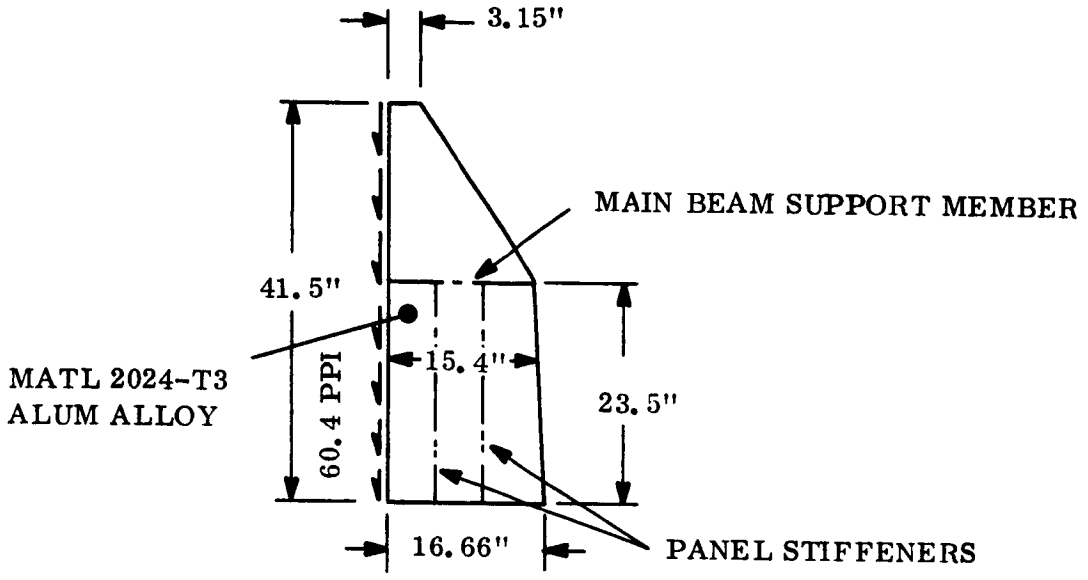
$$\frac{L}{\rho} = \frac{15.4}{0.147} = 104.7$$

$$F_c = \frac{\pi^2 E}{(L/\rho)^2} = \frac{\pi^2 \times 10.5 \times 10^6}{10960} = 9460 \text{ psi}$$

M.S. = + 0.02 Buckling (conservative)

Equipment Bay

SIDE PANEL - AXIAL LOAD, "Z" DIRECTION



ASSUME 2 PANEL STIFFENERS

b = 5.34 inch average

$\frac{b}{a}$ = 0.227

K = 5.3

t = 0.032 inch

$$q_{cr} = \frac{5.3 \times 10 \times 10^6 \times 0.032^3}{5.34^2} = 64.5 \text{ ppi}$$

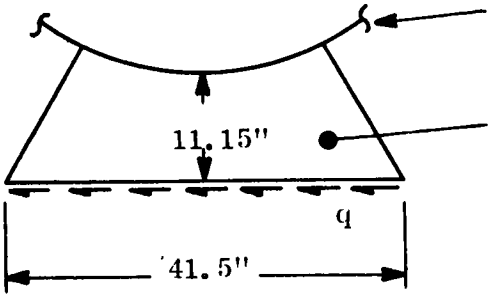
M.S. = + 0.07 shear buckling

Required $I_s = 7.2 \times 23.5 \times 0.032^3 = 0.0055 \text{ in.}^4$

$1 \times \frac{1}{2} \times 0.04$ ∠ adequate

Equipment Bay

BOTTOM PANEL-LATERAL LOAD, "X" AXIS



$q = \frac{1}{2} \times 0.0883 \times 12.3 \times 41.5 = 22.5$ ppi

b = 11.15 inch

a = 33 inch average

b/a = 0.338

K = 8.6 (long edges fixed)

t = 0.032

$$q_{cr} = \frac{8.6 \times 10.6 \times 10^6 \times .032^3}{11.15^2} = 24 \text{ ppi}$$

M.S. = 0.07 shear buckling

Lateral load, "Y" axis

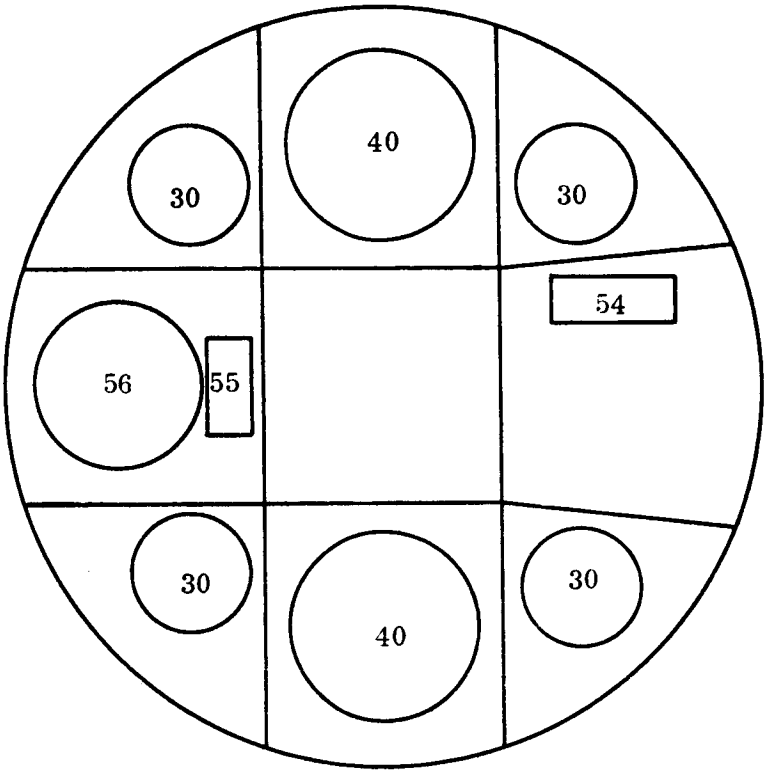
Bottom panel acts as web of beam 11.15 in. deep with ring and thermal panel edge member serving as beam caps. Max shear is less than 24 ppi.

Use 1 x 1 x .040 inch L's for all remaining panel edge members.

Tank Support Beams

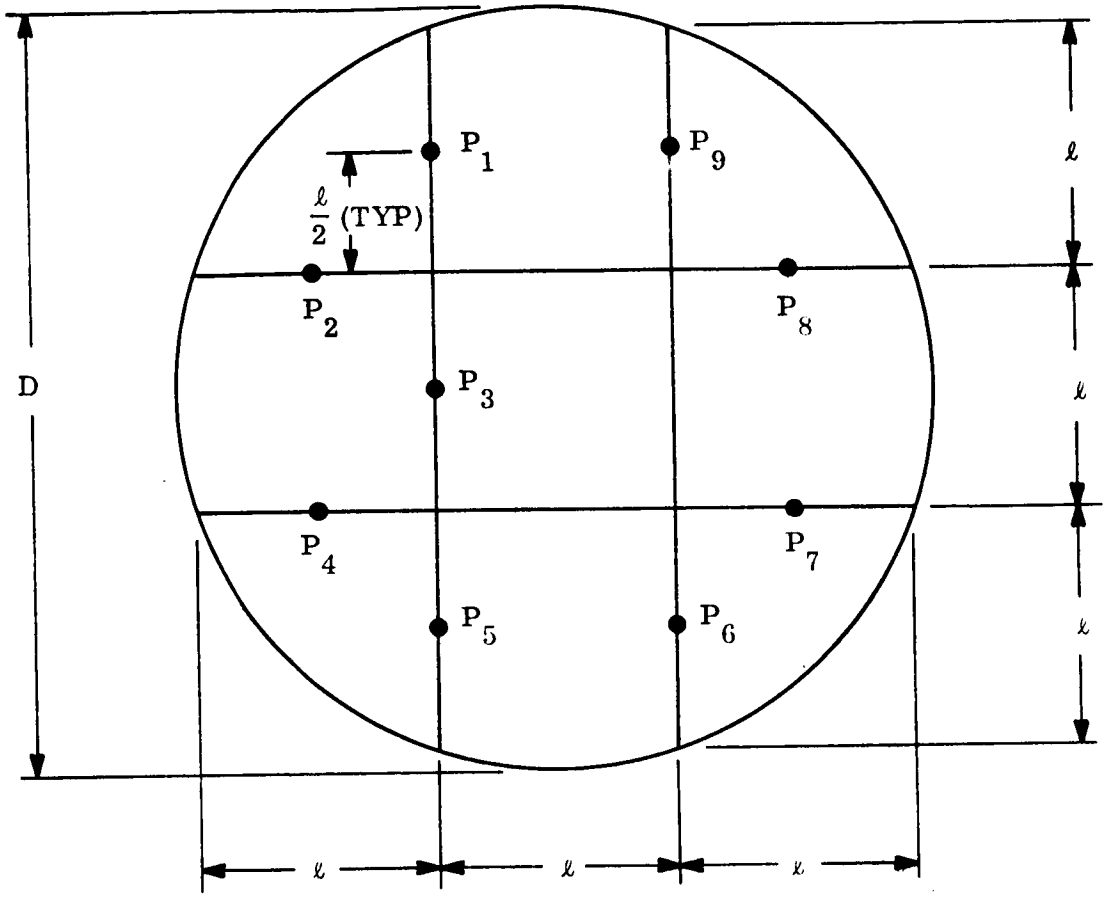
Loads $N_x = N_y = 12.3$ g ult.

$N_z = 33$ g ult.



Item	Weight
40	44 pounds each
30	25 pounds each
54	12 pounds
55	12 pounds
56	12 pounds

Idealized Structure



D_ℓ = 78.5 in.

D_s = 58 in.

$$\ell < \frac{1}{3}\left(\frac{78.5 + 58}{2}\right) \approx 22 \text{ in.}$$

d = Depth of beam = 18.5 in.

$$P_1 = P_5 = P_6 = P_9 = \frac{44 + 25}{2} = 34.5 \text{ pounds}$$

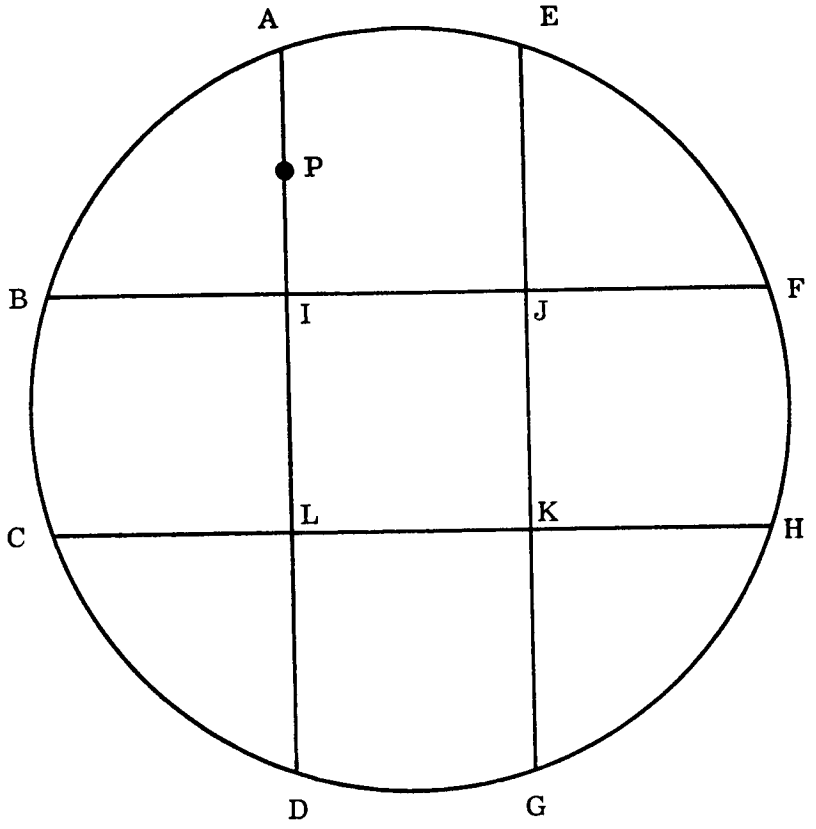
$$P_7 = \frac{25}{2} = 12.5 \text{ pounds}$$

$$P_2 = P_4 = \frac{25 + 12}{2} = 18.5 \text{ pounds}$$

$$P_8 = \frac{25}{2} + 12 = 24.5 \text{ pounds}$$

P_3 = 12 pounds

Unit Load Solution (Approximate)



For a load P into the paper, and assuming the reactions at G and H are equal the following reactions can be determined assuming redundant reactions are a function of the stiffnesses of the paths and determinant reactions are a function of the length of the paths.

$R_A = 0.74\ P$

$R_B = 0.21\ P$

$R_C = R_D = R_E = R_F = 0.012\ P$

$R_G = R_H = 0.001\ P$

} Approximate Solution

Reactions

$$R_{MAX} \approx N_z \left\{ 0.74\, P_1 + 0.21\, P_2 + \frac{P_3}{4} \right\}$$

$$= 33 \left\{ 0.74\ (34.5) + 0.21\ (18.5) + 3 \right\}$$

$$= 1070 \text{ pounds}$$

$$M_{MAX} \approx \frac{R_{MAX}\, \ell}{2} = \frac{1070\ (22)}{2}$$

$$= 11800 \text{ inch/pounds}$$

Stress Analysis

Compression load in caps $= \frac{M}{d} = \frac{11800}{18.5} = 640$ pounds

Shear stress in web (t = 0.032) $= \frac{R}{dt} = \frac{1070}{18.5\ (0.032)} = 1800$ psi

Max. Bending stress in cap (x loading) $= \frac{Mc}{I}$

$$= \frac{N_x\, P\, 1}{2 \times 4} \frac{c}{I} = \frac{12.3\ (34.5)(22)}{2 \times 4} \frac{c}{I}$$

$$= \frac{11.65}{Z}$$

Compression stress in caps $= \frac{640}{A}$

Cap Members

1.750 x 0.875 x 0.094 TEE 7075 - T6

$A = 0.240$

$Z = \frac{I}{c} = \frac{0.0393}{0.875} = 0.045$

$\sigma_b = \frac{1165}{0.045} = 25,900 \text{ psi}$

$\frac{b}{t} = \frac{0.875}{0.094} = 9.3$ $\qquad \sigma_{cc} = 26,000 \text{ psi}$ (Ref. 2)

$\sigma_c = \frac{640}{0.24} = 2679 \text{ psi}$

$$M.S = \frac{26000}{25900} - 1 = \underline{0.005}$$

Web

$q = 1800 (0.032) = 57.5 \text{ pounds/inch}$

Use 0.032 inch thick aluminum beaded panels

$q_{all} \approx 160 \text{ pounds/inch}$ (Ref. 4)

$$M.S. = \frac{160}{57.5} - 1 = \underline{1.78}$$

MEMBER 2 351 (STRAIGHT TUBE) FREQUENCY = 0

I JOINT, JOINT 2 - COORDINATES (7.5000 , 13.000 , 238.00) = RESTRAINT CODE (0, 0, 1, 1, 0, 0)
J JOINT, JOINT 351 - COORDINATES (39.250 , 0, 81.000) = RESTRAINT CODE (0, 0, 1, 1, 1, 0)
0 JOINT, REFERENCE - COORDINATES (29.000 , 0, 62.500)

REFERENCE TEMP = 0
RATIO = C

YOUNG'S MODULUS = 0.4000+08
SHEAR MODULUS = 0.1800+08
THERMAL COEFFICIENT = C
OUTSIDE RADIUS = 2.0000
TUBE THICKNESS = 0.7500-01
} SEE NOTE

TOTAL MEMBER WEIGHT = 9.9576
ROTOR SPEED = 0

WEIGHT DENSITY = 0.6700-01
TEMPERATURE GRAD 1 = 0
TEMPERATURE GRAD 2 = 0
TEMPERATURE AVERAGE = 0

TOTAL MEMBER LENGTH = 160.70
LENGTH BETWEEN FITTINGS = 152" ±

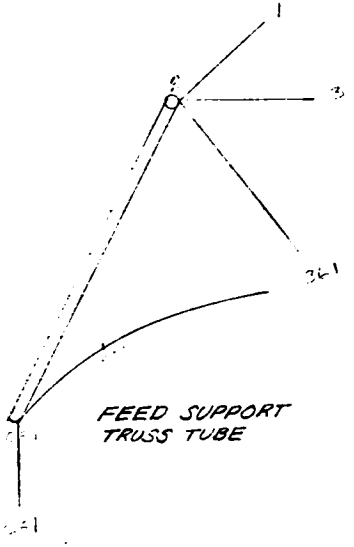
DISTRIBUTED LOADS 1 = 0
2 = 0
3 = 0
4 = 0
5 = 0
6 = 0

* * * CALCULATIONS * * *

		DIRECTION 1	DIRECTION 2	DIRECTION 3	DIRECTION 4	DIRECTION 5	DIRECTION 6
MEMBER LOADS	JOINT 2 (I)	2496.8	=1023.2	=0	=0	=0	=0.1236+05
	JOINT 351 (J)	=2498.8	1023.2	=0	=0	=0	0.1236+05
NORM. DEFLS.	JOINT 2 (I)	=5.8615	=1.4410	=0.2905-01	0.2839-02	0.3502-02	=0.6825
	JOINT 351 (J)	=1.1934	=1.3861	=0.2905-01	0.2839-02	0.3502-02	=0.2263
NORM. LOADS	JOINT 2 (I)	=0.3052-04	=0.1265+05	=0	=0	=0	0.3052-03
	JOINT 351 (J)	0.3052-03	0.1265+05	0	0	0	=0.4730-03

POTENTIAL ENERGY = 347.49

KINETIC ENERGY = 0



STRAIGHT BERYLLIUM TUBE

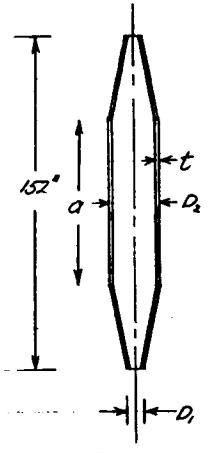
$$P_{CR} = 12650 = \frac{\pi^2 E I}{L^2}$$

$$REQ'D\ I = \frac{12650 \times 152^2}{\pi^2 \times 40 \times 10^6} = .74\ IN^4$$

WALL # THICK.	TUBE # DIA.	TOTAL WT.	f_a	F_{cc}
.050"	3.404"	32.2#	24000	
.055	3.299	34.2	22600	
.060	3.218	36.3	21300	
.065	3.141	38.3	20200	
.070	3.066	40.2	19,200	35000

PREFERRED 3.25" O.D. .060" WT →

NO CRIPPLING PROBLEM



2024-T3 ALUM ALLOY TUBE

D_2"	D_1"	t"	a"	NT.
4.0"	4.0"	.1207"	152"	134#
5.0	5.0	.0585	152	82.7
6.0	6.0	.0334	152	57.0
5.0	1.895	.083	51.7	92.7
6.0	1.33	.050	73	67.8

NO CRIPPLING PROBLEM

NOTE: THESE SECTION PARAMETERS WERE INPUT TO DETERMINE AXIAL TUBE LOADS. SINCE THE TRUSS IS STATICALLY DETERMINATE, THESE LOADS ARE APPLICABLE REGARDLESS OF SECTION OR MATERIAL. THE OPTIMUM FOR BOTH ALUMINUM & BERYLLIUM (WITHIN MFG. CAPABILITY) IS INDICATED HERE.

* M.S. = 0 (BUCKLING) ←

MEMBER 351 353 (CURVED BAR) FREQUENCY = 0

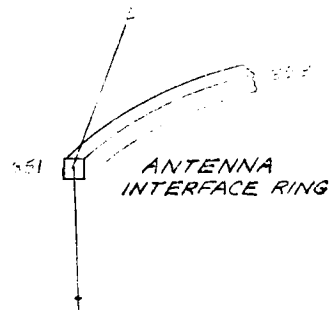
I JOINT, JOINT 351 - COORDINATES (39.250 , 0, 81.000) = RESTRAINT CODE (0, 0, 0, 0, 0, 0)
J JOINT, JOINT 353 - COORDINATES (37.910 , 10.160 , 81.000) = RESTRAINT CODE (0, 0, 0, 0, 0, 0)
O JOINT, REFERENCE - COORDINATES (0, 0, 81.000)

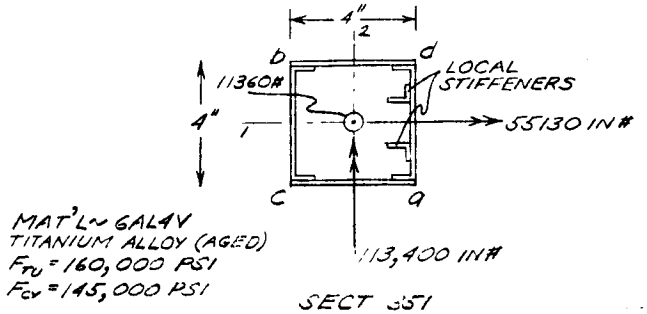
REFERENCE TEMP	=	0	TOTAL MEMBER WEIGHT	=	1.0524	RADIUS OF CURVATURE	= 39.249
RATIO	=	0	ROTOR SPEED	=	0	INCLUDED ANGLE	= 15.003
YOUNG MODULUS	=	0.1600+08	TORSIONAL CONSTANT	=	2.5600	DISTRIBUTED LOADS 1	= 0
SHEAR MODULUS	=	0.6200+07	SHEAR CONSTANT 1	=	0	2	= 0
THERMAL COEFFICIENT	=	0	SHEAR CONSTANT 2	=	0	3	= 0
CROSS SECTIONAL AREA	=	0.6400	WEIGHT DENSITY	=	0.1600	4	= 0
MOMENT OF INERTIA 1	=	2.9800	TEMPERATURE GRAD 1	=	0	5	= 0
MOMENT OF INERTIA 2	=	2.9800	TEMPERATURE GRAD 2	=	0	6	= 0
ROTATION OF AXIS	=	0	TEMPERATURE AVERAGE	=	0		

* * * CALCULATIONS * * *

		DIRECTION 1	DIRECTION 2	DIRECTION 3	DIRECTION 4	DIRECTION 5	DIRECTION 6
MEMBER LOADS	JOINT 351 (I)	6587.0	-0.1136+05	-0.1134+06	-0.5513+05	4143.9	-4417.6
	JOINT 353 (J)	-6587.0	0.1136+05	0.6370+05	0.1025+05	-0.1005+05	4417.6
NORM. DEFLS.	JOINT 351 (I)	-1.4611	0	0	0	-0.5424-01	1.1233
	JOINT 353 (J)	-1.3092	0.3568	-0.1850-01	-0.2003-01	-0.4532-01	1.0095
NORM. LOADS	JOINT 351 (I)	-6587.0	0.1136+05	0.1134+06	0.5513+05	-4143.9	4417.6
	JOINT 353 (J)	3227.6	-0.1263+05	-0.6370+05	-7296.1	0.1236+05	-4417.6

POTENTIAL ENERGY = 1046.2 KINETIC ENERGY = 0





MAT'L ~ 6AL4V
TITANIUM ALLOY (AGED)
F_{tu} = 160,000 PSI
F_{cy} = 145,000 PSI

SECT 351

$$f_a = \frac{11360}{.64} - \frac{113400 \times 2}{2.98} - \frac{55130 \times 2}{2.98} = -95{,}360 \text{ PSI COMP}$$

f_b = 130,840 PSI TENS.

M.S. = +.22 TENSION ←

f_c = +56,840 f_d = -21,360

SIDE a-d CRITICAL FOR BUCKLING

TWO LOCAL SIDEWALL RIBS REQUIRED TO PREVENT COMP. BUCKLING

MEMBER 251 351 (STRAIGHT BAR) FREQUENCY = 0

I JOINT, JOINT 251 - COORDINATES (34.411 , 0, 72.239) = RESTRAINT CODE (0, 0, 0, 0, 0, 0)
J JOINT, JOINT 351 - COORDINATES (39.250 , 0, 81.000) = RESTRAINT CODE (0, 0, 0, 0, 0, 0)
O JOINT, REFERENCE - COORDINATES (0, 0, 81.000)

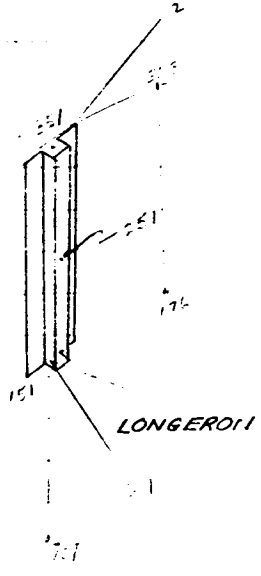
REFERENCE TEMP	=	0	TOTAL MEMBER WEIGHT	=	0.1777	TOTAL MEMBER LENGTH	= 10.009
RATIO	=	0	ROTOR SPEED	=	0		
YOUNG'S MODULUS	=	0.1050+08	TORSIONAL CONSTANT	=	0.9610-01	DISTRIBUTED LOADS 1	= 0
SHEAR MODULUS	=	0.3900+07	SHEAR CONSTANT 1	=	0	2	= 0
THERMAL COEFFICIENT	=	0	SHEAR CONSTANT 2	=	0	3	= 0
CROSS SECTIONAL AREA	=	0.1758	WEIGHT DENSITY	=	0.1010	4	= 0
MOMENT OF INERTIA 1	=	0.5610-01	TEMPERATURE GRAD 1	=	0	5	= 0
MOMENT OF INERTIA 2	=	0.5610-01	TEMPERATURE GRAD 2	=	0	6	= 0
ROTATION OF AXIS	=	0	TEMPERATURE AVERAGE	=	0		

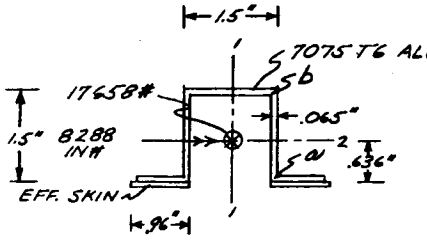
HALF SECT PROPERTIES
NO EFF. SKIN

* * * CALCULATIONS * * *

		DIRECTION 1	DIRECTION 2	DIRECTION 3	DIRECTION 4	DIRECTION 5	DIRECTION 6
MEMBER LOADS	JOINT 251 (I)	3888.2	0	0	0	-207.96	7938.9
	JOINT 351 (J)	-3888.2	0	0	-0	-4143.9	-7938.9
NORM. DEFLS.	JOINT 251 (I)	-1.0561	0.2290	0.8652-01	-0	0	0
	JOINT 351 (J)	-1.8221	0.2769	0.5424-01	0	0	0
NORM. LOADS	JOINT 251 (I)	434.82 HALF	-6829.2	-207.96	0	0	-0
	JOINT 351 (J)	-434.82 LOADS	6829.2	-4143.9	-0	-0	0

POTENTIAL ENERGY = 256.05 KINETIC ENERGY = 0





SECT 351

INCL. EFFECTIVE SKIN

$A = .4126$ SQ IN

$I = .1467$

$P_{CR} = \frac{\pi^2 \times 10.4 \times 10^6 \times .1467}{20.018^2} = 37{,}000\#$

$MS = +1.10$

$f_a = -\frac{17{,}658}{.4126} - \frac{8288 \times .636}{.1467} = 78{,}700$ PSI COMP.

$F_{cu} = F_{tu} = 77{,}000$ (REF. 1)

M.S. = −.021 COMPRESSION ←

AVG. WALL STRESS $= \frac{f_a + f_b}{2} = 42{,}800$ PSI COMP.

$b/t = 23.1$ $F_{cc} = 61{,}000$ PSI (REF. 2)

M.S. = +.13

MEMBER 701 151 (STRAIGHT BAR) FREQUENCY = 0

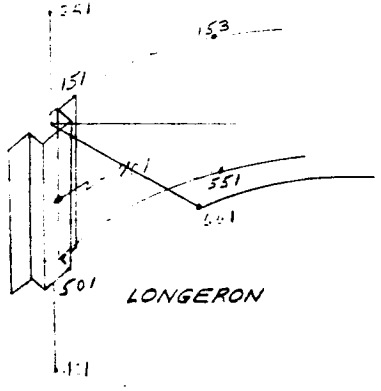
I JOINT, JOINT 701 - COORDINATES (28.370 , 0, 50.500) = RESTRAINT CODE (0, 0, 0, 0, 0, 0)
J JOINT, JOINT 151 - COORDINATES (29.000 , 0, 62.500) = RESTRAINT CODE (0, 0, 0, 0, 0, 0)
O JOINT, REFERENCE - COORDINATES (0, 0, 62.500)

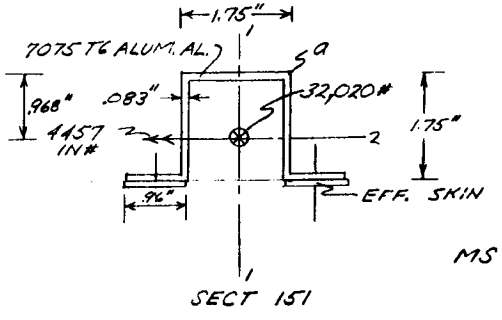
REFERENCE TEMP	=	0	TOTAL MEMBER WEIGHT	=	0.3168	TOTAL MEMBER LENGTH	= 12.017
RATIO	=	0	ROTOR SPEED	=	0		
YOUNGS MODULUS	=	0.1050+08	TORSIONAL CONSTANT	=	0.1972	DISTRIBUTED LOADS 1	= 0
SHEAR MODULUS	=	0.3900+07	SHEAR CONSTANT 1	=	0	2	= 0
THERMAL COEFFICIENT	=	0	SHEAR CONSTANT 2	=	0	3	= 0
CROSS SECTIONAL AREA	=	0.2610 } HALF SECT.	WEIGHT DENSITY	=	0.1010	4	= 0
MOMENT OF INERTIA 1	=	0.1165 } PROPERTIES-	TEMPERATURE GRAD 1	=	0	5	= 0
MOMENT OF INERTIA 2	=	0.1165 } NO EFF. SKIN	TEMPERATURE GRAD 2	=	0	6	= 0
ROTATION OF AXIS	=	0	TEMPERATURE AVERAGE	=	0		

* * * CALCULATIONS * * *

		DIRECTION 1	DIRECTION 2	DIRECTION 3	DIRECTION 4	DIRECTION 5	DIRECTION 6
MEMBER LOADS	JOINT 701 (I)	930.24	0	0	0	=531.44	0.1598+05
	JOINT 151 (J)	=930.24	0	0	0	2228.4	=0.1598+05
NORM. DEFLS.	JOINT 701 (I)	=0.1288	0.1838	0.6014=02	0	0	0
	JOINT 151 (J)	=0.2058	0.2540	0.1957=01	0	0	0
NORM. LOADS	JOINT 701 (I)	=141.22 HALF	=0.1601+05	-531.44	0	0	-0
	JOINT 151 (J)	141.22 LOADS	0.1601+05	2228.4	-0	-0	0

POTENTIAL ENERGY = 572.28 KINETIC ENERGY = 0





INCL. EFFECTIVE SKIN

$A = .5834$ SQ. IN.

$I = .2767$ IN^4

$P_{cr} = \frac{\pi^2 \times 10.4 \times 10^6 \times .2767}{24.034^2} = 49300\#$

$MS = \frac{49300}{32020} - 1 = +.54$ BUCKLING

$f_o = -\frac{32020}{.5834} - \frac{1457 \times .968}{.2767} = 70,500$ PSI COMP.

$\frac{b}{t} = 21.2$ $F_{cc} = F_{cy} = 68,000$ (REF. 2)

$MS = -.035$ CRIPPLING ←

MEMBER 501 701 (STRAIGHT BAR) FREQUENCY = 0

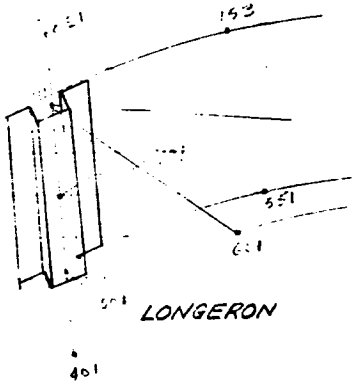
I JOINT, JOINT 501 - COORDINATES (27.740 , 0, 39.000) = RESTRAINT CODE (0, 0, 0, 0, 0, 0)
J JOINT, JOINT 701 - COORDINATES (26.370 , 0, 50.500) = RESTRAINT CODE (0, 0, 0, 0, 0, 0)
B JOINT, REFERENCE - COORDINATES (0, 0, 39.000)

REFERENCE TEMP	= 0	TOTAL MEMBER WEIGHT	= 0.3036	TOTAL MEMBER LENGTH	= 11.517
RATIO	= 0	ROTOR SPEED	= 0		
YOUNGS MODULUS	= 0.1050+08	TORSIONAL CONSTANT	= 0.2922	DISTRIBUTED LOADS 1	= 0
SHEAR MODULUS	= 0.3900+07	SHEAR CONSTANT 1	= 0	2	= 0
THERMAL COEFFICIENT	= 0	SHEAR CONSTANT 2	= 0	3	= 0
CROSS SECTIONAL AREA	= 0.2610 } HALF SECT.	WEIGHT DENSITY	= 0.1010	4	= 0
MOMENT OF INERTIA 1	= 0.1165 } PROPERTIES	TEMPERATURE GRAD 1	= 0	5	= 0
MOMENT OF INERTIA 2	= 0.1165 } NO EFF. SKIN	TEMPERATURE GRAD 2	= 0	6	= 0
ROTATION OF AXIS	= 0	TEMPERATURE AVERAGE	= 0		

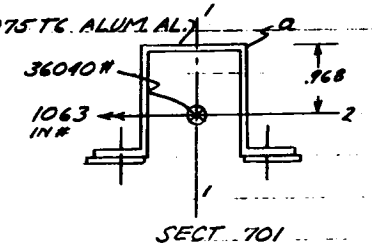
• • • CALCULATIONS • • •

		DIRECTION 1	DIRECTION 2	DIRECTION 3	DIRECTION 4	DIRECTION 5	DIRECTION 6
MEMBER LOADS	JOINT 501 (I)	1079.9	0	0	0	505.30	0.1799+05
	JOINT 701 (J)	=1079.9	0	0	0	531.67	=0.1799+05
NORM. DEFLS.	JOINT 501 (I)	=0.7007-01	0.1078	0.5890-02	0	0	0
	JOINT 701 (J)	=0.1292	0.1835	0.6014-02	0	0	0
NORM. LOADS	JOINT 501 (I)	=90,036 HALF	=0.1802+05	505.30	0	0	=0
	JOINT 701 (J)	90,036 LOADS	0.1802+05	531.67	=0	=0	0

POTENTIAL ENERGY = 683.11 K1NET1C ENERGY = 0



LONGERON



SECT. 701

INCL. EFFECTIVE SKIN
A = .5834 SQ. IN.
I = .2767 IN⁴

$f_a = -\frac{36040}{.5834} - \frac{1063 \times .968}{.2767} = 65{,}500$ PSI COMP.

$F_{cc} = 68{,}000$ PSI (REF. 2)

MS = +.04 CRIPPLING ←

MEMBER 501 551 (CURVED BAR)

FREQUENCY = 0

I JOINT, JOINT 501 - COORDINATES (27.740 , 0, 39.000) = RESTRAINT CODE (0, 0, 0, 0, 0, 0)
J JOINT, JOINT 551 - COORDINATES (24.020 , 13.870 , 39.000) = RESTRAINT CODE (0, 0, 0, 0, 0, 0)
O JOINT, REFERENCE - COORDINATES (0, 0, 39.000)

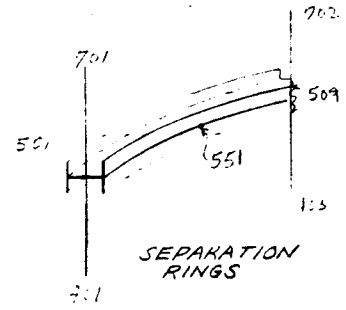
REFERENCE TEMP	= 0	TOTAL MEMBER WEIGHT	= 0.5986	RADIUS OF CURVATURE	= 27.738
RATIO	= 0	ROTOR SPEED	= 0	INCLUDED ANGLE	= 30.004
YOUNG'S MODULUS	= 0.1050+08	TORSIONAL CONSTANT	= 0.1200-02	DISTRIBUTED LOADS 1	= 0
SHEAR MODULUS	= 0.3900+07	SHEAR CONSTANT 1	= 0	2	= 0
THERMAL COEFFICIENT	= 0	SHEAR CONSTANT 2	= 0	3	= 0
CROSS SECTIONAL AREA	= 0.4080	WEIGHT DENSITY	= 0.1010	4	= 0
MOMENT OF INERTIA 1	= 0.3450-01	TEMPERATURE GRAD 1	= 0	5	= 0
MOMENT OF INERTIA 2	= 0.3723	TEMPERATURE GRAD 2	= 0	6	= 0
ROTATION OF AXIS	= 0	TEMPERATURE AVERAGE	= 0		

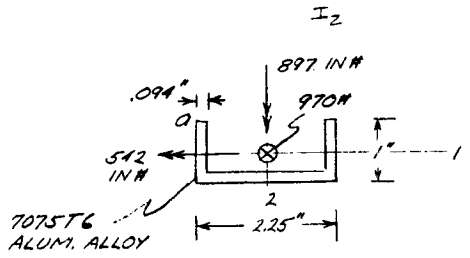
* * * CALCULATIONS * * *

		DIRECTION 1	DIRECTION 2	DIRECTION 3	DIRECTION 4	DIRECTION 5	DIRECTION 6
MEMBER LOADS	JOINT 501 (I)	-283.19	969.66	897.24	541.90	49.085	67.576
	JOINT 551 (J)	283.19	-969.66	-573.57	395.43	202.10	-67.576
NORM. DEFLS.	JOINT 501 (I)	-0.6407-01	0	0	0	-0.5898-02	0.1115
	JOINT 551 (J)	-0.5857-01	0.3640-01	0.3702-03	-0.3979-02	-0.3041-01	0.1634
NORM. LOADS	JOINT 501 (I)	283.19	-969.66	-897.24	-541.90	-49.085	-67.576
	JOINT 551 (J)	239.65	981.33	573.57	-443.50	22.718	67.576

POTENTIAL ENERGY = 4.3139

KINETIC ENERGY = 0





SECT 501

$$f_a = \frac{-970}{.408} - \frac{897 \times 1.125}{.3723} - \frac{542 \times .74}{.0346} = 16690 \text{ PSI COMP.}$$

$$\frac{b}{t} = \frac{1.0}{.094} = 10.6 \qquad F_{cc} = 47{,}500 \text{ PSI (REF. 2)}$$

MS = +1.85 CRIPPLING ←

MEMBER 153 602 (STRAIGHT TUBE) FREQUENCY = 0

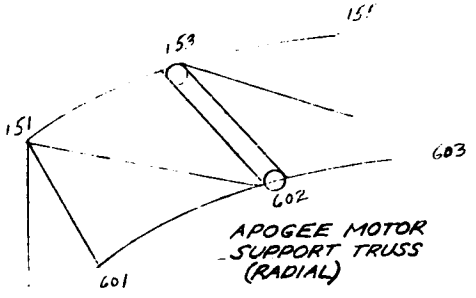
I JOINT, JOINT 153 - COORDINATES (14.500 , 25.110 , 62.500) = RESTRAINT CODE (0, 0, 0, 0, 0, 0)
J JOINT, JOINT 602 - COORDINATES (9.2500 , 16.020 , 52.000) = RESTRAINT CODE (0, 0, 0, 0, 0, 0)
O JOINT, REFERENCE - COORDINATES (14.385 , 24.560 , 50.500)

REFERENCE TEMP	= 0	TOTAL MEMBER WEIGHT	= 0.4504	TOTAL MEMBER LENGTH = 14.847
RATIO	= 0	ROTOR SPEED	= 0	
YOUNG* MODULUS	= 0.1050+08	WEIGHT DENSITY	= 0.1010	DISTRIBUTED LOADS 1 = 0
SHEAR MODULUS	= 0.3000+07	TEMPERATURE GRAD 1	= 0	2 = 0
THERMAL COEFFICIENT	= 0	TEMPERATURE GRAD 2	= 0	3 = 0
OUTSIDE RADIUS	= 1.0000	TEMPERATURE AVERAGE	= 0	4 = 0
TUBE THICKNESS	= 0.4000-01			5 = 0
				6 = 0

* * * CALCULATIONS * * *

		DIRECTION 1	DIRECTION 2	DIRECTION 3	DIRECTION 4	DIRECTION 5	DIRECTION 6
MEMBER LOADS	JOINT 153 (I)	54.019	=23.471	1182.6	=402.61	1140.9	317.58
	JOINT 602 (J)	=54.019	23.471	=568.35	=2730.6	=40.837	=317.58
NORM. DEFLS.	JOINT 153 (I)	0.8936-01	0.2452-01	-0.4042-02	0.1114-01	0.2672-01	=0.3451
	JOINT 602 (J)	0.1428	0.2344-01	0.3603-02	-0.9612-02	0.8186-02	=0.1789
NORM. LOADS	JOINT 153 (I)	=219.78	229.32	919.17	=280.08	1392.5	=58.579
	JOINT 602 (J)	219.78	=229.32	2344.0	=589.65	=1392.5	58.579

POTENTIAL ENERGY = 21.013 KINETIC ENERGY = 0



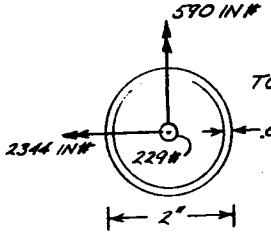
$$\text{MAX COMP. STRESS} = \frac{229}{.3003} - \frac{2344 \times 1}{.143} = -15640 \text{ PSI}$$

BENDING MODULUS OF RUPTURE $F_b = .91\, F_{TU}$ (REF. 1)

$$\text{MAX TORSIONAL SHEAR STRESS} = \frac{1393}{2\pi \times 1^2 \times .049} = 4530 \text{ PSI}$$

TORSIONAL MODULUS OF RUPTURE $F_{ST} = 26{,}000$ PSI (REF. 1)

$$MS = \frac{1}{\sqrt{\left(\frac{15640}{.91 \times 64000}\right)^2 + \left(\frac{4530}{26{,}000}\right)^2}} - 1 = +2.12$$ ← BENDING & TORSION



SECT 602

MAIL.~2024 T3 ALUM. AL.

$A = .3003\ IN^2$

$I = .143\ IN^4$

$D/t = 40.2$ $L/D = 7.424$

$F_{TU} = 64{,}000$ PSI (REF. 1)

MEMBER 151 602 (STRAIGHT TUBE) FREQUENCY = 0

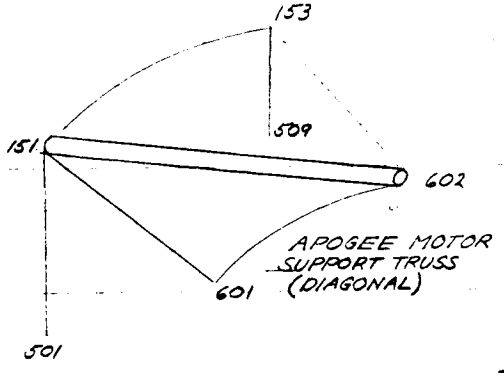
I JOINT, JOINT 151 - COORDINATES (29,000 , 0, 62,500) = RESTRAINT CODE (0, 0, 0, 0, 0, 0)
J JOINT, JOINT 602 - COORDINATES (9,2500 , 16,020 , 52,000) = RESTRAINT CODE (0, 0, 0, 0, 0, 0)
O JOINT, REFERENCE - COORDINATES (14,500 , 25,110 , 62,500)

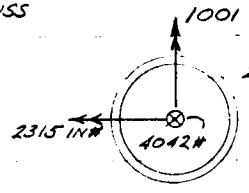
REFERENCE TEMP	= 0	TOTAL MEMBER WEIGHT	= 0.8346	TOTAL MEMBER LENGTH	= 27,513
RATIO	= 0	ROTOR SPEED	= 0		
YOUNGS MODULUS	= 0.1050+08	WEIGHT DENSITY	= 0.1010	DISTRIBUTED LOADS 1	= 0
SHEAR MODULUS	= 0.3900+07	TEMPERATURE GRAD 1	= 0	2	= 0
THERMAL COEFFICIENT	= 0	TEMPERATURE GRAD 2	= 0	3	= 0
OUTSIDE RADIUS	= 1.0000	TEMPERATURE AVERAGE	= 0	4	= 0
TUBE THICKNESS	= 0.4900-01			5	= 0
				6	= 0

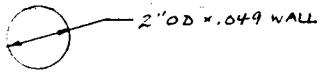
* * * CALCULATIONS * * *

		DIRECTION 1	DIRECTION 2	DIRECTION 3	DIRECTION 4	DIRECTION 5	DIRECTION 6
MEMBER LOADS	JOINT 151 (I)	=2981.6	2351.0	755.51	1016.3	2196.8	=1397.0
	JOINT 602 (J)	2981.6	=2351.0	576.59	1290.0	1519.6	1397.0
NORM. DEFLS.	JOINT 151 (I)	=0.1140	0.7889-01	=0.7398-02	0.1409-01	=0.1139-01	=0.3403
	JOINT 602 (J)	0.4407-02	0.1142	=0.7767-02	0.9143-02	=0.4950-02	=0.1996
NORM. LOADS	JOINT 151 (I)	74.248	=4042.4	=1001.3	2314.9	=261.25	148.67
	JOINT 602 (J)	=74.248	4042.4	=1041.5	1775.5	261.25	=148.67

POTENTIAL ENERGY = 69.405 KINETIC ENERGY = 0







SECT. 151

SAME MAT'L & SECT. PROPERTIES AS MEM. 153-602

$P_{CR} = \frac{\pi^2 EI}{L^2} = \frac{\pi^2 \times 10.5 \times 10^6 \times .143}{27.5^2} = 19600$

MS = HIGH BUCKLING

$f_c = \frac{4042}{.3003} = 13,450$ PSI

$F_c = F_{cy} = 42,000$ PSI (REF 1.)

$R_c = \frac{f_c}{F_{cy}} = .32$

$f_b = \frac{2315 \times 1}{.143} = 16,200$ PSI

$F_b = .91 \times 64,000 = 58,250$ PSI

$R_b = .278$

NEGLECT TORSION

$MS = \frac{1}{R_b + R_c} - 1 = +.67$ BENDING & COMP. ←

PLATE 302 502 401 402 FREQUENCY = 0

I JOINT, JOINT 302 = COORDINATES (26.270 , 3.4600 , 16.000)
J JOINT, JOINT 502 = COORDINATES (27.500 , 3.6200 , 39.000)
K JOINT, JOINT 401 = COORDINATES (27.130 , 0. , 27.500)
L JOINT, JOINT 402 = COORDINATES (26.200 , 7.0200 , 27.500)

REFERENCE TEMP = 0
TOTAL MEMBER WEIGHT = 0.7526

RAD OF CURVATURE I-J = 0
RAD OF CURVATURE K-L = 27.128
THICKNESS OF PLATE = 0.7200-01
YOUNG'S MODULUS = 0.6500+07
SHEAR MODULUS = 0.2400+07

THERMAL COEFFICIENT = 0
POISSONS RATIO = 0.3000
WEIGHT DENSITY = 0.6390-01
PRESSURE ON PLATE = 0

TEMPERATURE JOINT I = 0
TEMPERATURE JOINT J = 0
TEMPERATURE JOINT K = 0
TEMPERATURE JOINT L = 0
THERMAL GRADIENT = 0

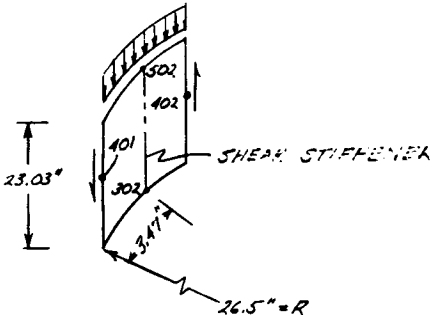
* * * CALCULATIONS * * *

			DIRECT	EDGE	TRANSVERSE	BENDING	TORSION
NORMALIZED DEFLECTIONS	JOINT 302	(I)	-0.2474-01	-0.5218-02	-0.4029-01	0.6611-02	-0.4266-02
	JOINT 502	(J)	-0.5067-01	0.1019-01	0.6499-01	-0.1130-01	0.1514-02
	JOINT 401	(K)	-0.3551-03	-0.5612-01	-0.1090-02	0.4183-04	-0.6021-02
	JOINT 402	(L)	0.3993-02	-0.2830-01	0.1059-01	-0.2683-02	-0.4021-02
NORMALIZED LOADS	JOINT 302	(I)	4396.1	3055.3	-21.506	-129.15	-0.3055
	JOINT 502	(J)	-3216.6	-2846.0	4.1406	149.84	0.2621
	JOINT 401	(K)	-911.95	-0.1619-05	-106.30	-65.020	-0.3714
	JOINT 402	(L)	703.19	9006.3	-87.984	81.447	1.4147

POTENTIAL ENERGY = 132.75 KINETIC ENERGY = 0

STRESS CALCULATION 1054

STRESSES	DIRECT	EDGE	TRANSVERSE	BENDING
JOINT 302	-8622.29	5992.52	42.1815	-21108.4
JOINT 502	-6308.91	5581.87	8.12116	-24490.5
JOINT 401	-549.895	6141.90	64.0947	-3267.17
JOINT 402	-424.017	5430.68	53.0534	-4092.62



$f_s = 6142$ PSI

$F_{SCR} = \frac{K E t^2}{b^2}$ REF. 2

FOR $\frac{a}{b} = \frac{23.03}{3.47} = 6.64$

$\frac{b}{\sqrt{Rt}} = 2.51$

$K = 5.4$

$F_{SCR} = 15,100$

$R_s = \frac{6142}{15,100} = .406$

$f_c = 8622$

$F_{CR} = \frac{1}{6}\frac{E}{1-\mu^2}\left[\sqrt{12(1-\mu^2)}\left(\frac{t}{R}\right)^2 + \left(\frac{\pi t}{b}\right)^4 + \left(\frac{\pi t}{b}\right)^2\right]$ REF. 6

$F_{CR} = 16,900$

$R_c = .510$

$MS = \frac{2}{R_c + \sqrt{R_c^2 + 4R_s^2}} - 1 = +.36$ ← COMBINED SHEAR & COMA BUCKLING

MEMBER 301 302 (CURVED BAR) FREQUENCY = 0

I JOINT, JOINT 301 - COORDINATES (26.500 , 0, 16.000) = RESTRAINT CODE (0, 0, 0, 0, 0, 0)
J JOINT, JOINT 302 - COORDINATES (26.270 , 3.4600 , 16.000) = RESTRAINT CODE (0, 0, 0, 0, 0, 0)
O JOINT, REFERENCE - COORDINATES (0, 0, 16.000)

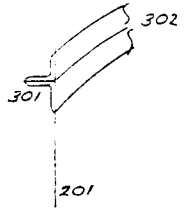
REFERENCE TEMP	= 0	TOTAL MEMBER WEIGHT	= 0.1585	RADIUS OF CURVATURE	= 26,498
RATIO	= 0	ROTOR SPEED	= 0	INCLUDED ANGLE	= 7.5032
YOUNGS MODULUS	= 1.1050+08	TORSIONAL CONSTANT	= 0.3300-02	DISTRIBUTED LOADS 1	= 0
SHEAR MODULUS	= 0.3900+07	SHEAR CONSTANT 1	= 0	2	= 0
THERMAL COEFFICIENT	= 0	SHEAR CONSTANT 2	= 0	3	= 0
CROSS SECTIONAL AREA	= 1.4523	WEIGHT DENSITY	= 0.1010	4	= 0
MOMENT OF INERTIA 1	= 0.~~1338~~.1176	TEMPERATURE GRAD 1	= 0	5	= 0
MOMENT OF INERTIA 2	= 0.~~1442~~.0660	TEMPERATURE GRAD 2	= 0	6	= 0
ROTATION OF AXIS	= 0	TEMPERATURE AVERAGE	= 0		

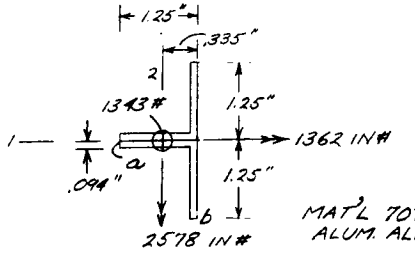
* * * CALCULATIONS * * *

		DIRECTION 1	DIRECTION 2	DIRECTION 3	DIRECTION 4	DIRECTION 5	DIRECTION 6
MEMBER LOADS	JOINT 301 (I)	=411.30	1342.6	2577.7	=1361.5	=39.854	=290.10
	JOINT 302 (J)	=411.30	=1342.6	=1459.2	357.69	=25.966	290.10
NORM. DEFLS.	JOINT 301 (I)	0.3025-01	0	0	0	=0.9348-03	0.2720-01
	JOINT 302 (J)	0.4157-01	=0.5187-02	0.4386-02	=0.2093-02	0.6609-02	0.2253-01
NORM. LOADS	JOINT 301 (I)	411.30	=1342.6	=2577.7	1361.5	39.854	290.10
	JOINT 302 (J)	=252.40	1384.8	1459.2	=351.24	72.452	=290.10

POTENTIAL ENERGY = 0.3763 KINETIC ENERGY = 0

401





MAT'L 7075 T6 ALUM. ALLOY

SECT 301

FIELD JOINT RINGS

$f_a = -\frac{1343}{.452} - \frac{2578 \times .915}{.066} = 38720$ PSI COMP.

$f_b = -\frac{1343}{.452} - \frac{2578 \times .335}{.066} - \frac{1362 \times 1.25}{.1176} = 30{,}520$ PSI. COMP.

$\frac{b}{t} = \frac{1.25}{.094} = 13.3$ $F_{cc} = 39{,}500$ PSI

MS = +.02 CRIPPLING ←

6.7.1.5 References for Structural Analysis

1. "Mil-HDBK-5", August 1962.
2. "General Electric Structures Manual"
3. "General Electric Structural Data Sheets"
4. Bruhn, E. F., "Analysis and Design of Flight Vehicle Structures," Tri-State Offset Company, 1965.
5. Timoshenko, S., "Strength of Materials," Part II, 1956.
6. Roark, R. J., "Formulas for Stress and Strain," Third Edition, 1954.

6.7.2 SEPARATION AND DEPLOYMENT

6.7.2.1 Design Criteria

Design objectives considered in the antenna/solar array deployment mechanism study included:

a. Positive, controlled antenna and solar array deployment motion

b. Structural adequacy for minimum weight

c. No deployment structure within the antenna reflecting field, which might contribute to rf losses or interference

d. Minimum number of power packages to reduce "Key event" occurrences necessary for separation and deployment.

e. Positive lock at full deployed position taking into account uneven deployment behavior of the individual panels

6.7.2.2 Deployment Mechanism Selection

6.7.2.2.1 Antenna Deployment System Selection

The recommended parabolic antenna deployment system generally consists of a system of single point driven ball screw actuators which pull the twenty antenna trusses in outward radial arcs to move the antenna petals from the cylindrical packaged state to the deployed parabolic form. This system is shown in detail in Subsection 5.4.

A major factor in the selection of ball screw actuators over other forms of actuating devices was the need for a controlled rate antenna deployment with positive positioning throughout the cycle. Such control is mandatory to control and reduce dynamic forces which result upon the sudden release of the stored energy in the stowed antenna when the cinching band is separated and again near the full deployed position when each individual panel hinge snaps through center to assume the final contoured shape.

The ball screw actuator fulfills this requirement very effectively in addition to serving as a fixed structural member, both in the stowed and deployed antenna positions.

Other antenna actuating systems were considered during the study, including an "umbrella" type and a hydraulic system.

The "umbrella" type deployment system, as previously discussed, is potentially the simplest approach to deploying the antenna. The concept consists of a central multi-extend ball screw jack acting as a structural column with radiating struts (arranged in "spoke" fashion) attaching to the antenna trusses. This system does not meet the requirement for minimal rf losses or interference within the selected vehicle configuration since the twenty actuating struts would span the reflecting area. Also, cutouts in the antenna petals would be necessary for the actuating struts to be attached to the solar panel trusses. For these reasons, the concept was rejected. A positive displacement hydraulic feed back system consisting of a synchronized master actuator which would displace slave actuators was briefly considered, but was rejected because of life requirements of the mission and the weight and problems associated with a hydraulic system in space.

An alternate drive system to replace the chosen torque tube system for driving the twenty ball screw jacks might consist of a continuous perforated tape system as shown in Figure 6.7-5. Small chain or studded belt drives might be substituted for the perforated tape in such a system. Several alternate drive systems would be a major area of study in any ensuing preliminary design effort.

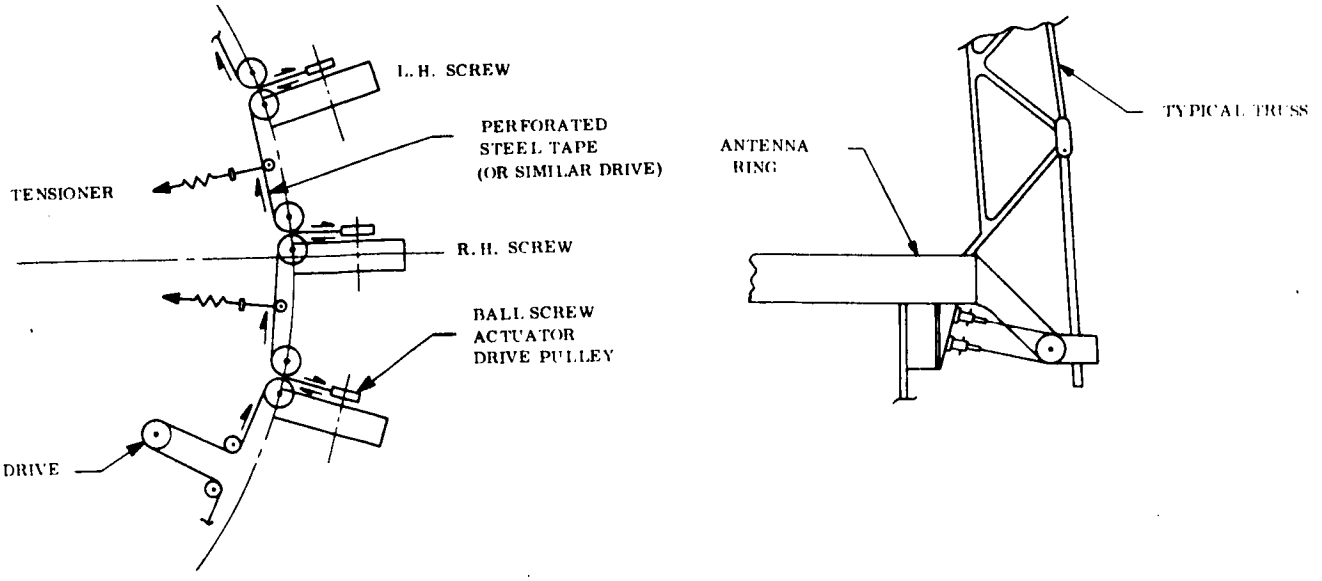


Figure 6.7-5. Tape Drive Deployment System

6.7.2.2.2 Solar Paddle Deployment System Selection

The deployment of the solar paddles is secondary to the successful deployment of the parabolic antenna from the standpoint of optimum mission completion. One or more solar paddles can remain in a stowed position in the recommended vehicle configuration without catastrophic effects on mission accomplishment. Such failure of a solar panel to deploy would merely require that the use of power and operating times would have to be programmed in such a way as to give the batteries more recharge time. On the other hand, the failure of the antenna to deploy would result in partial mission failure. Therefore, extreme care must be exercised in the design of the solar paddle deployment mechanism to guarantee non-interference with antenna deployment.

The recommended solar paddle deployment system shown in Figure 5.9-12 is intended to portray a "typical" arrangement which could be used to couple mechanically the solar paddle unlock system to the antenna drive mechanism, and, by using a damped spring panel deployment

drive, eliminate extra power sources on the vehicle. Several alternate systems were investigated as discussed below.

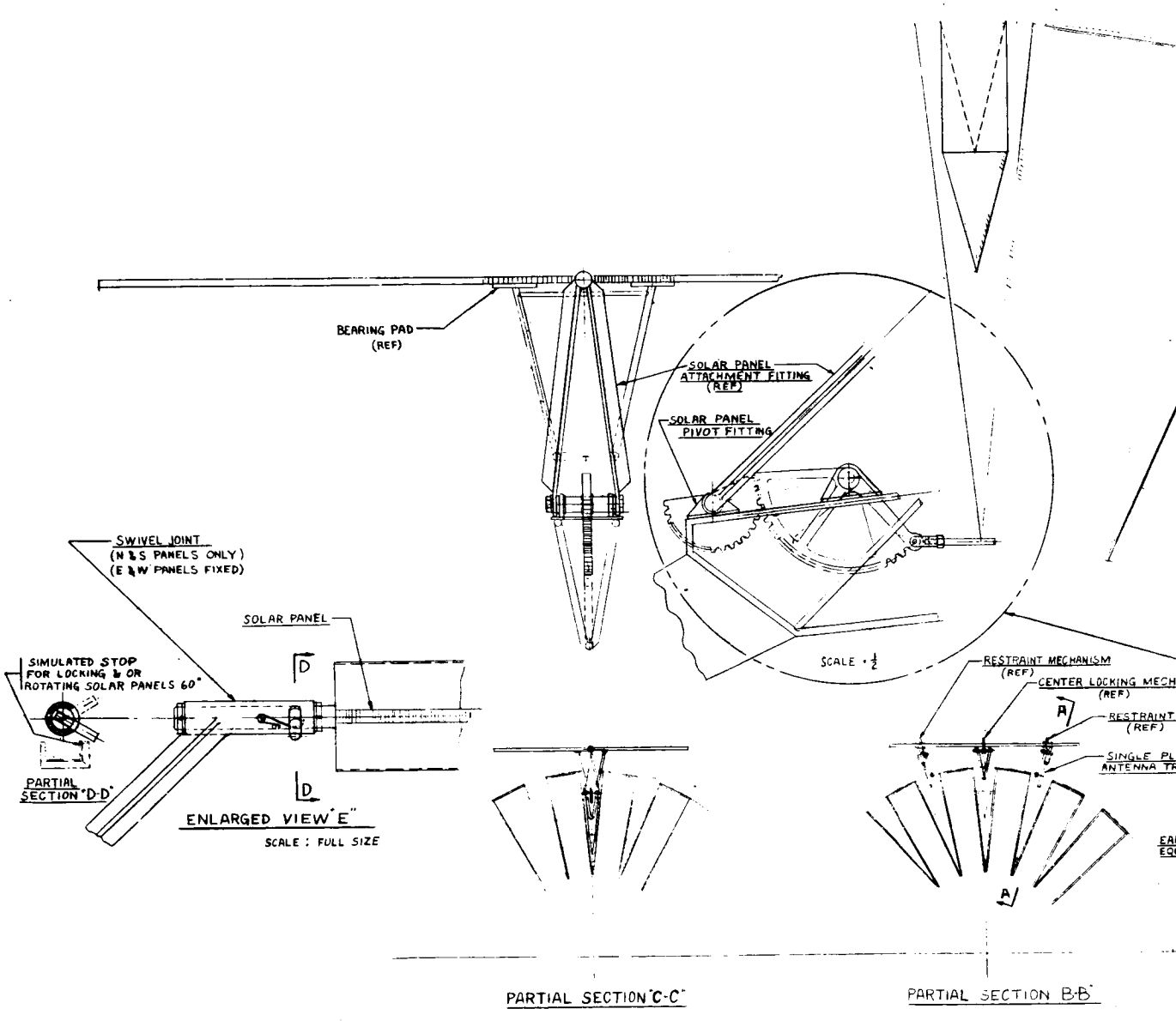
6.7.2.2.2.1 Solar Array Alternate Configurations - An alternate configuration which was considered for solar array stowage is shown in Figure 6.2-19. In this configuration, the solar paddles are stowed alongside the Earth viewing equipment module in roughly the same relationship to the stowed antenna as they would be in the orbit deployed position. The solar arrays are locked to and stabilized by the viewing equipment module during the launch phase and are unlocked prior to initiation of antenna deployment. Little or no further motion of the solar arrays is necessary for orbit positioning (except for rotation of the North and South panels)since the antenna/solar array relative positions remain constant and deployment of the antenna automatically deploys the solar arrays in the correct orbiting configurations.

This configuration is considered an alternate approach, but has the following disadvantages when compared to the selected configuration:

a. The solar arrays completely surround the Earth viewing module during launch and coast, blocking the thermal control shutters, orientation control sensors, and thruster nozzles.

b. A "Key event" is added to the deployment sequence in the form of paddle unlock. All four paddles are necessarily unlocked before the antenna can be deployed.

Another configuration which was considered as an alternate to the selected spring actuated solar array drive consisted of mechanically coupling both the "unlock" and the solar panel deployment cycle to the antenna drive mechanism. This approach is shown in Figure 6.7-6, and in addition to utilizing linkage for the unlocking of the arrays, an additional link extending to the solar array pivot is incorporated. This link imparts deployment motion to the solar array through a gear segment arrangement and is operated by the antenna deployment mechanism. In this manner, the deployment rate of the solar panels is positively controlled throughout the cycle by being directly coupled to the antenna motion. This design, although attractive from a rate control standpoint, was found not to be problem free because of the possibility of antenna "hang-up" which could result if the solar array and/or linkage


BEARING PAD
(REF)
SOLAR PANEL
ATTACHMENT FITTING
(REF)
SOLAR PANEL
PIVOT FITTING
SCALE • ½
SWIVEL JOINT
(N & S PANELS ONLY)
(E & W PANELS FIXED)
SOLAR PANEL
SIMULATED STOP
FOR LOCKING & OR
ROTATING SOLAR PANELS 60°
PARTIAL
SECTION "D-D"
ENLARGED VIEW "E"
SCALE : FULL SIZE
RESTRAINT MECHANISM
(REF)
CENTER LOCKING MECH
(REF)
RESTRAINT
(REF)
SINGLE PL
ANTENNA TR
PARTIAL SECTION "C-C"
PARTIAL SECTION B-B

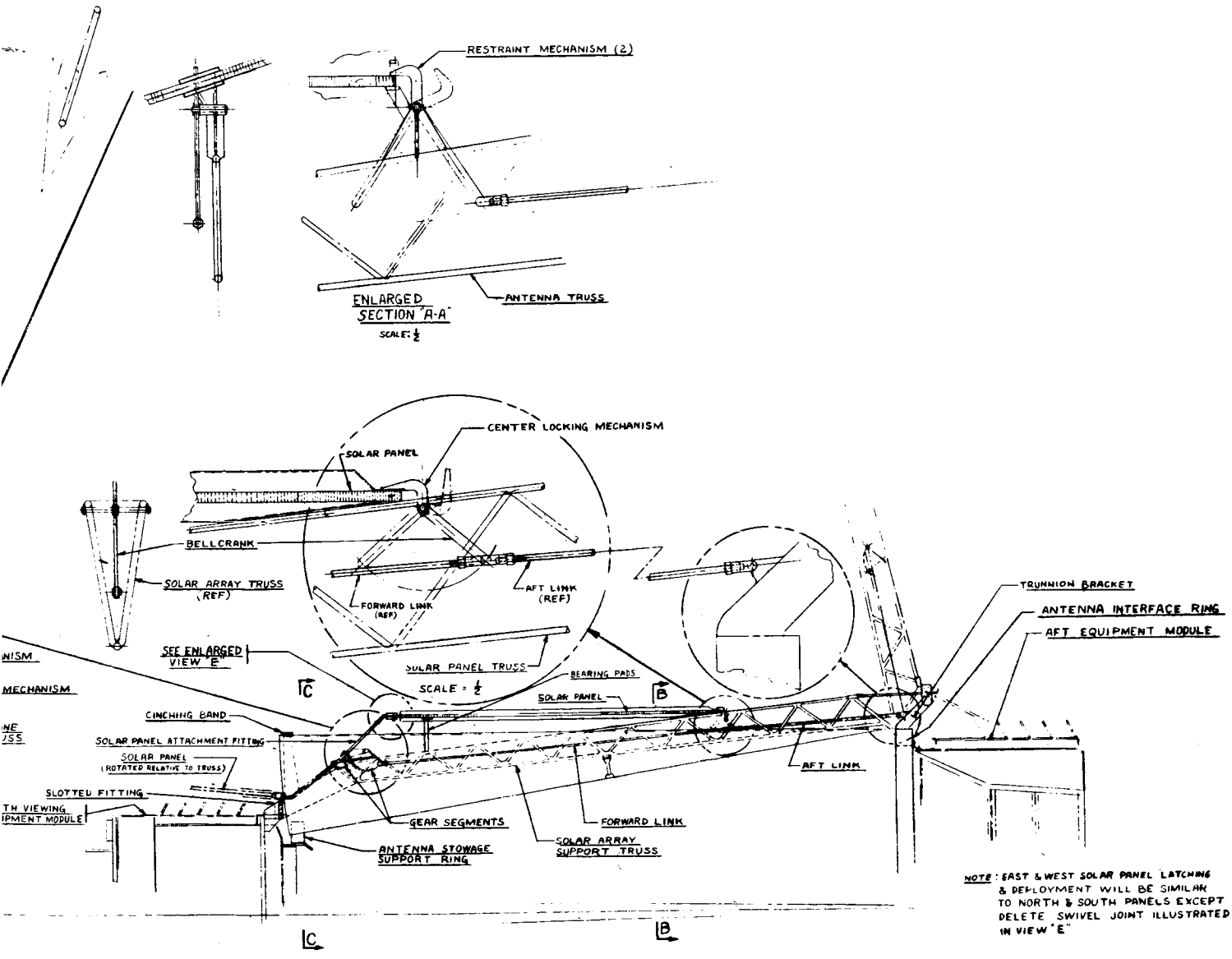


Figure 6.7-6. Solar Panel Latching and Deployment Design

should jam due to gear tooth chipping. Several modifications could be incorporated to prevent such occurrence. One such modification could consist of "sensing" the rotation angles of each solar paddle. If one paddle indicated an out of phase condition (of some predetermined amount, say 15 degrees) with the other three, this would indicate a "hang up" of that particular paddle. Such indication could automatically fire an explosive device on the defective solar panel drive link, thus severing the link and relieving the load on the antenna drive to allow the antenna to complete its full deployment cycle. Another approach is to eliminate the gear drive entirely in favor of a multiple bar linkage mechanism which could accomplish the same motion.

These and other alternate approaches should be fully investigated and applied to the solar paddle deployment system during a preliminary design phase.

6.7.2.3 Spacecraft/Booster Separation System

The type of pyrotechnic separation systems used to separate a spacecraft from its adapter (or booster) generally depends on its structural configuration. Spacecraft which have a continuous monocoque or honeycomb skin to carry the load to the adapter are usually separated by linear explosive cords or a continuous Marman Clamp. Spacecraft which are attached to the adapter (or booster) at discrete points are usually separated by pyrotechnic devices at each point. While both linear explosive cords and Marman Clamps can be readily adapted to discrete point release systems, the problem is to choose a readily available and reliable system which can meet the requirements peculiar to the ATS-4 program. The considerations leading to the choice of the preferred separation system are described in the following paragraphs.

The spacecraft is attached to its adapter at six discrete points and therefore release devices at each point are much easier to adapt than to change the structural configuration to separate by cutting monocoque with linear explosive cords or to use a continuous Marman Clamp. Therefore, these systems were eliminated from further consideration. Five devices were considered for attaching the spacecraft to the adapter, (1) Marman Clamp with six (6) shoes, (2) tension straps, (3) explosive bolts, (4) pin-pullers and (5) separation nuts. A summary of these devices and tradeoff factors is shown in Table 6.7-2.

Table 6.7-2. Separation Device Tradeoff Chart

Separation System	Other Programs	Availability	Installation	Shock and Contamination	Reliability	Cost	Comments
Separation Nuts (power cartridges)	Surveyor OAO Sprint Mil. Prog.	Readily Available	Easy	Low shock, and no contamination	0.9999 with two cartridges per nut.	Approx. $200 nut	Low weight depending on catches and bolt size. Recommended for ATS-4
Linear Explosive Cords	Polaris Sprint Gemini	Modification of proven design	Very Easy	High shock, and dirty	Can be very high	Low per unit. high development cost	Generally used for continuous structures. Fairly light
Marman Clamp (continuous structures)	Pershing Delta-Agena Thor-Delta GGTS Nimbus	Modification of proven design	Very Difficult	High shock, no fragmentation	Very high	High	Used for continuous structures. Generally very heavy
Marman Clamp (shoes with tension band)	Mariner	Modification of proven design	Very Difficult	High shock, no fragmentation	Very high	High	Generally heavy. Must be retained with booster.
Tension Straps	Saturn Apollo	Modification of proven design	Easy	High shock and dirty	Can be high	High development cost	Complicated method when simpler devices available
Explosive Bolts	Agena A Mercury	Can be off-shelf	Easy	High local shock - rather dirty	As high as 0.999 per bolt	Approx. $100 bolt	Low weight but might have reliability problems
Pin-pullers	Mil. Prog. Agena B Surveyor	Can be off-shelf. Any changes require redesign.	Fairly Easy, depends on adapters	Low shock and no contamination	Can be high	Approx. $400 unit	Fairly low weight, depending on the complexity of the mechanical fittings required.
Separation Nuts (MDF initiated)		Proven feasibility, not developed	Fairly Easy	Low shock and no contamination	Expected to be very high	May have high development cost	This method will improve reliability, lower power drain and improve simultaneity of operation.

The Marman Clamp arrangement consists of six V-shaped shoes held in place by a tension band which can be pyrotechnically cut or released. This method has been used successfully on several programs (i.e. Mariner). The drawbacks to this system are: (1) the system must be designed to suit the vehicle, (2) turnbuckles must be installed to equalize tension so that one or more V-shoes do not hang up, (3) installation is usually difficult, (4) the system is heavy and must be retained with the adapter. Tension straps can be bolted at the six load carrying points and then cut by pyrotechnic guillotines or linear explosive cords to effect separation. This method has been used on the Apollo and Saturn programs. However, the straps were rejected for the following reasons: (1) fragmentation tends to contaminate the vehicle, (2) the system must be designed and developed for this vehicle, (3) high local shock, (4) weight is comparatively high. In general, this is a complicated method when compared with the release devices below.

Explosive bolts operate by an explosive charge rupturing or breaking the bolts. The major disadvantages with the use of these bolts are high local shock and rather heavy fragmentation. Explosive bolts have been used on many programs. But for direct release, jamming problems may occur unless the bolt parts can be expelled after operation. The reliability of the explosive bolts is increased by adding two detonators per bolt. The increased shock and fragmentation must be weighed against the gain in reliability.

Pin-pullers have been used on various programs for release of Marman Clamps, deployment of antennas, platforms, etc., and for spacecraft separation. They are clean, and with two electroexplosive devices for operation, can be highly reliable. A disadvantage in using pin-pullers is that the weight of brackets, clevis fittings, and other mechanical devices necessary for attachment can be quite heavy. Other disadvantages are: (1) if turnbuckles are used to hold the system in tension, proper torquing must be maintained to prevent jamming, (2) mechanical designs using pin-pullers are usually complex, (3) changes in pin diameter or stroke length of available, qualified units require redesign. The pin-puller arrangement most attractive was the arrangement used successfully on the Surveyor program. However, several major objections were apparent. The sensitivity of the electroexplosive device used on the Surveyor did not meet the range requirements of AFETRM 127-1, and the pin was

too small. Since a new electroexplosive device as well as a new pin were required, a redesign of the Surveyor pin-puller would be necessary; thus a design, development and qualification cycle would have to be completed. Other qualified pin-pullers could possibly be found but the total assembly (new pin-puller and Surveyor hardware) would have to be requalified. Separation nuts also have been qualified on other programs and have the advantage of allowing a simpler attachment arrangement as well as meeting the range safety requirements. For these reasons, separation nuts were chosen as the release device and are fully described in Section 5.9.4.3.

6.7.3 STRUCTURAL DYNAMICS

The selected configuration represents the end result of a series of configuration studies. Evaluation for configural suitability was based on the rf restrictions for the antenna, deployment reliability considerations, packaging requirements, weight requirements, orbital frequency, and stationkeeping restrictions, etc., of this program. The result of these studies is the selection of a single configuration which is best suited to meet program objectives. The primary structure is optimized and sized for qualification vibration environment in its launch configuration. From a structural dynamic standpoint, with this basic sizing, the orbital behavior of the selected configuration meets the design criteria for minimum frequencies, orientation control and stationkeeping, and associated dynamic load considerations.

6.7.3.1 Design Criteria

The most significant structural design condition is the vibration test environment in the launch configuration. To minimize the dynamic loads during vibration testing, a mass ratio criterion is applied to the relative mass of Earth viewing equipment module to the aft equipment module in order to reduce the large lateral accelerations. The mass ratio investigation is outlined in Section 5.9.5 and the conclusion is that alteration of this final mass ratio would reduce lateral accelerations further at the expense of large increases in axial accelerations. Frequency criteria are also applied in structural size determination. These criteria are reported in earlier sections of the report and are now summarized. For the launch configuration a minimum lateral frequency of 10 cps is required for primary structure in the design to prevent coupling of the spacecraft with the booster autopilot.

For the orbital configuration a structural link of 10 cps minimum is required between Orientation Control system sensors and force generators for control purposes. In addition it is a design objective that major structural response frequencies must be kept above 2 cps.

6.7.3.2 Dynamic Environment

6.7.3.2.1 Launch and Boost Environments

A compilation of flight data for four Atlas/Centaur flights has been made. Table 6.2-3 lists the worst case recorded flight environments for these four flights in the lateral and axial direction.

Specifications for sinusoidal vibration testing of the ATS-4 spacecraft are presented in Table 6.7-3. These specifications are in compliance with NASA/GSFC philosophy of shaker testing space vehicles. The values include an ultimate load factor of 1.5.

Table 6.7-3. Sinusoidal Vibration Testing Specifications

Frequency (cps)	Axis	Sweep Rate	Level (Peak g)
5 - 250	Thrust	2 octaves	± 3.0
250 - 400	Z - Z	per minute	± 3.7
400 - 2000			± 7.5
5 - 250	Lateral	2 octaves	± 1.5
250 - 400	X - X	per minute	± 3.0
400 - 2000	Y - Y		± 7.5

The vibration test levels provide a more severe structural environment than the powered flight loads presented in Table 6.2-3. It is recognized that structure designed to these test levels will be conservative for anticipated flight loads and as a consequence carry a weight penalty.

By agreement with GSFC, the random vibration and torsional test conditions are not considered in design at this time, since preliminary estimates indicate that the other vibration conditions will be limiting. However, these preliminary conclusions will be reexamined during the final design.

Torsional Vibration

Frequency (cps)	Axis	Sweep Rate	Level (Rad/sec^2)
20 - 60	Thrust	2 octaves	$\pm$ 12.9
60 - 150	Z - Z	per minute	$\pm$ 25.8

The conditions of vibration which may be encountered at ATS-4 spacecraft and apogee motor interface, due to the apogee motor operation, will be determined for final design.

Random Vibration

Frequency (cps)	Test Duration (Each Axis)	Acceleration (g-rms)	PSD Level (g^2/cps)
10	4 minutes	overall	0.030*
22 - 175	duration	level	0.065**
530 - 1000	per axis	15.8	0.200***

*Increasing from 10 cps at a constant rate of 3 dB/octave.

**Increasing from 175 cps at a constant rate of 3 dB/octave.

***Decreasing from 1000 cps at a constant rate of -6 dB/octave.

Booster Sustained Acceleration

Axis	Level (g)	Duration (minutes)
Combined *Thrust and Lateral	$9.7 \vec{+} 3 = 10.2$	1

*9.7 (thrust), 3 g (any lateral axis), added vectorially and apply at the spacecraft adapter and booster interface.

Shock - Shocks caused by ignition, cutoff, staging, etc., will occur during vehicle operation. However, the shock environment will be less severe than the vibration requirements.

6.7.3.2.2 Orbital Environments

The orbital disturbances for orientation control and stationkeeping are force pulse inputs of 0.00286 pounds in the vehicle X and Y directions and zero pounds in Z direction. The worst case wheel rotational torques of 0.25 in./lb can occur about any of three vehicle axes for the condition of momentum wheel stall out.

The fundamental frequency of the spacecraft is well above the periodic orbital disturbance frequency, and, as such, there will be no strong interaction of the structural dynamic system with the orbital dynamic environment. Since the two systems are separable, the orbital environment forces (e.g., solar pressure gravity, etc.) are treated as static loads on the spacecraft.

An assumption of linear inertial loading has been made for the effects of structural interaction with control system forces. Such higher order effects as Coriolis acceleration, and centrifugal force are ignored. This simplification is considered valid for configuration comparison and initial establishment of control system parameters. In the next phase of study the effects of these terms will be included in all overall structural-control system interaction solution.

6.7.3.3 Methods of Analysis

An important part of any dynamic analysis is the establishment of a mathematical model which is representative of the actual physical system and also contains those characteristics of the physical system which are to be investigated. The assumptions used in modeling the spacecraft in its orbital configuration are made so that the low frequency behavior of the spacecraft is adequately defined. The low frequency structural response has a most important effect on control system/structure interaction and it is desired to measure the magnitude of that effect.

The launch configuration is also modeled for low frequency behavior, however, not all structural elements are included in the model. Primary structural elements are included in the model to provide amplification factors at the locations of the major mass items. These amplifications are used to determine the loads that the primary structure must withstand in its launch configuration.

Lumped parameter techniques with a finite number of degrees of freedom are used in the formulation of the equations of motion of these models. The equations of motion are formulated as a set of simultaneous, linear, second order differential equations. The data for the equations is organized into matrix arrays and solved for frequencies and mode shapes using standard eigenvalue techniques.

The frequencies and mode shapes are then manipulated to determine control transfer functions to unit load impulses at the location of the orientation control force generators. The procedure for determination of these transfer functions is found in Appendix J.

In addition to the control transfer functions, the acceleration response of the orbital configuration to Dirac Delta inputs is determined.

The Dirac Delta response technique for determination of orbital response accelerations to orientation control inputs is used because these inputs are of short duration relative to the significant structural frequencies excited. The Dirac Delta approach is therefore, a good approximation to orbital control excitations.

Beginning with Equation 5 of Appendix J:

$$M^* \ddot{\xi} + C^* \dot{\xi} + K^* \xi = F^* \qquad (6.7\text{-}1)$$

where

$F^* = F_0^* g(t)$

$F_0^* = \phi^T F_0$

F_0 = Forcing function amplitude

$g(t)$ = Function of time

ϕT = Set of mode shapes

Taking the r^{th} equation of the matrix set and rearranging some terms

$$\ddot{\xi}_r + 2\alpha \dot{\xi}_r + \omega^2 \xi_r = \frac{f_{or}^*}{m_r} g(t) \qquad (6.7\text{-}2)$$

$$2\alpha_r = \frac{c_r}{m_r}$$

$$\omega^2 = \frac{k_r}{m_r}$$

Using Laplace transform notation and solving for modal coordinate

$$S(\xi_r) = \frac{F_{or}^*}{M_r^*} \left[\frac{\zeta [g(t)]}{s^2 + 2\alpha s + \omega_r^2} \right] = \frac{f_{or}^*}{m_r} S\left[h_r(t)\right] \qquad (6.7\text{-}3)$$

By transforming back from complex coordinates to modal coordinates through the inverse Laplacian transform

$$\xi_r = \frac{F_{or}^*}{M_r} h_r(t) \qquad (6.7\text{-}4)$$

Transforming from modal to physical coordinates and summing over r modes

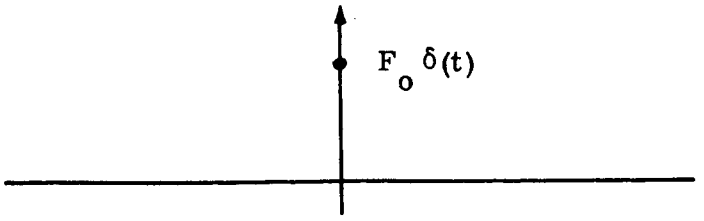
$$q = \phi M^{*-1} (H(t) \phi^T F_o \qquad (6.7\text{-}5)$$

$$H(t) = \sum_{r=1}^{n} h_r(t)$$

where

$h_r(t)$ remains to be defined

The Dirac Delta pulse graphically takes the form of



From Laplace transform theory it can be shown that the pulse for the r^{th} mode is given by

$$h_r(t) = \left\{ \frac{\rho - \alpha_r t}{\omega^2 \alpha_r^2} \sin (\omega - \alpha_r^2)^{1/2} t \right\} \qquad (6.7\text{-}6)$$

$$\alpha_r = \omega \zeta_r$$

Since assumed damping value is 0.001 the equation becomes after neglecting some negligibly small terms

$$h_r(t) \approx \frac{e^{-0.001 \omega t}}{\omega} \sin \omega t \qquad (6.7\text{-}7)$$

Since a computer simulation for a time history of response would yield many insignificant loading conditions besides the significant ones (maximum), the time history portion of pulse was maximized

$$h_r(\max) = \frac{1}{\omega} \qquad \sin \omega t = 1, \quad \omega t = \pi/2 \qquad (6.7\text{-}8)$$

$$H(\max) = \Sigma h_r(\max) = \frac{1}{\lambda^{1/2}}$$

where

λ = diagonal of eigenvalues

Assuming sinusoidal response

$$\ddot{q} = \lambda q$$

from Equations 6.7-5 and 6.7-8 the final result is

$$\ddot{q}_{max} = \phi \omega \phi^T F_O \qquad (6.7\text{-}9)$$

For the launch configuration, the following procedure is used to determine the launch amplification factors for adapter base excitations.

Beginning with Equation 5 of Appendix J

$$M^* \ddot{\xi} + C^* \dot{\xi} + K \xi = F^* \qquad (6.7\text{-}10)$$

and partitioning into forced (base) and unforced coordinates and assuming sinusoidal response, algebraic manipulations reduce the equation to

$$\left[\lambda + i \omega C^* - \omega^2 I \right] \xi_1 = F^* \qquad (6.7\text{-}11)$$

for a unit base displacement.

Where

$\lambda = \phi^T K_{11} \phi$

$C^* = \phi^T C_{11} \phi$

$I = M^* = \phi^T M_{11} \phi$

$F^* = \phi^T K_{12}$

K_{11} = Unforced stiffness set

K_{12} = Stiffness coupling terms between forced and unforced coordinates

ϕ = Matrix of fixed-free mode shapes

The modal coordinate is the sum of real and complex component so that Equation 6.7-11 can be written as:

$$\begin{bmatrix} \lambda - \omega^2 I & -\omega C^* \\ \omega C^* & \lambda - \omega^2 I \end{bmatrix} \begin{bmatrix} \xi_r \\ \xi_\phi \end{bmatrix} = \begin{bmatrix} F^* \\ 0 \end{bmatrix} \qquad (6.7\text{-}12)$$

solving for ξ_ϕ

$$\xi_\phi = - \left[(\lambda - \omega^2 I)^2 + \omega^2 C^{*2} \right]^{-1} \omega C^* F^*$$

Since a time history response calculation produces insignificant response conditions in addition to the maximum condition (resonance), the time history approach is rejected and only the resonant response is investigated.

Since resonant response consists almost entirely of quadrature response, the quadrature response at resonance is used for the response calculations.

The resonant value of quadrature component of modal response is then transformed back into the physical coordinate and the final result is

$$q = - \frac{1}{2} \phi_i \frac{1}{\zeta \omega^2} \phi_i^T K_{12} \qquad (6.7\text{-}13)$$

In addition to these analytic procedures, another development is made to determine an expression for the dynamic behavior of the spacecraft in the spin stabilization portion of the flight. The development of this expression for the change in cone angle with energy dissipation through damping is presented in Appendix K.

6.7.3.4 Configuration Selection Support Studies

A sequence of design concepts have been analyzed for their dynamic response to various orbital and launch perturbances.

Four of these configurations are considered of particular interest.

a. A configuration consisting of an aft equipment module connected by a flexible center support tube to an Earth viewing equipment module. The antenna mounts to the aft equipment module and the solar panels extend beyond the perimeter of the antenna on a pantograph linkage from the aft equipment module.

b. Antenna mounted solar arrays were investigated in an early configuration, featuring a front deploying antenna with cassegrain feed and earth viewing electronics below the feed. This configuration is shown in Figure 6.7-3.

c. The deployed feed configuration of Section 6.2.5 is modeled in Figure 6.7-7.

d. The selected configuration Figure 5.9-1; modeled in Figure 6.7-8.

(These last two configurations (c and d) are compared in detail commencing in Paragraph 6.7.3.4.1.)

Configuration (a) exhibited the largest acceleration responses to station keeping pulses of any configuration investigated. The resulting loads, however, were not significant when compared with those developed in deploying in a 1g field. This method of deploying solar panels was rejected because of low dynamic stiffness.

The antenna mounted solar array configuration (b) provides an evaluation of the capability of the antenna to support the solar panels mounted in its periphery. An orientation control analog simulation was performed using the results of the analysis of this concept.

Modeling of this concept utilized 34 degrees of freedom. The coordinate locations and conventions are shown in Figure 6.7-9.

The front deployment column is considered rigid in transmitting axial load and as a two element beam in bending (two directions). In torsion, it is considered as a torque tube between the Cassegrain reflector and the satellite body.

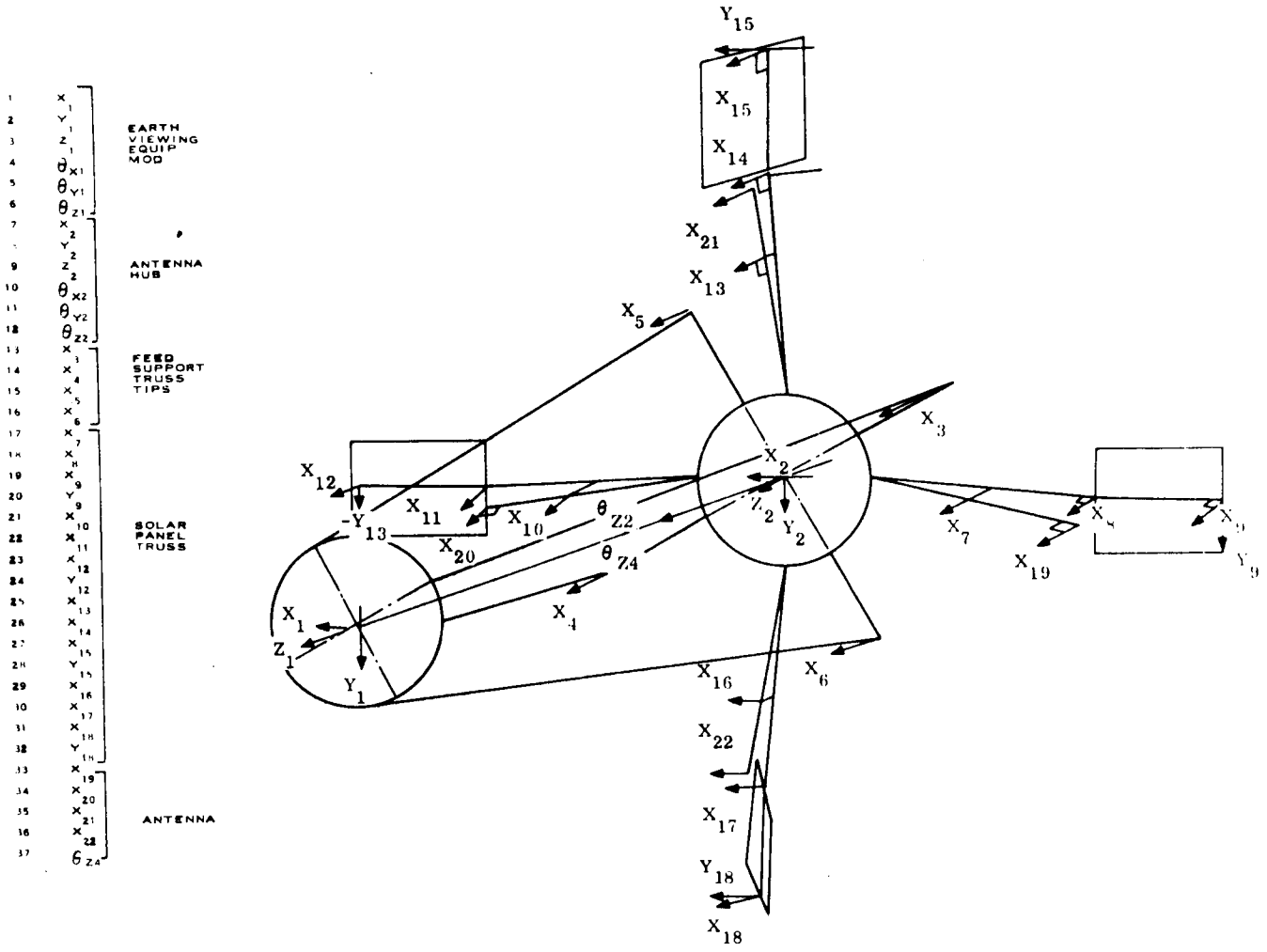


Figure 6.7-7. Coordinate Convention and Locations, Deployed Configuration

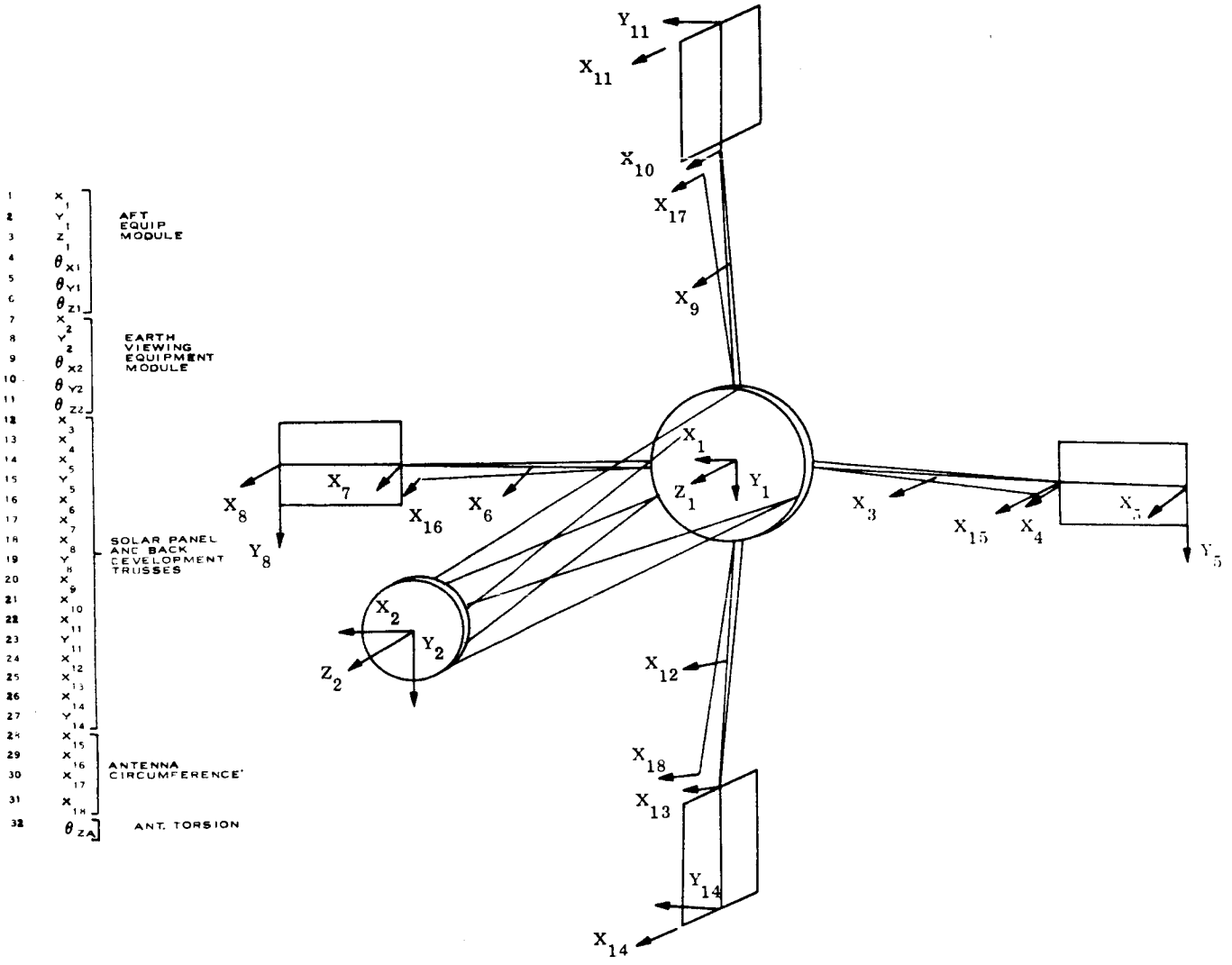


Figure 6.7-8. Coordinate Convention and Locations, Selected Configuration

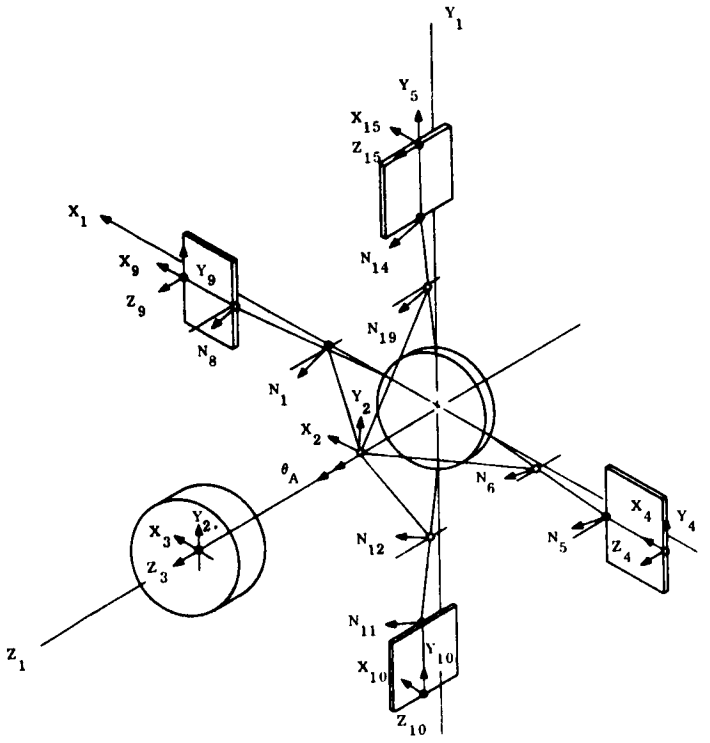


Figure 6.7-9. Coordinate Conventions and Locations, Antenna-Mounted Solar Array Configuration

The parabolic antenna is modeled for a description of its low frequency (nonextensional) modes. This is accomplished by assuming four orthogonally oriented radial node lines and basing section properties on active wedges between node lines. Antenna motions in circumferential directions are regarded as rigid (in terms of beam bending) and motions normal to the petal surface are modeled as beam deflections.

Wedge curvature is found to provide the primary source of bending stiffness and section properties are based on averaged element dimensions at: hub connection, deployment link connection and antenna perimeter. Finally, a torsional coordinate for the antenna is derived based on the shear deflection of the antenna modeled as circular disc.

Each of the four solar panels is modeled as a 4 x 5 foot honeycomb panel weighing 20 pounds each. A stiffness for the hinge linking the antenna and the solar panel is approximated and used to connect the solar panel to the antenna. The panel torsional coordinate along the

length of the panel is included and the torsional moment reacted by normal forces on the antenna circumference on adjacent petals.

The deployment linkage is modeled as axial load carrying members relating normal displacements at the linkage connection to the antenna with normal displacements at point 2 on the deployment column. A mass matrix consistent with the modeling coordinates is developed from weights data for the spacecraft and the resulting 34 degree freedom system is decomposed into its natural frequencies and normal mode shapes.

Transfer functions are presented in Table 6.7-4. The table contains the translational and rotational velocities at the antenna-satellite-deployment column intersection due to unit force (moment) inputs applied at point one (Figure 6.7-9).

Transfer functions are provided only for those mode shapes whose frequency is less than 10 cps and whose response magnitude is greater than 1 percent of the rigid body response.

A Dirac Delta calculation was also made for this configuration. The Dirac Delta was used to obtain response of each mode to a unit impulse. The absolute value of the maximum acceleration response in each mode was then summed over all modes to obtain a conservative estimate of total acceleration response to a unit impulse. This procedure is used with the selected and alternate configurations also.

Table 6.7-5 lists the results of this summation and columns one through six give dynamic component of acceleration for impulses at point one on the deployment column in the direction of X, Y, and Z axes and moments about X, Y, and Z axes. Units for displacement coordinates are in g's per g and rotational coordinates in radians per sec^2 per g.

The Dirac Delta approach to obtain an envelope yields response accelerations which are weighted by the square of the modal frequency. As evidenced from the tabulated results larger values of acceleration occur at coordinate locations which describe high frequency behavior with smaller values at those coordinates which describe low frequency behavior.

Table 6.7-4. Transfer Functions for ATS-4 Configuration with Antenna Mounted Solar Arrays

Frequency rad/sec	Damping	Eigenvalue	$\dot{A}_x$	$\dot{A}_y$	$\dot{A}_z$	$\dot{A}_{\theta_x}$	$\dot{A}_{\theta_y}$	$\dot{A}_{\theta_z}$	Mode
Unit Fx [3] Pt 1									
0	0	0	0.391					0.00251	Rigid Body
4.94	0.012	24.4	0.0257					0.00051	First Antenna Anti-Symmetric
10.17	0.012	103.4	0.00755					0	Solar Array Symmetric
17.38	0.012	302.0	0.0112					0.00032	Second Antenna Anti-Symmetric
Unit Fy [3] Pt 1									
0	0	0		0.391		-0.00251			Rigid Body
5.54	0.012	30.7		0.0268		-0.00053			First Antenna Anti-Symmetric
17.76	0.012	315.0		0.0105		-0.00029			Second Antenna Anti-Symmetric
Unit Fz [3] Pt 1									
0	0	0			0.391				Rigid Body
4.54	0.012	20.6			0.0083				First Solar Array/Antenna-Symmetric
5.09	0.012	25.9			0.0152				Second Solar Array/Antenna-Symmetric
16.28	0.012	265.0			0.0034				Antenna Petal Mode
16.98	0.012	288.0			0.0240				Third Solar Array/Antenna-Symmetric
Unit Mx [3] Pt 1									
0	0	0		0.00251		2.0×10^{-5}			Rigid Body
5.54	0.012	30.7		0.00053		1.06×10^{-5}			First Antenna Anti-Symmetric
17.76	0.012	315.0		0.00029		0.822×10^{-5}			Second Antenna Anti-Symmetric
Unit My [3] Pt 1									
0	0	0	0.00251				2.08×10^{-5}		Rigid Body
4.94	0.012	24.4	0.00051				1.00×10^{-5}		First Antenna Anti-Symmetric
17.38	0.012	302.0	0.00032				0.885×10^{-5}		Second Antenna Anti-Symmetric
Unit Mz [3] Pt 1									
0	0	0						4.50×10^{-5}	Rigid Body
11.75	0.012	138.2						2.44×10^{-5}	First Torsion

A similar analysis for the selected and deployed configuration is discussed in Section 6.7.3.4.3.

Table 6.7-5. Maximum Acceleration Due to Unit Load or Moment Impulse at Point One on Deployment Column

ATS-4 - Configuration (b)
Spacecraft Weight = 1050 Pounds

	1	2	3	4	5	6
Coord.*	R_x	R_y	R_z	R_{m_x}	R_{m_y}	R_{m_z}
X_1	0.113	-	-	-	0.0045	-
Y_1	-	0.128	-	0.0054	-	-
Z_1	-	-	0.027	-	-	-
θ_{x1}	-	0.005	-	0.0004	-	-
θ_{y1}	0.004	-	-	-	0.0004	-
θ_{z1}	-	-	-	-	-	0.0001
X	0.948	-	-	-	0.0379	-
Y^2	-	0.968	-	0.0403	-	-
X^2	0.146	-	-	-	0.0075	-
Y^3	0.027	0.150	-	0.0081	-	-
θ_{x3}	-	0.029	-	0.0014	-	-
θ_{y3}	-	-	-	-	0.0012	-
θ_{z3}	-	-	-	-	-	-
Y_4	-	0.595	-	0.0559	-	0.0132
Z_4	0.011	-	0.008	-	0.0025	-
θ_{x4}	-	0.003	-	-	-	-
Y_9	-	0.595	-	0.0559	-	0.0132
Z_9	0.011	-	0.008	-	0.0002	-
θ_{x9}	-	0.003	-	-	-	-
X_{10}	0.010	-	-	-	-	0.0006
Z_{10}	-	0.012	0.013	-	-	-
θ_{y10}	0.003	-	-	-	-	-
X_{15}	0.010	-	-	-	-	0.0006
Z_{15}	-	0.012	0.013	0.0003	-	-
θ_{y15}	0.003	-	-	-	-	-
N_5	0.016	-	0.018	-	0.0007	-
N_6	0.185	-	0.238	-	0.0358	-
N_7	0.185	-	0.238	-	0.0358	-
N_8	0.016	-	0.018	-	0.0007	-
N_{11}	-	0.016	0.024	0.0007	-	-
N_{12}	-	0.169	0.243	0.0344	-	-
N_{13}	-	0.169	0.243	0.0344	-	-
N_{14}	-	0.016	0.024	0.0007	-	-
θ_A	-	-	-	-	-	-

*X, Y, Z, and N Quantities are in g per g

θ Quantities are in rad/g sec^2

As part of the early configuration studies, an investigation was made into the effects on antenna frequencies by varying the deployment linkage from a front mounted strut type to back mounted truss type and varying the antenna f/D ratio. Results of the previously described configurations are used as a basis for this investigation and the results are contained in Table 6.7-6. The lowest antenna fundamental frequency (1.7 cps) is obtained with back deployment linkage, antenna mounted solar panels and f/D = 0.5. The highest frequency (4.5 cps) is obtained with front mounted deployment linkage, body mounted solar panels and f/D = 0.4.

Changing the deployment linkage from the tubular struts on the front side of the antenna to a truss network on the back side of the antenna provides a softer structural support which lowers antenna frequencies as shown in Table 6.7-6.

Varying the antenna f/D ratio alters the area moment of inertia of the petals by changing the petal curvature which is the primary source of petal stiffness. An investigation into the change in area moment with f/D ratio provides an extrapolation to the probable effect on the shift in antenna natural frequencies which are presented in Table 6.7-7. Cases two and four in Table 6.7-6 are used as baseline cases and data for f/D equal to 0.3 and 0.5 are obtained using the section property variation.

In view of the lower frequencies obtained with an antenna mounted solar panel approach, it was decided to support solar panels on separate truss structure. This support structure is the only structure of the selected configuration specifically designed by the 2 cps orbital stiffness requirement.

6.7.3.4.1 Launch Phase Dynamic Analysis

The selected configuration is represented as a three-mass system for the dynamic response in the launch configuration. Coordinate locations are at the top and bottom of feed deployment truss, adapter-aft equipment module interface, and adapter base (See Figure 6.7-10). The mass distribution is shown in Table 6.7-9.

Table 6.7-6. Antenna with f/D = 0.4

Case	Description	Fundamental Antenna Frequency (cps)
1	Antenna mounted solar arrays with front mounted tabular deployed linkage	2.7
2	Antenna mounted solar arrays with back mounted truss deployed linkage	2.0
3	Antenna used with body mounted pantograph solar arrays and front mounted tubular deployed linkage	4.5
4	Antenna used with body mounted pantograph solar arrays and back mounted truss deployed linkage	3.5

Table 6.7-7. Frequency Shift with f/D Variation

Case	f/D	Fundamental Antenna Frequency (cps)
2	0.3	2.4
2	0.4	2.0
2	0.5	1.7
4	0.3	4.0
4	0.4	3.5
4	0.5	2.8

Considerable lateral amplification at the Earth viewing module is evidenced. In order to best meet the 10 cps minimum lateral frequency, it is desirable to include most of the required structural stiffness in the launch configuration at the adapter for two reasons: first, it reduces the amplifications at the Earth viewing equipment module (EVM) which is severely loaded; secondly, because this mass remains with the booster allowing for a greater useful payload in orbit.

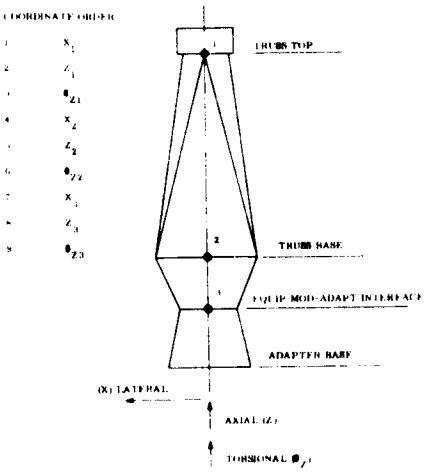


Figure 6.7-10. Response Coordinate Locations, Selected Configuration

As can be seen in Table 6.7-8, large launch amplifications occur at the EVM and when combined with the mass allocation at the coordinate (Table 6.7-9) provide the design criteria for the truss tubes (3-1/4 inch OD beryllium x 0.060 wall).

A flexible description of the solar panel trusses and solar panel has been omitted from the model as these provide little or no structural support between the aft equipment module and EVM. However, future effort will include these items in order to more accurately determine their behavior under launch loading conditions. The solar panels are assumed to be tied to the EVM and therefore these mass properties are included at the EVM coordinates. Similar modeling techniques are applied to the antenna with mass properties introduced at the Aft equipment module and EVM.

The resulting minimum lateral frequency for the spacecraft is 11 cps, being most influenced by the aft equipment module and adapter structure.

The deployed feed, configuration (c), is represented as a two mass system for dynamic response in the launch configuration analysis. Coordinate locations are at the antenna hub and the apogee-equipment module interface as shown in Figure 6.7-11. The mass distribution is in the Table 6.7-9.

Modeling assumptions for this configuration include a 0.040 inch wall thickness for the equipment module and 0.046 wall for the apogee module.

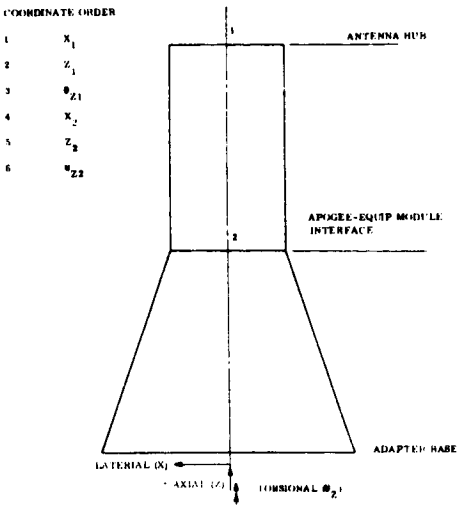


Figure 6.7-11. Launch Response Coordinate Locations, Deployed Configuration

Comparison of amplification factors (Table 6.7-8) for the selected and deployed feed configuration show that the factors are almost identical. Mass distributions for these concepts (Table 6.7-9) are also similar at the top of each launch structure, therefore, the lateral launch loads for both concepts are essentially the same, so that the increased load capability of the shell construction can be utilized to decrease its wall thickness with a subsequent weight reduction.

The resulting minimum lateral frequency of the deployed feed configuration is 18.5 cps.

Table 6.7-8. Launch Accelerations for the Selected and Deployed Configuration Due to A One-g or 1 rad/sec^2 Input

Selected Configuration		Deployed Configuration	
Coordinate Location	Lateral Response	Coordinate Location	Lateral Response
1	12.0 g	1	12.5
2	2.9 g	2	2.4
3	1.2 g		
	Axial Response		Axial Response
1	10.0 g	1	12.8
2	9.2 g	2	8.6
3	4.7 g		
	Torsional Resp.		Torsional Resp.
1	13 rad/sec^2	1	11.3
2	1.2 rad/sec^2	2	10.0
3	1.1 rad/sec^2		

Table 6.7-9. Mass Distribution

	Orbital Mass Distribution		Launch Mass Distribution	
	Selected Configuration	Deployed Configuration	Selected Configuration	Deployed Configuration
Coord.	Mass	Mass	Mass	Mass
1	3.94	2.75	1.26	1.55
2	4.04	2.75	1.26	1.55
3	4.60	2.75	725.00	2230.00
4	7980.00	9660.00	4.00	4.66
5	7350.00	9660.00	4.00	4.66
6	4680.00	1470.00	3220.00	2660.00
7	0.97	0.75	3.30	
8	0.97	0.75	3.30	
9	536.00	0.75	2450.00	
10	536.00	2220.00		
11	357.00	2220.00		
12	0.022	3540.00		
13	0.028	0.036		
14	0.024	0.036		
15	0.024	0.036		
16	0.022	0.036		
17	0.028	0.019		
18	0.024	0.025		
19	0.024	0.025		
20	0.022	0.025		
21	0.051	0.019		
22	0.047	0.025		
23	0.047	0.025		
24	0.022	0.025		
25	0.051	0.019		
26	0.047	0.048		
27	0.047	0.048		
28	0.011	0.048		
29	0.011	0.019		
30	0.011	0.048		
31	0.011	0.048		
32	3678.00	0.048		
33		0.011		
34		0.011		
35		0.011		
36		0.011		
37		1840.00		
Remarks	Coord. Located in Figure 6.7-8	Coord. Located in Figure 6.7-7	Coord. Located in Figure 6.7-10	Coord. Located in Figure 6.7-11

Launch deflections for shroud clearance analysis of the selected configuration are approximated by application of the amplification factors to the Earth viewing equipment module motions obtained from assumption of simple harmonic response. Based on available flight data a first modal flight lateral amplitude of 0.06 inch at a maximum frequency at 5 cps and second modal flight lateral amplitude of 0.03 at maximum frequency of 8 cps have been encountered at station 173 in four Atlas-Centaur flights.

For a worst case example, it is assumed that the booster first mode is tuned to the spacecraft lateral mode (11 cps actual). Earth viewing equipment module lateral deflection would be 0.06 x 12 = 0.72 inch. Since a 3-inch spacecraft excursion is permitted in the shroud clearance design criteria, displacement interference is not anticipated.

6.7.3.4.2 Cost Period Dynamic Analysis

The development of an equation to express the change in cone angle in terms of modal parameters can be found in Appendix K. Using the results of this derivation and typical values for ATS-4 inertias, spin rate, etc., it was determined that the cone rate was 0.052 degree/hr, which should not create any problems.

6.7.3.4.3 Orbital Dynamic Analysis

The selected configuration (Reference Figure 5.9-1) is modeled with a 152-inch, six member diagonal feed support truss connecting the aft equipment module with the Earth viewing equipment module. Attached to the aft equipment module is the antenna interface ring with attached parabolic antenna and back deployment trusses. The solar array panel trusses and panels are attached to both the aft equipment module and the Earth viewing module, the latter, through the preloaded antenna band.

The deployed configuration (Reference Figure 6.2-15) differs in that the one equipment module is coupled to the antenna hub directly in the launch phase and is deployed from the antenna on 4 struts in orbit.

A frequency comparison of the two configurations is shown in Table 6.7-10. In general, the selected configuration shows slightly higher frequencies than the deployed configuration although the differences are not significant. The significance of the mode shapes associated with these frequencies is established strongly in the transfer functions and is discussed in Section 6.7.3.4.4.

The low frequency lateral response of the solar array trusses results from the fact that the trusses in both models were not considered to be attached laterally to the antenna. Some lateral stiffening of the truss is provided by the antenna torsional shell-type stiffness but for a conservative approximation to control transfer functions, no account is taken of this stiffening. Appreciable transfer functions to θ_z excitation for the lateral truss modes represent an upper limit (Table 6.7-11).

Solar panel trusses are sized for 2.0 cps normal bending modes and they approach this design value in the selected design since they are in effect hard mounted in this concept. Mounting of the trusses on the soft feed support truss of the deployed configuration moves the solar array truss maximum response frequency up to 6 cps. However, since in both configurations the antenna and solar array truss are mounted to a common hard structure, little difference is observed in antenna frequency.

The antenna fundamental frequency is the result of the flexibility of the inner section of the antenna where curvature is rather shallow and not much section depth is available for bending resistance. It is primarily dependent upon the back deployment structure for support in this area. The antenna then behaves as a simply supported beam (connections at hub and back deployment linkage) with an overhang load (outer section of antenna). This method of modeling the antenna results in a lower frequency (2.37 cps) than that of the detailed computer analysis discussed in Section 6.3.3.4 (3.3 cps), and is conservative for control system analysis.

Table 6.7-10. Frequency Comparison Selected and Deployed Feed Configuration

Selected Configuration		Deployed Configuration	
Frequency (CPS)	Mode	Frequency (CPS)	Mode
0.91	Solar Array Truss Lateral (Y_{11}, Y_{14})	0.58	Solar Array Hinge
1.02	Solar Array Truss Lateral (Y_{11}, Y_{14})	0.64	Solar Array Hinge
1.96	Solar Array Truss Normal Bending	1.22	Solar Array Hinge
1.97	Solar Array Truss Normal Bending	1.26	Solar Array Hinge
2.37	Antenna Fundamental	1.5	Solar Array Truss Lateral
2.50	Antenna Fundamental	1.8	Solar Array Truss Lateral
2.51	Antenna Fundamental	2.49	Antenna Fundamental
2.53	Antenna Fundamental	2.50	Antenna Fundamental
2.45	Solar Array Truss Normal Bending	2.50	Antenna Fundamental
2.57	Solar Array Truss Normal Bending	2.50	Antenna Fundamental
3.07	Solar Array Truss Lateral (Y_5, Y_8)	2.56	Solar Array Truss Lateral
3.44	Solar Array Truss Lateral (Y_5, Y_8)	2.76	Feed Support Truss
6.94	Solar Array Lateral (X_{11}, X_{14})	2.89	Feed Support Truss
6.99	Solar Array Lateral (X_{11}, X_{14})	3.17	Solar Array Truss Lateral
7.18	Solar Array Normal (X_5, X_8)	5.31	Feed Support Truss
7.21	Solar Array Normal (X_5, X_8)	6.0	Feed Support Truss
10.7	Feed Support Truss Torsion	6.5	Solar Array Truss Normal Bending
19.5	Feed Supt. Truss Lateral Y-Z Plane (First Mode)	7.6	Feed Support Truss
19.7	Feed Supt. Truss Lateral X-Z Plane (First Mode)	8.3	Solar Array Truss Normal Bending
30.25	Feed Supt. Truss Lateral Y-Z Plane (2nd Mode)	10.7	Solar Array Truss Normal Bending
30.45	Feed Supt. Truss Lateral X-Z Plane (2nd Mode)	15.2	Solar Array Bending
32.43	Solar Array Truss Second Mode	15.9	Solar Array Bending
32.93	Solar Array Truss Second Mode	63	Solar Truss Normal Bend Second Mode
33.82	Solar Array Truss Second Mode	63	Solar Array Truss Normal Bend Second Mode
33.0	Solar Array Truss Second Mode	65	Solar Array Truss Normal Bend Second Mode
90	Antenna Torsion	65	Solar Array Truss Normal Bend Second Mode
		175	Feed Supt. Truss Axial Elongation of Truss Tubes
		175	Feed Supt. Truss Axial Elongation of Truss Tubes
		175	Feed Supt. Truss Axial Elongation of Truss Tubes
		178	Feed Supt. Truss Axial Elongation of Truss Tubes
		180	Antenna Torsion

Table 6.7-11. Dirac Delta Response Comparison

Selected Configuration				Deployed Feed Configuration			
Coord.	Response to F_x	Response to F_y	Response to F_z	Coord.	Response to F_x	Response to F_y	Response to F_z
X_1	0.006	0.001	0.00006	X_1	0.01	0.002	-
Y_1	0.001	0.006	-	Y_1	0.002	0.01	-
Z_1	0.00006	0.00001	0.0015	Z_1	-	-	0.052
θ_{x1}	0.00009	0.00046	-	θ_{x1}	0.00003	0.00018	-
θ_{y1}	0.0005	0.0001	-	θ_{y1}	0.0002	0.00003	-
θ_{z1}	-	-	-	θ_{z1}	-	-	-
X_2	0.025	0.003	0.0002	X_2	0.02	0.003	-
Y_2	0.0035	0.025	0.00003	Y_2	0.003	0.022	-
θ_{x2}	0.0002	0.002	-	Z_2	-	-	0.05
θ_{y2}	0.002	0.003	-	θ_{x2}	0.00002	0.0004	-
θ_{z2}	-	-	0.00003	θ_{y2}	0.0004	-	-
X_3	0.195	0.051	0.075	θ_{z2}	-	-	-
X_4	0.057	0.012	0.036	X_3	0.50	0.29	0.89
X_5	0.014	0.0011	0.020	X_4	0.50	0.29	0.89
Y_5	0.001	0.008	0.004	X_5	0.29	0.50	0.89
X_6	0.195	0.051	0.077	X_6	0.29	0.50	0.89
X_7	0.058	0.012	0.037	X_7	0.026	-	0.067
X_8	0.014	0.0011	0.021	X_8	0.069	-	0.133
Y_8	0.001	0.008	0.004	X_9	0.009	-	0.009
X_9	0.066	0.178	0.089	Y_9	-	0.035	-
X_{10}	0.015	0.034	0.026	X_{10}	0.026	-	0.067
X_{11}	0.007	0.011	0.014	X_{11}	0.070	-	0.133
Y_{11}	0.004	0.002	0.004	X_{12}	0.009	-	0.009
X_{12}	0.071	0.178	0.089	Y_{12}	-	0.035	-
X_{13}	0.015	0.034	0.026	X_{13}	-	0.025	0.047
X_{14}	0.006	0.011	0.014	X_{14}	-	0.046	0.108
Y_{14}	0.004	0.002	0.004	X_{15}	-	0.004	0.004
X_{15}	0.008	0.001	0.017	Y_{15}	0.008	-	-
X_{16}	0.008	0.001	0.016	X_{16}	-	0.025	0.047
X_{17}	0.007	0.001	0.014	X_{17}	-	0.046	0.108
X_{18}	0.006	0.001	0.014	X_{18}	0.008	-	-
θ_{Z_A}	-	-	-	Y_{18}	0.008	0	0
				X_{19}	0.011	-	0.013
				X_{20}	0.011	-	0.013
				X_{21}	-	0.012	0.014
				X_{22}	-	0.012	0.014
				θ_{Z_A}	-	-	-

The design criteria for the feed support truss are different for the two configurations. The selected configuration locates the orientation control sensors and the force generators in separate modules connected by the feed truss. In this arrangement a rigid (>10 cps) structure connecting the two modules is required. In the deployed configuration the location of the orientation control sensors and the force generators in a single module eliminates this requirement. This difference is shown in the higher grequency support truss mode in the selected configuration.

Acceleration response to unit force impulses are tabulated in Table 6.7-10 for the two configurations. For the selected configuration accelerations of 0.195 g occur on solar panel trusses at antenna connection when excited by a lateral impulse at the aft equipment module. This situation reflects the relatively high frequency motion associated with those coordinates (32 cps).

For the deployed concept, maximum accelerations of 0.89 g occur in the deployment truss in the truss tube axial direction when subjected to a one-g axial impulse at the Earth viewing equipment module. This connection likewise reflects high frequency behavior, (axial elongation of struts). Low accelerations can be evidenced in most of the other coordinates.

6.7.3.4.4 Control Transfer Functions

Comparison of the control transfer functions for the selected and deployed configuration, Table 6.7-12, shows that low frequency motions dominate the deployed feed configuration transfer functions and, when weighed with the magnitude of the transfer functions, offers more control problems than does the selected design. Transfer function admittances for the selected configuration with the exception of the torsional condition, are in general smaller than corresponding values in the deployed feed configuration and together with the higher natural frequencies give a less severe dynamic response to control action. The large torsional transfer function previously mentioned in the selected design is offset by the high frequency of an antenna torsional mode so it is not a severe problem area. It is interesting to note that in the deployed feed configuration, there was no appreciable transfer function from antenna torsional mode to the response at the aft equipment module which indicates

Table 6.7-12. Control Transfer Functions

Selected Configuration				Deployed Configuration			
Mode	$A_{\ddot{y}}$	$A_{\ddot{\theta}_x}$	Frequency (cps)	Mode	$A_{\ddot{y}}$	$A_{\ddot{\theta}_x}$	Frequency (Cps)
θ_x Excitation							
Rigid	8.94×10^{-4}	2.3×10^{-5}	-	Rigid	9.1×10^{-4}	2.2×10^{-5}	-
				Sol. Pan. Hinge	-2.12×10^{-4}	6.5×10^{-6}	0.63
Antenna Fundamental	1.05×10^{-4}	-	2.51	Ant. Fundamental	-3.82×10^{-5}	1.1×10^{-6}	2.50
				Sol. Pan Truss Lat.	8.16×10^{-4}	3.2×10^{-5}	2.56
Feed Supt. Truss Lateral	-5.7×10^{-4}	3.2×10^{-5}	19.5	Feed Supt. Truss	5.35×10^{-4}	3.31×10^{-5}	2.9
Feed Support Truss Lateral	3.4×10^{-4}	3.6×10^{-5}	30.2	Feed Supt. Truss	-1.16×10^{-4}	1.14×10^{-6}	6.0
Solar Array Truss	-1.8×10^{-4}	1.9×10^{-5}	33.8				
θ_y Excitation							
Mode	$A_{\ddot{x}}$	$A_{\ddot{\theta}_y}$	Frequency (Cps)	Mode	$A_{\ddot{x}}$	$A_{\ddot{\theta}_y}$	Frequency (Cps)
Rigid	9.55×10^{-4}	2.72×10^{-5}	-	Rigid	1.09×10^{-3}	2.97×10^{-5}	-
				Sol. Array Pan. Hinge	1.06×10^{-4}	3.31×10^{-6}	1.26
				Sol. Array Truss Lat.	0.97×10^{-5}	2.16×10^{-6}	1.51
Antenna Fundamental	-2.41×10^{-5}	1.29×10^{-6}	2.53	Antenna Fundamental	3.65×10^{-5}	1.32×10^{-6}	2.50
Feed Supt. Truss Lat. First Mode	3.61×10^{-4}	3.25×10^{-5}	19.7	Feed Supt. Truss	-1.29×10^{-3}	6.22×10^{-5}	2.76
Feed Supt. Truss Lat. Second Mode	2.86×10^{-4}	3.29×10^{-5}	30.4	Feed Supt. Truss	9.91×10^{-5}	1.05×10^{-6}	7.6
Sol. Array Truss Normal Bend Second Mode	2.91×10^{-4}	3.10×10^{-5}	33.8				
θ_z Excitation							
Mode	$A_{\ddot{z}}$	$A_{\ddot{\theta}_z}$	Frequency (Cps)	Mode		$A_{\ddot{\theta}_z}$	Frequency (Cps)
Rigid		5.18×10^{-5}	-	Rigid		6.12×10^{-5}	-
Sol. Array Truss Lat.		1.84×10^{-5}	1.02	Sol. Array Truss Lat.		3.20×10^{-5}	1.79
Sol. Array Truss Lat.		2.48×10^{-5}	3.41	Sol. Array Truss Lat.		1.39×10^{-5}	3.17
				Feed Supt. Truss		1.12×10^{-4}	5.3
Antenna Torsion		9.39×10^{-5}	90.				

the isolating effect of the 2.5 cps feed support truss used in this configuration; instead there is a significantly large transfer function from the support truss itself.

Control structural transfer functions were also determined for a gravity stabilization rod, in the event that this was to be included as an experiment.

Assumptions made regarding the spacecraft are as follows:

a. Spacecraft centerbody CG and inertias are identical to the equivalent configuration without a gravity gradient rod.

b. The spacecraft weighs 2000 lb.

The BeCu gravity gradient rod is divided into five equal length elements for purposes of obtaining all modes below 10 cps. The results of this analysis indicate that this was met, with upper frequencies ranging from 2 to 13 cps for six cases investigated.

The consistent mass approach is used in the mass modeling of the gravity gradient rod. Six combinations of rod length, diameter and tip-weight are investigated and listed in Table 6.7-13. The control transfer functions listed are those relating unit forces and moments to corresponding responses at the vehicle end of the gravity gradient rod. The numerators relating translational responses to forces are labeled as A_y and those relating rotational responses to moment inputs are labeled as A_{θ_x}.

Transfer functions which are less than 1 percent of the rigid transfer function are neglected. As expected the largest transfer functions are those obtained from low frequency modes and the major contribution is from the fundamental cantilever mode. The numerators approximate the rigid body contribution of the rod and when combined with the low frequency produce significantly large transfer functions. Fundamental frequencies range from 0.002 to 0.001 cps.

Table 6.7-13. Transfer Functions for Gravity Gradient Rods

Case			Rigid Body Mode	First Mode	Rigid Body Mode	First Mode	Frequency
Rod Diameter	Length	Tip Wt.	A_x	A_x	A_{ey}	A_{ey}	
0.5	130	20	$1.04(10^{-4})$	$-9.9\ (10^{-5})$	$6.41(10^{-6})$	$3.02(10^{-5})$	$1.267(10^{-2})$
1.0	130	20	$1.06(10^{-4})$	$-9.6\ (10^{-5})$	$6.25(10^{-6})$	$3.01(10^{-5})$	$3.51\ (10^{-2})$
0.5	65	20	$1.35(10^{-4})$	$-1.33(10^{-4})$	$1.70(10^{-5})$	$1.99(10^{-5})$	$2.22\ (10^{-2})$
1.0	65	20	$1.37(10^{-4})$	$-1.34(10^{-4})$	$1.68(10^{-5})$	$2.00(10^{-5})$	$6.28\ (10^{-2})$
0.5	130	5	$7.46(10^{-5})$	$-6.97(10^{-5})$	$1.60(10^{-5})$	$2.07(10^{-5})$	$1.55\ (10^{-2})$
1.0	130	5	$8.16(10^{-5})$	$-7.23(10^{-5})$	$1.49(10^{-5})$	$2.15(10^{-5})$	$4.33\ (10^{-2})$

6.7.3.4.5 Damping

An important element in the prediction of the structural dynamic responses of the ATS-4 spacecraft is the magnitude of damping. The nature of damping, the dissipation of energy, is easy to recognize and it is not a difficult task to measure its magnitude on an actual structure. However, damping is a most complicated phenomenon. The analytical prediction of damping for a new structure is, at present, an art not a science.

The damping measured on an actual spacecraft is the total energy dissipated by the vibrating system. This energy dissipation occurs through miscellaneous means, such as the impacting of parts, noise, airpumping, fretting at the faying surfaces, visco elastic and material damping. Perhaps the best understood form of damping is material damping. Unfortunately, the other means of dissipating energy are generally larger.

Fortunately, similar structures respond to similar environment in a similar manner. This allows utilization of past experience with similar structures in predicting damping for the new structure. The analysis performed in this study have drawn heavily on past experience and intuition in arriving at the magnitude of damping.

It must be emphasized that the range of damping values used in this study are a best estimate and the final design study will use values determined from experiments performed on actual major structural components of the ATS-4 spacecraft.

For the launch study and the responses to base shaker input, the value of damping is chosen as 5 percent of critical viscous damping. This nominal value has been used with reasonable success in the past development of similar spacecraft structures (measured damping values for the Nimbus spacecraft ranged from 1 percent to 8 percent of critical viscous damping).

It is understood that the form of damping considered here is modal damping. In that context a reasonable comparison of analytic results and tests are available from the Nimbus spacecraft data. It becomes especially interesting in that during the Nimbus modal survey it was found that the value of measured damping varied by as much as 4 to 1 dependent upon the method of calculating damping and the transducer location. (Methods used for calculating damping in this series of tests were: frequency of peak in-phase component before and after resonance, half power point band width and log decrement.)

For the cone angle study, a large value for damping is assumed for the spinning spacecraft. The large value is chosen in order to exaggerate the rate of cone angle increase. Since this is obviously a conservative assumption and no detrimental effects are produced, it will not be discussed further.

A range of damping values was chosen for the orbital control response study. This is a problem area in which experience in the form of data for similar spacecraft is not existing. From data available, a range of damping values of 0.6 to 0.1 percent of critical viscous damping was chosen as being reasonable and attainable in the actual spacecraft.

It is pertinent to point up a measure of the difficulty in predicting damping at this time. It is recognized that the magnitude of damping for a structure in a vacuum approaches that of material damping. In a recent work by Granick and Stern of NASA-GSFC, reporting

tests on aluminum cantilever beams in a vacuum, the method of Zener for predicting damping is shown to agree with test.

Using the method of Zener, values of equivalent viscous damping of 0.088 percent for aluminum and 0.041 percent for titanium are calculated for the ATS-4 antenna.

A generally accepted method of calculating material damping is that of Lazan (Shock and Vibration Handbook, by Harris and Crede). Using the method of Lazan, values of equivalent viscous damping of 0.15 percent for aluminum and 0.075 percent for titanium are calculated for the ATS-4 antenna.

It is concluded that accepted techniques predict values of damping which differ by a factor of two. Although, these results are interesting and indicate the need for further basic work, it must be recognized that none of the results are truly representative of the ATS-4 structure. Correct values of damping can only be obtained by measuring the magnitude of damping in ATS-4 structural elements in a vacuum. The experimentally derived values will be used in the final analysis for confident prediction of the ATS-4 behavior in orbit.

6.7.4 ELECTRONIC PACKAGING

6.7.4.1 Design Criteria

Reliability and other program requirements dictate the following design criteria:

a. Space ratable off-the-shelf electronic equipment will be used wherever possible in the electronics subsystems.

b. Proven methods and techniques of electronic packaging for reliability and long life will be used.

c. Heat producing and heat sensitive assemblies will be mounted on heat rejection panels.

d. The electronics will be structurally integrated into the vehicle with sufficient utilization of available volume to provide space for additional electronic equipment which may be found to be necessary during system development.

e. Electronic assemblies and components will be packaged into subsystem assemblies according to subsystem function as much as is practical without violating thermal and mass-balance requirements.

f. Proven methods and techniques of system and subassembly wiring based on past experience with standard wire, cables, and harness will be used.

g. During the system development phase, the selected harness design will be sufficiently flexible to accept changes in interconnection, shifts in subsystem and subassembly locations, and changes in quantity and type of wire and cables.

h. Cables will allow for the application of parallel redundancy techniques as found necessary for critical signal and return wires and connections.

i. The harnesses will provide for separation or grouping and isolation of sensitive and noisy signals, shielding and grounding as necessary for control of electromagnetic and electrostatic interference.

j. The complexity of the on-board systems and requirements for redundancy may result in a great many interconnections. Means will be employed to reduce the magnitude of the termination problem by such methods as:

    1. Judicious location of individual electronic assemblies within the limits of thermal and mass-balance considerations

    2. Sharing signal, control, and return lines without affecting operation reliability, or obviating EMI control measures

    3. Commoning of multiple use lines by reliable distribution methods such as buss bars, or splices which reduce the total number of wires and connections

6.7.4.2 Selected Configuration

The selected method of packaging the electronics in the ATS-4 spacecraft was considered over the other techniques requiring standardized electronics modules such as those used in Nimbus and Voyager (discussed in Section 6.7.4.3). Some of the advantages of this selection are delineated below:

a. It permits the use of some off-the-shelf equipment without the added expense of repackaging into a standardized configuration.

b. Better thermal control can be realized because all of the heat sensitive and heat producing electronic components will be mounted on the heat rejection panels.

c. Hinged or removable panels provide access to the electronics for test, trouble-shooting, and repair without disconnecting the panel or its associated electronic components from the system wire harness.

d. Growth potential can be realized by the use of module structural members and the addition of bulkheads for mounting of additional electronic equipment which is relatively insensitive to heat.

It is recommended that for those components requiring redesign and repackaging, a standard format, as discussed above, be selected.

6.7.4.2.1 Electronic Assemblies

To assure that reliability requirements for space borne equipment will be met, as much of the electronic equipment as practicable will be packaged in welded cordwood modules. The advantages of cordwood construction are:

a. It allows high packaging density without over complicating the interconnection system.

b. It provides protection for fragile electronic parts and interconnections from the most severe environments with high reliability.

c. The disciplines of design, manufacture, testing, and maintenance are performed in discrete, logical steps.

Electronic parts are mounted cordwood style, with their axial leads extending through the top and bottom insulating layers of Mylar film. Interconnection is accomplished by welding nickel ribbon between leads according to the circuit printed on the Mylar film. Interconnections between Mylar layers are made by nickel riser pins welded to ribbons on the top and bottom layers. After interconnections and testing are completed, a freeze coating of epoxy resin is applied and cured on the parts as a cushion against mechanical and thermal shock. A final encapsulation converts the assembly into a solid plastic parallelopiped with terminal pins protruding from one face which may be used as the mounting face if desired.

6.7.4.2.2 Harnessing

The ATS-4 Spacecraft wiring will provide the capability of electrically interconnecting subsystems with assurance of the successful transmission of all electrical signals whenever required without degradation for the flight mission lifetime. It will be designed to function under all combinations of pre-space and space environments.

Spacecraft components will be interconnected by the:

a. Intermodule Harness

b. Module Harnesses

c. Electronic Assembly Harnesses

The intermodule harness will interconnect power and signal functions between the Earth viewing and aft modules. The harness will be attached to the spacecraft structure with cable grouping, separation, shielding, and thermal barriers employed as required for EMI control and for protection from the space environments.

The module harnesses will be composed of separated signal, command, telemetry and power bundles as required to interconnect the electronic equipment panels with each other and with the intermodule harness interface.

The electronic assemblies and components on each equipment panel will be interconnected by an electronic assembly harness. Destinations of signal and power functions which are external to the panel will be terminated at connectors to interface with the module harness.

6.7.4.3 Alternate Approaches

The following alternate approaches were considered for packaging the electronic equipment:

a. Standardized electronic module configuration

b. Standardized electronic equipment panels with separate removable subassemblies or components

c. Functional subsystem groupings with all components comprising a subsystem physically integrated and interconnected as a removable subsystem

Approach (a) is similar to that used on Nimbus with the modularized electronic packages, considered as Level II modules of standard configurations, only mounted in a ring around the vehicle equipment modules (called Level I). The ring does not depend upon these modular boxes for stiffness or support but rather the boxes present loads on the ring structure. There is no requirement for grouping boxes by function and the mounting and thermal design allows these to be located anywhere in the ring.

Advantages of this approach are as follows:

a. Standard modular boxes of the same configuration and mounting simplifies the task of designing boxes. The same basic design can be used for all electronic components.

b. Standard boxes of same design reduce the manufacturing engineering and planning problems and high tooling costs normally encountered when fabricating boxes of different designs.

c. The design of the vehicle structure can proceed independent of the electronic components.

d. Structural integration and thermal analyses can be simplified.

e. Mass balancing can be simplified by shifting boxes as necessary.

f. Design flexibility due to being able to shift boxes as required.

g. Growth potential exists inside less dense boxes and to unoccupied slots or dummy spare modules.

Some disadvantages are:

a. Inefficient utilization of volume

b. Additional weight of vehicle structure and modular boxes

c. Thermal paths may not be optimized

d. Off-the-shelf equipment cannot be used

e. Growth of circuitry in heavily packaged module requires change to next larger size box or splitting function into more than one box

f. Interconnections and vehicle harness become exceedingly complex

Approach (b) provides for standardization by equipment panel only. The panel may be one complete component in a subsystem or contain separate removable component or subassemblies in black box form. Components or subassembly configurations are restricted only by maximum envelope dimensions and preferred thermal and mounting requirements. Components are grouped on a panel by related function and efficient use of mounting space. Figure 6.7-12 illustrates this concept as developed for another program.

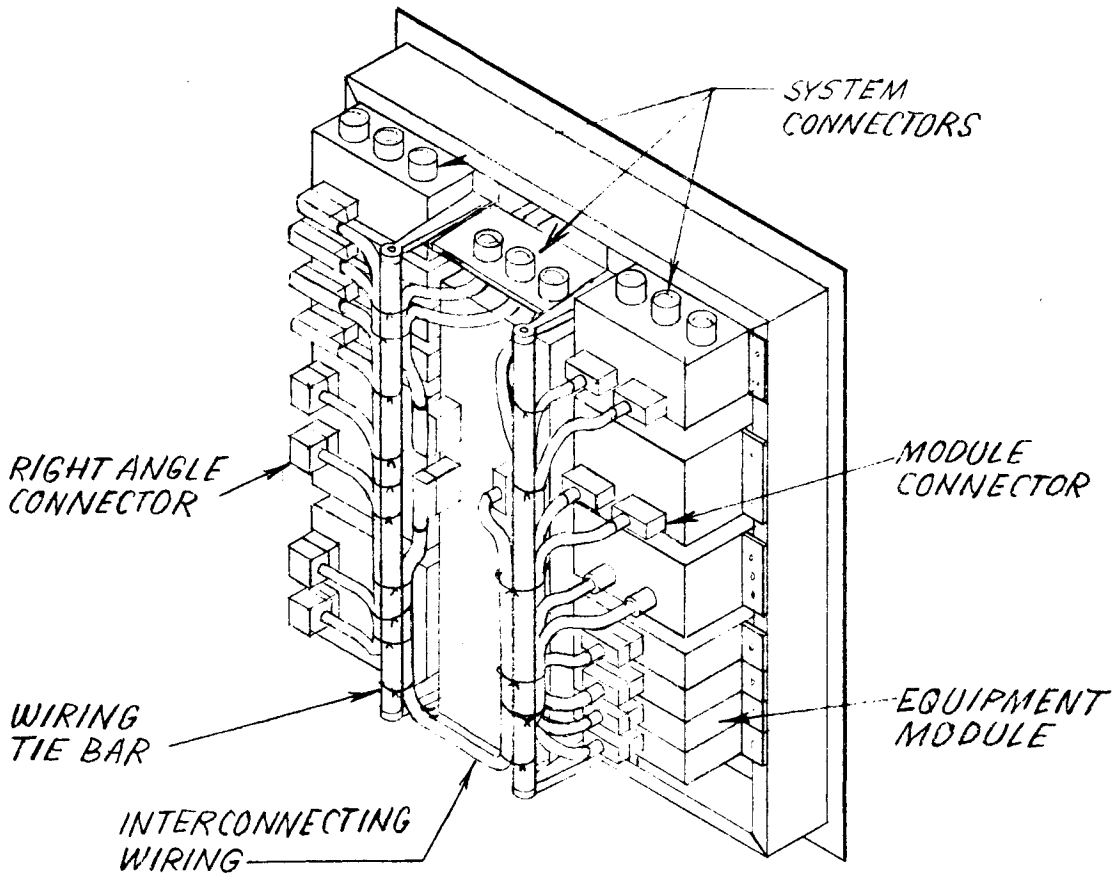


Figure 6.7-12. Typical Electronic Panel, Alternate Approach

Advantages of this approach are:

a. The bare panel can be sufficiently stiffened to integrate the panel into the primary vehicle module structural load paths.

b. Grouping components by related function reduces the complexity of the interconnecting wiring and vehicle harness.

c. The design of the vehicle module structure can proceed independent of the separate black box components.

d. Off-the-shelf hardware meeting the maximum configuration envelope restrictions can be used. Some of these will require intermediate bracketry.

e. Hot components can be grouped to improve the heat distribution by more efficient use of temperature controlled surfaces.

Disadvantages are as follows:

a. Individual boxes structurally load the panel

b. Some common tooling necessary for mounting between panel and vehicle structure

c. Not all off-the-shelf components and hardware can be used

d. Grouping and mounting restriction complicate the thermal design and may result in increased part temperatures

Approach (c) is similar to that developed for the Voyager Program with a subassembly of electronics packaged in the form of a standard box or tray tied structurally into a standard panel assembly. When assembled, this integrated package gives rigid support to the electronics, stabilizes the vehicle equipment module structure and provides heat paths between the electronics, the vehicle structure and heat rejection surfaces. Figure 6.7-13 shows an exploded view of a standard electronic panel.

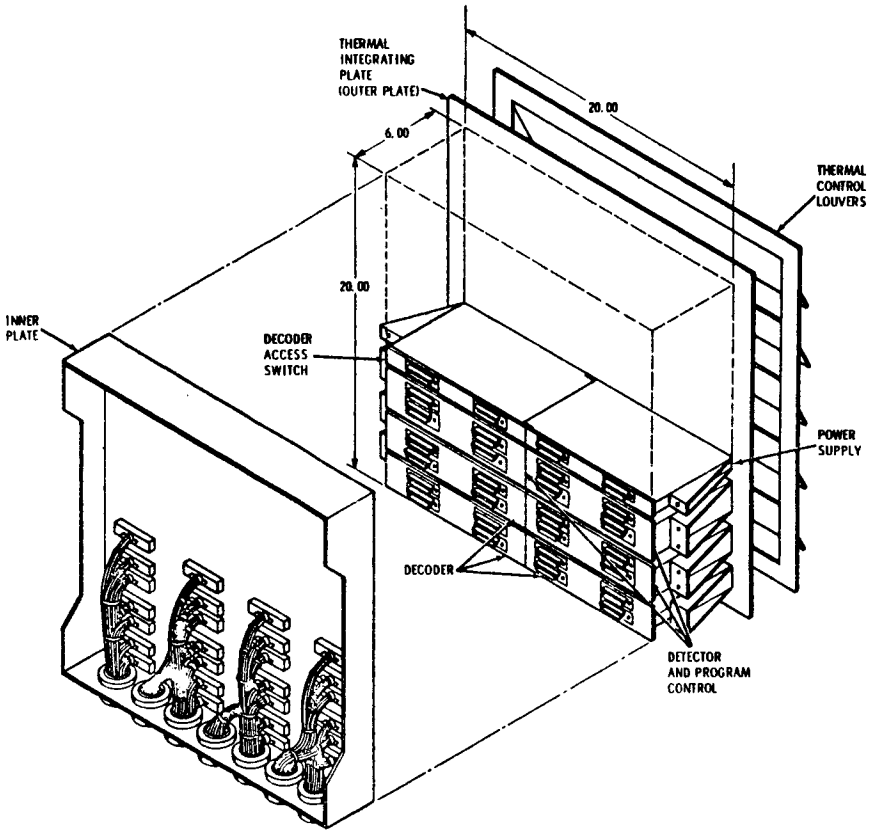


Figure 6.7-13. Voyager Standard Panel

Advantages of this method are:

a. Standard assembly gives great flexibility for functional, thermal, and center-of-gravity balancing

b. The stiffening provided by the electronic subassemblies allows weight saving in the structure

c. The stiffness of the subassemblies improve the reliability of the electronics by increasing the inherent resistance to environmental stress

d. Short thermal path to heat rejection surfaces possible

e. Structure and component design can proceed independently by virtue of standardization of interface

Disadvantages are:

a. Cannot use previously designed components

b. Requires disassembly of structure to remove electronics since standard panel is part of the vehicle structure

c. Unused slots require dummy modules or stiffener

6.7.4.4 Areas for Further Study

The final designs and physical locations of the electronic assemblies and components can be determined only after a thorough study and making tradeoffs of:

a. The function of the assembly or component

b. Heat dissipation and/or heat sensitivity of the assembly or component

c. Duty cycle of assembly or component

d. Mass-balance within the spacecraft

e. Harnessing considerations

6.8 APOGEE MOTOR SELECTION

6.8.1 INTRODUCTION

The study of apogee motors was preceded by a brief consideration of alternate propulsion techniques, which indicated that the use of a solid motor would maximize the use of available hardware and cost far less than an equivalent liquid bipropellant system. Additionally, a payload weight superiority is achieved by the solid motors within existing and 1969 state of the art.

The function of the apogee motor is to provide sufficient velocity to the spacecraft at the apogee of the elliptical transfer orbit to establish the synchronous equatorial orbit. By combining circularization and inclination shift into a single velocity increment, the transfer orbit is circularized and the plane changed.

A survey of apogee motors for both the Atlas (SLV-3A)/Agena-D and the Atlas (SLV-3C)/Centaur launch vehicles was performed. Three classes of motors were considered: available motors which could be used as is, modified existing motors, and lastly, new motors which would be optimized for this application. Contacts were made with motor vendors to obtain realistic estimates of performance and cost.

Early in the study, serious consideration was given to the use of the Burner II apogee stage for this application. Meetings were held with the Burner II contractor to discuss this in depth. However, the Burner II approach was eliminated from consideration because of the following:

a. In the case of the Atlas/Centaur launch vehicle, the Burner II apogee motor fuel loading would have to be significantly increased to circularize the anticipated payload, resulting in development and requalification. If used with the Atlas/Agena launch vehicle, the propellant loading of the present Burner II engine would be decreased by a small amount, but the weight of the guidance, apogee motor casing, and structure makes this application unattractive due to the limited payload capability of this launch vehicle.

b. The present Burner system is designed for a short-coast and a low-earth-orbit insertion. For our application, it is doubtful that the drift of the strap-down gyros could be tolerated for the several days required for initial acquisition. For this reason, the guidance systems would have to be re-designed or it might be necessary to include sensors to update the gyros periodically during the mission. This would result in development and qualification effort.

c. The vernier thrusting capability of the Burner, as designed, is almost an order of magnitude less than that required for the ATS-4 mission. For this reason, the vernier subsystem would require a complete re-design.

d. The primary batteries used as the power supply for the Burner II apogee stage would not be sufficient for the time period anticipated for the initial acquisition of the ATS-4 spacecraft. It is possible that secondary batteries could be carried and that the spacecraft's solar array could be used for regeneration. This would require a development program and would increase the interface complexity.

e. The separate apogee motor approach is incompatible with the selected spacecraft geometry and available fairing extentions. However, it could be used with the alternate spacecraft configuration (deployed feed approach).

6.8.2 APOGEE MOTOR REQUIREMENTS

Synchronous equatorial orbit insertion of payloads from a transfer ellipse, starting at 100 nautical miles, requires the addition of approximately 6050 feet per second. This value varies with the selected launch azimuth and the amount of plane change that takes place at perigee. The payload weight, in addition to the required ΔV, specifies the apogee motor total impulse requirements.

The process of matching apogee motor capability to launch vehicle capability requires tradeoffs to obtain the optimum payload into orbit. For example, if the launch vehicle can place more payload into the transfer orbit than a selected apogee motor can circularize and plane change, the excess energy is used to perform a partial plane change at perigee. Table 6.8-1 illustrates the capability of the Improved Delta third stage (used as an apogee motor) as a function of the plane change angle required at apogee. This motor is proposed for use with the Centaur. The Centaur capability into the transfer orbit as a function of plane change can be compared to the values in this table, where the total plane change required would equal the park orbit inclination.

Table 6.8-1. Payload Capability Using TE-364-3 Delta Motor

Plane Change Angle (deg)	ΔV	W_1	Net P/L
18	5400	3260	1681
20	5500	3210	1631
21	5560	3180	1601
22	5630	3160	1581
24	5780	3100	1521

Where: ΔV - The velocity added by the apogee motor

W_1 - The payload into the transfer orbit

P/L - The payload into orbit capability (not including the apogee motor dry weight)

6.8.3 APOGEE MOTOR SELECTION - SLV-3A/AGENA D

Five apogee motors were considered for the Agena configuration. A tradeoff was made based on a booster payload capability of 2300 pounds and a park orbit inclination of 28.5 degrees. These are:

a. Cutback Surveyor (Thiokol)

b. Enlarged FW-4S (UTC)

c. (Two) ALTAIR II, X-258 (Hercules)

d. Enlarged Alcor (Aerojet)

e. New state-of-art motor (Aerojet)

Of these motors, the modified Alcor required development but could not be modified sufficiently to maximize payload and was dropped from further consideration. Refer to Table 6.8-2 for design parameters obtained from the respective motor manufacturers.

Table 6.8-2. Apogee Motor Tradeoff Matrix

Atlas SLV-3A/Agena-D

	Two Hercules Altaire II X-258-B1	Enlarged FW-45(UTC)	Cutback Surveyor (Thiokol)	Aerojet ALCOR Modified	Aerojet New Unit
Apogee P/L Wt (lb)	2050	2300	2300	1964.3	2.300
ΔV (fps)	6050	6050	6050	6000	6050
W_1/W_2		1.97	1.91		1.87
Gross Spacecraft Wt (lb)	1048.0	1170	1202	1047.6	1230.0
Wt of Motor Case (lb)	137.0	70	122	110.6	119.0
Net Spacecraft Wt (lb)	911.0	1100	1080	937.0	1111.0
Motor Design Data:					
Length (in)	59.25/each	84	52.3	95	46.244
Diameter (in)	18/each	19.6	37	20.5 (Chamber) 29.2 (Nozzle)	38,346
Vac. Max Thrust (lb_f)	6,800	----	9250	----	
Vac. Avg Thrust (lb_f)	6,480	----	8330	9,050	7,343
I_{sp} (lb_f-sec/lb_m)	280	278	(Classified)	296.6	300
Propellant Wt (lb)	501.4/engine	1130	1098	916.7	1070.0
Total Wt, Motor (lb)	574.5/engine	1220	1220	1027.3	1189.0
Burnout Wt (W_2, lb)	68.4/engine	70	122	110.6	119.0
Thrust Time (sec)	21.6	----	36.7	30.0	43.5
Total Impulse (lb-sec)	140,300/each	314,000	(Classified)	271,820	321,700
Non-Recurring Cost	Developed	≈500K	≈650K	----	≈1,800K including 6 motors
Per Unit Cost	32-35K	30-40K	95K	----	
Temperature	400°F	500°F	----	----	-----
Max g	12.4	----	6.9, max: 8	8.67	3.95
Delivery Time (Month)	6-8	----	14	18-24	18-24
Total Cost for 6 Motors	420K	≈710K	≈1220K	----	≈1,800K

The FW-4S modification, which offers excellent performance, was dropped because of the long thin shape of the case, which would make packaging very difficult. The two "new" motors were studied, and it was decided that the lower cost of the cutback Surveyor design, coupled with the existing technology base from which the motor would be developed makes this the optimum motor selection rather than the totally new design proposed by Aerojet General.

The Surveyor motor was developed by the Thiokol Chemical Corporation. An inert weight of 122 pounds is based on an assumed use of a titanium case and carbon cloth nozzle. The environmental temperature limits are 10^{o}F to 110^{o}F. The Surveyor motor has a 50 percent smaller g loading and an 17.5 percent greater payload capability than the two Hercules Altairs, but the Surveyor TE-364 delivery cost of six engines is 60.6 percent higher than the two Hercules Altairs. Therefore, the use of the dual Altair motors represents a backup minimum cost selection resulting in less payload capability than realized with the Surveyor Motor. The packaging of two Hercules Altair engines requires only 7 inches more space in length than the Surveyor TE-364-2 and approximately the same width. The Surveyor TE-364 meets ΔV and payload requirements. It has maximum g force less than 8, and its cost is moderate. It is not the least expensive, but it will meet program requirements and can be packaged with only moderate problems (it is not as long and slender as the FW-4S and the modified Altaire II). The development risk of this engine is moderate to low because of the advanced technology of the existing Surveyor engines and the small steps between the TE-364 series engines.

6.8.4 APOGEE MOTOR SELECTION - SLV-3C/CENTAUR

Initially in the study a SLV-3C/Centaur payload capability of 4300 pounds into the transfer orbit was considered. The capability was later changed to 4000 pounds. Apogee motors have been evaluated for both capabilities. Following is a list of the motors initially considered for use with the Atlas Centaur ATS-4 configuration:

a. Antares I
b. Cutback Antares II
c. Extended Surveyor
d. Aerojet new unit
e. Existing Antares II
f. Antares II with shortened nozzle

To evaluate the above six motors, a ΔV of 6050 fps and a payload of 4300 pounds were used. This tradeoff (Table 6.8-3) shows the physical and performance data on the six motors.

The existing Antares II and short nozzle Antares II are too powerful for this application and were eliminated. The proposed Aerojet Motor was eliminated in favor of the Surveyor Extension Design which would have a firmer technology base from which to grow and would involve, therefore, lower developmental risk. The final motor selection process narrowed to consideration of:

a. Antares I
b. Cutback Antares II
c. Surveyor extension motor
d. Delta motor

Table 6.8-4 presents pertinent design information for the candidate apogee motors.

Antares I (X254-A1)

Allegany Ballistics Laboratory (ABL) developed the solid propellant fueled Antares I rocket motor for use in the third stage propulsion system of the NASA Scout Launching Vehicle. The motor became operational in January 1960. By mid-1963, the Antares I had completed 28 successful flights. Figure 6.8-1 is a drawing of the X254-A1.

Antares II

Antares II was developed by Allegany Ballistics Laboratory (ABL) to comply with technical requirements stipulated by NASA and the Bureau of Naval Weapons for use as an advanced third stage propulsion unit for the Scout Launch Vehicle.

Table 6.8-3. Atlas SLV-3C/Centaur

	Antares I X-254-1A	Cut Back Antares II	Thiokol Surveyor Extension	Aerojet New Motor	Existing Antares II	Antares II With Shortened Nozzle (ϵ = 2.0)
Apogee P/L Wt (lb)	4000	4300	4300	4300	5162	4682
ΔV (fps)	6050	6050	6050	6050	6050	6050
W1/W2	2.085	1.95	1.91	1.87		
Gross spacecraft wt (lbs)	1915	2202	2250	2300	2700	2130
Wt of motor case (lb)	170	223	140	223	233	188
Net spacecraft wt (lb)	1745	1979	2110	2077	2477	1942
Motor design data:						
Length (in.)	114.68	114.00	68.101	56.525	114	84
Diameter (in.)	30.02	30.05	36.912	47.240	30.05	30.05
Vac. max. thrust (lb)	16,500	---	13,355	----	23,500	23,500
Vac. avg. thrust (lb)	14,100	---	11,800	11,153	21,400	18,000
Isp (lbf-sec/lb_m)	256	282	(Classified)	300	281	288
Propellant wt. (lb)	2085	2098	2050	2000	2562	2562
Total wt., motor (lb)	2285	2288	2190.77	2223.0	2785	2750
Burn out wt (lb)	170	190	122.7	223.0	200	165
Thrust time (sec)	38.1	---	49.59	53.54	55.5	33.9
Total impulse (lb-sec)	533,760	592,000	(Classified)	600,800	620,300	610,000
Nonrecurring cost	Developed	200K	1,340,000 (Thiokol)	2,100,000 incl.	Developed	55K
Per unit cost	42-45K	50-55K	115,000	6 motors	50-55K	45K
Reliability		90% of flights were a success				
Temperature	400°F	400°F				
Max g	8.63	---	≈ 7.5	≈4.83	8.7	11.05
Delivery time (months)	6-8	---	18	18-24		
Total cost 6 months	270K	530K	2,030,000	2,100,000	33.5K	325K

Table 6.8-4. Data on Candidate Apogee Motors

		Antares I X-254	Off-loaded Antares I X-254A	Off-loaded Antares II X-259	Extended Surveyor TE-364-4	Delta TE-364-3
Isp	sec	256	256	284.1	(classified)	(classified)
Average thrust	lbf	14100	14100	27500	14000	10000
Burn time	sec	37.1	38.0	21	42	48
Max g		8.8	≈8.9	≈ 12	≈7.5	5.7
Total impulse	lb-sec	533760	525000	541600	(classified)	415000
Propellant weight	lb	2085	2049	1925	1909	1440
Inert weight	lb	200	200	223	126	139
Burnout weight	lb	170	170	200	NDA	NDA
Total weight	lb	2285	2249	2148	2035	1579
Motor length	inches	115	115	114	63 + igniter	52.3
Motor diameter	inches	30.020	30.020	30.05	37	37
Nozzle length	inches	45.5	45.5	45.5	≈32.0	≈17
Throat diameter	inches	5.76	5.76	6.67	≈3.8	NDA
Average chamber pressure during burn	psi	314	314	410	600	600
Chamber material		Spiralloy	Spiralloy	Spiralloy	Titanium	Steel

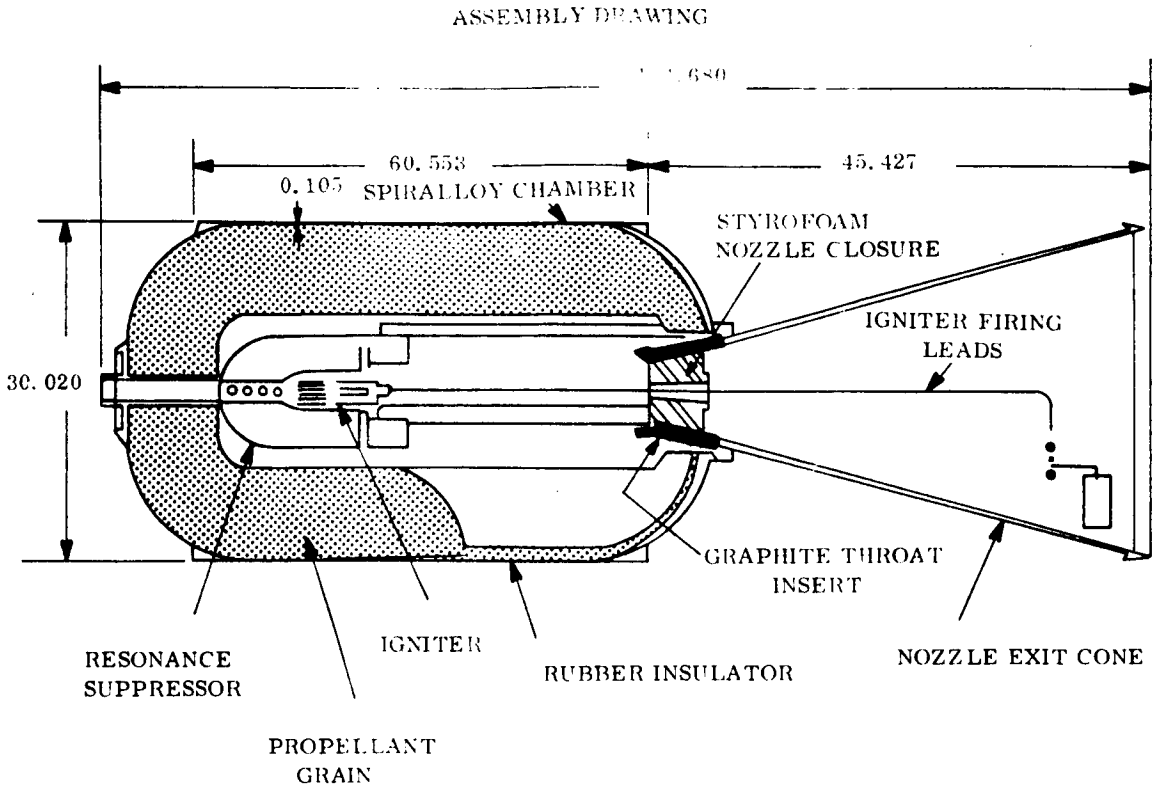


Figure 6.8-1. Antares I (X254-A1)

The development program consisted of 15 static test firings, including four simulated altitude firings at Arnold Engineering Development Center (AEDC). By mid-June of 1963 the Antares II had completed 10 successful flights. Figure 6.8-2 presents the Antares II design.

Improved Delta Motor (TE-M-364-3)

The improved Delta motor was developed from the Surveyor Motor Design. Currently approaching qualification, this motor is larger than the Surveyor design (1440 pounds propellant versus 1250 pounds for the latter) and represents a design point intermediate between the Surveyor and Extended Surveyor Designs.

Figure 6.8-3 shows the basic layout and the physical sizing of the motor. The improved Delta motor, built by Thiokol for Douglas, has completed development testing and is ready to start a qualification program which includes six motors. Some of these six motors will be AEDC tested. The Delta motor has a steel case at present, but consideration

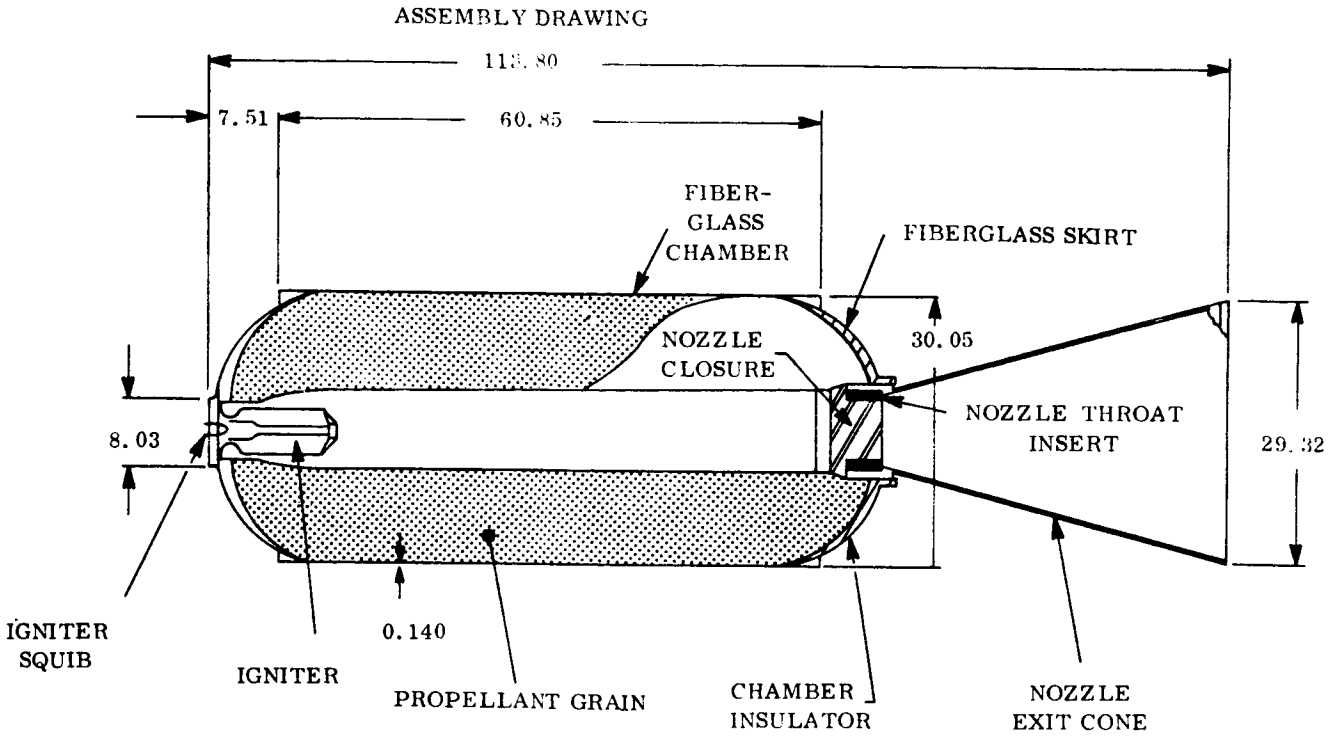


Figure 6.8-2. Antares II (X259-A2)

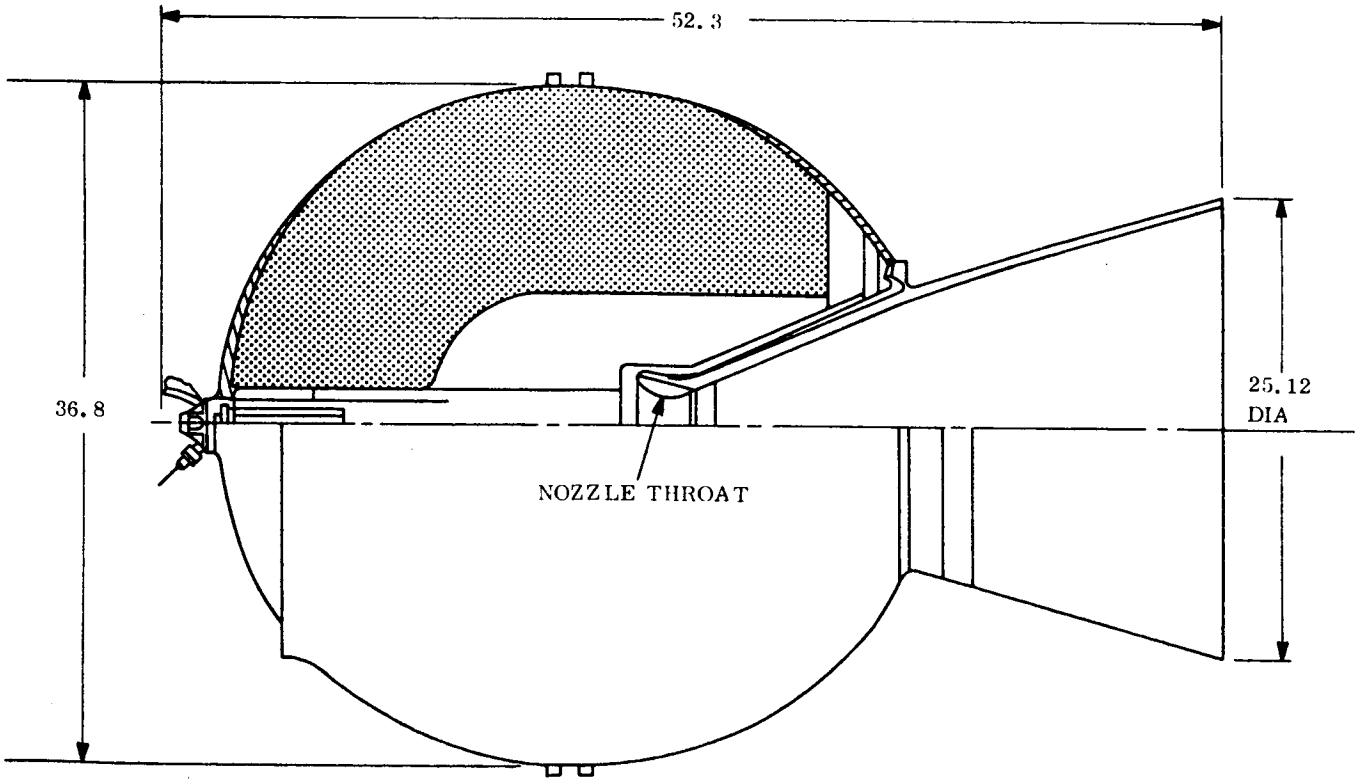


Figure 6.8-3. Delta Motor (TE-M-364-3)

of a change to Titanium will be made prior to qualification. A carbon cloth nozzle is also to be incorporated. Error tolerance in the total impulse is 1 percent, as in other members of the Surveyor "family."

Surveyor Extension

The Surveyor Extension Motor (Figure 6.8-4) is a proposed design by Thiokol Chemical Corporation - Elkton Division.

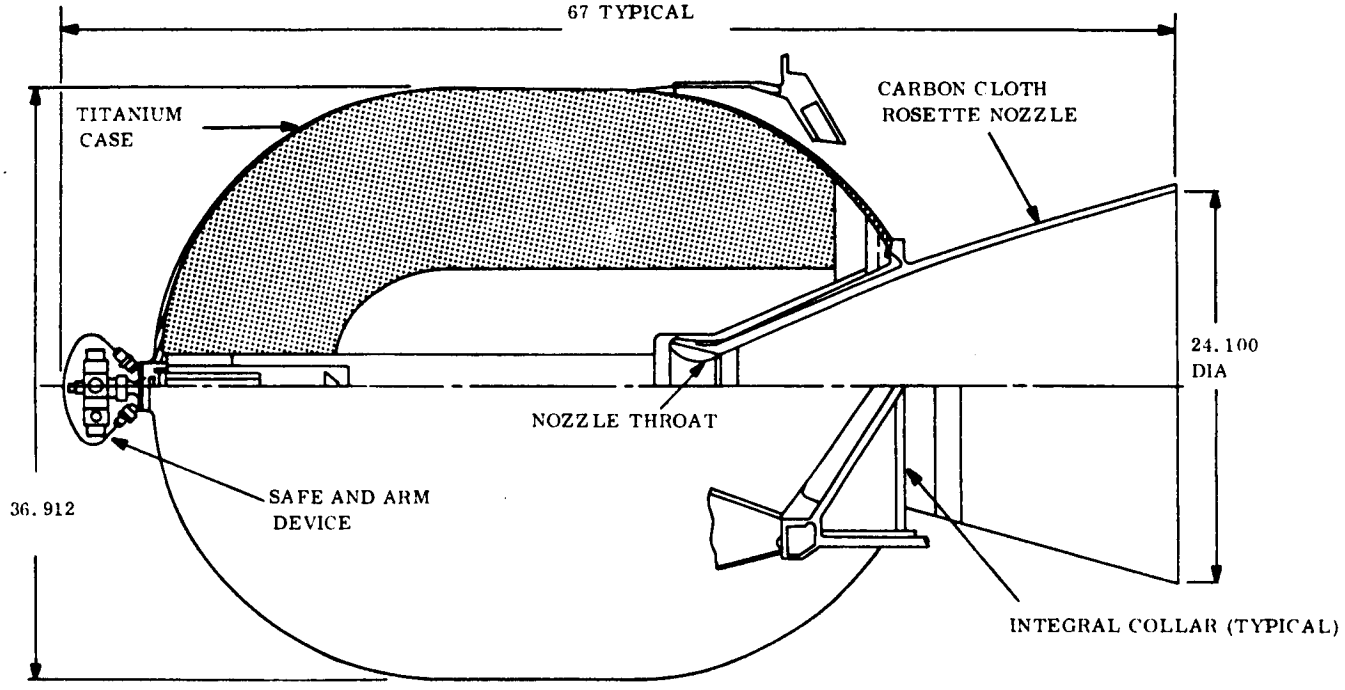


Figure 6.8-4. Extended Surveyor Motor

The design approach proposed has been to modify the existing Surveyor Motor only to the extent required to meet the specific objectives of the ATS-4 program. As a result, most design features of the proposed rocket motor have been extensively tested. Where changes have been made, they are logical extensions of demonstrated technology and will not introduce significant development risk. This approach has been previously used on other adaptations of the Surveyor motor with complete success. The design approach also permits high confidence in the performance and weight data.

Two adaptations of the Surveyor Motor have already been made successfully. One of these is for Boeing Burner II upper stage and the other is for the Douglas Improved Delta third stage. Both adaptations involved minimum test programs and have been successful.

6.8.4.1 Final Apogee Motor Selection Tradeoffs for the SLV-3C/Centaur

A second apogee motor ΔV requirement was considered. Because of this, the apogee motor selection study was redone to consider an increased ΔV at apogee of 6160 fps (vs 6050 fps used previously) and a decreased Atlas SLV-3C/Centaur apogee payload of 3894 pounds at start of motor burn (vs 4300 pounds used previously). Increased emphasis on minimizing apogee motor costs has resulted in the elimination of the Aerojet proposal. The proposed motor is felt to be a sound design; however, it is not based on as much related experience as the Thiokol version. The choice may be best summarized in the following five alternates:

a. Use existing Antares I
b. Use slightly off-loaded Antares I
c. Use off-loaded Antares II
d. Use extended Surveyor design
e. Use Delta motor with Centaur dogleg

Table 6.8-5 presents details for each of the options. The off-loaded Antares I would offer the least expensive and simplest solution, but it is limited in growth capability and its shape makes packaging very difficult. For these reasons it has been eliminated from further consideration. (The use of the existing Antares I requires 65 pounds increase in the Atlas/Centaur capability.) If maximization of payload weight is important, the Surveyor extension motor returns a 13 percent improvement over the cheap and simple off-loaded Antares I and a 9.25 percent improvement over the higher risk off-loaded Antares II. Because of Antares II packaging problems, the Improved Delta Motor is the best motor on the basis of cost.

Table 6.8-5. Apogee Motor Selection Tradeoff Chart

Option	Motor	Isp (sec)	Max Thrust (lb)	Time (sec)	Max g	Total Impulse (lb-sec)	Length (in)	Dia (in)	Prop Weight (lb)	Inert Weight (lb)	Burnout Weight (lb)	Total Weight (lb)	Net*P/L Weight (lb)	Subcontract Nonrecurring Cost (K*)	Cost Per Unit (K*)	Comments
I	Antares I	256	16500	38.1	8.8	534K	114.7	30.0	2085	200	170	2285	1675*	2.5 (Eng. only) +45.0 (batch assurance firing)	42-45	Requires an Atlas Centaur apogee payload capability of 3960 lb. This is 65 lb higher than that currently quoted but may be attainable.
II	Slightly off-loaded Antares I	256	16500	38	≈8.9	525K	114.7	30.0	2049	200	170	2249	1645*	5 (Eng) +45 (batch firing)	42-45	This is a low-risk change which should require only a nominal batch assurance firing.
III	Off-loaded Antares II	181.4	27500	21	≈12	541.6K	113.8	30.1	1925	223	200	2148	1702*	10 (Eng) 165 (3 firings)	50-55	Note that this change requires a 25 percent cutback in the propellant loading of the existing Antares II and should require at least three firings to establish the reproducibility of the adjusted total impulse.
IV	Extension of Surveyor design	----	14900	42	≈7.5	Classified	63+igniter	37	1905	126	NDA	2035	1859*	1340 (18 mos)	111	Although relatively expensive, this is a program offering a high probability of success based upon Thiokol experience with the Surveyor Motors. A significant payload advantage is realized, also.
V	Delta motor	----	10,000 (ave)	48	5.7	Classified	52.3	37	1440	139	NDA	1579	(1)	100 (12 mos)	90K	

*Exclusive of motor, but including MTG attachments and structure

(1) Payload is a function of plane-change at perigee.

Note that approximately a 30-pound payload improvement would be realized if the ΔV is 6050 fps instead of 6160 fps for the Surveyor extension motor (the ΔV in this case is a function of the inclination of the parking orbit). In addition, the nonrecurring cost quoted are those estimates developed for the rocket motor suppliers' costs and do not include AEDC test costs (GFE), NASA cognizant engineering or GE cognizant engineering.

6.8.4.2 Recommended Apogee Motor for the Atlas/Centaur Configuration

The final selection of an apogee motor for the Atlas/Centaur configuration involves the tradeoff between payload weight and cost. As previously discussed, the Delta motor is the minimum cost option, offering the lowest motor costs of the packageable motors but somewhat less payload capability than the extended Surveyor Design. The present study results indicate a design optimization with the extended Surveyor motor and minimum cost with the Delta motor.

6.8.4.3 Surveyor Motor Development Requirements

The specific design changes required for the adaptation of the Surveyor motor to the ATS-4 spacecraft are:

a. Addition of a 10.75-inch cylinder between the hemispheres
b. Increase in nozzle throat area

The addition of the 10.75-inch cylinder between the hemispheres on the 3894 pound spacecraft version of the motor is a straightforward way of providing the additional case volume required for the increase in propellant weight, without major changes to existing component tooling. For this motor, the case hemispherical ends will be fabricated in exactly the same manner as those for the Surveyor motor. The one-piece cylinder will be machined from a rolled-ring forging, and a weld will be used to join each hemisphere to the cylindrical section. Thiokol has employed this technique to generate an elongated motor case for use in the Surveyor Program and Delta Program. In this instance a 12-inch cylinder was added between the hemispheres of a heavy-weight steel case. This is a very efficient way to increase the performance of the motor, since many of the components remain

unaffected. For instance, the head-end hemisphere, the ignition system, the aft hemisphere, and the basic nozzle structure remain unchanged. The internal pressure is maintained at exactly the same level for the two motors by adjusting the throat area. This, of course, minimizes the changes and permits maximum use of identical components.

The increase in throat area is accomplished by moving the throat section of the nozzle downstream. An increase in throat area is specified so that the internal pressure will be kept at the same level for the two motors.

Since the internal pressure is unchanged, it is entirely feasible to move the throat portion of the nozzle downstream and increase its diameter accordingly without expecting synergistic effects in the remainder of the nozzle. For instance, the attachment ring portion of the nozzle will be unaware of any difference in the throat region. Local conditions within the nozzle structure will change; however, based on test experience it is believed that the margins of safety are sufficiently high so that no change in nozzle station thickness is required. The increase in nozzle throat diameter from 3.290 to 3.9 inches represents a radial increase of approximately 0.5 inch. This has a second order effect on the nozzle structure requiring a minor tooling adaptation to accommodate the larger throat area.

Note that the principal design features of the Surveyor, Burner, and the Delta motors have remained completely unchanged so that the proposed ATS-4 apogee kick motors can realize the maximum benefit from these programs. The ignition system, basic nozzle structure, case hemisphere, propellant, liner, insulation, fasteners, and O-rings will be identical for both motors. In addition, these are identical to items already developed and successfully tested under the Surveyor, Burner, and Delta Programs.